

DESIGN AND DEVELOPMENT OF NON-EQUILIBRIUM PLASMAS FOR THE MEDICAL
FIELD

A Dissertation

by

MATTHEW BURNETTE

Submitted to the Office of Graduate and Professional Studies of
Texas A&M University
in partial fulfillment of the requirements for the degree of
DOCTOR OF PHILOSOPHY

Chair of Committee,	David A. Staack
Committee Members,	Waruna Kulatilaka
	Dion S. Antao
	Balakrishna Haridas
Head of Department,	Andreas A. Polycarpou

December 2020

Major Subject: Mechanical Engineering

Copyright 2020 Matthew Burnette

ABSTRACT

There is great interest in the plasma research community on the potential medical applications of non-equilibrium plasmas, called cold atmospheric plasma (CAP), yet currently no such plasma device is approved by the US Food and Drug Administration (FDA). This dissertation seeks to take a holistic look at five novel plasma systems with potential use in the medical field. These systems are all analyzed from an engineering point of view to characterize the plasma and basic biocompatibility from an electrical and thermal approach. The overall design life-cycle for these devices is also examined, with an emphasis on deciding an approval pathway through the Food and Drug Administration, where the intended use of the device is the driving factor.

The first device considered is a nanosecond puling circuit devised for skin electroporation. An electrode is developed to help maximize the electric field applied to a substrate and ensure user safety. Voltage and current traces and optical emission spectroscopy are used to characterize the plasma generated for various substrates, showing the non-equilibrium behavior of the plasma for a wide operating range. The second device considered is an existing FDA-cleared electrosurgical device power supply and hand piece, which has been modified for use as a CAP source. By varying the tube length the plasma can be operated in a non-equilibrium state. The third device is a direct write system for depositing thin films in a controlled pattern. This system consists of a dielectric barrier discharge jet attached to a three-dimensional printer head for spatially controlling the plasma location. Various methods of depositing material are used, including directly onto biological substrates. The final two devices are for improving the strength of additively manufactured parts intended for use in custom printed prosthetics. The first is a nanosecond pulsed discharge onto a printed part, which shows 100% strength improvement from the plasma treatment. The second is a planar dielectric barrier discharge mounted onto the head of a three-dimensional printer, which is able to print parts with the same strength as injection molded parts.

DEDICATION

To my dad, for pushing me into engineering and being more excited to have a son with a Ph.D.
than his son is getting it.

And also to Chet and Francesca Butler, the next generation, to show them that learning is
something they should never stop doing.

ACKNOWLEDGMENTS

First and foremost I have to praise and thank my Creator and Lord for His help and guidance in my life. He has blessed me abundantly and graciously allowed me to continue my education to learn about a very small part of this incredible world He made.

I heard some good advice before going into graduate school: “Make sure you get a good advisor who will support and mentor you well.” Dr. Staack has certainly been that for me. He has made me think critically about my research and guided me very well. He knows that we learn best by our mistakes and has been willing to step back and watch me fail before stepping in to explain patiently how to better refine my approach. He has challenged me to go beyond the lab as well, voluntelling me to teach twice, but I learned so much about what it really means to teach through those experiences—it’s a lot harder than it looks. He has also been willing to send me literally around the world, enabling me to travel to Turkey, Germany, and Canada to present research.

My labmates in the Plasma Engineering and Non-Equilibrium Processing “Plasma” Lab (and sometimes still called the Plasma Engineering and Diagnostics Lab because *PEDL* is so much better of an acronym than *PENEPL*) have also been such a support. It is always good to know you are not going through the tough times of grad school alone, and I am so grateful for the help they have given me in listening to me talk through a problem, troubleshooting stubborn equipment, destressing with long Friday lunches, and being there in a myriad of other ways.

I am also so grateful for my family away from family, Aggieland Christian Church. So many people have taken in this “poor, starving grad student” and fed me, spend time with me, or helped me decompress after a long day in the lab.

Lastly, I want to thank my family. Dad, thank you for pushing me to pursue engineering and helping me get out here to Texas. Mom, thank you for understanding that your son is working and doesn’t call you as often as he should. Nik, thank you for your practical wisdom in all the little things in life. Chet and now Francesca, thank you for not realizing Texas is so far from Virginia and loving your uncle when he can make it home to see y’all.

CONTRIBUTORS AND FUNDING SOURCES

Contributors

This work was supported by a dissertation committee consisting of Professor David Staack, Professor Waruna Kulatilaka, and Professor Dion Antao of the Department of Mechanical Engineering and Professor Balakrishna Haridas of the Department of Biomedical Engineering. I am grateful to all of these men for sacrificing their time and effort to help me successfully complete this program.

Research cannot be done alone. Many people have helped contribute time and effort into the work presented herein. Those that I know and remember are as follows: Peng Xiao and Nicholas Gawloski helped in the initial data acquisition for the data in the electroporation chapter (Section 4.5.1); Nicholas Gawloski helped with the construction of the custom power supply and arrays in the electroporation chapter (Section 4.4.1 and Section 4.4.2); Sameer Kalghatgi from EP Technologies, LLC conducted the electroporation efficiency testing (Section 4.6); Joe Kelsey helped with some of the plasma mode testing for the electrosurgical generator (Section 5.5.1); Rhys Michna conducted the inactivation study in the electrosurgical device chapter (Section 5.5.5); Andrew Nelson and Kenton Cozart helped in setting up the 3D printer for the direct writing of DBD jet films (Section 6.4); Brittany Spivey helped with data collection for the direct writing of DBD jet films, primarily with the metallic films (Section 6.5); Chin Cheng “Jim” Shih was instrumental in the FID treated AM improvement project as this was his master’s thesis work (Section 7.4); and Charles Brandon Sweeney was the main investigator for the CNT-loaded filament with the AM improvement work done in conjunction with Essentium, Inc. which was part of his doctoral work (Section 7.5). To the best of my knowledge, all other work conducted for this dissertation was completed independently.

Though not directly involved in the work, I have had many useful discussions and teaching moments (both teaching and being taught) to improve my understanding of this material. For

those moments I am particularly indebted to my labmates in the Plasma Engineering and Non-Equilibrium Processing Lab. I must also give credit to Professor Alan Brewer for teaching me all about the internal working of the FDA in his two biomedical engineering classes that I attended.

Funding Sources

Having worked on such a diversity of projects there are many funding sources to note. First, I was awarded the Sally & Ray Bowen '58 Fellowship my first year in graduate school. For the electroporation chapter, that work was funded by EP Technologies, LLC. Lynntech supported some of the work in the direct writing of DBD jet films chapter, primarily the polymer film work. Essentium, Inc. hired me part time to support their work in the AM improvement of CNT-loaded filaments, namely the FlashFuse system. A number of other side projects also supported me during my tenure as a graduate student whose projects are not included in this dissertation, including the Defence Advanced Research Projects Agency (DARPA), Army Research Lab, 3M, NASA, and Physics Materials and Applied Mathematics Research, LLC (PM&AM).

NOMENCLATURE

3D	Three-Dimensional
510(k)	Premarket Notification for Substantial Equivalence
AC	Alternating Current
AM	Additive Manufacturing
C_i	Capacitor i or Capacitance of i
CAP	Cold Atmospheric-Pressure Plasma
CCD	Charged Coupled Device
CE	Conformité Européenne (European Conformity)
CuAcac	Copper(II) Acetylacetonate
DBD	Dielectric Barrier Discharge
DC	Direct Current
De Novo	Latin Phrase Meaning “From the New”
e	Electron
E	Electric Field
\mathcal{E}	Energy
EGDMA	Ethylene Glycol Dimethacrylate
EMI	Electromagnetic Interference
FDA	Food and Drug Administration
FE	Floating Electrode
FE-DBD	Floating Electrode Dielectric Barrier Discharge
FFF	Fused Filament Fabrication
FID	Fast Ionization Dynister (Power Supply)

FWHM	Full Width Half Maximum
GCP	Good Clinical Practice
GLP	Good Laboratory Practice
GMP	Good Manufacturing Practice
HV	High Voltage
ICCD	Intensified Charged Coupled Device
IPA	Isopropyl Alcohol
ISO	International Organization for Standardization
MMA	Methyl Methacrylate
NIST	National Institute of Standards and Technology
OES	Optical Emission Spectroscopy
PA	Polyamide
PECVD	Plasma Enhanced Chemical Vapor Deposition
PLA	Polylactic Acid
PMA	Premarket Approval
PMT	Photo-Multiplier Tube
Q	Charge
RC	Resistor-Capacitor
R_i	Resistor i or Resistance i
RBD	Resistive Barrier Discharge
RMS	Root Mean Squared
RMSE	Root Mean Squared Error
SEM	Scanning Electron Microscope
T_e	Electron Temperature
T_{elx}	Electronic Excitation Temperature

T_{rot}	Rotational Temperature
T_{trans}	Translational Temperature
T_{vib}	Vibrational Temperature
TMEVS	Tris(2-methoxyethoxy)vinylsilane
UV	Ultraviolet (Light)
V_b	Breakdown Voltage
V_i	Voltage or Voltage Drop across i
V_{max}	Maximum (Peak) Voltage
V_{pp}	Peak-to-Peak Voltage
VTMS	Vinyltrimethoxysilane
XPS	X-ray Photoelectron Spectroscopy
ε	Permittivity
λ	Wavelength
ν	Frequency
ρ	Space Charge or Resistivity

TABLE OF CONTENTS

	Page
ABSTRACT	ii
DEDICATION	iii
ACKNOWLEDGMENTS	iv
CONTRIBUTORS AND FUNDING SOURCES	v
NOMENCLATURE	vii
TABLE OF CONTENTS	x
LIST OF FIGURES	xv
LIST OF TABLES.....	xxiii
1. INTRODUCTION.....	1
1.1 Background.....	1
1.1.1 Medical Uses for Plasma	2
1.1.2 Medical Device Approval	3
1.2 Motivation	4
1.3 Research Objectives	5
1.4 Dissertation Overview	6
2. PREREQUISITE KNOWLEDGE & LITERATURE REVIEW	8
2.1 Introduction.....	8
2.2 Plasmas	8
2.2.1 Types of Plasma	10
2.2.1.1 Dark Discharge	11
2.2.1.2 Breakdown.....	13
2.2.1.3 Glow Discharge	14
2.2.1.4 Arc Discharge	15
2.2.1.5 Streamers and Related Discharges.....	15
2.2.1.6 Dielectric Barrier Discharge	16
2.2.1.7 Resistive Barrier Discharges	17
2.2.1.8 Plasma Jets.....	18
2.2.2 Energy In a Plasma	20
2.2.2.1 “Hot” Versus “Cold” Plasma	22

2.2.2.2	Plasma Collision Processes	24
2.2.2.3	Energy Distribution Function	27
2.2.3	Effect of Plasma on Materials.....	29
2.2.3.1	Electric Field Influence	29
2.2.3.2	UV Light Emission.....	30
2.2.3.3	Radical Species Generation.....	30
2.3	The Design Life-Cycle.....	31
2.3.1	Testing Considerations	33
2.3.1.1	Bench Top Testing	33
2.3.1.2	Animal Testing	34
2.3.1.3	Clinical Testing	34
2.3.2	Quality System	36
2.3.2.1	Good Manufacturing Practices	36
2.3.2.2	Design History File.....	37
2.3.3	Business & Financial Considerations.....	37
2.4	Medical Device Approval.....	38
2.4.1	The Food and Drug Administration	38
2.4.1.1	Premarket Approval	41
2.4.1.2	510(k)	42
2.4.1.3	De Novo	42
2.4.1.4	510(k) Exempt Devices	43
2.4.1.5	Humanitarian Device Exception.....	43
2.4.1.6	Custom Device Exception	44
2.4.1.7	Combination Products.....	44
2.4.1.8	Emergency Use Authorization.....	45
2.4.2	Other Countries	47
2.5	Low Temperature Plasma Medicine.....	48
2.5.1	Medical Uses of Low Temperature Plasmas	49
2.5.1.1	Plasma-Tissue Interaction Mechanisms	50
2.5.1.2	Wound Treatment	51
2.5.1.3	Cancer Treatment & Cell Death	53
2.5.1.4	Other Applications	55
2.5.2	Development of Low Temperature Plasma Devices	56
2.5.2.1	The kINPen MED	58
2.5.2.2	The PlasmaDerm	59
2.5.2.3	The MicroPlaSter.....	60
2.5.2.4	The plasma care	62
2.5.2.5	The Plasma ONE	63
2.5.2.6	Other Devices.....	64
2.5.3	Standards for Low Temperature Plasma Devices	66
3.	PLASMA CHARACTERIZATION	69
3.1	Introduction.....	69
3.2	Electronic Characterization	69

3.2.1	Power Supply Considerations	69
3.2.1.1	Spellman HV DC Power Supply	72
3.2.1.2	Information Unlimited HV AC Power Supply	72
3.2.1.3	FID Power Supply	72
3.2.2	Voltage, Current, & Charge Measurements	73
3.2.2.1	Measuring Voltage	74
3.2.2.2	Measuring Charge and Current	76
3.2.2.3	Electric Field	78
3.2.2.4	Oscilloscope Considerations	79
3.2.3	Lissajous Analysis	79
3.3	Imaging Systems	82
3.3.1	Nikon Camera	83
3.3.2	Stanford ICCD	83
3.3.3	Optical Microscopy	83
3.3.4	Scanning Electron Microscopy	84
3.4	Optical Emission Spectroscopy	85
3.4.1	Spectrometers	85
3.4.1.1	SPEX Spectrometer	85
3.4.1.2	B&W Tek Modular Spectrometer	86
3.4.1.3	Ocean Optics Modular Spectrometer	86
3.4.2	Species Identification	87
3.4.3	Temperature Determination	88
3.4.3.1	Theory of Temperature Determination	89
3.4.3.2	Implementation of Temperature Determination	91
3.4.3.3	Temperature Determination in Practice	94
4.	ELECTROPORATION SYSTEM	96
4.1	Introduction	96
4.2	Electroporation Background	96
4.3	Device Life-Cycle Overview	99
4.3.1	FDA Approach	101
4.3.2	Device Outlook	102
4.4	Device Design	103
4.4.1	RC Pulse Generator Circuit Design	103
4.4.2	Electrode Array Design	110
4.5	Device Characterization	113
4.5.1	Initial FID Testing	114
4.5.1.1	Array Imaging	114
4.5.1.2	Spectra	122
4.5.2	RC Pulse Generator Testing	126
4.5.2.1	Array Imaging	127
4.5.2.2	Spectra	132
4.5.3	Computational Model of the Electric Field in Skin	136
4.5.4	Electric Field Measurement	139

4.5.5	Time-Resolved Discharge Imaging	142
4.6	Electroporation Efficacy	145
4.7	Chapter Summary & Future Work	145
5.	MODIFICATION OF AN ELECTROSURGICAL SYSTEM	148
5.1	Introduction.....	148
5.2	Electrosurgery Background.....	148
5.3	Device Life-Cycle Overview	149
5.3.1	J-Plasma System.....	150
5.3.2	Other Electrosurgical Systems as a Cold Plasma	151
5.3.3	FDA Approach	152
5.3.4	Device Outlook	152
5.4	Bovie Modification.....	153
5.5	Device Characterization	154
5.5.1	Discharge Mode Imaging	156
5.5.2	Voltage and Current Characterization	158
5.5.3	Broadband Spectra	159
5.5.4	Temperature Determination	163
5.5.5	Inactivation Study	165
5.6	Chapter Summary & Future Work	169
6.	DIRECT WRITE OF FILMS USING A DIELECTRIC BARRIER PLASMA JET	171
6.1	Introduction.....	171
6.2	Project Background	171
6.2.1	Direct Writing	171
6.2.2	Ambient Plasma Enhanced Chemical Vapor Deposition	173
6.2.3	Applications of PECVD.....	174
6.2.3.1	Sprayable Bandages.....	174
6.2.3.2	Epidermal Electronics.....	174
6.3	Device Life-Cycle Overview	176
6.3.1	FDA Approach	176
6.3.2	Device Outlook	177
6.4	Experimental Setup	178
6.4.1	Physical Experimental Setup.....	178
6.4.2	3D Printing Pattern Considerations	180
6.5	Metal Film Results	184
6.6	Silane Film Results	187
6.6.1	Initial Material Selection	188
6.6.1.1	TMEVS Initial Testing	189
6.6.1.2	EGDMA Initial Testing	195
6.6.1.3	VTMS Initial Testing.....	195
6.6.1.4	MMA Initial Testing	198
6.6.2	Optimization Study	199
6.6.2.1	Initial Eight Samples	200

6.6.2.2	Further Iteration	206
6.6.3	Testing on Biological Substrates.....	208
6.7	Chapter Summary & Future Work	214
7.	IMPROVEMENT OF ADDITIVE MANUFACTURING.....	216
7.1	Introduction.....	216
7.2	Background of Additive Manufacturing	216
7.3	Device Life-Cycle Overview	218
7.3.1	FDA Approach	219
7.3.2	Device Outlook	220
7.4	Nanosecond Pulsed System.....	220
7.4.1	System Description & Experimental Setup	220
7.4.2	Device Characterization Results	223
7.4.2.1	Mechanical Results.....	223
7.4.2.2	Plasma Characterization	226
7.5	The FlashFuse System	229
7.5.1	System Description.....	229
7.5.2	Device Characterization Results	231
7.5.2.1	Voltage and Current Characterization	231
7.5.2.2	Spectroscopic Results	235
7.5.2.3	Material Property Results	236
7.6	Chapter Summary & Future Work	239
8.	CONCLUSIONS & FUTURE WORK.....	240
8.1	Conclusions.....	240
8.1.1	Electroporation System	242
8.1.2	Modified Electrosurgical System	242
8.1.3	Direct Write System Using a Plasma Jet	243
8.1.4	Nanosecond Pulsed System for Additive Manufacturing.....	243
8.1.5	The FlashFuse System	244
8.2	Future Work	244
8.2.1	Electroporation System	245
8.2.2	Modified Electrosurgical System	245
8.2.3	Direct Write System Using a Plasma Jet	246
8.2.4	Nanosecond Pulsed System for Additive Manufacturing.....	247
8.2.5	The FlashFuse System	248
REFERENCES	249
APPENDIX A.	DOUBLE SPARK GAP DISCHARGE GENERATOR USER GUIDE.....	288
APPENDIX B.	MATLAB CODE TO CONTROL THE 3D PRINTER	318

LIST OF FIGURES

FIGURE	Page
2.1 Plasma as a State of Matter	9
2.2 DC Steady State Voltage-Current Curve for Plasma	10
2.3 Schematic of the Electron Avalanche Process	12
2.4 Schematic of Different Types of Plasma Jets	19
2.5 Basic Energy Flow Diagram in a Low Temperature Plasma	20
2.6 Schematics of the Various Energy Modes for Atoms and Molecules in a Plasma	21
2.7 Infrared Images of a Plasma Discharge Operating in a “Hot” Mode and a “Cold” Mode	24
2.8 Plot of the Maxwell–Boltzmann (Maxwellian) Distribution Function for Multiple Temperatures on Both a Linear and Logarithmic Scale	28
2.9 Basic Schematic of the Design Life-Cycle for a Medical Device	32
2.10 Basic Flowchart for Approaching the FDA with a Medical Device	40
2.11 Image of the kINPen MED	58
2.12 Image of the PlasmaDerm	60
2.13 Images of the MicroPlaSter Being Used in a Clinical Setting and Its Electrode Configuration	61
2.14 Images of the plasma care and Its Electrode Configuration	62
2.15 Image of the Plasma ONE	63
2.16 Image of the Canady Helios™ Cold Plasma Scalpel in a Clinical Setting	65
3.1 Schematic of the Three Primary Types of Plasma Power Supplies with Represen- tative Voltage Traces	70
3.2 Measured Voltage and Current Traces from the FID Power Supply	73

3.3	Schematic of a Resistive Divider Circuit.....	75
3.4	Schematic of Three Different Methods for Measuring Current or Charge	76
3.5	Typical DBD Voltage and Current Traces with the Resulting Lissajous Curve	80
3.6	Annotated Ideal Lissajous Plot for a DBD System	81
3.7	Spectrum of the FlashFuse System.....	88
3.8	Spectral Fitting Showing the Non-Independence of T_e and Relative Concentration of N_2^+ in Modeling the 2 nd Positive System of N_2 and the 1 st Negative System of N_2^+	92
3.9	Measured Experimental Spectrum with a Model Fit of $T_{rot} = 598$ K and $T_{vib} = 4244$ K with Detailed Insets	93
3.10	Spectra of Various Wavelengths and Detectors for Bands in the 2 nd Positive System of N_2 with Temperature Fits	94
4.1	Electron Micrographs of Flash Frozen Cells Exhibiting Electroporation	97
4.2	Schematic of Electroporation with Uses Including Protein Insertion, Foreign Matter Introduction, and Cell Membrane Destruction	97
4.3	Schematic and Image of the Array for Epidermal Electroporation Applications	100
4.4	Schematic of the RC Pulse Generator.....	105
4.5	Image of the RC Pulse Generator with the Lid of the Housing Open	106
4.6	Comparison of Voltage Traces for Dielectric and Conductive Substrates with the RC Pulse Generator for a $V_C = 9$ kV and $V_C = 27.5$ kV Breakdown Voltage Case ...	107
4.7	Comparison of Voltage and Current Traces for a $V_C = 9$ kV Breakdown.....	108
4.8	Comparison of Voltage and Current Traces for a $V_C = 27.5$ kV Breakdown	109
4.9	Schematic of the 2D Electric Field Model for the Array Tip Electrode and Graph of the Resulting Modeled Electric Field	111
4.10	Schematic of the Array Electrode	112
4.11	Image Showing the Design of the Array Electrode.....	112
4.12	Discharge Imaging Comparison of the Three Array Electrodes	112
4.13	Temperature Comparison of the 3 Arrays.....	114

4.14 Schematic of the Array Testing Setup.....	115
4.15 Images of the Array Testing Setup with Dielectric and Conductive Substrates.....	115
4.16 FID Discharges with Air Flow onto a Dielectric	116
4.17 FID Discharges with No Gas Flow onto a Dielectric.....	117
4.18 FID Discharges with N ₂ Flow onto a Dielectric	117
4.19 FID Discharges with Ar Flow onto a Dielectric	118
4.20 FID Discharges with He Flow onto a Dielectric	118
4.21 FID Discharges with Air Flow onto a Conductor.....	119
4.22 FID Discharges with No Gas Flow onto a Conductor	119
4.23 FID Discharges with N ₂ Flow onto a Conductor	120
4.24 FID Discharges with Ar Flow onto a Conductor	120
4.25 FID Discharges with He Flow onto a Conductor	121
4.26 FID Discharges with No Gas Flow onto Pig Skin	121
4.27 Spectra of FID N ₂ Discharges for Various FID Power Supply Settings	123
4.28 Spectra of FID Discharges for Other Gases at 10 kHz and 30 kV	124
4.29 Plot of Rotational and Vibrational Temperatures of the FID Discharges.....	126
4.30 Images of the Array's First Mode with the RC Pulse Generator for the Biological Substrate Showing Streamers Only on the Edge of the Array with Only Variations in Light Intensity for Changing Discharge Conditions	128
4.31 Images of the Array's First Mode with the RC Pulse Generator for the Conductive Substrate Showing Streamers Only on the Edge of the Array with Only Variations in Light Intensity for Changing Discharge Conditions	129
4.32 Images of the Array's First Mode with the RC Pulse Generator for the Dielectric Substrate Showing Streamers Only on the Edge of the Array with Only Variations in Light Intensity for Changing Discharge Conditions	130
4.33 Images of the Array's Second Mode with the RC Pulse Generator for the Dielectric Substrate Showing Spreading of the Streamers on the Substrate for a Variety of Conditions All with an Electrode-Substrate Gap of 0 mm with Only Variations in Light Intensity for Changing Discharge Conditions.....	131

4.34	Images of the Array's Third Mode with the RC Pulse Generator for the Conductive Substrate Showing Brighter Discharges for Certain Conditions Where the Streamers Have Transitioned to Higher Energy Spark Discharges with Changes in the Applied Voltage and Electrode-Substrate Gap Distance	132
4.35	Temperature Comparison Using the RC Pulse Generator for Varying the Substrate with $V_{\max} = 25 \pm 2$ kV, FWHM = 26 ± 1 ns, Gap = 7 mm, and No Air Flow	133
4.36	Temperature of Array Discharges for Varying the Applied Voltage, Pulse Duration, Air Flow Rate, Substrate, and Electrode-Substrate Gap.....	134
4.37	Spectrum of 2 nd Positive System of N ₂ for the Second Mode of the RC Pulse Generator Showing Many Iron Peaks and Some Continuum Emission, Making Temperature Determination Impossible.....	135
4.38	Temperature of the Second Mode for the RC Pulse Generator With Small Gaps Not Modelled Due to Iron Peaks in the Spectrum.....	135
4.39	Schematics of the Comsol Model for the Electric Field in Skin with and without a Plasma Streamer.....	137
4.40	Plot of the Modelled Electric Field Magnitude into the Skin Along Multiple Directions	138
4.41	Image of the Fluorescent Dye Setup for Electric Field Measurements in an Agar Substrate	140
4.42	Fluorescence Spectra from the Rhodamine-640 Perchlorate Dye Varying the Applied Duration	140
4.43	Ratio of Peak Intensities Plotted Against the Applied Voltage for the Dye Fluorescence Spectra	141
4.44	Deconvolution of Dye Fluorescence Spectrum Using Three Pseudo-Voigt Profiles ...	141
4.45	Time-Resolved ICCD Imaging Setup Schematic.....	142
4.46	Time-Resolved ICCD Imaging Setup Image	143
4.47	Select ICCD Images Showing the Time-Resolved Discharge with 2 ns Exposures....	144
4.48	Voltage Trace and Background Subtracted Image Brightness as a Function of Time .	145
4.49	Fluorescence Gene Uptake Comparing Conventional Electroporation to Electroporation Using the Array Electrode	146
5.1	J-Plasma Operating in Cold and Hot Plasma Modes	151

5.2	Image of the Modification to the Bovie Electrosurgical Tip Electrode	154
5.3	Schematic of the Bovie Power Supply Setup	155
5.4	Image of the Bovie Power Supply Setup.....	156
5.5	Bovie Power Supply, Laboratory AC Power Supply FE-Direct Jet, and Laboratory AC Power Supply FE-DBD Jet Operating in a Diffuse Mode and a Concentrated Mode.....	157
5.6	Different Operating Modes for the Bovie Power Supply as a Function of Electrode-Substrate Gap and Power Setting for a Flow Rate of 3.97 SLPM	157
5.7	Initial Voltage and Current Pulses for the Diffuse and Concentrated Modes with the Bovie Power Supply	159
5.8	Current and Voltage Traces for the Bovie FE-Direct Plasma Jet, the Laboratory AC Power Supply FE-Direct Jet, and the Laboratory AC Power Supply FE-DBD Jet for Both Diffuse and Concentrated Modes.....	160
5.9	Broadband Spectra for the Bovie and Laboratory AC Power Supply FE-Direct Jets for Both Diffuse and Concentrated Modes.....	161
5.10	Boltzmann Plots Derived from the Broadband Spectra of the Bovie and Laboratory AC Power Supply FE-Direct Jets for Both Diffuse and Concentrated Modes	162
5.11	Various Wavelengths for the 2 nd Positive System of N ₂ with Temperature Fits for the Bovie Power Supply and Laboratory AC Power Supply FE-Direct Jets	164
5.12	Setup Schematic for the Plasma Jet Sterilization Treatment	165
5.13	Plates After 1 Day Incubation of <i>E. Coli</i> and <i>Aspergillus Flavus</i> for Both FE-DBD Jet and Bovie Jet for 30 s, 90 s, 180 s Trials and 180 s No Plasma Control Condition .	167
5.14	Number of <i>E. Coli</i> Colonies Counted After Various Plasma Treatments.....	167
5.15	Number of <i>Bacillus</i> Colonies Counted After Various Plasma Treatments	168
5.16	Number of <i>Aspergillus Flavus</i> Colonies Counted After Various Plasma Treatments..	168
6.1	Schematic of Both Sprayable (Paint-On) Bandages and Epidermal Electronics Showing Conventional Systems and a Direct Write Plasma Jet System.....	175
6.2	Image of the Direct Write DBD Jet Setup	179

6.3	Schematic of the Direct Write Setup Showing the Heated Sublimation Cell for Solid Precursors and the Nebulizer and Syringe Pump for Liquid Precursors with Inset Images of the Heated Sublimation Cell Partially Unwrapped from the Heating Tape and the Nebulizer Spraying into the DBD Jet	179
6.4	Comparison of Printer Paths and Their Time Per Unit Area Coverage over a Discretized Grid.....	181
6.5	Image of Hydrocarbon Deposition Using IPA Without Controlling for Equal Area Treatment Yielding a Thicker Outline, Thin Infill, and Thick Centerline	182
6.6	Image of Hydrocarbon Deposition using IPA of an Equal Area Treatment with Black Spots from Hot Spots in the Plasma Discharge and Plume Deposition	183
6.7	Images of Hydrocarbon Deposition Using a Micro-DBD Jet for Small Feature Sizes Varying with the Printer Head Speed	184
6.8	Voltage and Current Traces for the Copper (II) Acetylacetonate Deposition	185
6.9	Image of Copper Direct Write Deposition onto Glass Creating a Copper Film.....	186
6.10	Image of Iron Oxide Direct Write Deposition onto Glass Using Ferrocene as the Precursor.....	187
6.11	Images of Initial Droplet Tests Using TMEVS	189
6.12	Optical Images and SEM Images for Initial TMEVS Nebulizer Tests	191
6.13	Images of Further TMEVS Depositions on Various Substrates with Specs Appearing in the Deposited Film	192
6.14	Optical Images of the Half-Masked TMEVS Deposition	192
6.15	SEM Images of the Half-Masked TMEVS Deposition.....	193
6.16	Images of TMEVS Depositions onto Various Meshes	194
6.17	Images of Initial Droplet Tests Using EGDMA	196
6.18	SEM Images of Initial EGDMA Tests	197
6.19	Images of Stainless Steel Substrate Tests Using EGDMA	197
6.20	Images of Initial Droplet Tests Using VTMS.....	198
6.21	Images of MMA Depositions on Various Substrates	199
6.22	Voltage and Current Traces of the DBD Jet with the Nebulizer Spraying TMEVS....	201

6.23	Images of the Initial Eight TMEVS Samples Shortly After Deposition	202
6.24	Low Resolution Micrographs of the Initial Eight TMEVS Samples	203
6.25	High Resolution Micrographs of the Initial Eight TMEVS Samples	204
6.26	Images of the Initial Eight TMEVS Samples After Drying in Ambient Air	205
6.27	SEM Images of the Inital TMEVS Sample 2	206
6.28	Profilometer Results For Samples 2, 3, and 6 of the Initial Eight TMEVS Samples ..	207
6.29	Images and Micrographs for TMEVS Repeatability Trials	209
6.30	SEM Images of TMEVS Sample 3A	210
6.31	Optical Micrographs of TMEVS Sample 4A	210
6.32	Image of TMEVS Sample 8A Using a Lower Nebulizer Flow Rate	211
6.33	Images of the Initial Pig Skin DBD Jet Treatment with a Droplet of TMEVS.....	212
6.34	Image of the Removal of the TMEVS Deposition from Pig Skin	213
6.35	Images of the Initial Test Spraying TMEVS onto a Pig Skin Substrate for Film Deposition	213
6.36	Optical Micrographs of Pig Skin with TMEVS Deposition and the Scrapings of the TMEVS Films for Higher Helium Flow Rates	214
7.1	Schematic of Strength Variation in a 3D Printed Part	218
7.2	Schematic and Image of Plasma Treatment for the Nanosecond Pulsed System	221
7.3	Schematic of Test Part for Testing the Nanosecond Pulsed Plasma System	222
7.4	Image of the Custom Designed Shear Bond Test Apparatus	223
7.5	Force vs. Time Plots from the Shear Bond Test for All Test Conditions	224
7.6	Bar Chart of the Required Shear Force to Remove the Top Layer.....	225
7.7	Bar Chart of the Work Done Until Fracture of the Top Layer	226
7.8	Broadband Spectrum from the Nanosecond Pulsed System for AM	227
7.9	Spectra with Temperature-Fitted Modeled Spectra from the Nanosecond Pulsed System for AM	228

7.10 Schematic of the FlashFuse System	230
7.11 Image of the FlashFuse System Running In Situ	231
7.12 Image of the FlashFuse System as a Bench Top Setup	232
7.13 Voltage and Current Traces of the FlashFuse System	233
7.14 Lissajous Diagram of the FlashFuse System.....	234
7.15 Broadband Spectrum of the FlashFuse System	235
7.16 FlashFuse Spectrum with Temperature Model Fits.....	236
7.17 Plot of the Error Associated with the Temperature Fit Shown in Figure 7.16.....	237
7.18 XPS Survey Spectrum of the Polymer Surface with and Without the FlashFuse Treatment and the Relative Atom Percentage of the Observed Species	238
7.19 Temperature Plot of the Partially Printed Part as a Function of Z Height with Flash- Fuse Treatment	238
7.20 Stress-Strain Curve and Radar Chart Showing Some Material Properties of the DBD Welded Part Compared to a Control and Injection Molded Part	239

LIST OF TABLES

TABLE	Page
4.1 Comparison of the Design Parameters for the Three Array Electrodes	113
5.1 Comparison of Bovie and Laboratory AC Power Supplies	154
6.1 Four Monomers Tested For Direct Write Film Deposition.....	188
6.2 Testing Conditions for Initial Eight TMEVS Samples	200
6.3 Sample Conditions for Further Testing of TMEVS Film Deposition.....	206
7.1 Various Treatment Conditions for PLA Samples	221

1. INTRODUCTION

1.1 Background

Non-equilibrium plasma discharges are a quickly growing field with a wide range of possible applications including medical uses. These plasmas have come from scaling existing discharges to higher pressures and lower temperatures. Low pressure plasmas have found extensive use in microelectronics for etching, deposition, ion implantation, and surface activation and functionalization. [1] In particular, plasma-enhanced chemical vapor deposition, has allowed a wider variety of thin films to be deposited for various surface treatments. Atmospheric pressure plasma discharges are typically high power discharges and are commonly used to provide the activation energy for various processes such as combustion. These include some of the first laboratory discharges discovered, such as arc and spark discharges discovered in 1803 [2] as well as dielectric barrier discharges. [3]

Non-equilibrium plasma is created by balancing energy inflow and outflow to avoid a full thermodynamic equilibrium from developing. Plasma, being a collection of ions, electrons, and neutral gas species, typically has an energy input that preferentially excites only some of these constituents. For example, an electric field imparts energy primarily into the electrons, since they are electrically charged and have a much smaller mass than ions. There are various energy loss mechanisms that can also occur, such as diffusion of energetic particles out of the plasma or collisions with the cooler walls surrounding the discharge. If the average energy of all of the various plasma constituents are equal, then the plasma has become an equilibrium plasma. However if there is an energy imbalance between some of the species, typically electrons with a high average energy and neutral gas species with a much lower average energy, then a non-equilibrium plasma discharge has developed. A special case of non-equilibrium plasma is a low temperature plasma, where the bulk gas temperature is near ambient conditions. For typical low temperature atmospheric pressure plasma, the gas temperature is near or under 40°C. As such, this is also often called cold

atmospheric plasma (CAP).

Research is now being done on these low temperature plasma discharges to achieve many of the applications that have already been done with low pressure plasma sources or high temperature plasmas. These discharges allow for high temperature chemistry to occur at ambient or near ambient conditions. The advantage of using ambient conditions is that new substrates can be used that are not vacuum compatible or temperature sensitive, such as biological substrates. When used for medical purposes, this is called plasma medicine.

Discovering an important finding in medical science is not enough; it has to be given to the general populace to have real-world effect. To transition the results from this new field of plasma medicine out of the lab and to a physician for practical implementation, devices need to be created to meet specific medical needs. The next two subsections will discuss the two main aspects of this transition: identifying specific medical uses for plasma discharges and the process of developing a medical device.

1.1.1 Medical Uses for Plasma

The first use of a plasma discharge for a medical use was on October 1, 1926, when Dr. William Bovie used an electrosurgical generator with surgeon Dr. Harvey Cushing to remove a large brain tumor. [4] This plasma was a lower energy thermal (equilibrium or near equilibrium) discharge that helped maintain hemostasis during the surgery by sealing blood vessels during incisions. This type of system is still in use today for similar applications of minimizing blood loss, both for coagulation of blood as well as cauterization.

Low temperature plasmas have been investigated much more recently for potential medical benefits, predominantly starting in the 1990s. [5] One of the first uses found was bacterial inactivation. In addition to sterilization of surfaces, it was found that the plasma can be applied to skin, where the bacteria can be inactivated without damaging human cells. This has developed into treating chronic wounds with biofilms, the only application for which there are marketed low temperature plasma medical devices. In addition to bacteria being more sensitive to low temperature plasma, cancer cells have also been found to be more susceptible to plasma. [6] This has led to

extensive research being done on plasma as a potential cancer treatment.

Electric fields, which if high enough will invariably create plasma discharges, are also being investigated for a number of uses. They have been shown to have a wide range of effects on cells, ranging from electroporation of cell membranes to inducing apoptosis. [7]

Plasma can also be used indirectly for medical use. The most common example is in surface sterilization, such as autoclaves. However, plasma discharges can also create gaseous species with medicinal benefit, such as nitric oxide (NO) used in NO therapy. Plasma can also modify other materials for later medical use, such as plasma activated water, which has been shown to have sterilization potential. [8] Lastly, plasma can also modify solids, such as enhancing the strength of additively manufactured parts as discussed in Chapter 7.

1.1.2 Medical Device Approval

Medical devices follow a design life-cycle, which begins with idea generation and identifying a specific need to ultimately marketing the device and implementing an end-of-life plan. They generally have four stages: basic research, design development, device testing, and device marketing. Initially an idea is explored to discover if there is sufficient benefit to create a medical device. If there is sufficient benefit a device is developed to meet the need. After undergoing verification and validation, a final design is found, which then undergoes testing for a marketing submission to the regulatory body for approval.

This regulatory body acts as a gatekeeper for how a medical device is distributed to the masses. Nearly all regulatory bodies, such as the US Food and Drug Administration (FDA), examine devices with two concepts in mind: safety and efficacy. They ensure the device is safe for end users, not posing an undue risk to the consumer, while also examining the efficacy of the device to ensure that it effectively treats the specified condition, called the intended use of the device. They do this by examining the evidence gathered by the testing of the final design. Devices are also normally broken into groups based on the amount of risk they pose; higher risk devices receive more careful scrutiny, while low risk devices can quickly be processed.

If a device is adequately shown to be safe and effective, it receives approval to be marketed.

Typically there are also requirements to continue monitoring the device to ensure that good manufacturing practices continue to be followed as well as longer term studies to ensure there are no long term adverse effects from using the device. Device manufactures may also consider end-of-life plans such as ways to recycle the device after its useful life is finished.

Designing and marketing a medical device, especially in a novel field such as low temperature plasma medicine, is a serious undertaking. It involves balancing technological development, maintaining cash flows for a burgeoning business, and navigating a complex regulatory environment. All of these aspects must be kept in mind throughout the device development process, so that the early designs flow smoothly to a final design ready for testing for regulatory approval.

1.2 Motivation

Innovation in medicine is always desired. In the case of plasma medicine, clinical studies have already been conducted in which wounds have been shown to heal to the extent that amputation of the limb is no longer needed. [9] Further development in cancer therapy may lead to treatments for various cancers, as shown currently with in vitro and animal models. [6] These results would lead anyone into investigating these and other uses for plasma as a medical tool, as the results show promise to be substantially better than those currently being used in the medical field, improving quality of life for patients and even possibly saving patients' lives.

For those with less of an altruistic side, this is a novel yet burgeoning market currently with very few companies. The United States' medical device market is worth \$156 billion, accounting for 40% of the world's medical device market. [10] The low temperature plasma market is expected to double in size in the next 5 years, primarily in wound treatment. [11] There is plenty of opportunity as there is currently no approved low temperature medical devices in the US market, showing incredible room for growth and also the potential benefit of being the first to the market.

The work presented in this dissertation is motivated by finding a variety of uses and plasma sources for medical treatments. This is intended to provide a more holistic approach than is typically done in a laboratory setting, attempting to bridge the gap from basic research to targeted medical device development to meet a specific intended use.

1.3 Research Objectives

How can a low temperature plasma medical device be developed effectively in the US?

This dissertation seeks to answer this question by looking at five low temperature plasma medical devices in four different aspects of their design.

1. **Device development** can encompass the entire range from idea exploration and prototype creation through marketing approval and post-marketing studies. [12] It can even be broadened to include the entire design life-cycle, which seeks to examine a device from the initial idea (or even before with idea creation) to the end-of-life of the device. Four of the five devices discussed in this dissertation are early in their development, but their entire design life-cycle is investigated at least briefly, with an emphasis on the early characterization of the designs.
2. **Regulatory approval** can be a key hurdle in attempting to market a device. The approach is driven by the intended use of the device, which determines the level or rigor the testing of the device will require, which can ultimately lead to years of additional development time. Understanding the regulatory environment is crucial for properly developing the device. The various approaches that these new devices can take for marketing submissions to the FDA are explored, examining the strengths and weaknesses of the various approaches.
3. **Plasma characterization** is the main thrust of this dissertation, seeking to characterize the plasma discharges of these five devices for their respective applications. The control of the plasma is key for achieving the end result for the different designs.
4. **Biocompatibility** is critical to plasma medicine. It is very easy for a plasma discharge to become dangerous or even lethal, thus careful control over the plasma is necessary to ensure that minimal current is introduced into the substrate, the temperature remains low to avoid thermal damage, and no dangerous chemicals are generated in the plasma. Note, however, that a fully biocompatibility analysis is not performed in this work. For example,

the amount of potentially hazardous gaseous species generated such as NO and ozone was not quantified, solvents such as methanol were not replaced with a biocompatible alternative, nor were histological studies conducted to determine if and to what extent thermal damage was done to the biological tissues.

1.4 Dissertation Overview

This dissertation is divided into two primary sections, a background section consisting of two chapters (Chapters 2 and 3) and an exploration of five potential low temperature plasma medical devices (Chapters 4 through 7). Chapter 8 concludes this work and examines the future work to be done for developing a low temperature plasma medical device as well as the future work for each of the systems described in the earlier chapters. Two appendices are also included for further information on the power supply developed in Chapter 4 (Appendix A) and the code developed to directly interface with a 3D printer to create uniform area coverage for film deposition discussed in Chapter 6 (Appendix B).

The following chapter, Chapter 2, explores the plasma medical device field. It does this by first presenting some prerequisite knowledge of plasma operation, followed by a brief overview of medical device development, particularly examining the approval pathways for devices for marketing a device. This chapter concludes looking at the current state of the field of plasma medicine, examining the potential uses, current devices, and standards that are being developed for plasma medical devices. The next chapter, Chapter 3, discusses the specific techniques used in this dissertation to characterize the five plasma devices discussed, examining the applicability of the various techniques and their limitations.

The next four chapters of this dissertation cover the five potential low temperature plasma medical devices. Each of these chapters begins with an introduction of the material followed by relevant literature and background for that specific device that was not covered in the more general discussion in Chapter 2. Next, the device's design is examined, noting where it is in the overall design life-cycle as well as steps to carry the design forward. The possible regulatory approaches are also laid out, in particular how to approach the FDA. Then, the physical design

and development are discussed, noting the characterization that has been conducted thus far on the device. Each chapter then concludes with a brief summary of the work completed as well as a future outlook for the device with the necessary design and development work still to be done.

This work has generated four journal papers thus far, with three further papers being prepared for submission as well. The electroporation system (Chapter 4) was published as “Development of a Substrate-Invariant 2-D Array of Nanosecond-Pulsed Streamer Discharges”, [13] with a future publication planned on the timing circuitry for imaging the discharge (as shown in Section 4.5.5). A publication is being written on the modification of the electrosurgical power supply to create a low temperature plasma discharge. Characterization of the metallic depositions discussed in Section 6.5 has been published as “Copper Film Deposition Using a Helium Dielectric Barrier Discharge Jet”, [14] which is a continuation of Cliff Tsai’s graduate work. [15] A further publication is being finalized on the direct write aspects of Chapter 6. The nanosecond pulsed system for assisting additive manufacturing (Section 7.4) was published as “Effects of Cold Plasma Treatment on Interlayer Bonding Strength in FFF Process”. [16] The FlashFuse system was published as “Dielectric Barrier Discharge Applicator for Heating Carbon Nanotube-Loaded Interfaces and Enhancing 3D-Printed Bond Strength”. [17]

2. PREREQUISITE KNOWLEDGE & LITERATURE REVIEW

2.1 Introduction

This chapter will describe the prerequisite knowledge necessary for understanding plasma discharges and the core literature for the context of this dissertation. The next chapter will go into detail on the diagnostics used to characterize the plasma systems, which will include any relevant literature describing those diagnostics. In addition, each chapter will begin with a background including the relevant literature necessary for that specific plasma system; as such, only the literature and relevant background information that spans multiple systems will be described here.

This chapter will first describe what a plasma is, going into some detail for various types of discharges, how energy propagates in a plasma discharge, and the effect plasma has on the materials exposed to it. Second, a discussion of the design life-cycle for a medical device is given. This provides the context of where the devices discussed in this dissertation are in their development as well as the general approach needed for further development through marketing and end-of-life considerations. Next, medical device approval for marketing is discussed, with a focus on the US Food and Drug Administration (FDA). Finally, low temperature plasma medical devices are reviewed, examining the effect of plasma on live tissue, current systems in development, and finally standards that are being developed for these systems.

2.2 Plasmas

First, one must understand what a plasma is. Plasma is the 4th state of matter.¹ If one keeps adding energy to a system it will eventually end up becoming a plasma, as shown in Figure 2.1. A plasma also differs from a gas in that the material may not be of a uniform composition; there can be free electrons, ions, and neutral gas species all present. Due to the presence of free electrons (i.e. electrons no longer bound to an atom) and ions, a plasma responds to electric and magnetic

¹This is sometimes confused with blood plasma, which is a completely different material. Interestingly though, electrical plasma is named after blood plasma as the collection of ions, electrons, and neutral gas species were reminiscent of blood plasma. [18] Both definitions derive from the Greek word *πλάσμα*, meaning *moldable substance*

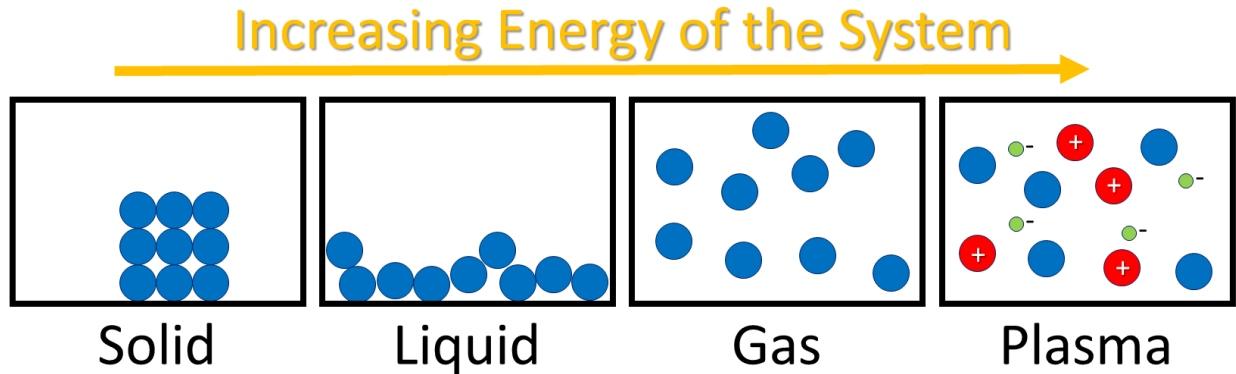


Figure 2.1: Plasma as a State of Matter

fields. However, unlike a solid, liquid, or gas, there is no distinct phase change that occurs to create a plasma.²

Plasmas can be created multiple ways. If energy is uniformly added to a quantity of material to maintain equilibrium, a thermal (or equilibrium) plasma results. This is called such because all of the plasma's constituents (the electrons, ions, and neutral species) are at the same temperature. There is sufficient energy that the thermal energy alone has created the excitation process that created the free electrons and ions. Two examples of this process are the most common examples of plasmas people know: the sun (via compression heating of a material) and the latter stages of lightning (via Joule heating). In contrast to this type of plasma is a non-thermal (or non-equilibrium) plasma. Energy is often added only into the free electrons via a strong electric or magnetic field which begins to ionize a fraction of the neutral gas. Once a sufficient fraction has been ionized that the gas begins to show collective behavior (i.e. it begins responding to electromagnetic fields, etc.), the gas is now a plasma. The ionization fraction at which this occurs can be extremely low; for example, a fluorescent lamp has an ionization fraction around 4 parts per million [21]. This type

²There is some trickiness with definitions here. In general the terms *phase* and *state of matter* are nearly synonymous, meaning a portion of material that is homogeneous in its chemical and physical structure, separated by other phases by a phase boundary. [19] By this definition, a plasma is not a phase of matter because it is not homogeneous per se nor is there a distinct phase change or boundary to differentiate it from a gas. However, at some point with sufficient ionization, the behavior of a plasma is different enough from a gas that a new way of describing it is required. This is perhaps analogous to the lack of a phase change between a liquid or gas when it becomes a supercritical fluid. Nevertheless, it is fairly well established in literature that a plasma is a state of matter. [20]

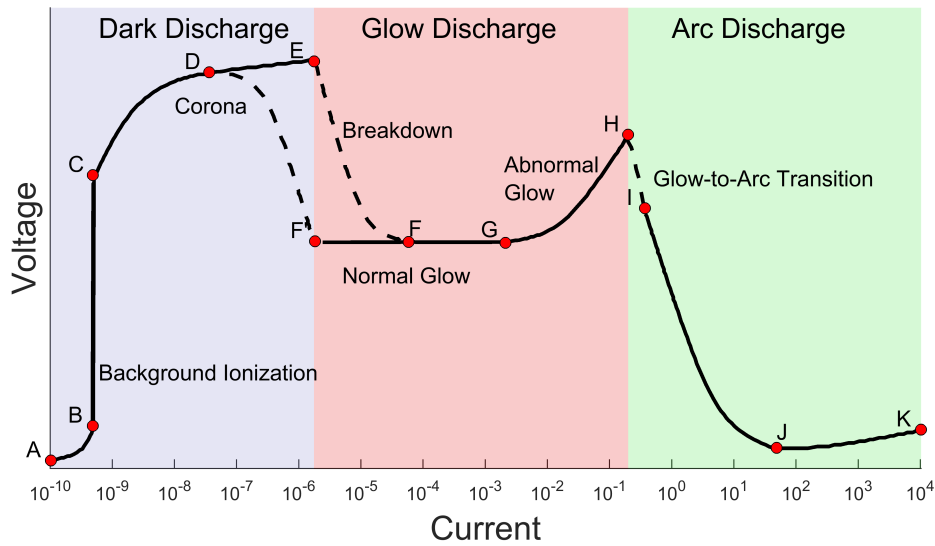


Figure 2.2: DC Steady State Voltage-Current Curve for Plasma

of plasma does not have a single temperature that can be used to describe the energy in every type of particle (or even the amount of energy within the energy modes of a given particle).

2.2.1 Types of Plasma

A plasma can be thought of as any other circuit element with its own voltage-current characteristics. Just as Ohm's Law ($V = IR$) relates voltage and current for a resistor, there is a standard "equation" that relates voltage and current for a plasma, which is shown in Figure 2.2. Note, however, that this diagram is specifically for a DC steady-state plasma; some behavior of fast-changing voltages may deviate from this. This relation is obviously much more complicated for a plasma than for a resistor. The next few subsections deal with each portion of this voltage-current relationship in more detail.

The voltage and current are functions of time as well as other parameters in the external circuit. For example, the external circuit may not be able to supply the amount of power that the plasma may be attempting to draw; as such the external circuit may place an external influence on the plasma by limiting the amount of current through it. Figure 2.2 also does not display the time-scales that the various plasma processes occur at; there are physical processes (e.g. the physical

movement of electrons and ions in the plasma each of which have characteristic time-scales) occurring that are coupling with the electrical circuit. Note that due to the complexity of the plasma voltage-current relationship, it cannot be averaged out using RMS equivalents as is commonly done for impedance with resistors, capacitors, and inductors. Thus three types of transient discharges, streamers, dielectric barrier discharges (DBDs), and resistive barrier discharges (RBDs), are also discussed in the following subsections.

Lastly, a section on plasma jets is included. Since plasma jets are usually operated using an AC power supply, rather than a DC power supply, some different considerations arise. These also deserve mentioning as the most commonly used plasma discharge in plasma medicine is a plasma jet.

2.2.1.1 Dark Discharge (A-E)

Initially there will be a few free electrons (i.e. not bound to an atom) in any gas. This occurs because there will always be some cosmic rays or rare high energy collisions that will ionize a few gas particles. Normally the electrons would quickly recombine with the gas around them; however, if a small voltage is applied these free electrons will have a small amount of net motion producing a minute amount of current (Position A in Figure 2.2). As the voltage is increased, these electrons will move faster, leading to a larger amount of current until a saturation value is reached (Position B-C), which corresponds to all these spontaneously created electrons contributing to the current flow. If the voltage is further increased, at some voltage value these electrons gain enough energy from the applied electric field to ionize some of the neutral gas molecules they collide with as they travel to the anode. As a result, there are more free electrons (for a binary system there is the free electron that collided with and ionized the neutral gas particle and now the new free electron that was created from this ionization collision), which allows for an increase in the current (Position C-E) since there are more charge carriers (i.e. free electrons).

An electron avalanche begins. This is where one seed electron collides with a neutral gas particle and creates a second free electron. Then these two electrons are accelerated by the electric field and both can then collide with other neutral gas particles creating an additional two electrons.

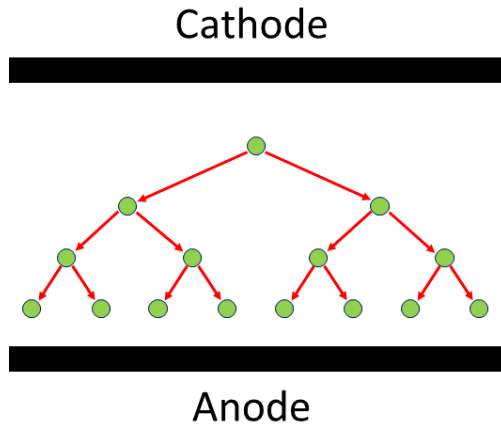


Figure 2.3: Schematic of the Electron Avalanche Process

These four electrons continue this process as they travel toward the anode, creating a large population of energetic free electrons. This process is shown schematically in Figure 2.3. The parameter often used to describe this process is called the Townsend ionization coefficient, α , [22] which is the number of electrons produced per unit length. If this electron avalanche does not reach electrical ground (i.e. it is from a very high electric field, such as sharp points on an electrode, or simply a very high voltage, often ≥ 20 kV) a very dim discharge called a corona discharge has developed. However, electrons can also be lost by electron capture processes with electronegative gases, such as oxygen. This is described using the second Townsend coefficient, β , which can be significant in air, but is ignored in many other gases, where electron capture is rare. Sometimes this type of discharge is called a Townsend discharge (from John Sealy Townsend who first described the electron avalanche process), however a Townsend discharge is specifically when the discharge is at least partially sustained by secondary electron emission. [23] Secondary electrons are those that are released from the cathode by collisions of ions with the cathode surface. This is described by the third Townsend coefficient, γ , which gives the number of secondary emitted electrons per incident ion. This value is typically much smaller than 1.

2.2.1.2 Breakdown (E-F)

If the electron avalanche shown in Figure 2.3 is able to cross the entire gas gap, a conductive channel is formed. This is referred to as breakdown, because the gas is no longer acting as a dielectric; it has *broken down*. The voltage at which this process occurs is called the breakdown voltage (Position E in Figure 2.2), which is often a fairly constant value for a given system. For perfectly planar electrodes the breakdown voltage is only a function of the gas and the product of the pressure (p) and the anode-cathode gap spacing (d); this is called Paschen's Law. In reality surface roughness can greatly affect the breakdown voltage, so the exact value is almost always experimentally determined. In addition, the preexisting conditions of the gap can affect the breakdown voltage, such as an unusually large presence of free electrons (e.g. a laser partially ionizing the gap or residual electrons from a previous discharge event that has extinguished).

Historically Paschen's Law was only used to describe breakdown processes at low values of pd (i.e. pressure times gap spacing). Instead as the electron avalanche begins occurring local space charge becomes significant leading to streamers or smaller filaments forming instead of a more volumetric breakdown as described by Paschen's Law. This breakdown process is sometimes called streamer breakdown, filamentary breakdown, or Raether-Meek breakdown (after the physicists who first described it). [24, 25] This will be described in more detail in Section 2.2.1.5.

Since the electron avalanche creates a conductive path, a much larger current is able to flow and a lower voltage than the breakdown voltage is able to sustain the resulting discharge. This breakdown process is sometimes referred to as having negative resistance since a decrease in the voltage corresponds to an increase in the current. Note that there is hysteresis that occurs (Positions E-F-F'-D). After breakdown, a lower current is able to sustain the discharge than the current initially arrived at; however, depending on the system this hysteresis may be small. This breakdown (E-F) and extinguishing (F'-D) of the discharge gap are inherently unstable processes, hence the dashed lines in Figure 2.2.

There are other possible breakdown mechanisms than high electric fields. Magnetic fields can at minimum assist in the breakdown phenomenon if not initiate it as well. [26] Optical breakdown

is also common using lasers, although this can be explained by the intense magnetic and electric fields present in the light (an electromagnetic wave). Gravity can also supply the necessary energy, as this is how stars operate, to create internal confinement fusion, which is a plasma.

2.2.1.3 *Glow Discharge (F-H)*

After breaking down, often a glow discharge will be created, depending on the voltage and current supplied by the external circuit. A glow discharge is characterized by secondary electron emission sustaining the discharge. Secondary electron emission is when free electrons are generated by ion collisions with the cathode. Often only one out of every 1000 or more ions that collide with the cathode will eject an electron from the surface. The exact number, called the secondary emission coefficient, γ (as described in Section 2.2.1.1, is dependent on electrode geometry, material, and the gas; it is usually experimentally determined. The difference between a glow and a Townsend discharge, which is also sustained by secondary electrons, is that a glow discharge bridges the gap, while a Townsend discharge does not.

A glow discharge has a few recognizable features, the most common being the negative glow, the Faraday dark space, and an anode glow. [2] There are many more potential features, but these three are the most evident, even at atmospheric pressure. The negative glow is close to the cathode and is often the brightest part of the discharge. There are slightly more electrons than ions hence the name negative glow. The Faraday dark space separates the negative glow from the anode glow. The anode glow is a region with constant electric field, where electron production equals electron loss. This is not a necessary part of the glow discharge and will disappear if the gap is too short, but it will expand if the gap is increased in size. This is the primary part of the discharge seen in “neon” signs used in advertising (where neon is one of the common gases added for these glowing signs).

Typically a glow discharge has a fairly constant voltage over a wide range of currents (Positions F-G in Figure 2.2). The current density is fairly constant; increases in the current correspond to an increase in the discharge size in the negative glow. An abnormal glow is when the plasma has exceeded the size of the electrode (Positions G-H), so any further increase in current also increases

the current density and voltage. An abnormal glow is generally not noted at atmospheric pressures since the discharge area is typically not limited. [27] Even in pin-to-pin discharges the cathode will wrap around the edge of the pin electrode to increase in area.

2.2.1.4 *Arc Discharge (I-K)*

An arc discharge is characterized by thermionic emission of electrons (Positions I-K in Figure 2.2). The cathode has heated up to a sufficient extent that the electrons are able to overcome the work function of the cathode material and are ejected in sufficient quantity to sustain the discharge. This is a very high temperature discharge. The exact transition from a glow to an arc discharge can be due to Joule heating in the plasma or in the electrode until the electrode surface is hot enough to thermionically eject electrons (Positions H-I). The glow-to-arc transition is often thought to arise in the cathode fall region of the glow discharge, where there is a large voltage drop. [28] This is also an unstable process like electrical breakdown (see Section 2.2.1.2).

2.2.1.5 *Streamers and Related Discharges (Transitory Plasmas)*

Unfortunately there is little consensus in the literature around the distinction between a corona, streamer, and streamer-corona (or corona-streamer) discharge. In general, a corona is a weakly luminous steady-state discharge centered around a region of high electric field (typically a sharp point on an electrode), where the discharge does not have direct electrical contact with ground. The charge is slowly dissipated into the ambient environment, where the free electrons dissipate their energy by collisions with neutral species until recombination occurs. The space charge is generally low enough to not greatly affect the overall electric field of the discharge gap. Coronas are typically seen around high voltage ($>\sim 20$ kV). This type of discharge is responsible for the characteristic hum of high voltage power lines.

A streamer discharge is a single electron avalanche process (called the streamer head) and the ionized channel behind the avalanche, where the generated high voltage wave is propagating toward ground. These growing ionized channels often have significant space charge to affect the electric field of the discharge gap. The difference in the literature is that some authors term the in-

dividual filaments that form a corona as streamers. To further complicate this definition are pulsed discharges. These discharges may form a steady-state corona discharge or perhaps transition to a glow if they were sustained, but due to the pulsed nature of the supply voltage they quickly extinguish. As such, some authors use the term streamer-corona to describe these pulsed discharges.

Another related discharge is a spark. A spark discharge is a transient discharge that has a fast breakdown (electron avalanche) and quickly begins to heat up transitioning toward an arc discharge. (You can think of this as a discharge that very quickly goes from position A to position I in Figure 2.2, although the exact current and voltage measurements may not exactly correspond to Figure 2.2.) However, the external circuit is not able to sustain the discharge, so it quickly dies out. This commonly occurs when discharging capacitors, where the charge stored on the capacitor discharges quickly, but as the charge leaves the capacitor the voltage it is supplying drops. There is again disagreement whether the entire process is a spark or if a streamer discharge, upon reaching ground becomes a spark only when a significant amount of current begins flowing and Joule heating occurs. This is analogous, if not identical, to the glow-to-arc transition.

2.2.1.6 Dielectric Barrier Discharge (A Transitory Plasma)

A dielectric barrier discharge (DBD) consists of at least one dielectric barrier and a gas gap between the anode and cathode. The dielectric barrier prevents charge from flowing between the two electrodes, ensuring the system always has some capacitance. Due to this, a dielectric barrier discharge must have either a periodic or pulsed voltage waveform applied—DC circuits will not work for DBDs. Thus a DBD is a transitory discharge.

A DBD often consists of numerous microdischarges. These show up as individual filaments in the discharge gap. Each microdischarge begins as an electron avalanche (see Section 2.2.1.2) that occurs in the gas gap at some location along the dielectric barrier. This creates a conductive channel across the gas gap. The electrons, however, are not able to complete the circuit due to the dielectric barrier and a local build-up of electrons occurs on the dielectric barrier's surface. As a result of the charge build-up, the voltage locally across the gas gap decreases, since more voltage is dropped across the dielectric barrier (the dielectric barrier is a capacitor with some charge now,

which is governed by the equation $Q = CV$). The conductive channel that was formed from the electron avalanche is not able to become a sustained discharge due to the reduced voltage across the gas gap and the discharge extinguishes. This essentially corresponds to traveling from positions A to G and then back to A in Figure 2.2 for the local discharge.

However, DBDs are normally driven by a sinusoidal voltage waveform, so after the first half cycle a half cycle with the opposite polarity occurs, where the electrons deposited on the dielectric barrier are then driven across the gas gap in the opposite direction. This leads to another discharge in the opposite direction, and as a result no net charge moves for a full voltage cycle. For large surface area DBDs, there can be hundreds or thousands of microdischarges that occur for each half-cycle of the voltage, so the local discharges have an overall aggregate effect of shorting the gas gap capacitor when the voltage is above the breakdown voltage. The driving frequency is normally on the order of kilohertz, so to the eye it appears as a continuous discharge.

Over certain ranges of gap distance and pressure a DBD may take on a diffuse glow rather than having filamentary discharges all across the surface. In general this occurs for lower pressures and gap distances which corresponds to Paschen breakdown rather than streamer breakdown (see Section 2.2.1.2). The diffuse mode may be more advantageous for gas processing due to its uniformity.

DBDs have been used primarily as ozone generators and gas purifiers. They are also potentially very useful due to the dielectric barrier, which helps prevent large currents from flowing through the discharge, since all currents are only displacement currents. This makes DBDs advantageous for medical devices, since the dielectric barrier makes them inherently “safe”.

2.2.1.7 Resistive Barrier Discharges

A similar system to a dielectric barrier discharge is a resistive barrier discharge (RBD). An RBD replaces the dielectric barrier with a material that has a high distributed resistance. Unlike a DBD, net charge can flow through an RBD. Similar in operation to a DBD, an RBD often has pulses where the plasma is intermittent, only due to a larger voltage drop across the local resistor rather than a local dielectric. An advantage of the RBD is that it can be operated at lower fre-

quencies, even as a DC discharge (in which case it will become a continuous discharge, rather than intermittent discharges).

2.2.1.8 *Plasma Jets*

Plasma jets come in a wide variety of types and electrode configurations, but their distinguishing feature is that the discharge occurs in a gas flow. Some example electrode configurations are shown in Figure 2.4. The floating electrode-DBD (FE-DBD) jet is used in this work in Chapter 6 and has been used extensively in our lab [15, 29–31], which stands in contrast to the more common non-floating electrode counterpart, where the ground electrode is also included on the outside of the dielectric tube. [32] The floating electrode (FE) direct plasma jet is used Chapter 5; however its non-floating counterpart is much more common; in particular, it is used in the kINPen plasma jet, [33] which will be discussed in more detail in Section 2.5.2.1. The final example shows some of the diversity in the possibilities of electrode configuration, where the plasma discharges laterally across the gas flow in the jet and the effluent of the plasma discharge exists the tube; this is used in the COST jet, which is often used as a reference microplasma jet. [34, 35] Some other jet configurations are detailed in various plasma jet review articles. [36, 37]

Typically a plasma jet uses a pulsed DC waveform or an AC waveform. This is a necessity for DBD jets, as no current would flow across the dielectric barrier in DC operation. Other plasma jets can operate in DC; however they often require either higher voltages or currents for operation and are thus difficult to operate in a low temperature plasma mode.

The plasma is not continuous, rather it comes in ionization waves termed plasma bullets. Though this may seem obvious for a pulsed DC operation, this also holds true for AC excitation. Often only one plasma bullet occurs per cycle or half-cycle of the AC excitation source; however it can happen multiple times per cycle. [29] They are easily noted in current traces, as each plasma bullet corresponds to a current spike. The plasma bullet travels on the order of 10^6 – 10^7 cm/s depending upon the excitation voltage, although the current draw continues long after the bullet has traversed the gap. [38]

Plasma jets are a very commonly used source of low temperature plasma. This is because

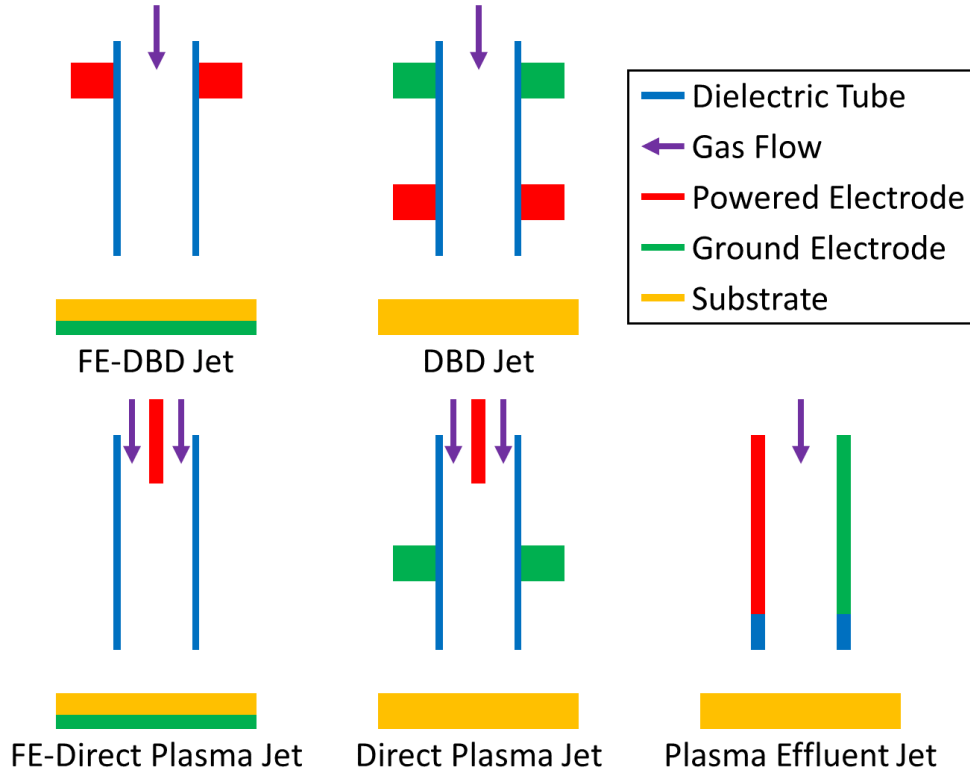


Figure 2.4: Schematic of Different Types of Plasma Jets

they have a lot of versatility. The high voltage is easily shielded either by a dielectric barrier or a long distance to the substrate, allowing easier low temperature operation. This operation is also substrate independent for many jets as the only effect of the plasma is in its effluent (such as the non-floating electrode DBD jet, the direct plasma jet, and the plasma effluent jet in Figure 2.4). By varying the distance between the jet and the substrate different chemistry is possible, such as using a more direct plasma contact or large distances with only long-lived species being able to reach the substrate. In addition, the gas can be varied yielding a wide variety of possible treatments. Noble gases can be used for easier operation (e.g. lower operating powers [39]). They also provide a wider variety of chemistry, in particular helium with extremely high electronic excitation energies. Lastly, the ability to have an admixture of different gases or various precursors in the gas stream while still being able to run in ambient air allows for nearly unlimited possibilities for plasma jets. Some applications are discussed in Chapter 6.

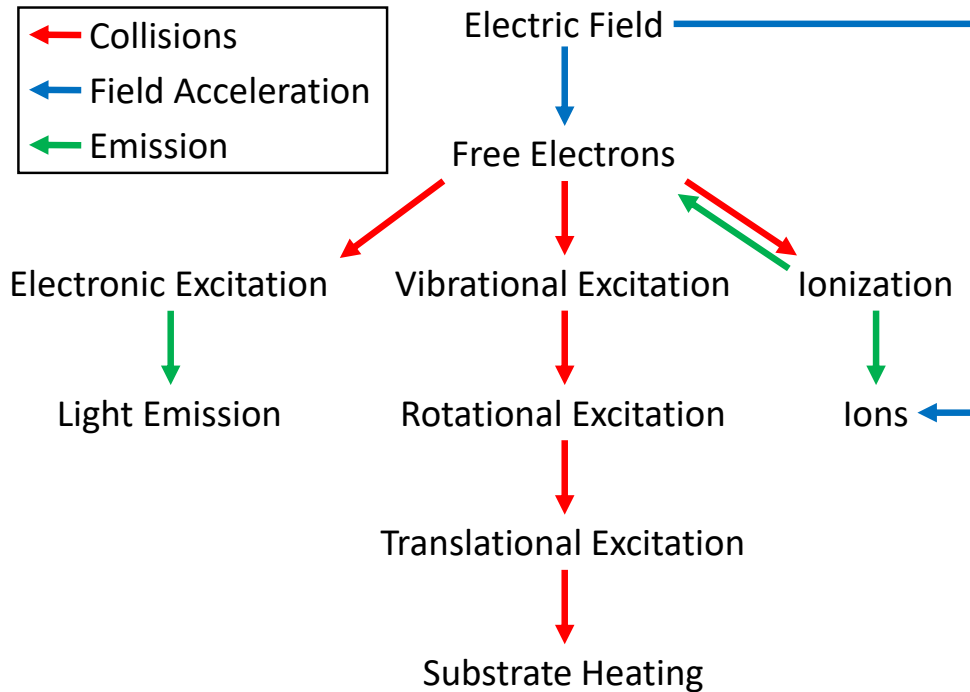


Figure 2.5: Basic Energy Flow Diagram in a Low Temperature Plasma

2.2.2 Energy In a Plasma

To get a general understanding of how a plasma works, it's useful to understand where the energy goes. Initially with a voltage applied across a gas gap, the energy is stored in the electric field. Any free electrons are accelerated by that electric field and as those electrons gain energy from the electric field they begin a number of processes, imparting energy to the neutral gas, as shown in Figure 2.5. In general, at low energies (a small electric field for the number of particles) electrons impart energy to vibrational modes of the gas, which then spread to rotational and translational modes in the gas via collisions. As the electrons gain more energy, they begin to electronically excite the gas, and at higher energies they begin to ionize the gas.

The gas molecules (atoms for atomic gases like helium) are also moving around and colliding with each other. In these collisions they exchange energy. The average translational kinetic energy of the gas particles corresponds with the temperature of the gas that we feel (where more kinetic energy means a warmer gas). Energy can also be stored in other modes that just the translational

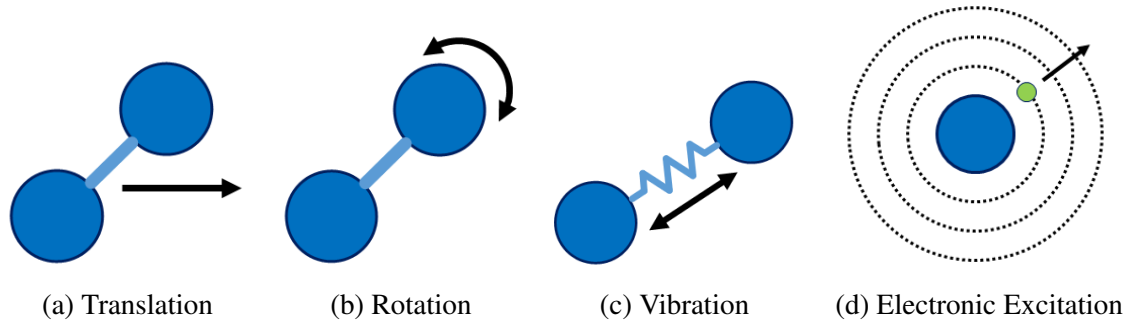


Figure 2.6: Schematics of the Various Energy Modes for Atoms and Molecules in a Plasma

motion of the gas molecules, as shown in Figure 2.6. They can rotate, vibrate (where the bond between the two nitrogen or oxygen atoms acts like a spring), or undergo electronic excitation (which also occurs for atomic species). Rotational energy couples very well with translational energy; this means that when two molecules collide energy moves easily between translational and rotational modes. Since these collisions happen often (due to the high density of gas molecules), it usually takes less than a nanosecond for the rotational temperature (the average energy stored in rotational energy modes) to equilibrate with translational temperature. The vibrational energy modes take longer to equilibrate than the rotational and translational modes. This can be measured using spectroscopy.

The concept of temperature only applies in equilibrium. This is when the energy is distributed according to a Maxwellian distribution, as will be discussed in more detail in Section 2.2.2.3. However, there can be a pseudo-equilibrium within an energy mode, which is often approximately true for many low temperature plasma systems. Temperature is a measure of the spread of the distribution of the energy present in the system, in this case the energy mode. As the temperature increases, there are more particles that have a higher energy.

The energy in the vibrational modes can be normally distributed, but at a substantially higher temperature than the energy in the rotational modes. However, within each mode, there can exist an equilibrium in the energy distribution. This is then by definition a non-equilibrium plasma, because the various modes do not have the same temperature. For low temperature plasmas discussed in

this dissertation, the temperature (energy) distribution among the various modes is

$$T_e > T_{\text{elx}} > T_{\text{vib}} > T_{\text{rot}} \approx T_{\text{trans}} = T_{\text{gas}} \quad (2.1)$$

where the free electrons have the most energy due to their small mass but charge leading them to be excited by the electric field. The electrons excite the gas electronically and vibrationally via collisions, hence elevating those temperatures by imparting energy into those energy modes. The energy slowly spreads to rotational modes via collisions, which quickly equilibrate with the translational energy modes of the gas. The translational temperature is the gas temperature that one feels.

2.2.2.1 “Hot” Versus “Cold” Plasma

The definition of cold atmospheric plasma (CAP) generally given in the literature is that the plasma temperature does not exceed 40°C at the point of application to the substrate. [40, 41] However, the concept of a plasma being “hot” or “cold” is really a misnomer. This is a term applied only to the observable gas temperature, namely the translational temperature. However, there can still be a substantial amount of energy in other energy modes, yielding quite hot temperatures for those modes, often even over 10,000 K! In particular, the average energy of the electrons can be quite high. Nevertheless, the “cold” plasmas are able to be used on temperature sensitive substrates, such as human patients, without the gas feeling “hot”. This often has more to do with the thermal load of the plasma than its temperature.

For a proper definition of CAP, one needs to consider at least three aspects of the system:

- **Translational temperature**, which is a measure of the average speed of the gas particles and thus the rate of energy transfer to the substrate. This rate would be expressed by Newton’s Law of Cooling and has the potential to change drastically if the substrate changes temperature (such as using cryogenic cooling, but this is not expected in a medical situation) or the discharge changes modes (see Section 5.5.1, for example).
- **Thermal load**, which measures the amount of heat traveling into the substrate, taking into

account the heat capacity of the plasma and the substrate. Since many cold plasma treatments are using a weakly ionized plasma jet, the thermal mass of the plasma is quite small, often leading to a small thermal load. In addition, the substrate for medical treatments has a large water content and thus has a very large heat capacity and thermal mass compared to the plasma.

- **Duty cycle**, which is the amount of time the plasma is “on”. Most cold plasma systems are pulsed either directly or indirectly by using an AC excitation, and thus they can have a low duty cycle, where the plasma is not “on” for a majority of the treatment time.

These aspects are not necessarily independent of each other. For example, the translational temperature of the plasma may vary greatly over time, with a peak temperature significantly above the 40°C suggested temperature limit. However, if the duty cycle is low, the thermal load may be small and the time-averaged (over many cycles) translational temperature may also be near the ambient temperature due to thermal diffusion into the surrounding environment. It is also possible to have what may be considered a “warm” plasma (>40°C translational temperature, thus not a “cold” plasma per the literature definition), but the substrate temperature does not increase greatly due to a high heat capacity or effective cooling system. This should however be considered a “cold” plasma since it is not heating the substrate, even though it does not meet the literature definition of a “cold” plasma.

Thus a better definition for CAP may be: “The interaction of the plasma does not cause the treated material (typically a substrate, but can be the bulk gas in applications without a substrate) to exceed a local temperature rise of >5°C.” This does not deal directly with the the plasma but rather with its interaction with the substrate, thus accounting for the thermal load. This is also easily measurable using a temperature sensor on the substrate or a thermal imaging system and is expected to be time-averaged over the interaction time of the plasma, thus also accounting for the duty cycle of the plasma treatment. The main issue with this definition, which also plagues the literature definition, is that the temperature or temperature rise is an arbitrary value.

The difference between a “hot” plasma and a “cold” plasma is illustrated in Figure 2.7, where

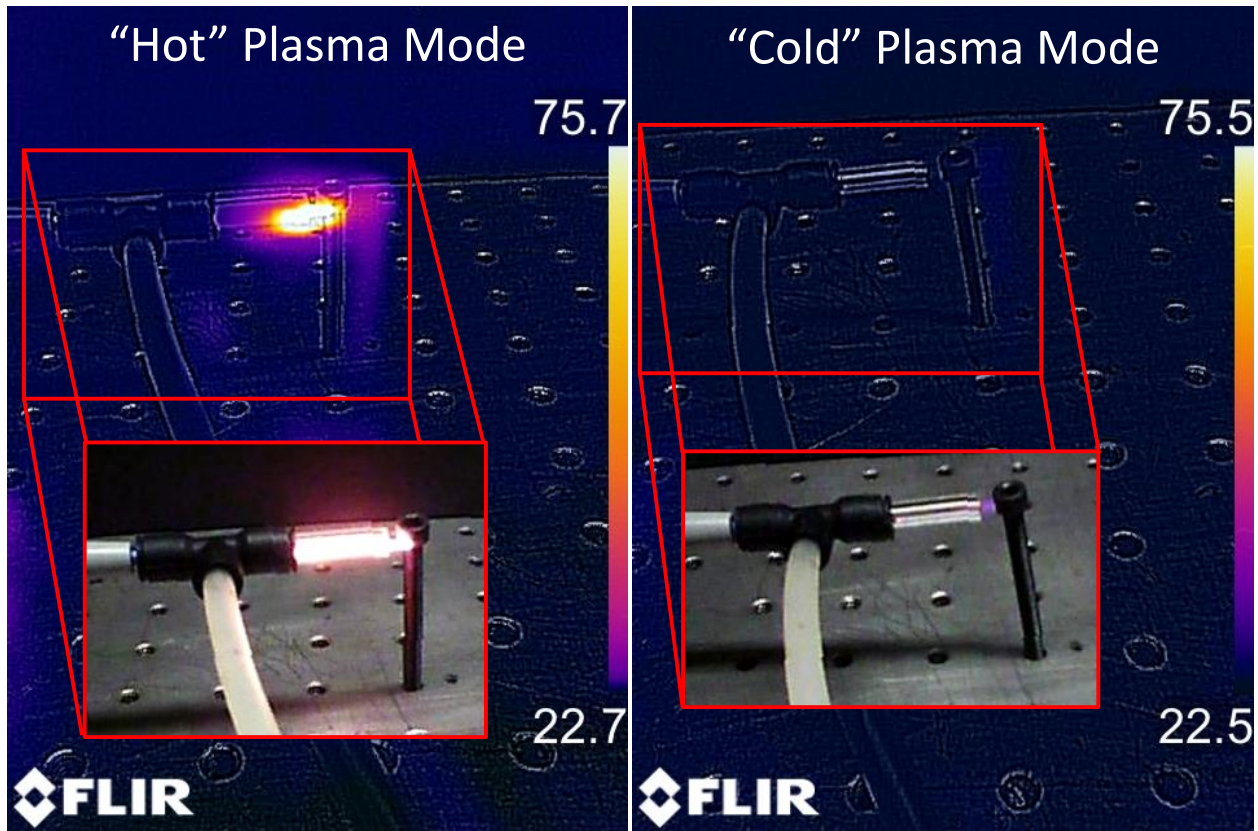


Figure 2.7: Infrared Images of a Plasma Discharge Operating in a “Hot” Mode and a “Cold” Mode (Note the Temperature Scale Bar Has Units of Celsius, °C)

a significant rise in temperature is noted due to the interaction with the “hot” plasma, but this is not noted with the “cold” plasma. The plasma source in this figure is the Bovie power supply, where the “hot” and “cold” plasma conditions roughly correspond to the diffuse and concentrated modes discussed in Section 5.5.1.

2.2.2.2 Plasma Collision Processes

One of the key ways to understand a plasma is to understand some of the basic collisional processes that occur. Though many processes can occur only a few are highlighted below.

- **Electron Impact Ionization** is when an electron, e collides with a neutral gas species, A , and imparts enough energy to remove another electron. This is one of the main ways that a plasma is created. The electrons are accelerated by the electric field until they have enough

energy to ionize the gas species. This produces more electrons which help sustain the discharge.



- **Electronic Excitation** is when a gas species is excited but not ionized. A valence electron is excited to a higher energy level, and a metastable state is created; after a certain amount of time the electron will lose energy either via collision with another gas species or via photon emission.



- **Photon Emission** is when an excited gas species loses energy by emitting light. The photon energy, $h\nu$, corresponds to the decrease in energy of the gas species. This is the main source of the light emitted by a plasma. Since the energy of the photons corresponds to electronic and other internal energy modes of the gas species this light can be collected and used to characterize the plasma. This is called optical emission spectroscopy (see Section 3.4). Information that can be determined from this light is the temperature of the rotational and vibrational states (assuming there are molecular species in the gas) as well as the degree of ionization of the gas.



- **Photoionization** is when a photon of light ionizes the gas species. The photon must have at least enough energy as the ionization energy of the gas species. This process can become significant when a gas with high electronic states (normally helium, He, or argon, Ar) is introduced into the bulk gas.



- **Penning Ionization** is when a species with a high energy metastable state, M^* , collides with a species with an ionization energy lower than the energy stored in the metastable state. This can be a significant ionization mechanism for some species in a mixture. Helium is often

the metastable species since it has extremely high electronic excitation energies often well above the ionization energies of other gases.



- **Recombination** is when an electron is captured by an ionized gas species. This is one way that electrons are lost in a plasma. A third body, M , is usually needed to carry away the excess energy from this recombination event to prevent the electron from immediately being re-emitted.



- **Electron Capture** is when an electron is captured by a neutral gas species. This usually only occurs with electronegative gases, such as oxygen. As such, this is negligible in many gases, such as noble gases and N_2 ; however this process is significant for air. Like recombination, often a third body is needed to carry away the excess energy to prevent the electron from being re-emitted.



- **Elastic Collision (Diffusion)** is when there is no net energy loss in a collision; this is the typical billiard ball collision. Often the particles travel in a different direction. This can lead to electrons diffusing out of the discharge and is one of the main loss mechanisms of electrons for plasmas.



2.2.2.3 Energy Distribution Function

Each of the reactions in Section 2.2.2.2 has an associated rate constant, k_i that describes the rate this reaction will occur, expressed as

$$k_i = \int_0^{\infty} \sigma_i(\mathcal{E}) \left(\frac{\mathcal{E}}{2m} \right)^{\frac{1}{2}} f(\mathcal{E}) d\mathcal{E} \quad (2.10)$$

where $\sigma_i(\mathcal{E})$ is the energy-dependent cross section (a measure of probability in units of area), m is the mass of the species, and $f(\mathcal{E})$ is the distribution function. This is often highly dependent on the energy of the species (often electrons), thus knowing the distribution of the species in energy space becomes critical to understanding a plasma's behavior. One of the main distribution functions is a Maxwell–Boltzmann distribution function (also commonly called a Maxwellian distribution) which is shown in Figure 2.8 and is given by the equation

$$f(\mathcal{E}) = \frac{2}{\sqrt{\pi}(k_B T)^{\frac{3}{2}}} \mathcal{E}^{\frac{1}{2}} \exp\left(\frac{-\mathcal{E}}{k_B T}\right) \quad (2.11)$$

where $f(\mathcal{E})$ is the energy distribution function, the initial term is a normalization term (total area under f is 1), \mathcal{E} is the species's energy, k_B is the Boltzmann constant, and T is the temperature. Only a single parameter, the temperature (T), determines this distribution. The Maxwellian distribution function describes equilibrium, which is rarely completely true for the electrons, but may be a reasonable approximation for heavier species in a plasma; nevertheless they are often tending towards this type of distribution. This is technically the only way temperature is defined; if the distribution of particles does not fit an equilibrium distribution, then the temperature of those particles is not defined.

Particularly for electrons, the electron energy distribution function (EEDF) can become skewed. This often occurs due to a depopulating effect particularly for higher energy electrons. This is because many processes, such as ionization, have an energy threshold upon which the process suddenly becomes dominant (based on the reaction cross section, σ_i , which is a component of the rate

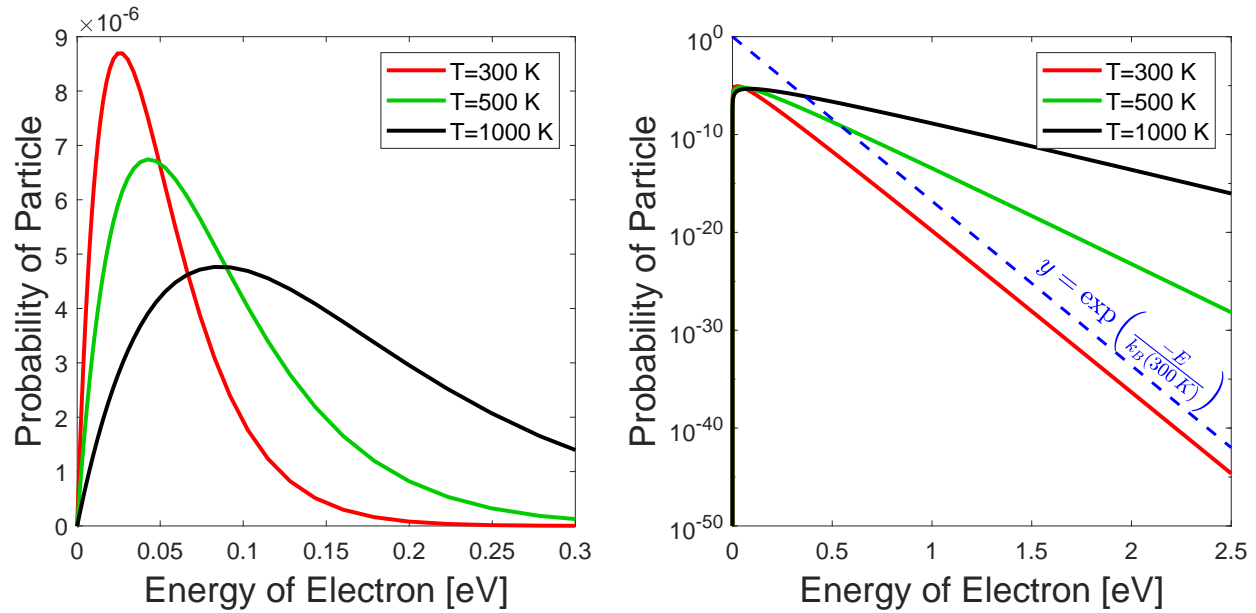


Figure 2.8: Plot of the Maxwell–Boltzmann (Maxwellian) Distribution Function for Multiple Temperatures on Both a Linear and Logarithmic Scale

coefficient, k_i). As such, it is often easier to plot the EEDF on a semi-log plot (see Figure 2.8), upon which any nonlinearity is easily visible, because the exponential portion of the distribution function dominates at higher energies (i.e. it is linear on a semi-log plot). For comparison, a simple exponential curve (blue line) is also plotted in Figure 2.8. Often other types of distributions are used instead of a Maxwellian, such as the Druyvesteyn distribution or other more generalized distributions, to adequately model the EEDF. These distributions better capture the physics for the high energy tail in the EEDF. Only a small fraction of the electrons need to have sufficient energy for ionization to sustain a plasma, while the other electrons may participate in electronic excitation reactions, which leads to the characteristic light emission of a plasma. [42, 43]

For other species, the distribution function can deviate from equilibrium due to an unbalanced energy input, where some input is preferentially exciting only certain states, such as a laser tuned to specific energy transition. This can also occur as the energy input rate, such as from electron impact processes, does not have time to equilibrate in the system, especially compared to energy outflow rates. However, though the energy may not be in equilibrium between various internal

energy modes, internally to each energy mode there may be at least a quasi-equilibrium. This is especially useful, since this can be probed spectroscopically to determine not only the degree of non-equilibrium, but also the distribution function, which yields the temperature of the various energy modes. However, the translational energy cannot be determined due to not being able to resolve the various translational lines.

2.2.3 Effect of Plasma on Materials

The effect a plasma has on a substrate can be quite diverse. This section will break those effects apart into three different aspects of the plasma, namely the electric field, the ultraviolet (UV) light generated, and the radical species created, and each will be discussed separately. For the potential medical applications of these effects, see Section 2.5.1.

2.2.3.1 Electric Field Influence

A plasma is generated from a high electric field such that the normally conducting air or other gas has broken down and has become conducting. If the substrate is sensitive to changes in the electric field, substantial changes can occur. One such example is electroporation of cells which is discussed in Chapter 4. Another example is the effect of electric fields on piezoelectric materials, where a change in the voltage across the material creates a physical change in the material. This occurs because the electric field causes a change in the unit cell of the crystal, in an effect called polarizability. [44] This effect has been explored in the plasma field. [45–48]

The applied electric field can also cause charges in the substrate to move. This movement can be dissipated in the form of heat in the substrate. If the substrate is a dielectric, the dipole moment of the molecules can reorient themselves to the applied electric field rather than having bulk charge movement. If the field is oscillating fast enough this causes substantial heating, which occurs in microwave ovens. This effect was also explored to heat additively manufactured parts. [49] If the substrate is conducting, this heating effect is called Joule heating, which is exploited in Section 7.5 for additively manufactured parts. This is also one of the main drivers for the gaseous heating occurring in plasma discharges.

2.2.3.2 *UV Light Emission*

Plasmas are the most common UV generating source for UV lamps. Direct UV light is a common bactericide. [50] This is a common sterilization technique that can be used with a plasma system, either as the main use or as a beneficial aspect apart from its primary goal, such as wound healing (see Section 2.5.1 for more information on the biomedical uses of plasma). UV light can also induce polymerization in polymers; this is called photopolymerization or photocrosslinking. [51] This was the first type of additive manufacturing developed, where a UV laser polymerizes a liquid monomer. [52] However, research in this area is still ongoing to explore the various types of materials that can be used. [53] Photopolymerization occurs by UV light imparting enough energy to create a radical species that will participate in polymerizing reactions. This radical species can be a metastable state, an ionic species (i.e. created via photoionization), or a radical created from the UV light breaking a bond. [54] When degradation of a material occurs due to UV exposure, this is called photodegradation; this is commonly seen in color degradation of materials left outside to sun exposure.

2.2.3.3 *Radical Species Generation*

Plasma can also generate a huge variety of radical species that can interact with a substrate. Particularly for air discharges these are often called reactive oxygen and nitrogen species (RONS). These species can interact and bond with surfaces (as noted in XPS results in [17]). Many of these species have biological significance as well, leading to enhanced sterilization, [5, 55, 56] immunoresponse, [57] etc., which will also be discussed further in Section 2.5.1.

Plasma-generated species are also used for surface modification. These can be various depositions from plasma enhanced chemical vapor deposition, where a film is deposited on various substrates. [58, 59] Everything from polymers [30] to metals [14] to dielectrics [60, 61] can be deposited. Etching of surfaces is common with low pressure discharges, particularly in microchip fabrication, [1] although it has also been noted with atmospheric pressure plasmas. [62] Surface functionalization is another application, where a surface can be treated to increase wettability for

later processing. [62, 63] This is especially common using corona discharges and DBDs. [64, 65]

2.3 The Design Life-Cycle

The design life-cycle is a concept to look at the entire design process from the initial idea generation to the end-of-life of the product. [66] In particular for medical products, the design life-cycle is shown in Figure 2.9. The design begins with an idea, often from identifying a need. Initial exploratory studies are conducted to examine what possible device could meet the identified need. This is the current status of most of the devices discussed herein; only the FlashFuse system has been carried forward to a market launch. In addition, market research is conducted to determine if there is a sufficiently sized market for a device to meet this need. Ultimately a more formal feasibility assessment is conducted to determine if this idea deserves full consideration to carry forward into developing a device. If there is a sufficient market need with enough scientific knowledge to produce a suitable device to meet the need, a formal needs statement is developed. The needs listed in the needs statement have to be well defined such that a device can be tested against them. A prototype device is generated that attempts to meet these needs. The design is iterated on and tested, making sure the device is verified to act as intended. In this process, there may be many design review steps until a “final” design is created. This “final” design must pass validation against the needs to ensure it adequately meets the intended use. [67] The US Food and Drug Administration (FDA) has the ability to regulate the device controls; thus the developer must ensure that the device development starting with the needs statement is properly documented in the design history file.

After a “final” device design has been settled upon, testing is conducted for confirmation of the design to support a marketing submission to the FDA (see Section 2.4.1 for the various considerations with approaching the FDA). If the device fails at any point in this process it can go back to the development stage to produce a new “final” device design. Device testing is conducted to ensure that good laboratory practice (GLP) is followed, making sure everything is properly documented and all controls are followed. Bench top testing usually leads to animal testing in support of ultimately conducting clinical testing, where good clinical practice (GCP) is followed. If all testing is

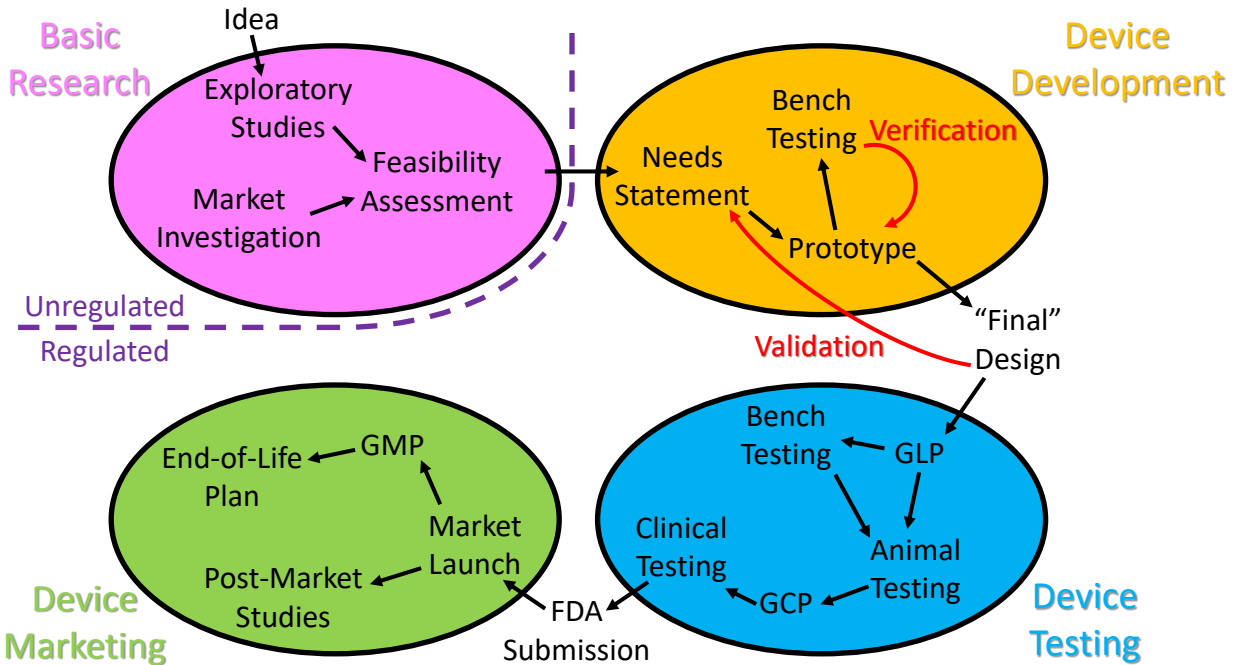


Figure 2.9: Basic Schematic of the Design Life-Cycle for a Medical Device

a success and enough data is acquired to prove the safety and efficacy of the device, a submission to the FDA can be made so that the device can be marketed.

Upon acceptance by the FDA, the device can be marketed. The device can be put into production and distributed to end users. There should be continual monitoring of the device in the form of post-market studies, to ensure that no issues may occur once the device is used on a broader population. Further, good manufacturing practice (GMP) should be followed to ensure a quality device is being produced. Lastly, the end-of-life for the device should be considered, such as final disposal or possible recycling of the device.

The following subsections provide more detail on some aspects of the design life-cycle. The next subsection examines the various types of testing a device will undergo. Other considerations, such as designing a quality system, are then discussed. For specifics on the marketing approval aspects, including further information on the FDA, see the next section, Section 2.4.

2.3.1 Testing Considerations

Testing is crucial to device development, as this is the way to both verify a device is acting as desired as well as validate the device that it meets the need it was created to meet. Testing results are also required as part of any marketing submission to the FDA. Thus testing ensures both the manufacturer and the FDA that the device is safe and effective for its intended use. There are three main tiers of testing: bench top testing, animal testing, and clinical testing. These will each be addressed in the following subsections.

2.3.1.1 Bench Top Testing

Bench top testing is an informal term used to refer to preclinical studies, often even before animal studies are conducted. This can include all testing from initial idea experimentation to pre-GCP studies. These can generally be broken down into prototype testing and pre-GLP validation studies.

Prototype testing is testing done to experiment on the design of a medical device and can include anything from testing in one's garage to large-scale tests to verify and validate a design. The goal of this type of testing is to iterate on the design to achieve a final design that can be consistently and reliably manufactured as well as doing as much as possible to verify that the design meets all of the design criteria. These types of studies are not regulated, thus the FDA is not concerned with them and no records need to be kept from the regulatory standpoint. This is the scope of all testing done in this dissertation.

The next phase of bench top testing is when regulation begins. This is known as pre-GLP testing, where the device design should be stable. Any changes deemed necessary to the design may lead one back to conducting more prototype testing. Pre-GLP testing includes final verification of design aspects as well as holistic design verification. This testing generally supports a submission to an institutional animal care and use committee (IACUC) for subsequent animal testing. In rare cases this may be sufficient for an FDA submission, almost certainly only for a 510(k) submission (see Section 2.4.1.2) where this level of testing was sufficient to prove substantial equivalence to

an existing device.

2.3.1.2 *Animal Testing*

It is often unethical to test a new device directly on a human subject due to the unknown risks associated with the device. Instead, testing is often done first on animals. This can also serve a two-fold purpose, possibly helping the device to be used for veterinary use as an alternative market as well as establishing the safety and efficacy of the device on an animal model before running clinical trials.

All testing done with animals involves getting approval from an institutional animal care and use committee (IACUC). The IACUC will review the study protocol to ensure that it is done in the most ethical and humane manner possible. In particular, the protocol is examined with respect to what is known as the four *R*'s: replacement, reduction, refinement, and re-use. Replacement is to determine if the animal can be replaced with a lower class of animal, such as swapping a vertebrate out for an invertebrate. Reduction is to determine if a statistically significant result can still be obtained using fewer animals. Refinement is to determine if the protocol can be changed to ensure humane treatment of animals while still meeting the endpoints of the study, such as using a different analgesic, rather than not treating the animal for pain. Re-use is to determine if an animal can be used for multiple parts of a study or multiple studies, such as serving as its own control or even rarely using the same animal in multiple studies that have non-conflicting endpoints. In general, animal studies are to support later clinical studies, rather than being sufficient alone for an FDA submission. This is because an animal is not a perfect analog to a human; what works for an animal may not work for a human.

2.3.1.3 *Clinical Testing*

Clinical testing is highly regulated due to a number of abuses over the years, from unethical treatment and experimentation during the Nazi regime in Germany (leading to the Nuremberg Code) to the often cited Tuskegee syphilis study in the US, where patients were not adequately informed of alternative treatments among other abuses. [68] Now the process is wrapped up in what

is called good clinical practice (GCP). GCP includes following a protocol approved by an institutional review board (IRB), getting freely given informed consent, following a study monitoring plan, and properly documenting all aspects of the study. [69] Some of the details here pertain solely to the US, but similar rules are in effect in other countries.

An IRB is an independent body that acts to protect the rights, safety, and well-being of human subjects. They have the power to approve, require modification or disapprove research. They are composed of at least 5 members with diverse backgrounds.

Informed consent is the permission of the study participant. It generally takes physical form in a document that must be provided to study subjects informing them about the study, what treatments will be provided, and any and all risks associated with the treatment. Alternative treatments that they can seek must also be disclosed. The study participants must have adequate time to consider if they want to join the study, understand the informed consent document, and cannot be coerced in their decision about joining the study. Further, the informed consent document must explain that the study participants are not waiving any of their rights by joining the study, nor are the study providers released from any liability. Study participants are allowed to revoke their informed consent at any time during the study. Lastly, a point of contact must be provided if they have any questions or concerns in regards to the study.

To be able to use an unapproved device for a clinical study, the manufacturer has to have permission, in this case via an investigational device exception (IDE) from the FDA. However, if an IRB approves the device as not posing a significant risk an IDE is not required. Some devices are IDE exempt; if they are noninvasive, do not have a high risk sampling procedure, do not introduce energy into the patient, and are not a sole diagnostic for a condition. To file an IDE, a manufacturer should follow design controls, have IRB approval, and properly label the device as unapproved; they are exempt from most other regulations, since the device is not approved yet. However they must monitor the study and ensure all records are kept in case they are audited by the FDA. The FDA evaluates an IDE within 30 days (or it is assumed approved).

2.3.2 Quality System

A quality system, also known as a quality management system, is concerned with ensuring that the quality of the product (a medical device in this case) does not degrade. This is encompassed in ensuring that good manufacturing practices (GMP) are followed, as well as good laboratory practice (GLP) and good clinical practice (GCP) are followed during testing of the device. This system ensures design controls are followed, corrective and preventative actions are taken appropriately, the production is properly followed, and everything is properly documented in case an audit occurs. The end goal of this system is to ensure that the device being manufactured is the same as the device that was approved by the FDA. Though a quality system is not necessarily part of the device development, it must be in place before the device can be marketed, and many aspects are also needed during device testing. Quality systems are enforced by the FDA in the code of federal regulations (CFR) under 21 CFR 820; the European counterpart is ISO 13485, as a medical device specific standard rather than solely relying on ISO 9001, the general quality management system's standard. [70]

2.3.2.1 Good Manufacturing Practices (GMP)

Good manufacturing practices form a system to ensure that the manufacturing process are producing a consistent product. They are to prevent any adulteration in the product; these could be in the form of small deviations in manufacturing equipment adding up to large changes in the end product or even poor hygiene contaminating an otherwise sterile product.

Good manufacturing practice is especially important with additively manufactured parts. Specifically "AM may introduce variability into the manufacturing process that would not be present when using other manufacturing techniques." [71] Special considerations are given to the entire workflow process for AM parts. This includes the design aspect of the device (such as defining tolerance ranges for parts or ensuring the imaging technique used to match a AM device to a patient), the materials used, the build process (how the part is printed), post-processing on a part (such as how a surface finish is applied), and final testing done on the device (to ensure no defects or de-

iciencies exist in the final part). These are challenging especially with patient-matched devices (PMD), that is devices custom designed for an individual patient.

2.3.2.2 Design History File

A file is created for every design even at the research stage that continues into manufacturing, called the design history file. This contains all aspects of the device's design and any changes that have been made to it. Specifically the manufacturer's design history file contains "the records necessary to demonstrate that the design was developed in accordance with the approved design plan and the requirements of this part." [70]

2.3.3 Business & Financial Considerations

It would be remiss to not at least briefly mention the business and financial considerations that go into the device design. The technical side would not exist if the needed financial capital was not being supplied. Often device development is done in small companies, thus venture capital is one of the primary funding mechanisms. In addition protecting the intellectual property of the device is important, usually done through patents.

The primary influence of the business side on the specific design is do decide whether a design will be pursued at all. A useful device without a market will not be developed; there must be a reasonable return on investment to get any device created. Business strategy also becomes involved in determining what sort of approval pathway to use. By selecting a more difficult pathway (e.g. a PMA over a De Novo request, see Section 2.4.1 for details), a precedent is set that can serve as a large barrier to entry for other companies, effectively blocking them from the market. However this means a much harder approval process that requires substantially more time and funding to accomplish, which may be too much for some companies. Without having a patent on the idea, any other company can manufacture the same device, thus there is no protection of the intellectual property. Many investors will not consider a venture unless they are certain there are protections on the intellectual property of the device being developed.

2.4 Medical Device Approval

Creation of a medical device is not sufficient. The device also needs to be marketed to have any significant impact on the health of the community. Different countries approach the process of device regulation in a variety of ways. This dissertation will primarily focus on the US; however there are currently devices being marketed in Europe, which serve as useful examples of how to approach device design.

2.4.1 The Food and Drug Administration (FDA)

The United States Food and Drug Administration (FDA) “is responsible for protecting the public health by ensuring the safety, efficacy, and security of human and veterinary drugs, biological products, and medical devices; and by ensuring the safety of our nation’s food supply, cosmetics, and products that emit radiation... FDA is responsible for advancing the public health by helping to speed innovations that make medical products more effective, safer, and more affordable and by helping the public get the accurate, science-based information they need to use medical products and foods to maintain and improve their health.” [72] Thus all medical devices must have either FDA clearance or approval in order to be sold as such.

The FDA was established in 1930 in response to the growing concern of unsafe products on the market in the US.³ Its authority and scope have grown since, starting with the 1938 Federal Food, Drug, and Cosmetic Act (FFDCA). It grew to cover responsible device manufacturing (added in 1976 as the Medical Device Amendment to the FFDCA), including the design for devices (added in 1990 under the Safe Medical Device Act).

The FDA classifies a medical device as “an instrument, apparatus, implement, machine, contrivance, implant, in vitro reagent, or other similar or related article, including any component, part, or accessory, which is

1. recognized in the official National Formulary, or the United States Pharmacopeia, or any supplement to them,

³The duties of the FDA, however, have existed under control of a differently named regulatory body since at least 1906 with the passage of the Pure Food and Drugs Act.

2. intended for use in the diagnosis of disease or other conditions, or in the cure, mitigation, treatment, or prevention of disease, in man or other animals, or
3. intended to affect the structure or any function of the body of man or other animals, and

which does not achieve its primary intended purposes through chemical action within or on the body of man or other animals and which is not dependent upon being metabolized for the achievement of its primary intended purposes.” [73] A device stands in contrast to a drug (chemical action) and a biologic.

Devices are classified as Class I, Class II, or Class III devices, where higher classes receive more scrutiny and restrictions. All previously approved devices have a product classification in the FDA regulations that can be consulted, which lists the device class and approval method. Especially for new devices, the manufacturer should first undergo a risk assessment of their device to determine the appropriate classification before approaching the FDA. In general any CAP device will most likely be a Class II device, since this class requires special controls to ensure safety but is not a high risk (e.g. life-sustaining) device. These special controls can be as simple as including special labeling (e.g. high voltage warnings) or as complex as following a performance standard established by some regulating body (such IEEE, ASME, etc.). [74] Since nearly any CAP device will require high voltage to operate, there will be some form of special controls required to ensure safety. These special controls are beyond the nine general controls for devices (not adulterating the product, not misbranding, registering and listing the device, following the relevant premarket notification, not marketing a banned device, notifying of device changes, keeping all relevant records and reports, restricting the use of the device as needed, and following good manufacturing practices). [75]

There are three main pathways for approaching the FDA with a medical device: premarket approval (PMA), 510(k) clearance, and a De Novo request. These will be discussed in some detail in the next subsections, along with other lesser known mechanisms for device marketing and related considerations. The basic process for classifying these devices and determining the appropriate pathway is shown in Figure 2.10.

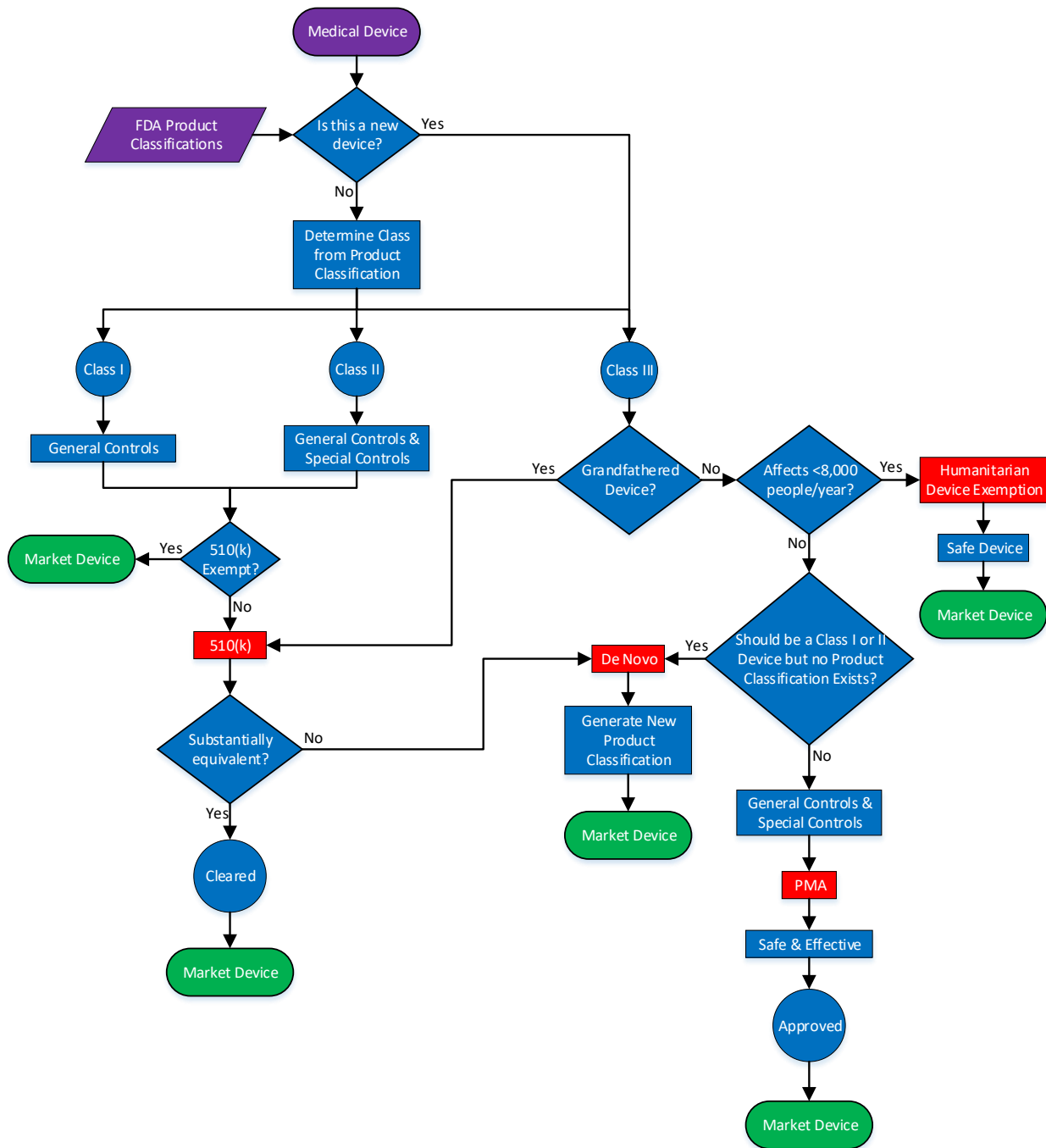


Figure 2.10: Basic Flowchart for Approaching the FDA with a Medical Device

2.4.1.1 *Premarket Approval (PMA)*

The FDA only *approves* devices that go through the premarket approval (PMA) pathway, which is the default pathway for a device. A PMA⁴ is required for nearly all Class III devices. If a device does not have a class because it is a new device it is automatically assigned a Class III designation. “PMA approval is based on a determination by FDA that the PMA contains sufficient valid scientific evidence to assure that the device is safe and effective for its intended use(s).” [76] Since the PMA must prove the device is safe and effective it often requires years of clinical trials to support this, making this a very time-consuming and expensive process. It does not help that a PMA submission to the FDA carries a price tag of \$340,995. [77] Average development costs to the manufacturer though are substantially higher, averaging \$94 million. [78]

An older version of the FDA’s PMA website [76] also mentioned that “an approved PMA is, in effect, a private license granting the applicant (or owner) permission to market the device.” This is one advantage of a PMA for a company—it is a large barrier to entry for any competitors, since they must also go through this approval pathway for their device. A competitor’s only alternative is to petition the FDA to reclassify the device into a lower risk class (via a process called 513(e) from its location in the act establishing the FDA), which can take up to years to finally get approved through the system. However, this can also have the unintended side effect for devices that are later deemed “safe” (via the 513(e) process) and do not warrant this approval pathway. The company that initially went through the effort to get the device approved opened the door for other companies to use a 510(k) clearance for their devices, greatly reducing a competitor’s barrier to entry in the market. As a result the FDA may have unintentionally stifled innovation for new “safe” medical devices until creating the De Novo pathway.

⁴Though technically the term *PMA* refers to the final granting of approval by the FDA, this term is applied to the submission and process, as well. It is often done without regard to the meaning of the acronym, too.

2.4.1.2 510(k)

Under the 510(k) pathway⁵, also called a premarket notification, a device is not *approved*, rather it is *cleared* by the FDA. This is because the device is compared to an existing device called the predicate device. The device must demonstrate substantial equivalence to the existing device. To be substantially equivalent the new device must have:

1. The same intended use as the predicate and
- 2a. The same technological characteristics of the predicate or
- 2b. Different technological characteristics that do not raise new questions of safety and effectiveness as well as being at least as safe and effective as the predicate device. [79]

This is often used for small modifications to an existing device. As such, it is the least difficult pathway, with the smallest submission cost (only \$11,594 [77]) and the shortest review time of 90 days. Nevertheless, the total development costs average \$31 million. [78]

Generally 510(k) clearances are for Class I or Class II devices; however, rarely Class III devices that have been grandfathered into the regulations (i.e. existed before these regulations were implemented) and have not been reassigned into a lower class or explicitly required to use a PMA pathway can also use this pathway for marketing approval. This is not necessarily a straightforward pathway as no CAP device is currently on the market for use as a predicate device; thus any predicate device will have different technological characteristics of the predicate device. Care must then be taken to ensure the most appropriate predicate is chosen and sufficient testing is done to show there are no new questions on the safety or efficacy of the device.

2.4.1.3 De Novo

Since a PMA is a very burdensome pathway for a new device without a predicate, a third pathway was introduced and is becoming more popular called the De Novo pathway. When it was first introduced, it was only a viable option after a 510(k) submission was rejected as not being

⁵This pathway is named from section 510(k) of the Food, Drug, and Cosmetic Act.

substantially equivalent. It was only later created as a new option as a direct De Novo request for a new device. However, in so doing, the price has increased to \$102,299. [77] An older version of the FDA's website [80] read "The de novo process provides a pathway to classify a low to moderate risk device for which general controls or general and special controls provide reasonable assurance of safety and effectiveness, but for which there is no legally marketed predicate device. De novo is a risk-based and evidence-based classification process. Devices that are classified into Class I or Class II through the de novo process may be marketed and used as predicates for future premarket notification [510(k)] submissions."⁶ The De Novo pathway serves as an intermediate pathway between the PMA and 510(k) for devices that have no predicate, making it a viable option for many CAP systems.

2.4.1.4 *510(k) Exempt Devices*

Some devices pose a low enough risk they do not require a 510(k) for marketing. [81] These are generally Class I devices, but a few Class II devices (i.e. low risk devices that still require special controls) are considered low enough risk to not require a 510(k), such as mercury thermometers. [82] Due to the possible shock hazard with any plasma device, it will never be deemed a 510(k) exempt device; however, it may assist in creating medical devices that are 510(k) exempt devices, such as prosthetics, [83] as discussed in Chapter 7.

2.4.1.5 *Humanitarian Device Exception*

Certain conditions are rare, defined as affecting under 8,000 people per year. For these cases, a humanitarian device exception (HDE) can be made that has to only show that it is safe at treating the condition, rather than the safe and effective requirement for a PMA. [84] The device will then be designated as a humanitarian use device (HUD). This is done so that device developers can create and market devices to treat these rare conditions without having to go through the same rigorous testing of a PMA. This would be especially difficult in patient recruitment for clinical studies. This is often used to get a device to market quicker for a condition that has a subset condition that affects

⁶In more recent publications the FDA has decided to capitalize the words *De Novo*, which is how this dissertation will treat the term.

fewer people. This allows a company to market a device, as well as collecting some useful clinical data, and begin making a small profit before expanding to a wider condition. This may be a useful strategy for certain conditions that a CAP could treat, such as certain types of wounds that cannot be treated by conventional methods.

2.4.1.6 Custom Device Exception

The custom device exemption allows only 5 units per year to be manufactured and is thus not a viable option for marketing a device. [85] Instead it is useful for devices that will only rarely be needed, such as changing the size of a device to accommodate a patient who is greatly different in size than the average population. Unless there is a medical use found for a CAP device that affects such a small population, this is generally not worth pursuing. Note that a device that is additively manufactured to meet the custom needs of a patient would not be considered under this exemption. [71]

2.4.1.7 Combination Products

A “combination product [is]

- A product comprised of two or more regulated components, i.e. drug/device, biologic/device, drug/biologic, or drug/device/biologic, that are physically, chemically, or otherwise combined or mixed and produced as a single entity (a ‘single entity’ combination product, such as a prefilled syringe or drug-eluting stent);
- Two or more separate products packaged together in a single package or as a unit and comprised of drug and device products, device and biological products, or biological and drug products (a ‘co-packaged’ combination product, such as a surgical or first-aid kit containing bandages and an antiseptic drug);
- A drug, device, or biological product packaged separately that according to its investigational plan or proposed labeling is intended for use only with an approved, individually specified drug, device, or biological product where both are required to achieve the intended

use, indication, or effect and where upon approval of the proposed product the labeling of the approved product would need to be changed (e.g., to reflect a change in intended use, dosage form, strength, route of administration, or significant change in dose) (a ‘cross-labeled’ combination product, as might be the case for a light-emitting device and a light-activated drug indicated for use together for treatment of a dermatologic condition); or

- Any investigational drug, device, or biological product packaged separately that according to its proposed labeling is for use only with another individually specified investigational drug, device, or biological product where both are required to achieve the intended use, indication, or effect (also a ‘cross-labeled’ combination product)

A combination product is assigned to an Agency Center that will have primary jurisdiction (i.e., ‘the lead’) for that combination product’s premarket review and regulation.” [86] As such, a combination product may be approved via a drug or biologic pathway even though it is *primarily* a device. Nevertheless, a combination product will go through the same rigorous treatment as if it were both a device and drug/biologic separately. In addition, any issues with the combination will also be evaluated. In general, a 510(k) clearance will only be given if the predicate is also a combination device.

This approach may be significant for a number of devices considered here. Particularly, the electroporation system considered in Chapter 4 would most likely be combined with a specific drug for uptake, which would most likely be considered a device-drug combination product. This would even be the case for an electrochemotherapy system involving a known and approved chemotherapy drug, such as bleomycin.

2.4.1.8 *Emergency Use Authorization (EUA)*

This is not an approval pathway but warrants a brief mention as this is a means that a low temperature device may be used in a clinical setting.⁷ In the event of an emergency declared by

⁷At the time of the writing of this dissertation the disease COVID-19 has become a worldwide pandemic. It is conceivable that a plasma-based device could be used either directly for sterilization, indirectly for ozone generation (which our lab is currently investigating as a fabric sterilization method), or some other means to help combat this viral spread, hence the brief treatment in this dissertation.

the Secretary of Homeland Security, Secretary of Defense, the Secretary of Health and Human Services, or the Secretary of Homeland Security the FDA has the authority to allow unapproved devices to be marketed to combat the emergency situation. The FDA does this by issuing an emergency use authorization (EUA) for a specific device after evaluating it. The EUA will expire either when the emergency ends, at which time the device can no longer be legally marketed, or if the approval status of the device changes, such as a device receiving a PMA during the emergency. [87]

For an EUA to be issued, the following criteria must be met:

1. A serious or life-threatening disease or condition exists,
2. There is evidence for effectiveness of the treatment,
3. The benefits outweigh the risks, and
4. There are no alternatives (at least that adequately meet the demand).

As such, when submitting a request for an EUA, a manufacturer should address at least the following in the submission:

- Product description with intended use, explaining which emergency and need this product will satisfy,
- Current FDA approval status (especially useful if extending the use of an already approved product),
- The need for the product, noting any alternatives and the availability of those alternatives (especially useful when alternatives exist but cannot meet the demand),⁸
- Safety and efficacy data on the product so that the FDA can evaluate the device,

⁸This occurred for the COVID-19 pandemic for personal protective equipment (PPE) and ventilators where the demand was much higher than the supply of these products.

- A risk-benefit discussion to determine if the known risks will outweigh the benefits of using this device,
- Details on the chemistry, manufacturing (including location and quantity that can be produced), and controls of the device, and
- Any instructions for use and all appropriate labelling to determine if this is sufficient for providers to understand and follow proper use of the device.

The FDA will do a review of the device, but it is not as thorough as a review done for an actual submission (such as a 510(k), PMA, or De Novo). This is because the FDA is trying to quickly get the device out to meet the emergency need; thus time is critical. A manufacturer can submit an EUA even before an emergency occurs; this is called a pre-EUA. The FDA can conduct most of the evaluation before the emergency occurs, allowing the EUA to be granted possibly within hours of an actual emergency being declared.

2.4.2 Other Countries

The US is the largest single market for medical devices, but there are a number of other important locations to consider. It can be advantageous for a company to approach multiple markets in hopes of receiving faster approvals and having an income stream while approaching another market. Often as well, studies can be conducted that will be used in multiple submissions for multiple countries, thus greatly saving costs for the company.

The standard for Europe (specifically the European Economic Area, consisting of the European Union, Iceland, Liechtenstein, and Norway, as well as Switzerland, Turkey, and the United Kingdom⁹) is the CE marking. [89] Each country has their own competent authority who ensures the medical device directives developed in common between the various countries is included in national law. The competent authorities designate notified bodies that act as third party assessors of the manufacturer's compliance with all relevant regulations.

⁹This includes the United Kingdom until at least January 1, 2021 pending any further changes as they fully transition out of the European Union (i.e. Brexit) [88]

Manufacturers determine the class of their device, and ensure they follow all relevant regulations, including developing a design dossier for the device as part of a quality management system per ISO 13485 (standard developed by the International Organization for Standardization). All relevant information is submitted to a notified body for certification before they can manufacture the device. Upon certification by the notified body, the manufacturer may apply the CE marking on their device, often with the number of the certifying notified body included. The manufacture, however, must still register with the competent authority in the country they are marketing the device. Post-marketing surveillance and monitoring is conducted to monitor the safety and efficacy of the device. [90,91] However, approval is often easier and quicker because the approval is based on safety and performance, rather than safety and efficacy, which is required for the US FDA. [66]

Japan is the second largest medical device market in the world, yet a challenging market due to language barriers in addition to a more rigorous approval system compared to some countries. [92] Like many other systems, Japan uses a risk-based assessment of devices, separating high and low risk devices. High risk devices require review by the Pharmaceutical Medical Devices Agency (PMDA); while low risk devices can have third party certification. [92] Ultimately the Ministry of Health, Labor, and Welfare (MHLW) has the final judgment in device approval. [93] Clinical trials are required for new or improved medical devices, often required to take place in Japan. [94]

Though there are some differences, most countries' approvals are done with a risk-based approach, allowing low risk devices to be approved easily, with more stringent requirements as the risk of using the device increases. Focus is increasingly being placed on quality management systems with standards such as ISO 13485, 21 CFR Part 820, or similar ones being developed in various countries. Further harmonization is expected as countries attempt to adapt their local policies to align with those of other countries. [95]

2.5 Low Temperature Plasma Medicine

Low temperature plasma medicine is a quickly growing field, with many publications that could be reviewed. This section is divided into three subsections with limits placed on the included sources to avoid this section from becoming too large. The first section deals with the

potential medical uses for low temperature plasmas. Only studies with relevant clinical studies, animal studies, or human cell lines are included. This excludes plasma sterilization of surfaces and bacterial inactivation as well as many computational studies. The second section attempts to find all devices that are currently marketed or are being developed for use as a marketed device. However, due to the ability for plasma devices to quickly be marketed in less-regulated countries, the investigated devices are limited to those being developed in the US and those with a CE marking or a number of journal articles for non-US devices. The third section examines the standards that are being developed for these types of systems. The broad standards that apply to many types of devices are briefly mentioned; the focus is given on the only plasma-specific standard, currently issued in Germany.

2.5.1 Medical Uses of Low Temperature Plasmas

Though high temperature plasmas have been in use by the medical community since 1926 when the first electrosurgery took place, [4] cold plasmas for direct medical use (as opposed to sterilization of equipment such as autoclaves) is a much more recent development. This began with efforts to use atmospheric pressure plasma for sterilization of surfaces, which then led to interest in wound sterilization; further effects were also discovered, such as enhancing phagocytosis and inducing apoptosis. [5] This led to the creation of the field of plasma medicine, the common name applied primarily to low temperature atmospheric pressure plasma use for medicinal effects. Though high temperature plasmas, such as electrosurgical devices, and lower pressure plasmas, such as some ethylene oxide sterilization units, can have medicinal benefits, they are generally not included under the term “plasma medicine”. [96]

Plasmas have been noted to have a diverse number of effects including killing microorganisms, inactivation of mammalian cells based on dose/time (senescence to apoptosis to necrosis), stimulating microorganism metabolism, detaching cells from matrices, modifying cell migration, changing cell surface proteins, stimulating cell proliferation and angiogenesis, and permeabilizing cells. These diverse effects are achieved by the high electric fields that create radical species in the plasma and are also achieved by the chemistry initiated by the plasma in the environment of the

cell, which is often a liquid. [96,97] As such, plasma-liquid interactions is also a growing field of study that also has relevance in the plasma medicine community.

This section is divided into four subsections. The first subsection will explore the mechanisms of plasma interaction with tissues. This forms the basis for the medical applications discussed in the following subsections. Then the following two subsections discuss the two main low temperature plasma applications: wound treatment and cancer treatment. A final subsection will discuss other applications. Any relevant studies using a specific marketed plasma device will be discussed in the next section rather than in the subsections below.

2.5.1.1 Plasma-Tissue Interaction Mechanisms

As previously discussed in Section 2.2.3, there are diverse effects of plasma on materials. The influence of the electric field on tissues, the main effect being electroporation (also called cell permeabilization), will be discussed in Section 4.2. Like other substrates, biological substrates can also be heated by the dissipation of the currents caused by the electric fields. The gas temperature, however, appears to only scale with average power for a plasma discharge. [98] However, the discharge current can also pose a hazard for electrical shock [99] but are often kept near or below the perception threshold for a patient and thus are far from risking loss of muscle control or shock. This can also be minimized by using a different electrode configuration, such as a those with a ground electrode that receives the majority of the current. [41]

UV light is often broken into three types based on wavelength: UVA (320–400 nm), UVB (290–320 nm), and UVC (200–290 nm) with differing effects for the different ranges. UVA is used by the body to regulate hormones. UVB can help with the synthesis of vitamin D. UVC can cause oxidative damage to lipids, proteins, and DNA, particularly with thymine and cytosine in DNA. [41] This is the main mechanism for UV sterilization. In general short term, low intensity exposure is safe, but longer exposure accumulates the amount of damage that occurs until a cell no longer becomes viable. However, since most plasma treatment uses low powers for short times, the UV light generated by plasmas is assumed to have negligible biological effect; other mechanisms dominate. [40] This has generally been proven true by insertion of a UV transparent medium

between the plasma and the substrate leading to know effect; however this also removes possible synergistic reactions involving UV light with other plasma effects. [100]

The dominant mechanisms involved in plasma medicine are based on the radical species that are generated, generally plasma generated radical gas species that are termed reactive oxygen and nitrogen species (RONS). The reactive oxygen species include ozone (O_3), hydrogen peroxide (H_2O_2), superoxide (O_2^-), singlet oxygen ($^1\Delta_g O_2$), and the hydroxyl radical (OH); reactive nitrogen species include nitric oxide (NO), nitrite (NO_2^-), and nitrate (NO_3^-). All of these radicals participate in an extensive number of biochemical reactions, such as modifying proteins and lipids and signaling molecules in immunoresponse mechanisms. [41, 57] However, these species may not directly cause these diverse biochemical responses; rather they initiate a series of chemical reactions that ultimately lead to these responses. These reactions predominantly take place in the liquid medium that the cells are in making characterization difficult. [40, 96, 100]

Most studies have shown that low doses of plasma (typically defined as low power density, $\sim 1 J/cm^2$, and shorter treatments, ~ 1 min, note that time of treatment is the most common way to increase the dose) have beneficial effects on cells, such as inactivation of bacteria while not affecting the human cells. Higher doses ($\sim 5 J/cm^2$) can cause some more serious but potentially beneficial effects, such as inducing apoptosis and repairable DNA damage, while some cases of cell proliferation have also been observed. Even higher doses ($\sim 10 J/cm^2$) can cause cell death and necrosis. [40, 57, 97, 100] These are described in more detail in Section 2.5.1.3 However, similar plasma sources can generate a wide range of species and other effects, leading to very different treatment results, thus careful investigation of each device is required. [101] This can also be exacerbated by small changes in setup, such as the well size or depth for cell treatments, affecting the results due to complex plasma-substrate interactions. [102]

2.5.1.2 Wound Treatment

There are two main goals with wound treatment using plasmas. The first is to inactivate any bacteria and possible biofilm that has built up in the wound preventing the body from healing properly. This is viable because bacteria have been shown to have a lower tolerance for plasma

treatment than human cells. [103] The second is to stimulate the body's immune system and encourage cell proliferation to heal the wound. [40] The relevant research on these two topics is discussed in this section. Clinical trials are discussed in Section 2.5.2, as nearly all of them have been to support CE marking for one of the devices discussed in that section.

Perhaps the greatest asset for plasma wound treatment is in biofilms, which are often a challenge to disinfect using conventional methods. There is disagreement in the literature as to whether gram-negative or gram-positive bacteria are more susceptible; this is most likely dependent upon the plasma source used. [104, 105]

One of the earliest studies on directly treating skin with a plasma used a floating electrode dielectric barrier discharge (FE-DBD), which used the skin as the second electrode in the circuit. This showed that direct low temperature plasma treatment was possible on a live patient. [106] The FE-DBD was shown to have skin damage (tested using live pig models) associated with dose rate (frequency of the discharge), which increases the gas temperature, as well as dose (input power); nevertheless, the damage to the skin occurs at a dose substantially larger than the dose that was found to inactivate bacteria (<2 min at 0.17 W/cm²). [107, 108]

However, plasma treatment has been effective in faster healing rates than conventional treatments. [104] The exact mechanisms are not understood but there are a number of theories. Nitric oxide (NO) therapy is an FDA approved therapy for vasodilation. As plasmas can produce NO some of the improved healing could be due to increased blood flow to the wounded region. [109] Growth factor proteins and genes can be stimulated, but the exact mechanism is not understood. [110–112] Angiogenesis has also been noted as a result of plasma treatment. [97, 113]

Further testing has been conducted on mice models using a different plasma source. Increased blood flow and faster wound closure was noted over three weeks with mice having an argon jet plasma treatment only on the initial day of the wound and even more for those with plasma treatments for the first three days. No mention was given of possible bacterial infection on the wounds. The authors imply the increased NO exposure from the plasma treatment is the mechanism but no control with NO therapy was given. [114] Using a similar treatment with an argon plasma, another

group also found improved healing over the course of 15 days for mice with plasma treatment. In this case, a 1 min plasma treatment was given daily over the course of the experiment. They noted higher amounts of growth factor hormones present in the mice with the plasma treatment. Though no bacterial load was intentionally added in the treatment, it was monitored; a statistically lower microbial load was only noted for days 3–7. [115]

Not every study has been completely positive. Using a plasma jet in a similar configuration as the kINPen (Section 2.5.2.1) on corneal injury induced in rabbits, CAP had no effect on wound healing. This was a small study with only 12 rabbits (5 in the treatment group) and the only study treating corneal injury. It is unclear if the eye behaves differently from wound on other parts of the body. Nevertheless, the treatment did not have any negative side effects; it simply yielded no better results compared to the control. [116]

It is worth noting that the optimal conditions for bacterial inactivation and accelerated wound healing may not be the same. For example, comparing the same plasma jet in a contact and non-contact mode by changing the distance between the plasma jet and the treated substrate yielded different results for bacterial inactivation and wound healing. [117] The contact mode was better at inactivating bacteria than the non-contact mode. The non-contact mode was better at wound healing; the contact mode was actually significantly worse than the control for wound healing, having a visibly larger wound even after 14 days. Thus the plasma treatment needs to be tailored for the specific treatment desired.

2.5.1.3 Cancer Treatment & Cell Death

Various amounts of plasma treatment can induce effects from senescence (stoppage of cell growth) to apoptosis (programmed cell death or “cellular suicide” [118]) to necrosis (cell death not undergoing a highly controlled programmed cell death). [96, 119] In addition, plasma treatment can stimulate the immune system possibly leading to induction of immunogenic cell death. [120] The mechanism is perhaps similar to that described in the previous section (Section 2.5.1.2) for stimulating the immune system for wound healing. The plasma treatment can also act synergistically with other treatments, such as nanoparticles. [121, 122]

The main advantage of plasma treatment is the selectivity of targeting and killing cancer cells rather than healthy cells. It achieves this by “by interfering with the mitotic cell cycle and inducing cell cycle arrest, DNA damage, and apoptosis via ATM [ataxia-telangiectasia mutated, a protein] expression and phosphorylation of p53” among other possible mechanisms yet to be explored. [6] For example, using a helium plasma jet for 90–120 s yielded at least 50% cell death for three glioma (cancer) cell lines with negligible cell death for healthy endothelial cells. [123] This has also been shown to kill a variety of types of cancer. [124]

In an attempt to determine the mechanism of cell death, a number of studies have been conducted. Using a shroud (or shielding) gas flow of either N₂ or air with an argon plasma jet, it was shown that oxygen chemistry is the dominant factor in viability of human immune cells. This was ascribed to H₂O₂, but further research is needed to adequately determine the mechanism. [125] Quantifying the amount of H₂O₂, NO₂⁻, and NO₃⁻ in a solution exposed to a helium plasma jet allowed for comparison of the viability of human fibroblasts to the plasma and solutions of those various chemicals. It was found that a synergistic combination of both H₂O₂ and NO₂⁻ yields comparable loss of viable cells. [126] Similar results were found with an argon plasma jet on human glioma cells, where a synergistic effect of both H₂O₂ and NO₂⁻ were required to have substantial cell death; however the corresponding amounts of those two species as those measured in the plasma activated medium had a lower effect compared to the plasma, suggesting other effects are also present to fully explain the loss of cell viability. In addition, healthy, non-cancerous mammary epithelial cells remained viable despite the plasma treatment or H₂O₂ and NO₂⁻ addition, showing good selectivity in the treatment for cancer cells. [127]

Using a nanosecond pulsed FE-DBD, it was shown that murine mesenchymal stem cells are no longer viable after increasing the energy delivered to the cells (higher frequency with the same energy per pulse, applied voltage, and treatment time). This same experiment was run attempting to exclude other plasma aspects to determine the mechanism. Running in an oxygen atmosphere yielded lower cell viability compared to air, while a nitrogen atmosphere showed no loss in cell viability; this also supports the conclusion that radical oxygen species are a main contributor to

cell death. Longer-lived species were exposed to the cells by using a copper mesh as a ground electrode (i.e. no longer a FD-DBD system) which showed some loss in cell viability but not as much as by using the FD-DBD for a more direct plasma treatment. The electric field (using a stronger dielectric to avoid plasma formation) and UV light (using quartz glass to shield the cells from the plasma) did not cause any loss in cell viability, although synergistic effects with these may yield more significant effects. A final condition with a larger gap distance was used to create a less uniform discharge with streamers present; lower cell viability was noted but most conditions were not statistically significant from the uniform case, suggesting the plasma chemistry is perhaps slightly more favorable in the streamers for creating the reactive species that resulted in cell death. [128] These results also appear to be consistent with other results for a longer pulse duration, which also measured the damage to DNA occurring as a result of direct plasma treatment but not indirect (using a grounded mesh or treating the medium and then plating the cells). [129] It was also shown with testing on melanoma cancer cells that the effect of inducing apoptosis in the cancerous cells is not based on a poisoning of the growth medium the cells were placed in but by direct action of the plasma. [130]

Electroporation has also been used as a method for killing cancer cells, in particular irreversible electroporation in which the pores induced by the high electric fields do not close leading to cell death. There is also a possibility that irreversible electroporation works in combination with the reactive species generated by the plasma. [131] Electroporation is discussed further in Section 4.2, with a focus on reversible electroporation.

2.5.1.4 Other Applications

Plasma treatment has a number of other applications. One of the first noted was blood coagulation, in addition to cauterization that occurs with “hot” plasma treatment (see Section 5.2). [100, 106] Electric fields, heating, calcium ion (Ca^{2+}), pH changes, and albumin modification were all excluded as the primary mechanism for this effect. The only mechanism that was found was direct conversion of fibrinogen into fibrin, although further mechanisms are expected to be significant as well. [132] This may be similar to other effects of cell mobility that have been noted, where cells

can detach from the extracellular matrix they are held in due to plasma treatment. [6]

Another field with extensive research is plasma dentistry. This is related to plasma sterilization, where bacteria can be inactivated and biofilms can be broken down by the plasma. [133] Plasma jets can be scaled down to even fit in small areas for use in root canal surgeries. [134] Plasma can also functionalize dentin to help with bonding implants to teeth. [135] It can also be used to whiten teeth as a plasma discharge can produce some of the same chemical compounds used to bleach teeth. [135]

Plasma activated media is another novel field, where the plasma interacts with a medium which is then transferred to cells for an effect remote from the plasma. This has been shown to have an antibacterial effect dependent upon the medium used. [55] Anti-cancer media have also been investigated, where the concentration of H_2O_2 was noted to change with various media for different storage conditions. This led to cell death 3 days after plasma treatment for certain media, noting that two amino acids, cysteine and methionine, were reduced apparently by the H_2O_2 in the stored plasma treated medium. [136]

Plasma could also be used in a system to clean hands for basic hygiene. A possible system was developed and shown to inactivate bacteria in a little as 5 s, leading to a possible use to supplement conventional hand washing or use of hand sanitizer. [137] Surface DBDs also can be used for either hand cleaning or surface sterilization as an atmospheric pressure, ambient temperature equivalent to an autoclave. [138]

2.5.2 Development of Low Temperature Plasma Devices

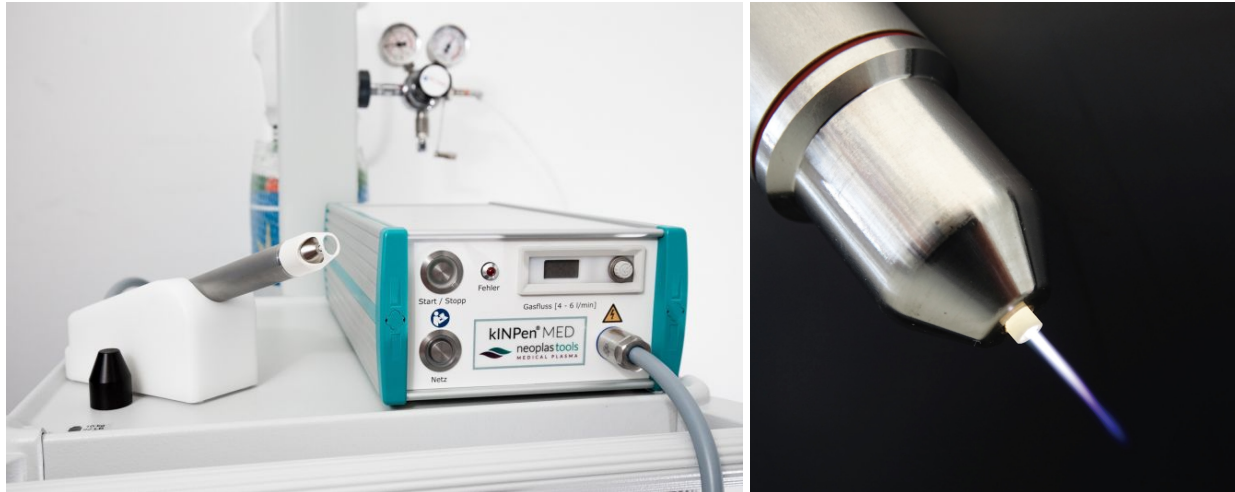
A variety of plasma devices have been used for biomedical applications. They are often divided into three general categories based on their electrode configuration: direct, indirect, and hybrid. [6] Direct devices use the body as one of the electrodes, as done in the PlasmaDerm, Drexel University's FE-DBD [106] or FE-DBD jet (used in Chapter 6). Indirect devices have both the high voltage and ground electrodes far from the patient, with gas flow carrying the plasma generated species to the treatment location, such as the MicroPlaSter or the kINPen MED. Hybrid devices have a ground electrode taking the majority of the current, but small currents may still pass through

the patient, such as the plasma care, a surface DBD. [6, 139] Despite the wide variety of devices being used in laboratory and research settings, very few are being developed as marketed devices, which is the primary focus of this section.

Unfortunately, most device development occurs in-house and does not become public knowledge, so for many of these devices there is limited information available. Fortunately five devices, which have all now also been approved for medical use in Germany (i.e. received a CE marking), [96, 140, 141] are being developed in close collaboration with universities. As such, there are a number of published studies on these devices. Numerous clinical studies have been done using them and have found that they are effective for healing chronic wounds, [142–144] have antibacterial effects, [145] and even reduce pain. [146] No device is currently approved by the FDA for use in the US; however one device has been used twice under the FDA's rule as a Compassionate Use Exemption for inoperable colon [147] and pancreatic [148] cancer and has started clinical trials. [149]

A number of devices are excluded, since they do not generate a cold plasma, per se. For example, the Plason, which uses an arc discharge to generate a high concentration of NO from atmospheric air, which is then quenched to reduce the temperature of the resulting NO-containing gaseous jet. [150] This is a common device used for NO therapy to help accelerate wound healing, where the concentration of NO can be regulated by the distance from the arc generating it. [109, 151] Other systems, such as electrosurgical systems that can be modified to generate a cold plasma, are discussed in Chapter 5.

The following subsections will examine each of the five devices that have currently received a CE marking in Germany: the kINPen MED, the PlasmaDerm, the MicroPlaSter, the plasma care, and the Plasma ONE, focusing on the characterization and development of these devices. A final subsection will investigate the various devices that are being developed in the US for FDA approval as well as other notable devices.



(a) Entire System

(b) Jet Head

Figure 2.11: Image of the kINPen MED (Reproduced under Fair Use from [154])

2.5.2.1 *The kINPen MED*

The most investigated low temperature plasma device is the kINPen MED¹⁰ developed by the Leibniz Institute for Plasma Science and Technology (INP Greifswald) and consequently spun off to into a company called neoplas tools GmbH. An image of the device is shown in Figure 2.11. It was the first low temperature plasma device to receive a CE marking in May 2013 for local treatment of chronic or infected wounds. [96] The kINPen MED is a direct radio frequency (1 MHz) argon plasma jet (see Figure 2.4), although small admixtures of other gases have also been explored to tailor the chemistry. For example, small admixtures of air greatly increase the amount of NO in the resulting effluent. [33,40] In addition, the kINPen MED is the instigation of the DIN-SPEC 91315 for low temperature plasma medical devices (Section 2.5.3). [153] As such, this device has been well characterized in regards to temperature and thermal output, light and gaseous emissions, current characteristics, inactivation of microorganisms, and effect on human cells. Further iterations on the kINPen MED are also under development. [33]

The kINPen MED has been studied extensively in vitro and ex vivo. [33,56,101,105,140,155–

¹⁰This device has undergone many iterations, where the medical device has limited controls compared to the research variations. The medical device is based off of the kINPen09. [33,152]

161] These studies have examined the resulting species generated by the plasma, [56, 101, 156, 158–160], bacterial inactivation, [105, 155, 157] and the toxicity of the plasma treatment to human cells. [56, 101, 140, 156, 158, 161] Overall, the kINPen MED has shown itself to be safe for human cells while still able to inactivate a variety of bacteria. The main complaint has been the small size of the kINPen MED jet, which requires significant time to treat a large area.

A number of clinical studies have been conducted with the kINPen MED. Initial studies investigated the biocompatibility of the plasma with skin. [162] Combining plasma treatment with conventional treatment of wounds with the antiseptic octenidine dihydrochloride yielded lower bacterial loads than either individually; plasma treatment and octenidine dihydrochloride were comparable to each other. [144] A number of trials on cancer patients have also been conducted. Plasma treatment on advanced squamous cell carcinoma was shown to reduce pain, lower microbial load, help with tumor shrinkage, and assist with wound healing. [146] Apoptosis of cancer cells was detected in patients with advanced head and neck cancer, reducing the size of the tumor. [163] A small study of two patients showed increased microcirculation as a result of plasma treatment, but due to the small size no conclusive results can be determined. [164]

2.5.2.2 *The PlasmaDerm*

The PlasmaDerm by Cinogy GmbH was the first FE-DBD device to receive a CE marking in 2013 (shown in Figure 2.12). [165] Initial tests showed it was successful at inactivating a number of bacteria in vitro, [155] including a range of difficult to kill species, such as methicillin-resistant *Staphylococcus aureus* (MRSA). [105] It was also well characterized to show it as a safe device, without producing unsafe levels of reactive species, introducing excessive current into the substrate, or damaging ex vivo skin samples. [166] A small clinical study was conducted on reducing the bacterial load in chronic wounds from 14 patients. [145] Patients received a 45 s/cm² treatment three times per week for eight weeks in addition to standard care. There was a significant reduction in bacterial load, but not a significant reduction in the size of the wound. Overall patients mentioned less pain with the plasma treatment as well. Further work is ongoing to elucidate the mechanisms of bacterial reduction and effects on human cells. [167]



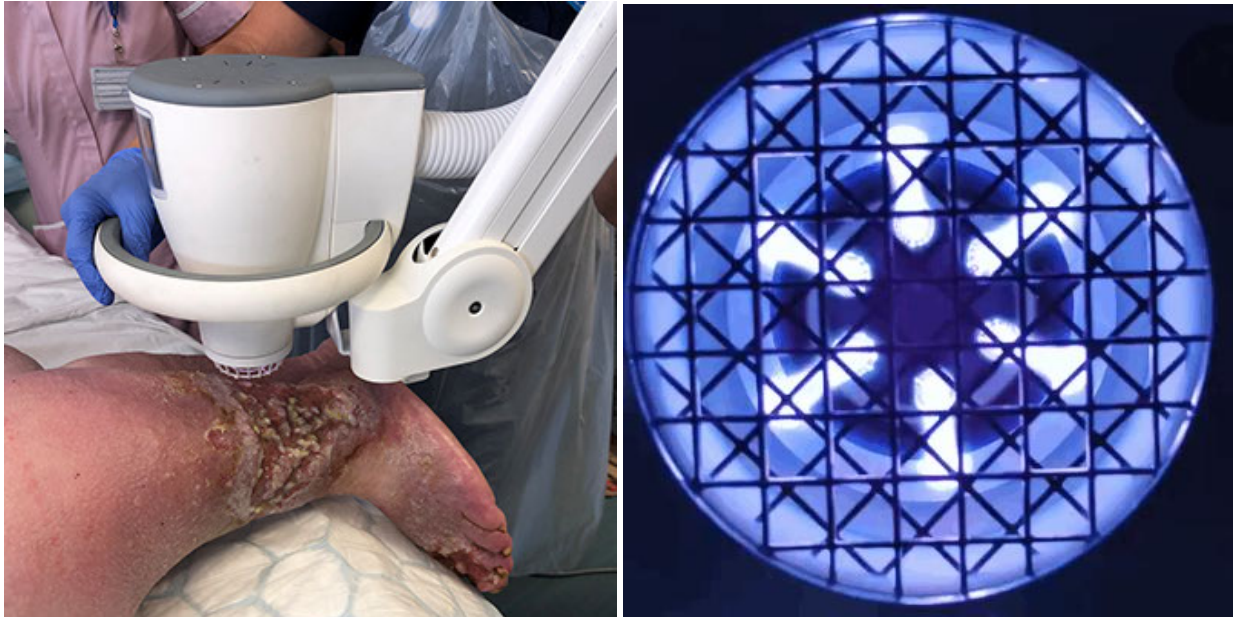
Figure 2.12: Image of the PlasmaDerm (Reproduced under Fair Use from [168])

2.5.2.3 *The MicroPlaSter*

The MicroPlaSter¹¹ was developed by the European branch of Adtec Plasma Technology Co. Ltd. in conjunction with the Max Planck Institute for Extraterrestrial Physics in Germany. [169, 170] The device is often classified as a plasma torch, since it is a microwave (2.45 GHz) argon plasma jet with six exposed electrodes in a grounded metal cylinder, as shown in Figure 2.13b. Additional air is used to ensure a low temperature output. [152] The device was shown to have low UVC output; most UV output appears to be OH and NO bands. [143, 171] It was shown to have large area bactericidal effects, which leads to chronic wound treatment as the primary use, as shown in Figure 2.13a. [170]

Unlike the previous two devices (the kINPen MED and PlasmaDerm), some of the first published studies are clinical trials (and the first clinical trials of a cold plasma device), suggesting that substantial development was done in-house to warrant these trials. These studies showed a substantial reduction in a wide range of bacterial loads in chronic wounds for both a 5 min [172]

¹¹This has been rebranded as the SteriPlas [169], but appears to be essentially the same device as the previous generations, the MicroPlaSter α and MicroPlaSter β (sometimes misspelled with an β or different capitalization, a 25% smaller unit than the α model), which are discussed in the literature. As such, the older name will be used in this dissertation.



(a) Clinical Treatment

(b) Exposed Electrodes

Figure 2.13: Images of the MicroPlaSter Being Used in a Clinical Setting and Its Electrode Configuration (Reproduced under Fair Use from [169])

and a 2 min [143] treatment time. This led to further studies, with secondary endpoints of wound healing in addition to the primary endpoint of bacterial load reduction. Significant wound size reduction was noted in addition to broad bacterial inactivation in the wounds. [173] No adverse effects have been noted from the plasma treatment. [139] Further clinical studies for wound healing in skin grafts and on herpes zoster were also conducted; treating skin grafts suggested a positive effect, [174] while the study on herpes zoster treatment showed faster clinical improvement and reduced pain. [175]

Further studies have investigated the MicroPlaSter in vitro and animal studies. Low levels of toxicity were noted for in vitro tests while no mutations were detected, supporting the use for clinical studies. [176] gram-negative bacteria were found to be more susceptible to plasma treatment than gram-positive bacteria. [104] In addition, thicker biofilms were noted to be more difficult to inactivate. Increased cell proliferation was noted from treatment leading to faster wound healing. [177]



(a) Clinical Setting

(b) Electrode Design

Figure 2.14: Images of the plasma care and Its Electrode Configuration (Reproduced under Fair Use from [178])

2.5.2.4 *The plasma care*

The most recent device to receive a CE marking is the plasma care from terraplasm medical GmbH, an offshoot company from the Max Planck Institute for Extraterrestrial Physics. The device is shown in Figure 2.14. The plasma care is a surface DBD, directly spun out of the university rather than working initially with an external company, such as Adtec, which had a partnership with the Max Planck Institute for Extraterrestrial Physics. [138] This device appears to be a variant of an Adtec device, which was originally called the FlatPlaSter (or some variant). [179–181] General characterization experiments were run showing that it does not produce unsafe amounts of reactive species yet still has sterilization potential. [138] Initial results for inanimate object sterilization proved effective even against difficult to kill bacteria. [180] This was continued for sterilization on a skin surrogate, where sterilization was effective without damaging the skin. [179, 182] The effect of destroying biofilms was also noted, which is one of the drivers for this device's clinical use. [183] Currently this is now being explored in vitro as a cancer therapy as well. [181] In addition, it is being marketed for household veterinary use. [184]



Figure 2.15: Image of the Plasma ONE (Reproduced under Fair Use from [188])

2.5.2.5 *The Plasma ONE*

The Plasma ONE by plasma MEDICAL SYSTEMS GmbH has also received its CE marking. [185] This is an unusual device compared to the previous four, as it does not appear to have been worked on extensively in a partnership with a university, and thus there are not many journal papers concerning it, making this more analogous to development that has been done in the US. It is mentioned to be a volumetric DBD in air, but the system appears to be a type of plasma jet in images (see Figure 2.15); typical treatments are done for 60 s with voltages from 3–18 kV, where the plasma was shown to assist in wound healing by increasing cell proliferation post treatment. [111,112] It has also been shown to reduce biofilms on titanium surfaces, a common material used for medical implants. [186] Nevertheless, not all results are positive; it did not successfully sterilize a number of bacteria for a number of run conditions in an aqueous setup intended to mimic the human mouth. [187] This shows that determining the appropriate conditions for a plasma system is highly non-trivial and requires fairly extensive study.

The company's website only lists two clinical trials that have been conducted using the Plasma ONE; [189] although a further one has been found. This last one, however, was most likely not

done in part of the CE approval process, as it has only a single patient, thus further clinical results may exist, just not in the open literature. As part of post-operative care for an ear carcinoma, one patient was prescribed treatment using the Plasma ONE to assist in wound healing. [190] Interestingly, as this was a carcinoma, this treatment could also be considered as an anti-cancer therapy, as this was apparently a reoccurring cancer. However, no long-term results are given to determine if this helped prevent resurgence of the cancer for this particular patient.

2.5.2.6 *Other Devices*

A number of startup companies have been created in the US, some of the earliest ones being Harmonic Cold Plasma, Plasma Technologies, and Sterionics, Inc., all with the intention of generating a plasma device for wound healing. Unfortunately it seems most of these companies no longer exist; at minimum their websites no longer exist. Harmonic Cold Plasma reached animal trials, but apparently progressed no further. [191] Sterionics, Inc. received a small business innovation research (SBIR) grant for “disinfection efficacy of a novel non-thermal-plasma-generating technology that produces a variety of reactive ionic species.” [192] However, since no further information is available since 2013, it is assumed that their CAP device intended for FDA approval was never realized. [193] Another more recent company ChiScan LLC is also operating in this space using a corona discharge device; however it appears they may have also gone out of business as their website also is unresponsive. [194]

However, US Medical Innovations is still doing well with their development of a low temperature plasma jet, called the Canady HeliosTM Cold Plasma Scalpel, named after a surgeon on staff at the company. [195] The system is shown in Figure 2.16 being used in a surgical procedure. This company already produces electrosurgical equipment, so there is perhaps minimal changes needed to their existing devices (e.g. see Section 5.4) to convert it to a low temperature plasma device. In addition to already having a revenue stream as an electrosurgical device manufacturer, US Medical Innovations is working with a number of universities with prominent cold plasma researchers. [196] They have already published preliminary bench scale research for operating conditions. [197] This device has already been used twice under the FDA’s rule as a Compassion-

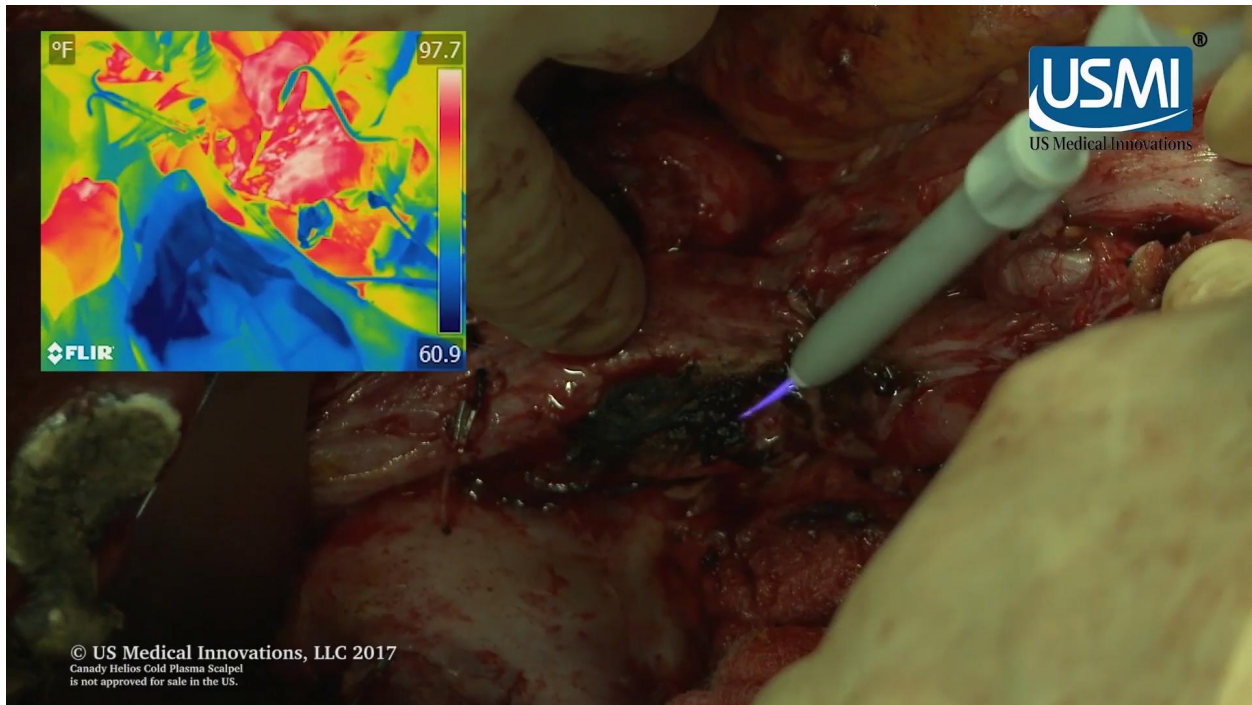


Figure 2.16: Image of the Canady Helios™ Cold Plasma Scalpel in a Clinical Setting (Reproduced under Fair Use from [195])

ate Use Exemption for inoperable colon [147] and pancreatic [148] cancer, as well as at least once outside of the US for retroperitoneal sarcoma. [198] This device has now also just been permitted to undergo clinical trials in the US for cancer treatment. [149]

Drexel University's FE-DBD has been used in clinical trials for wart removal in pediatric patients. [199] Though successful, this was a small-scale study needing further results with a larger population for conclusive results.

Another company with a device family, the Bioplasma Cell Modulator by Photo Bio Care in Thailand, also deserves mentioning due to the number of studies done. Two different systems are tested, one is a DBD similar to Drexel's FE-DBD system; the other is a direct plasma jet (see Figure 2.4) usually run with helium. The first study found used the FE-DBD system for acne treatment; skin oil production was reduced for up to 4 weeks after plasma treatment. [200] This is the only study found for acne using a cold plasma treatment, although there appears to be a device on the market in Australia claiming to use cold plasma for similar skin treatments. [201] Three

results were found using the direct plasma jet. DNA modification was investigated using the direct plasma jet with helium, showing that this device can modify bacterial DNA. [202] This plasma jet with a small admixture of oxygen in the helium has also been investigated for root canals, where it was shown to be useful in inactivating *E. faecalis*, especially when combined with the standard treatment. [203] Lastly a clinical study was conducted with the jet using argon rather than helium to heal pressure ulcers with a secondary objective of reducing the bacterial load in these ulcers. A significant reduction in size was noted after 1 week compared to the control group; the bacterial load was also reduced. [204]

2.5.3 Standards for Low Temperature Plasma Devices

There exist a number of standards for medical devices. These include general standards for medical devices such as ISO 13485 for “the design, production, installation and servicing of medical devices and related services.” [205] These general standards focus on the overall system that generates medical devices. Then there are some more specific standards that the FDA or another regulatory agency will recognize as pertaining to a device that can have a very narrow scope, such as “IEC TR 60878:2015 Graphical symbols for electrical equipment in medical practice.” The FDA usually relies on standards developed by other organizations rather than creating their own, particularly to “support a least burdensome regulatory framework.” [206] Thus any plasma device would have to follow a variety of standards that are relevant for such a device that is converting electrical energy to a medical use. Relevant standards that should be followed include electrical ones (such as ensuring minimal electromagnetic interference (EMI) is generated and patients are protected against electrostatic discharges [207]), as well as medical ones for the medical treatment being conducted.

However, in addition to these very general to relatively specific standards, there is a standard being developed specifically for low temperature plasma devices in Germany, namely DIN-SPEC 91315: General requirements for medical plasma sources. [208] The goal of this standard is not necessarily to address all aspects of plasma design and characterization for a medical device but to provide a basic set of characterization standards and performance metrics for low temperature

plasma devices; it is anticipated that other standards will be used as well or further standards will be developed that more fully address the mandatory metrics for low temperature plasma devices. [40, 153] Nevertheless, this standard is the first attempt to give reasonable standards for manufacturers who are beginning to develop a number of plasma medical devices. [153]

The DIN-SPEC 91315 characterization was designed primarily for plasma jets with applications in sterilization, such as the KINPen MED, but can be applied to any plasma medical device. [153] The specifications are divided into three sections: general requirements, physical assessment criteria, and biological assessment criteria. [208] The general requirements specify that any experiment should be as controlled as possible with all relevant factors noted (e.g. humidity, ambient temperature, etc.). It is also expected that sufficient tests will be conducted for some measure of statistical significance (i.e. all results presented in triplicate at a minimum).

Physical assessment criteria include measuring the temperature, thermal load, optical radiation, gas emissions, and electrical currents. For temperature, a variation along the plasma region is expected with a spatial resolution of 1 mm or smaller. The thermal load is to show the energy deposited by the plasma into the substrate. The optical radiation emitted is to determine the spectral rays emitted, particularly in the ultra-violet range (200–400 nm). The gas emissions should characterize the amount of ozone and NO₂ generated by the plasma to determine if they approach a hazardous level. Lastly, the ground leakage current should be determined to ensure minimal current flows through the patient.

Biological assessment criteria include measuring the inactivation of microorganisms, the vitality of cell cultures after plasma treatment, the detection of chemical species in liquids, and the determination of pH changes. For sterilization applications, the inactivation of a wide range of medically relevant microorganisms should be shown. This includes both gram-positive and gram-negative bacteria as well as fungal spores. The cell culture vitality is particularly for in vivo treatment. A wide variety of chemical species including nitrites and nitrates can be produced in water due to plasma treatment, which need to be characterized for a plasma system that may produce them on biological surfaces. Lastly, any change in the pH of a treated liquid should be measured.

Though no specific standard for low temperature plasma devices has been adopted by any medical device approving body (e.g. the FDA), showing that one is following a standard such as the DIN-SPEC 91315 would certainly help support any marketing application.

3. PLASMA CHARACTERIZATION

3.1 Introduction

Plasmas are notoriously difficult to characterize. They are a collection of particles moving at vastly different speeds, with dynamics occurring over sub-nanosecond timescales, with large amounts of energy being dissipated over extremely short timescales. This chapter introduces the diagnostic techniques used to characterize the plasma systems described in the following chapters, discussing their applicability and limitations. The subsequent chapters will refer back to sections in this chapter for more information on the systems used. First, the electrical characterization of the plasma is treated, observing how the plasma interacts as a circuit element as well as the difficulties and trade-offs that occur when taking these measurements. Second, imaging techniques are discussed. Next, optical emission spectroscopy of plasma discharges is discussed. The two main uses of species identification and plasma temperature are highlighted.

3.2 Electronic Characterization

This section will discuss the various aspects of the electronic side of plasma generation and diagnostics. Many of the systems used to generate or characterize the plasma systems discussed in later chapters will be described in detail here so that they need only be referenced in the later chapters. Initially plasma power supplies are discussed, followed by voltage, current, charge, and electric field measurements; lastly Lissajous analysis for DBD systems will be discussed.

3.2.1 Power Supply Considerations

As explained in Section 2.2.1, a plasma is coupled to its power supply (and the rest of the circuit powering it). As such, changing the power supply will affect the behavior of the plasma. This can be as simple as changing the capacitance that the plasma is drawing charge from, yet this can have profound impacts in plasma operation, such as a small change of increasing the length of wire in the system can then influence the plasma dynamics.

Power supplies for plasma systems come in one of three general types: DC, pulsed DC, and

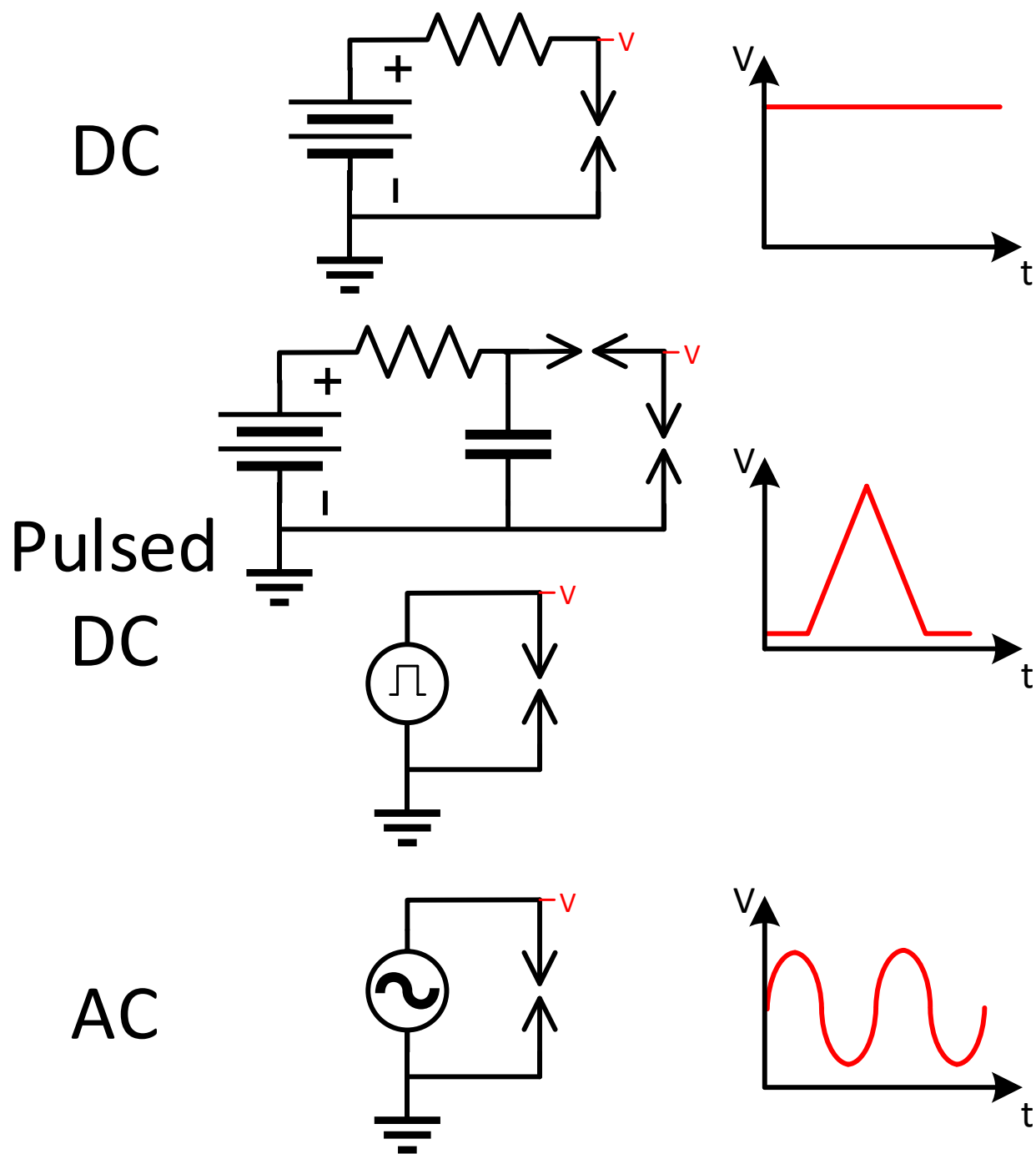


Figure 3.1: Schematic of the Three Primary Types of Plasma Power Supplies with Representative Voltage Traces

AC power supplies (see Figure 3.1). Current travels in only one direction for DC power supplies; thus they do not work for DBD systems, since the dielectric stops the flow of charge. However, DC power supplies can be used as charging power supplies for pulsed DC systems (see Section 4.4.1 and the first pulsed DC system in Figure 3.1). They are the simplest design from a basic circuit characterization standpoint, since the direction of the current is known. Since the source of power is typically a standard AC wall outlet, they must involve some relatively complex circuitry to both step up the voltage and rectify the current. As such, they typically have a relatively large output capacitance to ensure a relatively smooth rectified signal. Typically high voltage DC power supplies are used to power corona or glow discharges.

Pulsed DC power supplies deliver current in pulses in a single direction; they achieve this by having a single polarity voltage pulse, as shown in Figure 3.1. They can be constructed of a DC power supply with a fast switch to deliver stored charge (e.g. a spark gap, as shown in Figure 3.1 for the first pulsed DC power supply) or they can involve complex circuitry, such as the FID power supply (see Section 3.2.1.3). Pulsed DC power supplies can power nearly any type of plasma discharge, including DBDs. They are characterized by their duty cycle and pulse duration. Since pulsed DC power supplies only deliver short pulses, they tend to deliver lower average power than the other two types of power supplies. They are increasingly being used to drive low temperature plasmas, since one of the main ways to achieve a low temperature plasma is to have a low duty cycle, delivering high current over very short timescales either before significant gas heating occurs or so that the time-average gas temperature remains near ambient.

AC power supplies alternate the direction of charge flow, typically at fairly fast rates (10s of kHz, but can be up to 100s of MHz). Since the power supplies typically use wall power, they are relatively simple and can consist of simply a transformer to step up the low wall voltage to a high enough voltage to generate a plasma discharge. Further internal circuitry is needed to modify the frequency of the power supply. The main drawback of AC systems is that they need impedance matching to be able to deliver substantial power. This is often done with a matching network attached to the power supply for high power systems, but it can also be done by varying

the frequency of the power supply.

Three of the power supplies used for this research are described below. They are a DC high voltage power supply, an AC high voltage power supply, and a pulsed DC power supply system. Two further systems were used: a Bovie, which will be discussed in Chapter 5, and a custom AC high voltage power supply used in the FlashFuse system (see Section 7.5).

3.2.1.1 Spellman HV DC Power Supply

The high voltage DC power supply used in this work is a Spellman SL300 DC power supply. It is capable of outputting voltages from 0–40 kV and currents from 0–7.5 mA. Its output capacitance is on the order of 1 nF. It will operate in either a voltage or current controlled mode, depending upon whichever control (voltage or current) is limiting the power draw from the circuit. This power supply is used in conjunction with a double spark gap pulse-forming network in Section 4.4.1 to deliver nanosecond voltage pulses.

3.2.1.2 Information Unlimited HV AC Power Supply

The most common high voltage AC power supply used in this work is the PVM500 power supply from Information Unlimited (also known as Amazing1 from their website URL). This is an inexpensive radio frequency (RF) power supply capable of delivering 0–40 kV (peak-to-peak) over a frequency range of 20–70 kHz. This ability to adjust the frequency allows a resonance mode to be found for driving capacitive loads that maximizes the power output. This avoids needing to use a separate matching network to deliver maximum power to the load as is commonly used in RF plasma systems. This is used in this work to drive a plasma (usually a DBD) jet (see Chapter 5 and Chapter 6).

3.2.1.3 FID Power Supply

Some of the power supplies with the shortest pulse duration on the market are the fast ionization dynister (FID) power supplies from FID, GmbH. This work uses a model FPG 30-N, which delivers 5–30 kV high voltage pulses with a pulse duration of ~ 3 ns. The frequency of pulses can be internally varied from 800 Hz–10 kHz, but by externally triggering lower frequencies down to a

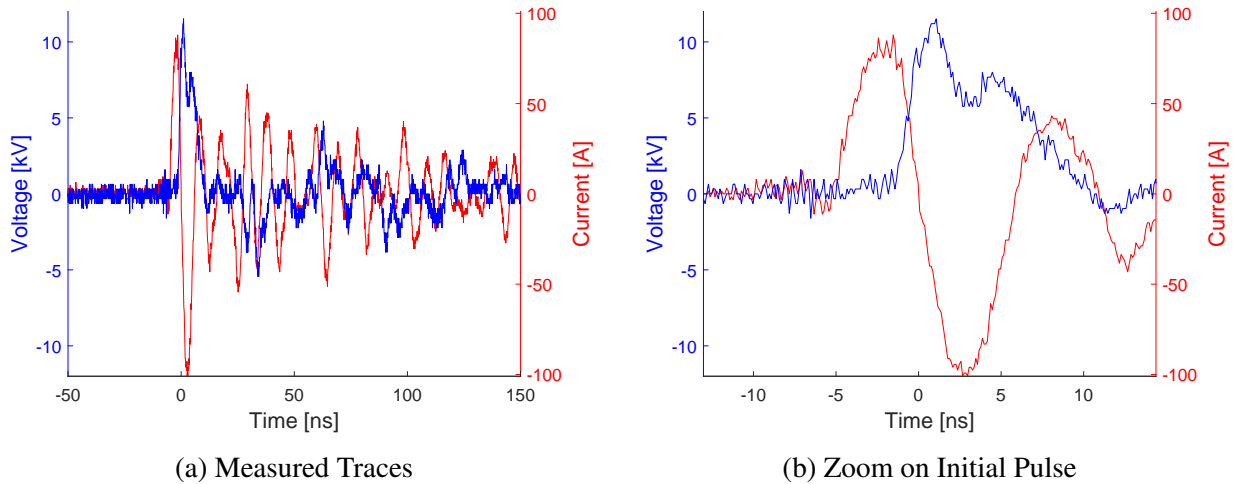


Figure 3.2: Measured Voltage and Current Traces from the FID Power Supply

single pulse are possible. Due to the extremely short pulse duration, the electrical characteristics of this power supply are difficult to measure. An attempt was made to measure the output voltage and current in Figure 3.2, but the pulse duration is not adequately measured because the pulse is faster than the voltage and current probes response times. There is also a significant amount of ringing in the circuit, possibly from voltage reflections at numerous points in the circuit. Nevertheless, this power supply has been measured to output ~ 3 mJ/pulse into a plasma load, which is its rated energy per pulse for a $200\text{--}500\ \Omega$ load. This power supply is used in this work in Section 4.4.2, Section 4.5.1, and Section 7.4.

3.2.2 Voltage, Current, & Charge Measurements

Usually a number of trade-offs have to be balanced to adequately measure a plasma discharge's electrical properties. This is often due to the large range of timescales that processes occur over. For example, current pulses can have a duration of only 10s of nanoseconds but the duty cycle of them can be on the order of milliseconds, thus necessitating capturing data to adequately resolve a 10 ns pulse while still attempting to capture multiple pulses to see the pulse-to-pulse variation—6 orders of magnitude range in time! This is often impossible for systems since 10s of millions of data points or more are necessary to measure a single signal. In addition to time, scaling the

signal magnitude can be difficult. Particularly for current traces in AC systems, there can be a low magnitude primary signal with large current spikes superimposed on it (e.g. the plasma bullets described in Section 2.2.1.8 or microdischarges as shown in Figure 3.5a). As the oscilloscopes used involve an analog-to-digital (A/D) conversion to acquire the signal, substantial data can be lost. There are attenuators that can be used to ensure a signal is within the range the oscilloscope can measure, but linear scaling may still cause important information in the signal to be lost. As a result, some researchers have investigated more complex circuitry that scales the input signal in a logarithmic fashion to not lose any important aspects of the data. [209] There are also a number of other considerations for each type of measurement, which will be discussed in the following subsections.

3.2.2.1 Measuring Voltage

The main difficulty in measuring the voltage drop across a plasma is due to the large voltages occurring. A good rule of thumb is that a plasma requires 3 kV/mm to break down an air gap (this value is the dielectric strength of air). As such, the voltage can easily be on the order of 10s of kilovolts. The easiest way to measure the voltage is using a high voltage oscilloscope probe; however, these can easily cost \$100s to \$1,000s for a probe with a high enough bandwidth (the range of measurable frequencies) and voltage rating. Even worse, at times probes cannot be commercially purchased (without custom builds) that can achieve the high bandwidths and voltage rating desired.

This brings up the second challenge in measuring the voltage drop across a plasma: they often operate at high frequencies. The bandwidth needed to fully measure the dynamics is generally beyond any probe, but high bandwidth probes (>100 MHz) are usually sufficient for most cases (the exception being the FID power supply or similar systems). Note here that the lower bandwidth is assumed to be 0 Hz so that a probe can measure DC voltages.

Another option to purchasing an expensive high voltage probe is to build your own high voltage probe, using a basic resistor divider circuit (see Figure 3.3). The bandwidth will not be optimal (at best on the order of 100 kHz, higher bandwidths require adding in a capacitive divider) and care

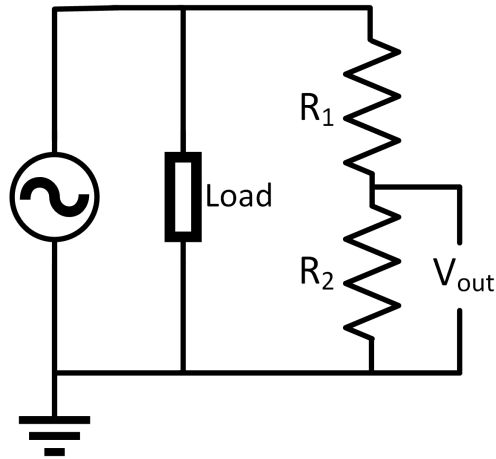


Figure 3.3: Schematic of a Resistive Divider Circuit

must be taken to ensure the proper voltage is being read by an oscilloscope, but this is a very cheap alternative to buying a high voltage probe. The resistors must be chosen so that very little current will flow through them ($R_1 + R_2 \geq \sim 10 \text{ M}\Omega$, but higher resistances may be necessary if the circuit element has a high resistance), and the output voltage is able to be input to an oscilloscope ($V_{out} = \frac{R_2}{R_1 + R_2} V_{in} \leq \sim 40 \text{ V}$). Care must be taken for proper impedance matching with the oscilloscope. (Often an oscilloscope has an input impedance of $1 \text{ M}\Omega$, but R_2 can also be the same order of magnitude; a simple solution might be to use an op-amp to isolate the resistive divider from the oscilloscope.) A custom-built voltage divider probe was used for initial diagnostics of the custom RC pulse generator and in determining the voltage across the capacitor (see Section 4.4.1 for circuit details) since this did not require a fast time response.

Placement of the voltage probe is important. The probe must be placed as close as possible to the circuit element of interest to minimize possible time delays between the measured voltage and the actual voltage across the circuit element (as noted in Figure 3.1). There ideally should be no other circuit elements between the circuit element of interest and ground to accurately measure the voltage (e.g. a shunt resistor may be used for current, but then the voltage difference can be used instead). This is because the probe often has a ground reference; floating this ground reference can potentially damage the oscilloscope, which often also has its own internal ground reference.

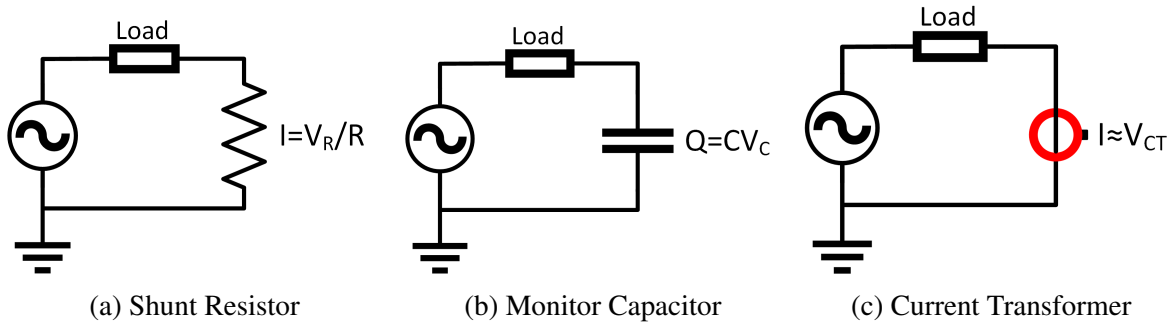


Figure 3.4: Schematic of Three Different Methods for Measuring Current or Charge

Differential probes can be used instead to avoid this, but they rarely are capable of measuring high enough voltages for use in plasma diagnostics.

For the work reported in this dissertation, three high voltage probes were used. The first is a Northstar PVM-4 with a bandwidth of 110 MHz, a maximum voltage rating of 40 kV, input resistance of 400 MΩ, and input capacitance of 10 pF. The second is a LeCroy PPE20KV with a bandwidth of 100 MHz, maximum voltage of 20 kV, input resistance of 100 MΩ, and input capacitance of <3 pF. A resistive divider probe (nominally $R_1 = 50 \text{ M}\Omega$ and $R_2 = 10 \text{ k}\Omega$, measured as $R_1 = 49.9 \text{ M}\Omega$ and $R_2 = 9.84 \text{ k}\Omega$) was used to measure the breakdown voltage on a capacitor (see Section 4.4.1), since this did not require a fast time response.

3.2.2.2 Measuring Charge and Current

Current (or charge) is possibly the most difficult part of a plasma system to measure. This is because for a DBD, the discharges last only 10s of nanoseconds, while the overall excitation (applied voltage sinusoid) is on the order of 10s of microseconds, and the pulses can sometimes be as high at 100s of amperes (see Figure 3.5a). Note that current or charge can be measured as a function of time. As long as there is sufficient temporal resolution, the other can be sufficiently determined by either integration or differentiation of the signal.

There are three main ways to measure current—a shunt resistor, a monitor capacitor, or a current transformer (see Figure 3.4). The downside for all of these systems is that the current (or charge) is linearly proportional to the output voltage. Though simple, this requires the oscilloscope

to have sufficient resolution to resolve both the low current and high current aspects of the system. More complex circuitry can be used to achieve logarithmic dependence, thus reducing the need to have a large resolution on the oscilloscope. [209]

A shunt resistor (Figure 3.4a) is a small resistance placed between the plasma load and ground. (it can be placed elsewhere, but then two voltage probes, or a differential voltage probe is needed to isolate the voltage drop across the resistor.) The voltage measured across the resistor is proportional to the current ($I = \frac{V}{R}$). The resistance must be small enough to not affect the circuit, but large enough that a measurable voltage drop across it occurs; often, this is in the range of 1 to 10 Ω but the values can range greatly depending upon the current magnitudes expected.

A monitor capacitor (Figure 3.4b) is similar to a shunt resistor, except that the voltage across the capacitor is proportional to charge rather than current ($Q = CV$). The charge must be differentiated to obtain current; however, this can be useful if a Lissajous figure is being obtained (see Section 3.2.3), since then there is no need to integrate a current signal. One difficulty of implementing this method is that charge can build up on the capacitor. If this occurs, the voltage across the capacitor continues to grow with each plasma discharge and will eventually affect the discharge characteristics. If this occurs, a moderately large resistor in parallel with capacitor may be necessary to remove the charge between discharge cycles, but the resistor must be large enough to not allow significant charge to flow through it during a discharge event. Finding an optimum value for this resistor may be difficult to impossible, thus this method of measuring current (after differentiating the measured charge signal) is not always feasible.

A current transformer (Figure 3.4c) uses the magnetic field from the flowing charges to induce a voltage. (It is a Rogowski coil with a integrating circuit on the output.) This voltage can then be measured by an oscilloscope. This is often one of the easiest ways to measure current, since the inductive loading on the circuit is typically small; however, it may be difficult (or expensive) to find a current transformer with a high enough current and bandwidth rating for a DBD system. An advantage of a current transformer over the other two methods is that the current transformer does not need to be placed between the load and ground, but can be placed anywhere the current

measurement is desired.

The primary method to measure current used in this dissertation was a Bergoz current transformer, model CT-D1.0, which has a maximum (peak) current of 1 kA, a rise time of 0.7 ns, and a bandwidth of 200 Hz–500 MHz. A Pearson current monitor model 6585 was also used which has a maximum (peak) current of 500 A, a rise time of 1.5 ns, and a bandwidth of 400 Hz–250 MHz.

3.2.2.3 *Electric Field*

For many applications, the voltage is not the desired result, rather the electric field. The electric field, E , is the gradient of the voltage, V expressed as,

$$E = -\nabla V \quad (3.1)$$

Space charge, ρ , however, develops in the discharge gap for any plasma system which greatly affect electric field, as given by Gauss's Law

$$\nabla \cdot E = \frac{\rho}{\varepsilon} \quad (3.2)$$

where ε is the permittivity of the medium.¹ This leads to difficulty or (much more often) even impossibility of measuring the local electric field, which is often necessary for a full characterization of many systems (such as an electroporation system described in Chapter 4). At a minimum, the local electric field cannot be estimated by only knowing the applied voltage at the electrodes.

There are two methods of observing the electric field directly. The first is an electric field probe. This is based off of the Pockel's effect, a well established electro-optical effect, where the index of refraction changes based on the applied electric field. [210] Though commonly used in lasers to control the pulse, similar devices can be used as sensors to measure the applied electric field. [211] They, however, suffer from poor spatial resolution and can have a substantial impact on the discharge if inserted directly into the plasma.

The second direct method of measuring the electric field is a dye measurement. A dye sensitive

¹Not to be confused with the vacuum permittivity, $\varepsilon_0 = 8.854 \times 10^{-12}$ F/m. The permittivity of the medium is often given by $\varepsilon = \varepsilon_r \varepsilon_0$, where ε_r is the relative permittivity. Either ε_r or ε are experimentally determined and tabulated.

to the applied electric field can be selected. The details of this are discussed in Section 4.5.4, where a rhodamine dye is used in an attempt to measure the electric field. The dye's fluorescence changes under the magnitude of the applied electric field. The challenge in this case is that the change is quite small and thus difficult to observe.

Indirect methods of measuring the electric field are typically optically based. For example, Stark polarization spectroscopy can be used to measure the electric field. [212] This measures the location of a normally forbidden transition that becomes allowed due to the electric field; however the line is very close to an allowed transition, making this measurement difficult. [212, 213] There is also a new technique using a variant of coherent anti-Stokes Raman spectroscopy, whereby non-linear mixing of three laser beams yields a signal that scales with the electric field. [214]

3.2.2.4 Oscilloscope Considerations

The behavior of the probes are meaningless unless a device, such as an oscilloscope, is used to capture the signal traces. Common oscilloscopes today are digital rather than analog. This may add some small complications with the A/D conversion, but a wide variety of other functions are possible, such as peak finding, various mathematical transformations, etc. Oscilloscopes are rated for the number of channels (2, 4, and 8 channels are the most common), bandwidth, sampling rate, and memory (for digital oscilloscopes). For all of the work reported in this dissertation, a 4 channel LeCroy 204MXi (2 GHz) oscilloscope with 10 GS/s.

3.2.3 Lissajous Analysis

A typical voltage and current trace for a DBD is shown Figure 3.5a, in this case from the FlashFuse system characterized in Section 7.5. The voltage is sinusoidal with a slight deviation at voltages greater than the breakdown voltage of the gas gap due to the plasma discharge. The current is roughly a sinusoid phase shifted from the voltage (since the overall system is mainly capacitive). However, there are large spikes superimposed on the current's sinusoidal behavior. These spikes are the plasma discharges; there is one spike for every filament. They come from large increases in the current due to the breakdown process. Their duration is in the range of 10 to

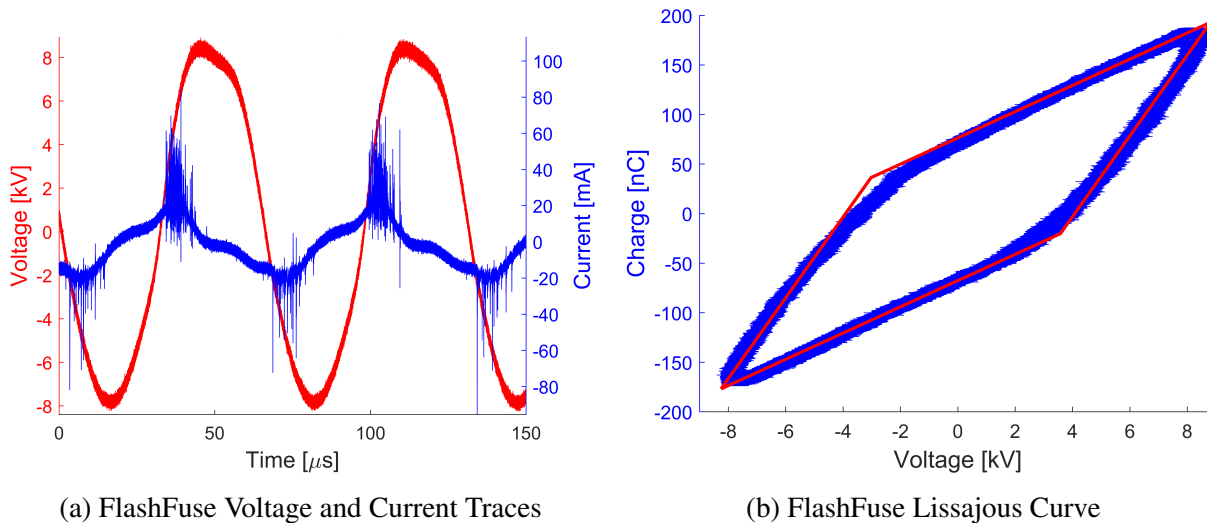


Figure 3.5: Typical DBD Voltage and Current Traces with the Resulting Lissajous Curve

100 nanoseconds, and the number of current spikes can vary from a single spike (fairly typical in DBD jets) to hundreds or more (common for planar DBDs as seen in Figure 3.5a). For a normal capacitor, there is no net power loss over a full cycle; however, for a DBD the plasma is dissipating some of the energy in the form of light emission and heat (Joule heating occurs, since a plasma does have a small resistance, typically on the order of $100\ \Omega$). Often the forward and reverse polarity do not match because the discharge gap is not symmetric (e.g. the FlashFuse system has a resistive additively manufactured part as one electrode), thus there is some difference in the number of spikes or their magnitude for the two polarities. Since these current spikes are so large in magnitude and so short in duration, accurately measuring them is very difficult, as discussed in Section 3.2.2.2.

Due to the cyclic nature of a DBD's voltage, it can be useful to use time as a parametric variable, since ideally each cycle is identical to all others. Plotting the voltage and charge of a DBD produces a Lissajous figure, which is an easy way to characterize the discharge. An ideal Lissajous figure is shown in Figure 3.6. From this diagram, the capacitance of the system can be determined. Capacitance is the slope on this diagram ($Q = CV$), so the capacitance of the dielectric (and any capacitance in the rest of the external circuit) is the slope during the discharge

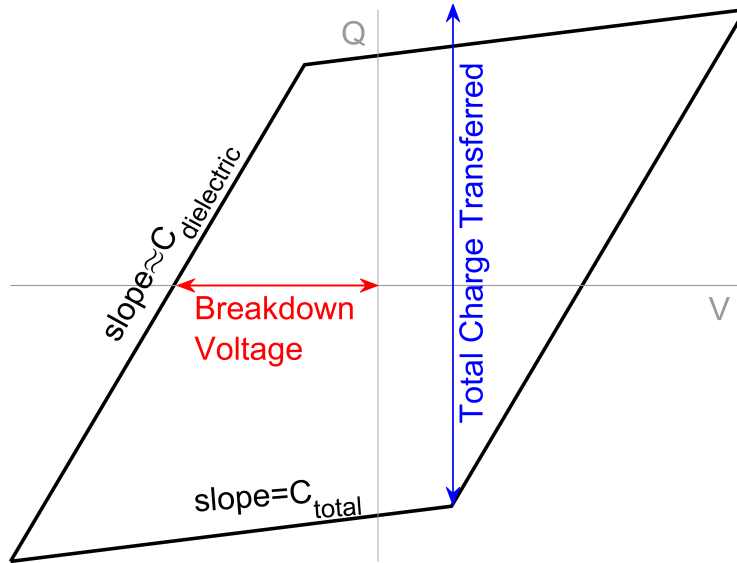


Figure 3.6: Annotated Ideal Lissajous Plot for a DBD System

event (steeper sloped lines in Figure 3.6). The system's total capacitance without a discharge is the slope of the curve not during a discharge event (shallower slopes in Figure 3.6) Note that the system's total capacitance is smaller than the dielectric capacitance due to this being a series capacitance of the gas gap and the dielectric, namely

$$C_{total} = \frac{C_{dielectric} C_{gas\ gap}}{C_{dielectric} + C_{gas\ gap}} \quad (3.3)$$

The breakdown voltage, V_b , is readily evident on a Lissajous figure as the voltage where the curve crosses the voltage axis. Likewise, the amount of charge transferred during each half-cycle, q_{max} is also easily noted on the Lissajous figure. [215].

In reality, the Lissajous figure for a DBD is rarely so clean. A Lissajous figure for the FlashFuse system is shown in Figure 3.5b with a parallelogram fit to the experimental data. The rounded corners on the figure come from resistance in the system, [216] and there is asymmetry denoting differences in the discharge with the positive and negative half-cycles. This is expected due to the asymmetry in the geometry of the FlashFuse system, which has a resistive part as one of the electrodes. Nevertheless an approximate system capacitance, dielectric capacitance, breakdown

voltage, and charge transferred can be determined from the Lissajous figure.

3.3 Imaging Systems

Imaging is one of the most basic methods for analysis, especially for a plasma discharge. This is typically done using a charged coupled device (CCD) or complementary metal-oxide-semiconductor (CMOS) sensor as a part of most standard cameras, which can also be attached to a microscope as opposed to using a standard camera lens, although a subsection below will discuss scanning electron microscopy, which images solid samples using electrons rather than photons and thus uses a completely different type of system. Though there are a number of possible parameters for imaging ($f\#$, focal length, ISO value, etc.) this discussion will focus mainly on quantum efficiency as a function of wavelength and exposure time.

The quantum efficiency is the ratio of the number of electrons generated by the incident light to the number of incident photons. The higher the quantum efficiency the more sensitive the detector is. This becomes useful for two reasons: color detection and photon counting. A typical CCD for a camera has three types of detectors that are sensitive to different wavelengths of light. This allows them to capture a color image. The color has some indication for the type of discharge. In general, cooler discharges typically have the majority of the light coming from specific narrow transitions, while hotter discharges become more broadband and thus white. However, a spectrometer is needed for a more accurate and full analysis. In a well calibrated system, the exact number of photons impinging on the detector (or their flux) can be determined, allowing for quantification of the total number of photons emitted by the plasma.

The exposure time for typical cameras ranges from fractions of a second to ~ 30 s. This is often substantially longer than the duration of a plasma phenomenon of interest, typically an ionization wave in a pulsed plasma system. However, an electronic gated system as opposed to a mechanical shutter is capable of extremely short exposure times that can temporally resolve these phenomena. To achieve this, timing circuitry must be used to ensure the camera gate opens at the desired time with as little jitter as possible, usually involving a timing circuit for the plasma discharge as well.

Two different imaging systems are treated in more detail in the first two subsections below

as they are used to characterize some of the plasma systems discussed in future chapters. The next subsection discusses optical microscopy, which used the Nikon cameras (Section 3.3.1) as the imaging system. The last subsection gives a brief overview of scanning electron microscopy and discusses the two scanning electron microscopes used in this work.

3.3.1 Nikon Camera

Three comparable cameras are used in our lab: a Nikon D90, a Nikon D3300, and a Nikon D5600, all of which use a CMOS sensor. They have an ISO range of 100 to 6400 (to 25,600 for D5600), and the exposure time can vary from 1/4000 to 30 s. Both cameras are able to accept a wide variety of lenses, typically a 105 mm focal length micro Nikkor lens with variable f# or similar. They are used for plasma imaging, in particular determining where a plasma discharge is occurring, which may be difficult for the unaided eye if the plasma is extremely dim, as well as for qualitative analysis between various discharge conditions.

3.3.2 Stanford ICCD

A Stanford Computer Optics 4Picos ICCD (intensified CCD) is used both for directly imaging the plasma as well as a detector for the SPEX Spectrometer (see Section 3.4.1.1). It is a gated ICCD capable of exposure times as small as 400 ps in a burst mode and 1 ns in normal operating mode. It can accept a TTL (transistor-transistor logic) signal for a trigger or can be self-triggered. This ICCD has a high quantum efficiency around 20% in the range of 200–450 nm, but it quickly decreases at higher wavelengths. This is why it is useful for capturing the 2nd positive system of N₂ for spectral analysis, but it is not extremely useful for broadband spectra.

3.3.3 Optical Microscopy

Optical microscopy uses a light microscope to image small features. The microscope used in this work, an AMScope, is a binocular stereo microscope with a magnification of 0.5 X–4 X along with an additional magnification on the eye-pieces. It has a C mount for mounting a camera as well, which was used extensively in Chapter 6 for imaging deposited films using a Nikon camera (see Section 3.3.1).

3.3.4 Scanning Electron Microscopy

Scanning electron microscopy uses electrons for imaging rather than photons. This is ultimately possible by the wave-particle duality of electrons as explained by de Broglie, [217] where the wavelength of electrons is varied by the accelerating voltage used. Electrons are emitted from a fine tip, either by thermionic emission or field emission. These electrons are then accelerated as a beam to the sample, which is rastered over the surface. The incident electrons cause secondary electrons to be emitted from the sample surface, which are collected by a detector, ultimately forming an image of the sample surface.

A number of factors affect the resolution of a scanning electron microscope (SEM). The most fundamental is the accelerating voltage, where faster electrons can produce smaller wavelengths; however, in practice other factors play a much larger role in the final image resolution. The pressure inside the SEM affects the resolution, since more particles in the residual background gas results in more collisions with the electron beam. This also limits what samples can be imaged with an SEM, as the sample may outgas or degrade in low pressure. The magnification of the SEM is done by a series of magnets (called lenses as an analog to light microscopy), which ensure the electron beam is well collimated; deviations in the beam profile can have large effects on the image quality. Important for some of this work is sample charging. The sample must be conductive to dissipate the electrons impinging on it. If the sample is not conductive, it will charge and the electron beam used for imaging will be repelled by the charge buildup on the sample surface.

Two different SEMs were used in this work. The first is a TESCON VEGA II LSU SEM, which uses a heated tungsten cathode. It has a probe current of 1 pA–2 μ A, using an accelerating voltage of 200 V–30 kV; mostly an accelerating voltage of 5 kV was used in this work. Magnification up to 1×10^6 X is possible. Due to the thermionic emission tip, this SEM is in general lower resolution than the other SEM used.

The second, higher resolution SEM used in this work is a JEOL JSM-7500F. It uses a cold cathode UHV field emission conical anode gun with accelerating voltages of 500 V–30 kV with probe currents of 100 fA–2 nA. Magnification up to 650,000 X is possible.

3.4 Optical Emission Spectroscopy

Optical emission spectroscopy uses the light emitted from a plasma to characterize it. The light is coming from photon emission of the various species in the discharge, as described in Section 2.2.2.2. Optical emission spectroscopy differs from other types of spectroscopy in that the system is naturally emitting light, rather than requiring an energy input to excite the species, as is done in a variety of laser techniques. As such, this is a completely non-intrusive technique; however, the amount of light is dictated solely by the physics occurring in the system. As such, the amount of light cannot be increased by varying the excitation process; the collection time must be increased to increase the amount of light collected. This technique is also not easily spatially resolved; the collection optics must be setup in such a way as to exclude certain areas for spatial resolution. This is in contrast to excitation spectroscopy techniques such as laser induced fluorescence, which are spatially resolved due to the excitation process that generates the signal.

3.4.1 Spectrometers

There are a number of types of spectrometers, but they all work on the same basic principals of breaking light up into its constituent wavelengths. This is usually done with a grating (although prisms can be used), commonly a diffraction grating (transmission gratings are also used at times). The diffraction grating splits the light up into its constituent wavelengths that are then detected by a light sensitive medium, such as a PMT or CCD.

The spectrometers used in this work are discussed in the following subsections. This will allow the details of their operation to be discussed here so that later chapters can refer to these subsections for more detail on the experimental setup.

3.4.1.1 SPEX Spectrometer

This is the main spectrometer used in this research. It is a SPEX 1 m focal length scanning monochromator spectrometer, model 1000M. It is a Czerny–Turner type spectrometer, containing a variable width entrance slit, two parabolic mirrors, and a reflective grating, such that the light travels in a *W* shape with the parabolic mirrors on one side and the entrance and exit slits and

grating on the other side. Two different detectors are used with this spectrometer, a Hamamatsu R928 photomultiplier tube (PMT) and an ICCD camera (see Section 3.3.2). The PMT has a spectral resolution of ~ 0.2 nm, as measured by the FWHM of the helium 706.5 nm peak, while the ICCD has a spectral resolution of ~ 0.04 nm, as measured by the FWHM of the iron 360.3 nm peak. As such, the resolution is substantially better (one order of magnitude) with the ICCD as the detector; however, scanning over wavelengths is possible with the PMT but has not been implemented with the ICCD. Thus the wavelength range is limited to ~ 5 nm when using the ICCD, which is sufficient for temperature determination using the 2nd positive system of N₂. The spectrometer wavelength dispersion was calibrated using a mercury lamp; a range of visible lines from 253.7 nm to 546.1 nm was used in the calibration.

3.4.1.2 *B&W Tek Modular Spectrometer*

The B&W Tek Inc. Glacier X thermoelectrically cooled CCD spectrometer is designed to have 0.5 nm spacing from 200–800 nm. The thermoelectric cooling allows for less thermal noise without a more complicated cooling mechanism (such as one requiring a coolant). The advantage of this system over the SPEX spectrometer is that the entire range is captured in a single acquisition without the need to scan over the wavelengths. This gives the entire spectrum at a single point in time, rather than relying on the assumption that the system is time-invariant, with the trade-off of having poor wavelength resolution. The disadvantage is that extremely short exposure times (<1 ms) are not possible.

3.4.1.3 *Ocean Optics Modular Spectrometer*

A second modular spectrometer (Ocean Optics Model HR4000) is used that has a narrower wavelength range from 325–421 nm, with a spectral resolution of 0.03 nm, which is sufficient for temperature determination using the N₂ 2nd positive system, since some rotational lines are able to be resolved. It has a set 5 μ m slit. This is an alternative to using the SPEX spectrometer, but is not able to provide the nanosecond time resolution that system is capable of achieving, due to the ability to gate the ICCD detector.

3.4.2 Species Identification

Figure 3.7 shows a measured spectrum from the FlashFuse system (see Section 7.5). The gas species present can be determined from the transitions (spectral lines) visible in the discharge. For the FlashFuse system, mostly nitrogen is visible, which is overexposed in Figure 3.7. This is to show some of the trace species, namely nitric oxide (NO), atomic carbon, and ionized nitrogen gas (N_2^+). In addition, different systems within a given species can be excited. This is shown where both the 2nd (C–B) and 1st positive system (B–A) of N_2 are both visible. The notation A, B, and C here correspond to different electronic transitions within a N_2 molecule. These transitions have different energies and thus appear at different wavelengths. The transition energy is given by the equation

$$\mathcal{E}_{initial} - \mathcal{E}_{final} = \Delta\mathcal{E} = h\nu = \frac{hc}{\lambda} \quad (3.4)$$

which relates the change in energy in the gaseous species ($\Delta\mathcal{E}$) to the light emitted (frequency ν or wavelength λ , where h is Planck's constant and c is the speed of light).

Various species can be identified because the electronic state is different for every atom and molecule, leading to differing spectra for each species. However, identification is not completely straightforward, sometimes considered an art rather than a science, because there can be many overlapping spectra which also can be excited in various ways leading to differing intensities or even different lines being observed. As such, a priori knowledge of what species are present (or likely to be present) in the system is crucial in making a determination of line identification.

In addition, understanding the method of excitation is helpful. For example, the dominant mechanism in the spectrum (a discharge in air) in Figure 3.7 is electron-impact excitation; however, O_2 is not observed (nor monatomic oxygen) due to the electron affinity of those species, which favors electron capture rather than electron excitation. Discharges with helium can also create a number of other species through Penning ionization or similar processes (see Section 2.2.2.2), since collisions with excited helium species can introduce a substantial amount of energy. There can also be large differences in the relative intensities of the emitting lines, even in systems that

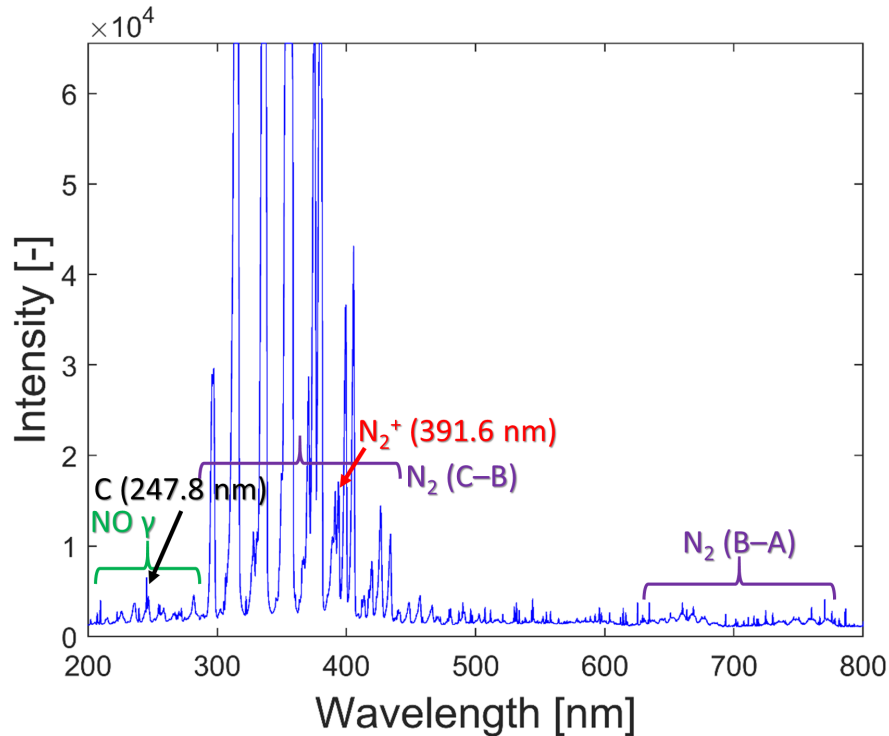


Figure 3.7: Spectrum of the FlashFuse System

appear quite similar. This is determined by how the various levels are excited, and can often be used to determine parameters about the discharge. For example, the ratio of various atomic lines can be used to determine the electronic excitation temperature, $T_{\text{el ex}}$, which is often assumed to be equal to the electron temperature, T_e , since the free electrons are causing the excitation of the various electronic states (see Section 3.4.3.1).

The stability of a state also is important. An excited species can lose energy via collisions rather than photon emission. This is called quenching, and is most commonly discussed in fluorescence applications, but can occur in plasma processes as well.

3.4.3 Temperature Determination

One of the primary ways to measure the temperature of a discharge is from the light emitted from it. The following subsections will discuss the theory of this method, the implementation in numerical software, and the practical issues in implementing it experimentally.

3.4.3.1 Theory of Temperature Determination

The light intensity emitted from a specific transition from an upper state u to a lower state l with upper state energy \mathcal{E}_u is proportional to the number of emitters there are, mathematically expressed as

$$I_l^u = k_l^u N_u \quad (3.5)$$

where I_l^u is the measured light intensity of the specific $u \rightarrow l$ transition, N_u is the number of emitters at the upper energy level of the transition, and k_l^u is a proportionality constant. The proportionality constant is a measure of the likelihood this transition will occur. It is described by the Einstein coefficient for electronic transitions (tabulated in the NIST database [218]) and becomes more complicated for molecular species, using the Franck–Condon factor for vibrational transitions and the Hönl–London factor for rotational transitions. [219–221] The number of emitters is given by the distribution function, typically a Maxwell–Boltzmann distribution (see Section 2.2.2.3), as described by quantum mechanics. For a single energy mode, say for the electronic excitation energy mode, the number of emitters at a specific energy level \mathcal{E}_u is given by

$$\frac{N_u}{N_{total}} = \frac{g_u}{Z} \exp\left(\frac{-\mathcal{E}_u}{k_B T_{\text{elec}}}\right) \quad (3.6)$$

where N_{total} is the total number of particles (of a given species, such as helium or N_2), g_u is the degeneracy of the upper level state, Z is the partition function of the energy levels, k_B is the Boltzmann constant, and T_{elec} is the electronic excitation temperature.

For a simple system of a single atomic species (i.e. no vibrational or rotational energy modes), the electronic excitation temperature can be explicitly solved for. The intensity of a particular transition $u \rightarrow l$ is given by

$$I_l^u = \frac{h\nu_l^u}{4\pi} A_l^u N_u = \frac{h\nu_l^u}{4\pi} \frac{g_u A_l^u}{Z} N_{total} \exp\left(\frac{-\mathcal{E}_u}{k_B T_{\text{elec}}}\right) \quad (3.7)$$

where the first factor comes from integrating the transition energy ($\Delta\mathcal{E} = \mathcal{E}_u - \mathcal{E}_l = h\nu_l^u$) over the

solid angle of a sphere and A_l^u is the Einstein coefficient for this transition. Taking the ratio of this transition with a second transition $i \rightarrow j$, where u and i are different upper level states yields

$$\frac{I_l^u}{I_j^i} = \frac{\nu_l^u g_u A_l^u}{\nu_j^i g_i A_j^i} \exp\left(\frac{\mathcal{E}_i - \mathcal{E}_u}{k_B T_{\text{elx}}}\right) \quad (3.8)$$

which yields a system that can be solved for the temperature as

$$T_{\text{elx}} = \frac{\mathcal{E}_i - \mathcal{E}_u}{k_B \log\left(\frac{I_l^u \nu_j^i g_i A_j^i}{I_j^i \nu_l^u g_u A_l^u}\right)} \quad (3.9)$$

For a more complicated system such as a diatomic molecule like N_2 , the intensity of a particular transition is a compilation of electronic, vibrational, and rotational energy modes that must be solved simultaneously.² Each energy mode is assumed to be in equilibrium internally, but not with the other energy modes. The state of the system is described by three quantum numbers, n , v , and J corresponding to the electronic, vibrational, and rotational energy modes, respectively. For a transition from an upper to a lower energy level, $n', v', J' \rightarrow n'', v'', J''$, the intensity is given by

$$I_{n'',v'',J''}^{n',v',J'} = k_{n'',v'',J''}^{n',v',J'} \frac{N_{\text{total}}}{Z} g_{n'} g_{v'} g_{J'} \exp\left(\frac{-\mathcal{E}_{n'}}{k_B T_{\text{elx}}} + \frac{-\mathcal{E}_{v'}}{k_B T_{\text{vib}}} + \frac{-\mathcal{E}_{J'}}{k_B T_{\text{rot}}}\right) \quad (3.10)$$

where the partition function is expressed as

$$Z = \sum_{n'} \sum_{v'} \sum_{J'} g_{n'} g_{v'} g_{J'} \exp\left(\frac{-\mathcal{E}_{n'}}{k_B T_{\text{elx}}} + \frac{-\mathcal{E}_{v'}}{k_B T_{\text{vib}}} + \frac{-\mathcal{E}_{J'}}{k_B T_{\text{rot}}}\right) \quad (3.11)$$

This is much more complicated than the case with a single energy mode, where the temperature could be explicitly solved for. Instead, it is easier to create a simulated spectrum, which can then be compared to the experimental spectrum, where the difference between the two spectra are minimized.

²The translational energy is normally treated separately since the quanta of energy are so small they are usually treated as a continuum. Doppler broadening and/or some other method are used to determine the translational temperature.

3.4.3.2 *Implementation of Temperature Determination*

Rather than attempting to look up every rotational and vibrational level to calculate the temperature by hand, it is convenient to use a computer program that has already implemented them, including deviations from the ideal cases, such as anharmonicity in intermolecular bonds and coupling between the energy modes. SpecAir [222] is a program that is capable of doing this, generating a spectrum of a variety of species including N_2 and N_2^+ given the necessary inputs of the various species and their fractions, the discharge temperatures (T_{trans} , T_{rot} , T_{vib} , and T_e), and gas density. However, this only produces a spectrum with a predetermined set of temperatures, rather than finding the actual temperature of a discharge. Since the equations in Section 3.4.3.1 cannot be solved explicitly, an iterative numeric approach is used to determine the temperature.

For this a MatLab routine is used to minimize the difference between the experimentally measured spectrum and the modeled spectrum from SpecAir. This code was developed by David Staack as a part of his graduate work [223] and was shown to successfully determine the temperature of atmospheric pressure glow discharges. [224] Some small changes were made to the code by Matthew Burnette, but no large changes in its behavior were implemented in this work. This is a highly nonlinear optimization for up to 9 dimensions: two spectral shifts (wavelength and intensity), one spectral stretch parameter (since the data is normalized only a wavelength stretch parameter is needed), four temperatures (T_{trans} , T_{rot} , T_{vib} , and T_e), a species number ratio (since only N_2 and N_2^+ are typically modelled), and an instrumental spread. The spectral shifts and stretch account for small spectral spread and shifts between the experimental and modelled spectra. The temperatures and species number ratio are accounted for in the simulated spectrum generated by SpecAir. Typically the translational temperature does not affect the spectrum significantly (it is implemented in SpecAir as Doppler broadening on the spectrum, which is typically too small to affect the result); in particular for low temperature plasmas this can be set equal to the rotational temperature, as these two modes equilibrate quickly. The electron temperature can be set equal to the vibrational temperature if there is no other information to better determine its value; it has a much larger effect on the spectrum when both N_2 and N_2^+ are both modelled, since this partially

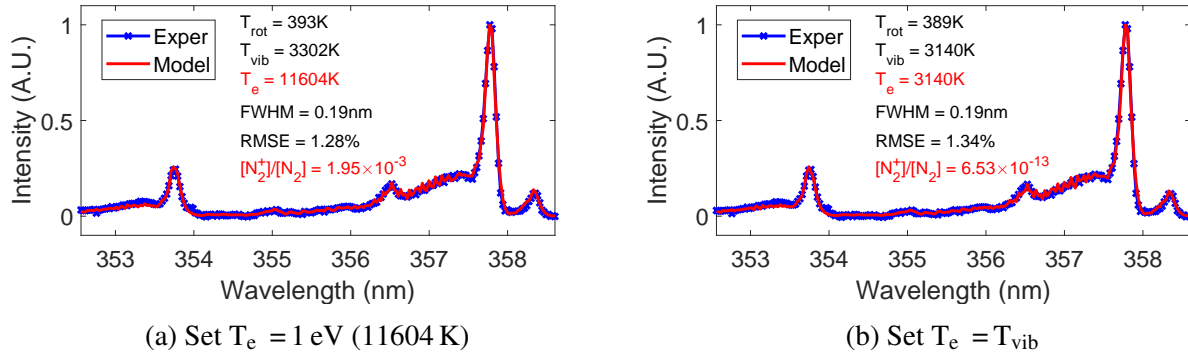


Figure 3.8: Spectral Fitting Showing the Non-Independence of T_e and Relative Concentration of N_2^+ in Modeling the 2nd Positive System of N_2 and the 1st Negative System of N_2^+

determines the amount of ionization occurring in the discharge. The ionization fraction (or species ratio in the general case) determines the ratio of N_2^+ to N_2 , thus determining the amount of each species spectrum in the overall result. Lastly, the instrument function, also called the slit function, is the spread of a Gaussian curve that is convolved with the modelled spectrum to best match the experimental spectrum. This is needed because the spectrometer does not have perfect resolution; it broadens the lines from what is actually emitted by the plasma due to the instrument's detector resolution and the physical inlet slit (via diffraction). Though different instrument functions can be used to better match the physical system (such as a Voigt profile or a trapezoidal profile), the simplicity of a Gaussian profile is used in place of a measured slit function. These various parameters are not necessarily independent of each other; in fact, in many cases they are not independent, as shown in Figure 3.8. To remove this dependence, further information is needed; for example, the electron temperature can be determined from Stark broadening of a hydrogen line in the spectrum.

The accuracy of modeling the temperature was shown to be up to 50 K for T_{rot} and <500 K for T_{vib} for the 2nd positive system of N_2 . An example fit of an experimental spectrum is shown in Figure 3.9 for the FlashFuse system (see Section 7.5), where inserts are included to show the fit for increasing or decreasing both T_{rot} and T_{vib} by 200 K and 500 K respectively.

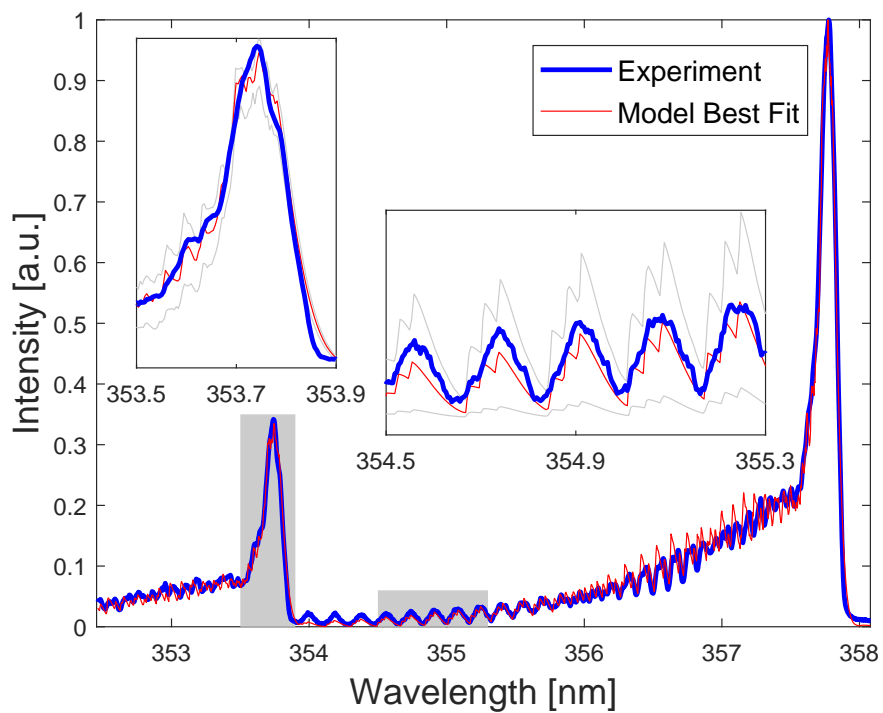


Figure 3.9: Measured Experimental Spectrum with a Model Fit of $T_{\text{rot}} = 598$ K and $T_{\text{vib}} = 4244$ K Along with Model Fits (Grey Curves in Insets) of $T_{\text{rot}} \pm 200$ K and $T_{\text{vib}} \pm 500$ K (+ Upper; - Lower Grey Fits)

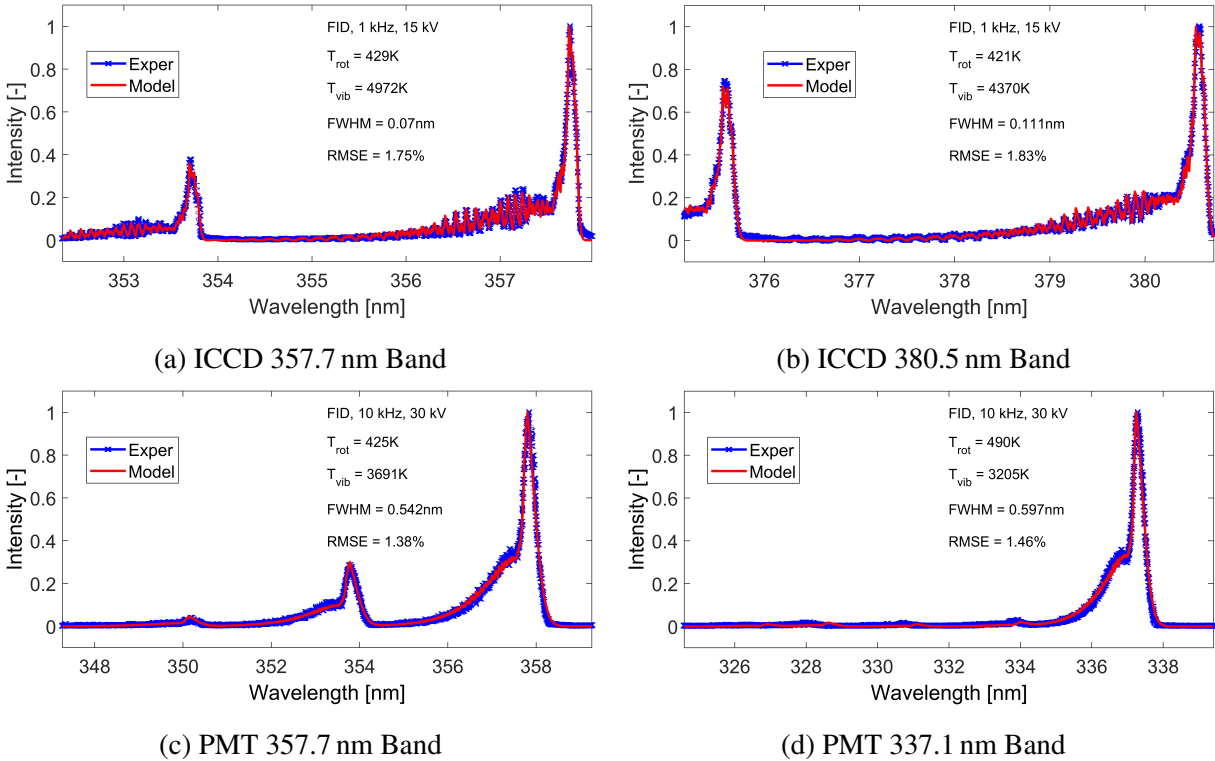


Figure 3.10: Spectra of Various Wavelengths and Detectors for Bands in the 2nd Positive System of N₂ with Temperature Fits

3.4.3.3 Temperature Determination in Practice

In practice, a number of factors can affect the accuracy of the temperature determination. The spectrometer resolution, band selection, and timing and light collection will be discussed.

The first is the resolution of the spectrometer and the resulting spectrum. The difference in resolution is noted by comparing Figure 3.10a with Figure 3.10c. Though these are the same system, band, and even the same spectrometer (including entrance and exit slit widths), the ICCD detector is able to achieve a much better resolution than the PMT detector (see Section 3.4.1.1 for a quantitative comparison). This is noted especially in the tail of the band heads, where the rotational lines are resolved in the ICCD spectrum, while they are not resolved in the PMT spectrum. This leads to more accurate T_{rot} when using the ICCD compared to the PMT.

The second main factor affecting the accuracy of the measured temperatures for a plasma dis-

charge is the band used for the temperature determination. The 357.7 nm band (Figure 3.10a) and the 380.5 nm band (Figure 3.10b) of the 2nd positive system of N₂ are roughly comparable to each other, although the 357.7 nm band also has a small influence from N₂⁺ which is absent in the 380.5 nm band. The main difference is with the 337.1 nm band (Figure 3.10d), where the additional vibrational levels are much smaller compared to the main band head. As such, an accurate T_{vib} is nearly impossible since only one band head is investigated.

The last aspect that can affect the accuracy of the temperature determination is the combination of the spectrometer timing and light intensity. Sufficient light must be collected to obtain a spectrum, but increasing the exposure time may have unintended consequences. The temperature of a discharge may not be a constant, and for all of the discharges investigated in this dissertation the temperature is highly time dependent. Thus the trade-off must be made between sufficient light collection and time resolution. In general, all of the temperatures reported in this dissertation are time averaged temperatures, because the dynamics of the discharge are occurring too quickly (~1–10 ns) for adequate light collection while maintaining any reasonable time resolution (i.e. exposures on the order of 1 ns). The gas temperature that would cause issues in a medical setting is a time averaged temperature, as well, further supporting this approach.

One way to work around the trade-off of light collection and time resolution is to assume that all discharge events are identical. Thus a gated system could be used where the light is collected many in short (~1–10 ns) increments before it is read off of the detector. This has been done with the ICCD, but not for any of the results reported in this dissertation. The main issue (beyond the complications in creating the timing circuitry between the discharge and light detector) that was found with this approach is that there is more noise for many short exposures of the ICCD compared to long exposures. As such, some testing was done in a dark room to limit influence from ambient light sources especially with long (up to 30 min) exposures.

4. ELECTROPORATION SYSTEM

4.1 Introduction

This chapter introduces an electroporation system that is designed to apply a high electric field to human skin with pulse durations ranging from ~ 3 ns to >20 ns. This system is designed to assist with drug delivery in dermal and epidermal applications. In addition to using a commercial pulsed power supply system (~ 3 ns pulse duration), a custom built RC pulse generating circuit, capable of delivering 2–40 kV pulses with variable pulse widths of >20 ns, is also devised as an inexpensive system to apply the fast electric field. An array electrode is developed of finely spaced tips which allows for gas flow through the array as the high electric field applicator. The system is characterized by high resolution imaging to observe uniformity across the array tips. Three distinct discharge modes are noted for the system using the custom pulsed system. Optical emission spectroscopy is used to determine some of the species created using this system, as well as a method of determining the temperature of the plasma discharge. The plasma discharge is noted to be substrate invariant for a range of conditions. The possible approval routes for marketing this system are explored.

4.2 Electroporation Background

Electroporation is the application of an electric field on a cell to induce pore formation in the cell membrane. Research began in earnest starting in the 1980s after transfection of plasmid DNA was shown to occur using electroporation. [225] This has only been perfected in more recent decades. [226] It was in the 1990s that it was determined that physical pores do form in cells as a result of electroporation. This was done by rapidly freezing cells before performing electron microscopy, which yielded images of 20–120 nm sized pores in the cell membranes. [227] These pores were observed to start to close after several seconds, showing that electroporation is only a transient effect (see Figure 4.1).

Electroporation is used to insert proteins into the cell membrane, introduce foreign matter into

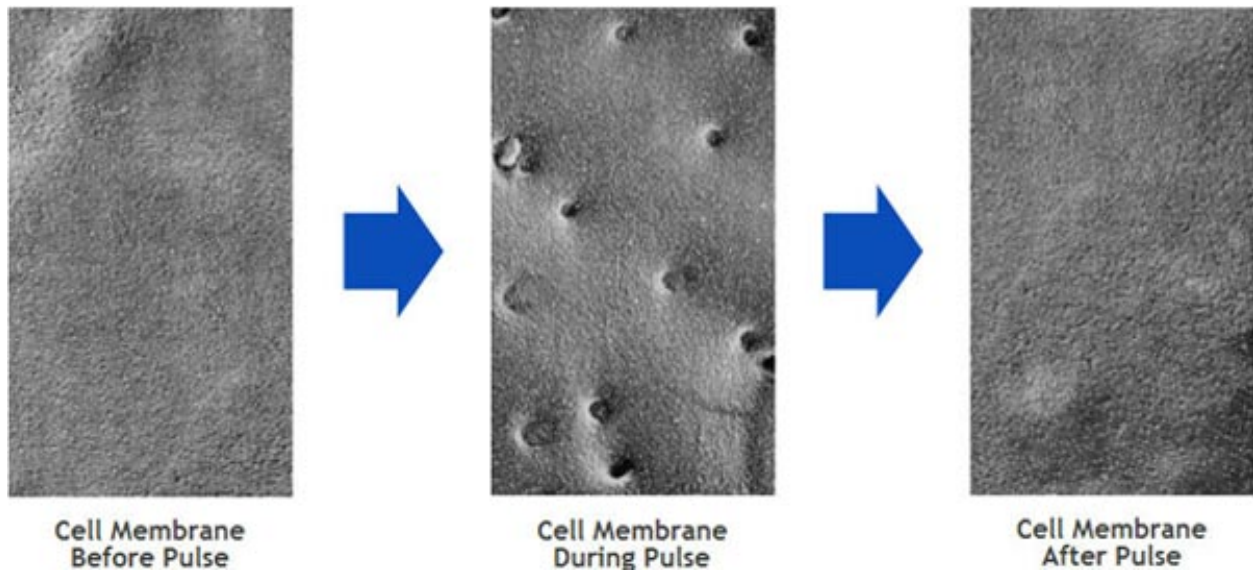


Figure 4.1: Electron Micrographs of Flash Frozen Cells Exhibiting Electroporation (Reproduced under Fair Use from [228])

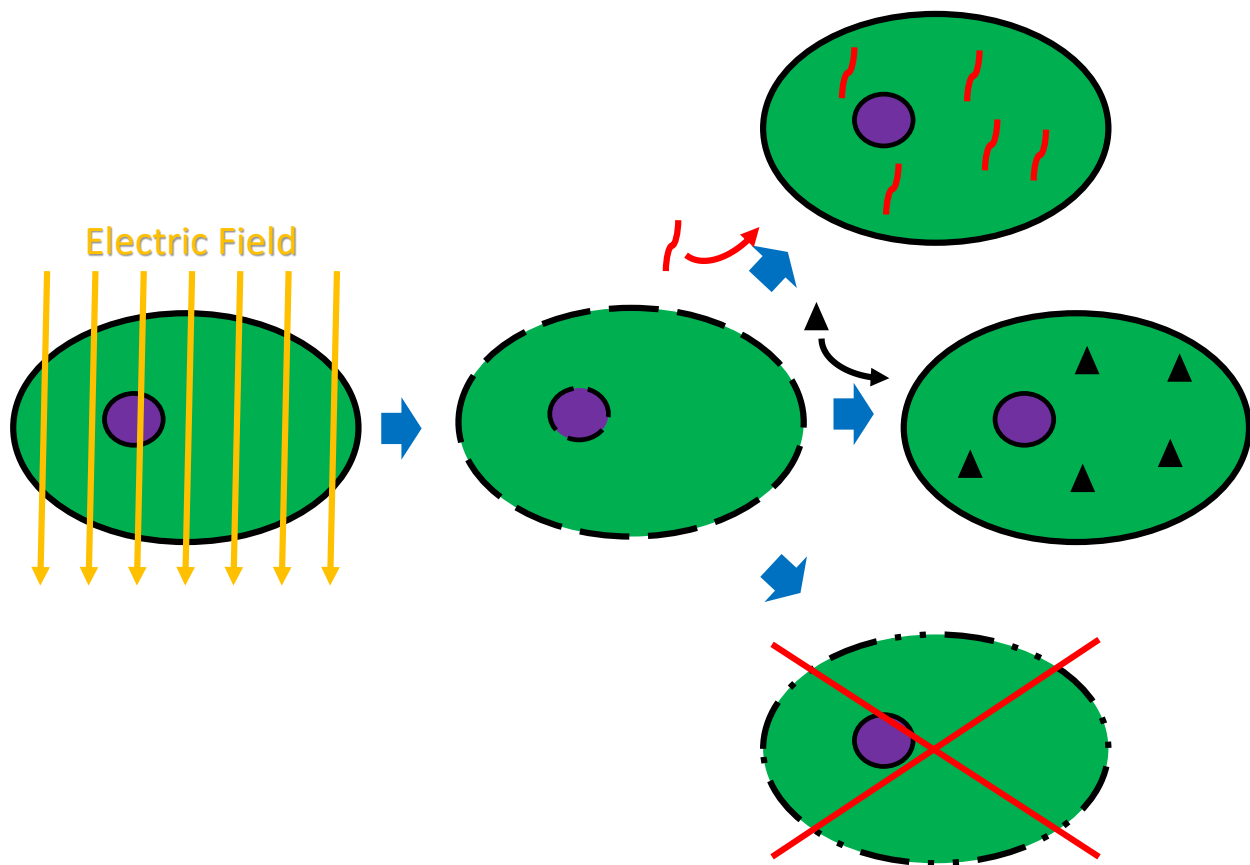


Figure 4.2: Schematic of Electroporation with Uses Including Protein Insertion, Foreign Matter Introduction, and Cell Membrane Destruction

the cell, or destroy the cell membrane, as shown in Figure 4.2. However if too high of a voltage is used, the electroporation is irreversible, and the cell will not recover after the electric field is removed. [229] Irreversible electroporation is not always undesired. It is one method of killing cells, although other methods may be more useful or efficient for a given setting; in particular, large areas of necrotic tissue often result if this is done in vivo. Often after electroporation a number of cells are no longer viable, particularly for in vitro electroporation where it is difficult to control the electric field magnitude for all cells. However newer electroporation techniques are being developed that are more selective in the cells that are electroporated leading to higher cell viability. Research shows that typically a transmembrane potential of around 1 V is sufficient to induce electroporation. [225] For in vivo applications, reversible electroporation occurs for an electric field around 350 V/cm and irreversible electroporation occurs around 600 V/cm, as found using rat liver tissue with eight 100 μ s pulses at 1 Hz. [229]

Clinical research is beginning to be done with electroporation; however it appears to solely be in the field of electrochemotherapy, that is the application of electroporation for the insertion of chemotherapy drugs directly into cancerous cells. Irreversible electroporation is not desired per se due to creating large sections of necrotic tissue; however, small amounts of irreversible electroporation may occur during electrochemotherapy. [230] The primary purpose is to assist in targeted delivery of the chemotherapy drugs directly to the tumor. A number of drugs have been investigated, predominantly bleomycin and cisplatin, which have been shown to have up to 1000 times and 80 times cytotoxic enhancement, respectively, due to electroporation treatment. [231] Even more, insertion of plasmid DNA is also being investigated for anti-cancer effect. [232] Though no device is on the US market to date, advanced clinical trials are ongoing in this space. [233]

Conventional electroporation can be done in vitro in electroporation cuvettes using low voltage pulses or in vivo where two electrodes are placed on opposite sides of a section of skin and a voltage pulse is applied. Usually long (micro- or millisecond) pulses are used, but new research has shown that nanosecond electroporation can also be used with some differing effects. Research shows that nanopores are created using nanosecond-pulsed electric fields. [234] Other effects can

occur such as inducing apoptosis, damaging DNA, modifying caspase activity, and modifying calcium functions in the cell. [7,234,235] Since the electric field is applied faster than the inherent charge time of ~ 100 ns for a cell, a higher electric field is possible before the charges migrate to reduce the applied electric field. [236] This is one reason that though irreversible electroporation was noted above 600 V/cm, [229] higher electric fields may still be used if they are applied over nanosecond durations. However, more research needs to be done to understand what threshold may exist for irreversible electroporation using a nanosecond pulsed electric field.

4.3 Device Life-Cycle Overview

The goal of this project was to develop and test a nanosecond-pulsed array and corresponding pulsed power system that is capable of creating a uniform discharge with high electric fields (100-150 kV/cm, note this is about 50 times the magnitude required for electroporation using microsecond pulses) and low current in ambient air that can also be operated using different working gases. The system should be stable, safe, and robust within the operation range, such that anyone with moderate training can use. This device seeks to be external to the patient, ideally without direct contact, thus the electric field must also penetrate through the epidermis and into the living cells in the dermis, a gap of $\sim 68.9 \mu\text{m}$ to the edge of the dermis. [237] Applying higher fields nanoseconds in duration is one way to achieve the necessary high fields at depth, but inevitably this will create a plasma, which is utilized in this project for device characterization. Plasma discharges have also been investigated for their electroporation effect. [238] This system is intended to be a novel nanosecond electroporation device for medical treatment.

As with most of the devices discussed in this dissertation, this device is very early in its development. The need has been at least partially identified as epidermal electroporation to assist in drug delivery through the skin and dermis (see Figure 4.3), but the market is a challenge due to the nature of the FDA. This is because, as a combination drug/device, each new drug used will require a separate approval process (see Section 2.4.1.7). As such, the need has to be further narrowed to a specific drug, which will most likely narrow this to a specific application. One possibility is using this to replace viral vectors currently used in gene therapy. [239] However, electrochemotherapy is

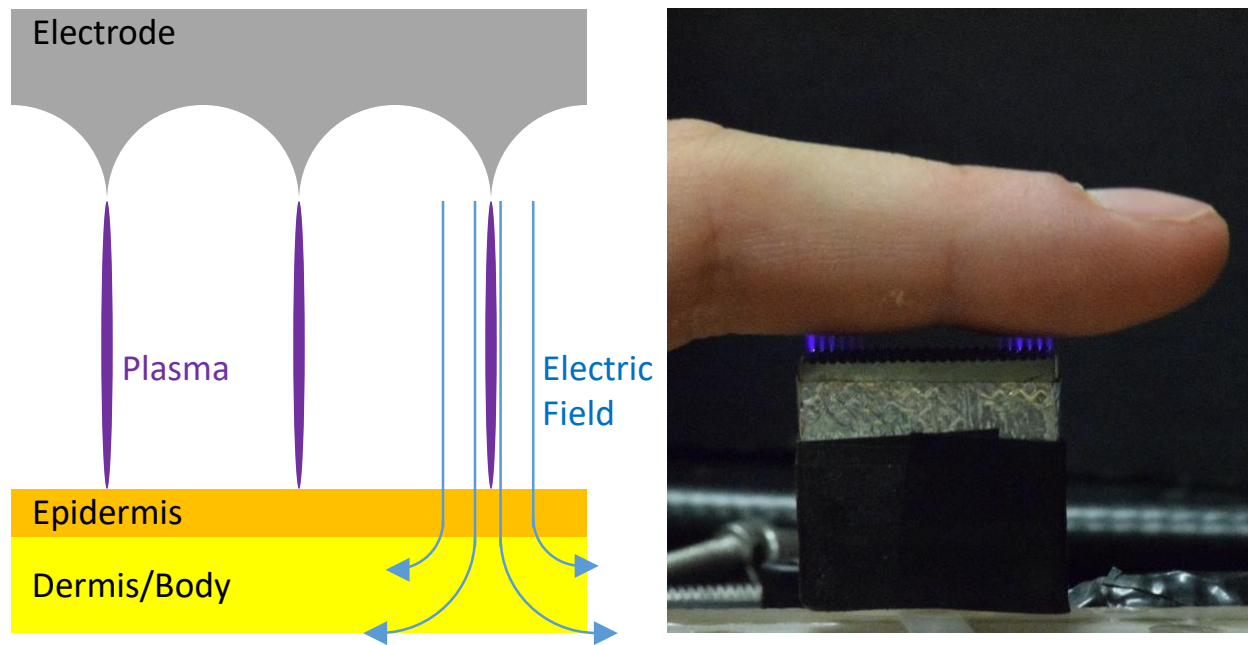


Figure 4.3: Schematic and Image of the Array for Epidermal Electroporation Applications

the most likely application as it has a large market, which also means many potential investors to see this device through to marketing.

Significant work has been done in electrochemotherapy with other devices. An earlier clinical trial was conducted in 2004, but it does not appear the FDA approved this device; most likely it has stopped in clinical trials, [240] since no further information on it is publicly available. This may be due to lack of funding to continue the project or may have occurred because poor results were obtained and the project was cancelled. [241] It is unclear if this may be a similar device that has been used successfully in Europe for electrochemotherapy. [242] There is a further clinical trial of an existing, FDA-cleared irreversible electroporation device, called the NanoKnife, being used for electrochemotherapy; [233] although it is unclear what FDA approach this system is taking, which can affect the approach for this device. In addition, there is at least one clinical trial attempting to use calcium, rather than bleomycin, as a device for electrochemotherapy, where calcium should have fewer side-effects than the standard chemotherapy drugs. [243]

4.3.1 FDA Approach

Most electroporation devices are designed for cell suspensions or similar setups rather than for direct medical treatment. An example of this is the prevalence of electroporation cuvettes. [225] This means that any device brought before the FDA will most likely be a novel device, requiring a De Novo request. There is a small probability that the FDA would view this as a Class III system and require a PMA, but this is unlikely, since the risks associated with an electroporation system can be mitigated with special controls. Lacking a clear predicate device, the 510(k) pathway does not seem to be a viable option, however a narrow use device may be possible via the 510(k) pathway. This would require finding a need where an electroporation system has the same intended use as the predicate device, but is operating with different technological characteristics; however this is unlikely to be found.

Though there are a number of FDA cleared systems for operation as irreversible electroporation devices [244, 245] (which all appear to be grandfathered into the FDA as derivatives of older devices, possibly dating back to the Bovie power supply for electrosurgery), this device is not designed for irreversible electroporation, and thus those existing systems cannot be used as a predicate device. No device for clinical non-irreversible electroporation was found except those used for electrochemotherapy (where small amounts of irreversible electroporation may occur); however none of these systems are FDA approved. The NanoKnife system, though, may offer the rare opportunity for a 510(k). If this system is cleared under a 510(k)¹ or is granted a De Novo request, this would allow further devices to seek a 510(k) clearance using it as the predicate device. However, the use would most likely be limited depending upon the exact wording of the intended use of the NanoKnife system predicate.

The main difficulty in this device is that it is designed to be paired with a drug to be delivered, which opens the possibility of complex reactions, since not only is the reaction of the tissue to the applied electric field needing to be considered but also the drug-tissue interactions, the drug-

¹A 510(k) clearance is unlikely, since this should be viewed as a combination device, and no similar drug/device combination is currently approved.

electric field interactions, and even the possibility of a drug modified by the electric field interacting with the tissue. This will require substantial study to show that there are no unintended results. As such, the De Novo request may be the best option. This is the most probable course for any device seeking a combination drug/device without a clear predicate, which is the most probable use for electroporation devices in a clinical setting.

However, electroporation by itself may yield enough benefit it can be used without pairing it with a drug or a drug may be applied after electroporating the tissue. In this case, a 510(k) option may be available. This would allow a limited number of drugs to be used that could be applied after the electroporation, thus avoiding potential plasma-drug interactions. This, however, may still be considered a combination product, but the risks are lower since the electroporation system and drug are applied in series rather than parallel. Later, the developer can begin trials with other drugs that cannot be applied in series, while being able to market the device and ideally turn a profit. This seems to be the general approach for AngioDynamics, Inc., the manufacturer of the NanoKnife system, who are currently using their 510(k) cleared device in clinical trials for electrochemotherapy, most likely in support of a De Novo or similar combination product (bleomycin, the drug, along with the device) submission. [233]

4.3.2 Device Outlook

For our device, the possibility of using nanosecond pulsed electric fields for electroporation of the epidermis is desired, without the need to insert electrodes into the dermis as is commonly done for electrochemotherapy systems. [230] Though we are not targeting a specific drug at this point, we would most likely also use an anti-cancer drug, such as bleomycin or even just intracellular calcium. [243] Thus we are considering how to ensure the safety of the device in our design such that it could be used in a clinical setting. The testing is also designed to show at least from a bench top scale, that this device is biocompatible and could be taken through further testing to become a clinical device. Nevertheless, further verification studies should be conducted on this device.

4.4 Device Design

The device consists of two main parts, a nanosecond pulsing circuit and an electrode to deliver a wide area high electric field treatment. These two parts will be discussed in the following subsections. Initially the FID power supply (see Section 3.2.1.3) was used as the nanosecond pulsing circuit; however, this power supply is prohibitively expensive for widespread use, so a custom RC pulse generating circuit is devised as detailed in the next subsection.

4.4.1 RC Pulse Generator Circuit Design

To maximize the desired high electric field (E), high voltage (V) and fast voltage rise time are required. Without movement of charges

$$E = -\frac{V}{d} \quad (4.1)$$

where d is the distance between two electrodes, thus clearly higher voltage produces higher electric fields. This gives an initial approximation to yield the desired electric field magnitudes of 100–150 kV/cm; using an applied peak voltage of 30 kV an electrode-substrate gap of 2 mm is needed. However if there are charges present in the form of free electrons or ions, these charges can build up on dielectric surfaces which then negate the applied electric field. Therefore the rise time on the voltage should be comparable to the ion transit time to allow for a high electric field before the ions have time to migrate and decrease the electric field. Since cells have an inherent charge time on the order of 100 ns, [234] a nanosecond pulsed system is required to maximize the electric field. To achieve a nanosecond rise time in voltage, a fast switch (i.e. operating on a nanosecond time-scale) is needed capable of supporting high voltage. The two main options are spark gaps or solid state devices, such as insulated-gate bipolar transistors (IGBTs). One main drawback to such a system is that high voltage usually means high energy since

$$\mathcal{E} = \frac{1}{2}CV^2 = \frac{1}{2}QV \quad (4.2)$$

where \mathcal{E} is the energy delivered, C is the capacitance being discharged (normally a constant for a given system, thus the energy applied scales with V^2), and Q is the charge transferred in the discharge. This large amount of energy is often incompatible with biological substrates. The main way to limit the energy delivered, while still maintaining the high voltage and fast voltage rise time, is to have another fast operating device in parallel to the load which is able to take most of the energy. This could be a resistor, inductor, etc. that is able to operate on the timescale of the voltage pulse. For our design detailed below, a second spark gap that is in parallel to the load is used to take most of the energy from the discharging capacitor.

For this project, an RC pulse generator was developed which consists of four switchable capacitors (5 nF, 500 pF, 50 pF, and stray capacitance), an optional secondary resistor to dampen the pulses, two independently adjustable spark gaps, and a third spark gap used for triggering the main spark gap. As this pulse generator was delivered to the project sponsor, a user guide for was developed to help ensure proper operation, which is included in Appendix A. The schematic of the RC pulse generator is seen in Figure 4.4, and the inside of the box housing the RC pulse generator is seen in Figure 4.5. The box is well insulated to ensure no undesired breakdown would occur in it or to its outer shell. It has the ability to be locked to avoid any unauthorized users from gaining access to it, as well as a top acrylic shield (not shown in the images) to allow basic diagnostics on it without being exposed to the high voltage.

Until the main spark gap (MSG) breaks down, the circuit is a standard RC charging circuit. A Spellman high voltage DC power supply (PS , see Section 3.2.1.1) initially charges the capacitor (C) through a resistor (R_1). Once sufficient charge has been built up on the capacitor to reach the breakdown voltage of the MSG , a spark occurs bridging the gap and resulting in a fast voltage rise downstream of the MSG . If the second spark gap (SSG) distance is small enough, it will discharge as a spark, taking most of the energy from the discharging capacitor and shortening the voltage pulse; if the SSG is too long, it will not break down resulting in significantly more energy being delivered to the array and substrate load and a much longer pulse duration will result ($\sim 1 \mu\text{s}$ for the single spark gap configuration compared to $\sim 20 \text{ ns}$ for the double spark gap configuration).

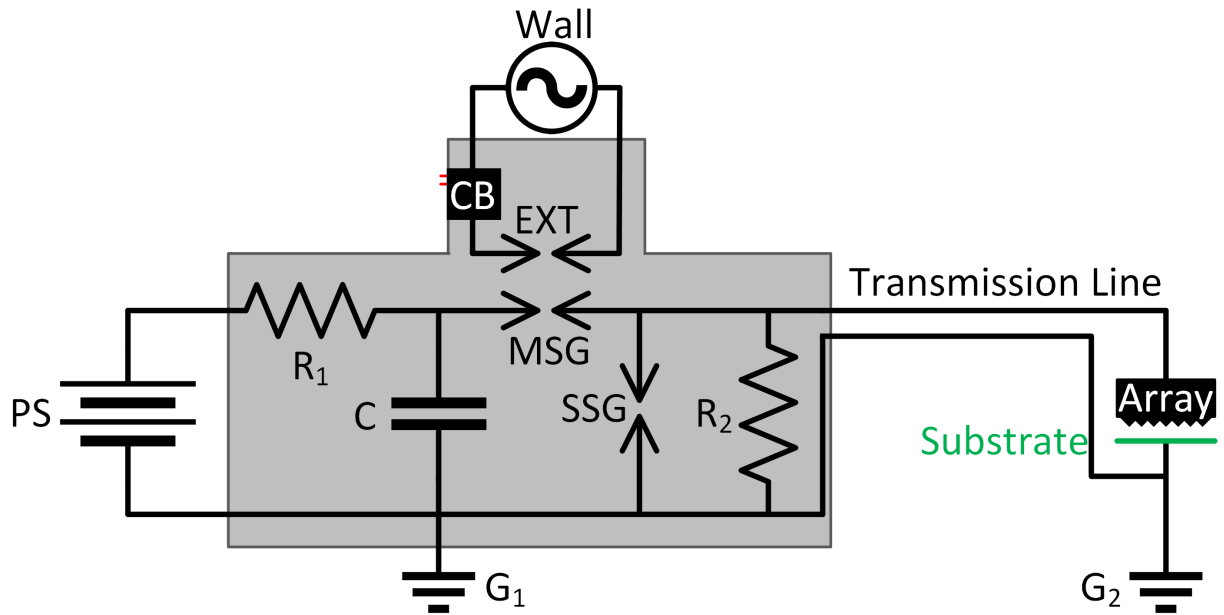


Figure 4.4: Schematic of the RC Pulse Generator

More details on this long pulse mode can be found in Appendix A. The voltage pulse travels down a meter-long twisted pair high voltage cable (a transmission line because the differential impedance is roughly constant along the wire due to a constant high voltage wire to ground wire distance with no change in the dielectric material separating them) connecting the array and substrate load to the RC pulse generator. If the load is conducting the current will travel through the array and substrate directly to ground; if the load is non-conducting, the voltage pulse will get partially reflected back to the RC pulse generator, resulting in a higher voltage across the load than the breakdown voltage of the *MSG* for the duration of the voltage pulse transit time in the transmission line. The load can still be non-conducting even if the substrate is conducting due to an array-substrate gap that is too large for complete breakdown to occur. The secondary resistor (R_2) is used to dampen any oscillations in the voltage pulse by slowly draining off excess charge. R_2 does not greatly affect the voltage pulse unless its resistance value is quite small ($\sim 100 \Omega$, see Appendix A). Two grounding locations are noted (G_1 and G_2) even though they are both *ground*. This is because for the duration of the voltage pulse (i.e. ~ 10 s of nanoseconds) they may not actually be at $V = 0$ due to stray

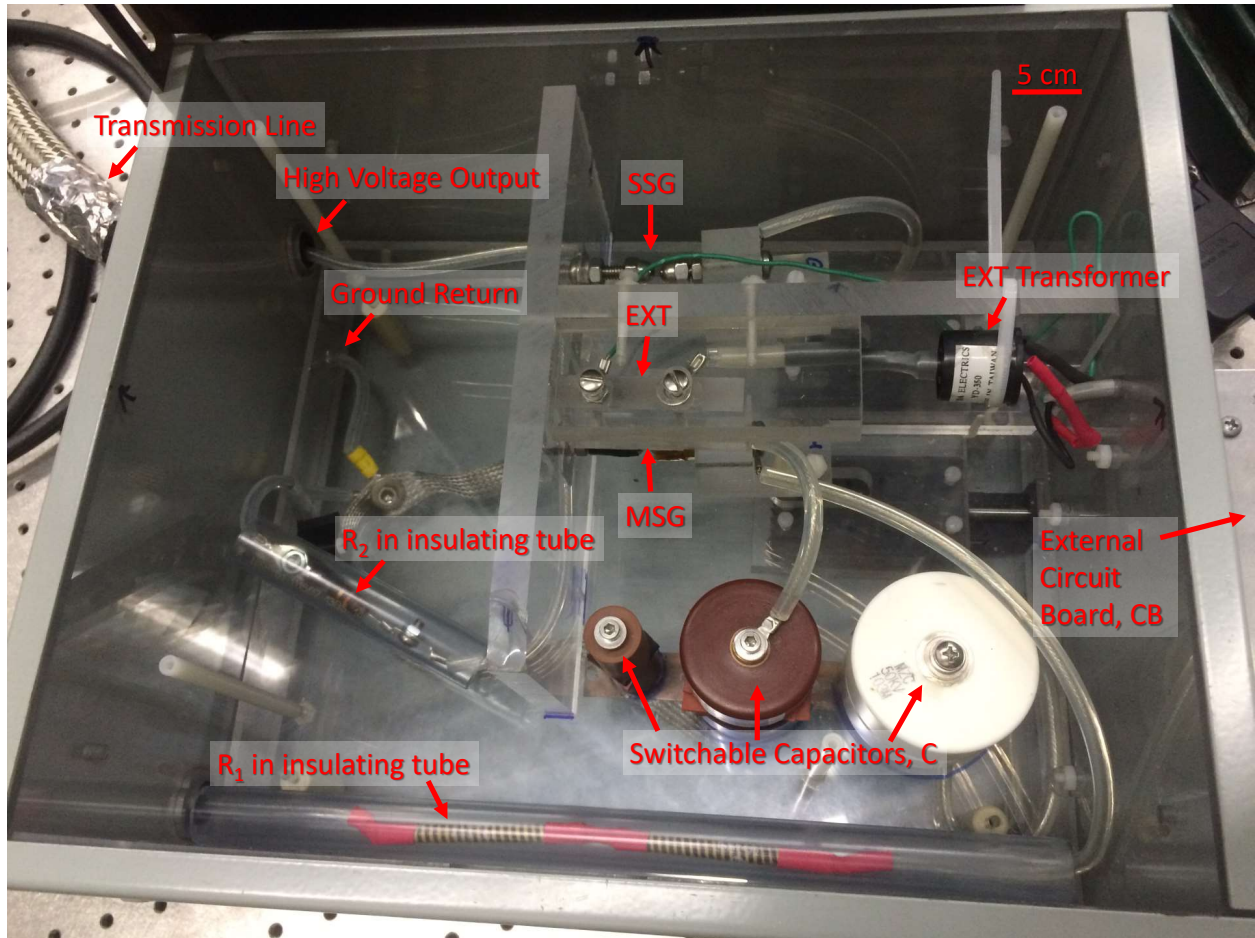


Figure 4.5: Image of the RC Pulse Generator with the Lid of the Housing Open

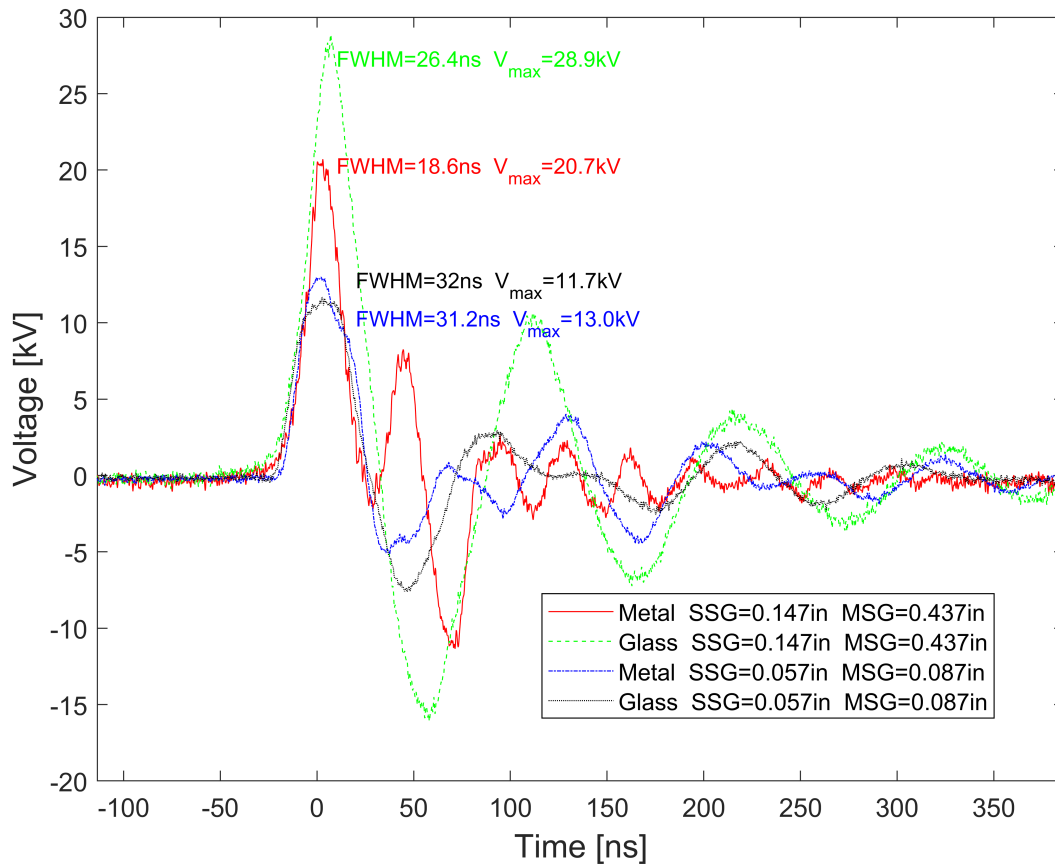


Figure 4.6: Comparison of Voltage Traces for Dielectric and Conductive Substrates with the RC Pulse Generator for a $V_C = 9$ kV and $V_C = 27.5$ kV Breakdown Voltage Case

inductance. This also clarifies that the ground side of the transmission line is actually connected directly to ground and not floating, relying on the ground reference inside of the box. The third spark gap (*EXT*) is operated by an external circuit board (*CB*, Ignitor10 power supply from Information Unlimited) mounted on the side of the main box housing the RC pulse generator. The *EXT* is able to trigger the *MSG* to fire when it is just below the breakdown voltage. It does this by introducing a few seed electrons (primarily by photoionization however due to its physically close location electron diffusion may also be significant) to initiate the breakdown process in the *MSG*.

By varying the spark gap distances of the *MSG* and the *SSG*, the desired pulse voltage and

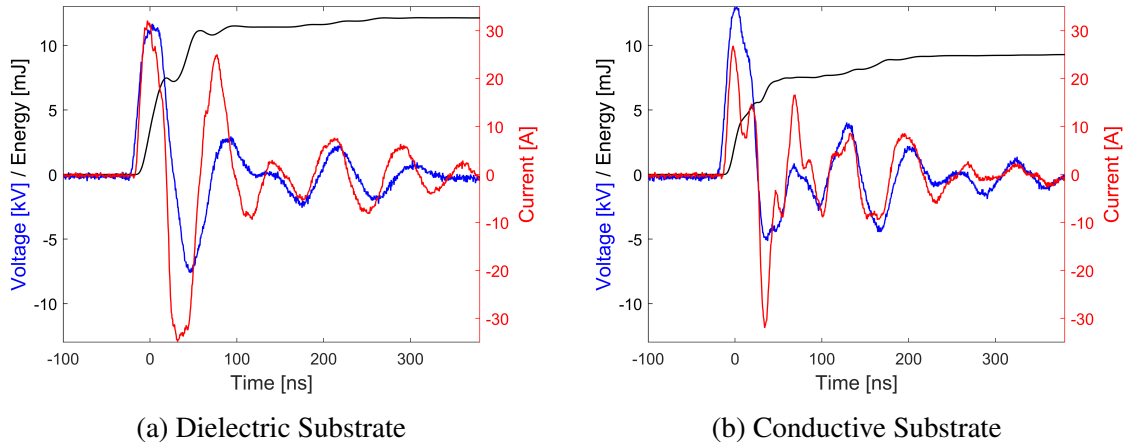


Figure 4.7: Comparison of Voltage and Current Traces for a $V_C = 9$ kV Breakdown

duration are able to be specified for a given load. The pulses from the RC pulse generator appear very repeatable, with a variance under 5%. Like any high voltage pulsed power supply, there is some load dependence on the pulse characteristics. For lower voltages (for a 5 mm electrode-substrate gap it was below 18 kV and 30 kV for a metal conductive and glass dielectric substrates, respectively) the air gap acts as a dielectric and voltage reflection can occur, leading to pulse voltages higher than the breakdown voltage on the capacitor, C . Some typical voltage pulses are shown in Figure 4.6. Nevertheless, peak pulse voltages were generally close (within about 3 kV) to the breakdown voltage on the capacitor (generally only slightly higher if voltage reflection occurred). This is because the characteristic impedance of the transmission line (the meter-long twisted pair high voltage cable) is not well matched with most of the loads. There was roughly a 1 kV/ns rise and fall on the voltage pulse if the SSG was set at or below an optimum value for a given load; larger SSG distances did not reliably fire, leading to longer pulse durations with substantially slower fall times. SSG distances below the optimum value reduced the peak pulse voltage but still maintained the 1 kV/ns rise and fall speeds. This *speed limit* on the rate of the voltage change is due to the characteristic impedance of the transmission line between the RC pulse generator and the load.

The voltage traces in Figure 4.6 are plotted together to show the effect of the load and break-

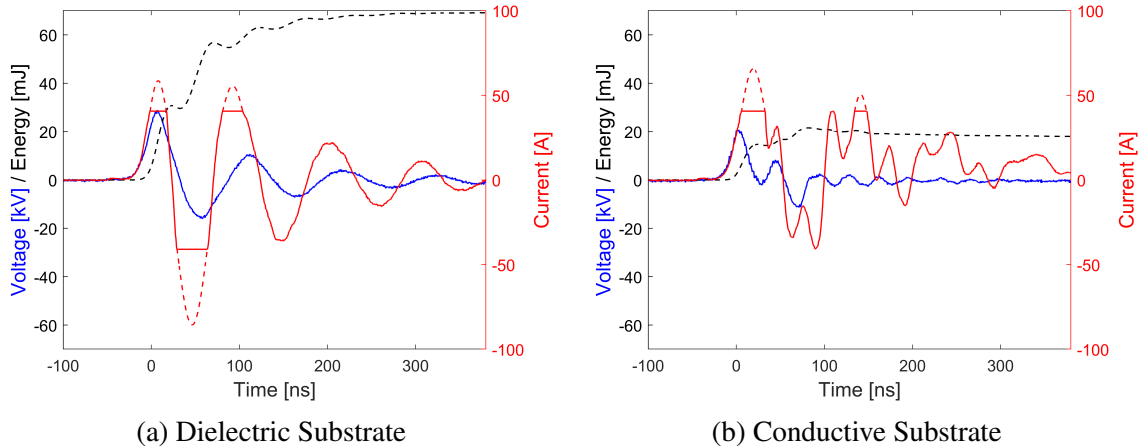


Figure 4.8: Comparison of Voltage and Current Traces for a $V_C = 27.5$ kV Breakdown

down voltage of the *MSG*. Despite nearly identical behavior for the lower breakdown voltage (measured across the capacitor as 9 kV), the two loads have very different voltage traces (both in maximum peak voltage attained and later ringing in the voltage) for the higher breakdown voltage case (measured to be 27.5 kV across the capacitor). These voltage traces are also shown in Figure 4.7 and Figure 4.8 for $V_C = 9$ kV and $V_C = 27.5$ kV breakdown voltages, respectively. In addition to the voltage trace the corresponding current is also displayed along with the energy, found by multiplying the instantaneous current and voltage (i.e. the instantaneous power) and then integrating. The oscilloscope was limited to only displaying ± 40 A, thus the current peaks for the $V_C = 27.5$ kV breakdown cases was cut off. Peak values were assumed (dashed lines) and thus an estimate on the instantaneous energy was also determined for those cases as well. The current traces and energy traces are comparable in the $V_C = 9$ kV breakdown voltage case, but there are significant differences in the $V_C = 27.5$ kV breakdown case. For all cases, it appears that the majority of the energy delivered occurred on the initial voltage and current rise (the higher breakdown voltages cases are possibly skewed slightly due to the current not being adequately measured), but further energy was delivered when the current fell; for the higher breakdown voltage case with the conductive substrate this current fall took longer to occur due to some ringing in the current signal. The total energy was nearly equivalent in the lower breakdown voltage case,

suggesting the air gap between the array and substrate did not completely break down; the streamers formed apparently did not form a fully conductive path to ground. Substantially more energy was delivered for the higher breakdown voltage cases. Counterintuitively, the dielectric substrate had substantially higher energy delivered for the higher breakdown voltage case compared to the conductive substrate. This occurred because the voltage and current magnitudes were higher for this load, especially the large fall in the current. This is most likely explained by better matching of the transmission line with this load than the conductive load.

The RC pulse generator is designed for a wide range of pulse frequencies from a single pulse up to ~ 100 Hz depending on the voltage and current supplied from the power supply (the power supply was limited to 7.8 mA). The pulse voltage has a minimum value around 2 kV, due to issues in reliably spacing the main triggering spark gap; the power supply was limited to 40 kV, serving as an approximate upper voltage limit, although higher voltages are possible if voltage reflection occurs. The *EXT* has some inherent jitter on the order of 1 μ s in triggering the *MSG* to break down, nor did it always trigger the main spark gap to break down since it had to be placed far enough away to avoid the high voltage side of the *MSG* from discharging to the ground of the *EXT*. For more detailed information on the operation of the RC pulse generator see the user guide in Appendix A.

4.4.2 Electrode Array Design

To achieve a uniform high electric field, a high density of sharp tips is desired. This is because the local electric field in the region of a sharp tip is determined by

$$E = \frac{V}{r} \quad (4.3)$$

where r is the radius of the tip. Sharper tips yield the higher electric fields. By creating an array of tips, the electric field will be approximately uniform ~ 0.5 mm from the tips, as determined by a 2D electrostatic model run in Comsol, shown in Figure 4.9.

This model (Figure 4.9) serves as a qualitative measurement of the effect that sharp tips have on

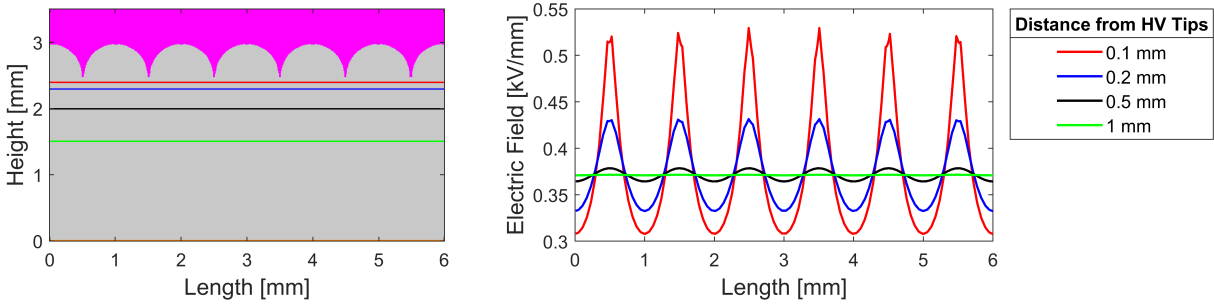


Figure 4.9: Schematic of the 2D Electric Field Model for the Array Tip Electrode and Graph of the Resulting Modeled Electric Field

enhancing the electric field. The model geometry has an array of 6 tips spaced 1 mm apart held at 1 kV (purple color) and ground 2.5 mm away at the bottom of the geometry (orange color). There are 4 lines where the electric field along the length is determined (red, blue, black, and green lines). The tips provide a local enhancement of the electric field, which becomes virtually non-existent at a distance of 1 mm from the tips. As such, for very short gaps (<0.5 mm) the electric field will be enhanced near the tips, leading to a more non-uniform electric field; farther away from the tips the electric field becomes lower than near the tips but approaches a uniform value.

The array was developed by using electrical discharge machining (EDM). Thin sheets of 1 in wide stainless steel were stacked together and portions were removed to create an array of tips along the length of each stainless steel sheet. U-shaped spacers were inserted between the EDM sheets to create a gas inlet, mixing chamber, and outlet near the tips by alternating their orientation, such that one opens up at the gas inlet and the other points in the opposite direction to be a gas outlet (see Figure 4.10). The array of tips was then placed in a block of Teflon to hold them together. The Teflon also acts as a good electrical insulator to protect the operator from the high voltage. A gas inlet was placed in the back of the Teflon block, and a high voltage wire was connected through the side to the stainless steel array. The final design is seen in Figure 4.11.

Three arrays were developed with varying tip spacing as noted in Table 4.1. Images of the different arrays are shown in Figure 4.12. Array #1 was used for all of the testing reported here except for the array comparison testing.

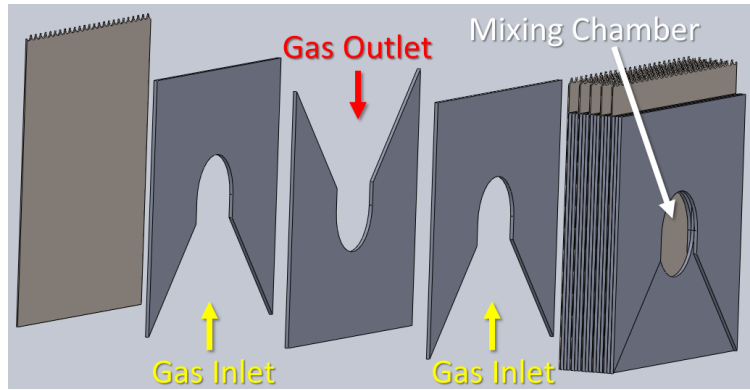


Figure 4.10: Schematic of the Array Electrode

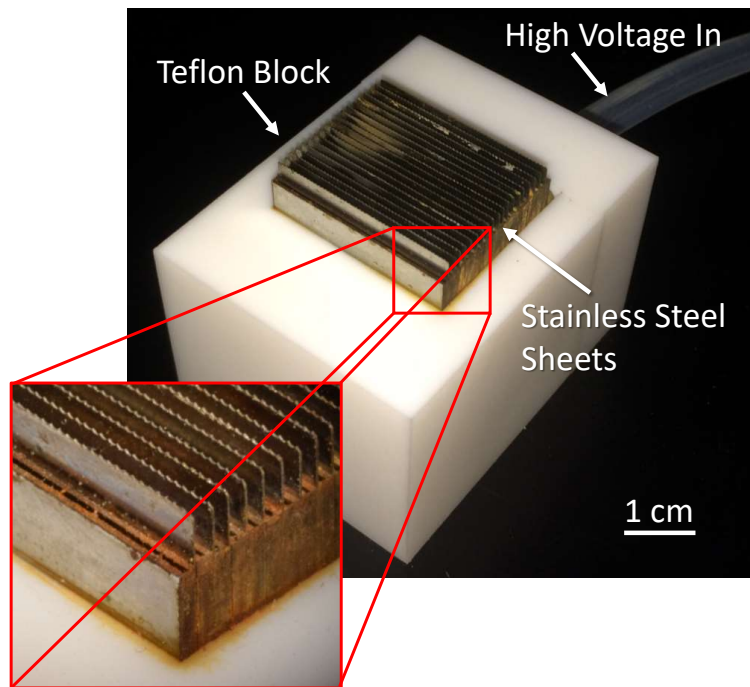
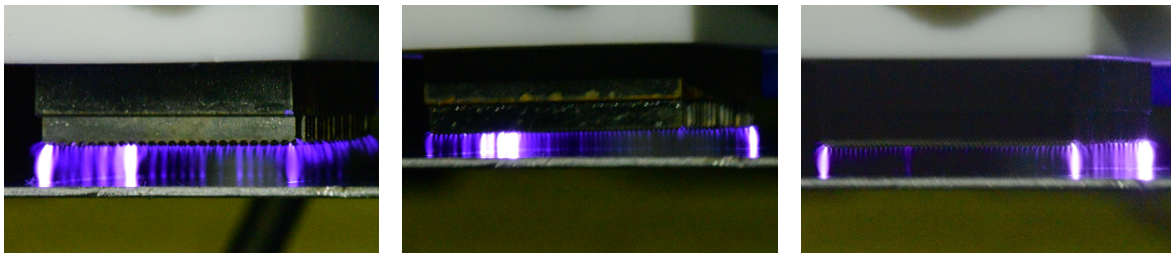


Figure 4.11: Image Showing the Design of the Array Electrode



(a) Array #1

(b) Array #2

(c) Array #3

Figure 4.12: Discharge Imaging Comparison of the Three Array Electrodes

Table 4.1: Comparison of the Design Parameters for the Three Array Electrodes

Array #	Tips/Sheet	Sheets	Number of Tips
1	25	19	475
2	51	19	969
3	51	48	2448

The three arrays were compared using the FID power supply at a voltage of 15 kV and a frequency of 1 kHz with a 3 mm gap. Array #1 appears to be the most uniform, but the differences may be due to slight alignment differences between the arrays. Nevertheless, all three arrays developed streamer discharges. Optical emission spectra was collected for two wavelength ranges with an ICCD camera (352–358 nm and 375–381 nm, see Section 3.4.1.1). The 2nd positive system of N₂ along with the 1st negative system of N₂⁺ was compared to modeled spectra from SpecAir to determine the rotational (T_{rot}) and vibrational (T_{vib}) temperatures of the nitrogen species in the gas (see Section 3.4.3.2). The results are shown in Figure 4.13. No clear trend seems to exist in the data, especially when one considers that the error in the temperature fitting is ~50 K for T_{rot} (see Section 3.4.3.2 for temperature determination considerations). The slight increase in temperature from Array #2 could be due to slight issues in alignment where the array was slightly closer to the ground electrode.

4.5 Device Characterization

The basic experimental setup is shown in Figure 4.14 with images in Figure 4.15. The main goals were

1. to observe uniformity of the tips lighting up on the array, which would suggest a fairly uniform electric field across each tip,
2. to identify the various species created from the discharge,
3. to determine the temperature of the discharge, and
4. to estimate conditions that would maximize the electric field in the substrate.

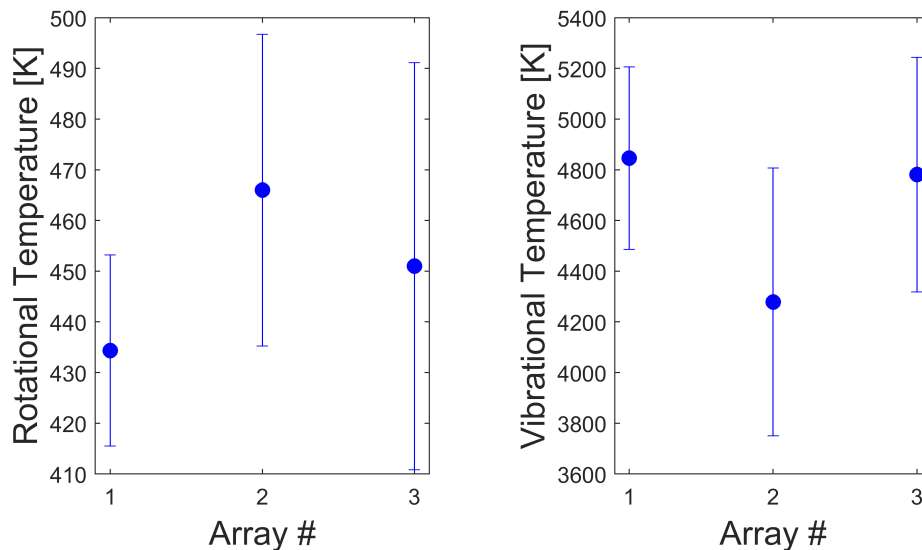


Figure 4.13: Temperature Comparison of the 3 Arrays (the Error Bars Shown Represent 1 Standard Deviation)

All testing was done in ambient air, although the gas flowing through the array was varied. Imaging was done with a Nikon D3300 camera (see Section 3.3.1 for details on the camera). Spectra was collected from 200–800 nm using a scanning monochromator (see Section 3.4.1.1 for details on the spectrometer) with a PMT detector for the FID testing and the ICCD (see Section 3.3.2 for camera details) for the nanosecond RC pulse generator circuit testing. Initial testing was done with the FID power supply before switching to the RC pulse generator.

4.5.1 Initial FID Testing

Initial testing was conducted using the FID power supply (described in Section 3.2.1.3) using Array #1 discharging into ambient air. Optical images were taken along with spectra to determine the species in the gas along with the temperature of the discharge.

4.5.1.1 Array Imaging

A parametric study was performed, with five gas flow conditions (air at 4.3 SLPM, argon at 3.61 SLPM, helium at 8.54 SLPM, nitrogen at 4.35 SLPM, and no gas all flowing into ambient air), four power supply conditions (1 kHz, 15 kV; 1 kHz, 30 kV; 10 kHz, 15 kV; 10 kHz, 30 kV),

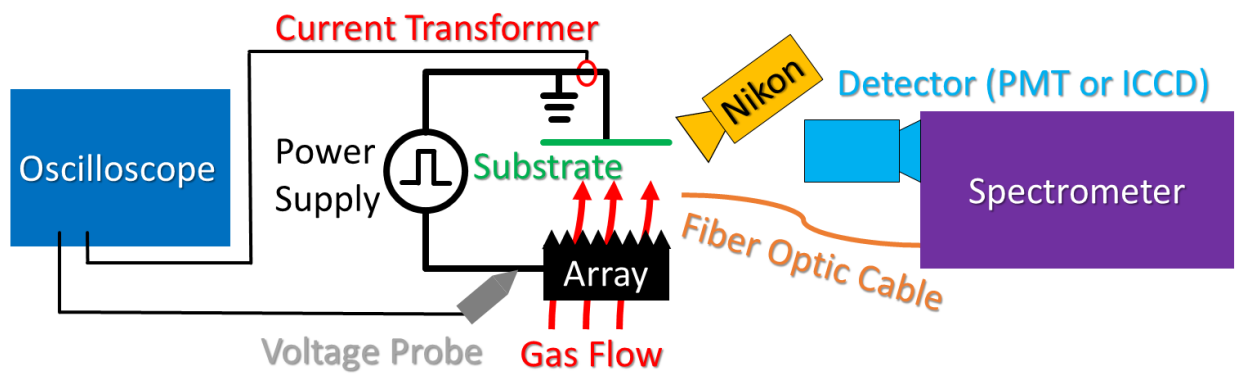


Figure 4.14: Schematic of the Array Testing Setup

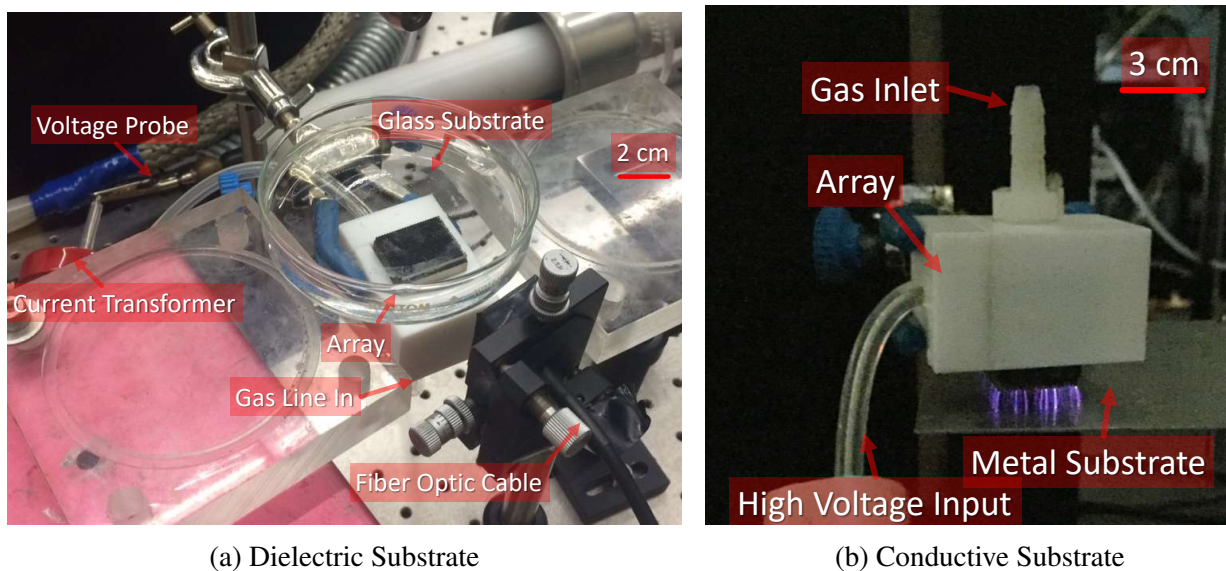


Figure 4.15: Images of the Array Testing Setup with Dielectric and Conductive Substrates

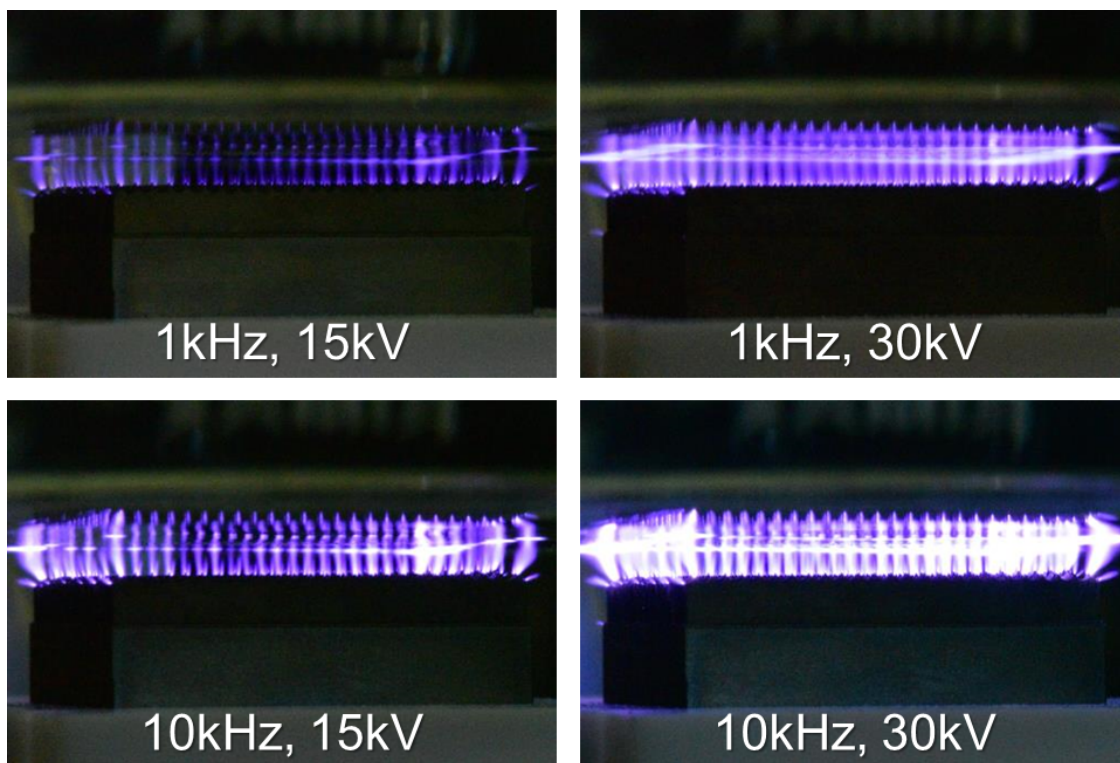


Figure 4.16: FID Discharges with Air Flow onto a Dielectric

and three substrates (metal plate, glass petri dish filled with grounded salt water to have a consistent dielectric, and pig skin thawed from frozen pork bought at the local grocer ~4 mm thick) to determine uniformity across all of the tips in the array. The results are shown in Figures 4.16–4.20 for the glass substrate and in Figures 4.21–4.25 for the metal substrate. Figure 4.26 shows the results for pig skin with no gas flow.

General trends were brighter and more uniform discharges at higher voltages. Helium created the most uniform discharge (Figure 4.20 and Figure 4.25), having all of the tips on the array lighting up; all other gases (and no gas flow) were comparable in uniformity. The color of the discharge varies depending on the gas due to various species and concentrations being created. The metal substrate generally led to brighter discharges (especially when it was grounded, though no floating metal images are shown here) compared to pig skin and the glass dielectric substrate. The dielectric glass substrate generally had a more uniform discharge across the tips. Uniformity on pig skin was difficult mainly due to non-uniformities in the pig skin itself (Figure 4.26). The metal substrate

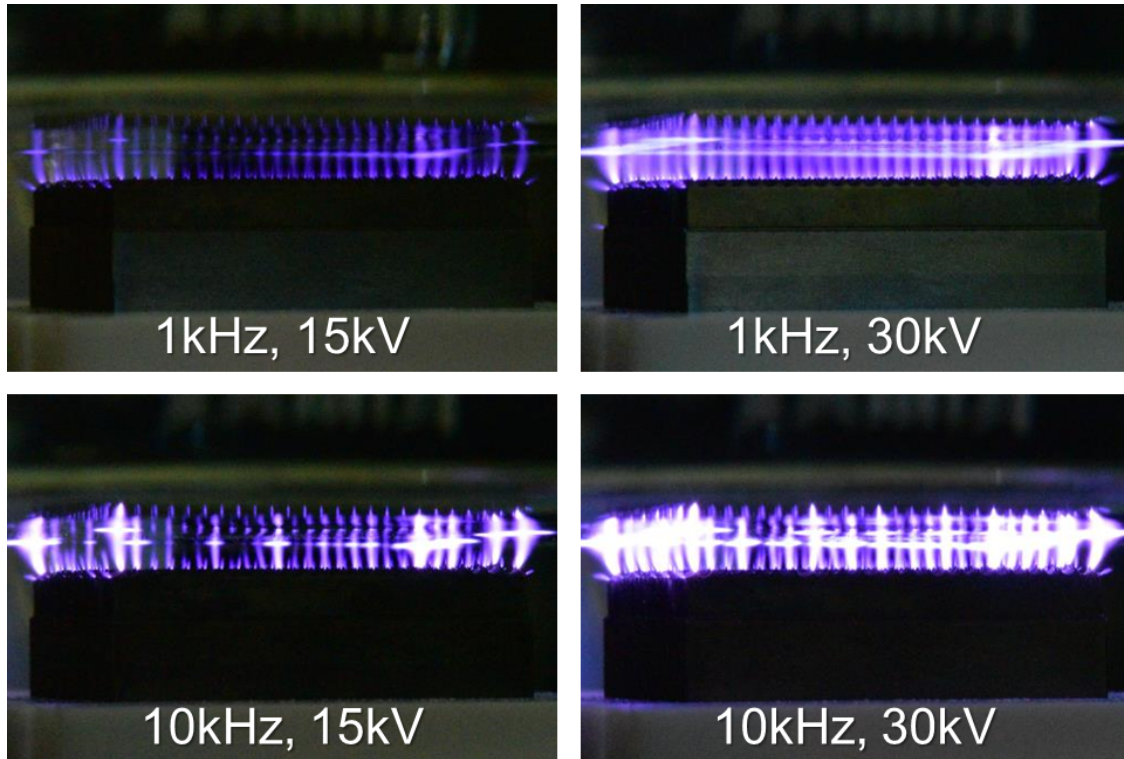


Figure 4.17: FID Discharges with No Gas Flow onto a Dielectric

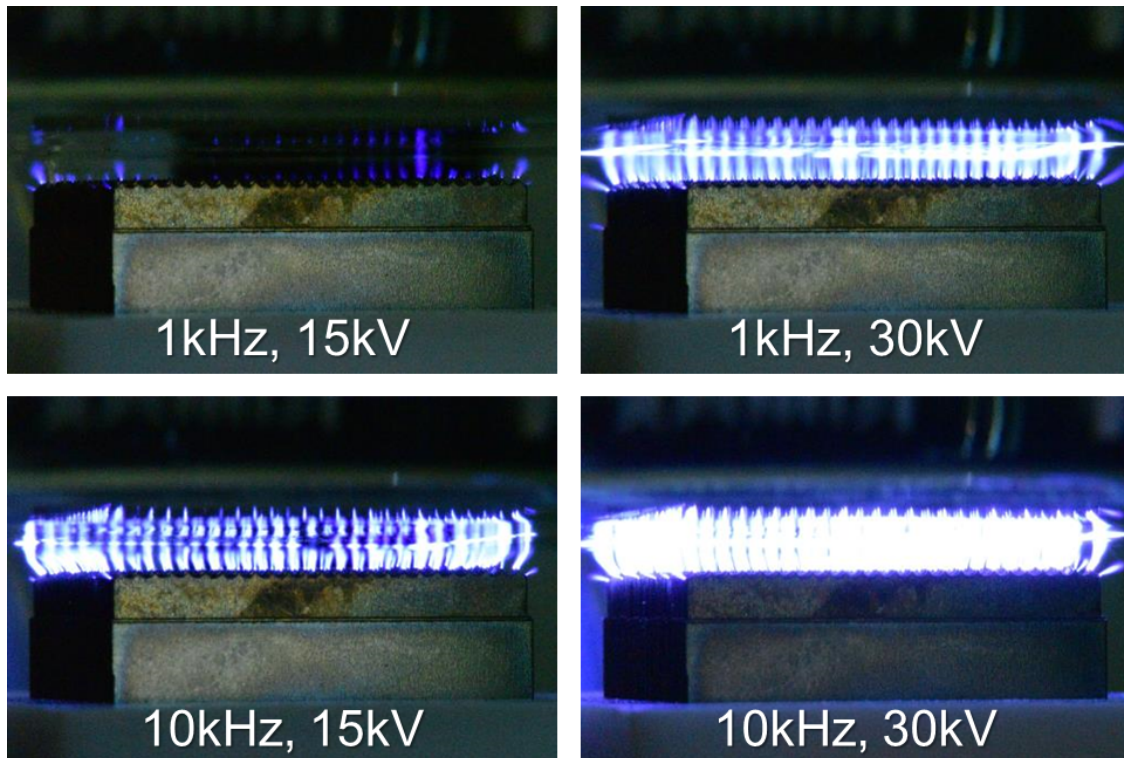


Figure 4.18: FID Discharges with N₂ Flow onto a Dielectric

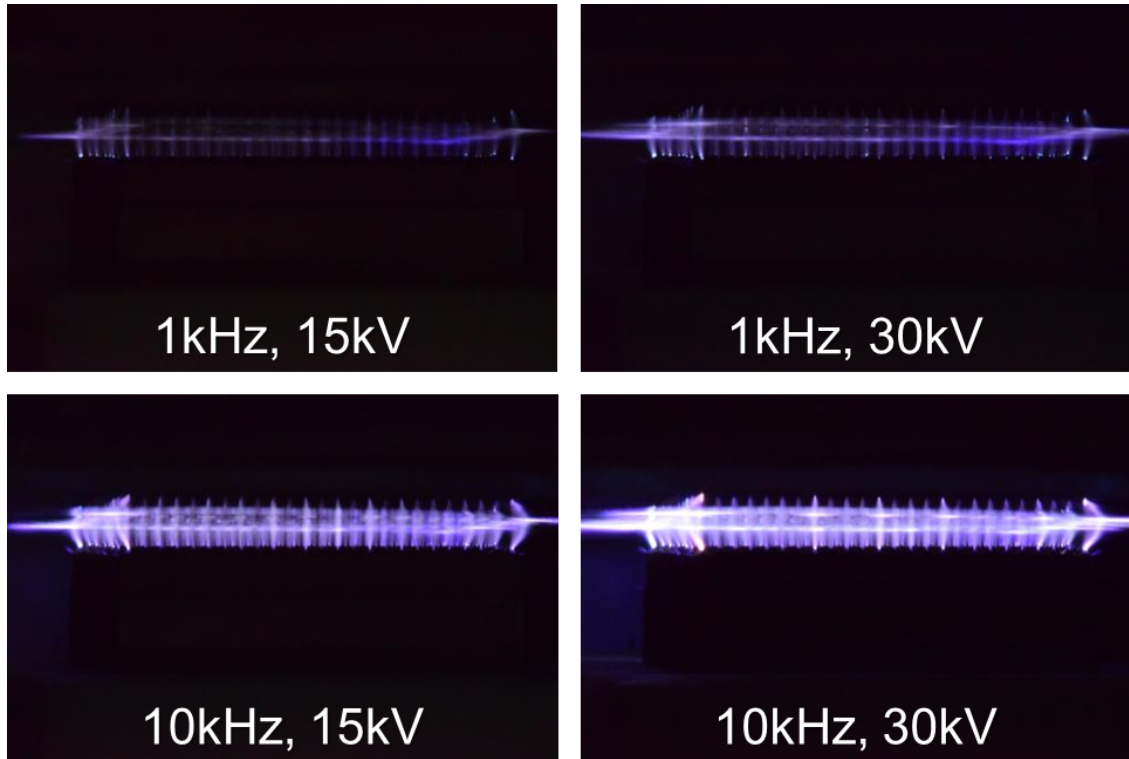


Figure 4.19: FID Discharges with Ar Flow onto a Dielectric

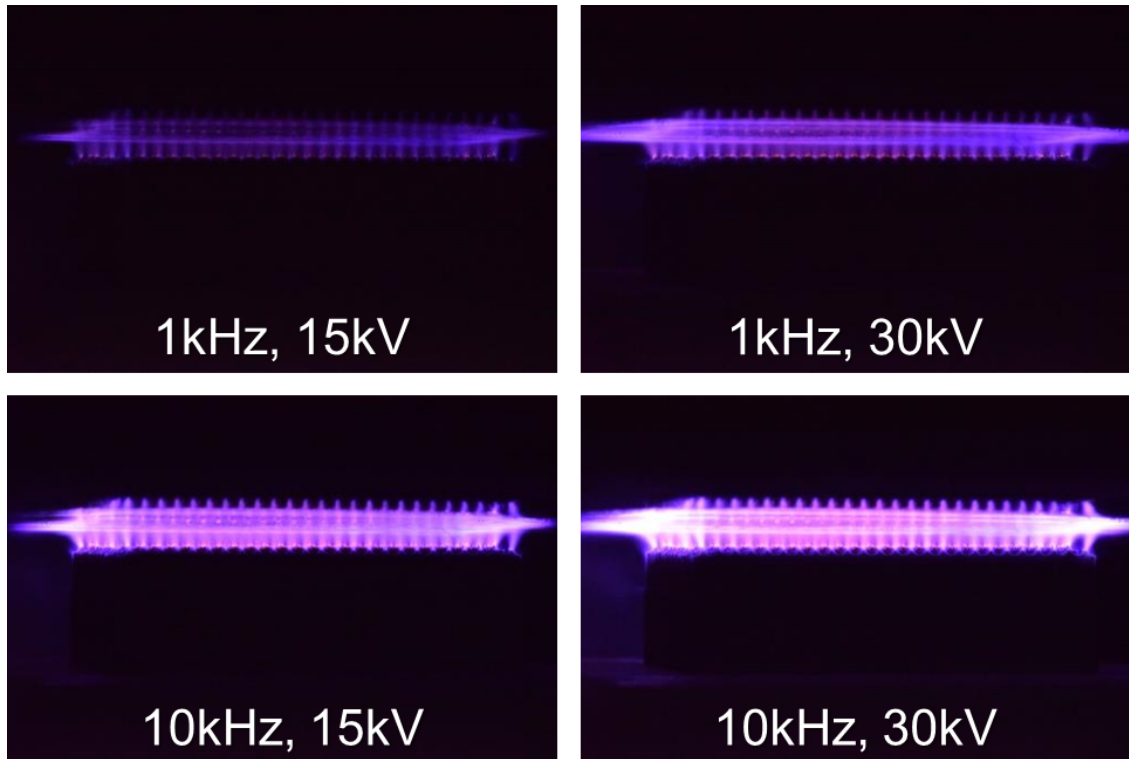


Figure 4.20: FID Discharges with He Flow onto a Dielectric

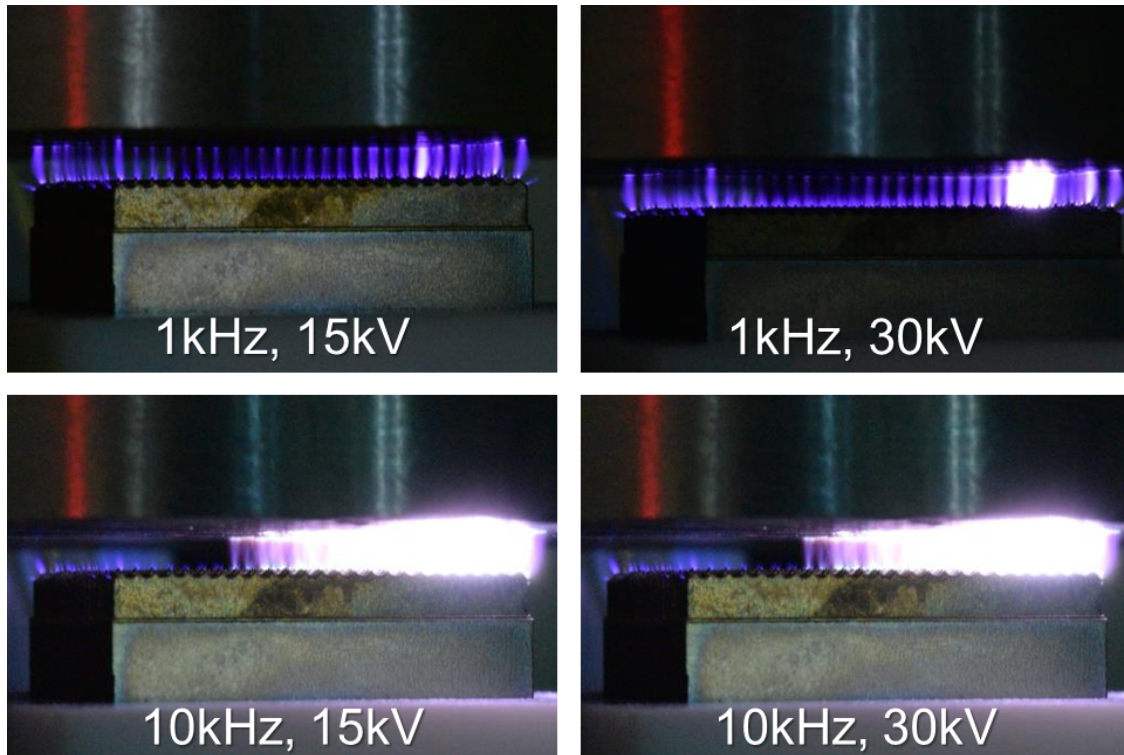


Figure 4.21: FID Discharges with Air Flow onto a Conductor

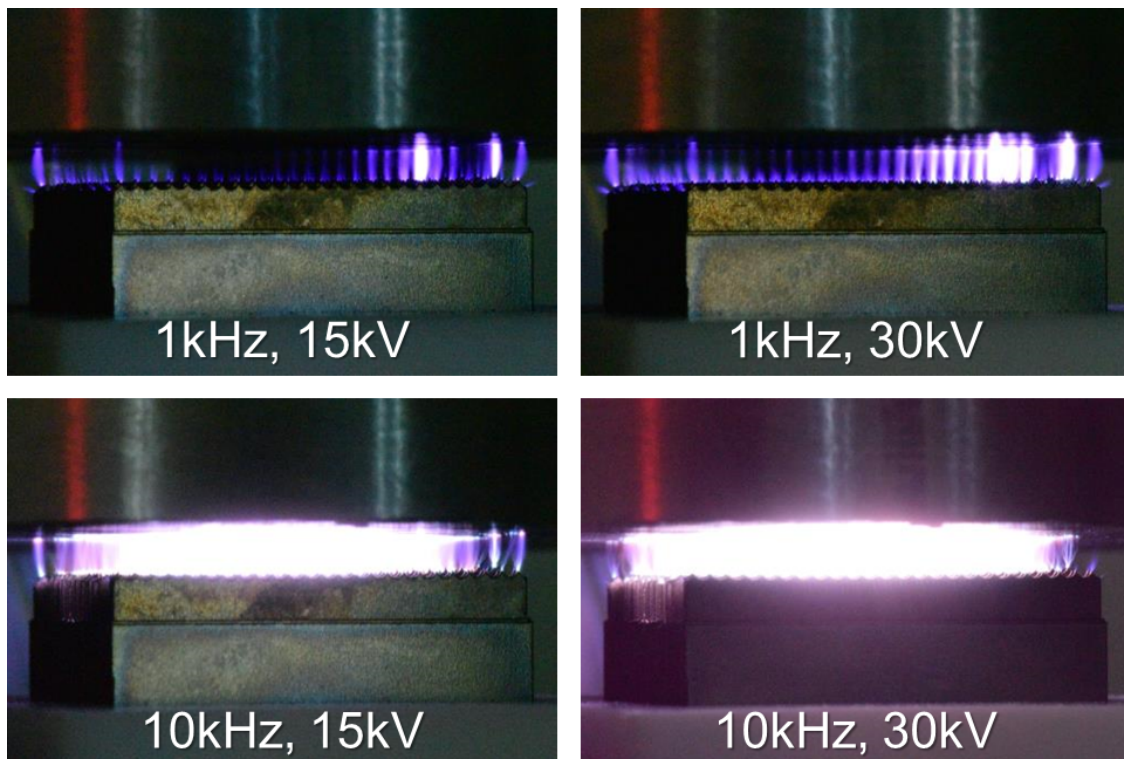


Figure 4.22: FID Discharges with No Gas Flow onto a Conductor

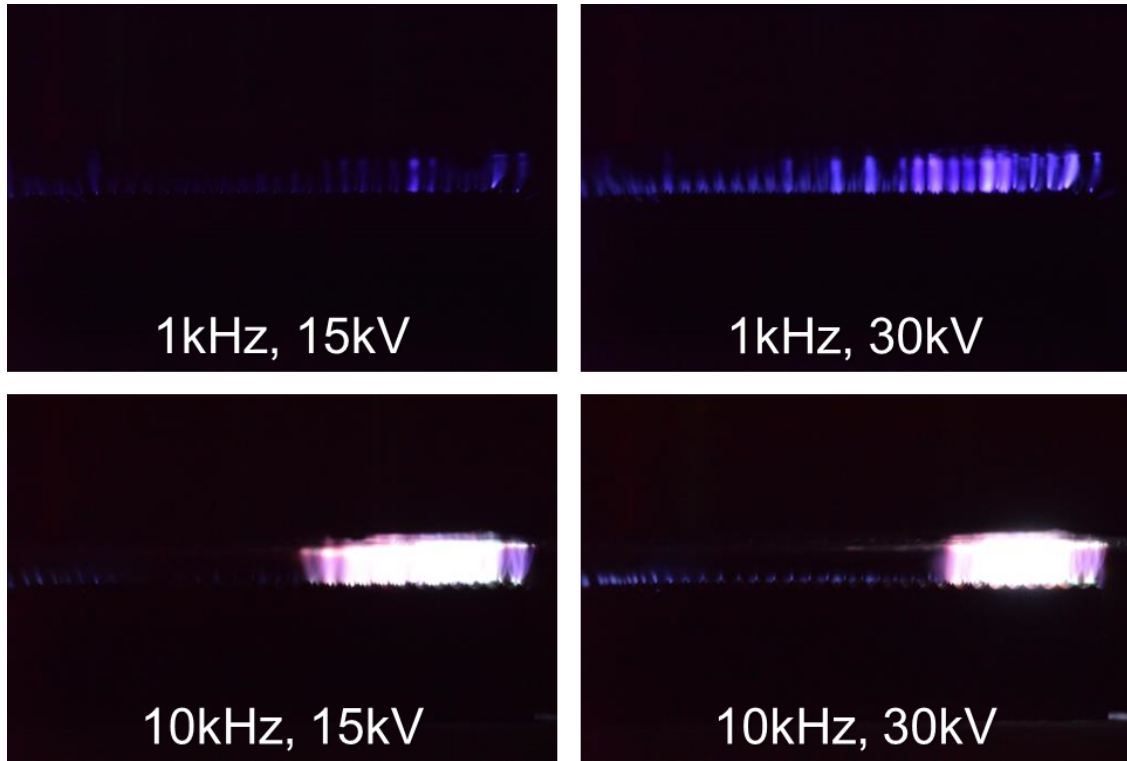


Figure 4.23: FID Discharges with N₂ Flow onto a Conductor

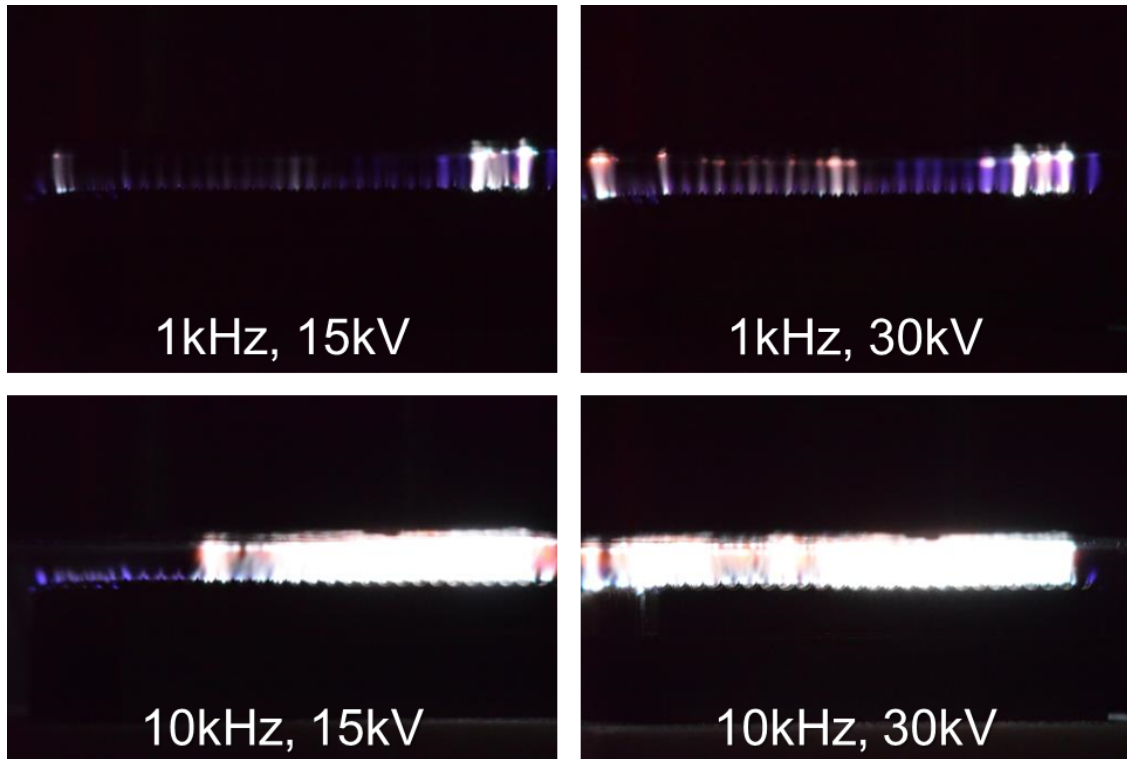


Figure 4.24: FID Discharges with Ar Flow onto a Conductor

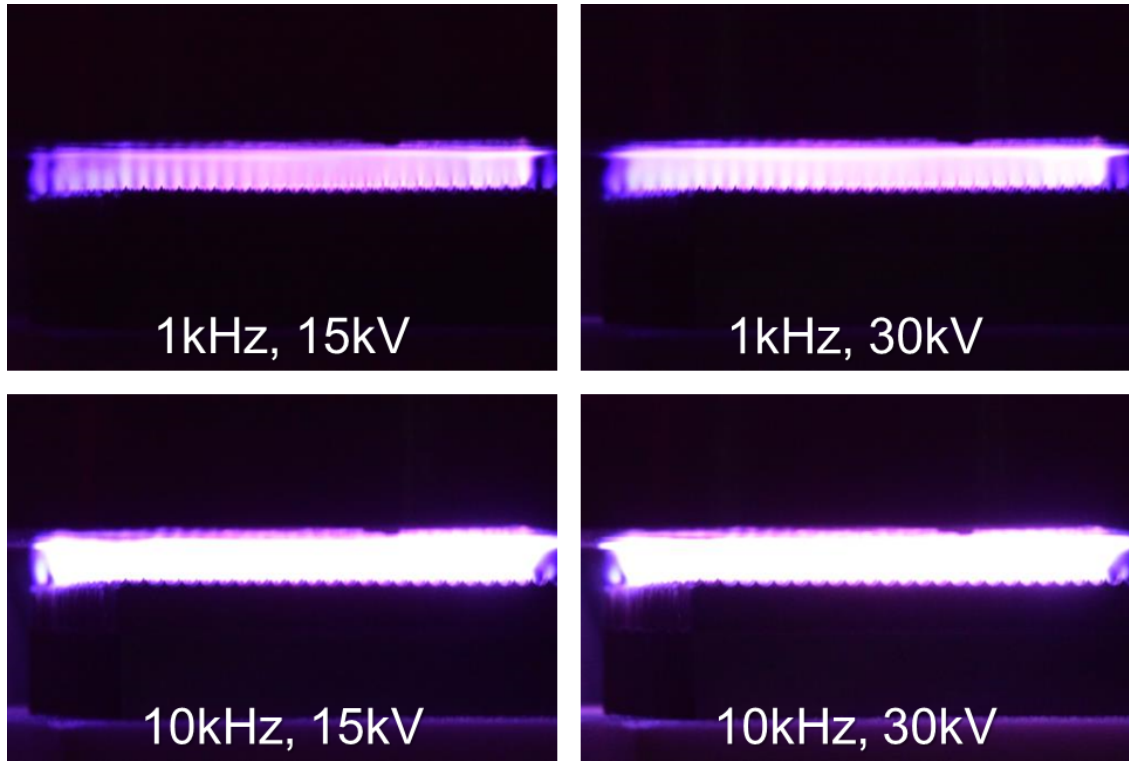


Figure 4.25: FID Discharges with He Flow onto a Conductor

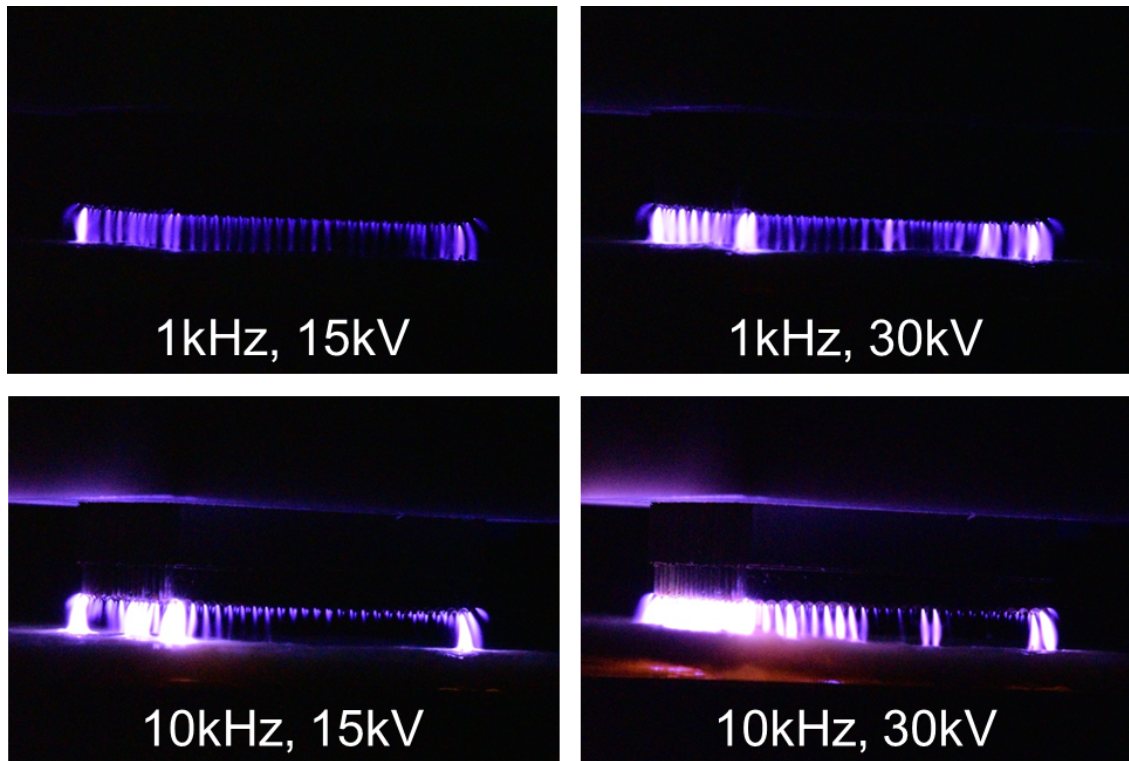


Figure 4.26: FID Discharges with No Gas Flow onto Pig Skin

was also very difficult to align, thus the right side is brighter due to being slightly closer to the array. The metal substrate easily developed individual streamers that transition toward a spark discharge. These are clearly seen in air (Figure 4.21 and Figure 4.22), N₂ (Figure 4.23), and argon (Figure 4.24) for the 1 kHz discharges, where one or two tips on the right side are brighter than the others. This is explained by one or two of the tips having a slightly more negative differential resistance. As the electron avalanche is initiated one or two of the tips will breakdown easier and faster than the others. Since a more conductive path begins to form on those tips the majority of the current flows through them, leading to a more intense discharge on them.

4.5.1.2 Spectra

Broadband optical emission spectra (OES) were collected from 200–800 nm with a PMT detector (see Section 3.4.1.1) for the dielectric substrate for five gas flow conditions (air (4.3 SLPM), Ar (3.61 SLPM), He (8.54 SLPM), N₂ (4.35 SLPM), and no gas all flowing into ambient air) and four power supply conditions (1 kHz, 15 kV; 1 kHz, 30 kV; 10 kHz, 15 kV; 10 kHz, 30 kV). The gas flow rates were chosen since they all have a consistent rotameter setting. OES were also collected for temperature determination of these conditions using three wavelength ranges (325–339 nm (T_{rot} only), 347–359 nm (T_{rot} and T_{vib}), and 363–382 nm (T_{rot} and T_{vib})). Spectra for the helium discharge was not modeled since the light levels for the 2nd positive system of N₂ were too low for accurate modeling. Note that the temperatures reported are the gas temperatures, not the substrate temperatures which can be much lower. An infrared (IR) thermometer was used to measure the substrate temperature, and no increases over 5°C were noted.

There was no observable change in the spectra other than increased light intensities for increasing voltage and frequency, as seen in the N₂ flow spectra in Figure 4.27, so the other reported spectra (Figure 4.28) are only for the brightest condition of 10 kHz and 30 kV. In the spectra for both no gas flow and air flow mostly only N₂ (2nd positive system) was observed with a few trace impurities. This is expected, since nitrogen is the dominant gas in air. Oxygen, being electronegative, does not emit light easily. In N₂, a significant amount of NO (γ system) was also observed; however no peak for atomic oxygen was noted. The additional NO lines are likely coming from a

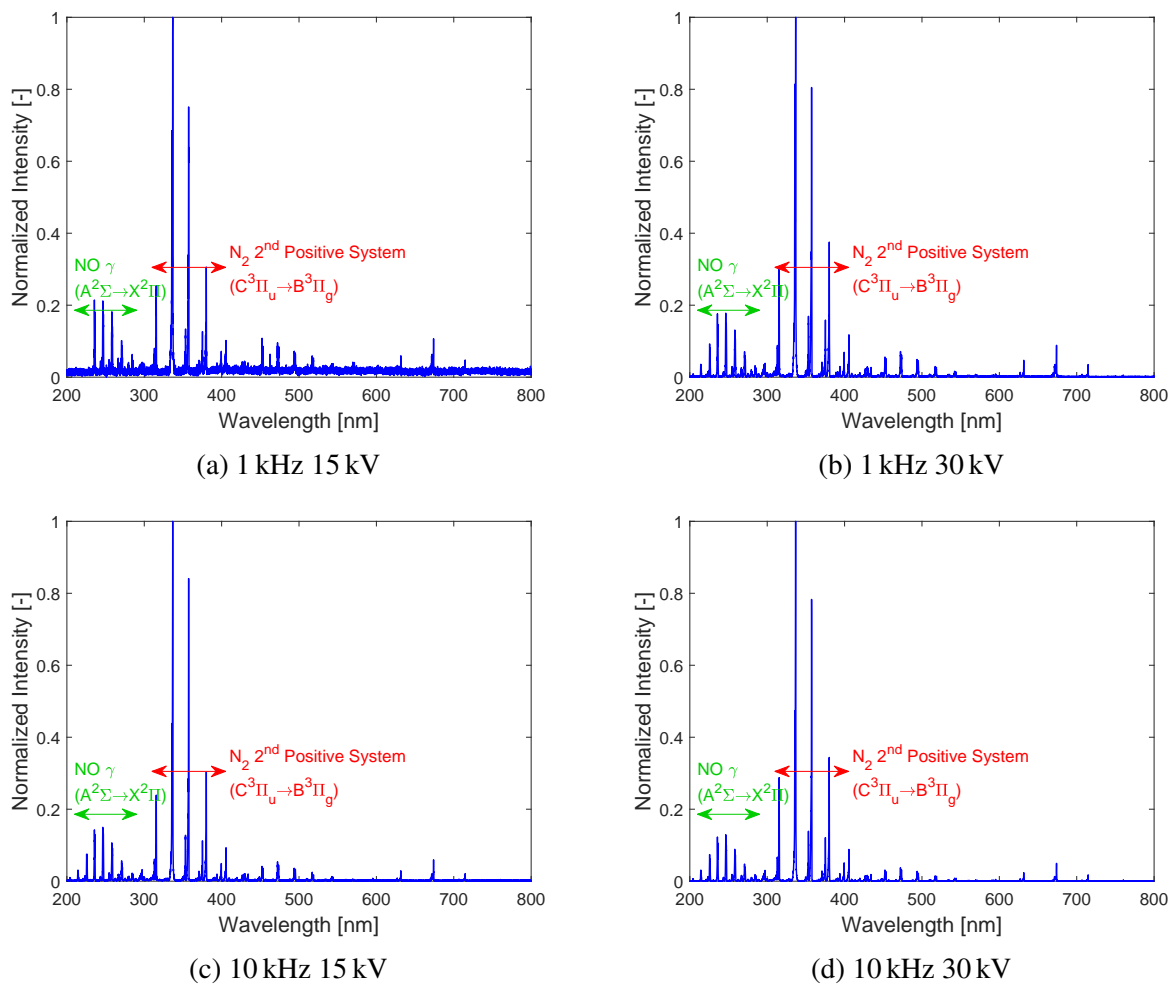


Figure 4.27: Spectra of FID N_2 Discharges for Various FID Power Supply Settings (Unidentified Peaks are Second Order Artifacts from the Spectrometer)

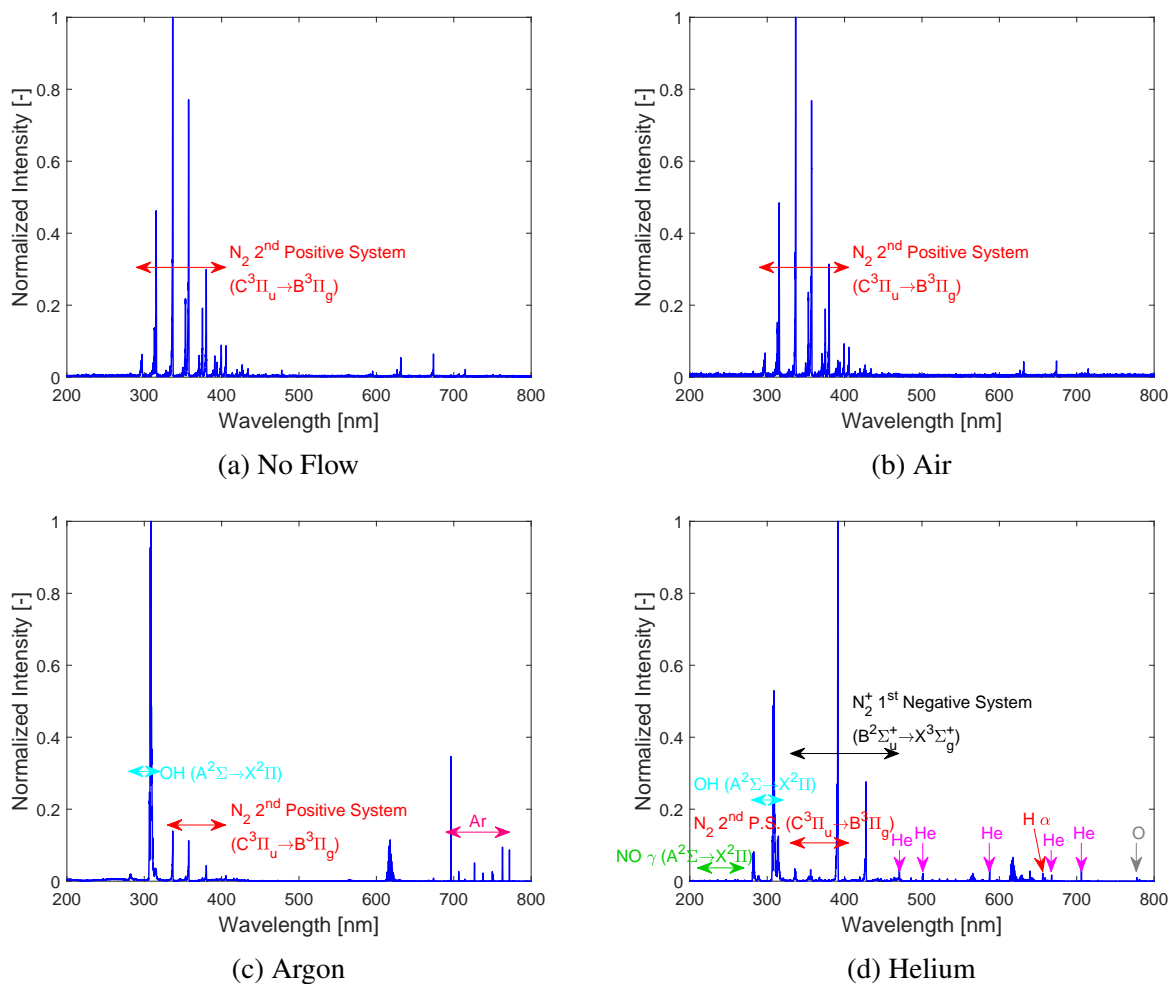


Figure 4.28: Spectra of FID Discharges for Other Gases at 10 kHz and 30 kV (Unidentified Peaks are Second Order Artifacts from the Spectrometer)

different electron temperature, T_e , in the discharge due to fewer electronegative O_2 molecules capturing free electrons. [246–248] This different T_e in turn changes the chemistry occurring in the discharge since different excited states are being created. For argon, OH (A-X system) dominated the spectra, with some N_2 (2nd positive system) and argon visible. Since argon has a high ionization energy (15.8 eV), an argon atom is able to store significant energy in its electronic states and then release it upon colliding with other species in the gas. The O-H bond in water has an energy of 4.8 eV, which is much lower than the amount of energy an excited argon atom could carry. The spectra indicates that the reaction between an excited argon ion and water, namely



is significant. No hydrogen lines are visible though, possibly due to them not gaining sufficient energy to subsequently emit or perhaps due to possible participation in further chemical reactions. Trace amounts of NO (gamma system), O (777 nm), and H (656 nm) were noted in helium along with various helium peaks. OH (A-X system) and N_2^+ (1st negative system) dominated the helium spectra. Similar to argon, helium has a high ionization energy (24.6 eV), thus it can store a significant amount of energy and release it upon collision with another species, such as water or nitrogen. Since the ionization energy for N_2 is 15.6 eV, which is comparable to the ionization energy of argon, it is observed in helium but not argon. If an argon atom had sufficient energy to ionize N_2 , it would instead be ionized, rather than storing that energy until colliding with a nitrogen molecule. The unlabeled peaks in the spectra are from the 2nd mode of the spectrometer, and thus correspond to doubled wavelengths of the brightest transitions noted in the spectra.

From modeling the temperatures, air (and no gas flow with discharge into ambient air) had the highest vibrational temperature and lowest rotational temperature (Figure 4.29). Argon had the highest rotational temperature and the lowest vibrational temperature; however this analysis may not be accurate since it does not account for excitation of the nitrogen species from collisions with

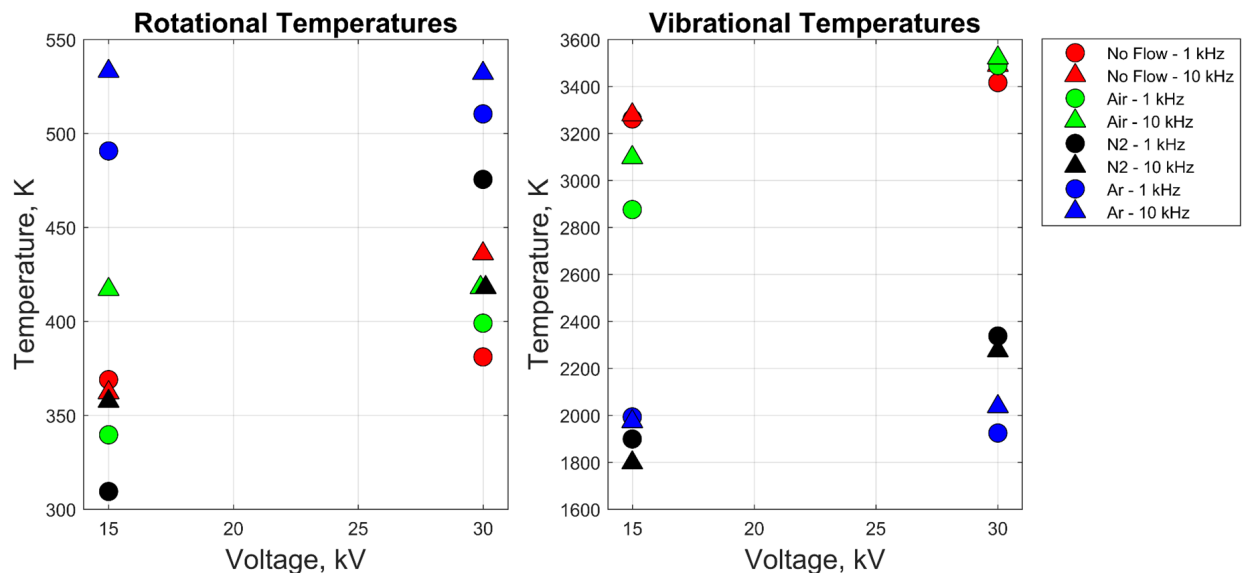


Figure 4.29: Plot of Rotational and Vibrational Temperatures of the FID Discharges

argon metastable species, namely



The analysis that yields these temperatures assumes only excitation by electron impact. Otherwise a non-Maxwellian distribution would result, which SpecAir cannot model. In general higher vibrational temperatures are correlated to higher electron temperatures which correspond to higher E/n , thus it is likely that air has a higher electric field. [249] This is supported by the fact that air is electronegative due to its relatively high oxygen content, making it harder to break down and requiring a higher E/n . There was no large trend in the spectra for higher voltages or frequencies.

4.5.2 RC Pulse Generator Testing

Further study of the array was conducted using the RC pulse generator using the same substrates previously discussed, namely a biological substrate (pig skin thawed from frozen pork bought from the local grocer ~ 4 mm thick), a conductive substrate (thin aluminum or stainless steel sheet), and a dielectric substrate (a glass petri dish filled with salt water and grounded through

a wire in the salt water). The main spark gap, second spark gap, electrode-substrate gap, and air flow through the array were varied. Having observed from the FID testing that air is possibly the best gas for enhancing the electric field further testing did not vary the type of gas flowing through the array. All data was taken at a pulsing frequency of 5 Hz using a BK Precision 4063 function generator to get the desired pulsing frequency via the external trigger spark (*EXT*) and circuit board (*CB*). The voltage pulse magnitude and duration (FWHM) were taken from oscilloscope traces (LeCroy WaveRunner 204MXi oscilloscope with North Star PVM-4 high voltage probe, see Section 3.2.2.4 and Section 3.2.2.1 for the oscilloscope and high voltage probe information, respectively).

4.5.2.1 Array Imaging

Overall three main discharge modes were noticed with the RC pulse generator. The first mode is streamers only visible on the edge of the array directed toward the substrate. This discharge mode occurred for all three substrates. There are variations only in light intensity with varying other conditions such as the pulse voltage, pulse duration, electrode-substrate gap distance, and air flow rate. This discharge mode is seen for pig skin in Figure 4.30. This first discharge mode is seen for the conductive metal substrate in Figure 4.31. Figure 4.31c shows a different angle as well to note that there are no visible discharges in the center of the array. This first discharge mode is also seen for the glass dielectric substrate in Figure 4.32. In Figure 4.32d a few streamers are visible in the center of the array (the benefit of having a transparent substrate of glass) though not nearly as densely occurring as at the edge of the array, where all of the tips are showing a streamer discharge. This is most likely due to a slightly higher negative resistance in the outer tips that is less noticed with the FID power supply due to the fast rise time of the voltage pulse. This is possibly analogous to the “donut” shape of the ionization wave noted in helium plasma jets. [250,251] In this case, the visible discharges may be travelling along the helium-air boundary, where breakdown is easier.

The second discharge mode was observed for the dielectric glass substrate with no gap between the array and the substrate as seen in Figure 4.33 (this has some of the same power supply conditions as Figure 4.32 with a larger gap, but since the gap has changed the capacitance of the load is

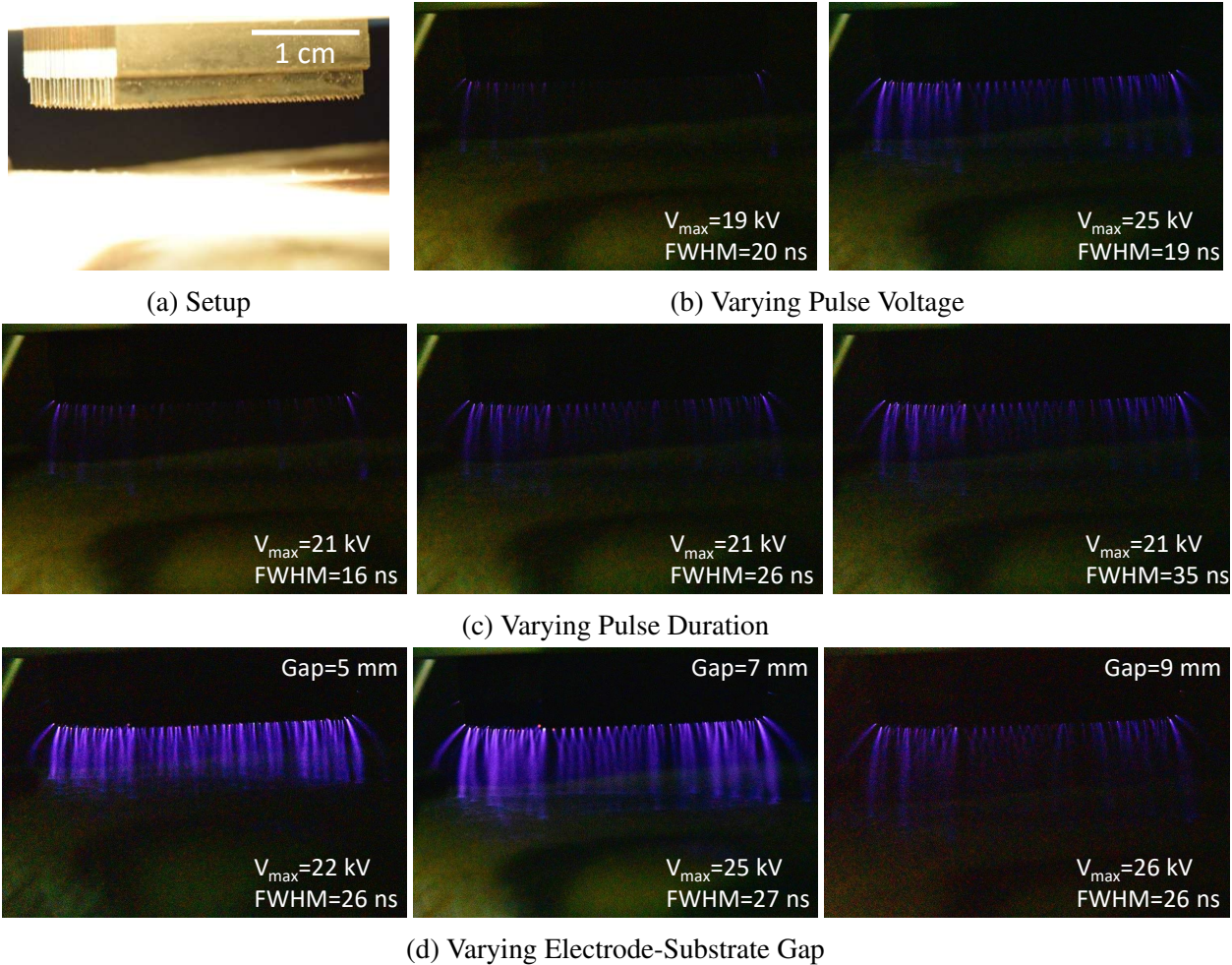
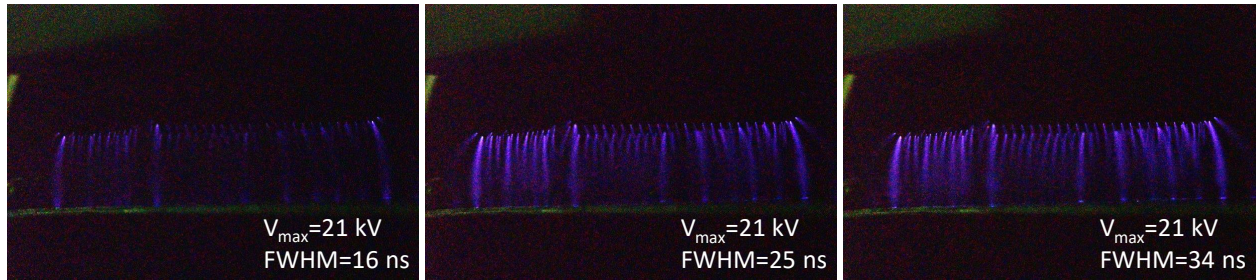


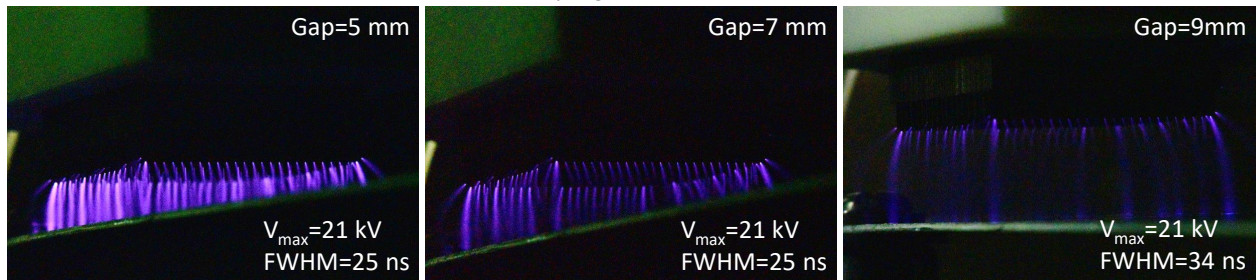
Figure 4.30: Images of the Array's First Mode with the RC Pulse Generator for the Biological Substrate Showing Streamers Only on the Edge of the Array with Only Variations in Light Intensity for Changing Discharge Conditions (All f#25, 10 s Exposure, 7 mm Gap, and No Air Flow Unless Noted Otherwise)



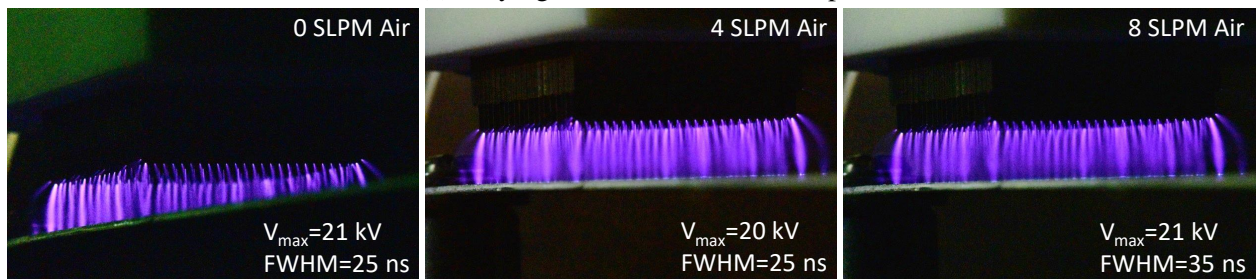
(a) Varying Pulse Voltage



(b) Varying Pulse Duration



(c) Varying Electrode-Substrate Gap



(d) Varying Air Flow Rate

Figure 4.31: Images of the Array's First Mode with the RC Pulse Generator for the Conductive Substrate Showing Streamers Only on the Edge of the Array with Only Variations in Light Intensity for Changing Discharge Conditions (All F#25, 20 s Exposure, 7 mm Gap, and No Air Flow Unless Noted Otherwise)

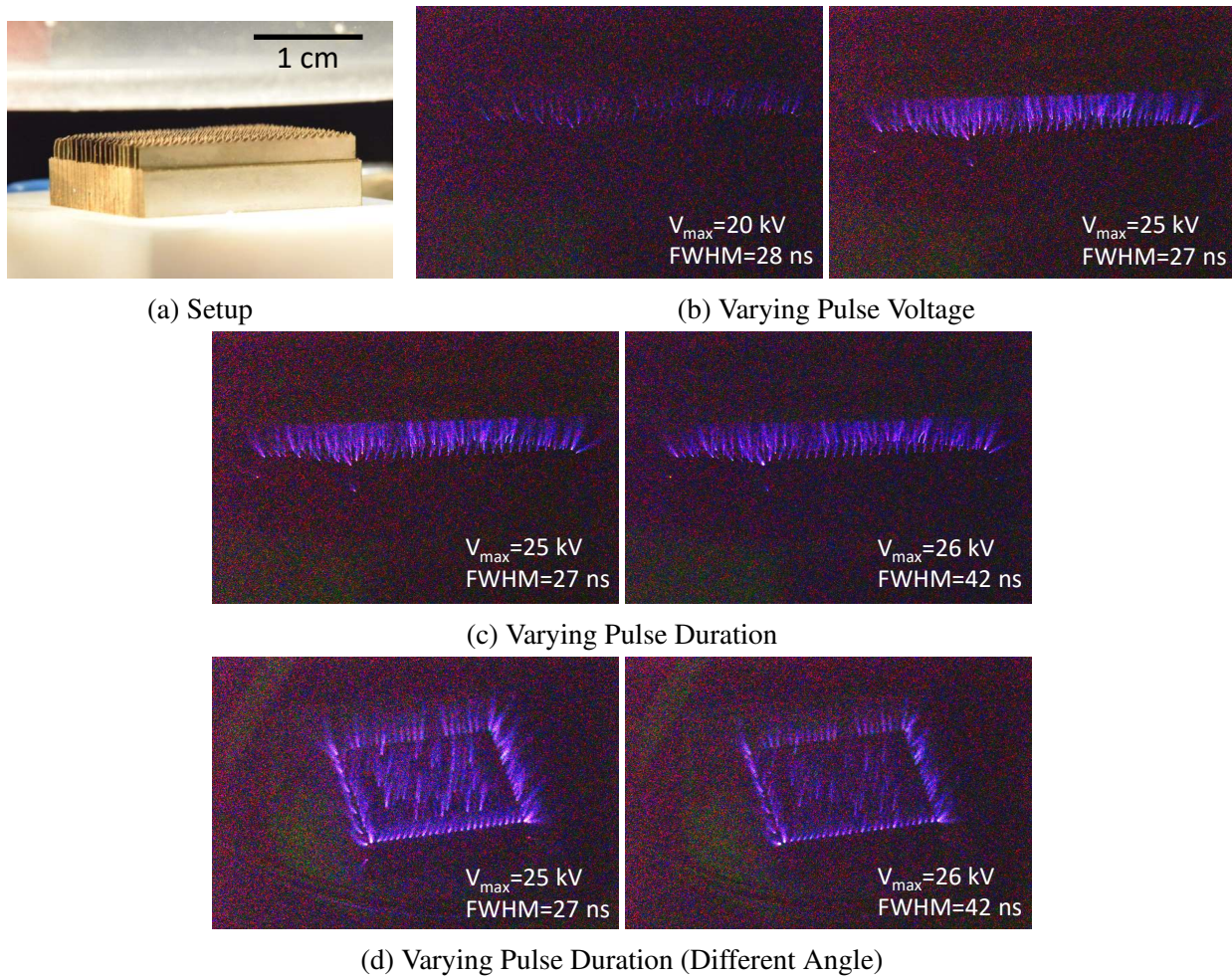
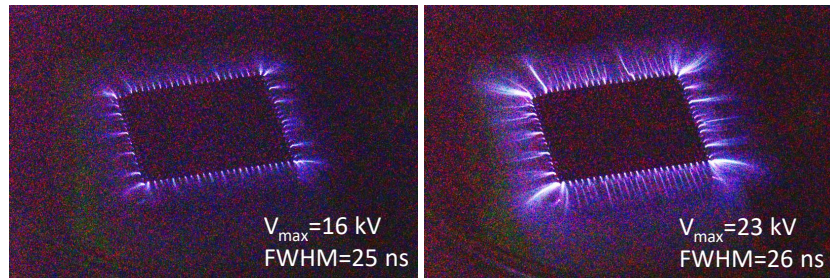
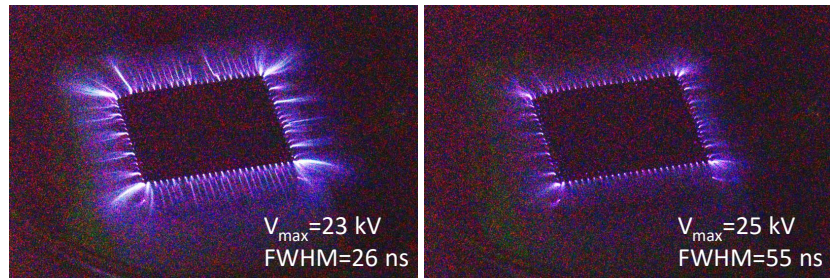


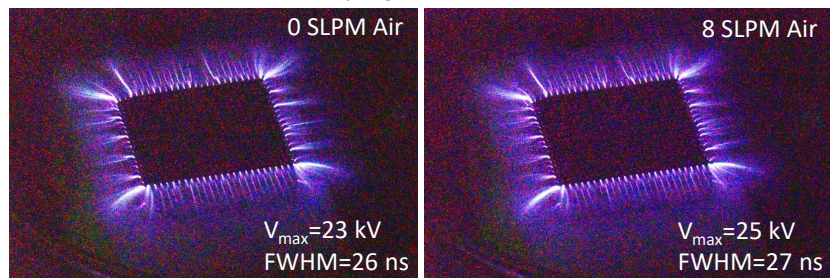
Figure 4.32: Images of the Array's First Mode with the RC Pulse Generator for the Dielectric Substrate Showing Streamers Only on the Edge of the Array with Only Variations in Light Intensity for Changing Discharge Conditions (All F#40, 30 s Exposure, 5 mm Gap, and No Air Flow)



(a) Varying Pulse Voltage



(b) Varying Pulse Duration



(c) Varying Air Flow Rate

Figure 4.33: Images of the Array's Second Mode with the RC Pulse Generator for the Dielectric Substrate Showing Spreading of the Streamers on the Substrate for a Variety of Conditions All with an Electrode-Substrate Gap of 0 mm with Only Variations in Light Intensity for Changing Discharge Conditions (All F#40, 30 s Exposure, and No Air Flow Unless Noted Otherwise)

different yielding different voltage pulse magnitudes and durations). In this second discharge mode the streamers, instead of being directed toward the substrate, spread out across the substrate. This occurs because the surface becomes charged, thus the streamers must spread out to find ground (i.e. a potential of zero). Similar to the first discharge mode, there are no visible streamers in the center of the array.

When the voltage was increased above a threshold or the electrode-substrate gap reduced below a threshold for the conductive substrate the third discharge mode was observed as seen in

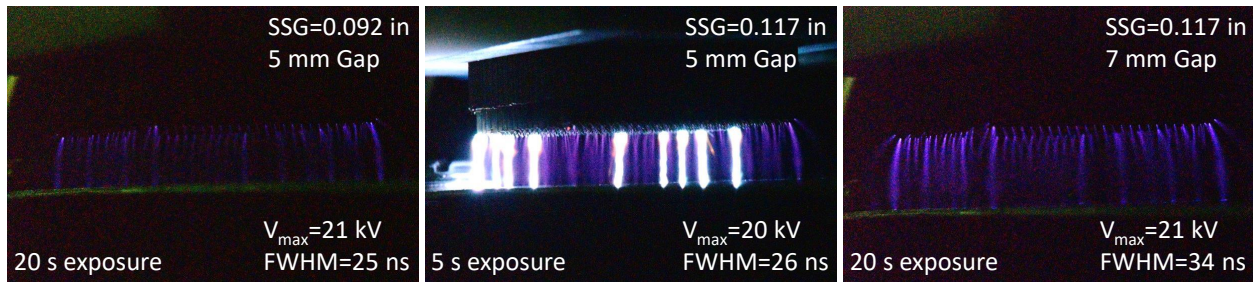


Figure 4.34: Images of the Array’s Third Mode with the RC Pulse Generator for the Conductive Substrate Showing Brighter Discharges for Certain Conditions Where the Streamers Have Transitioned to Higher Energy Spark Discharges with Changes in the Applied Voltage (Increasing SSG in This Case) and Electrode-Substrate Gap Distance (All F#25)

Figure 4.34. The discharge would begin like the first discharge mode, but then one or two of the streamers from individual tips would become a preferential path for current and thus grow much brighter as that streamer begins transitioning to a full spark discharge (note that the middle image in Figure 4.34 is actually 25 distinct discharge events, thus multiple spark discharges are seen).

4.5.2.2 Spectra

No broadband spectra was collected for the RC pulse generator. It is assumed to be similar to the FID power supply for the no flow or air conditions (see Figure 4.29). Broadband emission would have been much more difficult to acquire, since the array was only pulsed at 5 Hz, compared to 1–10 kHz for the FID spectra. Significantly longer exposure times would have been required.

Optical emission spectra were acquired for temperature data using two wavelength ranges (352–358 nm and 375–381 nm) with an ICCD detector (see Section 3.4.1.1). The emitted light was collected for around 10 minutes (usually 60 exposures each 10 seconds long to allow enough light to adequately expose the ICCD). The 2nd positive system of N_2 along with the 1st negative system of N_2^+ were compared to modeled spectra from SpecAir (see Section 3.4.3.2). Overall for all substrates the rotational temperatures are low, suggesting the discharge is not transitioning to a glow mode but remains as a streamer discharge (Figure 4.35). For a glow discharge in air, Staack et al. found a rotational temperature of 1320 K, which is much higher than the 389 K for the metal substrate. [39] This occurs because the voltage pulse is too short for the discharge to transition to

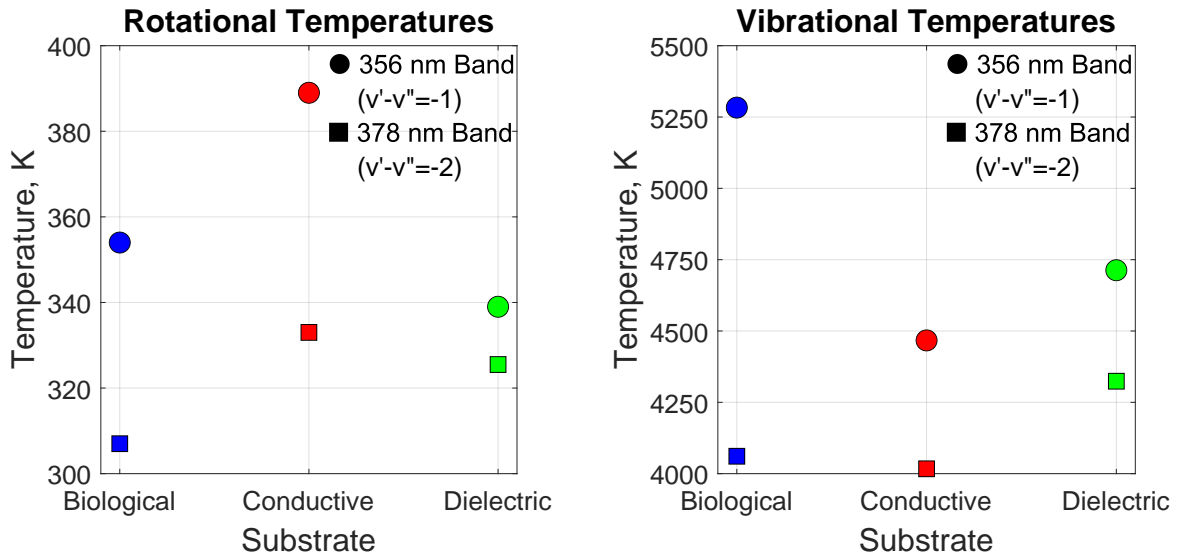


Figure 4.35: Temperature Comparison Using the RC Pulse Generator for Varying the Substrate with $V_{\max} = 25 \pm 2$ kV, $\text{FWHM} = 26 \pm 1$ ns, $\text{Gap} = 7$ mm, and No Air Flow

another mode, irrespective of the substrate used. The conductive metal showed a slightly higher rotational temperature and a corresponding lower vibrational temperature than the dielectric glass and pig skin substrates (Figure 4.35). This is most likely due to higher current (a slight transition toward a spark discharge compared to the other substrates) for the metal substrate, which is slightly heating the gas.

This low rotational discharge temperature holds true (see Figure 4.36) for varying the applied voltage (i.e. maximum peak pulse voltage) from 12.4 kV to 26.3 kV, varying the pulse duration (FWHM) from 15.9 ns to 33.8 ns, varying the air flow rate from 0 SLPM to 8 SLPM, and varying the electrode-substrate gap from 4 mm to 9 mm. No large effect of varying the gap distance is expected, since the variation in the gap size only affects the overall electric field (note: $E = -\frac{V}{d}$). However the streamer head produces a local electric field (which is initiated by the voltage pulse at the small radius of the tips which does not change), which does not vary with changing the electrode-substrate gap; thus overall the electric field is mostly constant. The effect of higher convection due to the air flow rate happens on a time scale much larger than the voltage pulse, thus the flow does not affect the plasma temperatures or electric field.

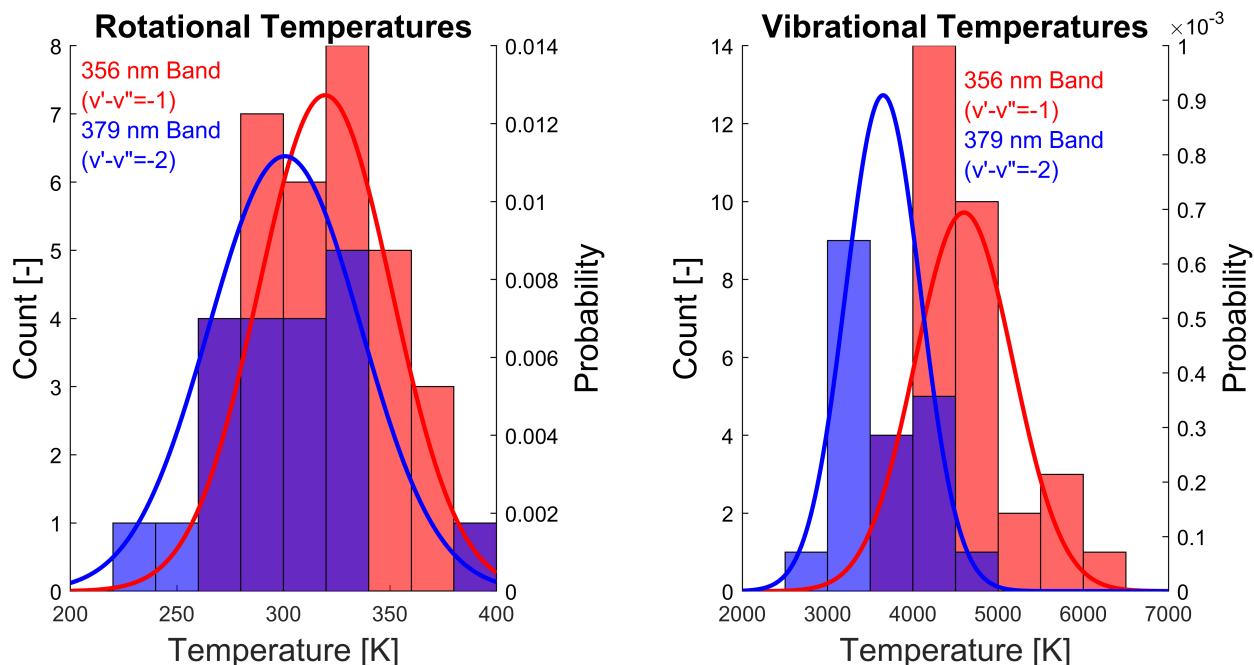


Figure 4.36: Temperature of Array Discharges for Varying the Applied Voltage, Pulse Duration, Air Flow Rate, Substrate, and Electrode-Substrate Gap

It was noticed that the 378 nm peak family consistently showed lower temperatures (both T_{rot} and T_{vib}) than the 356 nm family. This could be due to the greater effect of N_2^+ concentration on the modeled spectra in the 356 nm family, while no N_2^+ peaks appear in the 378 nm family. Overall, the temperatures were $T_{\text{rot}} = 310 \pm 35$ K and $T_{\text{vib}} = 4208 \pm 717$ K. Some rotational temperatures were observed to be lower than ambient. This is due to some error in the modeling; however it was consistent and should not affect any trends visible in the data.

A measurement of the temperature of the second discharge mode was also attempted, where there was sparking on every second or third pulse to the conductive substrate. As seen in Figure 4.37, there are a number of iron peaks in the N_2 spectrum, indicating electrode ablation, as this is the main constituent of the stainless steel array electrode. As the discharge changes mode, the electrode heats up and some of the electrode is ablated, introducing enough iron to obscure the spectrum. There also appears to be some continuum in the background, which also makes temperature determination nearly impossible for this spectral range. For another band in the 2nd positive

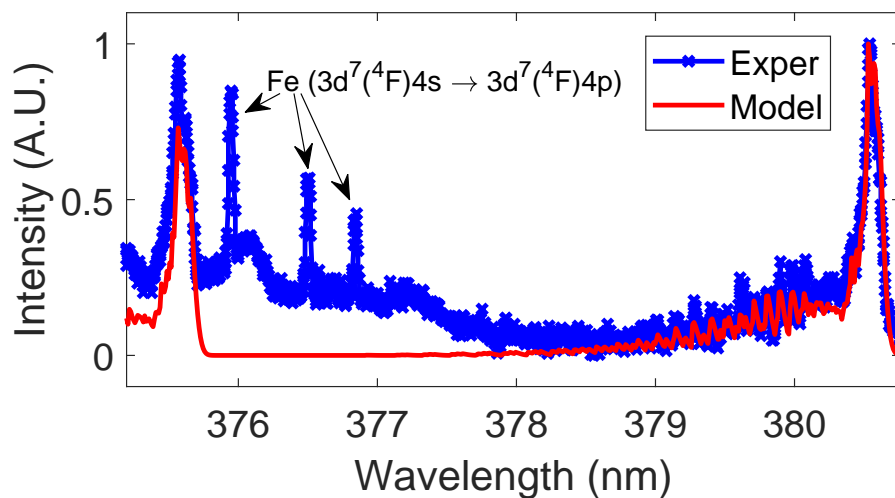


Figure 4.37: Spectrum of 2nd Positive System of N₂ for the Second Mode of the RC Pulse Generator Showing Many Iron Peaks and Some Continuum Emission, Making Temperature Determination Impossible (Model Spectrum Is for T_{rot} = 300 K and T_{vib} = 4500 K, and Was Not Fitted to the Spectrum)

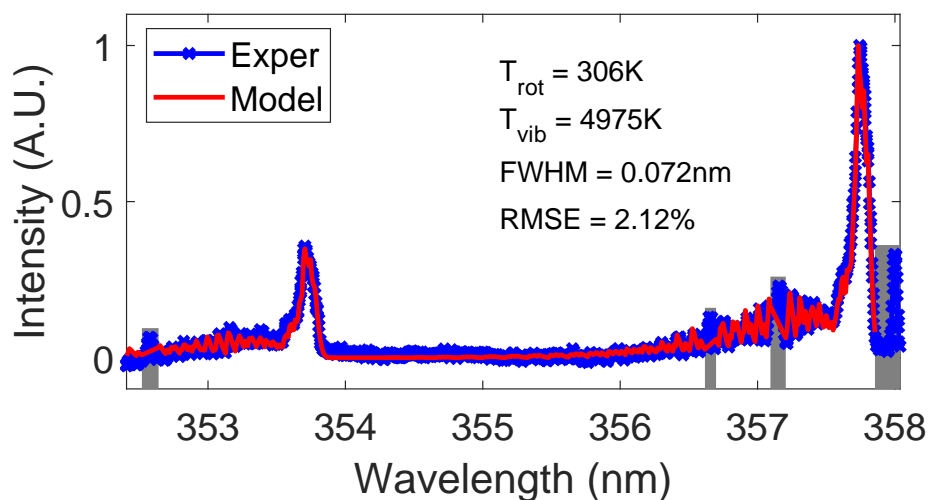


Figure 4.38: Temperature of the Second Mode for the RC Pulse Generator With Small Gaps (Gray Boxes) Not Modelled Due to Iron Peaks in the Spectrum

system of N₂, there were fewer iron lines that could be removed from the spectrum for temperature determination (see Figure 4.38). However, in addition to the iron peaks removed (gray boxes in Figure 4.38), there is an iron peak ($3d^6(^3G)4s4p(^3P^o) \rightarrow 3d^7(^2H)4s$) at 357.4 nm, which lines up near the band head of nitrogen ($C^3\Pi_u \rightarrow B^3\Pi_g, \Delta\nu = 0 \rightarrow 1$) at 357.6 nm which was not accounted for, possibly increasing the apparent height of the N₂ band head and incorrectly matching the temperatures.

4.5.3 Computational Model of the Electric Field in Skin

This section provides a basic computational model of the electric field in skin. This illustrates the benefit of using a streamer to apply the electric field closer to the skin and provides a rudimentary analysis of the depth of penetration of the electric field into the skin. At the request of the project sponsor, this model was done for a planar DBD rather than exactly matching the geometry of this setup. Nevertheless, the basic trends will stay the same. In addition, the modeling with a streamer is nearly the same as would be done without the dielectric barrier.

The electric field was modeled using Comsol (version 4.3) under four conditions:

1. With a 100 μm streamer head and a circular ground electrode on top of the substrate,
2. With plasma with 100 μm streamer head and a far away ground,
3. Without plasma but with a 2 mm air gap between the DBD electrode (1 mm thick quartz) and substrate and a circular ground electrode on top of the substrate, and
4. Without plasma but with a 2 mm air gap between the DBD electrode (1 mm thick quartz) and substrate and a far away ground.

Conditions 1 and 2 are seen schematically in Figure 4.39a, where condition 2 lacks the copper ground electrode. Conditions 3 and 4 are seen schematically in Figure 4.39b, where condition 4 lacks the copper ground electrode.

The model was conducted as a 2D axisymmetric system with the electrostatics package as a stationary (time independent) study. A zero potential was applied 4 mm deep into the skin and on

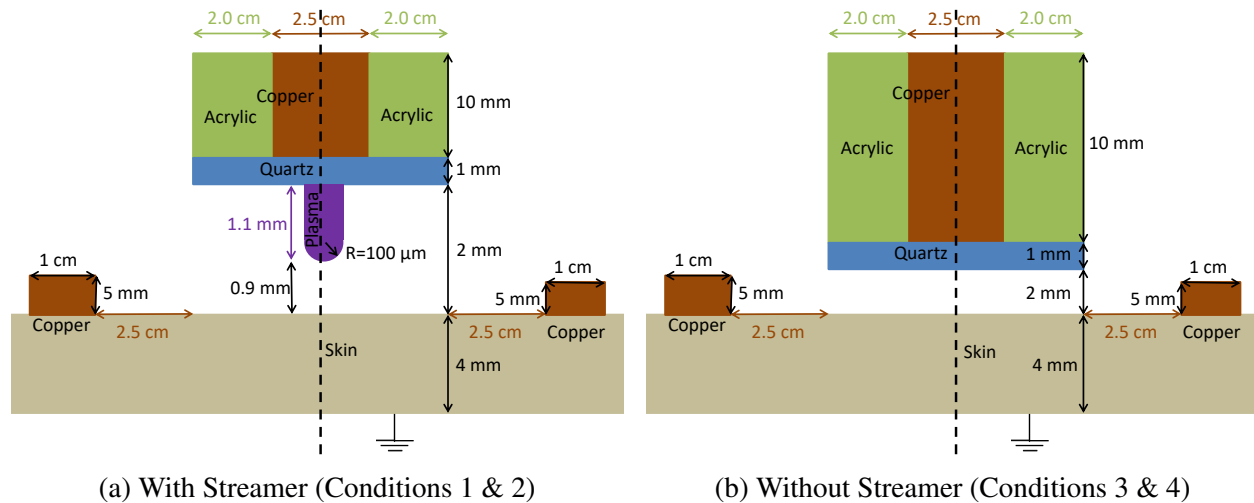


Figure 4.39: Schematics of the Comsol Model for the Electric Field in Skin with and without a Plasma Streamer (Note the Images are Not to Scale)

the copper ring ground electrode. A potential of 40 kV was applied to the high voltage electrode and to the plasma streamer. A boundary condition of dielectric shielding was applied to the air and far edge of the skin. Charge conservation was applied to all areas with an initial zero voltage. According to Sunaga et al. the relative permittivity of skin varies greatly, even for an individual. [252] For this study, the value of 120 was used, which is in relatively close agreement with both Gabriel et al. and Penn and Bell; [253,254] this is approximately the permittivity of human skin at 20 MHz (i.e. a pulse with a 50 ns period).

The magnitude of the electric field has been plotted below along two lines: the central axis for depth into the skin (Figure 4.40a) and radially through the skin halfway to ground at a depth of 2 mm (Figure 4.40b). Overall the ground electrode has nearly no effect on the electric field since it was too far away; instead, the ground 4 mm deep into the skin determined the voltage and electric field. The electric field was locally higher with the plasma streamer. This is seen in Figure 4.40a where the electric field directly under the streamer is ~ 1.2 times higher (~ 1700 V/cm compared to ~ 1400 V/cm) than the electric field without a streamer, but the field drops to a value very close to the electric field without a streamer as depth into the skin is increased. This locally higher electric field from the presence of the streamer also decreases quickly with radial distance away

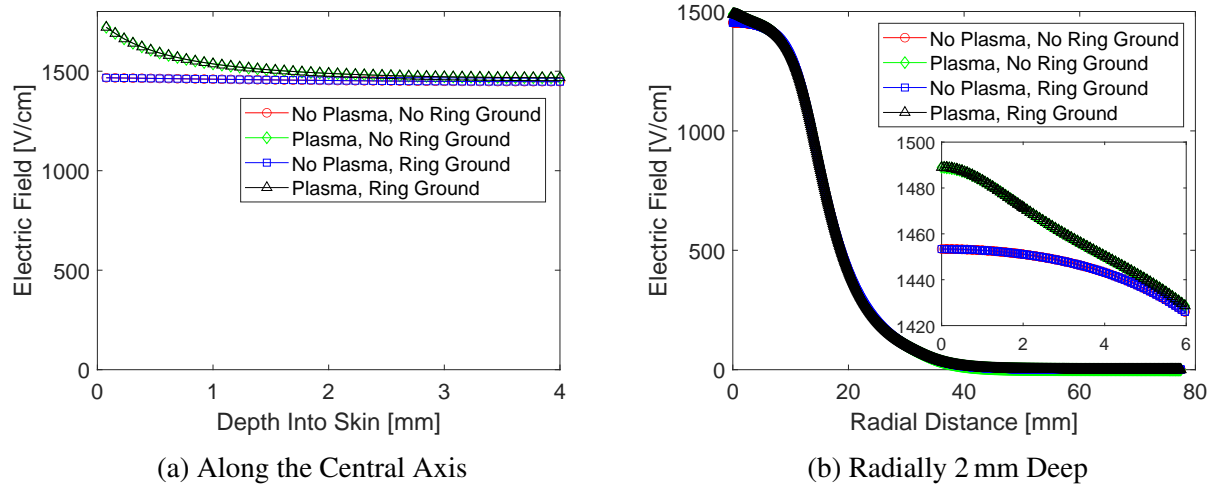


Figure 4.40: Plot of the Modelled Electric Field Magnitude into the Skin Along Multiple Directions

from the streamer, lasting only ~ 4 mm when 2 mm deep into the skin, as noted in the inset graph in Figure 4.40b.

Since this model does not account for moving charges (i.e. plasma, other than the presence of a streamer), the air and skin act as distributed capacitances; a simple 1D series capacitor equation describes the results fairly accurately. Assuming equal and constant cross-sectional areas (A_{cross}) for the skin and air (with thicknesses l_{skin} and l_{air} , respectively) and a uniformly applied electric field ($E = \frac{V}{l}$), the capacitor equation ($C = \frac{\epsilon A_{cross}}{l}$, for a parallel plate capacitor) yields

$$E_{skin} = \frac{V - V_{quartz}}{l_{skin} + \frac{\epsilon_{skin}}{\epsilon_{air}} l_{air}} \quad (4.6)$$

This equation shows that the electric field in the skin, E_{skin} , is roughly proportional to the applied voltage, V , assuming the voltage drop through the quartz dielectric (V_{quartz}) is small (no dielectric can also be used as is the case for the array). Decreasing the air gap distance will increase the electric field in the skin. This is observed in the model, where the presence of the streamer effectively halves the air gap. However the air gap, l_{air} , has a practical minimum value for a non-uniform substrate such as skin (which has a characteristic roughness value). The plasma, as well, has a minimum distance, on the order of 4–20 Debye lengths (the characteristic length scale of the

plasma, typically on the order of 100 μm). Though the permittivity of skin is frequency dependent, the frequency is set by the pulse duration, which does not vary greatly (it varies within one order of magnitude unless the second spark gap, *SSG*, in the RC pulse generator does not discharge). The ratio of permittivities, $\frac{\epsilon_{skin}}{\epsilon_{air}} \approx 120$, is approximately a constant; thus the denominator has a practical minimum value, yielding a maximum for the electric field in the skin at the smallest practical air gap.

4.5.4 Electric Field Measurement

Rhodamine-640 perchlorate dye (4.985×10^{-4} mol/L in methanol) was used in an agarose suspension (with mass fractions 6.845×10^{-3} agarose and 9.47×10^{-3} dye solution in DI water) to attempt to measure the electric field in the substrate by changes in the fluorescence from a 532 nm laser. Rhodamine dye was chosen as both easily available and due to its known fluorescence variation in an electric field; [255] while agarose was used to be a solid that better matches the dielectric properties of skin, rather than a water-methanol liquid alone. The agarose suspension was heated in a microwave for 3 minutes until nearly boiling, placed in a mold, and allowed to solidify. The resulting block of agarose and dye was placed under a glass slide (the agarose suspension had a resistance ~ 1.5 M Ω since it is mostly water). A high DC voltage was applied to the agarose block and glass slide. The setup is seen in Figure 4.41.

The fluorescence from the laser was measured as a function of applied voltage (Figure 4.42). Some variation was noted, but a large change was not noted, thus possibly limiting the use of this technique as a measure of applied voltage or electric field. Further, this system was noted to be extremely sensitive to optical fiber placement; small changes in the fiber placement would cause larger effects in the resulting signal than the applied voltage.

In an attempt to better quantify the changes of the electric field in the agar substrate, two different methods of measuring the peak intensity were used. The first method employed was to find the highest point in a 5 pixel range of the supposed peak. Two wavelengths were chosen, 600 nm and 624 nm, the location of the main fluorescence peak and the shoulder peak. This method is useful for its simplicity and at first yielded the clearest results (Figure 4.43), but the peak locations

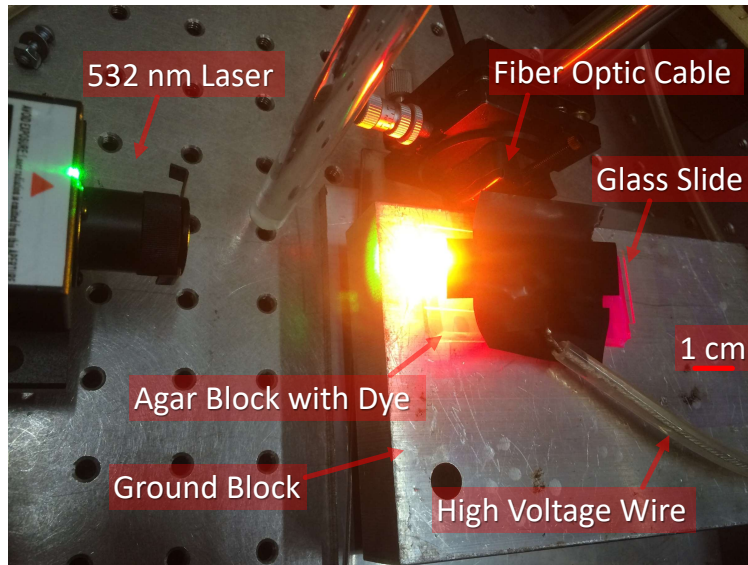


Figure 4.41: Image of the Fluorescent Dye Setup for Electric Field Measurements in an Agar Substrate

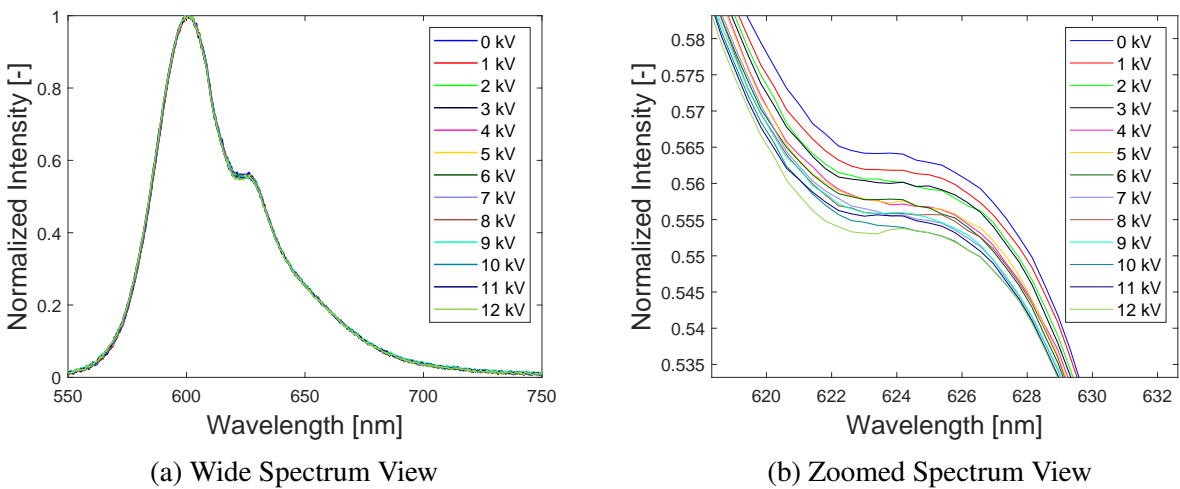
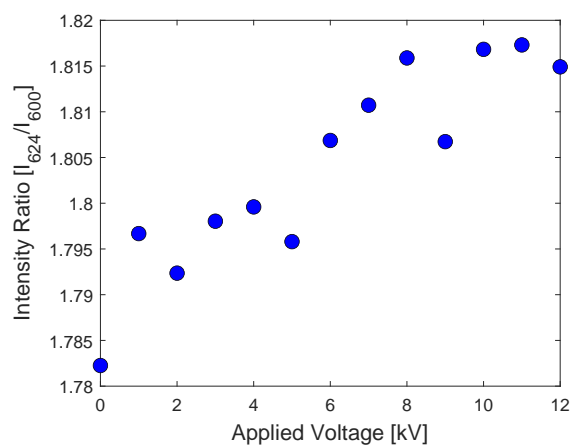
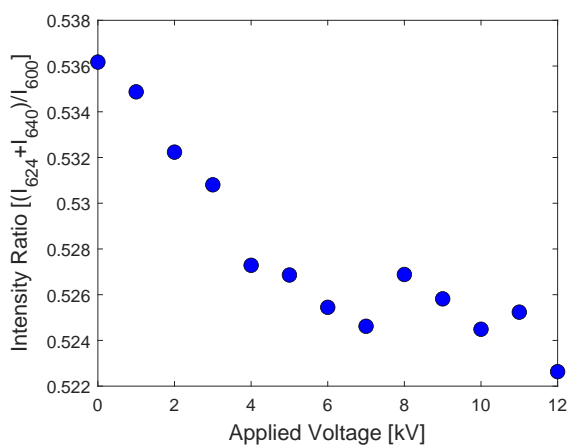


Figure 4.42: Fluorescence Spectra from the Rhodamine-640 Perchlorate Dye Varying the Applied Duration



(a) Highest of 5 Points Results



(b) Pseudo-Voigt Fitting Results

Figure 4.43: Ratio of Peak Intensities Plotted Against the Applied Voltage for the Dye Fluorescence Spectra

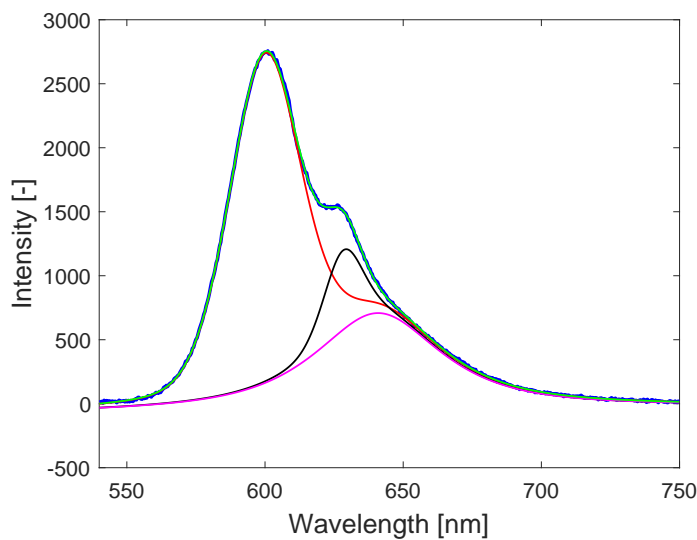


Figure 4.44: Deconvolution of Dye Fluorescence Spectrum (Blue Curve) Using Three Pseudo-Voigt Profiles (Red, Black, and Magenta Yielding Cyan Curve; Linear Offset Not Shown)

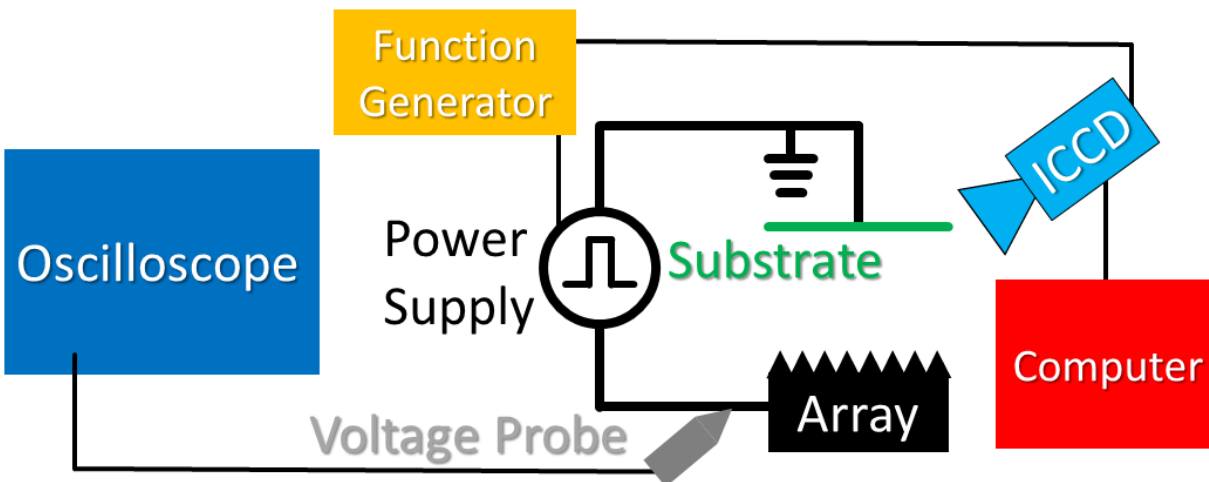


Figure 4.45: Time-Resolved ICCD Imaging Setup Schematic

are unfortunately fairly arbitrarily chosen and can be greatly affected by noise in the signal, thus calling into question the validity of this method. The second method employed was to fit two pseudo-Voigt profiles to the data. Poor fittings resulted until both a baseline correction and a third pseudo-Voigt profile were included, as shown in Figure 4.44, suggesting that the fluorescence is a combination of three different transitions. The clearest trend was found to be the ratio of the sum of the two shoulder peaks to the main fluorescence peak as shown in Figure 4.43. This may have become an option to adequately determine changes in the applied electric field, but was abandoned due to time constraints and anticipated further challenges in developing it to have sufficient spatial and temporal resolution for this system.

4.5.5 Time-Resolved Discharge Imaging

The ICCD camera was used to directly image the discharge over a grounded metal substrate (see Section 3.3.2 for camera information). A function generator (BK Precision 4063) was used to trigger both the camera and the discharge, and an oscilloscope (see Section 3.2.2.4 for oscilloscope details) was used to capture the voltage pulse at the high voltage electrode (i.e. the array) and the camera gate (that is the camera shutter). A schematic of the setup is shown in Figure 4.45, and Figure 4.46 shows the actual setup. The discharge was pulsed at 0.5 Hz with an electrode-substrate

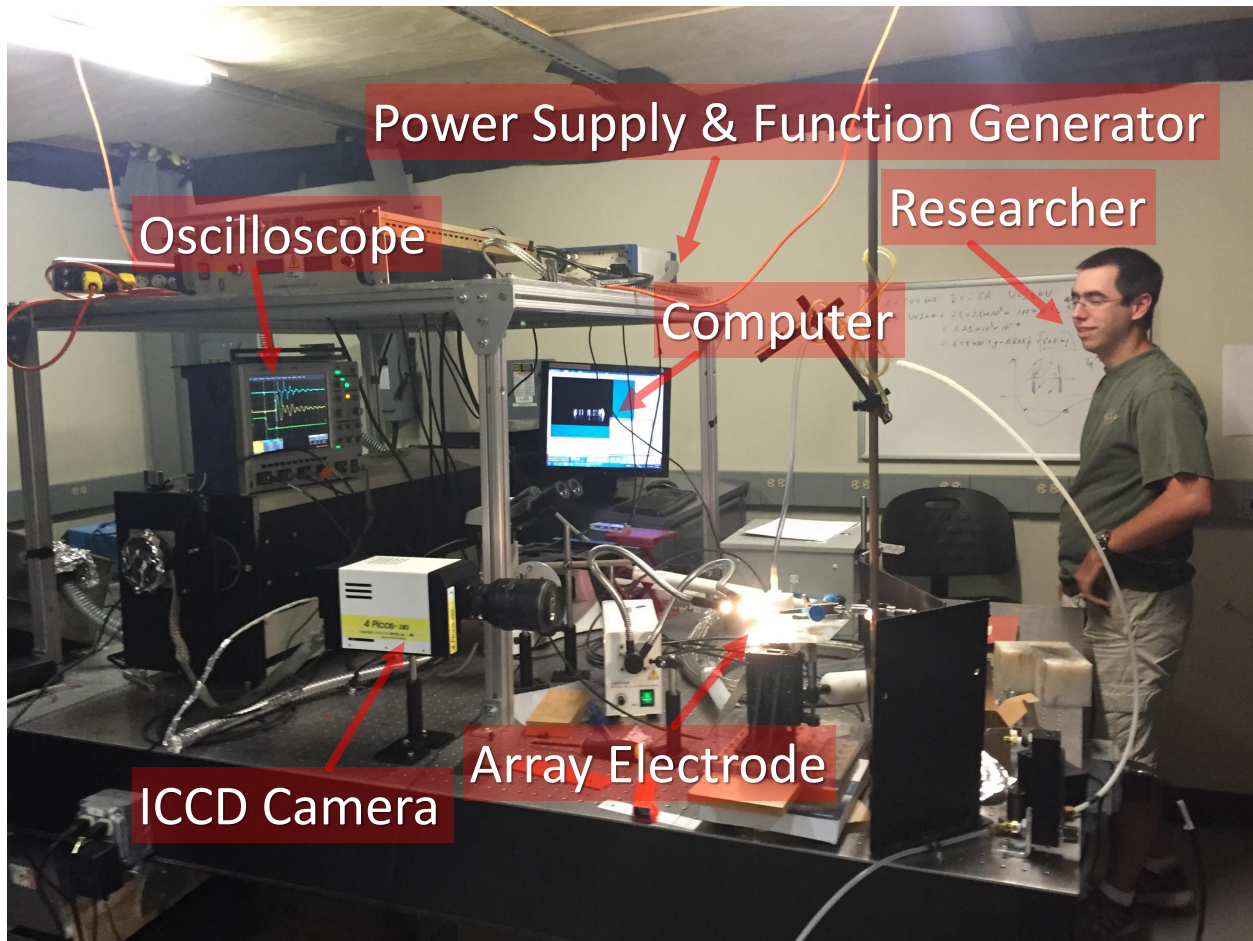


Figure 4.46: Time-Resolved ICCD Imaging Setup Image

gap of 5 mm, $MSG = 0.187$ in, and $SSG = 0.092$ in, yielding $V_{\max} = 20$ kV and $FWHM = 24$ ns. 350 images were taken with an exposure time of 2 ns. Since there is some jitter in the triggering of the discharge, the images were sorted in post-processing by the time delay measured on the oscilloscope traces (a 9 ns adjustment was based off of the cable lengths, which also agreed well with the data), where the zero point in time is taken when the voltage pulse is at 1 kV (above the noise in the measurement). The images without a discharge (41 in total) were used to get an average background, which is then subtracted from the other images.

Initially the discharge is visible at the tips of the arrays, as seen in Figure 4.47 for a delay time of -1.2 ns and -1.1 ns. The next image captured shows a full discharge approximately 1.6 ns after the previous image (at $t_{Delay} = 0.5$ ns). This shows that the streamer travels approximately the

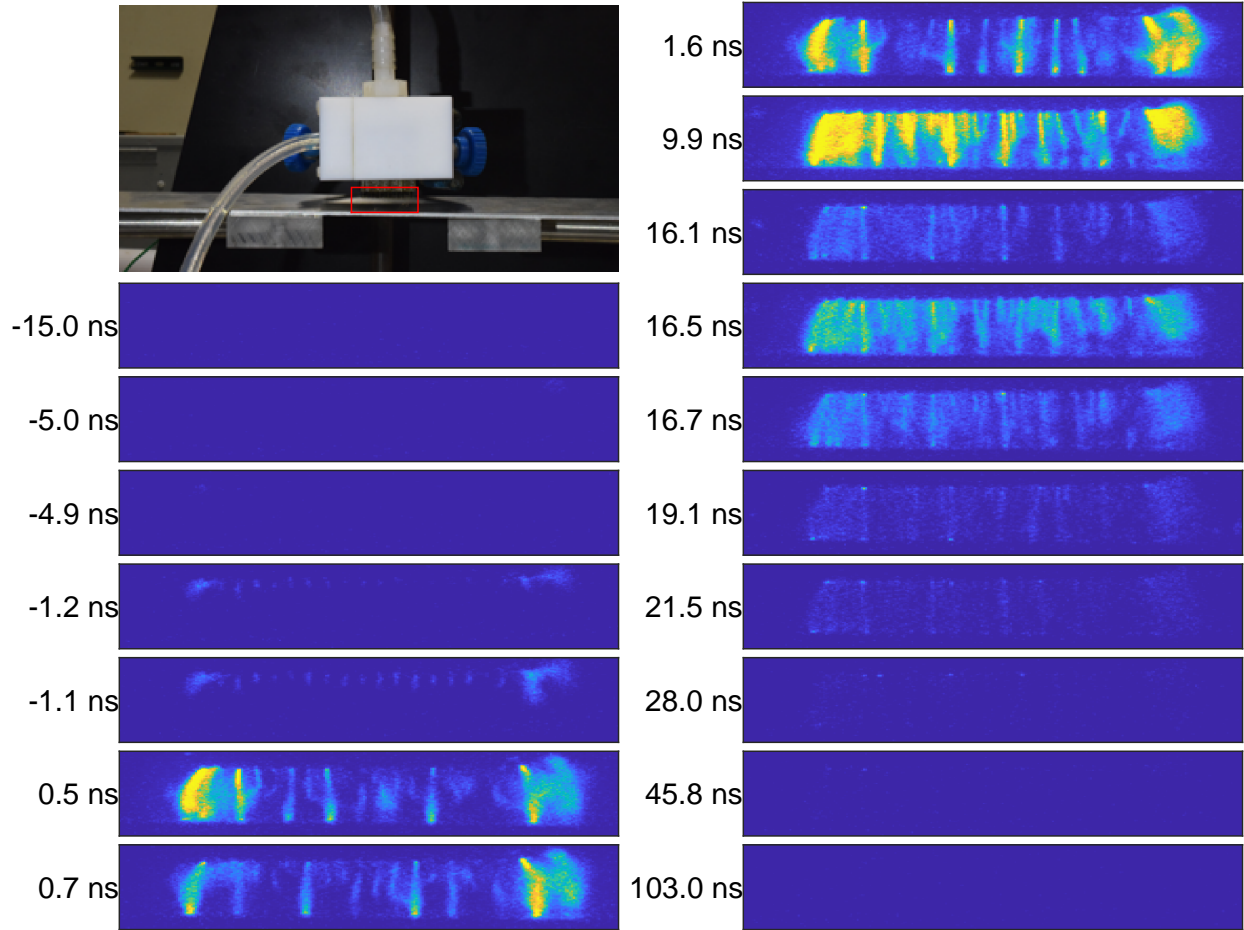


Figure 4.47: Select ICCD Images Showing the Time-Resolved Discharge with 2 ns Exposures

full gap distance of 5 mm in 1.6 ns, thus it is traveling around 3.1×10^6 m/s, which is $\sim 1\%$ of the speed of light. Though the electrons and ions may not be traveling this fast, the ionization wave is traveling around this speed, which is consistent with literature on fast ionization waves. [256–258] The plasma begins to decrease in light intensity after the initial brightness at the voltage rise and ultimately it fades out. The discharge is visible for only around 60 ns, but it is very bright for only a fraction of that time (~ 20 ns) as seen in Figure 4.48, which shows the brightness superimposed on the voltage pulse as a function of the delay time of the ICCD. There is no returning streamer observed (shown in Figure 4.47 at $t_{Delay} = 45.8$ ns), despite having a measured voltage around -8 kV in the voltage pulse.

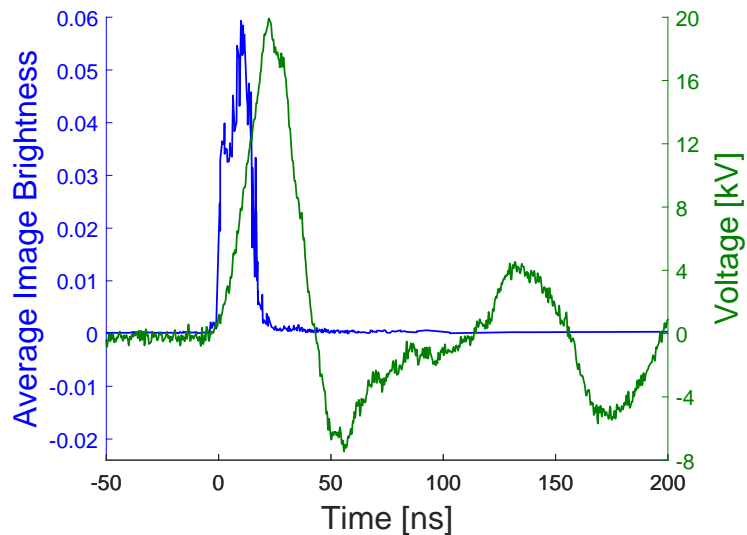


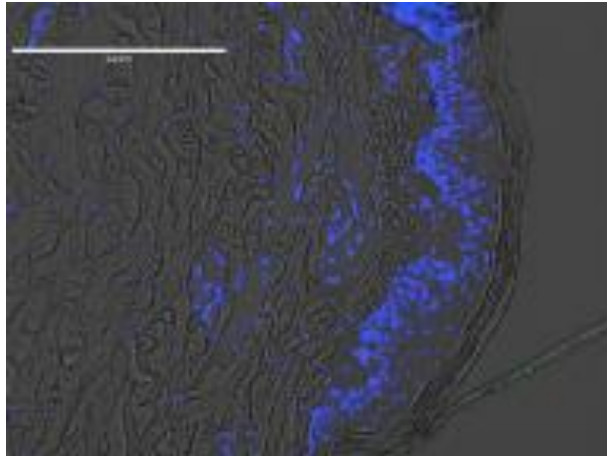
Figure 4.48: Voltage Trace and Background Subtracted Image Brightness as a Function of Time (5 mm Gap, $t = 0$ ns at $V = 1$ kV, Delay Adjustment Based Off of Cable Lengths)

4.6 Electroporation Efficacy

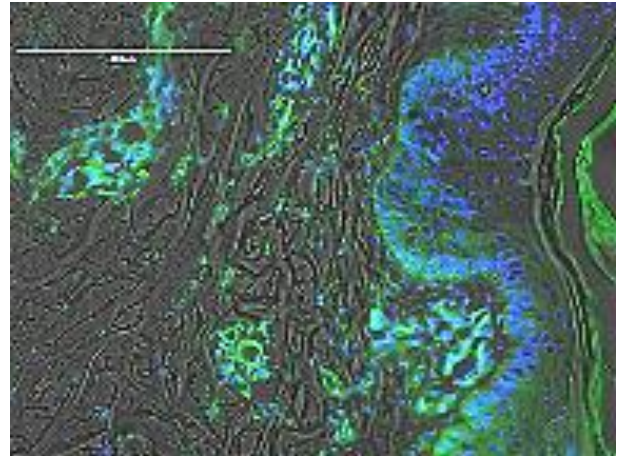
This system (both the array and the nanosecond RC pulse generator) was delivered to the project sponsor who shared some preliminary results of the electroporation efficacy of this array. The results are shown in Figure 4.49, comparing two different control cases (no electroporation but with and without plasmid DNA added) to a conventional electroporation and electroporation using the array electrode. The treatment with the array shows the most uptake of the plasmid DNA, observed by noting green fluorescence in the images.

4.7 Chapter Summary & Future Work

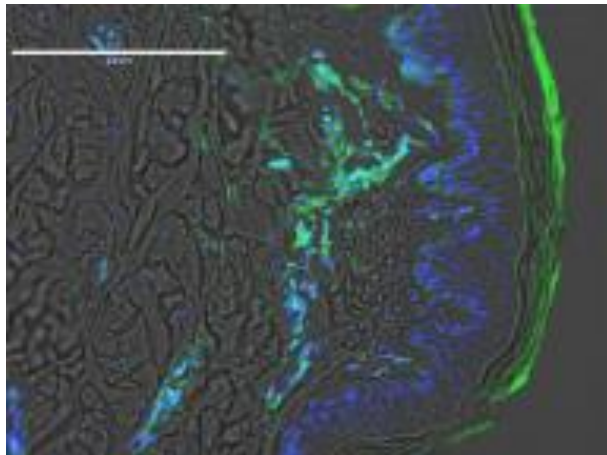
This chapter introduced a plasma system for inducing electroporation in biological substrates, with a focus on epidermal and dermal electroporation. A device such as this would most likely be paired with a drug for enhancing the uptake of the drug into cells, such as is done in some preliminary electrochemotherapy systems. This creates a more difficult pathway for marketing as this becomes a combination drug/device, which would most likely require a De Novo request (or the equivalent if assigned to the drug approval side of the FDA), since there are no existing systems



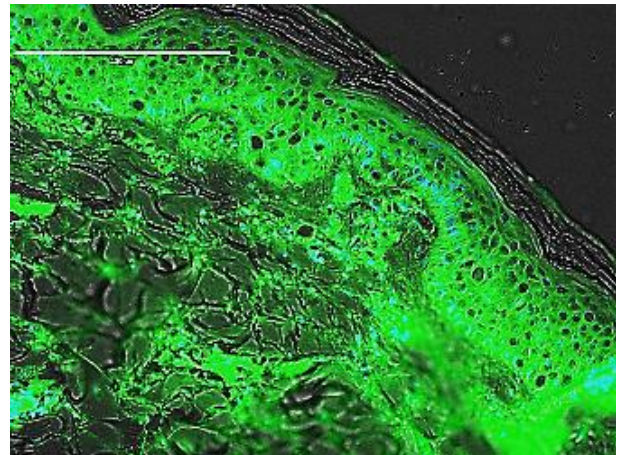
No Electroporation, No Plasmid DNA



Conventional Electroporation
16 pulses—200 V/cm, 150 ms



No Electroporation, Plasmid DNA



Array Electroporation
25 pulses— 20kV, 80 ns

Figure 4.49: Fluorescence Gene Uptake Comparing Conventional Electroporation to Electroporation Using the Array Electrode [Credit: Private Communication with EP Technologies, LLC.]

similar enough to serve as a predicate device.

The system was characterized to determine if all of the tips would develop a plasma to show good uniformity. This was sometimes observed with the FID power supply (depending upon uniformity of the substrate), but not with the custom RC pulse generator, most likely due to the difference in the individual tips' differential resistance having a larger effect with the longer pulse durations. A variety of gaseous species were noted to be generated depending upon the gas flow through the array, but few species were noted with air, which also appeared to have the highest electric field. Overall, the temperature of the discharge was noted to be quite low, owing to the short duration of the applied voltage pulse. The most interesting finding was that the array was substrate invariant for a wide range of conditions, including changing the substrate from a conducting one to a dielectric substrate.

Further work needs to be done to determine the electric field generated from this system. In particular, whether the electric field is roughly uniform underneath the entire array is of interest for wide area medical treatments. Further medical development needs to be done to validate the effect of electroporation, particularly *in vivo*.

5. MODIFICATION OF AN ELECTROSURGICAL SYSTEM

5.1 Introduction

Electrosurgical generators have been used in the medical industry for nearly 100 years; however, they produce a “hot” plasma that is used for destruction of tissue. This chapter introduces a method for converting an existing “hot” electrosurgical plasma into a “cold” plasma jet. This cold plasma jet can then be used for a variety of new uses, most obvious being sterilization applications in wound treatment such as the newly developed European plasma systems previously discussed (see Section 2.5.2). This plasma jet is compared using discharge imaging, electrical characteristics, and optical emission spectra to an existing system used for generating a low temperature plasma jet in laboratory applications. Two different electrical configurations of the existing laboratory plasma jet system are used. A preliminary inactivation study is shown to compare the efficacy of this new plasma jet to the laboratory plasma jet.

5.2 Electrosurgery Background

The first electrosurgery occurred on October 1, 1926, when Dr. Harvey Cushing and Dr. William Bovie removed a lemon-sized brain tumor. [4] The surgery was a success due to the newly developed electrosurgical generator developed by Dr. Bovie, who later patented the device. [259] Due to this success, the device quickly became synonymous with its inventor and all future devices are now known as “a Bovie”. [4]

Electrosurgery is particularly useful for its ability to maintain hemostasis. This is because high frequency currents do not penetrate the body but rather become dissipated in the form of heat. [260] This heat is able to quickly cauterize tissue, in particular sealing blood vessels as the surgeon is cutting them. A number of different terms are used to describe the type of mechanism that is occurring for a desired effect during electrosurgery, mainly cutting, desiccating, and fulgurating. All of these, however, operate on the same basic principle of supplying enough energy to vaporize the water in the tissue. [261] The water vapor along with other tissue fragments leave in the generated

“smoke”. Cutting occurs when the electrode touches the tissue and generates enough heat in the tissue to completely destroy it, passing through the tissue like a scalpel. This is done with a lower voltage sine wave, typically delivering 50–80 W into the tissue. A second type of waveform, called coagulation or *coag* for short, uses a higher voltage, often up to 9–10 kV, but with a much lower duty cycle. This waveform delivers 30–50 W of power into the tissue. The coagulation waveform does not heat up as large of a volume of tissue, so it is often used to seal blood vessels by locally cauterizing them, rather than cutting through bulk tissue. This is used in a contact method called desiccation to desiccate a local area of tissue. This can also be used in a non-contact method called fulguration, which is used to *spray* a region of tissue that is oozing blood, sealing any small capillaries in the region. [262] Between the cut and coagulation waveforms can be a variety of blend waveforms that have a moderate duty cycle (less than 100% and more than ~6%) and a moderate voltage.

There are also two different methods of applying this electromagnetic waveform to the body. The first is called monopolar configuration, where a large dispersive electrode is attached to the body to act as the ground electrode as a return path for current. The high voltage electrode is attached to the handpiece that the surgeon uses. The second is called bipolar configuration where forceps are used for the surgery, one of which is the high voltage electrode and the other is grounded. This localizes the deposited energy to the region of the handpiece, but requires a larger handpiece that has both the high voltage and ground electrodes along with sufficient high voltage shielding. This is much more difficult for laparoscopic surgery, where space is limited.

Electrosurgery is differentiated from electrocautery by the mechanism of heat application. Electrosurgery passes the electrical current through the tissue, while electrocautery uses the electrical energy to heat a filament which is then applied to the tissue to cauterize it.

5.3 Device Life-Cycle Overview

The initial motivation behind this project was that a new CAP device can be expensive to create and ultimately get FDA approval for, however an existing device can be modified with little effort and hopefully receive clearance quickly by using the 510(k) process. To that end an existing FDA-

cleared electrosurgical device is compared to an existing laboratory power supply. This is done by adding a small tube on the end of the electrosurgical generator with a helium gas flow. Helium is used since it has been well characterized in our lab, produces the lowest temperature plasma discharge, and is non-reactive as a noble gas. [29–31, 39] However, in researching the 510(k) submission pathway, it was noted that this pathway requires the same intended use for the new device. Since a CAP has very different effects on tissues, the intended use would not be the same as current, marketed electrosurgical systems, thus the 510(k) pathway would not be a viable option. However the De Novo pathway is a possible option, since the safety of the device has already been established; this would only extend its intended use to include CAP uses such as sterilization or wound treatment.

This then sets up an interesting situation, where the initial device is already done, since an existing device is being slightly modified. However, due to the drastic change in the nature of the plasma discharge going from a “hot” plasma to a “cold” plasma, substantial development is still needed. This is especially so since the entire intended use of the device is changing.

5.3.1 J-Plasma System

In the course of conducting this project, it was found that a newer Bovie system called the J-Plasma already has a tube with helium flow and a retractable electrode, essentially mimicking this setup. [263] However, this system is only being used as a “hot” plasma source for electro-surgery. This is observable in a promotional video of the J-Plasma system (the video appears to have recently been taken down, since it appears the J-Plasma system has been sold to another company), [264] where it initially generates a cold plasma in contact with an egg; only after decreasing the electrode-substrate gap does the plasma transition to a “hot” mode where it ends up “cooking” the top layer of the egg (see Figure 5.1). This is an interesting situation where an existing device can be used for a different intended use without any modification because the plasma already operates in multiple modes. However, like the modifications done on the Bovie system in this research, the intended use has changed, possibly requiring further development for the new intended use.

One study using the J-Plasma system has been conducted for its viability in killing cancer

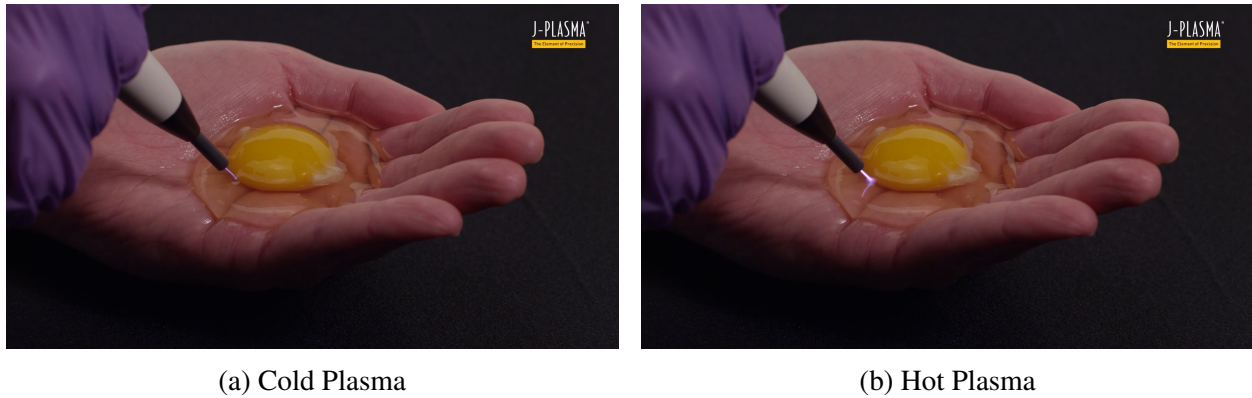


Figure 5.1: J-Plasma Operating in Cold and Hot Plasma Modes (Reproduced under Fair Use from [264])

cells. [265] This showed that the J-Plasma system could be used as a low temperature plasma source when operated with a low duty cycle. It was more successful in inactivating the cancer cells when they were in a liquid medium compared to plated in growth media. This is not explained by a pH change of the medium, rather this is due to biological effects resulting from the plasma treatment, most likely from long-lived reactive species created in the liquid medium. This suggests the J-Plasma system can be used as a post-operative treatment after removal of a cancerous tumor to help ensure any residual cancerous tissue is inactivated.

5.3.2 Other Electrosurgical Systems as a Cold Plasma

In addition to the J-Plasma system, a Maxium electrosurgical unit from Gebrüder Martin GmbH has been used as a cold plasma source specifically for sterilization of multidrug-resistant bacteria. [266] It appears that a low power was used for this in a coagulation mode, hence it is an argon beam coagulator as well. It appears a larger distance than for standard treatment was used, namely 0.5–1 cm to ensure the plasma did not transition to a “hot” mode. Eleven patients with a total of twenty-two wounds were treated; samples were taken directly before and after treatment. Eight wounds had a bacterial reduction by at least 3-logs; fourteen wounds were measured to have been completely sterilized, though this may also be due to a bacterial count too small to count (hence a reduction factor of less than 3-log for many wounds since fewer than 1×10^3 CFUs were

counted before treatment). All wounds showed some decrease in the bacterial load. Nevertheless, the design of this system is potentially suspect, since it requires the surgeon to maintain the high voltage electrode a safe distance away from the tissue to avoid it transitioning into a “hot” plasma discharge.

5.3.3 FDA Approach

In particular for the J-Plasma, this is an interesting situation where the device is already on the market, just under a different intended use. Since the Bovie electrosurgical generators are FDA cleared for “the removal and destruction of skin lesions and the coagulation of tissue,” [267] it seems unlikely that any effect of a cold plasma would be similar enough to use the same intended use. As such, the 510(k) pathway is not a viable option for a modified Bovie (or even the existing J-Plasma system) as a cold plasma device, unless a different device with the same intended use as the cold plasma system is found. Since these devices are already cleared as Class II devices, a De Novo request is a logical move to allow a modified device to become marketable under the FDA as cold plasma source.

5.3.4 Device Outlook

The main applications for a cold plasma device such as this would be for sterilization. In particular this is the use for similar devices currently marketed in Europe (see Section 2.5.2), particularly the sterilization of biofilms that have built up in chronic wounds. For this specific project, the Bovie is characterized as a cold plasma source and an initial bacteria inactivation study is done. However to have any hope of FDA classification as a Class II device (or even Class I device, but unlikely due to the Bovie already being a Class II device), substantially more work needs to be done to characterize the Bovie power supply for a wider range of conditions, and to prove the results of bacteria inactivation achieved with an already existing laboratory power supply can also be achieved with the Bovie. [30,31] In addition, at least one robust clinical study (a suitable animal model study may also be sufficient, but the FDA has become stricter for De Novo requests, so a clinical study may still be required) would be required to show this device

does behave like the various European devices for treating chronic wounds. However, in addition to showing efficacy, this system would also have to show superior performance to the existing, state-of-the-art treatments for wounds to be successful from a marketing point of view.

Though the system discussed here is not used for removal of cancerous tissue, a second approach for another system, such as the J-Plasma or a similar system, could be for cancer treatment. This opens up a market for systems that can operate in both a “hot” mode used for removing cancerous tissue and then switch to a “cold” mode for treating the nearby tissue that may have residual cancerous cells.

5.4 Bovie Modification

This project seeks to determine the similarities and differences between two power supplies listed in Table 5.1. The first power supply (Aaron 940) manufactured by Bovie Medical Corporation is used for thermal plasma treatment, i.e. electrosurgery. Specifically this unit is “intended for the removal and destruction of skin lesions and coagulation of tissue,” [268], which is solely done with a coagulation mode, that is with a lower duty cycle but higher voltages compared to the cutting mode of electrosurgery. As such, it is designed for high current and low voltage ($V_{pp} \leq 8$ kV) operation. The second power supply, the laboratory AC power supply, is manufactured by Information Unlimited (also known as Amazing1 from their website URL, a PVM500 model), which is used for research. The laboratory AC power supply has been well characterized for plasma operation in a FE-DBD jet configuration for non-equilibrium plasma generation previously in our lab. [15, 29] This project seeks to determine if the Bovie power supply is also capable of generating a controlled non-equilibrium plasma jet, which is typically done with higher voltages.

To make the Bovie power supply into a low temperature plasma jet, a small plastic tube was placed over part of the electrosurgical tip electrode. A T-shaped tube connector was then placed on the small plastic tube to make a seal around the electrode and tube. A gas inlet line was then connected to the tube connector and varying lengths of glass tube were attached to the third side to vary the electrode-to-ground distance. The modified electrosurgical tip was then inserted into the Bovie handpiece to be powered. The Bovie handpiece, the part of the power supply that houses

Table 5.1: Comparison of Bovie and Laboratory AC Power Supplies

	Bovie (Aaron 940)	Amazing1 (PVM500)
Voltage	~0–6 kV	~0–40 kV (peak-to-peak)
Power	40 W (max)	300 W (max)
Frequency	550 kHz (nominally, measured 455 kHz), 21 kHz repetition (pulse) rate (see Figure 5.8)	20-70 kHz
Waveform	Decaying sinusoid	Sinusoid
Cost	~\$1000	\$500

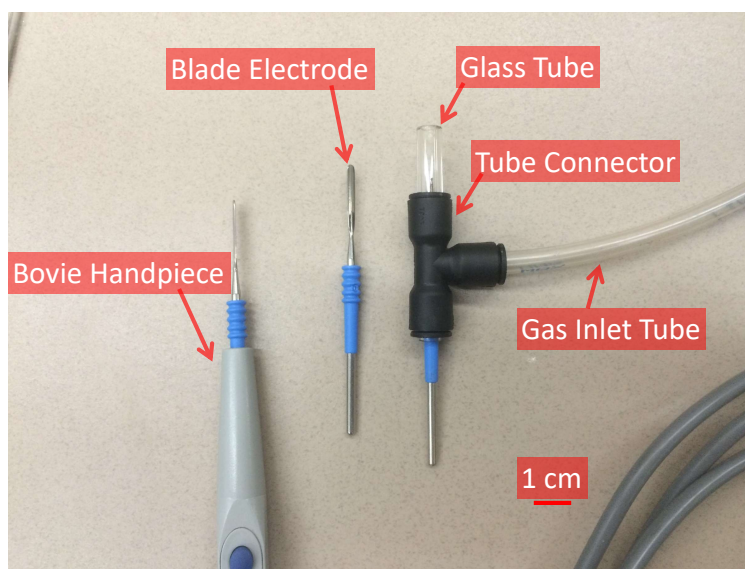


Figure 5.2: Image of the Modification to the Bovie Electrosurgical Tip Electrode

the control knobs and has a location to insert the high voltage electrosurgical tip electrode, was then connected to the setup. This modification is shown in Figure 5.2. For all testing done here, the blade electrode was used, rather than an electrode with a different geometry (such as a ball or needle tip).

5.5 Device Characterization

A glass tube (OD 0.25 in, ID 0.16 in) of varying lengths were used in testing. A helium gas flow was supplied around the electrode, usually at a flow rate of 3.97 SLPM. The electrode was suspended above a ground electrode plate. The Bovie handpiece was then connected to the setup. This is shown schematically in Figure 5.3, and an image is shown in Figure 5.4. Alternatively,

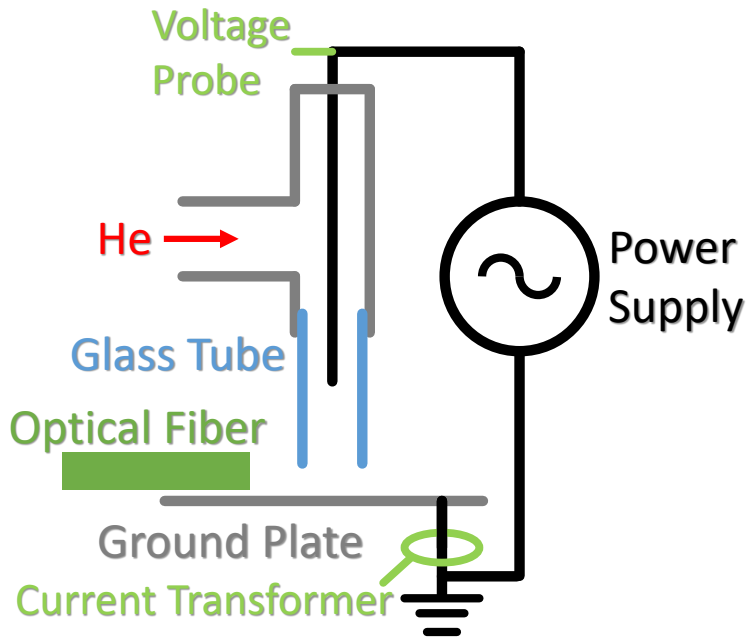


Figure 5.3: Schematic of the Bovie Power Supply Setup

the laboratory power supply could be connected in lieu of the Bovie power supply, thus the only difference would be the excitation waveform between the two devices; the electrode and all other connecting parts, such as the gas tube, would be the same.

Unfortunately, the Bovie power supply turns off if it overvoltages, thus there is a narrow operating range that it is able to create a low temperature plasma jet in; increasing the power or decreasing the tube length would cause it to enter a “hot” mode, and decreasing the power or lengthening the tube would cause it to overvoltage and turn off. This is due to a fail-safe in the power supply to avoid excessive power assumed to be due to failure of the insulation around the electrode. [269]

Initially the various modes of the two power supplies are investigated. Two different and possibly useful modes are identified for each power supply, a diffuse and concentrated mode, and these modes are further characterized by their voltage-current traces, broadband spectra to determine gaseous species present in the discharge, and discharge temperature. Lastly a brief bacterial inactivation study is conducted.

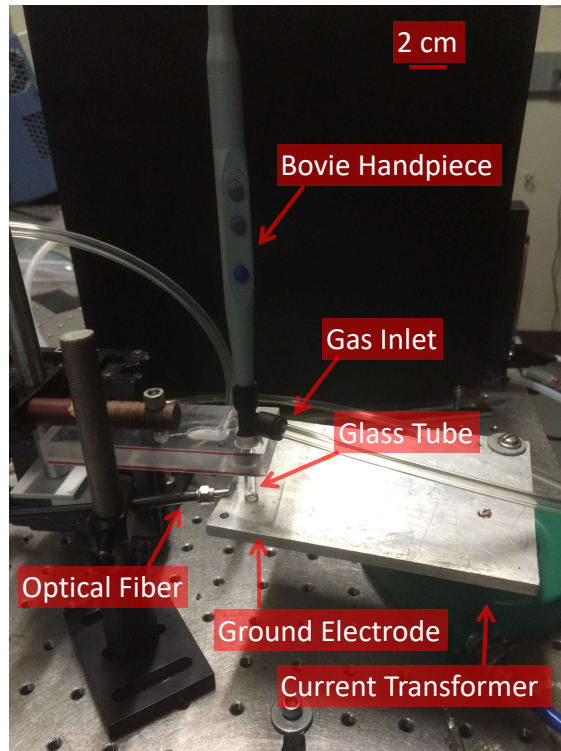


Figure 5.4: Image of the Bovie Power Supply Setup

5.5.1 Discharge Mode Imaging

The Bovie power supply was operated while varying the power and distance between the high voltage electrode and ground. A number of modes were observed at various conditions as shown in Figure 5.6. The circles represent measured data points; the background color is to demonstrate how the modes blend into each other. Modes of interest are the diffuse plasma (green, see Figure 5.5(a) with a 1.7 mm glass tube, 16 power setting), and the concentrated mode (purple, see Figure 5.5(b) with a 1.7 mm glass tube, 22 power setting). The preceding modes (red to orange, with a lower power settings) do not extend beyond the length of the tube, having either no discharge (red) or only a partial discharge (orange). The final mode (blue, a pulsing discharge) does not allow for continuous plasma since the power supply is being overvoltage and turns off intermittently with short pulses of plasma occurring at a frequency of ~ 1 Hz.

The laboratory AC power supply was operated in two different electrode configurations, in a

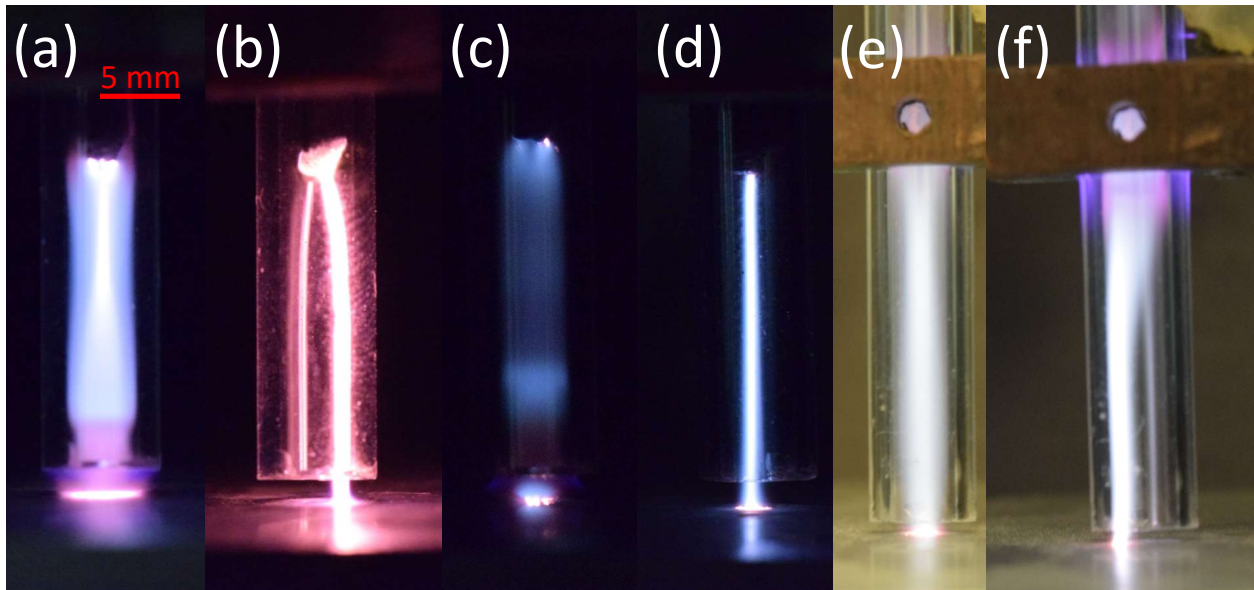


Figure 5.5: Bovie Power Supply Operating in (a) a Diffuse Mode and (b) a Concentrated Mode; Laboratory AC Power Supply FE-Direct Jet Operating in (c) a Diffuse Mode and (d) a Concentrated Mode; and Laboratory AC Power Supply FE-DBD Jet Operating in (e) a Diffuse Mode and (f) a Concentrated Mode

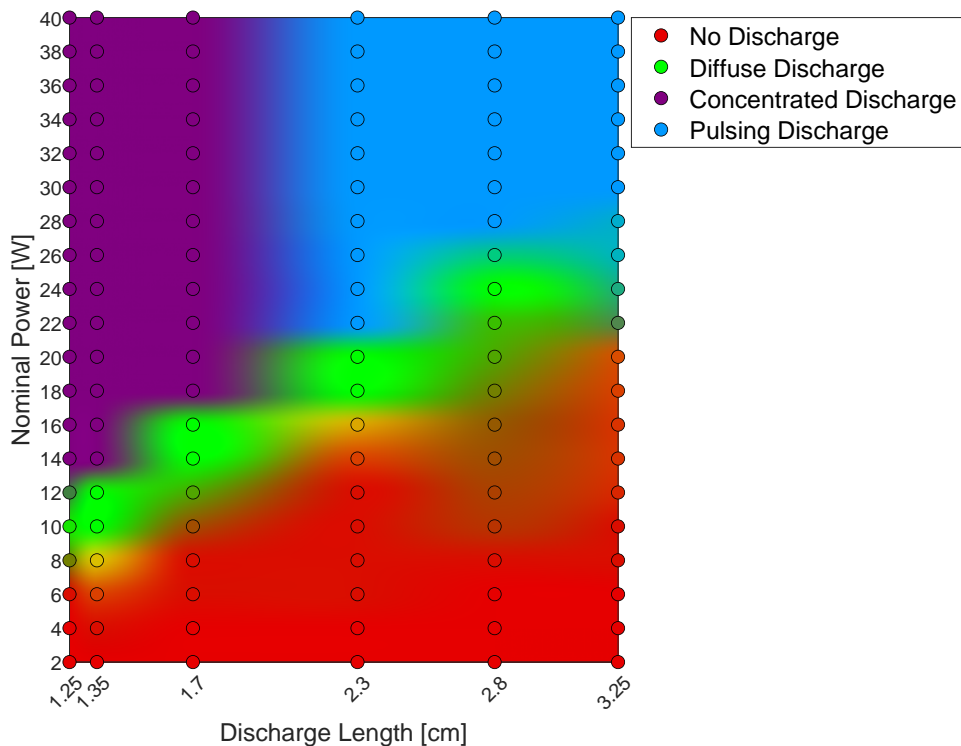


Figure 5.6: Different Operating Modes for the Bovie Power Supply as a Function of Electrode-Substrate Gap and Power Setting for a Flow Rate of 3.97 SLPM (Circles are Measured Data Points with the Background Color Approximating the Operating Mode Between Data Points)

floating electrode direct jet configuration the same as the Bovie power supply and in a FE-DBD jet configuration, where the high voltage electrode surrounds the dielectric tube rather than being inside it. The laboratory FE-direct jet was observed to operate in two main modes, a diffuse mode (Figure 5.5(c) with a 1.7 mm glass tube, 6% low power setting, 8.08 SLPM He flow) and a concentrated mode (Figure 5.5(d) with a 1.7 mm glass tube, 15% low power setting). The laboratory FE-DBD jet was also observed to operate in two main modes, a diffuse mode (Figure 5.5(e) with a 1.7 mm glass tube portion extending below the high voltage electrode, 10% low power setting, 13.8 SLPM He flow) and a concentrated mode (Figure 5.5(f) with a 1.7 mm glass tube portion below the electrode, 20% low power setting, 13.8 SLPM He flow). This is similar to what was found previously in our lab, [29] showing at least qualitatively that the modes exist for FE-direct plasma jets in addition to FE-DBD jets.

5.5.2 Voltage and Current Characterization

It was noted that the initial current and voltage pulse from the Bovie power supply was substantially higher than the subsequent pulses. This is seen in Figure 5.7. This is most likely due to the subsequent pulses having some preionization from earlier pulses, thus requiring a lower breakdown voltage to initiate the plasma discharge. This also explains the pulsing mode noted in Figure 5.6, where the gap is too large, requiring too large of a voltage to initiate the discharge. The first pulse creates a plasma discharge, but then the power supply turns off due to being overvolted. This process then repeats with only the initial pulse creating a plasma discharge, pulsing at the frequency the overvoltage control system allows (~ 1 Hz).

The steady state current and voltage traces are shown in Figure 5.8. The Bovie voltage traces between the two modes are similar; the diffuse mode has more decaying oscillations after the primary voltage pulse. The current, though, is two orders of magnitude larger for the concentrated mode compared to the diffuse mode. Similar to the voltage, the diffuse mode has significant ringing after the primary pulse, which is absent in the concentrated case. For the diffuse mode, the laboratory power supply behaves very similarly for both the laboratory FE-direct jet and the laboratory FE-DBD jet. The voltage and current traces are fairly sinusoidal; the laboratory FE-DBD

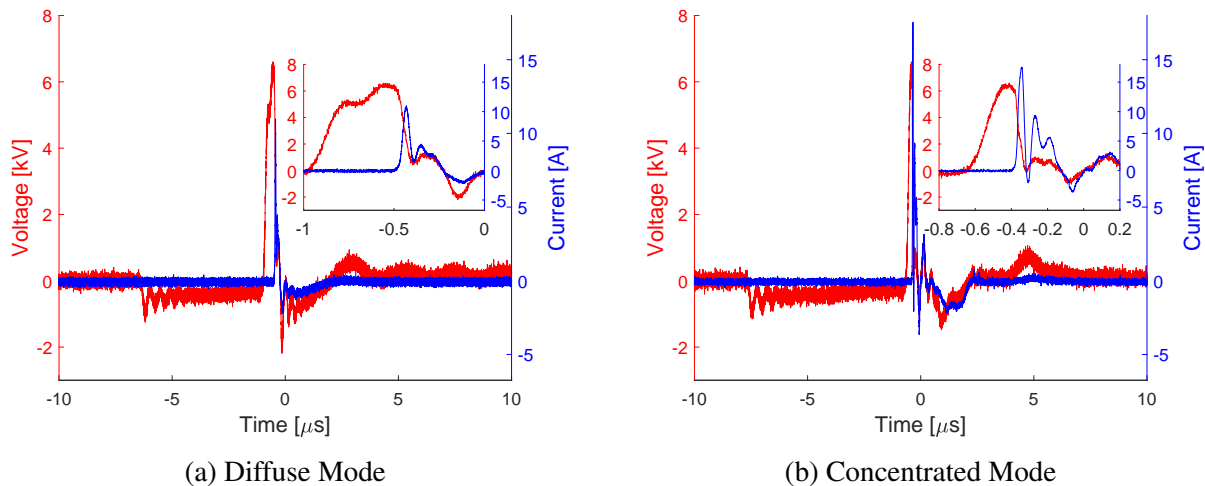


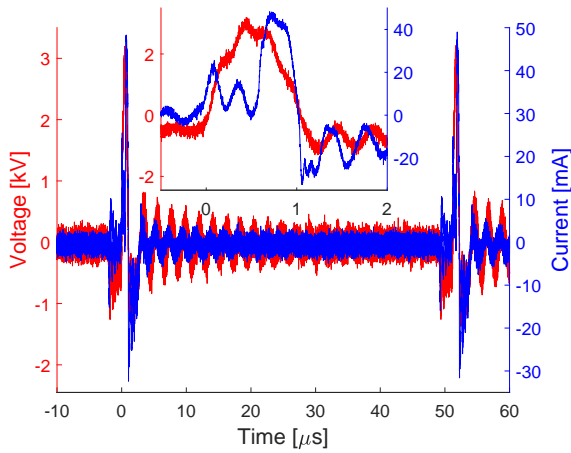
Figure 5.7: Initial Voltage and Current Pulses for the Diffuse and Concentrated Modes with the Bovie Power Supply

jet only requires slightly higher voltages due to the dielectric barrier, which in turn is causing a slightly higher current. No current spikes are noted, most likely being too small to notice. The concentrated mode for the laboratory FE-DBD jet is similar, with a few current spikes becoming noticeable. This is different than the very pronounced current spikes noted previously, [29] however this jet is running a substantially higher gas flow rate (13.8 SLPM compared to 2.9 SLPM). The concentrated mode for the laboratory FE-direct jet is quite different. The current spikes have consolidated into a single large spike (similar to previously noted FE-DBD jets [29]), that draws a large amount of power skewing the otherwise sinusoidal voltage trace. The large current spike (i.e. ionization wave) frequency is comparable to the repetition frequency of the Bovie power supply.

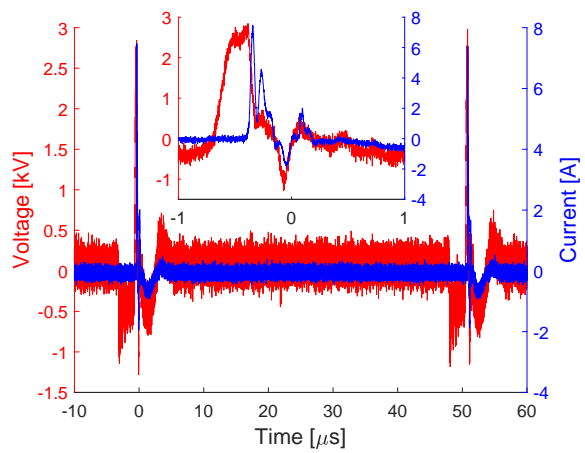
5.5.3 Broadband Spectra

Optical emission spectra were taken using a CCD spectrometer (see Section 3.4.1.2 for the spectrometer details). All spectra showed OH ($A^2\Sigma \rightarrow X^2\Pi$), N_2 2nd positive system ($C^3\Pi_u \rightarrow B^3\Pi_g$), He, He_2^1 , H ($H\alpha$ and $H\beta$ as well as very small $H\gamma$ in the Bovie spectra), and O (777 nm). The spectra for the various conditions are seen in Figure 5.9 corresponding to some of the condi-

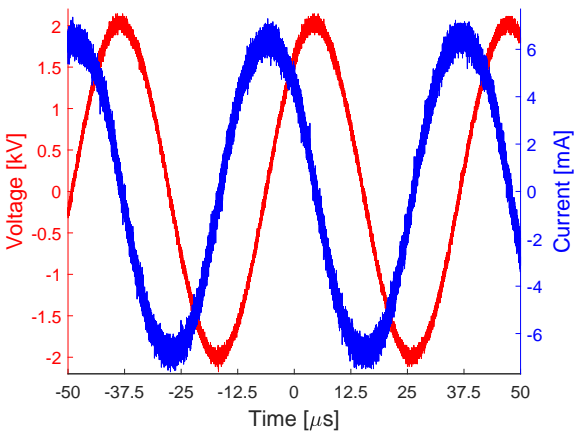
¹Unlike what is commonly taught in undergraduate chemistry, helium is capable of making bonds, albeit normally van der Waals bonds, which can nevertheless be considered molecules [270]. In this case, it is most likely from the collision of two helium atoms, where at least one is excited to a metastable state. [271]



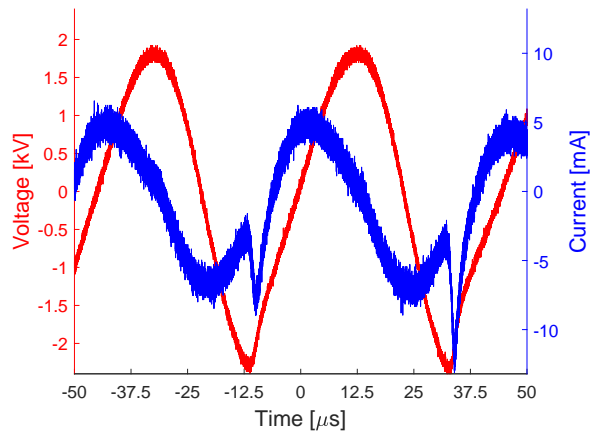
(a) Diffuse Bovie FE-Direct Jet



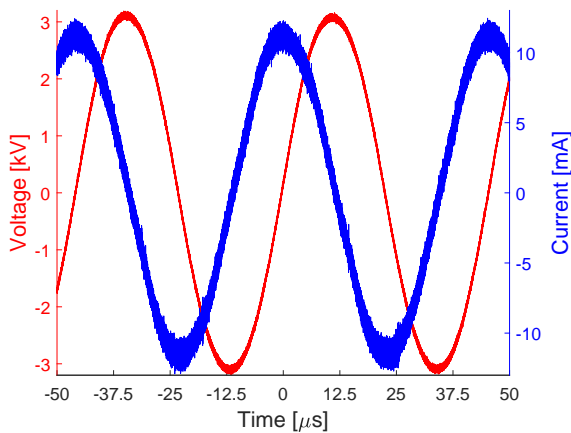
(b) Concentrated Bovie FE-Direct Jet



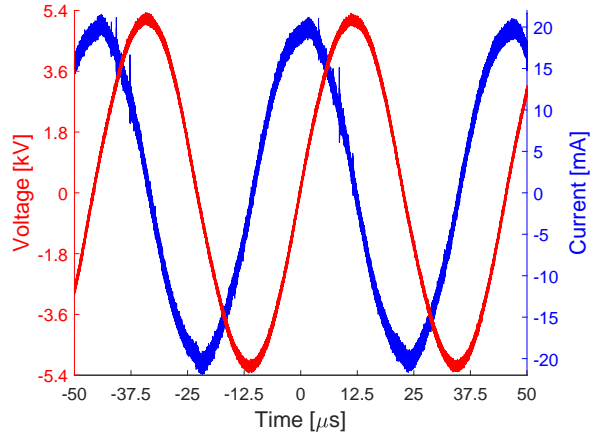
(c) Diffuse Laboratory FE-Direct Jet



(d) Concentrated Laboratory FE-Direct Jet



(e) Diffuse Laboratory FE-DBD Jet



(f) Concentrated Laboratory FE-DBD Jet

Figure 5.8: Current and Voltage Traces for the Bovie FE-Direct Plasma Jet, the Laboratory AC Power Supply FE-Direct Jet, and the Laboratory AC Power Supply FE-DBD Jet for Both Diffuse and Concentrated Modes

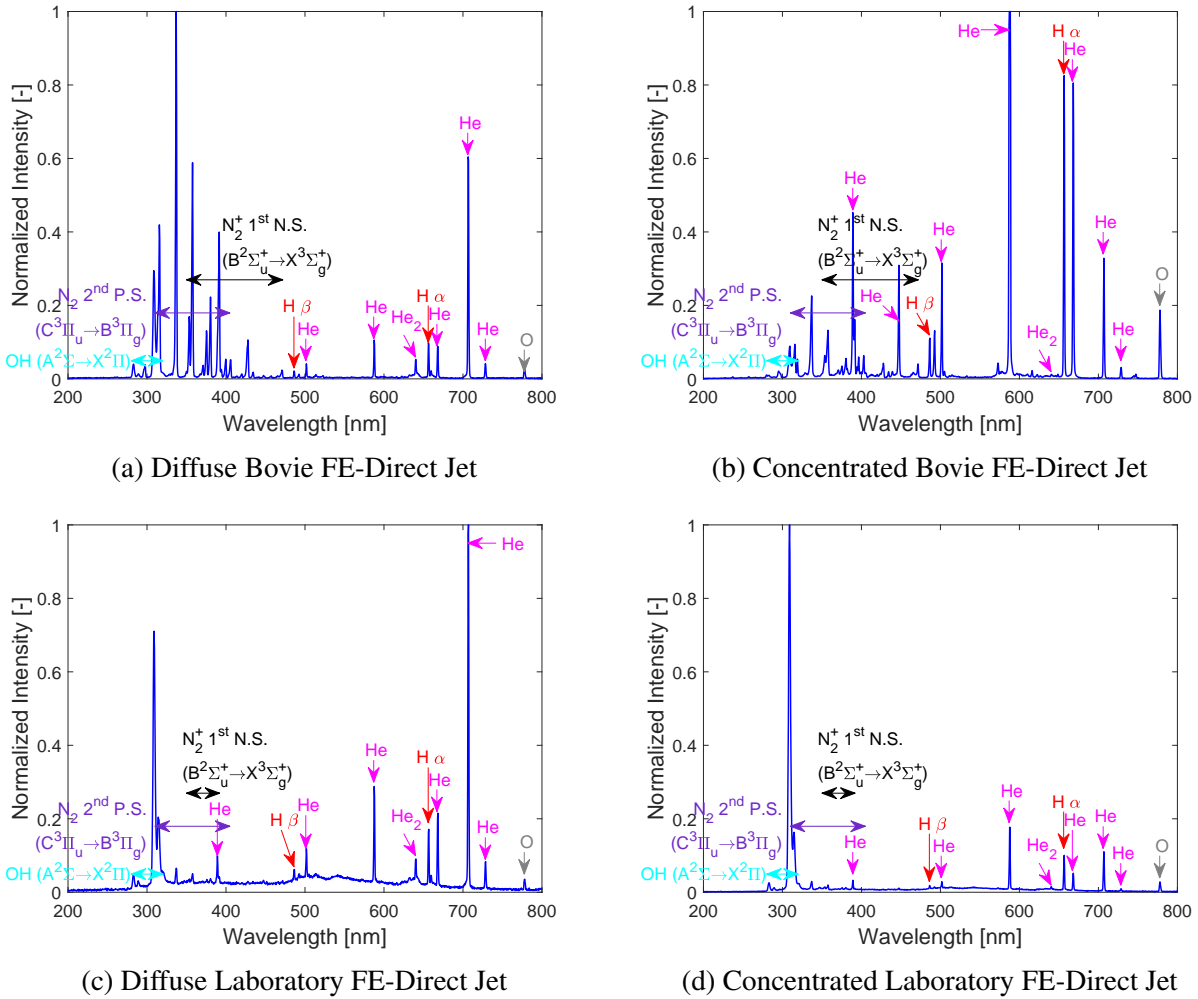


Figure 5.9: Broadband Spectra for the Bovie and Laboratory AC Power Supply FE-Direct Jets for Both Diffuse and Concentrated Modes

tions in Figure 5.5. Overall the spectra were similar other than differing relative intensities between lines, which was to be expected since all are discharges in a helium gas flow. The laboratory FE-direct jet produced more OH compared to the Bovie, which has a larger concentration of N_2 excited states. The Bovie also created N_2^+ ($B^2\Sigma_u^+ \rightarrow X^3\Sigma_g^+$), which was barely observed in the laboratory FE-direct jet's spectra, especially compared to the relative intensity of the OH and He peaks. Some of the non-flat baseline noted in the diffuse laboratory spectrum may be due to broad H_2 lines.

To attempt a more quantitative comparison, a Boltzmann plot (Figure 5.10) can be created for each condition. The Boltzmann plot is plotting the distribution of line intensities to their energy by

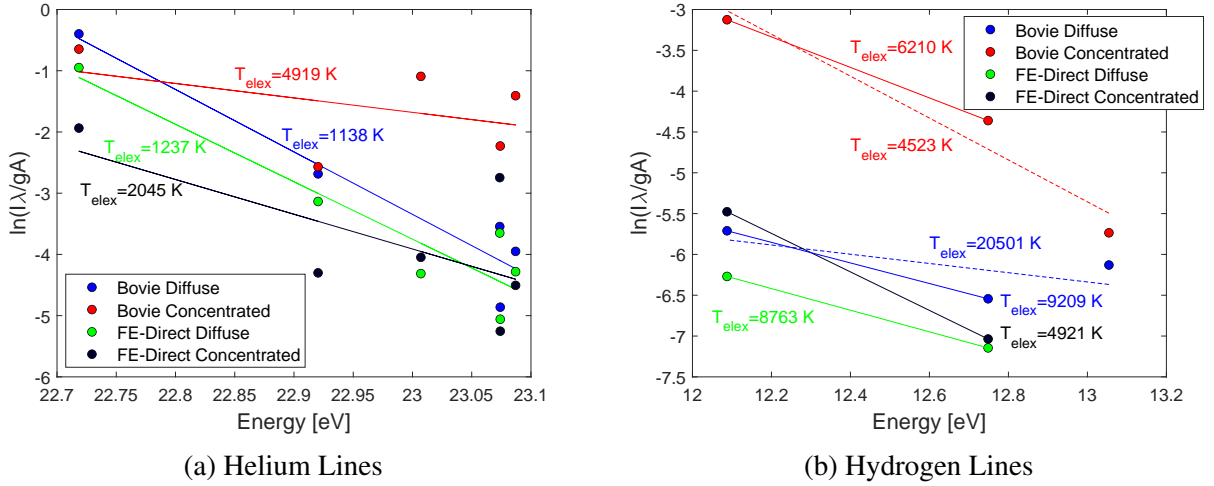


Figure 5.10: Boltzmann Plots Derived from the Broadband Spectra of the Bovie and Laboratory AC Power Supply FE-Direct Jets for Both Diffuse and Concentrated Modes

the equation

$$\ln \left(\frac{I_i \lambda_i}{g_i A_i} \right) = \left(\frac{-1}{k_B T_{\text{ellex}}} \right) \mathcal{E}_i + k \quad (5.1)$$

where I_i is the intensity of a specific transition i , λ_i is the wavelength, g_i is the degeneracy of the upper level, A_i is the Einstein coefficient, \mathcal{E}_i is the energy, k_B is the Boltzmann constant, and k is a constant (see Section 3.4.3.1 for more details on the theory). [272] This allows the electronic excitation temperature, T_{ellex} , to be determined from the slope of the line in the Boltzmann plot. The electronic excitation temperature is assumed to be similar to the electron temperature, T_e , since the primary mechanism of generating these excited states is from electron impact excitation processes (at least for helium, the excitation of the hydrogen can also be attributed to dissociation processes with water vapor). However various deexcitation processes are possible, such as photon emission as well as collisional losses, such as Penning ionization with neutral N_2 atoms, which can skew the resulting T_{ellex} determination. Two different Boltzmann plots are generated, one from various helium lines (388.9 nm, 501.6 nm, 587.6 nm, 667.8 nm, 706.5 nm, and 728.1 nm) and the other from the hydrogen lines ($H\alpha$, $H\beta$, and $H\gamma$, namely 656.3 nm, 486.135 nm, and 434.0 nm). The parameters g_i , A_i and, \mathcal{E}_i came from NIST. [218] Since the $H\gamma$ line was extremely dim (and

non-existent in two cases), T_{elx} is found with (dashed lines) and without its inclusion.

The electronic excitation states are not described by a Maxwellian distribution (and a single T_{elx} value²), since the electronic excitation temperature determined from the helium lines is significantly lower than the temperature determined from the hydrogen lines; although the concentrated Bovie case is close. That is because this system is tending towards an equilibrium discharge both within an energy mode (electronic excitation in this specific case) and across energy modes (see Section 5.5.4 for the rotational and vibrational temperatures). The hydrogen lines may give an approximate electron temperature for the N_2 excitation, since the C-state of N_2 (the upper state in the 2nd positive system) is approximately 11 eV above the ground state, which is close to the energy required to excite the hydrogen. This, however, is complicated by the fact that the hydrogen lines may not be electronically excited due to an electron impact excitation process but rather from a dissociation process from a water vapor molecule colliding with an excited helium atom, as is described by the equation



In this case, the electronic excitation temperature determined from hydrogen is not a good indicator of the electron temperature, T_e . Nevertheless, these different electronic excitation temperatures for the four measured cases result in the different relative intensities noted in the broadband spectra and are caused by the differing excitation mechanisms of the electrical systems. Interestingly, the two diffuse cases are comparable despite having vastly different intensities in OH, N_2 , and N_2^+ . Some of this could also be due to differing flow rates in helium, leading to a lower concentration of the ambient air species in the discharge.

5.5.4 Temperature Determination

Optical emission spectra were collected for 352–358 nm using an ICCD camera (see Section 3.4.1.1 for the spectrometer details). The 2nd positive system of N_2 along with the 1st neg-

²Some authors in the literature will use two T_{elx} values (typically broken into high energy and low energy fittings) to fit the entire distribution, which technically breaks from the strict definition of temperature as derived from an equilibrium Maxwellian distribution.

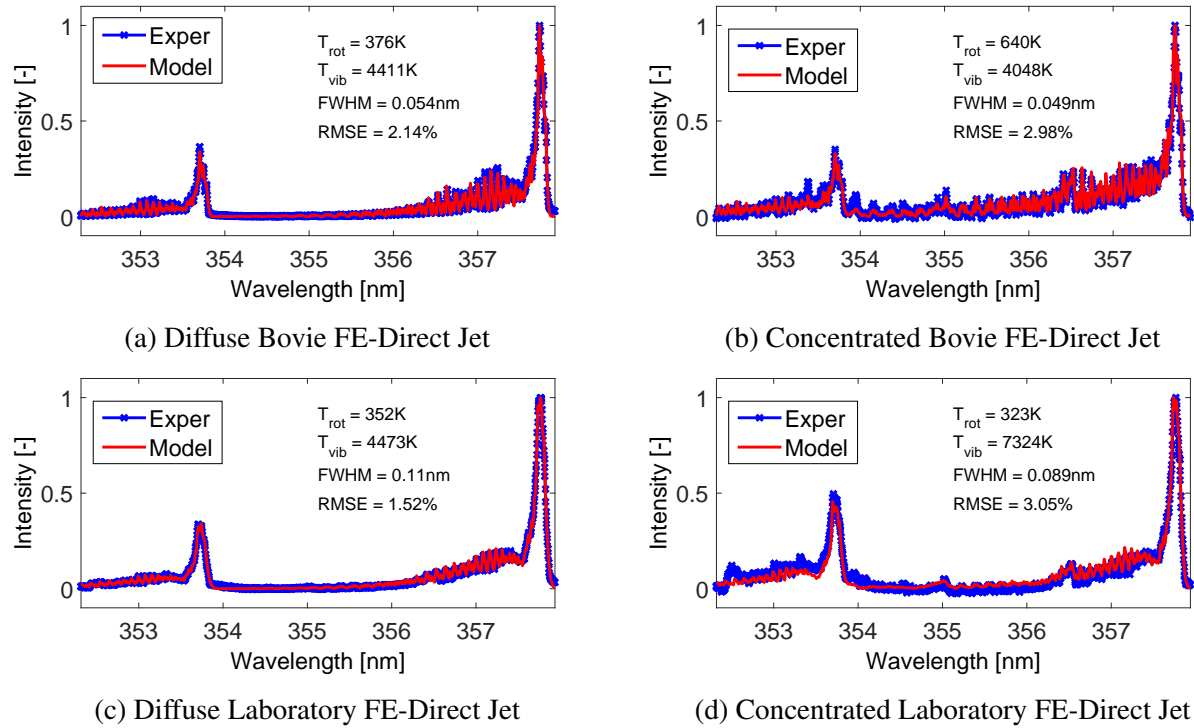


Figure 5.11: Various Wavelengths for the 2nd Positive System of N₂ with Temperature Fits for the Bovie Power Supply and Laboratory AC Power Supply FE-Direct Jets

ative system of N₂⁺ was compared to modeled spectra from SpecAir to determine the rotational (T_{rot}) and vibrational (T_{vib}) temperatures of the nitrogen species in the gas (see Section 3.4.3.2 for information on the temperature fitting algorithm). Spectra for the various conditions are seen in Figure 5.11 corresponding to the conditions in Figure 5.5. Both power supplies are non-equilibrium plasmas for both the diffuse and concentrated modes as determined by their rotational and vibrational temperatures. The diffuse mode for the Bovie has a very low gas temperature (approximately the rotational temperature), while both modes for the laboratory FE-direct jet have very low gas temperatures. Though in the concentrated mode the Bovie power supply is still a non-equilibrium plasma, it is closer to an equilibrium state than the other conditions, showing a higher rotational and lower vibrational temperature. For both power supplies in the concentrated mode, N₂⁺ was noted in the spectra; however, the concentration of N₂⁺ was negligible in the temperature fitting for both diffuse cases. The laboratory FE-direct jet has a larger concentration of N₂⁺ in the concen-

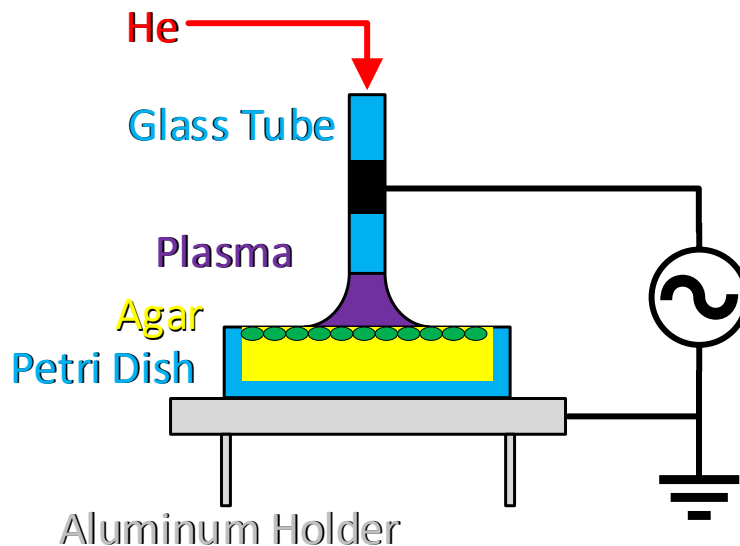


Figure 5.12: Setup Schematic for the Plasma Jet Sterilization Treatment

trated mode, with a relative number concentration of species $[N_2^+]/[N_2] = 4.7 \times 10^{-6}$ compared to 3.83×10^{-10} for the Bovie power supply. Nevertheless, this analysis was done assuming $T_e = T_{\text{vib}}$, rather than using the electronic excitation temperature found in Figure 5.10, since that temperature is assumed to better reflect the dissociation process rather than the true electron temperature.

5.5.5 Inactivation Study

A bacterial and fungal inactivation study was conducted to compare the Bovie (run at 21 W) and the laboratory FE-DBD jet (powered at $V_{pp} = 6$ kV and 23.8 kHz). The FE-direct plasma jet using the laboratory power supply was not used. This experimental work was performed by Rhys Michna, an undergraduate student; data processing was conducted by the author, Matthew Burnette. The setup is shown in Figure 5.12. The plasma jet, run with 15 SLPM industrial grade helium (99.95%), was placed ~ 1 cm over a petri dish with agar contaminated with 300 CFU of one of three strains, *E. Coli*, *Bacillus*, or *Aspergillus Flavus*. Three different treatment times were used, 30 s, 90 s, and 180 s, along with a control of 180 s treatment without a plasma discharge (i.e. just a helium gas jet). The samples were plated minutes before treatment, and images and counts were taken after 1 day of incubation. Three replicates of each trial were used.

Examples of the plated and incubated samples are shown in Figure 5.13. Cell count results for the entire petri dish are shown in Figure 5.14 for *E. Coli*, Figure 5.15 for *Bacillus*, and Figure 5.16 for *Aspergillus Flavus*. Results were compared using a *t*-test at a 5% significance level, all compared to the 180 s no plasma trial. No significant differences were noted for the laboratory FE-DBD jet with *E. Coli* or *Bacillus* compared to the control, suggesting that the laboratory FE-DBD jet is not effective at inactivating the bacteria, except for the 90 s treatment of *Bacillus* which was statistically significant ($p = 0.0286$). It is assumed this single case is due to a small variance from the small sample size, especially since neither shorter nor longer treatments were statistically significant. The 30 s and 90 s treatments of *Aspergillus Flavus* with the laboratory FE-DBD jet were both significant ($p = 0.0466$ and $p = 0.0260$, respectively). All of the *E. Coli* trials with the Bovie were significant ($p = 0.0044$, $p = 0.0061$, and $p = 0.0030$ for the 30 s, 90 s, and 180 s trials, respectively). The 30 s and 180 s trials of *Bacillus* ($p = 0.0293$ and $p = 0.0201$, respectively) were significant, and the 30 s treatment of *Aspergillus Flavus* was significant ($p = 0.0446$).

These results suggest that the Bovie is more effective at inactivating *E. Coli* than the laboratory FE-DBD jet. In particular, a much larger area in the center of the plates is bacteria free for the Bovie jet. The 180 s case for the laboratory FE-DBD jet and the control both show a small area in the center without colonies, suggesting this is most likely due to drying out of the agar. Neither jet was successful in inactivating *Bacillus*, where all trials were higher than the control. Both jets had moderate effectiveness against *Aspergillus Flavus*, although the fungus did not appear to thrive in any situation, experiencing the majority dying off in all cases. The laboratory FE-DBD jet actually shows a larger area in the middle of the plate that does not have any fungal growth. This is particularly pronounced at lower treatment times. This could be due to aqueous species being generated in the agar that are responsible for the anti-fungal effect, while longer times dry out the agar permitting growth of the fungus over the 1 day incubation. The Bovie shows only a small area of no fungal growth, suggesting it did not create as many aqueous anti-fungal species.

However, this is only a preliminary test and much more needs to be done. For example, better controls need to be conducted, rather than a single control at 180 s treatment time. A larger treat-

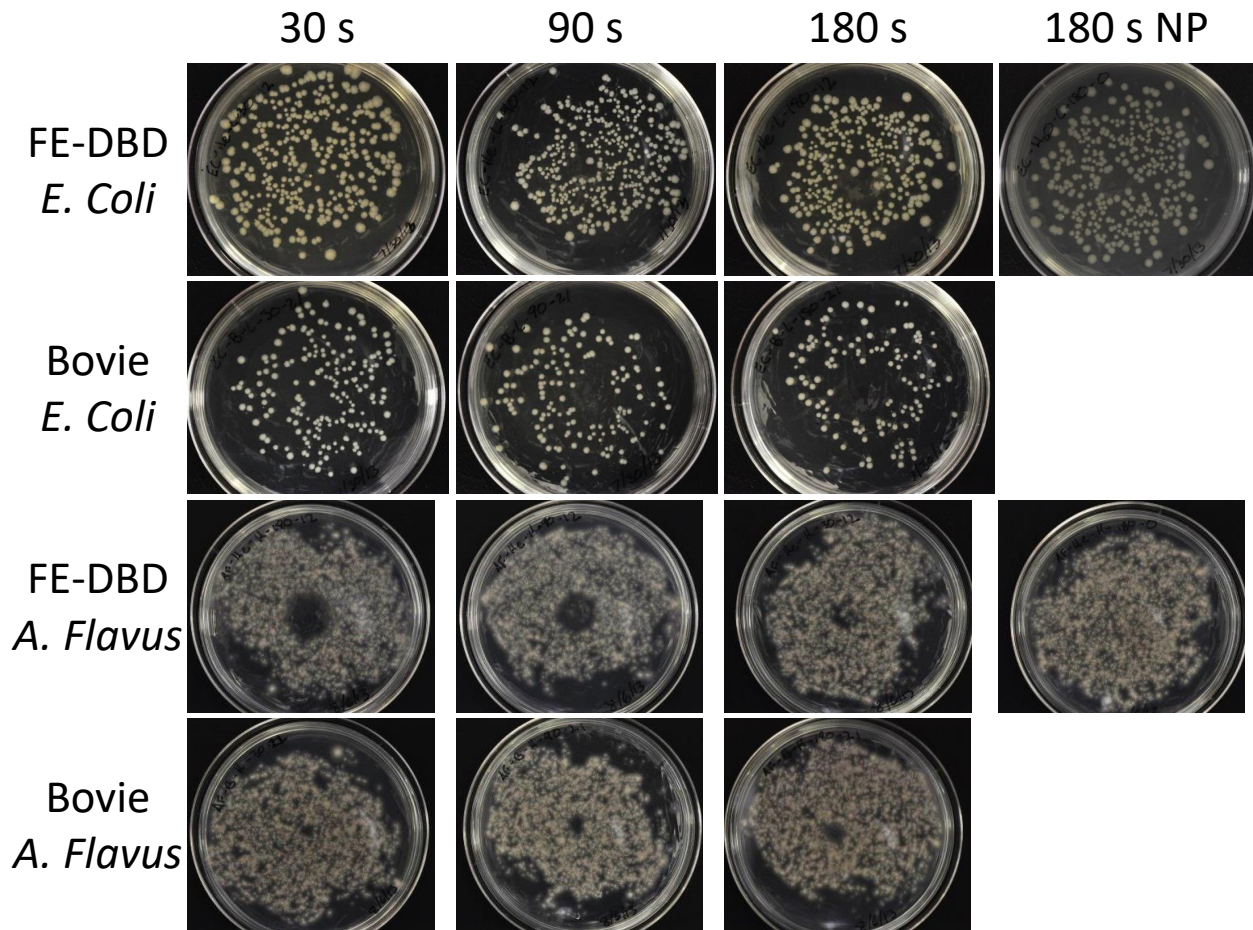


Figure 5.13: Plates After 1 Day Incubation of *E. Coli* and *Aspergillus Flavus* for Both FE-DBD Jet and Bovie Jet for 30 s, 90 s, 180 s Trials and 180 s No Plasma Control Condition

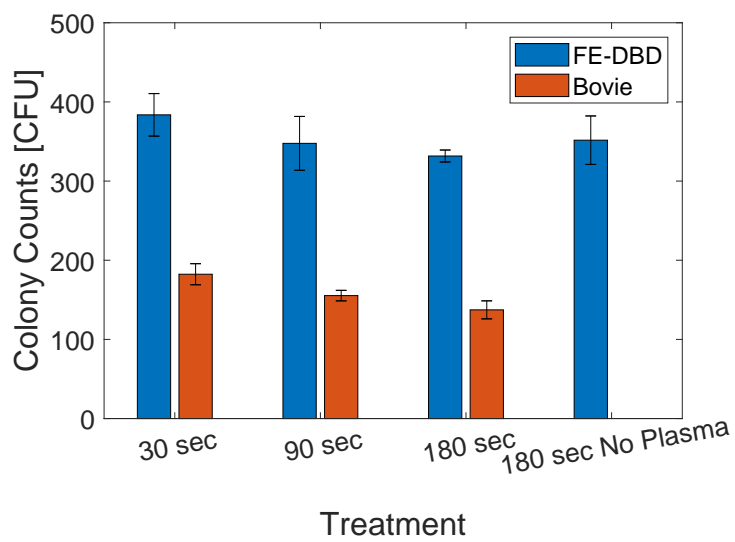


Figure 5.14: Number of *E. Coli* Colonies Counted After Various Plasma Treatments

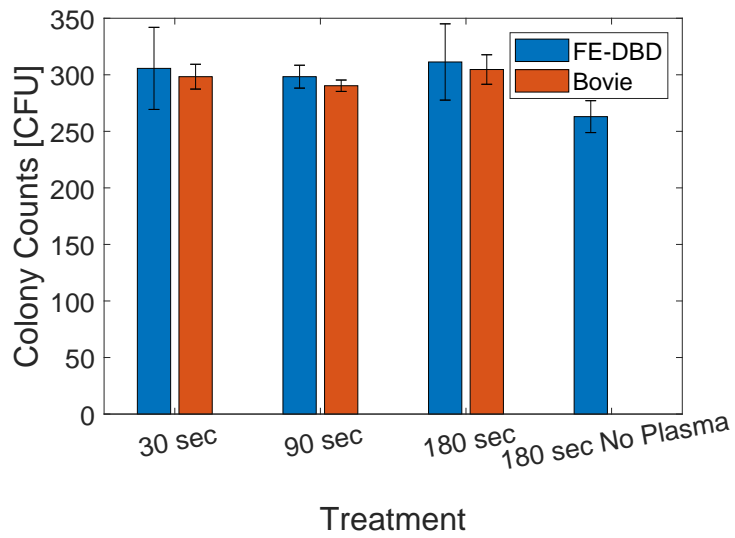


Figure 5.15: Number of *Bacillus* Colonies Counted After Various Plasma Treatments

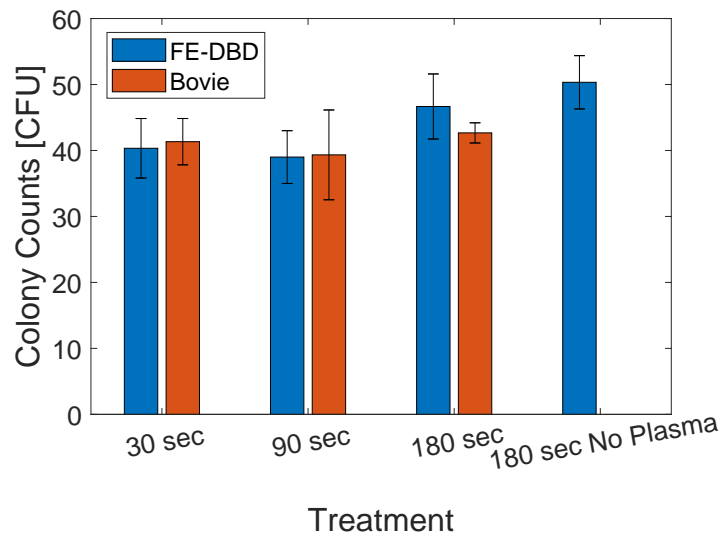


Figure 5.16: Number of *Aspergillus Flavus* Colonies Counted After Various Plasma Treatments

ment area should also be used, rather than treating the center of the petri dish. This could be done by using smaller petri dishes or a longer treatment time with a moving plasma jet, such as is used in Chapter 6. Since not all images were properly documented, further analysis on investigating a subset of the petri dish area as a better representative of the treatment area could not be obtained with statistically relevant results. Various incubation times could also be used, as well as treating samples that have already been partially incubated to better simulate wound treatments as well.

5.6 Chapter Summary & Future Work

In this chapter an existing FDA cleared electrosurgical device has been modified to create a low temperature plasma jet. The device is compared to an existing laboratory plasma system. Similar discharge modes were noted for the two devices, each having a diffuse mode and a concentrated mode. The generated species were noted to be spectographically similar, though differences were noted in their relative intensities. The diffuse modes had comparable temperatures near ambient for the rotational temperature, while the concentrated mode for the Bovie power supply was substantially hotter than the laboratory power supply. Inactivation of *E. Coli* was noted for the Bovie power supply, but further results are needed to show significant reduction of bacterial load to warrant further development of this as a device.

When first approached, it was desired to find a fast approval method for a low temperature plasma jet through the FDA. Though using an existing FDA cleared device may alleviate some concerns about the safety of the device, this does nothing to prove the efficacy of the device using a new intended use. As such, this is not likely to affect the speed of approval for such a device, since the intended use is a major driving factor for the approval of a device through the FDA. In addition, changes to the power supply may increase the efficacy, while not greatly affecting the safety of the device, thus changes to the device may be warranted. Nevertheless, this is a prime example of a medical system that could use the De Novo pathway for moderate approval speed (slower than a 510(k) but faster than a PMA).

Development on this specific design may not be carried forward, but the idea of using an electrosurgical generator for cold plasma treatment is now in the literature, including in clinical

trials in Europe. It is possible this may lead to further development of these devices in the US for cold plasma treatment.

6. DIRECT WRITE OF FILMS USING A DIELECTRIC BARRIER PLASMA JET

6.1 Introduction

A direct write plasma system is devised by replacing the printer head of a 3D printer with a floating-electrode dielectric barrier discharge jet. Various methods are employed to deposit the precursors, including vaporizing the precursor into the gas stream or spraying a liquid precursor into the plasma. Various materials can be deposited including metals (copper using copper (II) acetate and iron using ferrocene), polymers (a polymer from tris(2-methoxyethoxy)(vinyl)silane), and hydrocarbon compounds (using isopropyl alcohol). A variety of substrates are used ranging from conductive to dielectric and even to biological substrates, as the low temperature of the discharge allows patterning onto temperature-sensitive substrates. Factors affecting the deposition are explored, such as how higher concentrations of the precursor can be combined with faster motion to increase the deposition rate without overheating the substrate. The design constraints for fill pattern selection for the plasma printer are influenced by substrate heating, deposition area, and precursor consumption. Higher concentration of the precursor can be combined with faster motion and also higher discharge voltages and powers to increase the deposition rate without overheating the substrate. This is proposed as a method for a sprayable bandage or deposition of sensors directly onto skin or other tissue.

6.2 Project Background

The background is broken into three parts. The first section briefly discusses what direct writing is. Next, plasma enhanced chemical vapor deposition is discussed, which is the specific technique used here for direct writing of films. Finally, applications of this specific direct writing technique are examined, with emphasis given to two medically relevant applications.

6.2.1 Direct Writing

Direct writing, also known as maskless lithography, is a processing technique of laying down a patterned functional material onto a substrate. The thickness of the deposition can vary from

nanometers to millimeters in size. [273–275] As such, direct writing is typically differentiated from 3D printing by having a smaller length scale particularly in the height of the material being deposited, although there is overlap between the two techniques. Direct write techniques are generally classified under four main types based on how they deposit material: droplet, energy beam, flow, and tip. [275]

Droplet based techniques are often limited in resolution by the ink used; specifically the surface tension dictates the size of the droplets that form. [275] Aerosol direct write is one type of droplet technique that atomizes an ink which is then sprayed on to the substrate as an aerosol. The aerosol can be a variety of materials from metals, dielectrics, or even biological materials. [273] Energy beam techniques use a modified form of chemical vapor deposition, such as laser chemical vapor deposition and focused ion beam. These techniques cause the local excitation of a gas to create a chemical vapor that deposits onto the substrate. [273] The main downside of these techniques is that the substrate must be vacuum compatible. Flow techniques use a continuous flow of material rather than a series of droplets. An example of this is fused filament fabrication (FFF), a type of 3D printing, which will be discussed further in Chapter 7. Dip techniques use extremely fine tips, such as those used for atomic force microscopy, to deposit a small amount of ink. [276] As such, they are able to achieve extremely fine feature sizes on the order of 10 nm. [275]

However, there are other types that are difficult to classify into those four main groupings. For example, a glow discharge can be used to sputter a small diameter source electrode, which can then be moved over a conducting surface leaving a pattern of the sputtered material. [277,278] This system could also be implemented as a jet, spraying the sputtered material onto the substrate. [279]

Direct write techniques are used to fabricate sensors, such as thermocouples or strain gages directly onto a substrate. [273] They can also print a wide array of antennas for various sensors. Particularly, the energy beam techniques have shown great promise in the semiconductor industry leading to patterning off of the chip. [280]

6.2.2 Ambient Plasma Enhanced Chemical Vapor Deposition

Plasma enhanced chemical vapor deposition (PECVD) is a process that transforms a gas to a solid surface coating by use of a plasma process, using electrical energy rather than thermal energy to initiate the chemical processes. [281] Though historically a low pressure process, there has been a trend to increase the processing pressure of PECVD up to ambient conditions. Though this has the added benefits of being able to treat pressure sensitive substrates, such as biological substrates, and higher deposition rates due to higher concentrations of the reactive agents, high pressure PECVD suffers from gas contamination, higher power requirements, arcing risks, and difficulties in treating large areas. [282] A variety of plasma sources can be used, from DBDs to various plasma jets (microwave, RF, DBD, etc.) or even corona discharges. [281]

A variety of printed materials are also possible using an atmospheric pressure plasma system, with many available from earlier research on low pressure PECVD. These include hydrocarbons (using acetylene [283,284]), silicon (using silane [285]), silicon carbon nitride (using tetramethyldisilazane, hexamethyldisilazane, and triethylsilane [286]), silicon dioxide (using hexamethyldisiloxane [60,61,284]), and titanium oxide (using titanium tetrachloride [287], titanium isopropoxide [288], or titanium tetraisopropoxide [289]). These examples show that a variety of precursors can also be used to create the same film material. The precursor also does not need to be a complex compound from PECVD. For example, metal nanoparticles (cupric oxide nanoparticles [290]) or nanowires (silver nanowires [291]) can also be used. The substrate can also be coated in a metal-containing solution and selective areas can be plasma treated. [292]

Our lab has also previously shown polymeric and metallic (copper) deposition using a floating electrode dielectric barrier discharge (FE-DBD) jet (polymethyl methacrylate using the liquid monomer [30,31], and copper(II) acetylacetonate [14,31]). This system has also been shown to operate on temperature-sensitive biological substrates, such as onion skin, agar, and fingernails. [14,30,31]

6.2.3 Applications of PECVD

PECVD has a wide range of applications, since there are a wide range of possible coatings that it can create. These include optical coatings (e.g. anti-reflective coatings), wear and corrosion resistant coatings (e.g. diamond-like carbon), electrical insulation (e.g. SiO₂) and material synthesis (e.g. carbon nanotubes). [59, 293, 294] Two specific applications with direct medical relevance are sprayable bandages and epidermal electronics.

6.2.3.1 Sprayable Bandages

Paint-on liquid bandages (see Figure 6.1 for a schematic) are already FDA approved, [295] but sprayable bandages are not included per se. They are however approved for veterinary use. [296, 297] They are being considered in cases where a typical bandage is insufficient, mainly due to pain in the wound that would be exacerbated by current bandages and topical creams as well as cases where cross contamination could occur. [298] They are also combined with a drug for wound healing [299] or antimicrobial properties to prevent infection. [300, 301] The most commonly investigated materials for sprayable bandages are silane/siloxane polymers, cyanoacrylates, and hydrogels. [302]

6.2.3.2 Epidermal Electronics

A new field is growing of placing electronics directly onto skin for end use applications (see Figure 6.1). These epidermal electronics have mostly stemmed from work done by Rogers [303, 304] and Bao [305]. Kim, et al. [303] showed that fairly complex circuitry (antennas, LEDs, transistors, and a variety of other sensors) could be applied in a small package that can be applied directly to skin and even deform with the skin. This allows a variety of useful sensors to have access to the changing conditions of the epidermis. [304] Wang, et al. [305] has scaled this up to 347 transistors/cm². Small amounts of computational ability have even been demonstrated in some of these electronic systems. [306] Complex sensors can be made and integrated into small wearable devices (such as “smart” watches) that can give feedback during daily activities on a variety of systems, such as glucose, body temperature, and sweat. [307] Small tactile sensors can

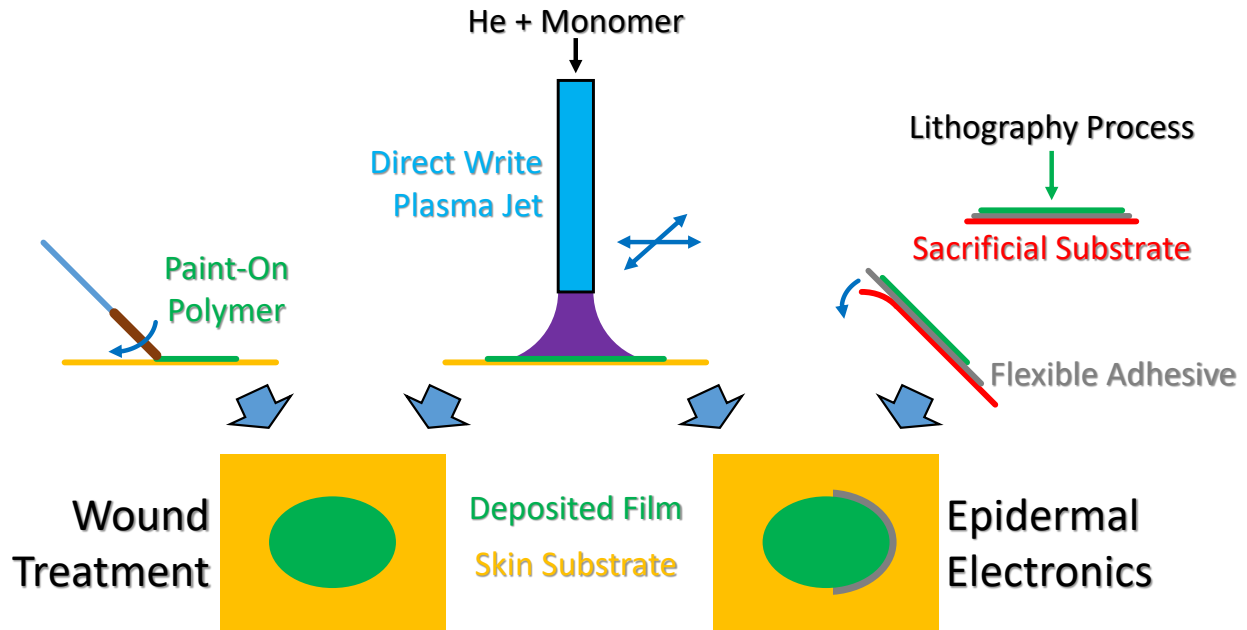


Figure 6.1: Schematic of Both Sprayable (Paint-On) Bandages and Epidermal Electronics Showing Conventional Systems and a Direct Write Plasma Jet System

also be created to measure a person's pulse or the amount of pressure applied to a surface. [308]

Often these circuits are not printed directly onto the biological tissue but are printed onto a surrogate material that is adhered to the skin or are transferred onto the skin, such as by hydrographic transfer. [309] Ink based solutions have also been used, where conductive ink can be drawn directly on a variety of surfaces to create sensors. [310] However care has to be taken that the substrate does not move, or at least have its movement tracked during the writing process for live patients, to ensure the pattern is properly printed. [311] The properties of these inks also become important, as they need to dry quickly (ideally within seconds) while still maintaining good conductivity through large bending, all the while ensuring biocompatibility of the ink materials. [312] These inks have been based on liquid metals such as gallium [312] or based on silver particles (nanowires [313] or small flakes [311]) in an alcohol solution.

6.3 Device Life-Cycle Overview

For development, a specific indication needs to be decided upon. The sprayable bandage may not be a viable option due to a number of cheap alternatives operating in that space; however, a niche in the field of sprayable bandages could be found leading to investors willing to support this device's development. In particular, if a drug is going to be included in the spray, extensive testing will be needed to ensure the plasma does not break it down.

The epidermal electronics application runs into the issue of other devices such as those out of Rogers' group using a less invasive method to create their electronics. They deposit the metal onto a flexible substrate which is then applied to the body as a sticker or removable tattoo, with fewer issues of biocompatibility concerns. As such, investors would be hard to attract to this method of electronics implementation. However, this method could fill a niche of connecting other electronic connections to the body, whether on the skin or inside of the body, such as for pacemaker leads. This requires extensive testing for biocompatibility as well as long-term operability.

6.3.1 FDA Approach

The two expected applications of sprayable bandages and epidermal electronics have different intended uses, requiring different considerations for approval pathways. The sprayable bandage is designed for wound care and could be paired with a drug that would help with pain, improve healing, etc., which would then require a combination drug and device application. This would warrant substantial testing to show it is safe, ensuring there are no adverse changes in the drug due to the plasma. Unless there is a similar predicate device, this would most likely require a De Novo request.

Without an additional drug, this system would most likely be similar enough to other existing bandage systems, in which case a 510(k) clearance would be viable. This becomes more difficult, however, particularly from a marketing standpoint, since there are similar devices under a Class I approval as liquid bandages. [295] This could even apply to some that are closer toward an aerosol. [314] A substantial improvement over the current state-of-the-art systems would be

needed to warrant the added complexity and cost of the plasma system. As such, some further benefit would need to be identified or utilized for successful marketing of this system (such as the addition of a drug). An example of this is a spray on system for burn treatment, which required a PMA. [315] A PMA was used because this is used for severe burns in which skin cells of the patient are sprayed on, thus requiring skin grafts from other areas on the body. A CAP system for depositing a bandage would most likely be deemed as a lower risk and could use a De Novo request pathway.

Epidermal electronics pose some unique challenges. If they are using antenna, then the devices need to ensure they do not have any Federal Communications Commission (FCC) regulations they also have to follow and are not emitting any hazardous radiation, which is under the FDA's purview. The biocompatibility of the materials needs to be considered; for example, a number of systems in the literature used silver, [311, 313] thus argyria (silver poisoning) needs to be avoided. Nevertheless, these hurdles can be overcome as shown in the pilot clinical studies for monitoring neonatal patients. [304] A system like this could choose any of the main pathways depending upon the exact intended use. A 510(k) pathway would be viable for printing a simple circuit on the body, such as a strain gauge to monitor the heart rate, as this would have a clear predicate device in other heart rate monitors. A De Novo request may be required for more complex circuitry and monitoring, unless there is a clear predicate device. There is also the possibility of using a system not just on the epidermis but for printing leads inside of the body. These could be used as a part of a pacemaker or some other electronic system, which would necessitate fairly stringent testing and lifetime requirements. The FDA has already established some performance standards for electrode lead wires that would need to be followed. [316] Any deposition inside the body would almost certainly require a PMA due to the high levels of risk.

6.3.2 Device Outlook

This particular design is merely a proof of concept, requiring extensive development for a particular indication. The particular indication will most likely be a niche market, since other systems are treating the proposed indications (bandages requiring a spray covering and epidermal

electronics) at a much lower cost than this device could attain. Nevertheless, this system does show a number of useful developments. This uses a floating electrode system, showing that deposition is possible without using a second ground electrode. The dielectric barrier also helps avoid the risk of large currents to the patient. Lastly, the variety of films possible show that as a single system a number of possible treatments are possible. A unique combination of conductive, dielectric, or other types of depositions may yield novel uses that cannot be obtained individually.

6.4 Experimental Setup

The physical setup of the system showing the various deposition methods is first introduced. Following that, the changes required to the 3D printer patterning is discussed. As the need for these changes was noted during the course of testing, many of the depositions reported later do not have all of the changes implemented into them, resulting in less than ideal films.

6.4.1 Physical Experimental Setup

The experimental setup consists of a 3D printer (3DStuffMaker Evolution Gen 1) that has had the heater and extruder removed from the printer head and an FE-DBD jet is mounted in their place (Figure 6.2). The z-axis has been disabled to avoid undesired changing of the jet length. The FE-DBD jet consists of an alumina tube with a high voltage copper electrode surrounding it. Helium is used as the working gas (flow rate controlled by a rotameter). Sufficient high voltage insulation is required to avoid discharging between the high voltage electrode and the printer chassis; in this case a custom acrylic mount was made to hold the alumina tube and provide electrical insulation. A high voltage AC source is used to excite the plasma (see Section 3.2.1.2 for power supply information). The power supply frequency is tuned for each condition to achieve the most stable discharge. The sample (usually either a silicon wafer or pig skin) is placed on the stage of the 3D printer under the DBD jet. This entire system is enclosed in a ventilation chamber (the framing of this chamber can be seen in the edge of Figure 6.2) with a removable side for access to the system.

Three different methods are employed to deposit the precursor into the plasma, as shown in the green boxes on the schematic in Figure 6.3. Solid precursors (copper (II) acetylacetonate,

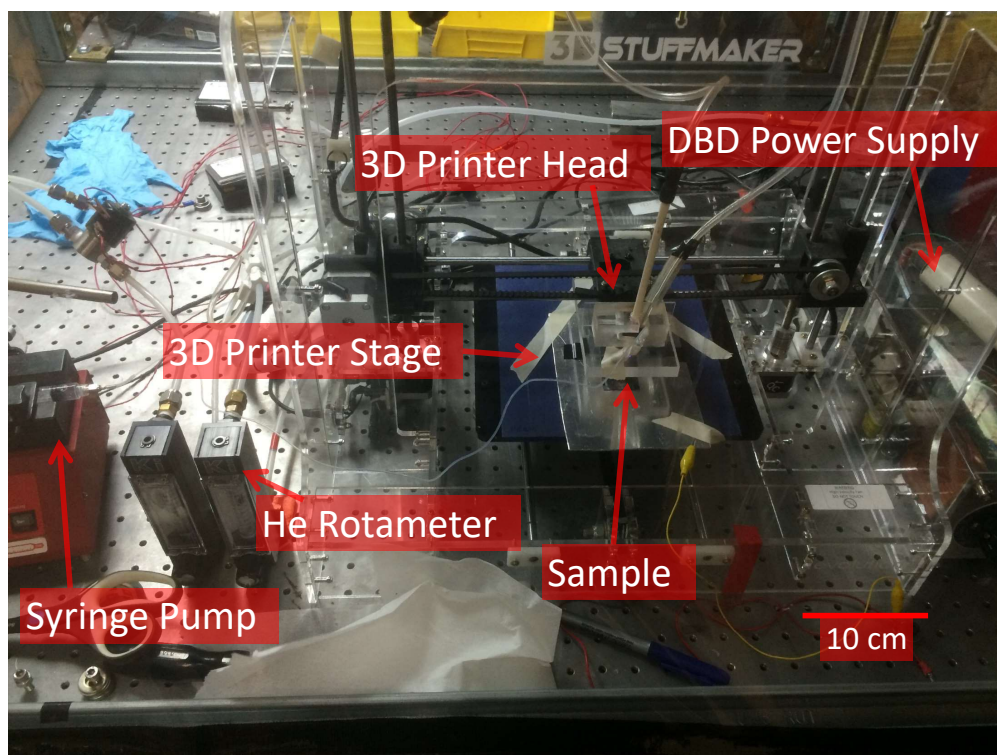


Figure 6.2: Image of the Direct Write DBD Jet Setup

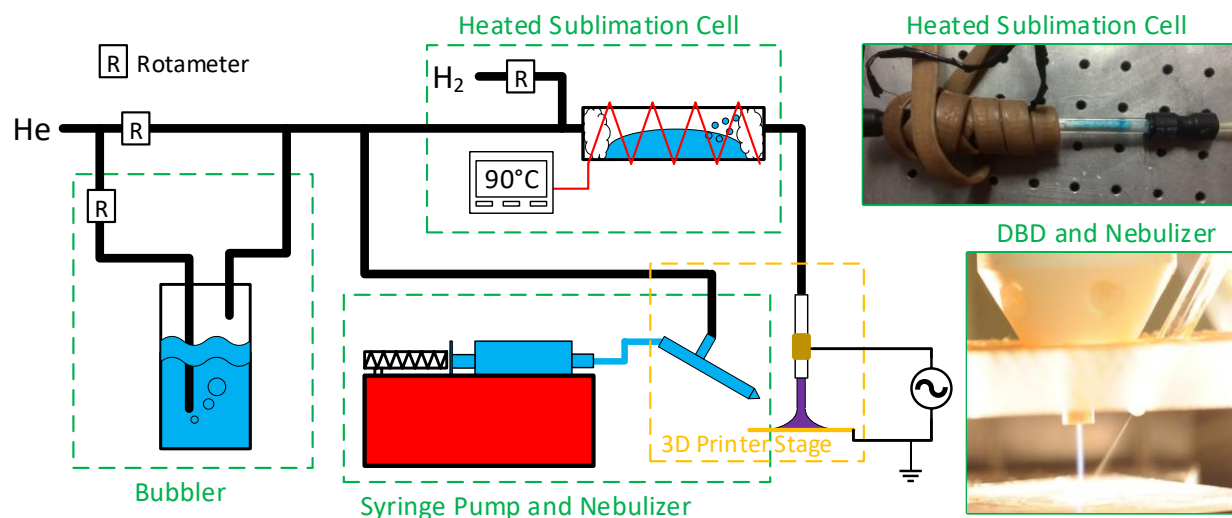


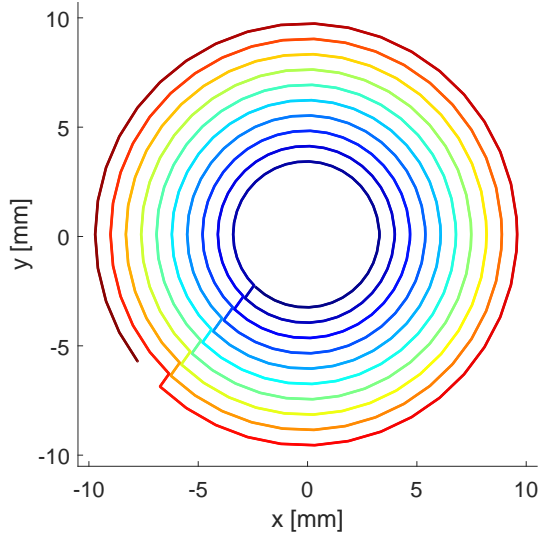
Figure 6.3: Schematic of the Direct Write Setup Showing the Heated Sublimation Cell for Solid Precursors and the Nebulizer and Syringe Pump for Liquid Precursors with Inset Images of the Heated Sublimation Cell Partially Unwrapped from the Heating Tape and the Nebulizer Spraying into the DBD Jet

referred to as CuAcac, and ferrocene) are sublimed into the gas stream. This requires heating of the precursor for a sufficient concentration to be vaporized. A small amount of hydrogen gas is mixed into the gas stream to etch away the ligands on the metal; without the hydrogen no material is deposited. High vapor pressure precursors are placed in a bubbler through which a controlled amount of helium is bubbled. This is used for initial testing with isopropyl alcohol (IPA) to determine the patterning requirements needed for the 3D printer (see Section 6.4.2) and for the methyl methacrylate (MMA) testing in Section 6.6.1. The low vapor pressure liquid precursor (tris(2-methoxyethoxy)(vinyl)silane, referred to as TMEVS, or ethylene glycol dimethacrylate) is sprayed by a nebulizer into the plasma region on the substrate. Each deposition method affects the voltage-current characteristics of the discharge, especially due to the presence of precursors in the gas stream.

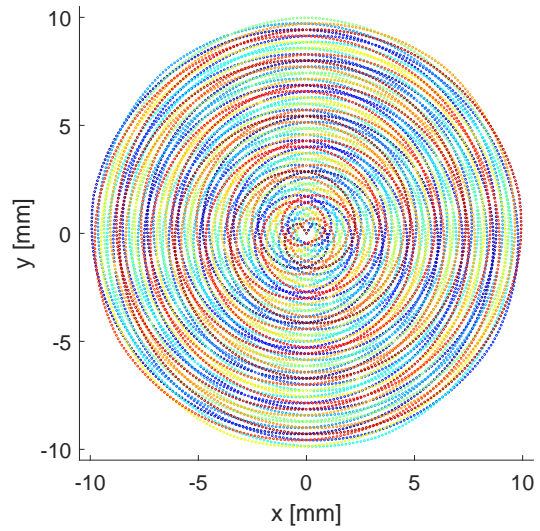
6.4.2 3D Printing Pattern Considerations

Thicker edges with little infill are commonly used for 3D printing, but are not desired for direct write applications, thus necessitating a custom GCode pattern, rather than a pattern generated by conventional 3D printer software, that achieves uniform coverage for the DBD jet (Figure 6.4). For a circular deposition a spiral pattern was chosen that provides much more uniform coverage (approximately equal area treatment) compared to the conventional 3D printing pattern. The Mat-Lab code used to generate this pattern and control the 3D printer are in Appendix B. This spiral pattern also ensures the film is deposited fairly uniformly, rather than one side receiving substantial deposition before another side, which could create edge effects from the plasma discharge. This non-uniformity in film thickness is noted in the hydrocarbon film in Figure 6.5. This was printed using the built-in slicer software (Slic3r) to generate the GCode, rather than a custom GCode, as evident in the thicker depositions for the outline and centerline. Normally these thicker areas would be needed for structural support in an additively manufactured part. For this print, a helium flow of 6.9 SLPM was used with an additional 0.7 SLPM helium flow through the isopropyl alcohol (IPA) filled bubbler.

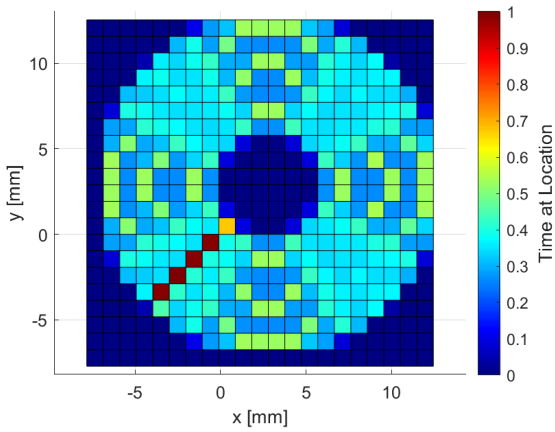
Other considerations that can affect the printing pattern are the treatment area of the plasma



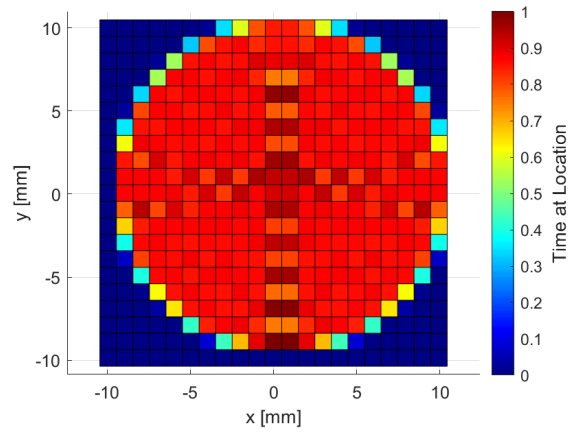
(a) Conventional 3D Printer Path



(b) Custom Spiral Path



(c) Conventional Pattern Area Coverage



(d) Spiral Pattern Area Coverage

Figure 6.4: Comparison of Printer Paths and Their Time Per Unit Area Coverage over a Discretized Grid

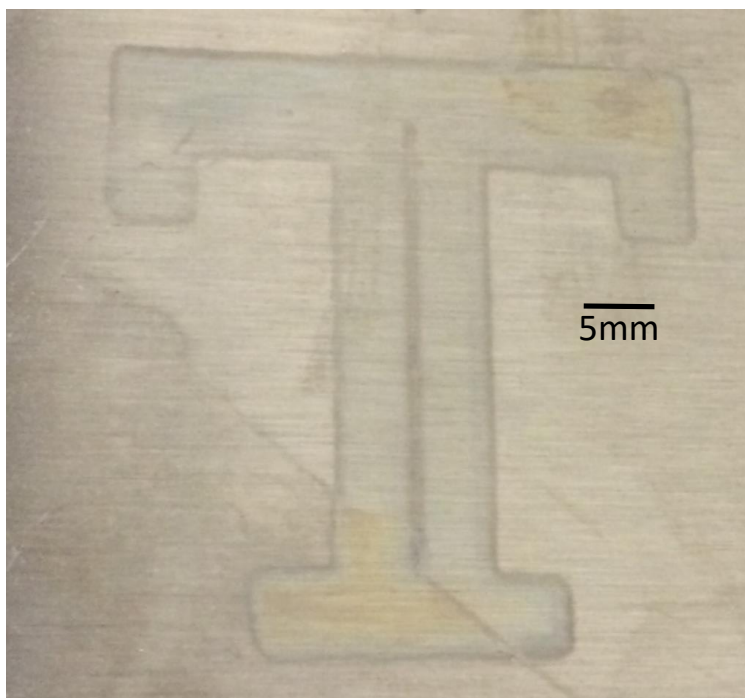


Figure 6.5: Image of Hydrocarbon Deposition Using IPA Without Controlling for Equal Area Treatment Yielding a Thicker Outline, Thin Infill, and Thick Centerline

jet, the speed of the printer head (residence time), and the temperature of the discharge. These may not be independent of each other. For example, if a dielectric material is being deposited onto a conductive substrate, the plasma will preferentially move to areas with a thinner coverage, possibly leading to hot spots developing in the discharge region which will affect the deposition. This appears to be the case in Figure 6.6, where a much thicker hydrocarbon deposition is used (325 passes compared to 4 passes in Figure 6.5). Black spots are noted in the film, most likely due to hot spots forming and changing the nature of the deposited film, producing more of a charred deposition; however this film has not been properly characterized to determine a difference between the brown and black areas. These hot spots can be mitigated by reducing the residence time of the plasma to avoid a thick layer being deposited, but then more passes of the jet will be required for a specified film thickness. This was one goal of using a spiral pattern (Figure 6.4b), so that no area builds up faster than any other. This becomes more complex to determine an optimal path for other geometries, since the deposition rate from the plasma must also be accounted for.

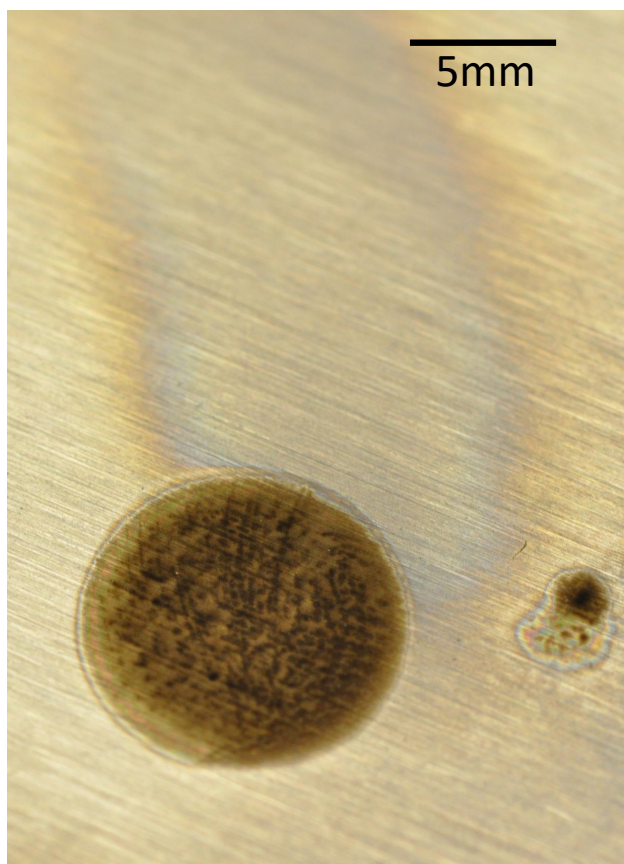


Figure 6.6: Image of Hydrocarbon Deposition using IPA of an Equal Area Treatment with Black Spots from Hot Spots in the Plasma Discharge and Plume Deposition

Also of note in Figure 6.6 is the large plume noted extending away from the discharge area. This plume is coming from a small flux of radicals leaving the plasma and depositing onto the substrate in undesired locations due to a small ambient air current during the deposition process. Better ambient air flow control could mitigate this issue.

Faster printing head speeds also effect the deposited film, which complicates the ability to move faster so less material is deposited per pass as a method to reduce hot spot formation. As noted in Figure 6.7 for a micro-DBD jet (created by pulling glass to achieve a smaller diameter tube), the speed of the printer head changed the width of the deposited film. This seems counterintuitive that a faster print would produce a wider deposition; however the height of this deposition is not measured, thus this does not necessarily correlate with the amount of material deposited. This

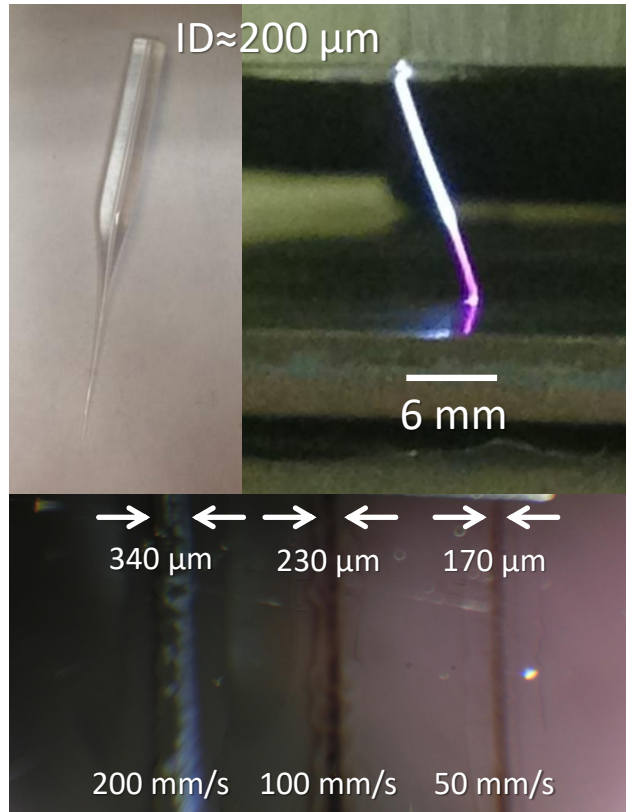


Figure 6.7: Images of Hydrocarbon Deposition Using a Micro-DBD Jet for Small Feature Sizes Varying with the Printer Head Speed

hydrocarbon deposition is likely conductive, thus a taller deposition may grow more rapidly than the area around it as it becomes closer to the plasma discharge. This also shows that smaller features can be created simply by changing the speed of the printer head. Further optimization is required to determine the smallest feature size that can be printed using this method.

6.5 Metal Film Results

Significant work has already been done previously on copper deposition. [14, 15] This includes characterizing the voltage and current traces of the DBD jet during operation [29] as well as characterizing the copper film. [14] The copper film was determined by X-ray photoelectron spectroscopy (XPS) to be >60% copper for a long distance away from the jet and >80% copper near the center of the deposition. The film's resistivity is between that of bulk copper and bulk iron. Though not directly measured, good adhesion of the films onto the substrate was noted, such that bending of

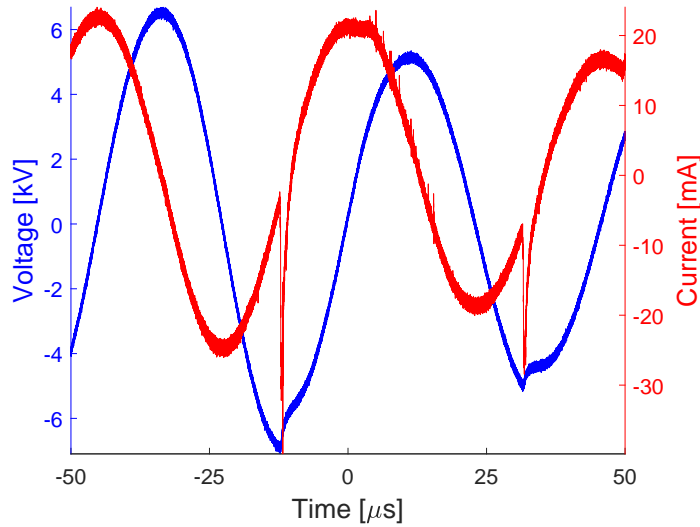


Figure 6.8: Voltage and Current Traces for the Copper (II) Acetylacetonate Deposition

material did not cause any visible film delamination. As such, this work seeks to extend it to a direct-write system.

Metal is deposited using the heated sublimation cell. A 1.85 SLPM helium gas flow mixed with 0.09 SLPM H_2 is flowed through the sublimation cell kept at $90^\circ C$ for the copper deposition (using copper (II) acetylacetonate, referred to as CuAcac), while a mixture of 2 SLPM helium and 0.09 SLPM H_2 with 9.9 SLPM N_2 as a shielding gas is used for the iron deposition (using ferrocene). The small admixture of hydrogen is necessary to create the film via hydrogen reduction of the compound. [317, 318] The majority of the experimental work in this section was done by Brittany Spivey under supervision of the author.

The voltage and current traces are shown in Figure 6.8. The voltage trace is a distorted sine wave, which is expected given the large current draw exceeding the power supply's power output. The current trace shows large spikes every half cycle, which is consistent with previous measurements. [15] There is a single large ionization wave per cycle, with possible smaller ones after a large one on the other half cycle. These are not noted on the first half cycle, suggesting they are only occurring due to a substantial amount of preionization. There is also a decrease in the voltage and current magnitude, suggesting that the average power is dropping from the power supply.

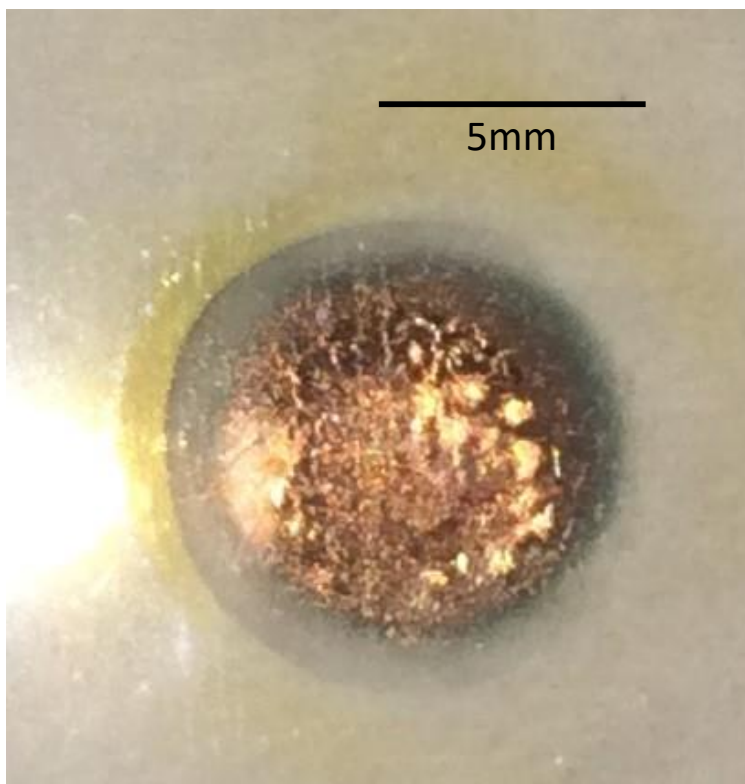


Figure 6.9: Image of Copper Direct Write Deposition onto Glass Creating a Copper Film

There could be a secondary duty cycle frequency, where an initial large ionization wave occurs with large subsequent ones every cycle and smaller ones every half cycle in between, but that the average power drops after a few cycles such that no discharge occurs, which then allows the average power to increase, precipitating another initial large ionization wave. This behavior is due to an unusual coupling between the power supply and the plasma, where the plasma is attempting to draw more power than the power supply can supply over a short time.

The copper deposition in Figure 6.9 is done with a tube-to-substrate length of 2.5 mm. The relatively slow rate of metal deposition is due to the small concentration of the metal in the plasma effluent. Increasing the compound's temperature to increase the rate of sublimation would yield faster deposition but would also increase the operating temperature of the jet. The various colors noted on the edges of the deposition in Figure 6.9 are due to variation in the percentage of copper in the deposition. [14, 15] Further exploration is necessary to determine if there is still good plasma

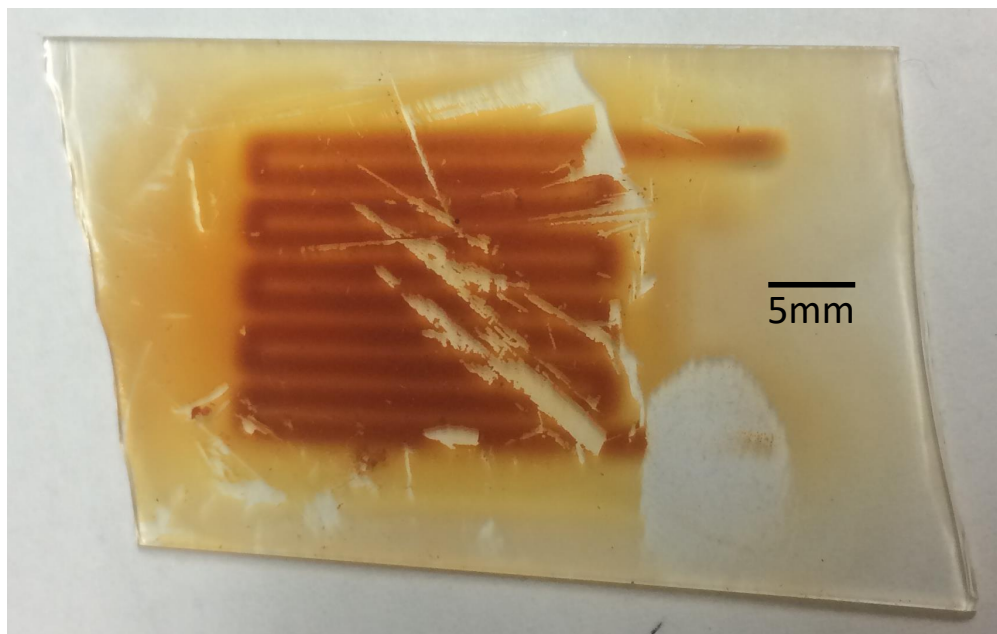


Figure 6.10: Image of Iron Oxide Direct Write Deposition onto Glass Using Ferrocene as the Precursor

stability at significantly higher concentrations of the organometallic compound along with metallic film deposition. Another way to increase the metal concentration to reduce printing time could also be to switch from using an organometallic compound to small metal particles. [290, 292]

An attempt is also made to deposit iron using ferrocene. The pattern in Figure 6.10 is created using a 16.7 mm/s raster with tube-to-substrate gap of 6.9 mm. However, despite trying a variety of conditions it appears that only iron oxide was deposited. This is most likely due to iron's greater affinity of producing oxides than copper, which naturally will form a passivation layer that protects the bulk copper, unlike iron which continually rusts.

6.6 Silane Film Results

This project intended to deposit thick ($\sim 1 \mu\text{m}$) films using a non-thermal plasma DBD jet as a sprayable bandage system. The goal is to optimize the discharge parameters for the thickest yet still uniform film as well as ensuring coverage over potentially non-uniform substrates. Fast deposition rates are also desired, with a goal to coat a 1 ft^2 area $1 \mu\text{m}$ thick within 10 minutes.

A variety of chemicals were initially tested using drying in air to determine the best chem-

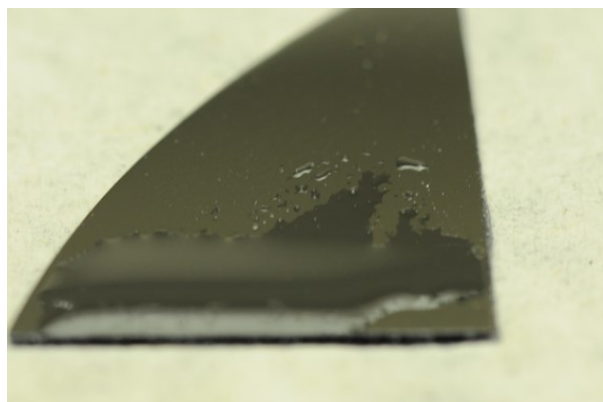
Table 6.1: Four Monomers Tested For Direct Write Film Deposition

Abbreviation	Chemical Name	Structure
TMEVS	Tris(2-methoxyethoxy)(vinyl)silane	
EGDMA	Ethylene Glycol Dimethacrylate	
VTMS	Vinyltrimethoxysilane	
MMA	Methyl Methacrylate	

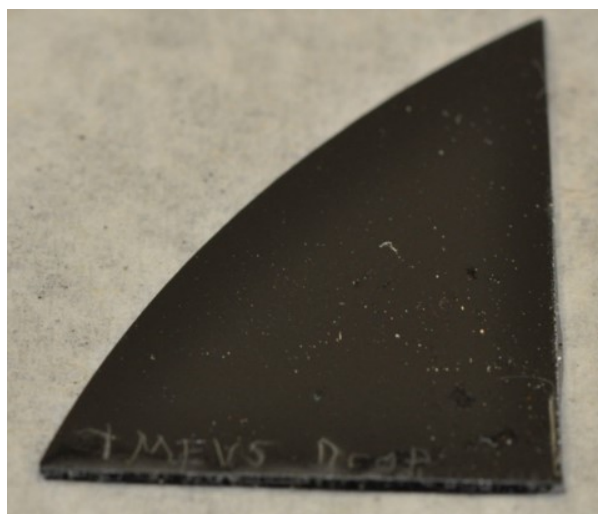
ical for a surrogate bandage. The most promising candidate, tris(2-methoxyethoxy)(vinyl)silane (TMEVS), was then carried forward into a small optimization study to determine the best conditions for film deposition. Later testing was then conducted on a biological substrate (pig skin) to determine if this could act as a bandage.

6.6.1 Initial Material Selection

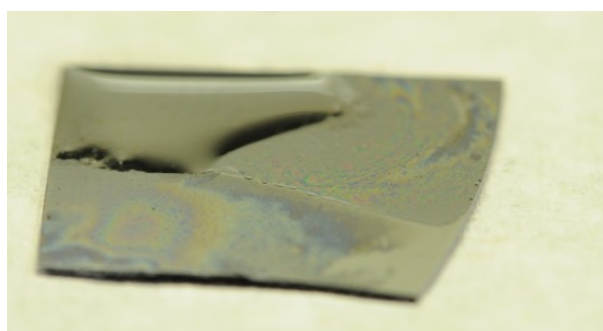
Four chemicals (as listed in Table 6.1) were tested for their volatility and film creation by exposure to ambient air and plasma treatment. These were selected due to their potential ability to create films and/or easy manufacturability for large-scale use. Overall, the best choice from this testing was TMEVS, which is carried forward in further testing.



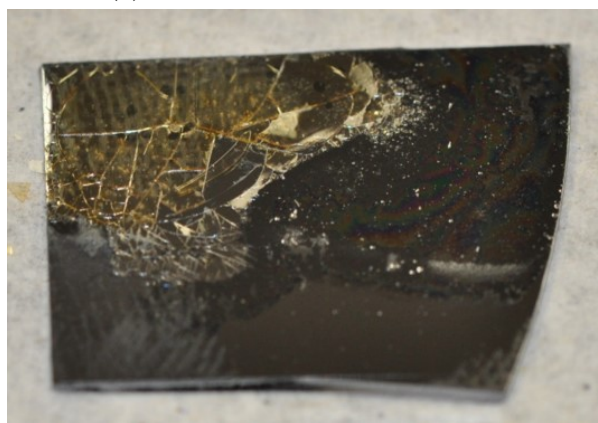
(a) Untreated and Air Dried



(b) Untreated and Heat Gun Dried



(c) Plasma Treated and Air Dried



(d) Plasma Treated and Heat Gun Dried

Figure 6.11: Images of Initial Droplet Tests Using TMEVS

6.6.1.1 TMEVS Initial Testing

Initial testing for tris(2-methoxyethoxy)(vinyl)silane (TMEVS) consisted of two tests, placing a droplet on a silicon wafer and allowing it to dry and placing a droplet on a silicon wafer, plasma treating it (5 min treatment, 40% low power, 1.04 SLPM He) to crosslink the monomers, and then allowing the film to dry to to remove the residual monomer. The droplet was left for 24 hrs and then dried using a heat gun to accelerate the drying process. This is seen in Figure 6.11. The untreated droplet appears to have mostly evaporated away due to the excess heat from the heat gun. The plasma treated droplet left behind a thin film; removing the excess monomer resulted in

a brittle film that easily cracked. Nonetheless, this shows that polymerization occurred as a result of the plasma treatment warranting further exploratory testing.

An initial nebulizer deposition was attempted using a 4 min treatment at 35% low power on the power supply with 13.4 SLPM He and a nebulizer flow rate of 50 $\mu\text{L}/\text{min}$ (10% TMEVS and 90% methanol solution, with 1.43 SLPM He through the nebulizer). Figure 6.12 shows the resulting deposition before and after being dried with a heat gun as well as two SEM images of the film (using the TESCON SEM, see Section 3.3.4 for more information). Overall the film appears fairly uniform, with some potential streaks in it due to the liquid flow being blown toward the outside of the deposition region by the helium jet flow.

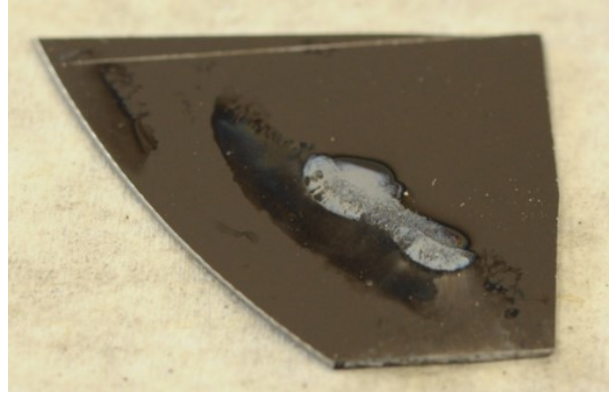
Further testing was conducted with the nebulizer using the 3D printer head in a circular pattern with the 10% TMEVS 90% methanol solution at a higher power (10 min treatment, 50% low power, 12.6 SLPM He, nebulizer at 10 $\mu\text{L}/\text{min}$ with 2.51 SLPM He). This yielded a black-specked deposition (Figure 6.13a), possibly from some hot spots developing in the plasma. However, at lower power (35% low power) a white-specked deposition was noted on a silicon substrate (Figure 6.13b). It is unclear if these are also hot spots in the discharge or possibly areas with a slightly higher film thickness.

Another test was conducted using a silicon wafer and masking half of the circle with a microscope slide to show the film thickness (Figure 6.14; 10 min treatment, 35% low power, 12.6 SLPM He, nebulizer run at 10 $\mu\text{L}/\text{min}$ of 10% TMEVS 90% methanol solution with 2.51 SLPM He). SEM images were taken of the film (Figure 6.15, using a JEOL JSM-7500F SEM, see Section 3.3.4 for more information on the SEM). Agglomerations were noted in the film, with larger agglomerations occurring near the masked edge of the film. It would appear that the plasma treatment creates small $\sim 1 \mu\text{m}$ “balls” of the polymer that can become aggregated where the plasma is more intense, such as by the mask.

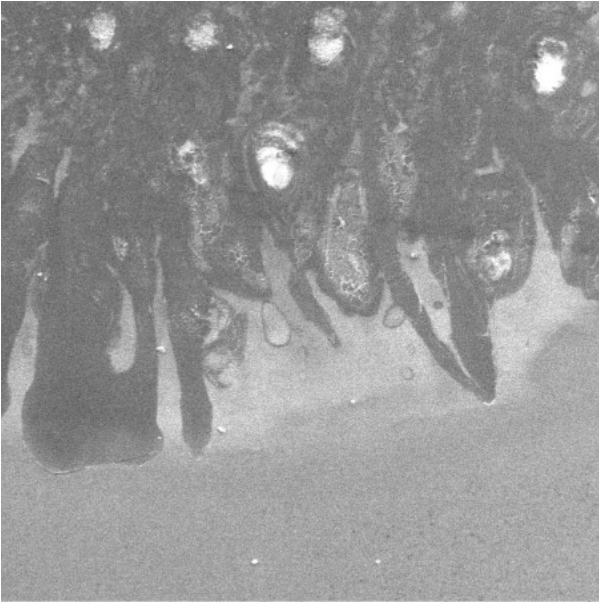
Depositions were attempted on various meshes to determine if the deposited film would be able to fill the gaps of the mesh. If so, this would serve as a better sprayable bandage as it would be less sensitive to the non-uniformity in the skin substrate. A nylon mesh was used initially



(a) Plasma Treated

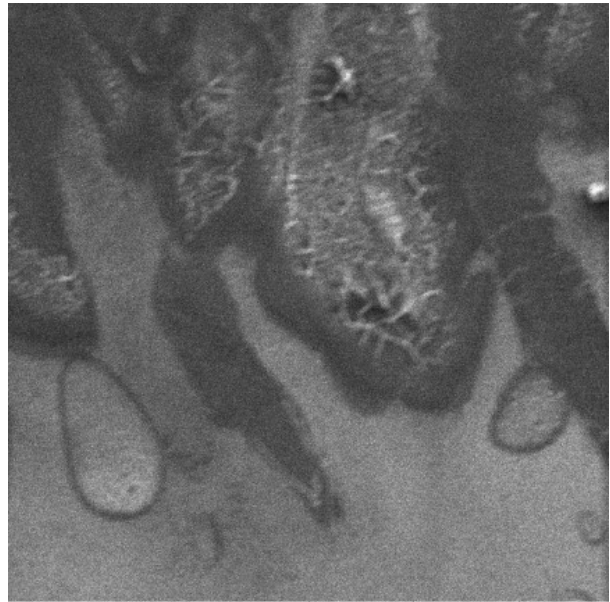


(b) Plasma Treated and Dried



HV: 5.00 kV WD: 25.6870 mm
View field: 2.08 mm DET: SE Detector
DATE: 05/13/14 guest 1 mm Vega ©Tescan
Digital Microscopy Imaging

(c) Wide View SEM Image



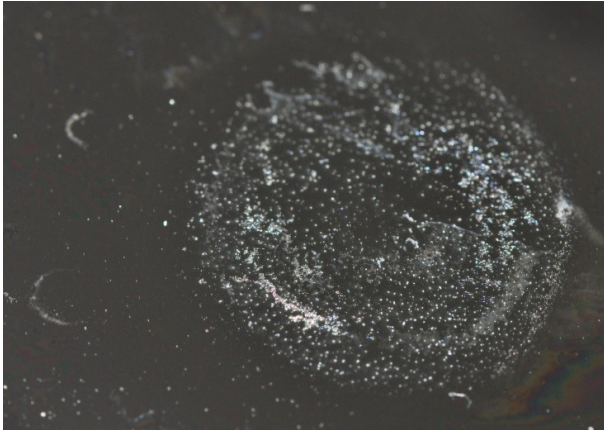
HV: 5.00 kV WD: 24.8800 mm
View field: 570.41 μm DET: SE Detector
DATE: 05/13/14 guest 200 μm Vega ©Tescan
Digital Microscopy Imaging

(d) Narrow View SEM Image

Figure 6.12: Optical Images and SEM Images for Initial TMEVS Nebulizer Tests

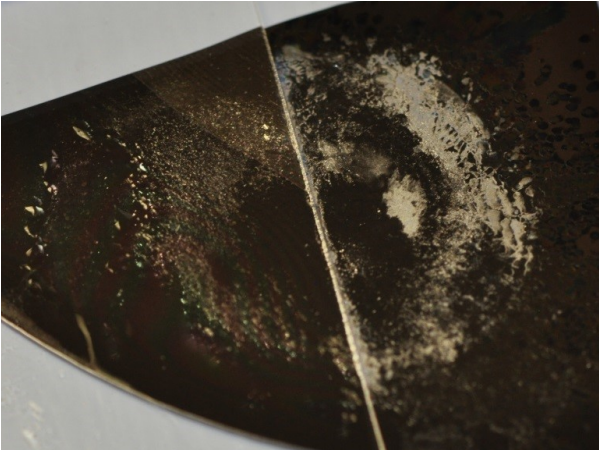


(a) Higher Powered Treatment on Stainless Steel Substrate with Black Specs

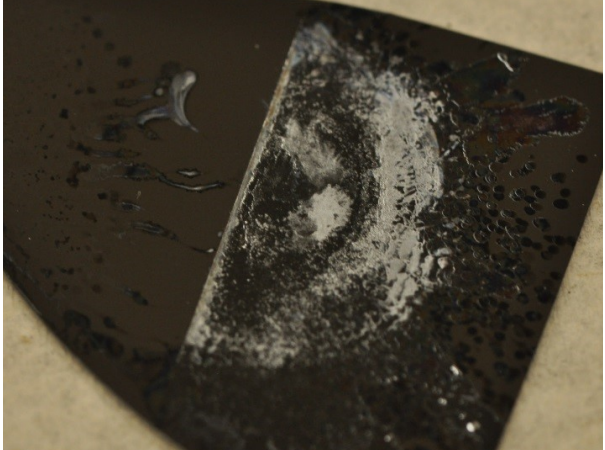


(b) Lower Powered Treatment on a Silicon Wafer with White Specs

Figure 6.13: Images of Further TMEVS Depositions on Various Substrates with Specs Appearing in the Deposited Film

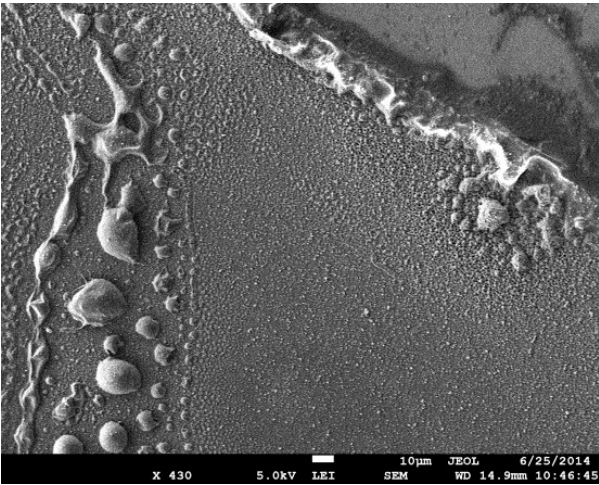


(a) Immediately Post Treatment

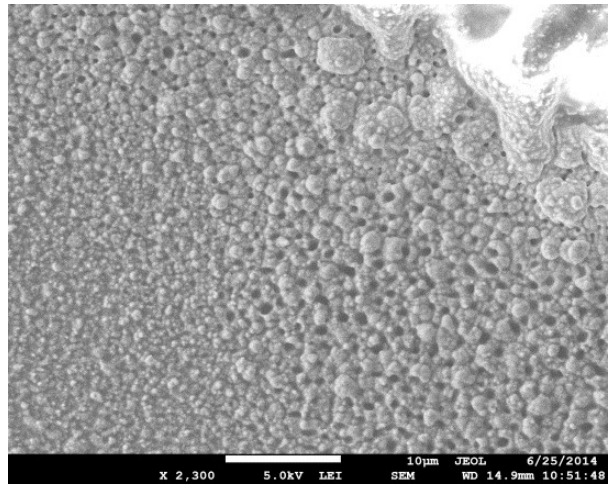


(b) After 3 Days to Dry

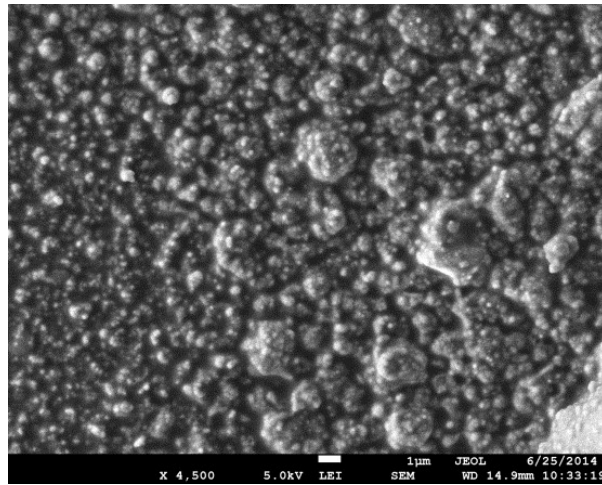
Figure 6.14: Optical Images of the Half-Masked TMEVS Deposition



(a) Wide View SEM Image



(b) Narrower View SEM Image



(c) Narrow View SEM Image

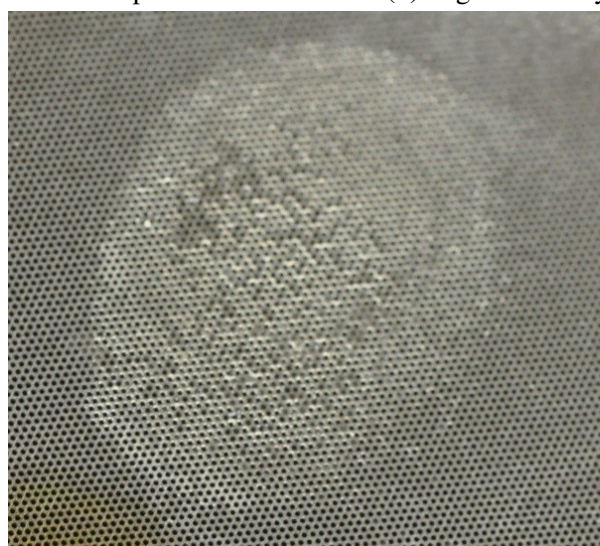
Figure 6.15: SEM Images of the Half-Masked TMEVS Deposition



(a) Low Power Nylon Mesh Deposition



(b) High Power Nylon Mesh Deposition



(c) High Power Metal Mesh Deposition

Figure 6.16: Images of TMEVS Depositions onto Various Meshes

showing some slight deposition (15 min treatment, 15% low power, 2.84 SLPM He, nebulizer run at 40 $\mu\text{L}/\text{min}$ with 10% TMEVS 90% methanol solution with 0.583 SLPM He), but mostly wetting of the nylon (Figure 6.16a). Higher powers usually caused melting of the nylon (Figure 6.16b; 15 min treatment, 20% low power, 2.84 SLPM He, nebulizer run at 30 $\mu\text{L}/\text{min}$ with 10% TMEVS 90% methanol solution with 0.724 SLPM He). Similar results with significant wetting were obtained for a stainless steel mesh (Figure 6.16c), but higher powers were able to be achieved (15 min treatment,

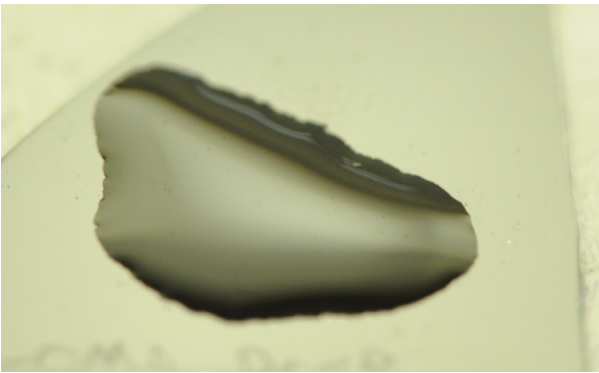
25% low power, 2.84 SLPM He, nebulizer run at 10 μ L/min with 10% TMEVS 90% methanol solution with 0.466 SLPM He). No cases were found where significant deposition occurred to begin closing the holes in the mesh, though.

6.6.1.2 EGDMA Initial Testing

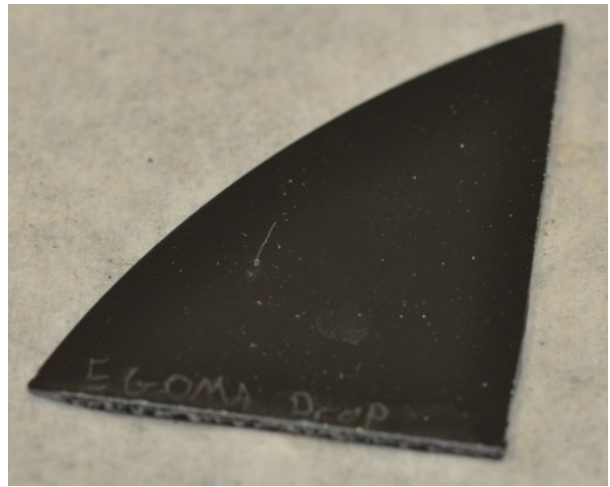
Like the TMEVS's testing, initial testing for ethylene glycol dimethacrylate (EGDMA) consisted of two tests, placing a droplet on a silicon wafer and allowing it to dry and placing a droplet on a silicon wafer, plasma treating it to crosslink the monomers (5 min treatment, 40% low power, 1.04 SLPM He), and then allowing the film to dry to remove the residual monomer. The droplet was left for 24 hrs and then dried using a heat gun to accelerate the drying process. This is seen in Figure 6.17. The untreated droplet appears to have mostly evaporated away due to the excess heat from the heat gun. The plasma treated droplet showed some possible polymerizing (i.e. white specks visible in the liquid) compared to simply letting the sample air dry. These became more evident with heat gun drying of the sample. SEM imaging was conducted on the plasma-treated film, showing the white specks appear to be larger structures compared to the bulk film (Figure 6.18, using the TESCON SEM, see Section 3.3.4 for more information on the SEM). Further testing on stainless steel (10 min treatment, 25% low power, 12.6 SLPM He, nebulizer run at 20 μ L/min with 10% EGDMA 90% methanol solution with 2.51 SLPM He) did not yield any significant visible deposition (see Figure 6.19a) even after drying with a heat gun so no further testing was conducted (see Figure 6.19b).

6.6.1.3 VTMS Initial Testing

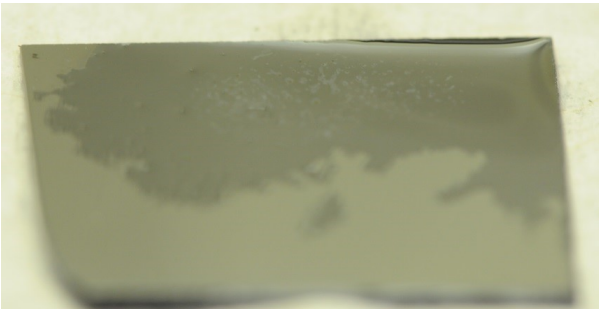
Like the TMEVS's testing, initial testing of vinyltrimethoxysilane (VTMS) consisted of two tests, placing a droplet on a silicon wafer and allowing it to dry and placing a droplet on a silicon wafer, plasma treating it to crosslink the monomers (5 min treatment, 40% low power, 1.04 SLPM He), and then allowing the film to dry to remove the residual monomer. The droplet was left for 24 hrs and then dried using a heat gun to accelerate the drying process; in this case, the heat gun was only used to briefly heat up the substrate to determine if a thin film may exist that would become



(a) Untreated and Air Dried



(b) Untreated and Heat Gun Dried

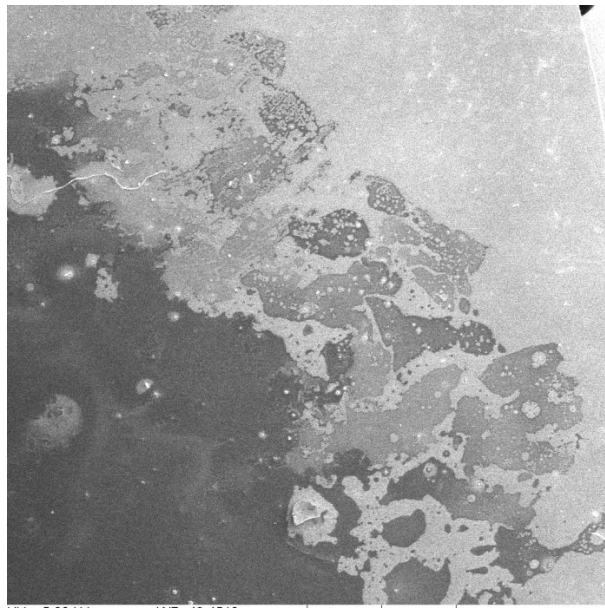


(c) Plasma Treated and Air Dried



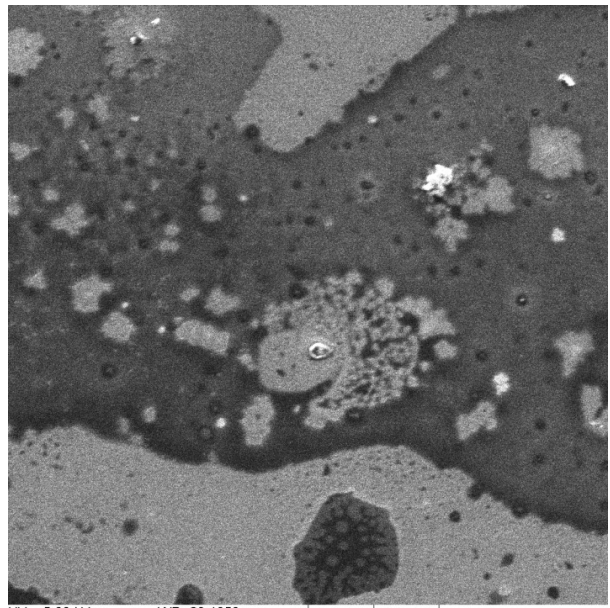
(d) Plasma Treated and Heat Gun Dried

Figure 6.17: Images of Initial Droplet Tests Using EGDMA



HV: 5.00 kV WD: 43.4510 mm
View field: 8.02 mm DET: SE Detector
DATE: 05/13/14 guest
2 mm Vega ©Tescan
Digital Microscopy Imaging

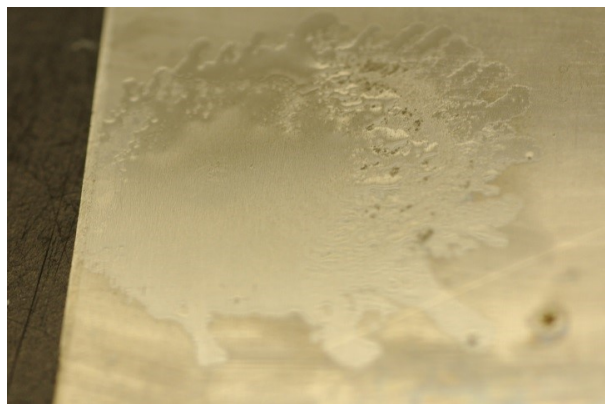
(a) Bulk Film



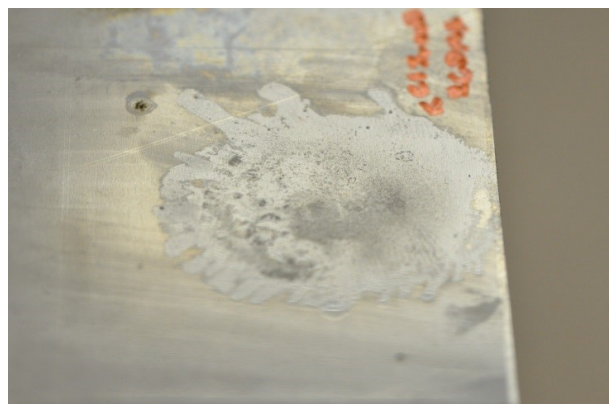
HV: 5.00 kV WD: 29.1850 mm
View field: 914.35 μ m DET: SE Detector
DATE: 05/13/14 guest
200 μ m Vega ©Tescan
Digital Microscopy Imaging

(b) Spots in Film

Figure 6.18: SEM Images of Initial EGDMA Tests

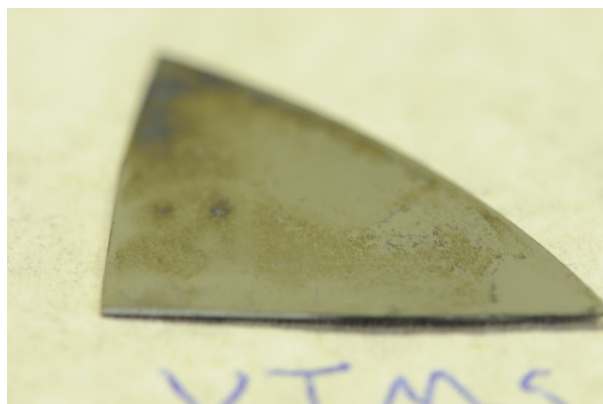


(a) Immediately After Deposition

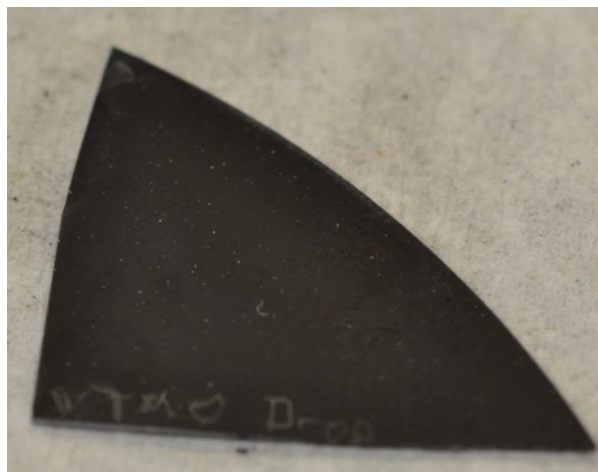


(b) Deposition Post Drying

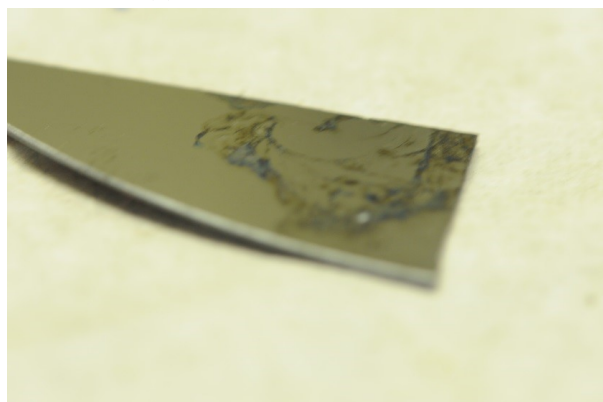
Figure 6.19: Images of Stainless Steel Substrate Tests Using EGDMA



(a) Untreated and Air Dried



(b) Untreated and Heat Gun Dried



(c) Plasma Treated and Air Dried



(d) Plasma Treated and Heat Gun Dried

Figure 6.20: Images of Initial Droplet Tests Using VTMS

more visible by heat. This testing is seen in Figure 6.20. Neither sample left any significant film, so no further testing was done. The main issue with VTMS appears to be its high vapor pressure, allowing it to evaporate before any significant treatment is conducted. Even the plasma did not sufficiently polymerize it to leave behind any significant deposition of a polymer.

6.6.1.4 MMA Initial Testing

Since methyl methacrylate (MMA) was successfully used before in our lab, [30, 31] a short test on two different meshes was attempted. As before, helium was bubbled through the MMA to produce a vaporized monomer for plasma-induced crosslinking and deposition. MMA was tested on silk above a quartz substrate (Figure 6.21a; 15 min treatment, 68% low power, 6.06 SLPM He

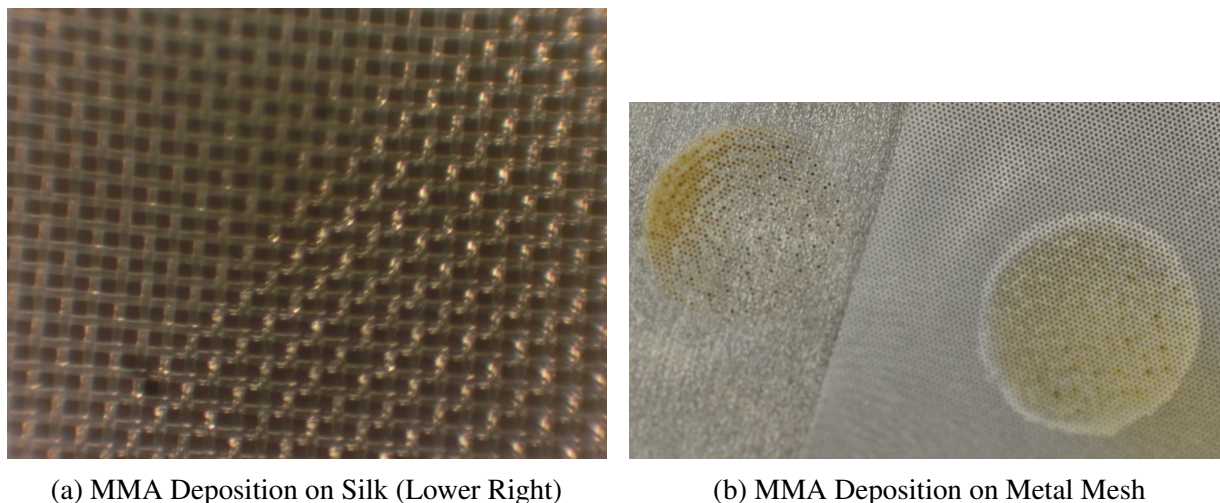


Figure 6.21: Images of MMA Depositions on Various Substrates

with ~ 0.01 SLPM through the bubbler). A clear deposition is noted, but no closing of the mesh occurred. MMA was also deposited onto a metal mesh (Figure 6.21b; 15 min treatment, 40% low power, 2.84 SLPM He with 0.25 SLPM through the bubbler). MMA penetrated the mesh and deposited on the substrate as well, but no closing of the mesh holes was noted. The deposition was also a light brown in color, although previously reported depositions were mostly clear. This is most likely due to a more intense discharge (in this case a metal substrate) which has changed the nature of the deposited film.

6.6.2 Optimization Study

TMEVS was identified as the best candidate for producing a thick and uniform film. Initially eight samples were used to understand the parameter space, varying the DBD jet's power, helium flow rate, and concentration of TMEVS in the deposition solution. Based off of the results from these eight samples, further iteration was conducted to ensure reproducibility and for further optimization of the film for thickness and uniformity.

Due to issues with the nebulizer becoming clogged or broken, no helium flow through it was used for this or further experimentation. Nevertheless, the inner tube of the nebulizer was still small enough (ID < 0.2 mm) that it could still be used to spray drops of solution onto the sample

Table 6.2: Testing Conditions for Initial Eight TMEVS Samples

DBD Power	Helium Flow Rate	10% TMEVS, 90% Methanol	50% TMEVS, 50% Methanol
15%	2.51 SLPM	Sample 1	Sample 8
15%	12.6 SLPM	Sample 2	Sample 7
30%	2.51 SLPM	Sample 3	Sample 6
30%	12.6 SLPM	Sample 4	Sample 5

without the gas flow, being run at a constant average flow rate of 50 $\mu\text{L}/\text{min}$ using the syringe pump.

6.6.2.1 Initial Eight Samples

Eight samples with a variety of conditions were used to probe the parameter space, with conditions noted in Table 6.2. A small portion of the wafer is masked using a microscope slide to allow for easier film thickness measurements. The parameters held constant for the initial eight samples to initially understand the sample space include the substrate (Si wafer), the DBD treatment time of 15 min, the ambient conditions (as much as possible; the tent flap to the hood was closed for all cases; samples 1 to 4 were run on a day earlier from samples 5 to 8, where the ambient temperature decreased from $\sim 26^\circ\text{C}$ to $\sim 24^\circ\text{C}$ for the second day, while the humidity decreased from $\sim 70\%$ to $\sim 50\%$ the second day), the pattern used for the 3D printer, and the time waited between the depositing and imaging the samples.

A representable voltage and current trace are shown in Figure 6.22. A relatively small voltage is required to ignite the discharge due to a fairly small jet length of ~ 16 mm from the electrode to the substrate and ~ 1.5 mm outside of the alumina tube. This is comparable to previous work, [29] albeit with a slightly smaller jet distance and electrode substrate gap, leading to the slightly lower voltages required. The current spikes observed are significantly smaller, but the substrate is fully conducting for this research as opposed to being a dielectric. Multiple discharge events are noted for each half-cycle.

All samples yielded thin films. Images of each film taken shortly after creating them are seen in Figure 6.23. Note that Samples 7 and 8 have different lighting conditions, since the films were

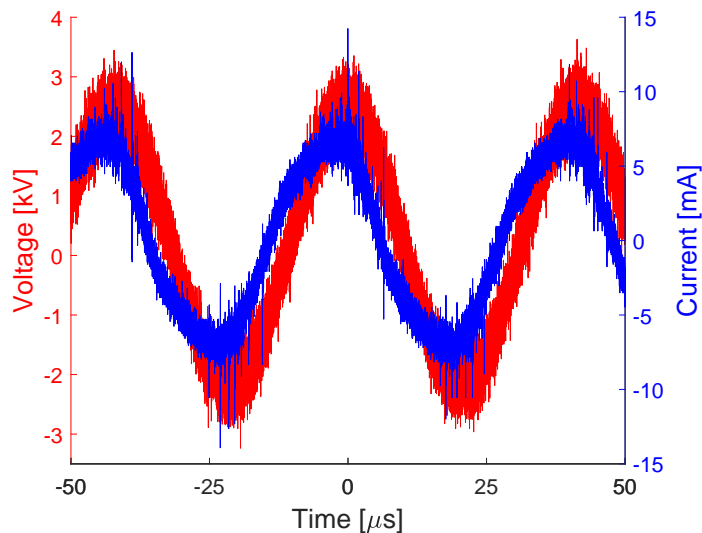
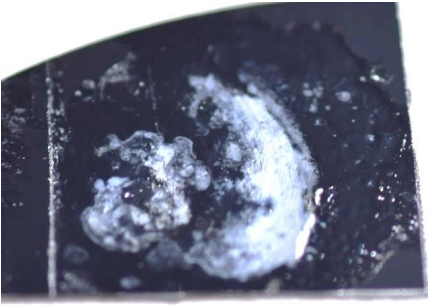


Figure 6.22: Voltage and Current Traces of the DBD Jet with the Nebulizer Spraying TMEVS

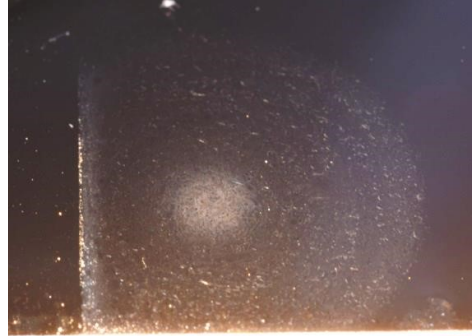
not otherwise visible by the ambient lighting. Optical micrographs of each film are shown in Figure 6.24 and with higher magnification in Figure 6.25. The film's appearance changed upon drying. After drying for 1 (samples 5 to 8) or 2 days (samples 1 to 4) the films are more visible as seen in Figure 6.26.

Increasing the concentration of TMEVS made the films appear more uniform but also created thinner films. In particular samples 7 and 8 were extremely thin films that were difficult to image or see until after they had dried for 24 hours. These were deposited using the lower discharge powers. The flow rate of helium did not seem to have any significant influence on the film. There may be a slight trend in increasing deposition with lower helium flow rates (compare Samples 5 and 6 or Samples 3 and 4) but the effect is not substantial; no profilometer data was acquired to verify this as well. As such, the lower flow rate was deemed better since it reduces the amount of helium used for depositing a thin film. Increasing the discharge power created thicker films (compare Samples 1 and 3 or Samples 6 and 8). However, Sample 3 shows what appear to be bubbles that have formed underneath the film or inside of it, possibly leading to a more porous film.

SEM imaging was attempted (using the TESCON SEM, see Section 3.3.4 for details on the SEM); however the SEM overheated after imaging only one sample, (Sample 2). The SEM images



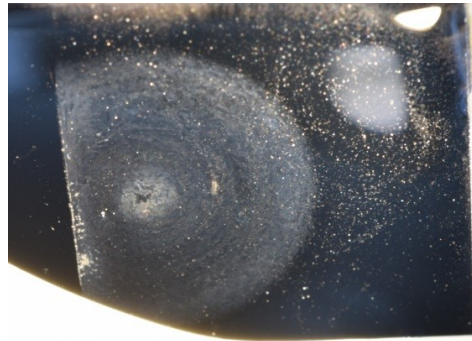
(a) Sample 1



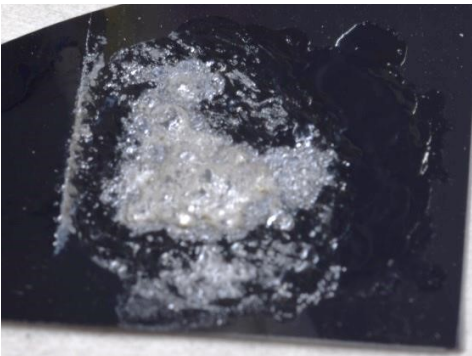
(b) Sample 8



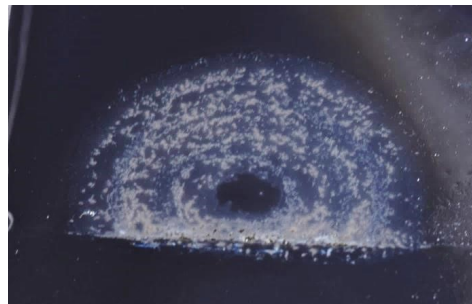
(c) Sample 2



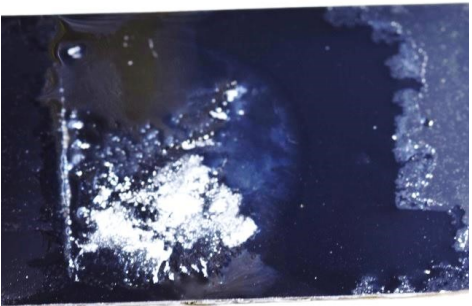
(d) Sample 7



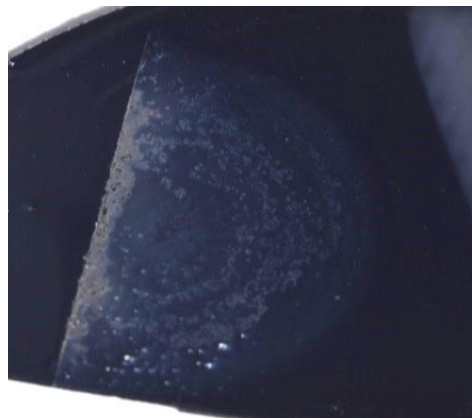
(e) Sample 3



(f) Sample 6

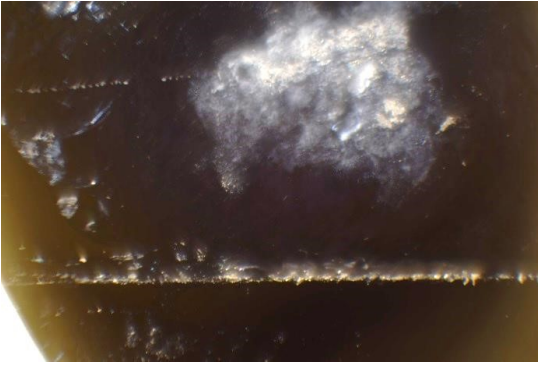


(g) Sample 4

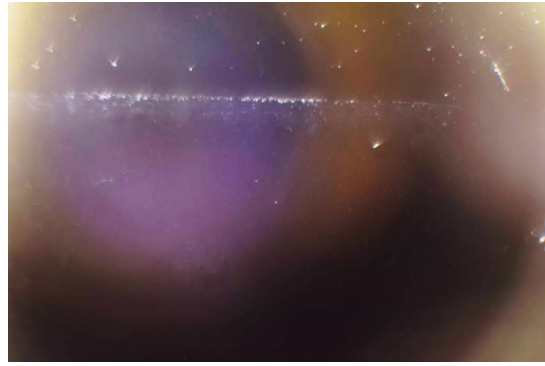


(h) Sample 5

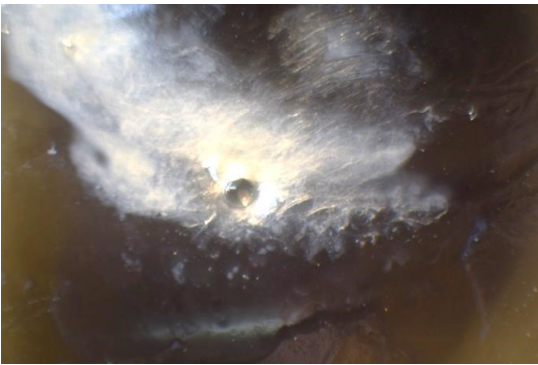
Figure 6.23: Images of the Initial Eight TMEVS Samples Shortly After Deposition



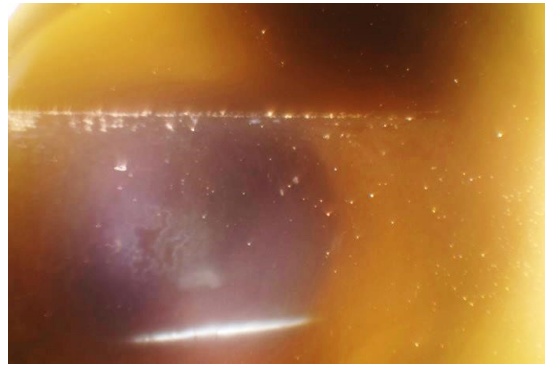
(a) Sample 1



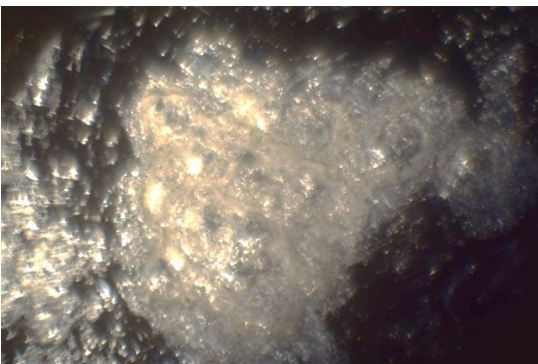
(b) Sample 8



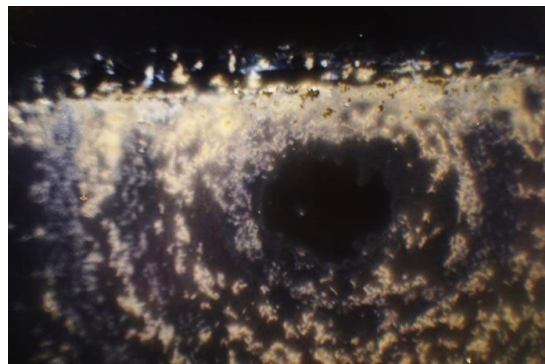
(c) Sample 2



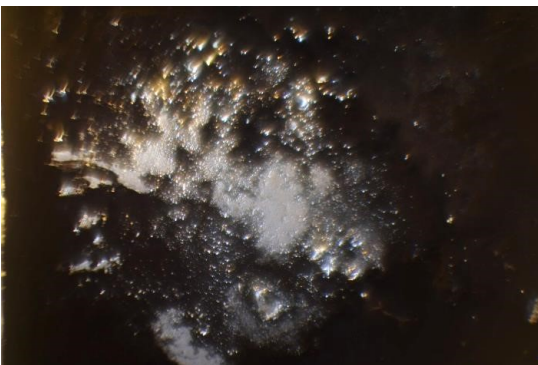
(d) Sample 7



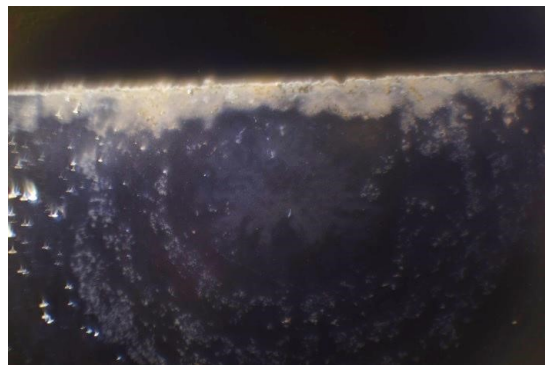
(e) Sample 3



(f) Sample 6

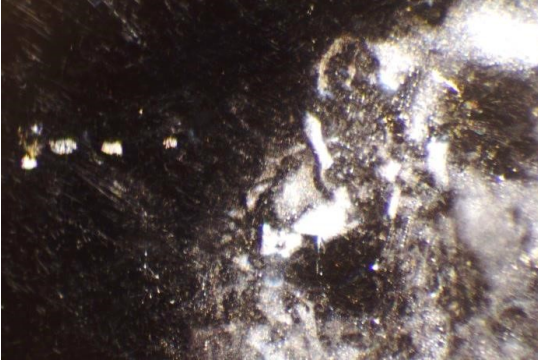


(g) Sample 4

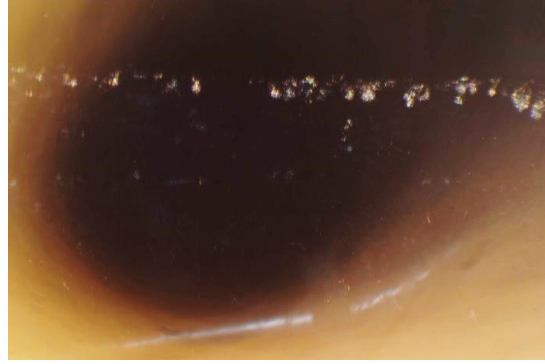


(h) Sample 5

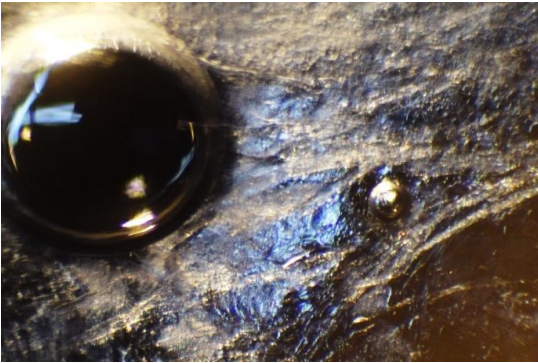
Figure 6.24: Low Resolution Micrographs of the Initial Eight TMEVS Samples



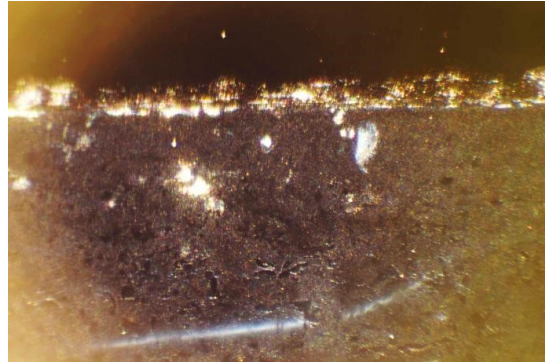
(a) Sample 1



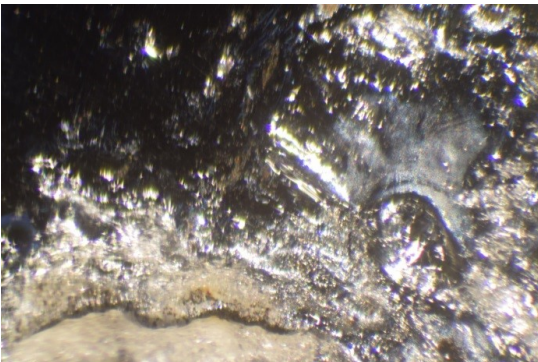
(b) Sample 8



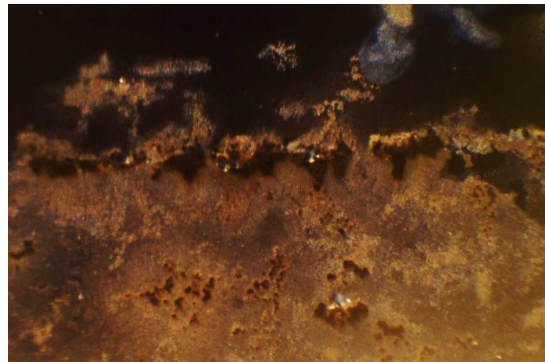
(c) Sample 2



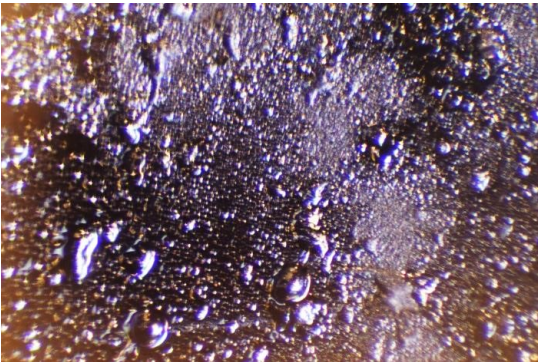
(d) Sample 7



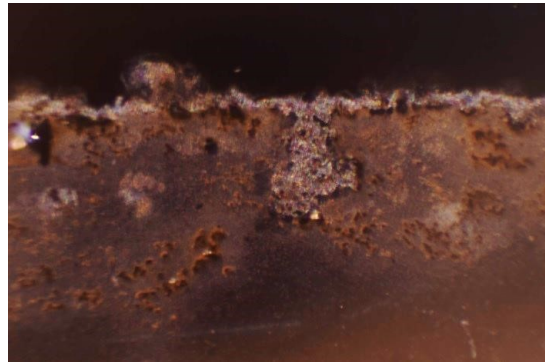
(e) Sample 3



(f) Sample 6

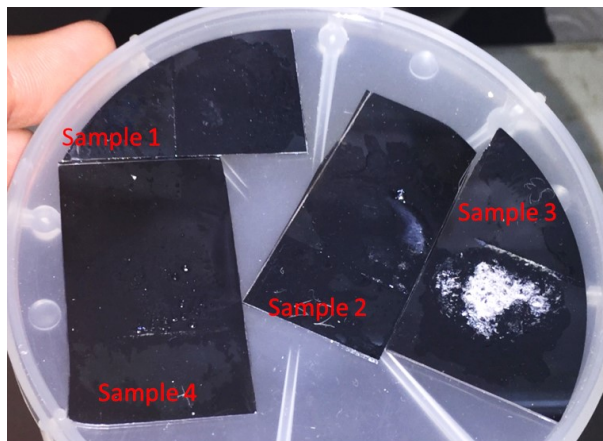


(g) Sample 4

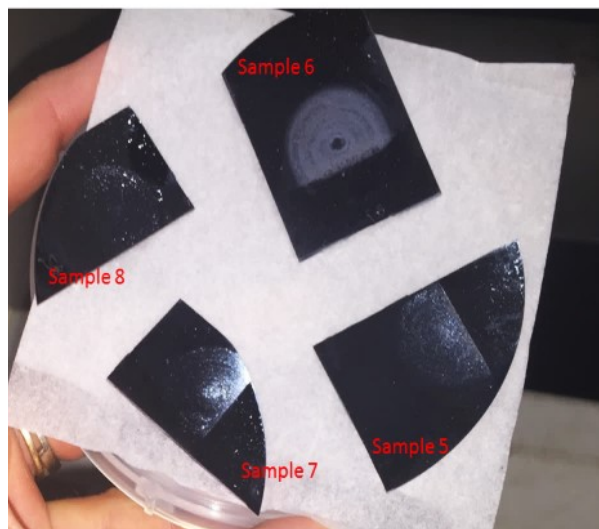


(h) Sample 5

Figure 6.25: High Resolution Micrographs of the Initial Eight TMEVS Samples



(a) Sample 1–4



(b) Sample 5–8

Figure 6.26: Images of the Initial Eight TMEVS Samples After Drying in Ambient Air

are seen in Figure 6.27. The film appears very uniform; however imaging was difficult due to charging of the film during image acquisition, which caused the image to become overexposed. It appears to be a piece of dust in the image near the center of the film, but the overexposed nature of the image makes it difficult to confirm.

To determine the thickness of the depositions, a profilometer was used, dragging the tip from a cleaner area on the silicon substrate across the edge of the film. Only three of the initial eight samples were tested (Samples 2, 3, and 6). The results are seen in Figure 6.28, where the images note roughly where the profilometer test was conducted. Sample 6 is noticeably thinner than the other two samples. Noticeable ridges exist apparently matching the rings of the printing pattern. This further supports the need to use a different pattern, such as the spiral pattern for direct write rather than conventional 3D printing patterns. Similarly, Sample 3 has a thin edge where the masking was done before increasing to a much thicker bulk film. Since mostly only the edges of the films were sampled, no hard conclusions can be made to the average thicknesses of the films, however they appear to be at least a micron thick, possibly much thicker to be on the order of $50\ \mu\text{m}$ or more.

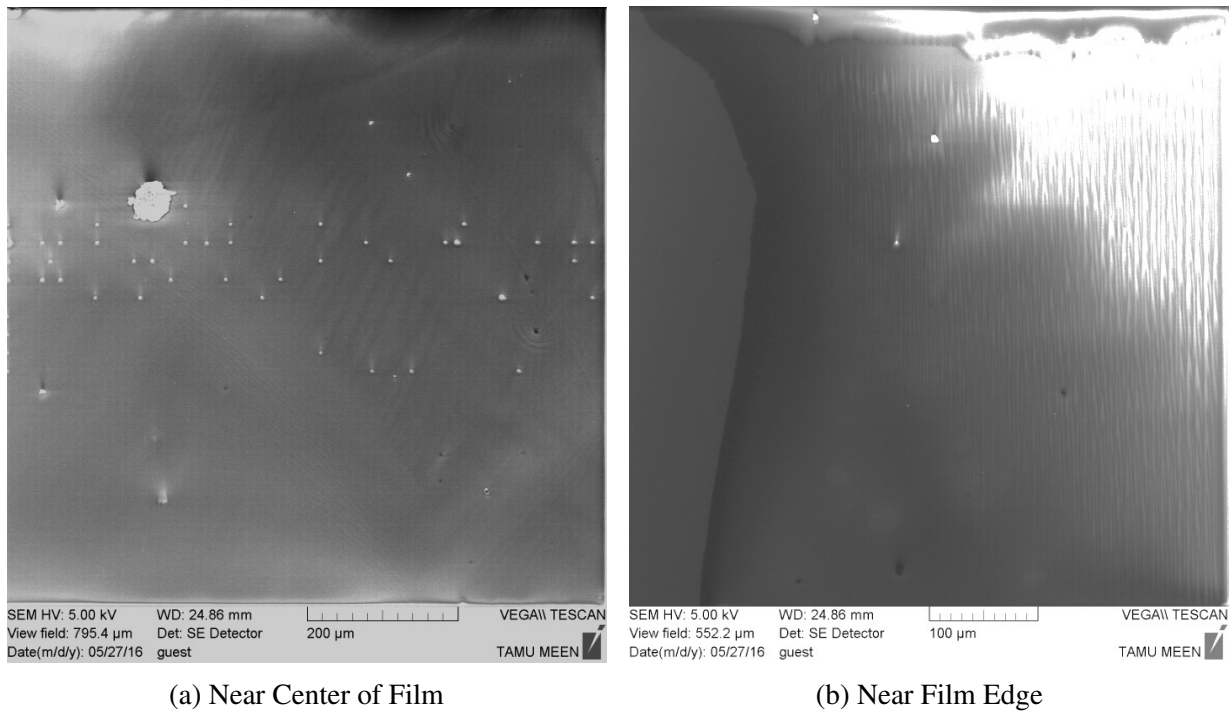


Figure 6.27: SEM Images of the Initial TMEVS Sample 2

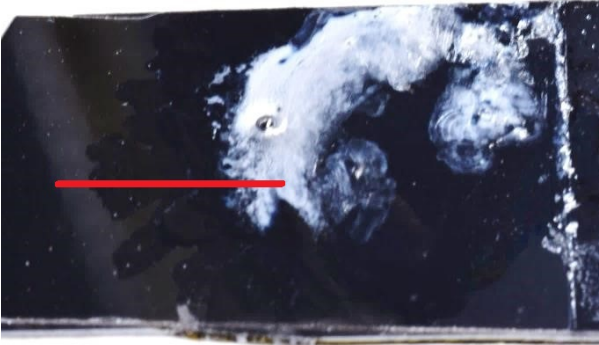
Table 6.3: Sample Conditions for Further Testing of TMEVS Film Deposition

Sample	DBD Power	Helium Flow Rate	TMEVS Concentration	Nebulizer Flow Rate
1A	15%	2.51 SLPM	10%	50 μ L/min
3A	30%	2.51 SLPM	10%	50 μ L/min
6A	30%	2.51 SLPM	50%	50 μ L/min
8A	15%	2.51 SLPM	50%	10 μ L/min
4A	30%	12.6 SLPM	20%	50 μ L/min

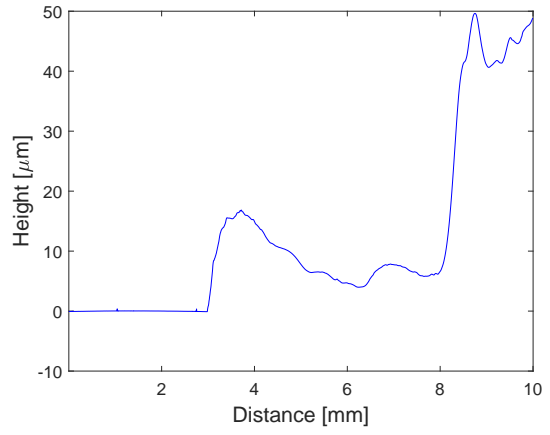
6.6.2.2 Further Iteration

Some further iteration on the printing pattern and other parameters was conducted. The testing conditions are shown in Table 6.3. All of these tests were run with the spiral pattern (Figure 6.4) for equal area treatment.

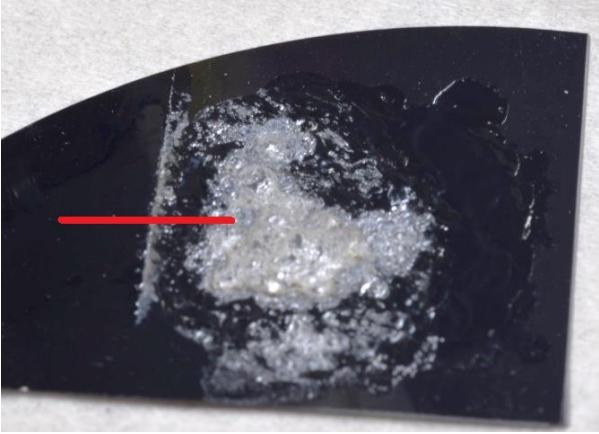
Samples 1, 3, and 6 were repeated without masking the silicon substrate with a piece of glass (called Samples 1A, 3A, and 6A), using the spiral pattern geometry that should be more uniform in covering all areas, and run for approximately 19 min instead of 15 min. The results are seen in



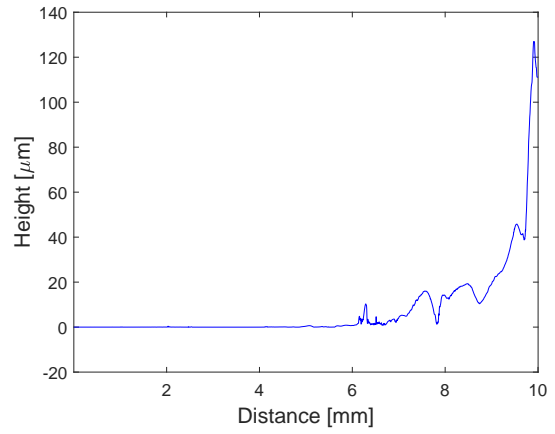
(a) Sample 2



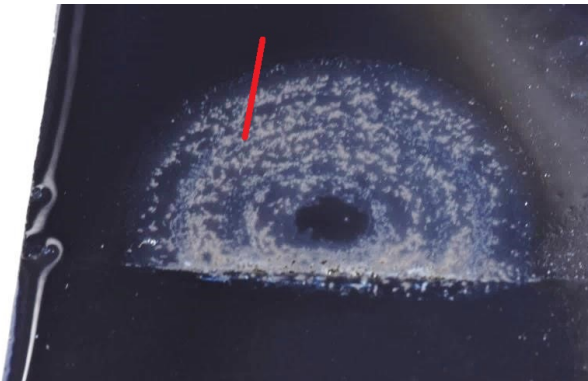
(b) Sample 2 Profile



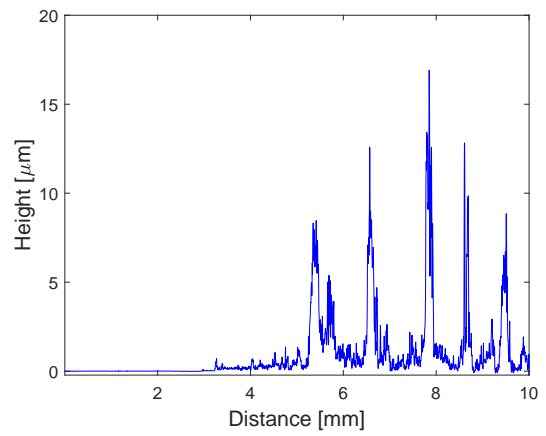
(c) Sample 3



(d) Sample 3 Profile



(e) Sample 6



(f) Sample 6 Profile

Figure 6.28: Profilometer Results For Samples 2, 3, and 6 of the Initial Eight TMEVS Samples

Figure 6.29, where all appear roughly the same as the previous trials, showing good repeatability. Optical micrographs are seen in Figure 6.29 where all conditions show a fairly uniform film, especially Sample 1A, where no pattern traces are easily visible.

Sample 3A was also further imaged using an SEM (JEOL JSM-7500F, see Section 3.3.4 for specifications on the SEM) that has better resolution and lower available probe currents to help reduce charging of the sample, which occurred previously. Overall the film appears moderately uniform with some surface roughness and agglomerations on the order of 10–50 μm in size (Figure 6.30). No significant pores are apparent in the film, nor were any bubbles visible as noted in Sample 3.

Another sample was created to determine if there may be more influence of TMEVS concentration on the films than initially noted. Sample 4A was run with 12.6 SLPM He, 30% power, and 20% TMEVS solution deposited at 50 $\mu\text{L}/\text{min}$ using the spiral pattern for 16 min. Micrographs of the deposition are shown in Figure 6.31. The film appears consistent with Samples 3A and 6A, suggesting less sensitivity as initially expected with the variation in the concentration of TMEVS.

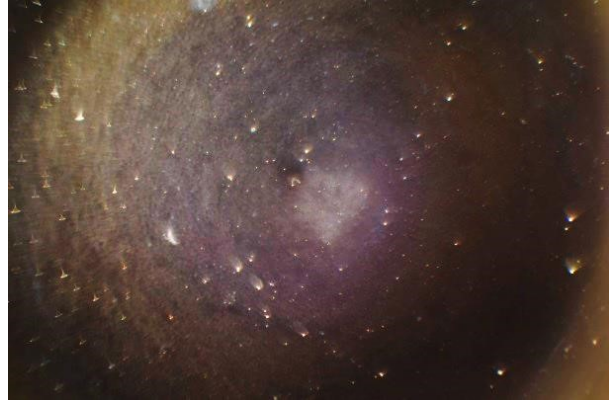
Another sample (called Sample 8A) was run with the same conditions as Sample 8, except the solution deposition rate was lowered to 10 $\mu\text{L}/\text{min}$ to reduce the excess liquid buildup noted on the sample. Again, after 15 min, no significant deposition was noted, so the solution deposition was turned off, but the DBD jet was left on for a further 15 min treatment. The resulting film is seen in Figure 6.32. The deposition appears thicker than Sample 8, but the film still appears very thin, confirming that the solution concentration is still a major factor, not the amount of excess solution left on the substrate during testing. Thus a large change occurs between a 20% solution (Sample 4A) and a 50% solution (Sample 8A).

6.6.3 Testing on Biological Substrates

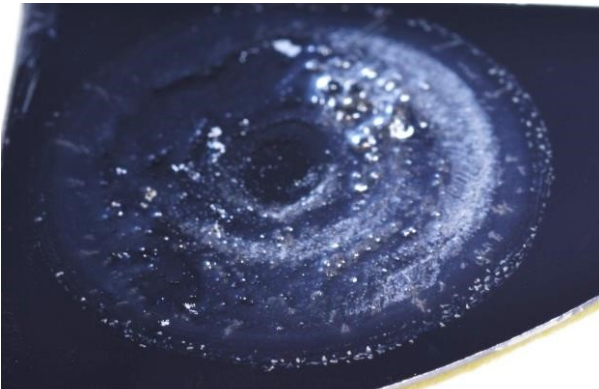
Testing was done on a pig skin as a biological substrate similar to human skin. Nevertheless, this is only to serve as a basic proof of concept and not as a proper measure for biocompatibility. Methanol was kept as the solvent for ease of use in testing, although it is known to not be biocompatible due to the risk of methanol poisoning. In addition, no histological studies are done to



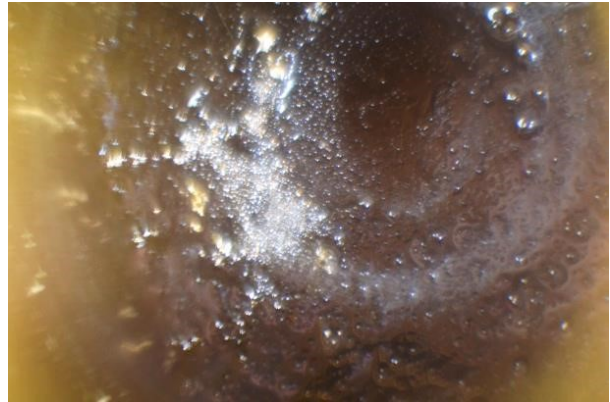
(a) Sample 1A



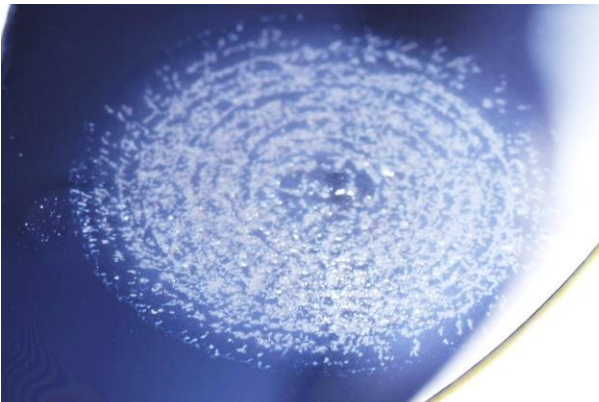
(b) Sample 1A Micrograph



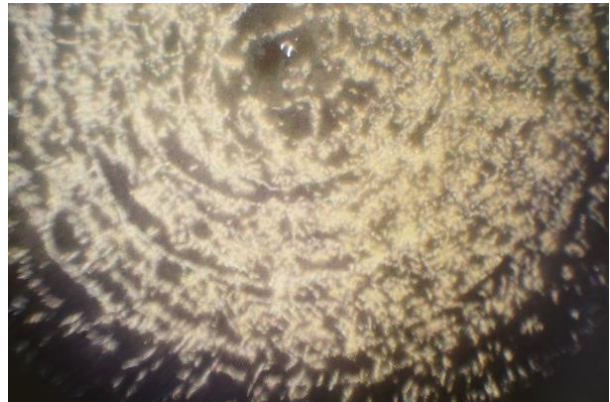
(c) Sample 3A



(d) Sample 3A Micrograph

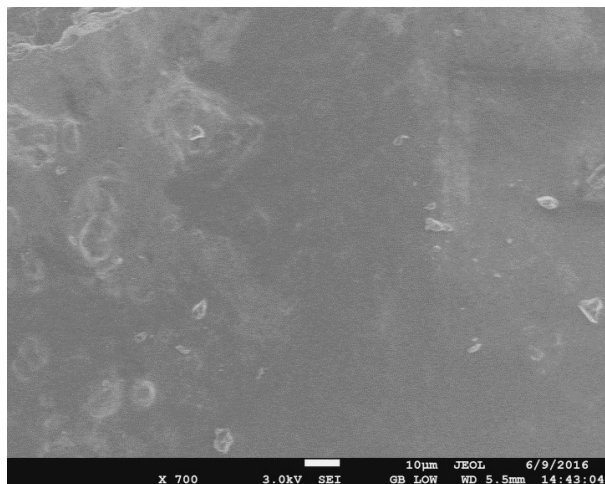


(e) Sample 6A

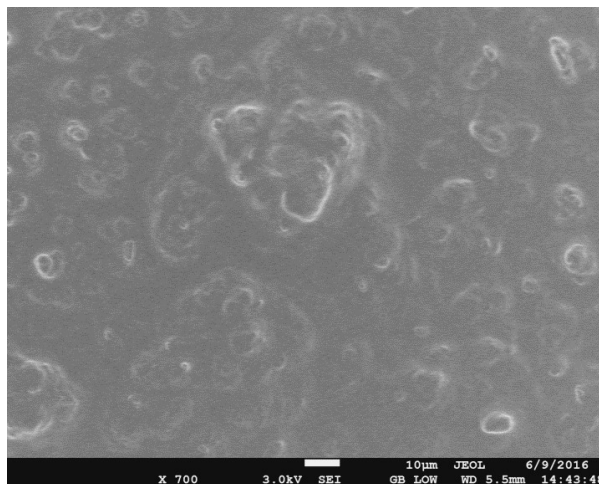


(f) Sample 6A Micrograph

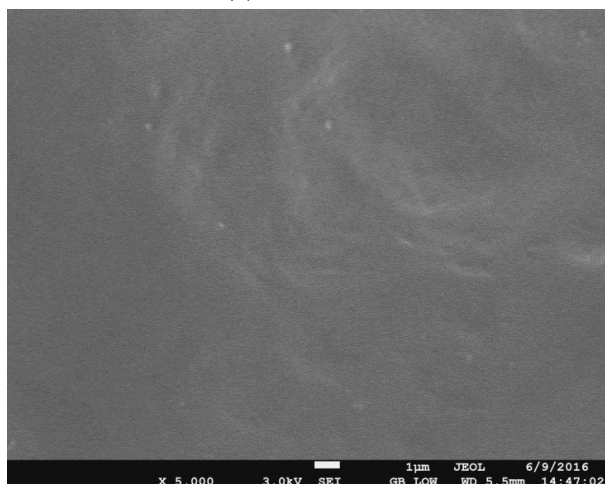
Figure 6.29: Images and Micrographs for TMEVS Repeatability Trials



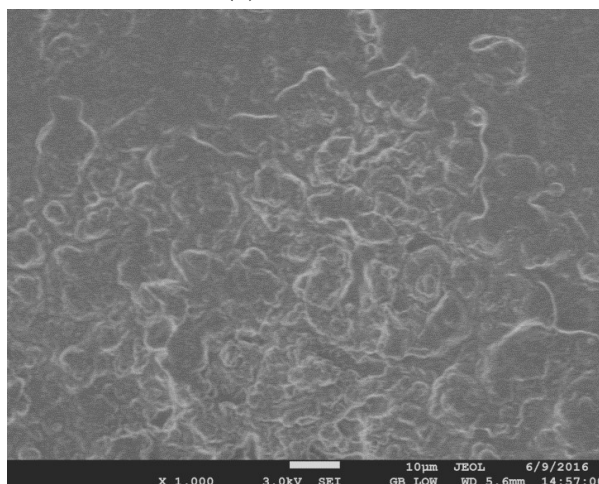
(a) Location 1



(b) Location 2

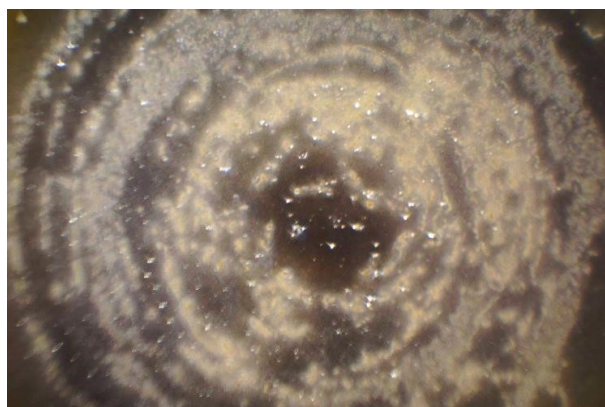


(c) Location 3

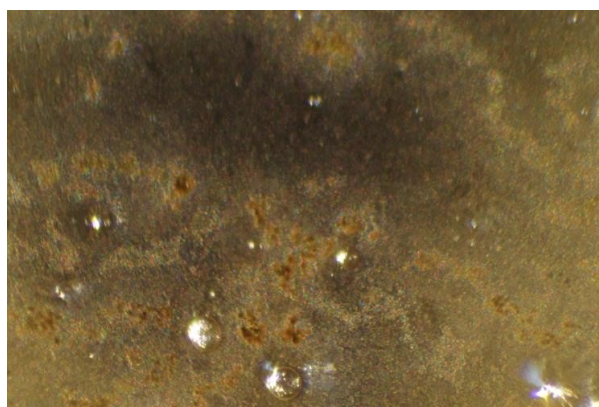


(d) Location 4

Figure 6.30: SEM Images of TMEVS Sample 3A



(a) 1 X Magnification



(b) 4.5 X Magnification

Figure 6.31: Optical Micrographs of TMEVS Sample 4A

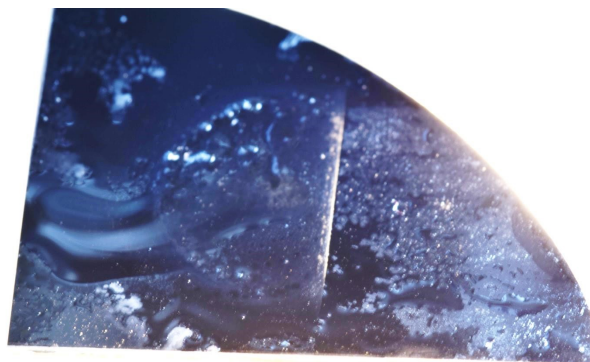


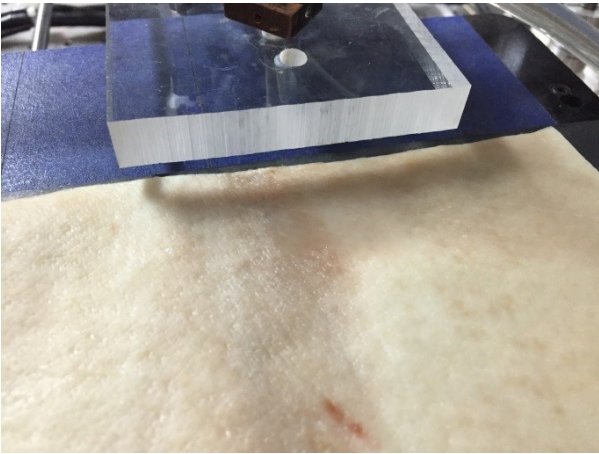
Figure 6.32: Image of TMEVS Sample 8A Using a Lower Nebulizer Flow Rate

determine if there was non-visible damage done to the skin.

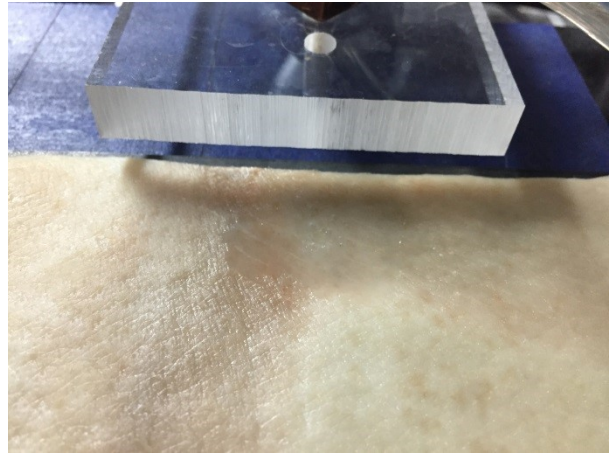
An initial test on pig skin was conducted with a few droplets of 10% TMEVS 90% methanol solution placed directly on the skin and then treated with the FE-DBD jet. The results are seen in Figure 6.33, showing the pig skin before during, and after treatment, as well as after drying of the skin briefly using a heat gun. A shinier area is seen where the skin was treated, especially in Figure 6.33d. Part of the deposited film was able to be exfoliated from the pig skin by scraping tweezers across the surface, as seen in Figure 6.34. This is desired for film porosity testing.

Three further tests on pig skin were attempted. The first was an attempt to replicate Sample 3A (2.51 SLPM He, 18% power, 10% TMEVS solution deposited at 50 $\mu\text{L}/\text{min}$, and the spiral pattern run for 10 min). The skin was noted to deform at higher powers, so a lower power of 18% (rather than 30%) was used. After 10 min of testing the skin was removed and imaged. It was noted that the deposition had substantial liquid components. Upon drying the excess liquid, there appeared to be no deposition as seen in Figure 6.35. The skin was noted to be dry and discolored post testing, suggesting the either the power was too high or the treatment time was too long suggesting possible thermal damage to the pig skin.

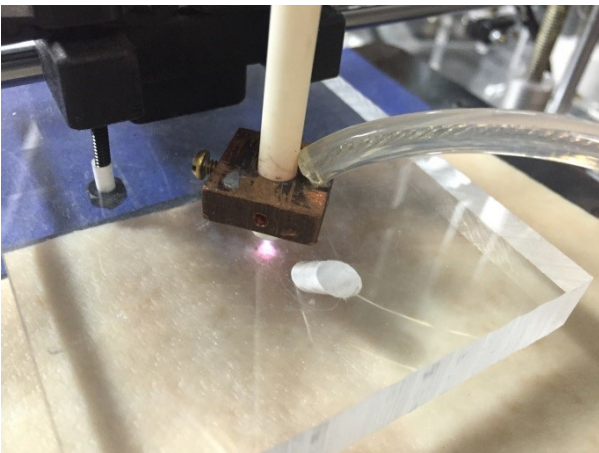
A second and third further attempts at using pig skin were made using higher He flow rates to cool off the skin. Both a low (10% TMEVS) and a high (50% TMEVS) concentration of the solution were used for two different runs (12.6 SLPM He, 30% power, TMEVS solution deposited



(a) Before Treatment



(b) After Treatment



(c) During Treatment



(d) After Treating & Drying

Figure 6.33: Images of the Initial Pig Skin DBD Jet Treatment with a Droplet of TMEVS

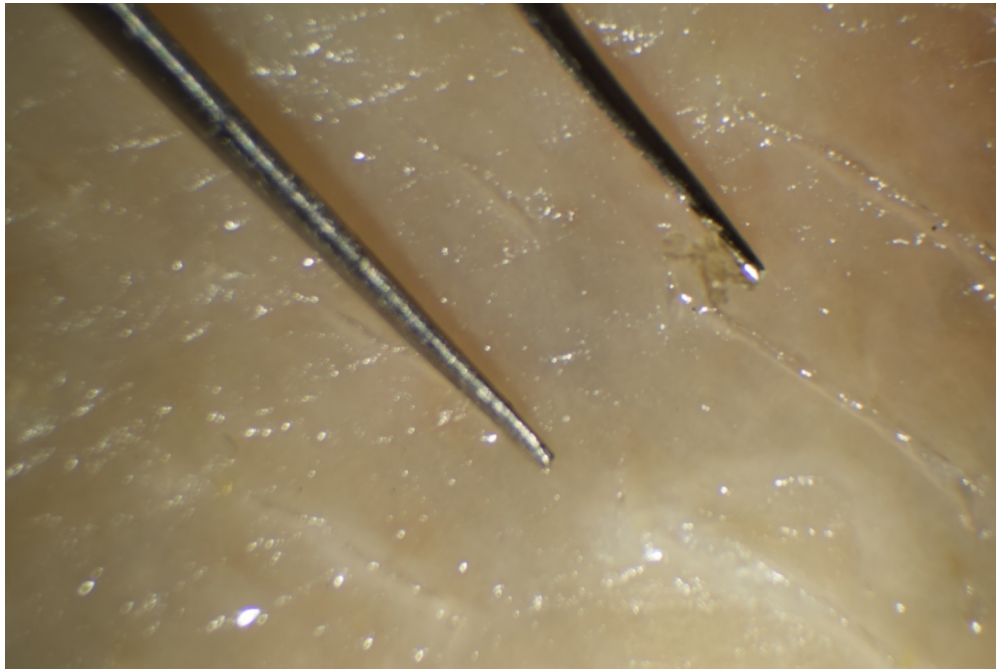
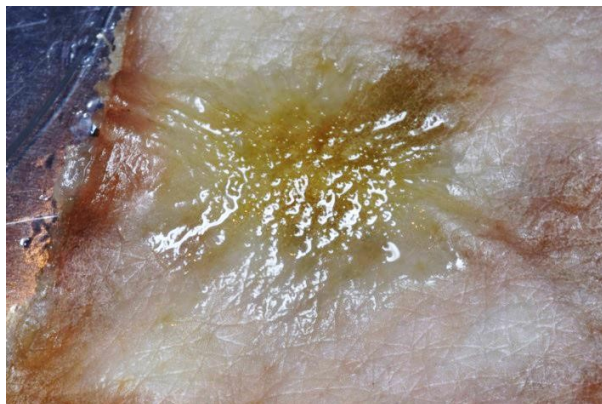
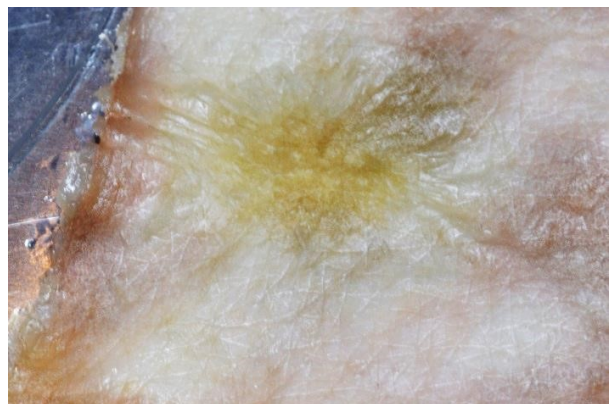


Figure 6.34: Image of the Removal of the TMEVS Deposition from Pig Skin



(a) After Testing

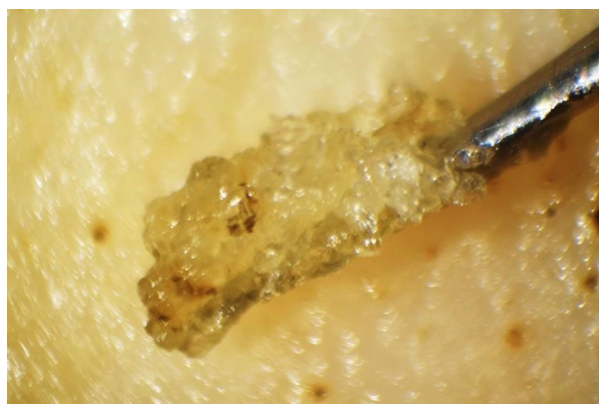


(b) After Deposition and Drying

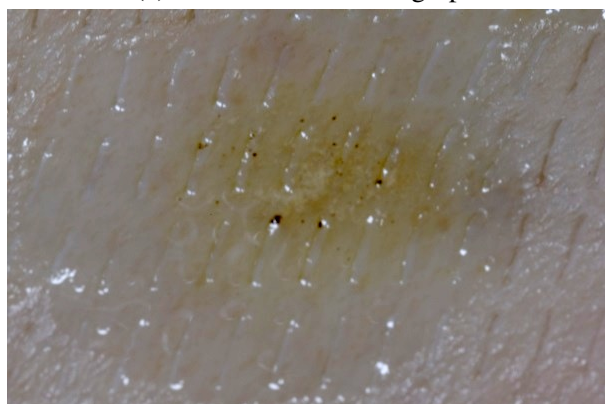
Figure 6.35: Images of the Initial Test Spraying TMEVS onto a Pig Skin Substrate for Film Deposition



(a) 10% TMEVS Micrograph



(b) 10% TMEVS Film Scrapings



(c) 50% TMEVS Micrograph



(d) 50% TMEVS Film Scrapings

Figure 6.36: Optical Micrographs of Pig Skin with TMEVS Deposition and the Scrapings of the TMEVS Films for Higher Helium Flow Rates

at $50 \mu\text{L}/\text{min}$ using the spiral pattern for 18 min). Both yielded films that were able to be scraped off of the surface of the pig skin using metal tweezers, seen in Figure 6.36; however the film was not able to be removed intact for film characterization, such as porosity testing.

6.7 Chapter Summary & Future Work

In this work, an existing fused filament fabrication (thermoplastic) 3D printer is modified to serve as a direct write system by mounting an FE-DBD jet in place of the printer head. Due to the change in application, different constraints on the printed pattern are needed to ensure optimized film depositions. A variety of deposition methods and precursors are used, with the primary goal of developing a system that can direct write onto biological substrates. Metal pat-

terns were attempted with the goal of using this as a method of printing epidermal electronics. A variety of materials were tested as possible sprayable bandages. The most likely candidate, tris-(2-methoxyethoxy)(vinyl)silane (TMEVS), was carried forward with an initial optimization study on a silicon substrate. In general, the helium flow rate in the DBD jet had little effect on the system; however higher flow rate helped cool the substrate, which was especially helpful in later depositions onto pig skin. Higher DBD powers tended to produce thicker films. The solution's flow rate did not seem to have a large effect on the films; any excess liquid would be blown off of the substrate by the jet. Lower concentrations produced thicker but less uniform films. The optimum conditions for a silicon substrate were found to be around 20% TMEVS solution (by volume in methanol) at a flow rate around 50 $\mu\text{L}/\text{min}$ with DBD jet parameters of 30% power and 2.51 SLPM helium flow rate. However, these conditions are not optimal for pig skin deposition, as this lower helium flow rate and higher DBD jet powers cause thermal damage. More research needs to be done on depositions on pig skin to determine optimal conditions for deposition.

In addition, the deposition rate is fairly slow. For this to be used in a medical device, faster deposition rates is desired, so that a patient does not have to lie still for minutes waiting for the deposition. Lastly, a clear market is needed for this device to warrant further targeted development. As it currently stands, existing technologies are cheaper and easier to use, so this device would not warrant funding from investors to get it through an FDA approval process.

7. IMPROVEMENT OF ADDITIVE MANUFACTURING

7.1 Introduction

This chapter investigates two different systems that use a plasma for improving the strength of additively manufactured parts. The first, uses a nanosecond pulsed plasma discharge. Due to the EMI-generating nature of the discharge, this plasma treatment was done external to the printer, however this also demonstrates that the effect is purely based on the plasma functionalizing the polymer surface and not based on a thermal effect. This treatment yielded >100% strength improvement in the bonding strength between layers. The second system is a commercial product called the FlashFuse system, which uses a DBD to treat polymers coated in carbon nanotubes. Since this system uses lower frequencies, EMI is less of a concern and parts are treated in situ during the printing process. The primary mechanism appears to be Joule heating in the additively manufactured parts where the plasma is coupling the power supply to the carbon nanotubes in the polymer. This heating allows sufficient time for the layers to weld together creating parts with the same strength as injection molded parts. The clearest path of using these processes for medical applications is in printing custom prosthetics, which is currently being done with the FlashFuse system.

7.2 Background of Additive Manufacturing

Starting from stereolithography systems developed in the late 1980s and thermoplastic extrusion printing in the early 1990s, additive manufacturing (AM), also known as 3D printing,¹ has become a huge field of research and innovation. [52] AM builds a part by selectively adding layers of material; this is in contrast to conventional “subtractive” machining, where parts of a material are removed to produce the finished part. There are many types of AM, from laser sintering of

¹Though the two terms are treated as synonymous by most authors, [319] some disagree [320] stating that *additive manufacturing* is more encompassing than *3D printing*, emphasising the entire manufacturing process including, for example, support structure design, part post-processing, and process considerations to ensure reproducibility in the design. This dissertation will follow the standard convention of treating them as synonyms and will primarily use the term *additive manufacturing*.

metallic powders to laminate based methods for paper; this work will focus on thermoplastic extrusion, namely fused filament fabrication (FFF), also known by the name fused deposition modeling (FDM), a name trademarked by Stratasys. [321]

FFF uses a thermoplastic that has a low glass transition temperature. When the material is heated up to or above its glass transition temperature it can be extruded out of a heated nozzle. Upon leaving the heated nozzle, the plastic will cool and reform into a solid, binding to the material nearby. By controlling the rate the material is extruded out of the nozzle as well as the location of the nozzle, a layer of material can be deposited in a controlled fashion. Successive layers can be laid down building a part layer by layer. This entire process can easily be automated by a computer, allowing the user to design a custom part in CAD software and quickly send it to a slicing program, which will create the commands to send to a printer for creating the part layer by layer. Though FFF may never quite meet the low cost of injection molding as a bulk manufacturing process, the advantages lie in that parts can easily be customized (without needing to create a new mold), various infills can be selected leading to varying material properties throughout the part, and a variety of materials can be printed simultaneously.

The biggest challenge for FFF is creating a strong interlayer bond. Along the filament direction, the strength is nearly identical to injection molded parts; however it is substantially weaker along the y and z directions (see Figure 7.1). This is because the bond is formed between the cooling filament as it leaves the nozzle and an already cooled thermoplastic layer. As a result, many groups have investigated methods of heating the printed layers to improve bond strength including using lasers [322], using infrared lamps [323], and microwaves [49].

The “gold standard” that is sought is to have additively manufactured parts with isotropic strength the same as that of injection molded parts. Since plasmas have demonstrated the ability to show surface modification of polymers (see Section 2.2.3), this is a viable method to improve the strength of additively manufactured parts as we have demonstrated. [16] In addition, Essentium, Inc. has shown adding a plasma to the printing process is a commercially viable option, which is demonstrated with the FlashFuse system. [17, 324]

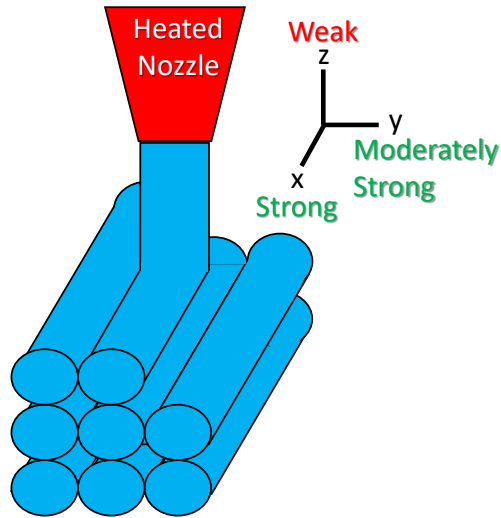


Figure 7.1: Schematic of Strength Variation in a 3D Printed Part

In addition to printing directly onto a biological substrate as done in Chapter 6, plasmas can be used to assist the 3D printing process for parts that will be used in the medical industry, such as creating customized parts for prosthetics or implants. Using plasma's ability to functionalize surfaces, a variety of potential uses exist, such as binding the layers together in a 3D printed part, adhering various surface coatings, and making other surface chemistry possible.

7.3 Device Life-Cycle Overview

This dissertation will focus on two systems: a nanosecond pulsed plasma system developed in-house in conjunction with Dr. Bruce Tai's lab and the FlashFuse system developed by Essentium, Inc. In particular, this dissertation will focus on the plasma characterization aspects as the mechanical characterization has been reported in the papers [16, 17] and coworker dissertations [325, 326] on these respective projects.

The nanosecond pulsed system requires substantial development to become a usable system. Two main issues currently exist: combining the current system into a single unified system rather than two disjointed parts of 3D printing and plasma treatment and greatly reducing or ideally eliminating the EMI generated from the system. If these can be solved, this will result in a method of creating parts with greatly enhanced strength compared to standard (i.e. non-plasma assisted)

FFF.

The FlashFuse system is by far the most developed system discussed in this dissertation. It is currently being used in commercial operation for a wide range of additively manufacturing processes to create parts with the injection molded strength. The most relevant is TriFusion Devices, a subsidiary of Essentium, Inc., which is using the FlashFuse system to produce prosthetic devices for amputees. The only last step in development for the FlashFuse system is to show a wider range of materials that can be used with the system, which is already claimed by the company's website. [324]

7.3.1 FDA Approach

The FDA has released non-binding guidance, which currently reflects the FDA's thinking in the area of 3D printed parts, to assist in company decisions. [71] Any patient-specific device created by a 3D printer is still subject to normal requirements; there is simply more of a focus on the process rather than the end product. As a result, following good manufacturing practices (GMP) is key, which may require some more scrutiny for a plasma-assisted printed device. This is because the plasma adds some additional controls over the printed part that need to be demonstrated to not adversely affect the end product. For example, the additional chemistry provided by the plasma may warrant additional testing to ensure no adverse chemicals were created. [55] However, these would most likely only need to be documented in the design file rather than requiring a new approval, just as changing out any other material source may be required to note in the device design file.

Essentium, Inc. and its subsidiary company TriFusion Devices are already operating in the area of custom prosthetic devices. [327] These devices are exempt from the 510(k) process as Class I devices, meaning no FDA approval is required for the device; however general controls such as proper labeling and GMP still apply. [83]

7.3.2 Device Outlook

Further work is being put into both of these designs. The nanosecond pulsed system is being more fully characterized to understand the mechanism for the improved strength. Though this is not developing it substantially as a potential medical device, it is planning to show that multiple 3D printers and materials can be used. In determining the mechanism a new plasma source may be able to be used that can be integrated easier into the printing process, especially one that does not generate so much EMI.

The FlashFuse system is already a marketed product. The only goal is that through the business side of Essentium, Inc. and TriFusion Devices this device can become wide-accepted and used in more systems.

7.4 Nanosecond Pulsed System

This system was developed in conjunction with Dr. Bruce Tai and his student, Chin-Cheng Shih, as a part of his master's work. [325] The plasma aspects of the system will have more of a focus in this dissertation as the other aspects of the project (running the 3D printer, bond strength testing, SEM, etc.) were Chin-Cheng Shih's contribution to this joint endeavor. Some results will only be mentioned in passing such as water contact angle changes and stress whitening noted on fractured samples, as these were done by Chin-Cheng Shih.

7.4.1 System Description & Experimental Setup

The system consists of two parts: a 3D printer (Dreameer, Flashforge) and a nanosecond pulsed power supply (FID power supply, see Section 3.2.1.3). Initially, small blocks of polylactic acid (PLA) are printed, measuring 20 mm by 12.5 mm by 12.5 mm so that they fit under the arrays previously described in Section 4.4.2 (Array #1 was used for all testing here). The printing process is then paused for treatment, and the printing platform is removed from the printer. Removal was necessary to avoid electromagnetic interference (EMI) during the plasma treatment. The blocks are then treated using the the FID power supply using two different treatment times of 30 s or 300 s (see Section 3.2.1.3 for information about the power supply). The plasma treatment is shown in

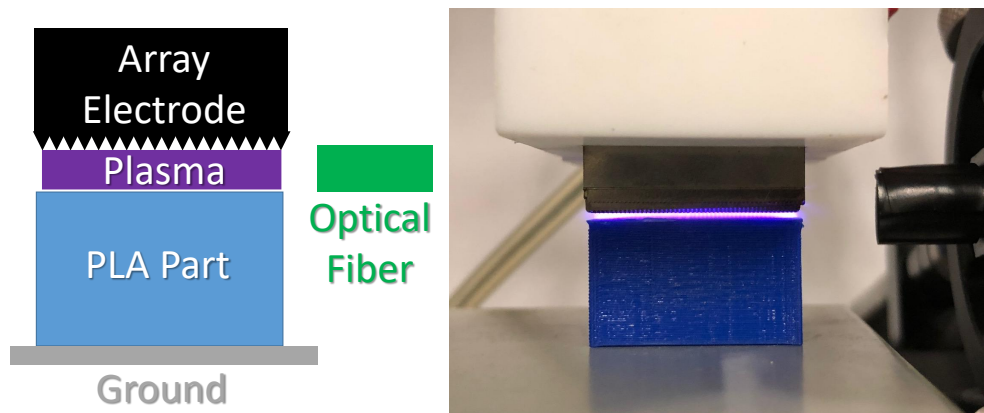


Figure 7.2: Schematic and Image of Plasma Treatment for the Nanosecond Pulsed System

Table 7.1: Various Treatment Conditions for PLA Samples

Notation	Name	Treatment Description
C	Untreated	Control (no treatment)
CPT30	Short Treatment	30 s plasma treatment
CPT300	Long Treatment	300 s plasma treatment
P	Polished	Polished with #180 grit sand paper
P+CPT300	Polished & Treated	Polished with #180 grit sand paper and then 300 s plasma treatment

Figure 7.2. The FID power supply was run at 20 kV and 2 kHz, with a 2.5 SLPM helium gas flow through the array; the discharge gap was maintained to be approximately 1 mm. In addition to a plasma treatment, a polishing treatment was given to some samples in lieu of a plasma treatment (manually polished with #180 grit sandpaper). A third treatment group was also conducted which included being polished and then having a 300 s plasma treatment. The different treatments are summarized in Table 7.1.

The two plasma treatment times were chosen to determine if there is any effect on the duration of treatment, assuming that longer treatments may have a greater effect on the surface. The polished samples were used to provide a control that has surface modification done on a macroscale level. In addition the polished surface showed itself to have the most wettable surface in water droplet tests, having a substantially smaller water contact angle ($\sim 10^\circ$) than both the control

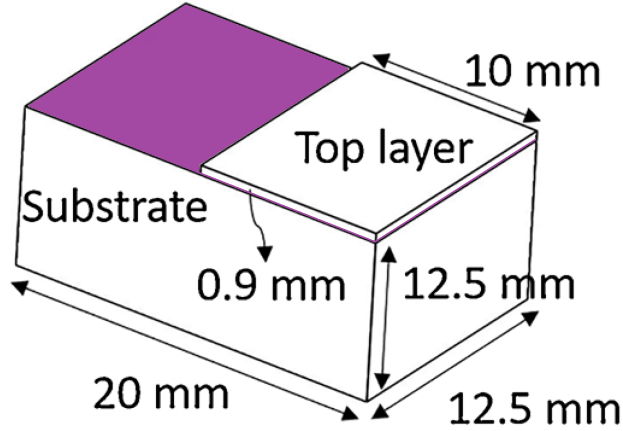


Figure 7.3: Schematic of Test Part for Testing the Nanosecond Pulsed Plasma System

($\sim 80^\circ$) and the 30 s plasma treatment ($\sim 45^\circ$).

After treatment, the printing platform was reinstalled and allowed to come back to thermal equilibrium with the bed temperature. Then a thin second layer measuring 10 mm by 12.5 mm by 0.9 mm is printed over half of the original block, as shown in Figure 7.3. The purple colored surface of the substrate is the plasma treated surface. This thin layer is then sheared off to measure the bond strength using a custom designed shear bond strength test apparatus (Figure 7.4), which measures the force applied as the layer is sheared off at a constant shearing rate of 12.5 mm/min. The work (or minimum energy expended, \mathcal{E}) required to remove the top layer is given by

$$\mathcal{E} = \int F \cdot v dt \quad (7.1)$$

where F is the instantaneous measured force, v is the velocity of the shearing tip, and t is time. This allows not only the force (strength) of the part to be measured, but also the work in removing the top layer of the material, showing how brittle the material is. This test is intended to be similar to the shear bond strength test used for dental composites. [328] This is done in place of the standard tensile test due to the small sample treatment area available using the array electrode.

In addition to the testing for the shear bond test, the plasma was characterized spectroscopically using the Ocean Optics modular spectrometer (see Section 3.4.1.3 for spectrometer details). No

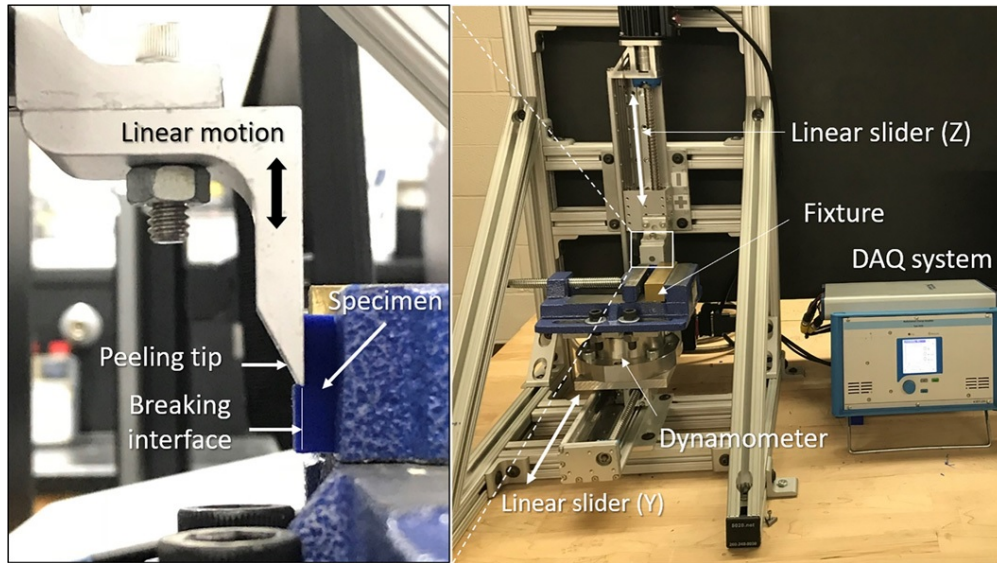


Figure 7.4: Image of the Custom Designed Shear Bond Test Apparatus (Reprinted with Permission from Shih, et al. [16] © 2018 Elsevier B.V.)

current or voltage measurements were taken due to the inability to measure the fast pulsing of the FID power supply (see Section 3.2.1.3 for power supply details).

7.4.2 Device Characterization Results

All of the interpretation of these results presented here is the author’s work. Further data and results are presented in the paper, most notably microscopic observations of the various treatments, which show stress whitening (crazing) of the plasma treated surfaces. “Stress whitening occurs when thermoplastic polymers are under an excessive tensile load, which causes the formation of microvoids due to the movement of molecular chains, thus changing the material refractive index.” [16] This supports the hypothesis that the plasma treatment increased the surface bonding between the layers, especially as this did not occur in the polished and control cases.

7.4.2.1 Mechanical Results

All trials for each case are plotted in Figure 7.5. Not only is there a substantial increase in the maximum force required to remove the top layer for the unpolished plasma treated samples (see Figure 7.6), the force is also much greater at longer times as well. The fast drop in the

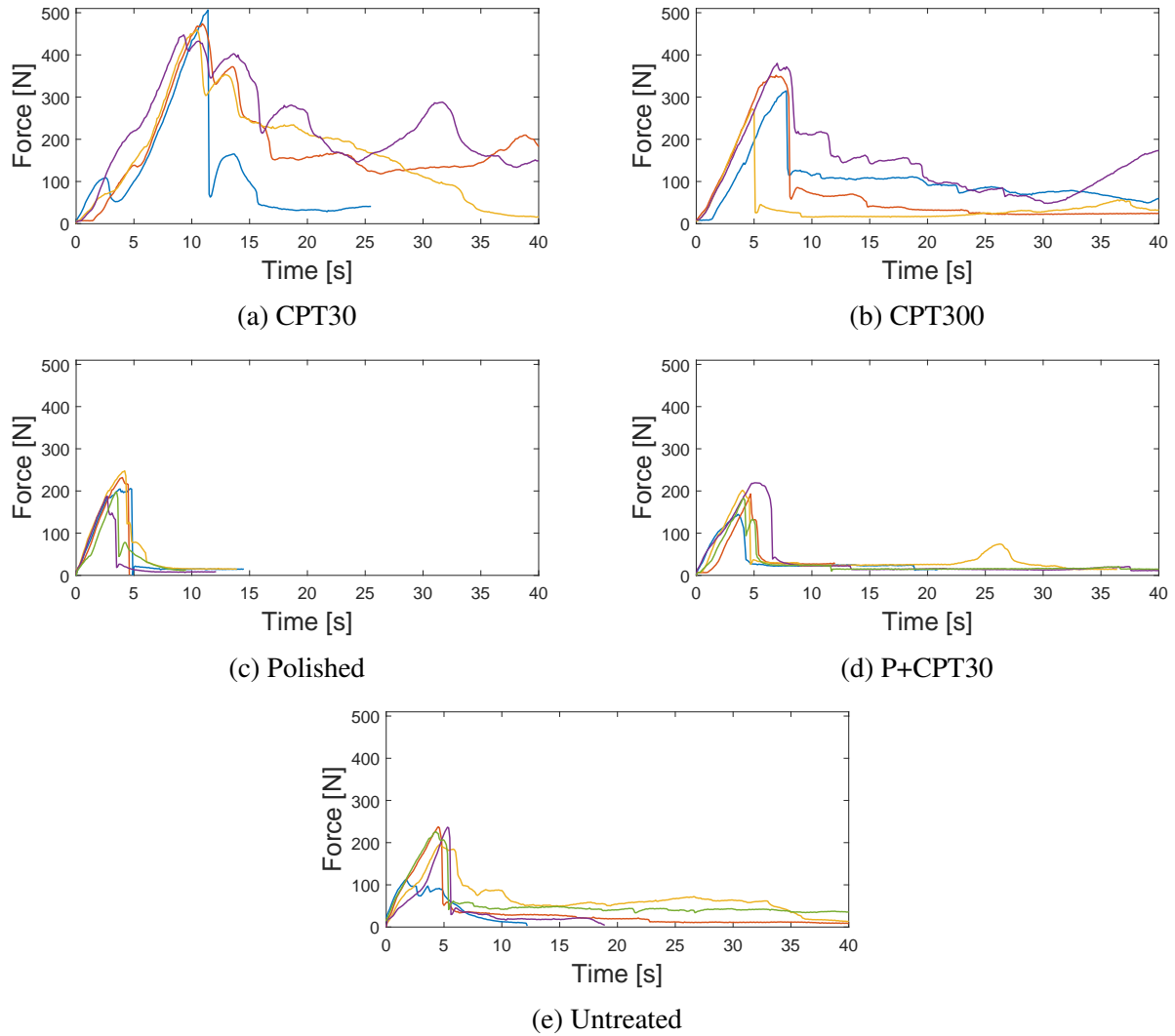


Figure 7.5: Force vs. Time Plots from the Shear Bond Test for All Test Conditions

required force for the untreated and polished cases suggests that brittle fracture occurred with a fast crack propagation along the interface. The plasma treated cases showed higher toughness, requiring a larger force throughout the duration of the test. The peak force required is shown in Figure 7.6, where the unpolished plasma treated samples have a significantly higher peak force compared to the untreated control samples ($p = 3.3662 \times 10^{-5}$ and $p = 0.0068$ for the 30 s and 300 s treatments, respectively), while neither of the polished cases are statistically different from the untreated control.

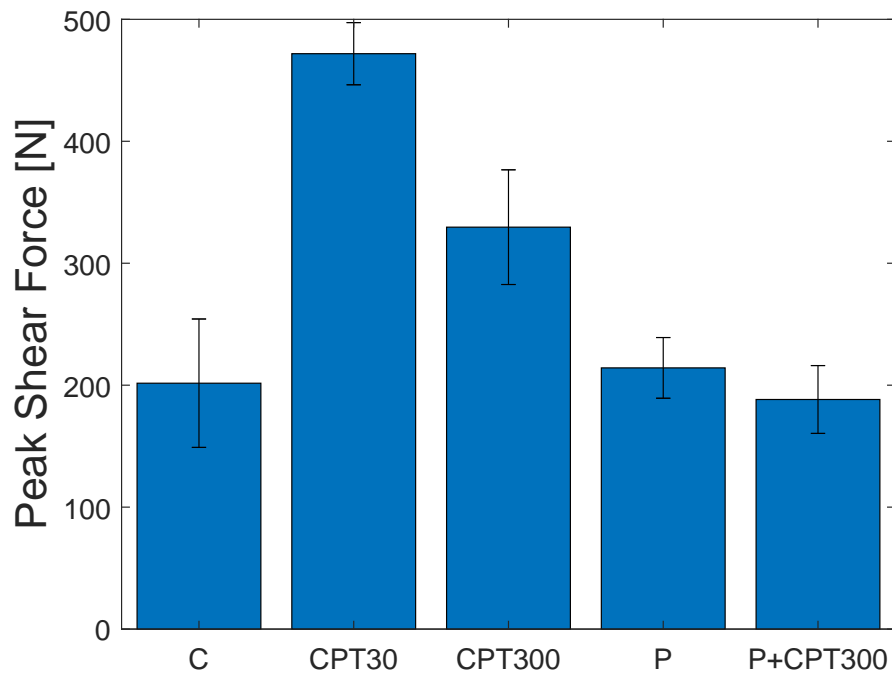


Figure 7.6: Bar Chart of the Required Shear Force to Remove the Top Layer (Error Bars are Standard Error)

Two other interesting results were noted. First, longer treatment times did not improve the bonding strength; rather longer treatment times resulted in worse results. The effect for this is not readily evident and is the subject of further ongoing research and hence not in this dissertation. The second interesting result was the effect of polishing the surface. Polishing showed similar peak forces as the untreated control, but had a faster fracture, suggesting that polishing may reduce the bonding toughness. Even further, combining the two effects (polishing and plasma treatment) had no significant effect.

There is considerably more variability in examining the total work done on the block until fracture occurred compared to the peak force. This work is shown in Figure 7.7, where only the 30 s plasma treatment is statistically different from the untreated control case ($p = 0.0052$). This mostly has to do with the time until fracture occurred. For the polished samples fracture occurred very quickly, while for a few of the unpolished plasma treated samples fracture only occurred after

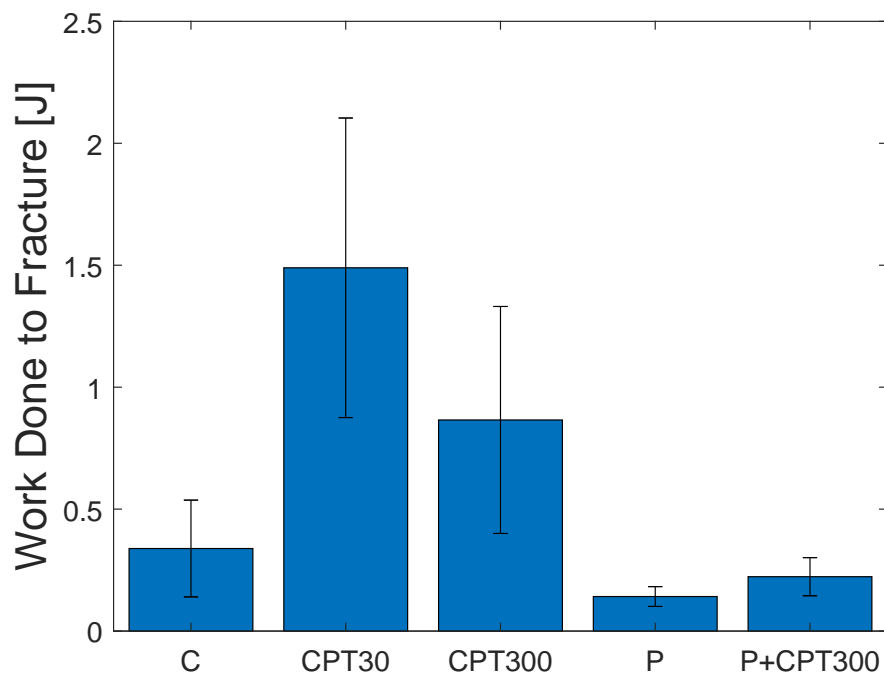


Figure 7.7: Bar Chart of the Work Done Until Fracture of the Top Layer (Error Bars are Standard Error)

the tip had sheared the entire top layer off. As noted in Figure 7.5, all of the polished samples either fractured off early (all polished samples) or had very little required force at later times (most polished and treated samples) suggesting only a small area had not fractured. There was greater variability in the other three cases, where one or more samples fractured significantly early, while some samples did not, requiring substantially more force at later times, suggesting a much higher surface energy. Further work is needed in this area to better characterize the initial surface energy as well as the effect of the plasma on increasing the surface energy, mostly to reduce the error or better characterize its source in the data of Figure 7.7.

7.4.2.2 Plasma Characterization

Due to the fast rise time of the power supply, all plasma characterization is optical in nature, since no equipment is able to adequately capture (i.e time resolve) the waveform of the FID power supply (see Section 3.2.1.3 for more details). Broadband spectra is shown in Figure 7.8 (see Sec-

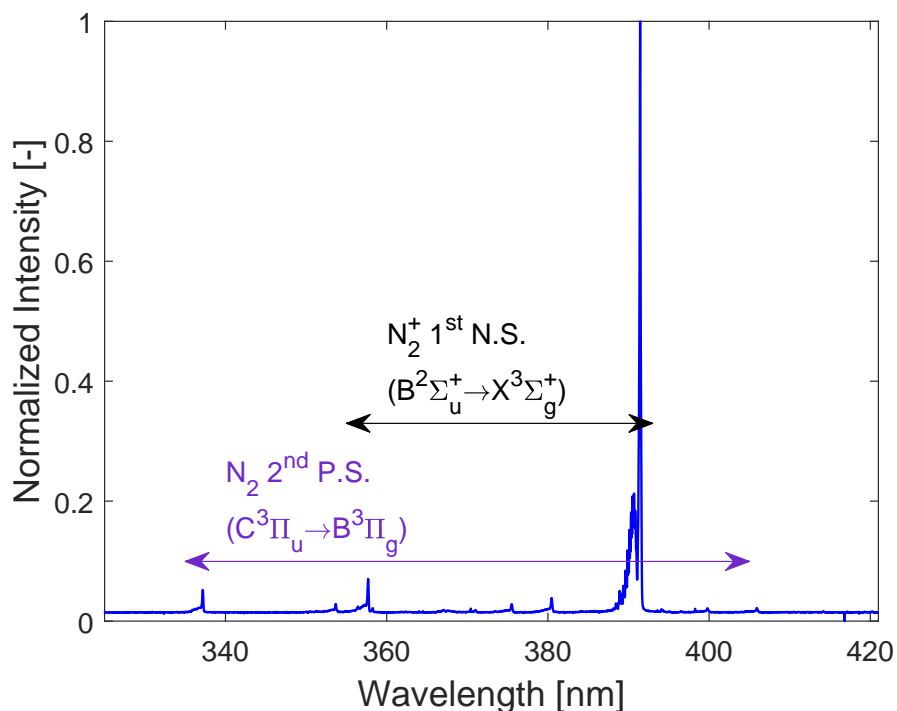
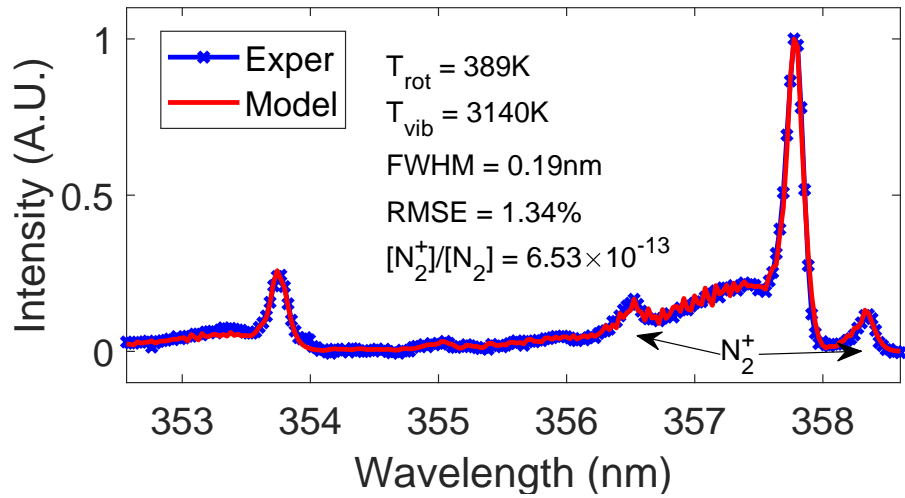


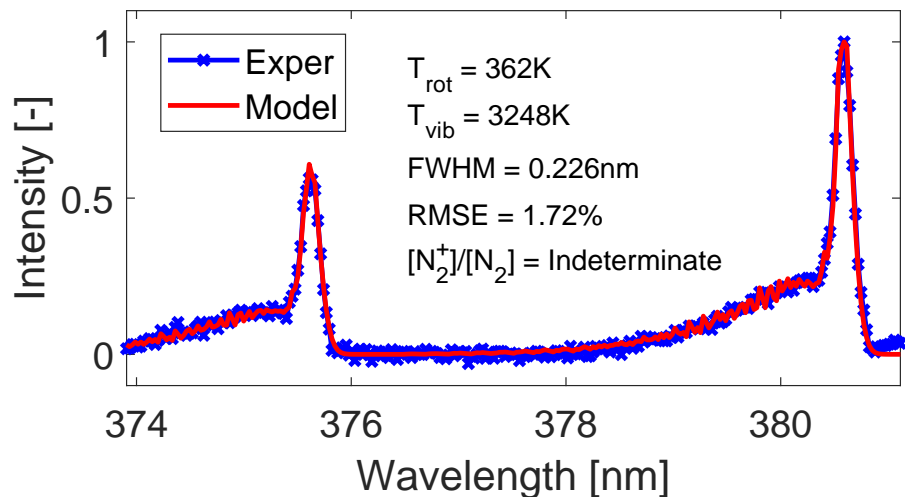
Figure 7.8: Broadband Spectrum from the Nanosecond Pulsed System for AM

tion 3.4.1.3 for details on the spectrometer). Only N_2 and N_2^+ lines are noted. Interestingly the bright helium line at 389 nm is not noted, but the spectrum is primarily dominated by N_2^+ . Broader spectra would most likely show other helium lines, just as a broader spectrum in Section 4.5.1.2 for a very similar setup showed many other species, including He, OH, and NO. Two different mechanisms could explain the large presence of N_2^+ , Penning ionization with helium and electron impact ionization (see Section 2.2.2.2 for explanation of these processes). It is assumed that Penning ionization is the dominant mechanism due to the large presence of helium ($\sim 100\%$ of the gas exiting the array is helium). Although it is also possible that electron impact ionization due to a large T_e caused by the fast application of the electric field is present, which would also cause ionization of N_2 . Without other evidence, such as multiple helium lines from which T_e may be approximated, the mechanism cannot be determined.

The spectra was also modeled for temperature fitting of the discharge, which is shown in Figure 7.9 (see Section 3.4.3.2 for information on the temperature fitting code). The gas temperature



(a) 356 nm Band



(b) 379 nm Band

Figure 7.9: Spectra with Temperature-Fitted Modeled Spectra from the Nanosecond Pulsed System for AM

(approximately T_{rot}) is quite low, which is to be expected for such a short pulsed DBD discharge primarily in helium to a dielectric substrate. The vibrational temperature (T_{vib}) is substantially higher showing the discharge to be highly non-equilibrium. This choice of wavelength range in Figure 7.9b was deliberate to ignore the contribution of N_2^+ , as no N_2^+ lines are in this range. The second range used in Figure 7.9a has peaks corresponding to N_2^+ . It is quite possible that the N_2 is not at the same temperature as N_2^+ due to different excitation methods between them; N_2 is predominantly excited by electron impact ionization, while N_2^+ is created by Penning ionization with helium. Since SpecAir cannot assign different T_{rot} and T_{vib} to the different species, it is best to use the wavelength range where there are not N_2^+ peaks. Nevertheless, in this case the two result in temperatures that do not differ from each other, being within the error of this method. This is due to the small influence of N_2^+ in the 356 nm band; other wavelength ranges with larger peaks of N_2^+ would differ more significantly.

7.5 The FlashFuse System

The FlashFuse system was developed at Essentium, Inc. in conjunction with Texas A&M University, from which the company was created. This system is an example of a production-ready system of integrating a plasma with a 3D printer for strength improvement of additively manufactured parts.

7.5.1 System Description

The FlashFuse system uses a DBD mounted to the head of a 3D printer to heat up polyamide (PA) filaments that have carbon nanotubes (CNTs) added to them. A schematic of the system is shown in Figure 7.10 and an image is shown in Figure 7.11. The system uses a custom-designed high voltage AC power supply that is integrated into the control system of the 3D printer. This system is designed to minimize the EMI generated to avoid disruption to the 3D printer's electronics. The goal is to generate a "warm" DBD discharge to keep the printed part heated near or above the glass temperature of the polymer so that sufficient time is allowed for increased mobility of the polymer chains to cross the boundary between the previously printed layers and the new

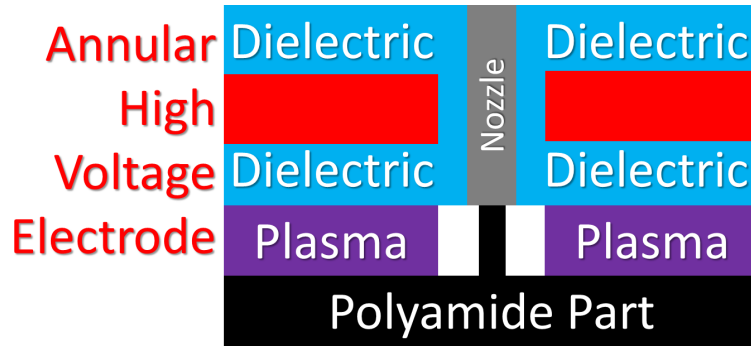


Figure 7.10: Schematic of the FlashFuse System

layers just extruded onto the part. If the DBD is too hot this can lead to undesired warping of the part from excessive melting of the polymer; if the DBD is too cold insufficient polymer chain movement in the welding process will occur leading to a weaker printed part. To ensure more even heating the polymer is mixed with a small amount of carbon nanotubes that will couple with the high frequency electric field leading to volumetric heating of the part via Joule heating. Higher heating will occur in the region with the highest electric field, as expressed by the equation for Joule heating

$$d\dot{Q} = j \cdot E dV = \frac{1}{\rho} E^2 dV \quad (7.2)$$

where $d\dot{Q}$ is the differential volumetric heat generation in the differential volume dV of the printed part, j is the local current density, E is the local electric field, and ρ is the local resistivity of the printed part caused by the carbon nanotubes. It should be noted that the small amount of carbon nanotubes does not impact the overall material properties (yield strength, elastic modulus, etc.). [49]

The high voltage electrode is an annular electrode that fits around the nozzle of the 3D printer and is fully encased to minimize the risk of electrical shock. For the purposes of characterization, a minimum setup was used, as shown in Figure 7.12. A high voltage feedthrough was created to allow voltage measurements. Current measurements were taken by a current transformer on the ground return path. Care was made to ensure a single ground path through the printed part existed, rather than multiple potential paths as may exist in the full system, such as a secondary discharge

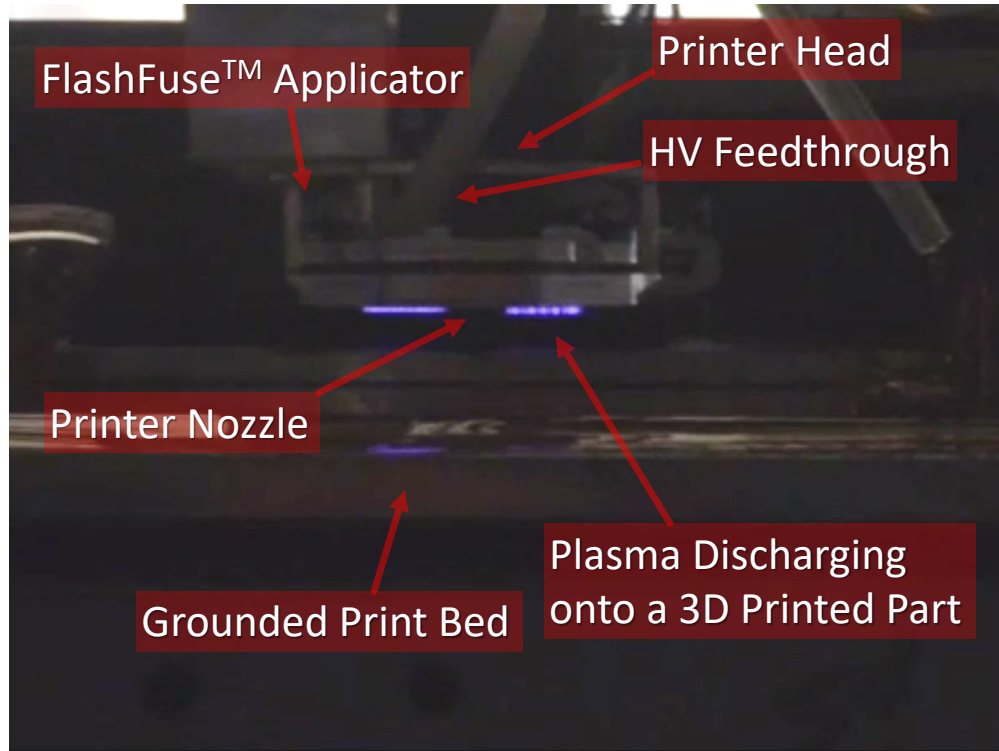


Figure 7.11: Image of the FlashFuse System Running In Situ

to the grounded printer nozzle, through the printed part and the print bed, or through the filament that is being extruded. Optical access was available via a fiber optic cable.

7.5.2 Device Characterization Results

The plasma characterization was done by the author; the material results were done by the coauthors on the resulting paper [17], namely members of Dr. Micah Green's lab or employees of Essentium, Inc.

7.5.2.1 Voltage and Current Characterization

The measured voltage and current for the FlashFuse system are shown in Figure 7.13. Note that some of this voltage is dropped across the additively manufactured part in addition to the plasma; nevertheless, care was taken to avoid an excessive distance through the part before the ground electrode to minimize the additional resistive drop through the part. As is characteristic of DBDs the voltage is roughly sinusoidal with a frequency of 15.4 kHz, though a notable drop is

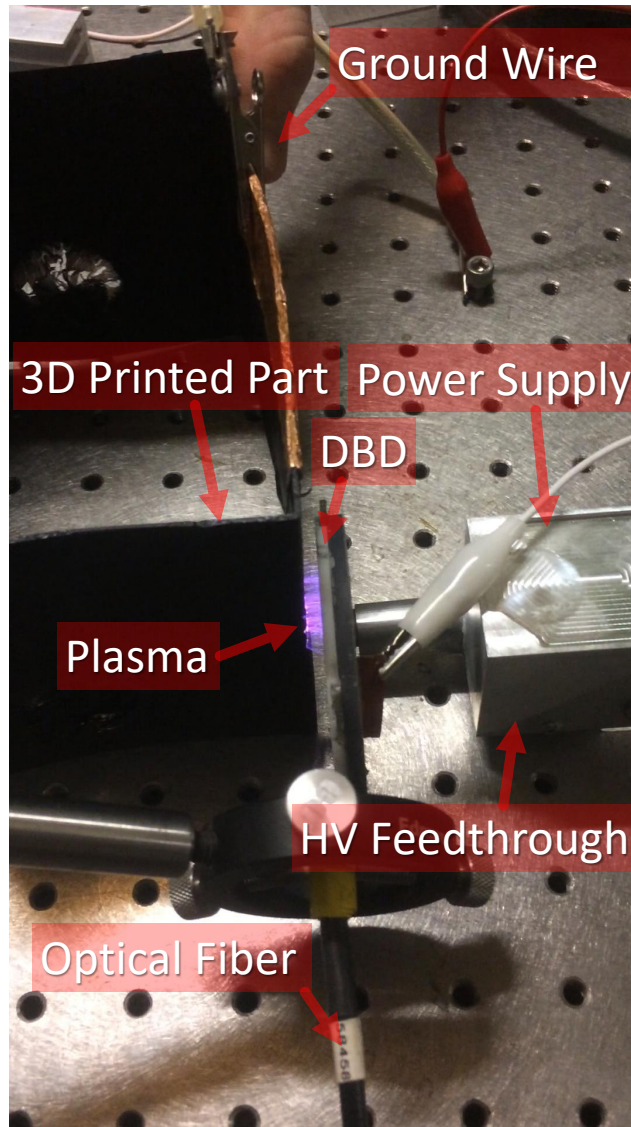


Figure 7.12: Image of the FlashFuse System as a Bench Top Setup

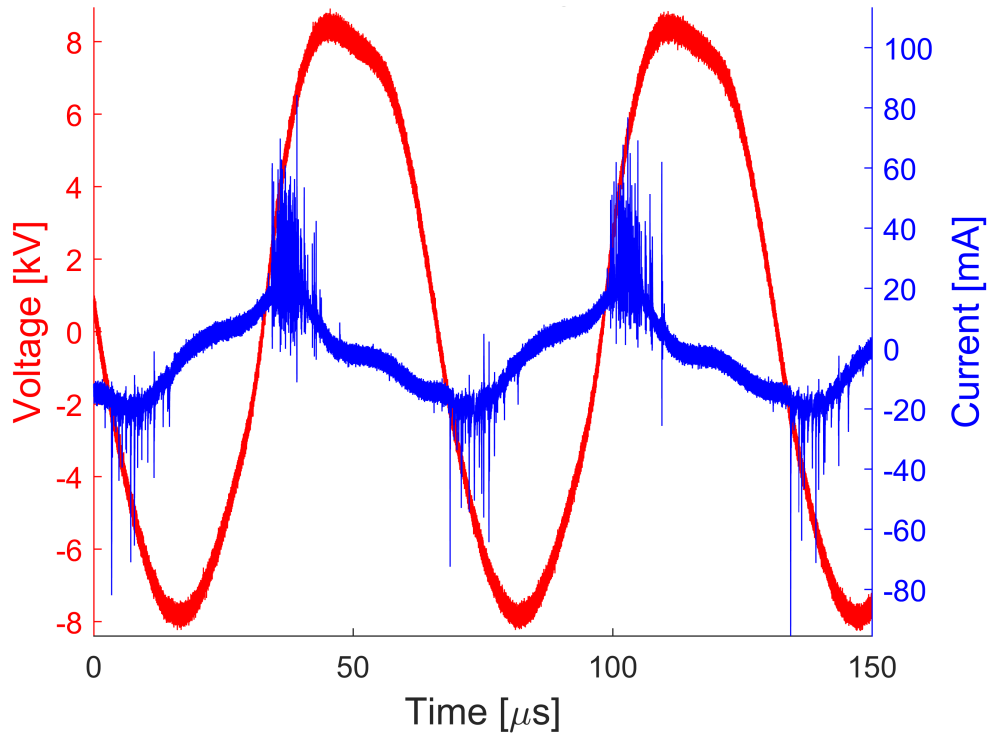


Figure 7.13: Voltage and Current Traces of the FlashFuse System

seen near the peak in the upper half of the sine wave. This is most likely due to an excessive power draw from the circuit beyond what the power supply is able to provide, leading to distortions in the waveform. Some asymmetry is expected since there is asymmetry in the geometry; there is a dielectric on one side of the gas gap, while there is a resistor on the other side, thus this system is partially a DBD and partially an RBD. Many current spikes are noted superimposed on a roughly sinusoidal current trace. The spikes are the individual microdischarges noted in the image of the setup (Figure 7.12).

The current trace can be integrated to yield the charge. Plotting the charge against the voltage yields a Lissajous figure, as shown in Figure 7.14. This figure allows for easier interpretation of a number of system parameters. The Lissajous figure is a parallelogram, where the rounded corners are more characteristic of a resistive discharge. [216] Since this discharge has a resistive barrier as one electrode (the printed part) some rounding is expected. The system total capacitance without a discharge (series capacitors of the dielectric barrier and the air gap) is the slope of the curve on the

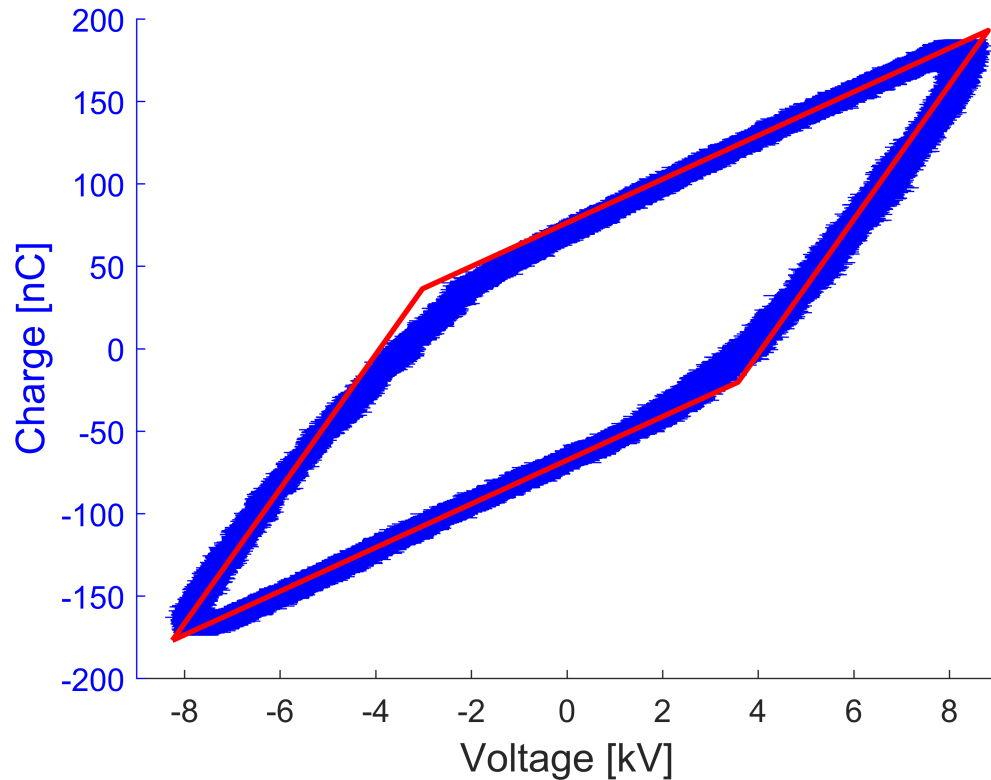


Figure 7.14: A Lissajous Diagram of the FlashFuse System, Corresponding to the Voltage and Current Traces in Figure 7.13

top and bottom of the parallelogram, measured to be 13.4 pF; the slopes of the left and right side of the parallelogram are the system's capacitance with a discharge (primarily from the dielectric barrier), measured to be 40.2 pF. The energy dissipated per cycle is found by the area enclosed inside of the parallelogram, measured to be 1.92 mJ, yielding a power of 29.6 W when multiplied by the frequency of the power supply. It is expected that the power density of 1.29 W/cm^2 (the power divided by the electrode area) will remain constant during the printing process, but this has yet to be verified. In addition, the power supply is designed to deliver a specified power, thus the voltage and frequency will be modulated by a microcontroller with a feedback loop to ensure the average power remains constant.

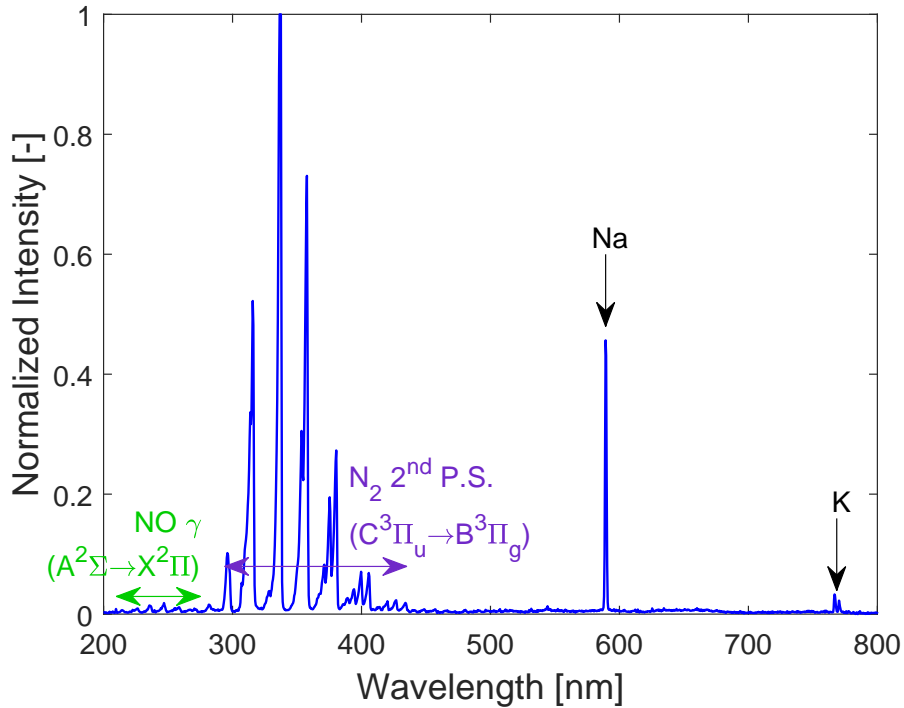


Figure 7.15: Broadband Spectrum of the FlashFuse System

7.5.2.2 Spectroscopic Results

The broadband optical emission spectra is shown in Figure 7.15 using a broadband spectrometer (see Section 3.4.1.2 for details on the spectrometer). Since this is a discharge in air, it is not surprising that the main constituent noted is N_2 . No N_2^+ was noted, although $NO \gamma$ was seen. Interestingly both sodium and potassium are observed, but these are assumed to be an impurity from excessive handling of both the additively manufactured part and the dielectric barrier.

The rotational temperature (T_{rot}) was determined spectroscopically (see Section 3.4.1.1 for the spectrometer details and Section 3.4.3.2 for the temperature fitting algorithm details) to be 598 K, and the vibrational temperature (T_{vib}) was determined to be 4244 K. The fitting for these temperatures is shown in Figure 7.16. To show the goodness of fit, the grey spectra plotted in the insets are modeled spectra with $T_{rot} \pm 200$ K and $T_{vib} \pm 500$ K. These show that increasing or decreasing the temperatures by those amounts leads to a clearly poorer fit. To better quantify the

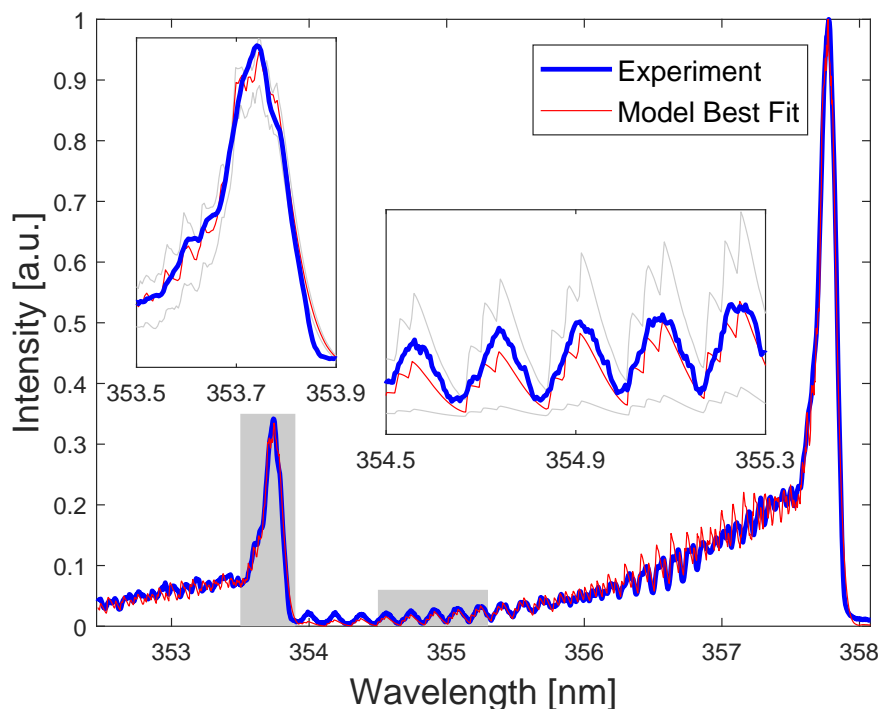


Figure 7.16: Spectrum (Blue) with Temperature Fit (Red) of the FlashFuse System, Noting the Temperatures of the Discharge are Approximately $T_{\text{rot}} = 598 \text{ K}$ and $T_{\text{vib}} = 4244 \text{ K}$ (Model Fits in Grey of $T_{\text{rot}} \pm 200 \text{ K}$ and $T_{\text{vib}} \pm 500 \text{ K}$ are also Shown)

error, the root mean squared error of the fit is plotted in Figure 7.17 as a function of the rotational and vibrational temperatures. This gives bounds on the fit that are on the order of 50 K for the rotational temperature and on the order of 400 K for the vibrational temperature, which is the approximate error of this technique. [224]

7.5.2.3 Material Property Results

X-ray photoelectron spectroscopy (XPS) was performed on a sample from the FlashFuse system. The results are shown in Figure 7.18. The main change was the increase of the nitrogen (N1s) concentration from ~ 0 to 5.7% due to the plasma. Oxygen (O1s) also increased slightly from 11.8% to 12.7%, while carbon (C1s) correspondingly decreased from 88.2% to 81.6%. This is interesting as PA is partially composed of nitrogen (the amide component of the structure, which is of the form $\text{RC}(=\text{O})\text{NR}'\text{R}''$), but no nitrogen component is noted in the control sample. The

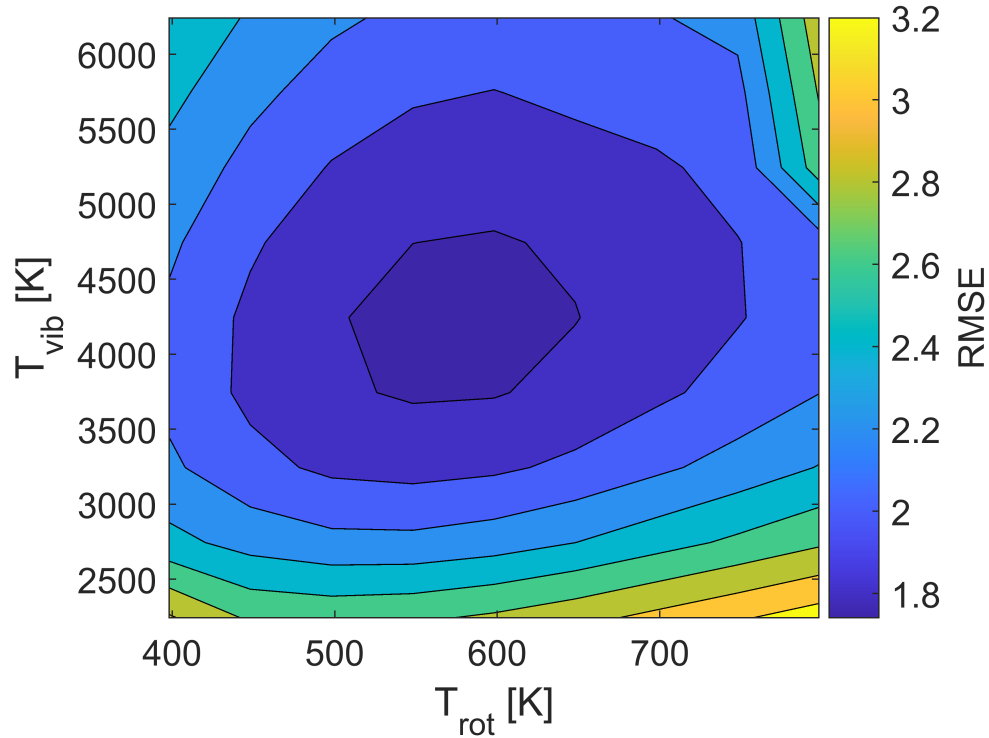


Figure 7.17: Plot of the Error Associated with the Temperature Fit Shown in Figure 7.16

plasma likely modified some surface bonds to allow nitrogen to appear in the treated spectrum.

Using the IR cameras, the temperature of the print was measured as a function of the z height. Figure 7.19 shows that the temperature of the printed part is substantially higher than glass temperature of PA (40–60°C) and close to the melting temperature of the polymer (189°C) for the DBD heated case. Since the degree of welding increases with increasing temperature, this large increase in temperature at least partially, if not wholly, explains why there is improved bonding between layers.

The material properties were enhanced compared to a control part, as shown in Figure 7.20. The tensile strength and elastic (Young's) modulus are nearly identical. The only material property that was not achieved to be the same as an injection molded part is the elongation at break, suggesting a more brittle fracture. Interestingly, this is the opposite result from the nanosecond pulsed system, which found a less brittle break after plasma treatment (see Figure 7.5). Nevertheless, two different materials (PA vs. PLA) and systems were used.

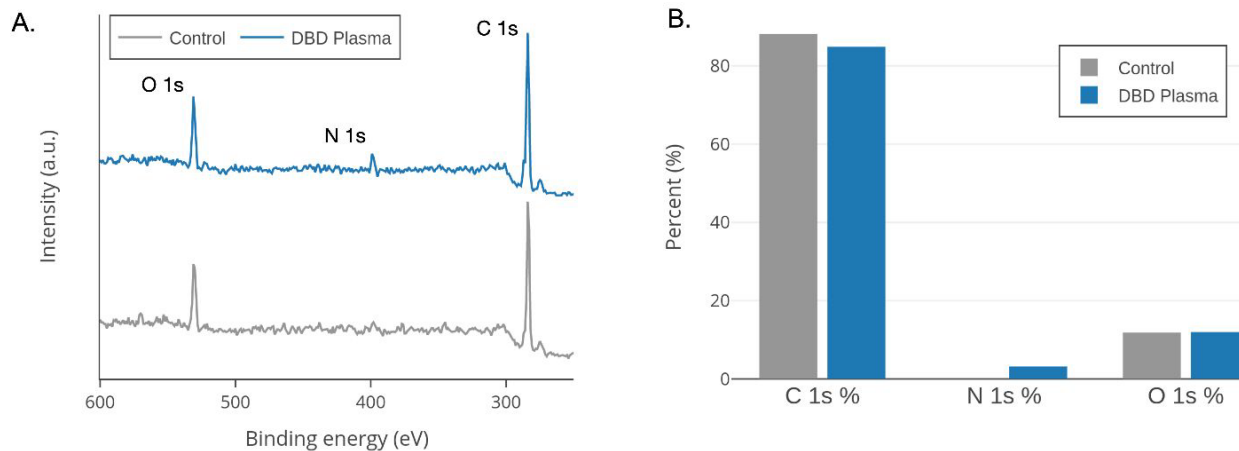


Figure 7.18: XPS Survey Spectrum of the Polymer Surface with (DBD Plasma) and Without (Control) the FlashFuse (DBD) Treatment and the Relative Atom Percentage of the Observed Species (Reprinted with Permission from Sweeney, et al. [17] © 2020 American Chemical Society.)

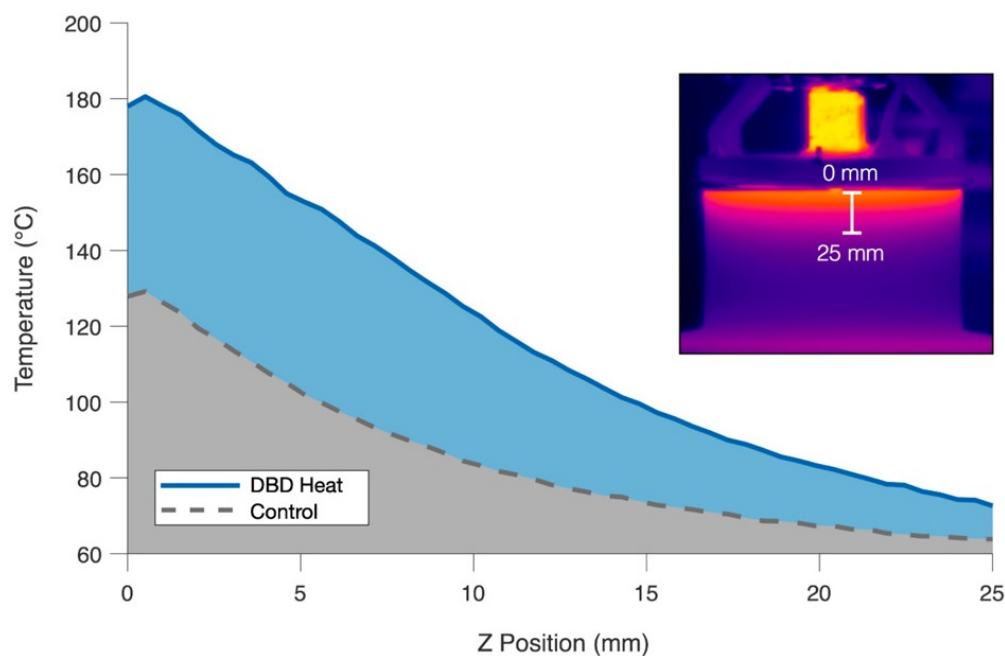


Figure 7.19: Temperature Plot of the Partially Printed Part as a Function of Z Height with Flash-Fuse Treatment (Reprinted with Permission from Sweeney, et al. [17] © 2020 American Chemical Society.)

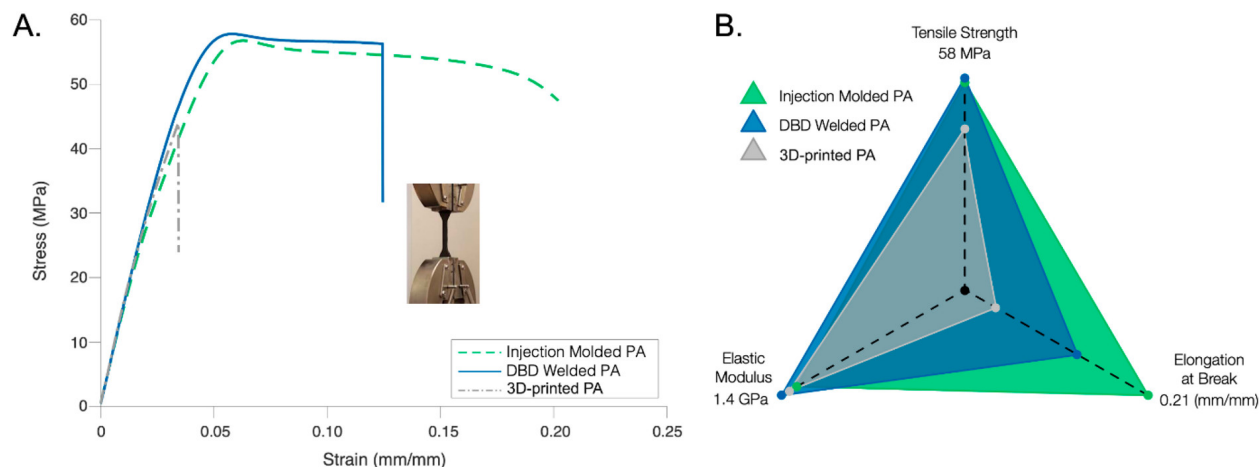


Figure 7.20: Stress-Strain Curve and Radar Chart Showing Some Material Properties of the DBD Welded Part Compared to a Control and Injection Molded Part (Reprinted with Permission from Sweeney, et al. [17] © 2020 American Chemical Society.)

7.6 Chapter Summary & Future Work

This chapter investigated two plasma systems that improve the strength of additively manufactured parts. Both systems show a large improvement in the strength of the parts, which can be used for prosthetics among a variety of other applications. This application is already being used for the FlashFuse system.

The exact mechanism for plasma improving the adhesion between the layers is unknown; this is the subject of ongoing research for the nanosecond pulsed system, while substrate heating appears to be one of the dominant mechanisms for the FlashFuse system.

From a design point of view, these systems are the easiest for medical devices since the plasma does not directly contact the patient; as such prosthetics are Class I devices not even requiring a 510(k) for approval. Nevertheless, further development is needed in these systems. Fully understanding the mechanism for strength improvement can lead to a more tailored plasma to optimize the strength improvement. For the nanosecond pulsed system, the plasma process needs to be integrated into the 3D printer as the FlashFuse system is to create a single process.

8. CONCLUSIONS & FUTURE WORK

8.1 Conclusions

Developing a low temperature plasma medical device is a complex initiative, requiring knowledge of how the plasma behaves and how that behavior can be leveraged for medical benefit. In addition, any given design must undergo extensive testing from the bench top to clinical trials to verify the system works as intended and validate that the design is achieving the desired medical results. Currently there are five devices in Germany that have received a CE marking and are thus approved for medical use. However, there are currently none approved by the US FDA. This is due in part to the stricter approval process of the FDA compared to the CE marking, which requires substantial proof of efficacy in addition to safety leading to more extensive clinical trials being required, as well as the number of universities in Germany that are at the forefront of the field of plasma medicine. Nevertheless, there are a number of companies attempting to produce a low temperature plasma medical device for the US market.

This dissertation addressed how to design low temperature plasma devices for the medical field, attempting to answer the question: *How can a low temperature plasma medical device be developed effectively in the US?* The biological aspects of the design were not the focus, which are nonetheless crucial to the overall development; rather an engineering approach and a more holistic view were taken. Four different aspects introduced for plasma medical devices were specifically examined in some detail:

1. **Device development** was examined at a more holistic level for the various devices considered. This was more speculative for these devices as nearly all of them (the FlashFuse being the only exception) are very early in their development. Nevertheless, potential issues were predicted and addressed, such as including substantial high voltage shielding for safe operation. Mostly these devices suffered from not having a clear indication to treat, leading to broader developmental considerations, rather than focusing on specific issues that would

become apparent when a specific indication is sought to be addressed. Many of these issues would become apparent in the verification and validation steps in the design process.

2. **Regulatory approval** drives the direction these devices must take in their development. The main driving force in regulatory approval is the intended use of the device. For some of these devices, the intended use can be narrowed to that of existing devices, allowing a 510(k) clearance for quicker approval. Nevertheless, some testing must be done to assure that the technological characteristics of the plasma do not raise any new questions on safety and efficacy. For other systems, a clear predicate device may not exist. Seeking a De Novo request is the clearest path forward for these devices.
3. **Plasma characterization** was successfully completed on all of these devices. All showed themselves to be non-equilibrium plasma discharges, most of them also meeting the definition of CAP systems (again the FlashFuse being an exception). In general, few unusual species were noted, with the exception of NO for some of the systems when flowing helium, but further testing is required to determine if other species, such as ozone, are generated and if they may be produced in quantities near or above regulatory limits. Voltage and current characterization was also conducted to minimize the amount of current flowing through into a patient.
4. **Biocompatibility**, at least at a cursory level, was sought in the characterization. Current was minimized whenever possible, predominantly by using dielectric barriers or fast pulsing to limit full development of the discharge. The discharge temperature was also sought to be minimized, mostly staying near ambient. Generally heating of the substrate was not noted; however, no histological studies were conducted to determine if thermal damage did occur. In regards to chemical species biocompatibility was neither well maintained nor satisfactorily measured. In some cases, NO was measured in the plasma emission spectrum but an absolute measurement was not obtained to determine if the levels generated poses a hazard. In addition, solvents such as methanol were used for their ease-of-use, rather than seeking to

determine a biocompatible alternative.

Specifically these four areas were addressed examining five different devices. The following subsections will explore the lessons learned from each device.

8.1.1 Electroporation System

The electroporation system is an interesting example of a combination product, where the plasma system assists in drug delivery by opening pores in the treated cells. Due to potential plasma-drug interactions this becomes a complex approval process, requiring an extensive amount of testing to receive regulatory approval.

The electrode and power supply were designed to maximize the electric field delivered to the substrate. This was achieved by having an array of sharp tips to create a locally higher electric field, using a short pulse duration to overvoltage the gap without undergoing a complete breakdown, and choosing a gas that should maximize the electric field during the discharge process. This device displayed very interesting and unusual behavior in being substrate invariant for a wide range of conditions. This is due to the short pulse duration of the system creating an incomplete breakdown of the discharge gap regardless of the conductivity of the substrate used.

8.1.2 Modified Electrosurgical System

A Bovie electrosurgical generator was modified to generate a low temperature plasma by adding a small tube around the electrode with helium gas flow. This provided a narrow operating regime where a low temperature plasma could be generated without overvolutaging the electrosurgical generator. The behavior was found to be similar to existing laboratory plasma jets, where both a diffuse and concentrated mode of the plasma discharge exist. A brief inactivation study was conducted showing that the modified electrosurgical generator is capable of inactivating *E. Coli* and *A. Flavus*.

Nevertheless, the original goal of being able to use a modified existing device for a faster approval process was flawed. This is because the intended use of the device is the driving factor for approval through the FDA. Since the modified system has a different intended use of microbial

inactivation compared to the existing system's intended use of tissue destruction or coagulation. This eliminates the 510(k) process using the current FDA approved systems as the predicate device. Unless a suitable predicate is found that uses different technological characteristics, a De Novo request is the best option, which will take substantially longer than a 510(k) clearance. Instead of using a modified existing device, a better system could be developed to better meet the new intended use.

8.1.3 Direct Write System Using a Plasma Jet

The direct write system was developed by modifying a 3D printer to use a DBD jet instead of thermoplastic. Due to the change in use, different patterning is required to achieve equal area treatment. It was found that the optimal patterning has to account for the speed of the printer head, the rate of deposition, the size of the plasma-treated area, and the desired treatment area. Nevertheless, this system is capable of creating a wide variety of films, from metallic copper to various polymers. Initial testing was done to create uniform films of both copper and a silane polymer on various substrates.

The economics of this system still need to be determined. Currently the two main intended uses, sprayable bandages and epidermal electronics, have cheaper alternatives. This requires finding a niche market that cannot be served by the alternatives to spur funding for the development of this system.

8.1.4 Nanosecond Pulsed System for Additive Manufacturing

The array developed in the electroporation chapter was used with helium to treat the surface of additively manufactured parts. This initial testing with a nanosecond pulsed helium plasma showed more than 100% strength improvement in the adhesion of a subsequently deposited thermoplastic layer using a shear bond test. This effect is not explained by increased wetting of the treated layer, since a polishing treatment which greatly improved the wettability did not increase the strength. Interestingly, longer treatment of 300 s compared to 30 s reduced the strength improvement. Further testing is underway to elucidate the mechanism for the strength improvement.

8.1.5 The FlashFuse System

The FlashFuse system was developed with Essentium, Inc. to create an in situ process of improving the strength of additively manufactured parts containing carbon nanotubes. The system is a DBD mounted around the nozzle of a 3D printer, where the ground electrode is the additively manufactured part, which is conductive due to the embedded CNTs. This system was able to print and plasma treat simultaneously, thermally welding the parts together. The plasma treated parts have the same tensile strength and elastic modulus as injection molded parts, just with a smaller elongation at the breaking point. This system is currently being used to create prosthetics in conjunction with TriFusion Devices, a subsidiary of Essentium, Inc.

8.2 Future Work

There is currently no low temperature plasma medical device approved by the FDA. As such there is still a tremendous amount of work to be done in developing such a device and even getting the existing systems currently being used in Germany to be used in the US. There are a number of companies working toward this goal, as mentioned in Section 2.5.2. However, most of this work will not become public until (or unless) the company becomes successful in marketing their device.

Nevertheless, there are a number of potential uses for low temperature plasma devices, which will certainly spur innovation in this field. The main question is whether the plasma offers a substantially better efficacy or cost compared to the existing treatment. This is questionable for many of the wound care treatments, where existing chemical treatments are already cheap and effective. Ultimately the market will determine if this is a viable treatment option for CAP. Cancer treatment currently appears to be the best option for CAP. There are no highly effective alternatives. Chemotherapy often has a number of undesirable side effects, so if CAP could be used in lieu of or in addition to the existing treatments to improve outcomes this would offer a substantial benefit.

For the individual systems explored in this dissertation, the future work to be done is explored in the following subsections.

8.2.1 Electroporation System

Electroporation is most likely going to be used in a combination product—using a device and drug/biologic to generate the desired effect. This is currently being investigated in our lab as a way of introducing new genes (a biologic) to plants, but the obvious reluctance of using gene therapy in humans means that this application of electroporation is going to be quite difficult for clinical practice. Nevertheless, the FDA has starting approving gene therapy, so this application may come sooner rather than later as an alternative to using viral vectors. [239] The other main use would be to insert a drug into cells as is done currently in electrochemotherapy. Either way, the FDA is going to require strenuous testing for approval to ensure there are no unintended plasma-drug interactions.

This system needs further testing to ensure minimal current is introduced to the patient and over what ranges of voltages and pulse duration a sufficiently low value is maintained. Further characterization of the electric field is desired. Since this is difficult to do experimentally, modeling of the system can be done computationally to determine the applied electric field.

8.2.2 Modified Electrosurgical System

The Bovie system tested in this dissertation could use some more design work to integrate the gas flow into the existing electrosurgical power supply; however, the J-Plasma system already has helium gas flow integrated into its design, removing the need for further design on that specific system. Further bench top testing is needed to determine how effective this exact system is beyond the single study done so far, [265] especially compared to existing marketed systems such as the kINPen MED plasma jet. Nevertheless, these existing systems have proven the technique; the J-Plasma would only be building off of their work in regards to their own device.

The FDA approach is fairly clear for this system; it is based off of a Class II device, thus unless a suitable predicate can be determined, the De Novo request is the clearest course of action to have this type of system used for wound treatment. The main question is why has Bovie not pursued this already? Is the market not feasible for them—either through lack of expertise in that

subfield of medicine or lack of a compelling enough business model? Since the J-Plasma system has been sold by Bovie to Apyx Medical, [263] it seems most likely the company is not doing well from a business perspective and is thus not pursuing a risky development effort. However, the Canady Helios™ Cold Plasma Scalpel is an outgrowth from electroporation systems developed by the same company, and this device is currently in clinical trials. [149] No matter the reason, it is reasonable to expect this technology will be used in the US in the near future, whether it will be a Bovie or Canady system branching into a new market, a homegrown new device, or one of the German devices entering the US market.

8.2.3 Direct Write System Using a Plasma Jet

The basic applications that were examined for this work are already being explored for marketing in the US. Epidermal electronic systems are already in clinical trials, but are not a plasma based system. [304] A variety of liquid bandages already exist as Class I devices, while sprayable bandages are approved for veterinary use. The addition of a plasma opens up a variety of novel uses and narrow applications, such as in vivo writing of these films that the existing technology may not be able to achieve. However, that comes with the added cost and complexity of the plasma system, and a strong case would have to be made that the added complexity is economically feasible for a company to pursue.

Substantial development is needed for these systems. Copper deposition has been achieved, but other metals have not been printed using a similar DBD jet system. The rate of deposition will also need to be increased greatly for feasible use as a medical application. Especially for epidermal electronic applications, the flexibility of the deposited metal film needs to be established without loss of conductivity. The use of hydrogen as well may need to be reevaluated to determine if this is allowable from a biocompatible and risk-mitigation approach.

Though the TMEVS films have undergone some optimization for film deposition, the viability of this material as a bandage has not been conducted. The TMEVS films also did not adhere to the pig skin substrate very well, suggesting this material may not be the optimal material for use as a sprayable bandage. If further development of this material is found useful for a sprayable bandage,

significant optimization needs to be done to determine the best conditions for rapid deposition, which was not achieved in this system. In addition, the methanol solvent is not biocompatible due to the risk of methanol poisoning. A new solvent will have to be considered both from a biocompatible standpoint and a functionality standpoint in the plasma.

8.2.4 Nanosecond Pulsed System for Additive Manufacturing

Further work on the nanosecond pulsed plasma system for improvement of additive manufacturing is ongoing. This is primarily to determine the mechanism for improvement of the interlayer bonding that was observed, as well as determining why that improvement was reduced with longer plasma treatment time. The various hypotheses being tested are:

1. **Nanoscale roughness increase.** This is expected to improve bond strength by increasing the surface area for bonding to take place. This will be measured using atomic force microscopy (AFM), which uses a nanoscale-sized tip to probe the surface of a material, including rastering over a surface to produce a three dimensional map of the local surface.
2. **Oxidation of the surface.** This is expected to decrease the bond strength. This effect can be eliminated by running in an inert environment, either by running in a glove box or with a shroud gas to avoid the entrainment of ambient air during testing. Conversely, this can be increased by running in an oxygen rich environment, by running in an oxygen atmosphere in a glove box, using a shroud gas of oxygen, or adding an admixture of oxygen to the gas flow through the array. This can also be measured using X-ray photoelectron spectroscopy (XPS), which observes the elemental composition and bonding on the surface of a material.
3. **Surface functionalization.** This is expected to increase the bond strength by adding a number of radical sites that will bond to the next printed layer. This should be observable using XPS, by noting a change in the surface elemental composition (such as an increase in the nitrogen content) or a change in the bonds of the surface (such as reducing the number of carbon-oxygen double bonds in the PLA thermoplastic).

By determining the dominant mechanism for the bond strength improvement, the plasma source can be tailored to maximize that effect. This may require switching to a different plasma source. Further optimization can be done including switching to a more economically feasible power supply (the FID power supply used costs \sim \\$30,000, while comparable ones can cost \sim \\$100s instead, such as was investigated in Section 4.4.1), as well as other changes that may be able to make this system integrate into a build process, rather than having to stop the print for treatment (which took \sim 30 min for each single layer test—clearly not feasible for a system that consists of 100s to 1000s of layers or more).

Further, this effect has only been observed in PLA. There are many more thermoplastics used in AM, and each one needs to be explored to determine if the same effect occurs as well as to what extent the effect may occur.

8.2.5 The FlashFuse System

The FlashFuse system could use further exploration to determine the extent that surface modification affected the bonding strength. Though this was assumed to not be a dominant mechanism compared to thermal heating in the paper [17], the exact extent of this effect was not explored. This could be done by running in an inert environment, such as an argon or helium atmosphere, which would not react chemically with the surface. Again, a thermal camera could observe the heating effect and XPS can be used to ensure there was no significant surface chemistry occurring.

Further development is ongoing in Essentium, Inc. to improve the FlashFuse system, such as determining the best dielectric material, trying to balance the cost as well as the dielectric strength of the material. Unfortunately, since this is a proprietary technology, most of the new developments may not be made public or published in the open literature.

REFERENCES

- [1] A. Bogaerts, E. Neyts, R. Gijbels, and J. van der Mullen, “Gas Discharge Plasmas and Their Applications,” *Spectrochimica Acta Part B* 57, vol. 57, pp. 609–658, 2002.
- [2] Y. P. Raizer, *Gas Discharge Physics*. Heidelberg: Springer-Verlag, 1991.
- [3] U. Kogelschatz, “Dielectric-barrier discharges: Their History, Discharge Physics, and Industrial Applications,” *Plasma Chemistry and Plasma Processing*, vol. 23, no. 1, pp. 1–46, 2003.
- [4] P. L. Carter, “The life and legacy of William T. Bovie,” *American Journal of Surgery*, vol. 205, no. 5, pp. 488–91, 2013.
- [5] M. Laroussi, X. Lu, and M. Keidar, “Perspective: The physics, diagnostics, and applications of atmospheric pressure low temperature plasma sources used in plasma medicine,” *Journal of Applied Physics*, vol. 122, p. 020901, jul 2017.
- [6] M. Keidar, “Plasma for cancer treatment,” *Plasma Sources Science and Technology*, vol. 24, no. 3, p. 033001, 2015.
- [7] S. J. Beebe, J. White, P. F. Blackmore, Y. Deng, K. Somers, and K. H. Schoenbach, “Diverse Effects of Nanosecond Pulsed Electric Fields on Cells and Tissues.,” *DNA and cell biology*, vol. 22, no. 12, pp. 785–796, 2003.
- [8] R. Thirumdas, A. Kothakota, U. Annapure, K. Siliveru, R. Blundell, R. Gatt, and V. P. Val-dramidis, “Plasma activated water (PAW): Chemistry, physico-chemical properties, applications in food and agriculture,” *Trends in Food Science and Technology*, vol. 77, no. May, pp. 21–31, 2018.
- [9] R. López-Callejas, R. Peña-Eguiluz, R. Valencia-Alvarado, A. Mercado-Cabrera, B. G. Rodríguez-Méndez, J. H. Serment-Guerrero, A. Cabral-Prieto, A. C. González-Garduño, N. A. Domínguez-Cadena, J. Muñoz-Infante, and M. Betancourt-Ángeles, “Alternative

- method for healing the diabetic foot by means of a plasma needle,” *Clinical Plasma Medicine*, vol. 9, no. August 2017, pp. 19–23, 2018.
- [10] International Trade Administration, “Medical Technology Spotlight.” <https://www.selectusa.gov/medical-technology-industry-united-states>, 2020.
- [11] MarketsandMarkets Research Private Ltd., “Cold Plasma Market by Industry, Application, Regime, Region - Global Forecast to 2024.” <https://www.marketsandmarkets.com/Market-Reports/cold-plasma-market-187065928.html>, 2020.
- [12] US Food and Drug Administration, “The Device Development Process.” <https://www.fda.gov/patients/learn-about-drug-and-device-approvals/device-development-process>, 2018.
- [13] M. Burnette and D. Staack, “Development of a substrate-invariant 2-D array of nanosecond-pulsed streamer discharges,” *Plasma Research Express*, vol. 2, p. 015001, jan 2020.
- [14] T.-C. Tsai, K. McIntyre, M. Burnette, and D. Staack, “Copper film deposition using a helium dielectric barrier discharge jet,” *Plasma Processes and Polymers*, jun 2020.
- [15] T.-C. Tsai, *Plasma Enhanced Chemical Vapor Deposition Modeling*. PhD thesis, Texas A&M University, 2012.
- [16] C.-C. Shih, M. Burnette, D. Staack, J. Wang, and B. L. Tai, “Effects of cold plasma treatment on interlayer bonding strength in FFF process,” *Additive Manufacturing*, vol. 25, no. September 2018, pp. 104–111, 2019.
- [17] C. B. Sweeney, M. L. Burnette, M. J. Pospisil, S. A. Shah, M. Anas, B. R. Teipel, B. S. Zahner, D. Staack, and M. J. Green, “Dielectric Barrier Discharge Applicator for Heating Carbon Nanotube-Loaded Interfaces and Enhancing 3D-Printed Bond Strength,” *Nano Letters*, vol. 20, pp. 2310–2315, apr 2020.
- [18] H. M. Mott-Smith, “History of Plasmas,” *Nature*, vol. 233, p. 1971, 1971.
- [19] M. J. Moran and H. N. Shapiro, *Fundamentals of Engineering Thermodynamics*. John Wiley & Sons, Inc., 5th ed., 2006.

- [20] B. S. Liley, S. Potter, and M. C. Kelley, "Plasma." <https://www.britannica.com/science/plasma-state-of-matter>, 2019.
- [21] W. J. Vogel, H. Ling, and G. W. Torrence, "Fluorescent Light Interaction With Personal Communication Signals," *IEEE Transactions on Communications*, vol. 43, no. 234, pp. 194–197, 1995.
- [22] A. Fridman, A. Chirokov, and A. Gutsol, "Non-thermal atmospheric pressure discharges," *Journal of Physics D: Applied Physics*, vol. 38, no. 2, 2005.
- [23] F. Massines, N. Gherardi, N. Naudé, and P. Ségur, "Glow and Townsend dielectric barrier discharge in various atmosphere," *Plasma Physics and Controlled Fusion*, vol. 47, no. 12 B, 2005.
- [24] H. Raether, "Untersuchung der Elektronenlawine mit der Nebelkammer," *Zeitschrift für Physik*, vol. 107, pp. 91–110, jan 1937.
- [25] J. M. Meek, "A theory of spark discharge," *Physical Review*, vol. 57, no. 1934, pp. 722–728, 1940.
- [26] S. Lebedynskyi, O. Karpenko, R. Kholodov, V. Baturin, I. Profatilova, N. Shipman, and W. Wuensch, "DC vacuum breakdown in an external magnetic field," *Nuclear Instruments and Methods in Physics Research, Section A: Accelerators, Spectrometers, Detectors and Associated Equipment*, vol. 908, no. Clic, pp. 318–324, 2018.
- [27] D. Staack, B. Farouk, A. Gutsol, and A. Fridman, "Characterization of a dc atmospheric pressure normal glow discharge," *Plasma Sources Science and Technology*, vol. 14, no. 4, pp. 700–711, 2005.
- [28] K. H. Becker, K. H. Schoenbach, and J. G. Eden, "Microplasmas and applications," *Journal of Physics D: Applied Physics*, vol. 39, no. 3, p. R55, 2006.
- [29] T.-C. Tsai and D. Staack, "Characteristics of precursor-dependent breakdown in helium dielectric barrier discharge jet," *IEEE Transactions on Plasma Science*, vol. 40, no. 11, pp. 2931–2945, 2012.

- [30] T.-C. Tsai and D. Staack, "Low-temperature polymer deposition in ambient air using a floating-electrode dielectric barrier discharge jet," *Plasma Processes and Polymers*, vol. 8, no. 6, pp. 523–534, 2011.
- [31] T.-C. Tsai, J. Cho, K. McIntyre, Y.-K. Jo, and D. Staack, "Polymer film deposition on agar using a dielectric barrier discharge jet and its bacterial growth inhibition," *Applied Physics Letters*, vol. 101, no. 7, p. 4pp, 2012.
- [32] D. B. Nguyen, Q. H. Trinh, M. M. Hossain, W. G. Lee, and Y. S. Mok, "Improvement of Electrical Measurement of a Dielectric Barrier Discharge Plasma Jet," *IEEE Transactions on Plasma Science*, vol. 47, no. 5, pp. 2004–2010, 2019.
- [33] S. Reuter, T. Von Woedtke, and K. D. Weltmann, "The kINPen - A review on physics and chemistry of the atmospheric pressure plasma jet and its applications," *Journal of Physics D: Applied Physics*, vol. 51, no. 23, 2018.
- [34] J. Golda, J. Held, B. Redeker, M. Konkowski, P. Beijer, A. Sobota, G. Kroesen, N. S. J. Braithwaite, S. Reuter, M. M. Turner, T. Gans, D. O'Connell, and V. Schulz-von der Gathen, "Concepts and characteristics of the 'COST Reference Microplasma Jet'," *Journal of Physics D: Applied Physics*, vol. 49, no. 8, p. 084003, 2016.
- [35] S. Kelly, J. Golda, M. M. Turner, and V. Schulz-Von Der Gathen, "Gas and heat dynamics of a micro-scaled atmospheric pressure plasma reference jet," *Journal of Physics D: Applied Physics*, vol. 48, no. 44, 2015.
- [36] J. Winter, R. Brandenburg, and K.-D. Weltmann, "Atmospheric pressure plasma jets: an overview of devices and new directions," *Plasma Sources Science and Technology*, vol. 24, no. 6, p. 064001, 2015.
- [37] M. Laroussi and T. Akan, "Arc-free atmospheric pressure cold plasma jets: A review," *Plasma Processes and Polymers*, vol. 4, no. 9, pp. 777–788, 2007.
- [38] A. Shashurin, M. N. Shneider, A. Dogariu, R. B. Miles, and M. Keidar, "Temporal behavior of cold atmospheric plasma jet," *Applied Physics Letters*, vol. 94, no. 23, pp. 2–4, 2009.

- [39] D. Staack, B. Farouk, A. Gutsol, and A. Fridman, “DC normal glow discharges in atmospheric pressure atomic and molecular gases,” *Plasma Sources Science and Technology*, vol. 17, no. 2, p. 25013, 2008.
- [40] K.-D. Weltmann and T. von Woedtke, “Plasma medicine—current state of research and medical application,” *Plasma Physics and Controlled Fusion*, vol. 59, no. 1, p. 014031, 2017.
- [41] M. G. Kong, G. Kroesen, G. Morfill, T. Nosenko, T. Shimizu, J. Van Dijk, and J. L. Zimmermann, “Plasma medicine: An introductory review,” *New Journal of Physics*, vol. 11, 2009.
- [42] F. F. Chen, *Introduction to Plasma Physics and Controlled Fusion*. Boston, MA: Springer US, 2nd ed., 1984.
- [43] A. A. Fridman, *Plasma Chemistry*. New York, NY: Cambridge University Press, 2008.
- [44] M. Teschke and J. Engemann, “Piezoelectric low voltage atmospheric pressure plasma sources,” *Contributions to Plasma Physics*, vol. 49, no. 9, pp. 614–623, 2009.
- [45] K. Teranishi, S. Suzuki, and H. Itoh, “A novel generation method of dielectric barrier discharge and ozone production using a piezoelectric transformer,” *Japanese Journal of Applied Physics*, vol. 43, no. 9B, pp. 6733–6739, 2004.
- [46] H. Itoh, K. Teranishi, and S. Suzuki, “Discharge plasmas generated by piezoelectric transformers and their applications,” *Plasma Sources Science and Technology*, vol. 15, no. 2, 2006.
- [47] H. Kim, A. Brockhaus, and J. Engemann, “Atmospheric pressure argon plasma jet using a cylindrical piezoelectric transformer,” *Applied Physics Letters*, vol. 95, no. 21, 2009.
- [48] M. J. Johnson and D. B. Go, “Piezoelectric transformers for low-voltage generation of gas discharges and ionic winds in atmospheric air,” *Journal of Applied Physics*, vol. 118, no. 24, 2015.

- [49] C. B. Sweeney, B. A. Lackey, M. J. Pospisil, T. C. Achee, V. K. Hicks, A. G. Moran, B. R. Teipel, M. A. Saed, and M. J. Green, “Welding of 3D-printed carbon nanotube–polymer composites by locally induced microwave heating,” *Science Advances*, vol. 3, no. 6, p. e1700262, 2017.
- [50] H. L. Bank, J. John, M. K. Schmehl, and R. J. Dratch, “Bactericidal effectiveness of modulated UV light,” *Applied and Environmental Microbiology*, vol. 56, no. 12, pp. 3888–3889, 1990.
- [51] P. Ferreira, J. F. J. Coelho, J. F. Almeida, and M. H. Gil, “Photocrosslinkable Polymers for Biomedical Applications,” in *Biomedical Engineering - Frontiers and Challenges*, vol. i, p. 13, InTech, aug 2011.
- [52] T. Wohlers and T. Gornet, “History of additive manufacturing,” tech. rep., Wohlers Associates, Inc., <http://www.wohlersassociates.com/history2014.pdf>, 2014.
- [53] C. Mendes-Felipe, J. Oliveira, I. Etxebarria, J. L. Vilas-Vilela, and S. Lanceros-Mendez, “State-of-the-Art and Future Challenges of UV Curable Polymer-Based Smart Materials for Printing Technologies,” *Advanced Materials Technologies*, vol. 4, no. 3, pp. 1–16, 2019.
- [54] N. G. Gaylord, “Participation of Excited Species in Propagation Step in Photopolymerization,” in *Ultraviolet Light Induced Reactions in Polymers*, vol. 25 of *ACS Symposium Series*, ch. 1, pp. 1–11, American Chemical Society, jun 1976.
- [55] J. Sebastian, *Experimental Investigation of Plasma Activated Ethanol Water Solution*. Master’s thesis, Texas A&M University, 2017.
- [56] J. Winter, K. Wende, K. Masur, S. Iseni, M. Dünnbier, M. U. Hammer, H. Tresp, K.-D. Weltmann, and S. Reuter, “Feed gas humidity: a vital parameter affecting a cold atmospheric-pressure plasma jet and plasma-treated human skin cells,” *Journal of Physics D: Applied Physics*, vol. 46, no. 29, p. 295401, 2013.
- [57] D. B. Graves, “Low temperature plasma biomedicine: A tutorial review,” *Physics of Plasmas*, vol. 21, no. 8, 2014.

- [58] L. Bárdos and H. Baránková, “Cold atmospheric plasma: Sources, processes, and applications,” *Thin Solid Films*, vol. 518, no. 23, pp. 6705–6713, 2010.
- [59] Y. Hamedani, P. Macha, T. J. Bunning, R. R. Naik, and M. C. Vasudev, “Plasma-Enhanced Chemical Vapor Deposition: Where we are and the Outlook for the Future,” in *Chemical Vapor Deposition - Recent Advances and Applications in Optical, Solar Cells and Solid State Devices*, InTech, aug 2016.
- [60] J. H. Lee, T. T. Pham, Y. S. Kim, J. T. Lim, S. J. Kyung, and G. Y. Yeom, “Characteristics of SiO₂-like thin film deposited by atmospheric-pressure PECVD using HMDS O₂ Ar,” *Journal of the Electrochemical Society*, vol. 155, no. 3, pp. 163–166, 2008.
- [61] S. E. Alexandrov, N. McSparran, and M. L. Hitchman, “Remote AP-PECVD of silicon dioxide films from hexamethyldisiloxane (HMDSO),” *Chemical Vapor Deposition*, vol. 11, no. 11-12, pp. 481–490, 2005.
- [62] S. A. Rich, T. Dufour, P. Leroy, L. Nittler, J. J. Pireaux, and F. Reniers, “Low-density polyethylene films treated by an atmospheric Ar-O₂ post-discharge: Functionalization, etching, degradation and partial recovery of the native wettability state,” *Journal of Physics D: Applied Physics*, vol. 47, no. 6, 2014.
- [63] V. Kudryavtseva, M. Zhuravlev, and S. Tverdokhlebov, “Surface modification of polylactic acid films by atmospheric pressure plasma treatment,” *AIP Conference Proceedings*, vol. 1882, 2017.
- [64] M. Goldman, A. Goldman, and R. S. Sigmond, “The corona discharge, its properties and specific uses,” *Pure and Applied Chemistry*, vol. 57, no. 9, pp. 1353–1362, 1985.
- [65] H.-E. Wagner, R. Brandenburg, K. Kozlov, A. Sonnenfeld, P. Michel, and J. Behnke, “The barrier discharge: basic properties and applications to surface treatment,” *Vacuum*, vol. 71, pp. 417–436, may 2003.

- [66] P. G. Yock, S. Zenios, J. Makower, T. J. Brinton, U. N. Kumar, F. T. J. Watkins, L. De-
nend, T. M. Krummel, and C. Q. Kurihara, *Biodesign: The Process of Innovating Medical
Technologies*. Cambridge: Cambridge University Press, 2 ed., feb 2015.
- [67] MaRS Discovery District, “Product development lifecycle: Medical device de-
sign and development.” [https://learn.marsdd.com/article/product-development-lifecycle-
medical-device-design-and-development/](https://learn.marsdd.com/article/product-development-lifecycle-medical-device-design-and-development/), 2020.
- [68] D. M. Pressel, “Nuremberg and Tuskegee: Lessons for contemporary American medicine,”
Journal of the National Medical Association, vol. 95, no. 12, pp. 1216–1225, 2003.
- [69] S. B. Hulley, S. R. Cummings, W. S. Browner, D. G. Grady, and T. B. Newman, *Designing
Clinical Research*. Philadelphia, PA, USA: Lippincott Williams & Wilkins, 4th ed., 2013.
- [70] US Food and Drug Administration, “Quality System Regulation.” [https://www.accessdata.
fda.gov/scripts/cdrh/cfdocs/cfcfr/CFRSearch.cfm?CFRPart=820](https://www.accessdata.fda.gov/scripts/cdrh/cfdocs/cfcfr/CFRSearch.cfm?CFRPart=820), 2019.
- [71] US Food and Drug Administration, “Technical Considerations for Additive Manufactured
Medical Devices - Guidance for Industry and Food and Drug Administration Staff.”
[https://www.fda.gov/regulatory-information/search-fda-guidance-documents/technical-
considerations-additive-manufactured-medical-devices-guidance-industry-and-food-and-
drug](https://www.fda.gov/regulatory-information/search-fda-guidance-documents/technical-considerations-additive-manufactured-medical-devices-guidance-industry-and-food-and-drug), 2017.
- [72] US Food and Drug Administration, “What We Do.” [https://www.fda.gov/about-fda/what-
we-do](https://www.fda.gov/about-fda/what-we-do), 2018.
- [73] US Food and Drug Administration, “Classification of Products as Drugs and Devices & Ad-
ditional Product Classification Issues: Guidance for Industry and FDA Staff.” [https://www.
fda.gov/media/80384/download](https://www.fda.gov/media/80384/download), 2017.
- [74] US Food and Drug Administration, “Regulatory Controls.” [https://www.fda.gov/medical-
devices/overview-device-regulation/regulatory-controls](https://www.fda.gov/medical-devices/overview-device-regulation/regulatory-controls), 2018.
- [75] US Food and Drug Administration, “General Controls for Medical Devices.” [https://www.
fda.gov/medical-devices/regulatory-controls/general-controls-medical-devices](https://www.fda.gov/medical-devices/regulatory-controls/general-controls-medical-devices), 2018.

- [76] US Food and Drug Administration, “Premarket Approval (PMA).” <https://www.fda.gov/medical-devices/premarket-submissions/premarket-approval-pma>, 2019.
- [77] US Food and Drug Administration, “Medical Device User Fee Amendments (MDUFA).” <https://www.fda.gov/industry/fda-user-fee-programs/medical-device-user-fee-amendments-mdufa>, 2020.
- [78] E. Silvestrini, “Premarket Approval (PMA).” <https://www.drugwatch.com/fda/premarket-approval/>, 2020.
- [79] US Food and Drug Administration, “Premarket Notification 510(k).” <https://www.fda.gov/medical-devices/premarket-submissions/premarket-notification-510k>, 2018.
- [80] US Food and Drug Administration, “De Novo Classification Request.” <https://www.fda.gov/medical-devices/premarket-submissions/de-novo-classification-request>, 2019.
- [81] I. C. Santos, G. S. Gazelle, L. A. Rocha, and J. M. R. Tavares, “Medical device specificities: Opportunities for a dedicated product development methodology,” *Expert Review of Medical Devices*, vol. 9, no. 3, pp. 299–311, 2012.
- [82] US Food and Drug Administration, “Sec. 880.2920 Clinical mercury thermometer.” <https://www.accessdata.fda.gov/scripts/cdrh/cfdocs/cfCFR/CFRSearch.cfm?FR=880.2920>, 2019.
- [83] US Food and Drug Administration, “Sec. 890.3420 External limb prosthetic component.” <https://www.accessdata.fda.gov/scripts/cdrh/cfdocs/cfcfr/cfrsearch.cfm?fr=890.3420>, 2019.
- [84] US Food and Drug Administration, “Humanitarian Device Exemption.” <https://www.fda.gov/medical-devices/premarket-submissions/humanitarian-device-exemption>, 2019.
- [85] US Food and Drug Administration, “Custom Device Exemption.” <https://www.fda.gov/regulatory-information/search-fda-guidance-documents/custom-device-exemption>, 2014.
- [86] US Food and Drug Administration, “Principles of Premarket Pathways for Combination Products Guidance for Industry and FDA Staff.” <https://www.fda.gov/media/119958/download>, 2019.

- [87] US Food and Drug Administration, “Emergency Use Authorization of Medical Products and Related Authorities.” <https://www.fda.gov/media/97321/download>, 2017.
- [88] E. & I. S. Department for Business, “CE Marking.” <https://www.gov.uk/guidance/ce-marking>, 2012.
- [89] BSI, “Want to know more about the Notified Body?.” <https://www.bsigroup.com/meddev/LocalFiles/nl-NL/Services/BSI-md-notifed-body-guide-brochure-UK-EN.pdf>, 2018.
- [90] E. French-Mowat and J. Burnett, “How are medical devices regulated in the European Union?,” *Journal of the Royal Society of Medicine*, vol. 105, pp. 22–28, apr 2012.
- [91] Global Legal Research Directorate Staff, “Approval of Medical Devices: European Union.” <https://www.loc.gov/law/help/medical-devices/eu.php>, 2014.
- [92] Emergo, “PMDA Medical Device Registration and Approval in Japan.” <https://www.emergobyul.com/services/japan/pmda-medical-device-registration-approval-process>, 2019.
- [93] A. Tamura, “Understanding Japanese Medical Device Requirements,” in *2011 AHC Workshop on Medical Devices: “Implementation of GHTF Documents”*, (Seoul, South Korea), 2011.
- [94] Pacific Bridge Medical, “Medical Device Registration in Japan.” <https://www.pacificbridgemedical.com/regulatory-services/medical-device/product-registration/japan/>, 2020.
- [95] World Health Organization, “Global harmonization task force (GHTF).” https://www.who.int/medical_devices/collaborations/force/en/, 2020.
- [96] T. Von Woedtke, H. R. Metelmann, and K. D. Weltmann, “Clinical Plasma Medicine: State and Perspectives of in Vivo Application of Cold Atmospheric Plasma,” *Contributions to Plasma Physics*, vol. 54, no. 2, pp. 104–117, 2014.

- [97] B. Haertel, T. von Woedtke, K. D. Weltmann, and U. Lindequist, “Non-thermal atmospheric-pressure plasma possible application in wound healing,” *Biomolecules and Therapeutics*, vol. 22, no. 6, pp. 477–490, 2014.
- [98] H. Ayan, G. Fridman, D. Staack, A. F. Gutsol, V. N. Vasilets, A. A. Fridman, and G. Friedman, “Heating Effect of Dielectric Barrier Discharges for Direct Medical Treatment,” *IEEE Transactions on Plasma Science*, vol. 27, no. 1, pp. 94–120, 2009.
- [99] C. F. Dalziel, “Electric shock hazard,” *IEEE Spectrum*, vol. 9, pp. 41–50, feb 1972.
- [100] D. Dobrynin, G. Fridman, G. Friedman, and A. Fridman, “Physical and biological mechanisms of direct plasma interaction with living tissue,” *New Journal of Physics*, vol. 11, 2009.
- [101] K. Wende, P. Williams, J. Dalluge, W. V. Gaens, H. Aboubakr, J. Bischof, T. von Woedtke, S. M. Goyal, K.-D. Weltmann, A. Bogaerts, K. Masur, and P. J. Bruggeman, “Identification of the biologically active liquid chemistry induced by a nonthermal atmospheric pressure plasma jet,” *Biointerphases*, vol. 10, no. 2, p. 029518, 2015.
- [102] X. Xu, X. Dai, L. Xiang, D. Cai, S. Xiao, and K. Ostrikov, “Quantitative assessment of cold atmospheric plasma anti-cancer efficacy in triple-negative breast cancers,” *Plasma Processes and Polymers*, vol. 15, no. 8, pp. 1–11, 2018.
- [103] B. K. H. L. Boekema, S. Hofmann, B. J. T. van Ham, P. J. Bruggeman, and E. Middelkoop, “Antibacterial plasma at safe levels for skin cells,” *Journal of Physics D: Applied Physics*, vol. 46, no. 42, p. 422001, 2013.
- [104] S. A. Ermolaeva, A. F. Varfolomeev, M. Y. Chernukha, D. S. Yurov, M. M. Vasiliev, A. A. Kaminskaya, M. M. Moisenovich, J. M. Romanova, A. N. Murashev, I. I. Selezneva, T. Shimizu, E. V. Sysolyatina, I. A. Shaginyan, O. F. Petrov, E. I. Mayevsky, V. E. Fortov, G. E. Morfill, B. S. Naroditsky, and A. L. Gintsburg, “Bactericidal effects of non-thermal argon plasma in vitro, in biofilms and in the animal model of infected wounds,” *Journal of Medical Microbiology*, vol. 60, no. 1, pp. 75–83, 2011.

- [105] G. Daeschlein, M. Napp, S. Von Podewils, S. Lutze, S. Emmert, A. Lange, I. Klare, H. Haase, D. Gumbel, T. Von Woedtke, and M. Jünger, “In vitro susceptibility of multidrug resistant skin and wound pathogens against low temperature atmospheric pressure plasma jet (APPJ) and dielectric barrier discharge plasma (DBD),” *Plasma Processes and Polymers*, vol. 11, no. 2, pp. 175–183, 2014.
- [106] G. Fridman, M. Peddinghaus, H. Ayan, A. Fridman, M. Balasubramanian, A. Gutsol, A. Brooks, and G. Friedman, “Blood coagulation and living tissue sterilization by floating-electrode dielectric barrier discharge in air,” *Plasma Chemistry and Plasma Processing*, vol. 26, no. 4, pp. 425–442, 2006.
- [107] D. Dobrynin, A. Wu, S. Kalghatgi, S. Park, N. Shainsky, K. Wasko, E. Dumani, R. Ownbey, S. Joshi, R. Sensenig, and A. D. Brooks, “Live Pig Skin Tissue and Wound Toxicity of Cold Plasma Treatment,” *Plasma Medicine*, vol. 1, no. 1, pp. 93–108, 2011.
- [108] A. S. Wu, S. Kalghatgi, D. Dobrynin, R. Sensenig, E. Cerchar, E. Podolsky, E. Dulaimi, M. Paff, K. Wasko, K. P. Arjunan, K. Garcia, G. Fridman, M. Balasubramanian, R. Ownbey, K. A. Barbee, A. Fridman, G. Friedman, S. G. Joshi, and A. D. Brooks, “Porcine intact and wounded skin responses to atmospheric nonthermal plasma,” *Journal of Surgical Research*, vol. 179, no. 1, pp. e1–e12, 2013.
- [109] G. Fridman, G. Friedman, A. Gutsol, A. B. Shekhter, V. N. Vasilets, and A. Fridman, “Applied plasma medicine,” *Plasma Processes and Polymers*, vol. 5, no. 6, pp. 503–533, 2008.
- [110] S. Kalghatgi, G. Friedman, A. Fridman, and A. M. Clyne, “Endothelial cell proliferation is enhanced by low dose non-thermal plasma through fibroblast growth factor-2 release,” *Annals of Biomedical Engineering*, vol. 38, no. 3, pp. 748–757, 2010.
- [111] B. Kleinedam, M. Nokhbehsaim, J. Deschner, and G. Wahl, “Effect of cold plasma on periodontal wound healing—an in vitro study,” *Clinical Oral Investigations*, vol. 23, no. 4, pp. 1941–1950, 2019.

- [112] B. Eggers, J. Marciniak, S. Memmert, F. J. Kramer, J. Deschner, and M. Nokhbehssaim, “The beneficial effect of cold atmospheric plasma on parameters of molecules and cell function involved in wound healing in human osteoblast-like cells in vitro,” *Odontology*, 2020.
- [113] J. M. Reinke and H. Sorg, “Wound repair and regeneration,” *European Surgical Research*, vol. 49, no. 1, pp. 35–43, 2012.
- [114] P. L. Shao, J. D. Liao, T. W. Wong, Y. C. Wang, S. Leu, and H. K. Yip, “Enhancement of wound healing by non-thermal N₂/Ar micro-plasma exposure in mice with fractional-CO₂-laser-induced wounds,” *PLoS ONE*, vol. 11, no. 6, pp. 1–15, 2016.
- [115] Nasruddin, Y. Nakajima, K. Mukai, H. S. E. Rahayu, M. Nur, T. Ishijima, H. Enomoto, Y. Uesugi, J. Sugama, and T. Nakatani, “Cold plasma on full-thickness cutaneous wound accelerates healing through promoting inflammation, re-epithelialization and wound contraction,” *Clinical Plasma Medicine*, vol. 2, no. 1, pp. 28–35, 2014.
- [116] R. Alhabshan, D. Belyea, M. A. Stepp, J. Barratt, S. Grewal, A. Shashurin, and M. Keidar, “Effects of In-vivo Application of Cold Atmospheric Plasma on Corneal Wound Healing in New Zealand White Rabbits,” *International Journal of Ophthalmic & Pathology*, vol. 02, no. 03, pp. 2–6, 2013.
- [117] S. Darmawati, A. Rohmani, L. H. Nurani, M. E. Prastiyanto, S. S. Dewi, N. Salsabila, E. S. Wahyuningtyas, F. Murdiya, I. M. Sikumbang, R. N. Rohmah, Y. A. Fatimah, A. Widiyanto, T. Ishijima, J. Sugama, T. Nakatani, and N. Nasruddin, “When plasma jet is effective for chronic wound bacteria inactivation, is it also effective for wound healing?,” *Clinical Plasma Medicine*, vol. 14, no. 18, p. 100085, 2019.
- [118] D. Mevorach, U. Trahtemberg, A. Krispin, M. Attalah, J. Zazoun, A. Tabib, A. Grau, and I. Verbovetski-Reiner, “What do we mean when we write "senescence," "apoptosis," "necrosis," or "clearance of dying cells"?” *Annals of the New York Academy of Sciences*, vol. 1209, no. 1, pp. 1–9, 2010.

- [119] G. Y. Park, S. J. Park, M. Y. Choi, I. G. Koo, J. H. Byun, J. W. Hong, J. Y. Sim, G. J. Collins, and J. K. Lee, “Atmospheric-pressure plasma sources for biomedical applications,” *Plasma Sources Science and Technology*, vol. 21, no. 4, 2012.
- [120] V. Miller, A. Lin, and A. Fridman, “Why Target Immune Cells for Plasma Treatment of Cancer,” *Plasma Chemistry and Plasma Processing*, vol. 36, no. 1, pp. 259–268, 2016.
- [121] D. Yan, J. H. Sherman, and M. Keidar, “Cold atmospheric plasma, a novel promising anti-cancer treatment modality,” *Oncotarget*, vol. 8, no. 9, pp. 15977–15995, 2017.
- [122] N. Berekzi and M. Laroussi, “Effects of low temperature plasmas on cancer cells,” *Plasma Processes and Polymers*, vol. 10, no. 12, pp. 1039–1050, 2013.
- [123] A. Siu, O. Volotskova, X. Cheng, S. S. Khalsa, K. Bian, F. Murad, M. Keidar, and J. H. Sherman, “Differential effects of cold atmospheric plasma in the treatment of malignant glioma,” *PLoS ONE*, vol. 10, no. 6, pp. 1–14, 2015.
- [124] D. Yan, A. Talbot, N. Nourmohammadi, X. Cheng, J. Canady, J. Sherman, and M. Keidar, “Principles of using Cold Atmospheric Plasma Stimulated Media for Cancer Treatment,” *Scientific Reports*, vol. 5, no. November, pp. 1–17, 2015.
- [125] S. Bekeschus, S. Iséni, S. Reuter, K. Masur, and K. D. Weltmann, “Nitrogen Shielding of an Argon Plasma Jet and Its Effects on Human Immune Cells,” *IEEE Transactions on Plasma Science*, vol. 43, no. 3, pp. 776–781, 2015.
- [126] P. M. Girard, A. Arbabian, M. Fleury, G. Bauville, V. Puech, M. Dutreix, and J. S. Sousa, “Synergistic Effect of H₂O₂ and NO₂ in Cell Death Induced by Cold Atmospheric He Plasma,” *Scientific Reports*, vol. 6, no. 2, pp. 1–17, 2016.
- [127] N. Kurake, H. Tanaka, K. Ishikawa, T. Kondo, M. Sekine, K. Nakamura, H. Kajiyama, F. Kikkawa, M. Mizuno, and M. Hori, “Cell survival of glioblastoma grown in medium containing hydrogen peroxide and/or nitrite, or in plasma-activated medium,” *Archives of Biochemistry and Biophysics*, vol. 605, pp. 102–108, 2016.

- [128] A. Lin, N. Chernets, J. Han, Y. Alicea, D. Dobrynin, G. Fridman, T. A. Freeman, A. Fridman, and V. Miller, “Non-Equilibrium Dielectric Barrier Discharge Treatment of Mesenchymal Stem Cells: Charges and Reactive Oxygen Species Play the Major Role in Cell Death,” *Plasma Processes and Polymers*, vol. 12, no. 10, pp. 1117–1127, 2015.
- [129] S. Kalghatgi, C. M. Kelly, E. Cerchar, B. Torabi, O. Alekseev, A. Fridman, G. Friedman, and J. Azizkhan-Clifford, “Effects of non-thermal plasma on mammalian cells,” *PLoS ONE*, vol. 6, no. 1, pp. 1–11, 2011.
- [130] G. Fridman, A. Shereshevsky, M. M. Jost, A. D. Brooks, A. Fridman, A. Gutsol, V. Vasilets, and G. Friedman, “Floating electrode dielectric barrier discharge plasma in air promoting apoptotic behavior in Melanoma skin cancer cell lines,” *Plasma Chemistry and Plasma Processing*, vol. 27, no. 2, pp. 163–176, 2007.
- [131] A. M. Hirst, F. M. Frame, M. Arya, N. J. Maitland, and D. O’Connell, “Low temperature plasmas as emerging cancer therapeutics: the state of play and thoughts for the future,” *Tumor Biology*, vol. 37, no. 6, pp. 7021–7031, 2016.
- [132] S. Kalghatgi, G. Fridman, M. Cooper, G. Nagaraj, M. Peddinghaus, M. Balasubramanian, V. N. Vasilets, A. Gutsol, A. Fridman, and G. Friedman, “Mechanism of Blood Coagulation by Non-Equilibrium Atmospheric Pressure Dielectric Barrier Discharge Plasma,” *IEEE Transactions on Plasma Science*, vol. 35, no. 5, pp. 1559–1566, 2007.
- [133] S. Cha and Y. S. Park, “Plasma in dentistry,” *Clinical Plasma Medicine*, vol. 2, no. 1, pp. 4–10, 2014.
- [134] M. Gherardi, R. Tonini, and V. Colombo, “Plasma in Dentistry: Brief History and Current Status,” *Trends in Biotechnology*, vol. 36, no. 6, pp. 583–585, 2018.
- [135] R. Ranjan, P. V. Krishnamraju, T. Shankar, and S. Gowd, “Nonthermal Plasma in Dentistry: An Update.,” *Journal of International Society of Preventive & Community Dentistry*, vol. 7, no. 3, pp. 71–75, 2017.

- [136] D. Yan, N. Nourmohammadi, K. Bian, F. Murad, J. H. Sherman, and M. Keidar, “Stabilizing the cold plasma-stimulated medium by regulating medium’s composition,” *Scientific Reports*, vol. 6, no. March, pp. 1–11, 2016.
- [137] I. Osman, A. Ponukumati, M. Vargas, D. Bhakta, B. Ozoglu, and C. Bailey, “Plasma-Activated Vapor for Sanitization of Hands,” *Plasma Medicine*, vol. 6, no. 3-4, pp. 235–245, 2016.
- [138] G. E. Morfill, T. Shimizu, B. Steffes, and H. U. Schmidt, “Nosocomial infections - A new approach towards preventive medicine using plasmas,” *New Journal of Physics*, vol. 11, 2009.
- [139] G. Isbary, T. Shimizu, Y.-F. Li, W. Stolz, H. M. Thomas, G. E. Morfill, and J. L. Zimmermann, “Cold atmospheric plasma devices for medical issues.,” *Expert review of medical devices*, vol. 10, no. 3, pp. 367–77, 2013.
- [140] S. Bekeschus, A. Schmidt, K. D. Weltmann, and T. von Woedtke, “The plasma jet kINPen – A powerful tool for wound healing,” *Clinical Plasma Medicine*, vol. 4, no. 1, pp. 19–28, 2016.
- [141] Adtec Europe Limited, “Adtec obtains CE Mark for cold plasma medical device.” https://www.medica-tradefair.com/en/News/Archive/Adtec_obtains_CE_Mark_for_cold_plasma_medical_device, 2014.
- [142] G. Isbary, G. Morfill, H. U. Schmidt, M. Georgi, K. Ramrath, J. Heinlin, S. Karrer, M. Landthaler, T. Shimizu, B. Steffes, W. Bunk, R. Monetti, J. L. Zimmermann, R. Pompl, and W. Stolz, “A first prospective randomized controlled trial to decrease bacterial load using cold atmospheric argon plasma on chronic wounds in patients,” *British Journal of Dermatology*, vol. 163, no. 1, pp. 78–82, 2010.
- [143] G. Isbary, J. Heinlin, T. Shimizu, J. L. Zimmermann, G. Morfill, H. U. Schmidt, R. Monetti, B. Steffes, W. Bunk, Y. Li, T. Klaempfl, S. Karrer, M. Landthaler, and W. Stolz, “Successful and safe use of 2 min cold atmospheric argon plasma in chronic wounds: Results of a

- randomized controlled trial,” *British Journal of Dermatology*, vol. 167, no. 2, pp. 404–410, 2012.
- [144] M. Klebes, C. Ulrich, F. Kluschke, A. Patzelt, S. Vandersee, H. Richter, A. Bob, J. von Hutten, J. T. Krediet, A. Kramer, J. Lademann, and B. Lange-Asschenfeld, “Combined antibacterial effects of tissue-tolerable plasma and a modern conventional liquid antiseptic on chronic wound treatment,” *Journal of Biophotonics*, vol. 8, no. 5, pp. 382–391, 2015.
- [145] F. Brehmer, H. A. Haenssle, G. Daeschlein, R. Ahmed, S. Pfeiffer, A. Görlitz, D. Simon, M. P. Schön, D. Wandke, and S. Emmert, “Alleviation of chronic venous leg ulcers with a hand-held dielectric barrier discharge plasma generator (PlasmaDerm® VU-2010): Results of a monocentric, two-armed, open, prospective, randomized and controlled trial (NCT01415622),” *Journal of the European Academy of Dermatology and Venereology*, vol. 29, no. 1, pp. 148–155, 2015.
- [146] H.-R. Metelmann, D. S. Nedrelov, C. Seebauer, M. Schuster, T. von Woedtke, K.-D. Weltmann, S. Kindler, P. H. Metelmann, S. E. Finkelstein, D. D. Von Hoff, and F. Podmelle, “Head and neck cancer treatment and physical plasma,” *Clinical Plasma Medicine*, vol. 3, no. 1, pp. 17–23, 2015.
- [147] US Medical Innovations LLC, “Cold Plasma Used In World’s First Clinical Surgical Procedure Performed To Selectively Kill Cancer Tumor Cells.” <https://www.prnewswire.com/news-releases/cold-plasma-used-in-worlds-first-clinical-surgical-procedure-performed-to-selectively-kill-cancer-tumor-cells-300066833.html>, 2015.
- [148] D. Song, “Cold Plasma: New Surgical Tool to Fight Pancreatic Cancer.” <https://www.rushu.rush.edu/news/cold-plasma-new-surgical-tool-fight-pancreatic-cancer>, 2016.
- [149] J. Ives, “FDA approves cold atmospheric plasma technology for first-ever use in clinical trial.” <https://www.news-medical.net/news/20190820/FDA-approves-cold-atmospheric-plasma-technology-for-first-ever-use-in-clinical-trial.aspx>, 2019.

- [150] Onkocet, “Air- plasma manipulator - basic element of the PLASON® device.” <http://www.onkocet.eu/en/produkty-detail/35/1/>, 2009.
- [151] A. B. Shekhter, V. A. Serezhenkov, T. G. Rudenko, A. V. Pekshev, and A. F. Vanin, “Beneficial effect of gaseous nitric oxide on the healing of skin wounds,” *Nitric Oxide - Biology and Chemistry*, vol. 12, no. 4, pp. 210–219, 2005.
- [152] T. von Woedtke, S. Reuter, K. Masur, and K. D. Weltmann, “Plasmas for medicine,” *Physics Reports*, vol. 530, no. 4, pp. 291–320, 2013.
- [153] M. S. Mann, R. Tiede, K. Gavenis, G. Daeschlein, R. Bussiahn, K. D. Weltmann, S. Emmert, T. von Woedtke, and R. Ahmed, “Introduction to DIN-specification 91315 based on the characterization of the plasma jet kINPen® MED,” *Clinical Plasma Medicine*, vol. 4, no. 2, pp. 35–45, 2016.
- [154] neoplas tools GmbH, “kINPen® MED.” <https://neoplas-tools.eu/en/produkte.html>, 2017.
- [155] G. Daeschlein, S. Scholz, A. Arnold, S. Von Podewils, H. Haase, S. Emmert, T. Von Woedtke, K. D. Weltmann, and M. Jünger, “In vitro susceptibility of important skin and wound pathogens against low temperature atmospheric pressure plasma jet (APPJ) and dielectric barrier discharge plasma (DBD),” *Plasma Processes and Polymers*, vol. 9, no. 4, pp. 380–389, 2012.
- [156] J. Winter, H. Tresp, M. U. Hammer, S. Iseni, S. Kupsch, A. Schmidt-Bleker, K. Wende, M. Dünnbier, K. Masur, K. D. Weltmann, and S. Reuter, “Tracking plasma generated H₂O₂ from gas into liquid phase and revealing its dominant impact on human skin cells,” *Journal of Physics D: Applied Physics*, vol. 47, no. 28, 2014.
- [157] J. Lademann, C. Ulrich, A. Patzelt, H. Richter, F. Kluschke, M. Klebes, O. Lademann, A. Kramer, K. D. Weltmann, and B. Lange-Asschenfeldt, “Risk assessment of the application of tissue-tolerable plasma on human skin,” *Clinical Plasma Medicine*, vol. 1, no. 1, pp. 5–10, 2013.

- [158] S. Bekeschus, A. Lin, A. Fridman, K. Wende, K. D. Weltmann, and V. Miller, “A Comparison of Floating-Electrode DBD and kINPen Jet: Plasma Parameters to Achieve Similar Growth Reduction in Colon Cancer Cells Under Standardized Conditions,” *Plasma Chemistry and Plasma Processing*, vol. 38, no. 1, pp. 1–12, 2018.
- [159] A. Schmidt-Bleker, J. Winter, A. Bösel, S. Reuter, and K.-D. Weltmann, “On the plasma chemistry of a cold atmospheric argon plasma jet with shielding gas device,” *Plasma Sources Science and Technology*, vol. 25, no. 1, p. 015005, 2016.
- [160] A. Schmidt-Bleker, J. Winter, S. Iseni, M. Dünnbier, K. D. Weltmann, and S. Reuter, “Reactive species output of a plasma jet with a shielding gas device - Combination of FTIR absorption spectroscopy and gas phase modelling,” *Journal of Physics D: Applied Physics*, vol. 47, no. 14, 2014.
- [161] J. Lademann, H. Richter, A. Alborova, D. Humme, A. Patzelt, A. Kramer, K.-D. Weltmann, B. Hartmann, C. Ottomann, J. W. Fluhr, P. Hinz, G. Hübner, and O. Lademann, “Risk assessment of the application of a plasma jet in dermatology,” *Journal of Biomedical Optics*, vol. 14, no. 5, p. 054025, 2009.
- [162] G. Daeschlein, S. Scholz, R. Ahmed, T. Von Woedtke, H. Haase, M. Niggemeier, E. Kindel, R. Brandenburg, K. D. Weltmann, and M. Juenger, “Skin decontamination by low-temperature atmospheric pressure plasma jet and dielectric barrier discharge plasma,” *Journal of Hospital Infection*, vol. 81, no. 3, pp. 177–183, 2012.
- [163] M. Schuster, C. Seebauer, R. Rutkowski, A. Hauschild, F. Podmelle, C. Metelmann, B. Metelmann, T. von Woedtke, S. Hasse, K. D. Weltmann, and H. R. Metelmann, “Visible tumor surface response to physical plasma and apoptotic cell kill in head and neck cancer,” *Journal of Cranio-Maxillofacial Surgery*, vol. 44, no. 9, pp. 1445–1452, 2016.
- [164] R. Rutkowski, M. Schuster, J. Unger, C. Seebauer, H. R. Metelmann, T. v. Woedtke, K. D. Weltmann, and G. Daeschlein, “Hyperspectral imaging for in vivo monitoring of cold atmo-

- spheric plasma effects on microcirculation in treatment of head and neck cancer and wound healing,” *Clinical Plasma Medicine*, vol. 7-8, no. June, pp. 52–57, 2017.
- [165] R. Tiede, J. Hirschberg, G. Daeschlein, T. von Woedtke, W. Vioel, and S. Emmert, “Plasma Applications: A Dermatological View,” *Contributions to Plasma Physics*, vol. 54, no. 2, pp. 118–130, 2014.
- [166] S. Emmert, F. Brehmer, H. Hänßle, A. Helmke, N. Mertens, R. Ahmed, D. Simon, D. Wandke, M. P. Schön, W. Maus-Friedrichs, W. Viöl, and G. Däschlein, “Treatment of chronic venous leg ulcers with a hand-held DBD plasma generator,” *Plasma Medicine*, vol. 2, no. 1-3, pp. 19–32, 2012.
- [167] C. Klinkhammer, C. Verlackt, D. Śmiłowicz, F. Kogelheide, A. Bogaerts, N. Metzler-Nolte, K. Stapelmann, M. Havenith, and J. W. Lackmann, “Elucidation of Plasma-induced Chemical Modifications on Glutathione and Glutathione Disulphide,” *Scientific Reports*, vol. 7, no. 1, pp. 1–11, 2017.
- [168] CINOGY System GmbH, “PlasmaDerm® – Innovative in wound healing stimulation and germ reduction.” http://www.cinogy.de/_EN/index.php, 2020.
- [169] Adtec Europe Limited, “About Us.” <http://www.adtecplasma.com/about.html>, 2019.
- [170] G. Isbary, J. L. Zimmermann, T. Shimizu, Y. F. Li, G. E. Morfill, H. M. Thomas, B. Steffes, J. Heinlin, S. Karrer, and W. Stolz, “Non-thermal plasma-More than five years of clinical experience,” *Clinical Plasma Medicine*, vol. 1, no. 1, pp. 19–23, 2013.
- [171] T. Shimizu, B. Steffes, R. Pompl, F. Jamitzky, W. Bunk, K. Ramrath, M. Georgi, W. Stolz, H. U. Schmidt, T. Urayama, S. Fujii, and G. E. Morfill, “Characterization of microwave plasma torch for decontamination,” *Plasma Processes and Polymers*, vol. 5, no. 6, pp. 577–582, 2008.
- [172] G. Isbary, G. Morfill, H. U. Schmidt, M. Georgi, K. Ramrath, J. Heinlin, S. Karrer, M. Landthaler, T. Shimizu, B. Steffes, W. Bunk, R. Monetti, J. L. Zimmermann, R. Pompl, and W. Stolz, “A first prospective randomized controlled trial to decrease bacterial load

- using cold atmospheric argon plasma on chronic wounds in patients,” *British Journal of Dermatology*, vol. 163, no. 1, pp. 78–82, 2010.
- [173] G. Isbary, W. Stolz, T. Shimizu, R. Monetti, W. Bunk, H. U. Schmidt, G. E. Morfill, T. G. Klämpfl, B. Steffes, H. M. Thomas, J. Heinlin, S. Karrer, M. Landthaler, and J. L. Zimmermann, “Cold atmospheric argon plasma treatment may accelerate wound healing in chronic wounds: Results of an open retrospective randomized controlled study in vivo,” *Clinical Plasma Medicine*, vol. 1, no. 2, pp. 25–30, 2013.
- [174] J. Heinlin, J. L. Zimmermann, F. Zeman, W. Bunk, G. Isbary, M. Landthaler, T. Maisch, R. Monetti, G. Morfill, T. Shimizu, J. Steinbauer, W. Stolz, and S. Karrer, “Randomized placebo-controlled human pilot study of cold atmospheric argon plasma on skin graft donor sites,” *Wound Repair and Regeneration*, vol. 21, no. 6, pp. 800–807, 2013.
- [175] G. Isbary, T. Shimizu, J. L. Zimmermann, J. Heinlin, S. Al-Zaabi, M. Rechfeld, G. E. Morfill, S. Karrer, and W. Stolz, “Randomized placebo-controlled clinical trial showed cold atmospheric argon plasma relieved acute pain and accelerated healing in herpes zoster,” *Clinical Plasma Medicine*, vol. 2, no. 2, pp. 50–55, 2014.
- [176] T. Maisch, A. K. Bosserhoff, P. Unger, J. Heider, T. Shimizu, J. L. Zimmermann, G. E. Morfill, M. Landthaler, and S. Karrer, “Investigation of toxicity and mutagenicity of cold atmospheric argon plasma,” *Environmental and Molecular Mutagenesis*, vol. 58, pp. 172–177, apr 2017.
- [177] S. Arndt, P. Unger, E. Wacker, T. Shimizu, J. Heinlin, Y. F. Li, H. M. Thomas, G. E. Morfill, J. L. Zimmermann, A. K. Bosserhoff, and S. Karrer, “Cold atmospheric plasma (CAP) changes gene expression of key molecules of the wound healing machinery and improves wound healing in vitro and in vivo,” *PLoS ONE*, vol. 8, no. 11, pp. 1–9, 2013.
- [178] terraplasma medical GmbH, “The plasma care®.” <https://www.terraplasma-medical.com/en/product/>, 2020.

- [179] T. Maisch, T. Shimizu, Y. F. Li, J. Heinlin, S. Karrer, G. Morfill, and J. L. Zimmermann, “Decolonisation of MRSA, *S. aureus* and *E. coli* by cold-atmospheric plasma using a porcine skin model in vitro,” *PLoS ONE*, vol. 7, no. 4, pp. 1–9, 2012.
- [180] T. G. Klämpfl, T. Shimizu, S. Koch, M. Balden, S. Gemein, Y.-F. Li, A. Mitra, J. L. Zimmermann, J. Gebel, G. E. Morfill, and H.-U. Schmidt, “Decontamination of Nosocomial Bacteria Including *Clostridium difficile* Spores on Dry Inanimate Surface by Cold Atmospheric Plasma,” *Plasma Processes and Polymers*, vol. 11, no. 10, pp. 974–984, 2014.
- [181] C. Schneider, L. Gebhardt, S. Arndt, S. Karrer, J. L. Zimmermann, M. J. Fischer, and A. K. Bosserhoff, “Acidification is an essential process of cold atmospheric plasma and promotes the anti-cancer effect on malignant melanoma cells,” *Cancers*, vol. 11, no. 5, 2019.
- [182] T. Shimizu, V. Lachner, and J. L. Zimmermann, “Surface microdischarge plasma for disinfection,” *Plasma Medicine*, vol. 7, no. 2, pp. 175–185, 2017.
- [183] F. Theinkom, L. Singer, F. Cieplik, S. Cantzler, H. Weilemann, M. Cantzler, K. A. Hiller, T. Maisch, and J. L. Zimmermann, “Antibacterial efficacy of cold atmospheric plasma against *Enterococcus faecalis* planktonic cultures and biofilms in vitro,” *PLoS ONE*, vol. 14, no. 11, pp. 1–15, 2019.
- [184] ASmax, “The "Plasma Akku Mobil" device.” <https://www.as-max.com/cold-plasma-devices/plasma-akku-mobil.html>, 2020.
- [185] S. Karrer and S. Arndt, “Plasmamedizin in der Dermatologie: Wirkmechanismen und Anwendungsmöglichkeiten,” *Hautarzt*, vol. 66, no. 11, pp. 819–828, 2015.
- [186] M. Ulu, T. Pekbagriyanik, F. Ibis, S. Enhos, and U. Ercan, “Antibiofilm efficacies of cold plasma and er: YAG laser on *Staphylococcus aureus* biofilm on titanium for nonsurgical treatment of peri-implantitis,” *Nigerian Journal of Clinical Practice*, vol. 21, no. 6, pp. 758–765, 2018.
- [187] S. Hafner, M. Ehrenfeld, A. C. Neumann, and A. Wieser, “Comparison of the bactericidal effect of cold atmospheric pressure plasma (CAPP), antimicrobial photodynamic therapy

- (aPDT), and polihexanide (PHX) in a novel wet surface model to mimic oral cavity application,” *Journal of Cranio-Maxillofacial Surgery*, vol. 46, no. 12, pp. 2197–2202, 2018.
- [188] plasma MEDICAL SYSTEMS® GmbH, “Plasma therapy with plasma ONE.” <http://www.plasmamedicalsystems.com/2/medical/plasma-therapy/>, 2020.
- [189] Plasma Medical Systems, “Competence and Research.” <http://www.plasmamedicalsystems.com/2/competence-research/kompetenzforschung/>, 2020.
- [190] W. Reich, A. Exner, E. Winter, B. Al-Nawas, and A. W. Eckert, “Complex functional and epithetic rehabilitation after ablation of recurrent retroauricular basal cell carcinoma - a case study.,” *GMS Interdisciplinary plastic and reconstructive surgery DGPW*, vol. 6, p. Doc18, 2017.
- [191] D. Pogorelc, “Cold plasma startup gets \$1 million for anti-infection wound healing device.” <https://medcitynews.com/2012/07/cold-plasma-startup-gets-1-million-for-anti-infection-wound-healing-device/>, 2012.
- [192] SBIR.gov, “SBIR Phase I: Non-Thermal Plasma Device for Wound Disinfection and Promotion of Wound Healing.” <https://www.sbir.gov/sbirsearch/detail/683096>, 2013.
- [193] C. Soder, “Tech startup Sterionics is developing pen-shaped device to treat wounds.” <https://www.crainscleveland.com/article/20130204/SUB1/302049981/tech-startup-sterionics-is-developing-pen-shaped-device-to-treat>, 2013.
- [194] ChiScan, “Next generation Non-Thermal Plasma Technology demonstrates effectiveness in the fight against tough infectious agents.” <https://www.prnewswire.com/news-releases/next-generation-non-thermal-plasma-technology-demonstrates-effectiveness-in-the-fight-against-tough-infectious-agents-300201388.html>, 2016.
- [195] US Medical Innovations LLC, “Canady Cold Plasma™ Technology for the Treatment of Cancer.” <https://www.usmedinnovations.com/canady-life-sciences/cold-atmospheric-plasma/>, 2020.

- [196] L. Ly, S. Jones, A. Shashurin, T. Zhuang, W. Rowe, X. Cheng, S. Wigh, T. Naab, M. Keidar, and J. Canady, “A New Cold Plasma Jet: Performance Evaluation of Cold Plasma, Hybrid Plasma and Argon Plasma Coagulation,” *Plasma*, vol. 1, no. 1, pp. 189–200, 2018.
- [197] W. Rowe, X. Cheng, L. Ly, T. Zhuang, G. Basadonna, B. Trink, M. Keidar, and J. Canady, “The Canady Helios Cold Plasma Scalpel Significantly Decreases Viability in Malignant Solid Tumor Cells in a Dose-Dependent Manner,” *Plasma*, vol. 1, no. 1, pp. 177–188, 2018.
- [198] Business Wire, “Canady Helios Cold Plasma Scalpel Successfully Used by Chaim Sheba Medical Center Surgeons to Remove Inoperable Retroperitoneal Cancer.” <https://www.businesswire.com/news/home/20200129005667/en/Canady-Helios-Cold-Plasma-Scalpel-Successfully-Chaim>, 2020.
- [199] P. C. Friedman, G. Fridman, and A. Fridman, “Using cold plasma to treat warts in children: A case series,” *Pediatric Dermatology*, pp. 1–4, 2020.
- [200] C. Chutsirimongkol, D. Boonyawan, N. Polnikorn, W. Techawatthanawisan, and T. Kundilokchai, “Non-thermal plasma for acne treatment and aesthetic skin improvement,” *Plasma Medicine*, vol. 4, no. 1-4, pp. 79–88, 2014.
- [201] Synergie, “An at-home device set to shake up the skincare industry.” <https://synergieskin.com/us/terris-blog/cold-plasma/>, 2020.
- [202] C. Yaopromsiri, L. D. Yu, S. Sarapirom, P. Thopan, and D. Boonyawan, “Effect of cold atmospheric pressure He-plasma jet on DNA change and mutation,” *Nuclear Instruments and Methods in Physics Research, Section B: Beam Interactions with Materials and Atoms*, vol. 365, pp. 399–403, 2015.
- [203] K. Saleewong, P. Wanachantararak, and P. Louwakul, “Efficacy of cold atmospheric pressure plasma jet against *Enterococcus faecalis* in apical canal of human single-rooted teeth: A preliminary study,” *IOP Conference Series: Materials Science and Engineering*, vol. 526, no. 1, 2019.

- [204] A. Chuangsuwanich, T. Assadamongkol, and D. Boonyawan, “The Healing Effect of Low-Temperature Atmospheric-Pressure Plasma in Pressure Ulcer: A Randomized Controlled Trial,” *International Journal of Lower Extremity Wounds*, vol. 15, no. 4, pp. 313–319, 2016.
- [205] International Organization for Standardization, “ISO 13485: Medical Devices.” <https://www.iso.org/iso-13485-medical-devices.html>, 2016.
- [206] US Food and Drug Administration, “Standards and Conformity Assessment Program.” <https://www.fda.gov/medical-devices/device-advice-comprehensive-regulatory-assistance/standards-and-conformity-assessment-program>, 2019.
- [207] US Food and Drug Administration, “Electromagnetic Compatibility (EMC).” <https://www.fda.gov/radiation-emitting-products/radiation-safety/electromagnetic-compatibility-emc>, 2018.
- [208] Deutsches Institut für Normung e. V., “DIN SPEC 91315,” 2014.
- [209] D. Ashpis, M. Laun, and E. Griebeler, “Progress toward Accurate Measurements of Power Consumption of DBD Plasma Actuators,” *50th AIAA Aerospace Sciences Meeting including the New Horizons Forum and Aerospace Exposition*, no. January, pp. 1–25, 2012.
- [210] L. Duvillaret, S. Rialland, and J.-I. Coutaz, “Electro-optic sensors for electric field measurements . I . Theoretical comparison among,” *Journal of the Optical Society of America B*, vol. 19, no. 11, pp. 2692–2703, 2002.
- [211] E. Robert, T. Darny, S. Dozias, S. Iseni, and J. M. Pouvesle, “New insights on the propagation of pulsed atmospheric plasma streams: From single jet to multi jet arrays,” *Physics of Plasmas*, vol. 22, no. 12, 2015.
- [212] A. Sobota, O. Guaitella, G. B. Sretenović, I. B. Krstić, V. V. Kovačević, A. Obrusnik, Y. N. Nguyen, L. Zajickova, B. M. Obradović, and M. M. Kuraica, “Electric field measurements in a kHz-driven He jet - the influence of the gas flow speed,” *Plasma Sources Science & Technology*, vol. 25, p. 065026, 2016.

- [213] M. Hofmans and A. Sobota, “Influence of a target on the electric field profile in a kHz atmospheric pressure plasma jet with the full calculation of the Stark shifts,” *Journal of Applied Physics*, vol. 125, no. 4, 2019.
- [214] M. Simeni Simeni, B. M. Goldberg, C. Zhang, K. Frederickson, W. R. Lempert, and I. V. Adamovich, “Electric field measurements in a nanosecond pulse discharge in atmospheric air,” *Journal of Physics D: Applied Physics*, vol. 50, no. 18, 2017.
- [215] A. V. Pipa, J. Koskulics, R. Brandenburg, and T. Hoder, “The simplest equivalent circuit of a pulsed dielectric barrier discharge and the determination of the gas gap charge transfer,” *Review of Scientific Instruments*, vol. 83, no. 11, 2012.
- [216] R. Brandenburg, “Dielectric barrier discharges: progress on plasma sources and on the understanding of regimes and single filaments,” *Plasma Sources Science and Technology*, vol. 26, no. 5, p. 053001, 2017.
- [217] L.-V. de Broglie, *Recherches sur la Théorie des Quanta*. PhD thesis, University of Paris, 1925.
- [218] NIST ASD Team, “NIST Atomic Spectra Database.” https://physics.nist.gov/PhysRefData/ASD/lines_form.html, 2019.
- [219] Q. Y. Zhang, D. Q. Shi, W. Xu, C. Y. Miao, C. Y. Ma, C. S. Ren, C. Zhang, and Z. Yi, “Determination of vibrational and rotational temperatures in highly constricted nitrogen plasmas by fitting the second positive system of N₂ molecules,” *AIP Advances*, vol. 5, no. 5, 2015.
- [220] C. Biloiu, X. Sun, Z. Harvey, and E. Scime, “An alternative method for gas temperature determination in nitrogen plasmas: Fits of the bands of the first positive system,” *Journal of Applied Physics*, vol. 101, no. 7, pp. 1–11, 2007.
- [221] Q. Yuan, P. Ren, S. Liu, J. Wang, and G. Yin, “The optical emission spectroscopy of nitrogen plasma driven by the 94.92 MHz/13.56 MHz dual-frequency,” *Physics Letters, Section A: General, Atomic and Solid State Physics*, vol. 384, no. 12, p. 126367, 2020.

- [222] C. O. Laux, "Radiation and nonequilibrium collisional-radiative models," in *von Karman Institute Special Course on Physico-chemical Modeling of High Enthalpy and Plasma Flows*, (Rhode-Saint-Genese, Belgium), 2002.
- [223] D. A. Staack, *Characterization and Stabilization of Atmospheric Pressure DC Microplasmas and their Application to Thin Film Deposition*. PhD thesis, Drexel University, 2008.
- [224] D. Staack, B. Farouk, A. Gutsol, and A. Fridman, "Spectroscopic studies and rotational and vibrational temperature measurements of atmospheric pressure normal glow plasma discharges in air," *Plasma Sources Science and Technology*, vol. 15, no. 4, p. 818, 2006.
- [225] J. Shi, Y. Ma, J. Zhu, Y. Chen, Y. Sun, Y. Yao, Z. Yang, and J. Xie, "A review on electroporation-based intracellular delivery," *Molecules*, vol. 23, no. 11, 2018.
- [226] R. Heller, M. Jaroszeski, A. Atkin, D. Moradpour, R. Gilbert, J. Wands, and C. Nicolau, "In vivo gene electroinjection and expression in rat liver," *FEBS Letters*, vol. 389, no. 3, pp. 225–228, 1996.
- [227] D. C. Chang and T. S. Reese, "Changes in membrane structure induced by electroporation as revealed by rapid-freezing electron microscopy," *Biophysical Journal*, vol. 58, no. 1, pp. 1–12, 1990.
- [228] The Vault, "Fusion Meso A Deeper Look." <http://www.thevaultdavenport.com/fusion-meso-a-deeper-look/>, 2018.
- [229] R. V. Davalos, L. M. Mir, and B. Rubinsky, "Tissue ablation with irreversible electroporation," *Annals of Biomedical Engineering*, vol. 33, no. 2, pp. 223–231, 2005.
- [230] N. Esmaeili and M. Friebe, "Electrochemotherapy: A Review of Current Status, Alternative IGP Approaches, and Future Perspectives," *Journal of Healthcare Engineering*, vol. 2019, 2019.
- [231] M. Wichtowski and D. Murawa, "Electrochemotherapy in the treatment of melanoma," *Wspolczesna Onkologia*, vol. 22, no. 1, pp. 8–13, 2018.

- [232] A. I. Daud, R. C. DeConti, S. Andrews, P. Urbas, A. I. Riker, V. K. Sondak, P. N. Munster, D. M. Sullivan, K. E. Ugen, J. L. Messina, and R. Heller, “Phase I trial of interleukin-12 plasmid electroporation in patients with metastatic melanoma,” *Journal of Clinical Oncology*, vol. 26, no. 36, pp. 5896–5903, 2008.
- [233] I. AngioDynamics, “AngioDynamics Receives FDA Approval to Initiate NanoKnife® DIRECT Clinical Study for the Treatment of Stage III Pancreatic Cancer.” <https://www.angiodynamics.com/news-and-events/73/AngioDynamics-Receives-FDA-Approval-to-Initiate-NanoKnife-DIRECT-Clinical-Study-for-the-Treatment-of-Stage-III-Pancreatic-Cancer/>, 2019.
- [234] W. Frey, J. A. White, R. O. Price, P. F. Blackmore, R. P. Joshi, R. Nuccitelli, S. J. Beebe, K. H. Schoenbach, and J. F. Kolb, “Plasma membrane voltage changes during nanosecond pulsed electric field exposure,” *Biophysical journal*, vol. 90, no. 10, pp. 3608–3615, 2006.
- [235] S. J. Beebe, P. M. Fox, L. J. Rec, K. Somers, R. H. Stark, and K. H. Schoenbach, “Nanosecond pulsed electric field (nsPEF) effects on cells and tissues: Apoptosis induction and tumor growth inhibition,” *IEEE Transactions on Plasma Science*, vol. 30, no. 1 II, pp. 286–292, 2002.
- [236] K. H. Schoenbach, R. P. Joshi, J. F. Kolb, N. Chen, M. Stacey, P. F. Blackmore, E. S. Buescher, and S. J. Beebe, “Ultrashort electrical pulses open a new gateway into biological cells,” *Proceedings of the IEEE*, vol. 92, no. 7, pp. 1122–1136, 2004.
- [237] J. Sandby-Møller, T. Poulsen, and H. C. Wulf, “Epidermal Thickness at Different Body Sites: Relationship to Age, Gender, Pigmentation, Blood Content, Skin Type and Smoking Habits,” *Acta Dermato-Venereologica*, vol. 83, no. 6, pp. 410–413, 2003.
- [238] M. Leduc, D. Guay, R. L. Leask, and S. Coulombe, “Cell permeabilization using a non-thermal plasma,” *New Journal of Physics*, vol. 11, 2009.
- [239] US Food and Drug Administration, “What Is Gene Therapy? How Does It Work?.” <https://www.fda.gov/consumers/consumer-updates/what-gene-therapy-how-does->

- it-work, 2017.
- [240] US Department of Health and Human Services, “Bleomycin With or Without Electroporation Therapy in Treating Patients With Stage III or Stage IV Melanoma.” <https://clinicaltrials.gov/ct2/show/NCT00006035>, 2004.
- [241] I. Inovio Pharmaceuticals, “Genetronics Granted FDA Fast Track Designation for its MedPulser® Electroporation Therapy System for Head and Neck Cancer.” <http://ir.inovio.com/news-and-media/news/press-release-details/2004/Genetronics-Granted-FDA-Fast-Track-Designation-for-its-MedPulser-Electroporation-Therapy-System-for-Head-and-Neck-Cancer/default.aspx>, 2004.
- [242] B. Pichi, R. Pellini, A. de Virgilio, and G. Spriano, “Electrochemotherapy: A well-accepted palliative treatment by patients with head and neck tumours,” *Acta Otorhinolaryngologica Italica*, vol. 38, no. 3, pp. 181–187, 2018.
- [243] US Department of Health and Human Services, “Confirmatory Trial in the Evaluation of Ca Electroporation for the Treatment of Cutaneous Metastases.” <https://clinicaltrials.gov/ct2/show/NCT03628417>, 2020.
- [244] US Food and Drug Administration, “NanoKnife 510(k) Letter K150089.” https://www.accessdata.fda.gov/cdrh_docs/pdf15/K150089.pdf, 2015.
- [245] US Department of Health and Human Services, “Outcomes of Ablation of Unresectable Pancreatic Cancer Using the NanoKnife Irreversible Electroporation (IRE) System.” <https://clinicaltrials.gov/ct2/show/NCT02041936>, 2014.
- [246] D. Mariotti, Y. Shimizu, T. Sasaki, and N. Koshizaki, “Gas temperature and electron temperature measurements by emission spectroscopy for an atmospheric microplasma,” *Journal of Applied Physics*, vol. 101, no. 1, pp. 1–8, 2007.
- [247] M. W. Ahmed, M. S. Rahman, S. Choi, U. Shaislamov, J.-K. Yang, R. Suresh, and H.-J. Leea, “Measurement of Electron Temperature and Number Density and Their Effects on

- Reactive Species Formation in a DC Underwater Capillary Discharge,” *Applied Science and Convergence Technology*, vol. 26, no. 5, pp. 118–128, 2017.
- [248] S. Z. Li, J. G. Kang, and H. S. Uhm, “Electrical breakdown characteristics of an atmospheric pressure rf capacitive plasma source,” *Physics of Plasmas*, vol. 12, no. 9, pp. 1–8, 2005.
- [249] D. Staack, B. Farouk, A. Gutsol, and A. Fridman, “Stabilization of the ionization overheating thermal instability in atmospheric pressure microplasmas,” *Journal of Applied Physics*, vol. 106, no. 1, 2009.
- [250] X. Lu, M. Laroussi, and V. Puech, “On atmospheric-pressure non-equilibrium plasma jets and plasma bullets,” *Plasma Sources Science and Technology*, vol. 21, no. 3, p. 034005, 2012.
- [251] X. Lu, G. V. Naidis, M. Laroussi, and K. Ostrikov, “Guided ionization waves: Theory and experiments,” *Physics Reports*, vol. 540, no. 3, pp. 123–166, 2014.
- [252] T. Sunaga, H. Ikehira, S. Furukawa, H. Shinkai, H. Kobavashi, Y. Matsumoto, E. Yoshitome, T. Obata, S. Tanada, H. Murata, and Y. Sasaki, “Measurement of the electrical properties of human skin and the variation among subjects with certain skin conditions.,” *Physics in medicine and biology*, vol. 47, no. 1, pp. N11–N15, 2002.
- [253] C. Gabriel, S. Gabriel, and E. Corthout, “The dielectric properties of biological tissues: I. Literature survey.,” *Physics in medicine and biology*, vol. 41, no. 11, pp. 2231–49, 1996.
- [254] E. L. Bell and J. W. Penn, “Electrical Parameter Values of Some Human Tissues in the Radiofrequency Radiation Range,” Tech. Rep. February, USAF School of Aerospace Medicine, 1978.
- [255] R. Code, Z. D. Popovic, and J. H. Sharp, “Electric-field-induced modulation of fluorescence from rhodamine 610 dye in a thin plastic film,” *Chemical Physics*, vol. 83, pp. 181–186, jan 1984.

- [256] S. M. Starikovskaia, A. Y. Starikovskii, and D. V. Zatsepin, “The development of a spatially uniform fast ionization wave in a large discharge volume,” *Journal of Physics D: Applied Physics*, vol. 31, no. 9, pp. 1118–1125, 1998.
- [257] S. M. Starikovskaia, N. B. Anikin, S. V. Pancheshnyi, D. V. Zatsepin, and A. Y. Starikovskii, “Pulsed breakdown at high overvoltage: development, propagation and energy branching,” *Plasma Sources Science and Technology*, vol. 10, no. 2, pp. 344–355, 2001.
- [258] A. Starikovskiy, “Fast ionization wave development in atmospheric-pressure air,” *IEEE Transactions on Plasma Science*, vol. 39, no. 11 PART 1, pp. 2602–2603, 2011.
- [259] W. T. Bovie, “Electrosurgical Apparatus.” Patent No. US1813902, 1931.
- [260] I. Alkatout, T. Schollmeyer, N. A. Hawaldar, N. Sharma, and L. Mettler, “Principles and safety measures of electrosurgery in laparoscopy,” *Journal of the Society of Laparoscopic Surgeons*, vol. 16, no. 1, pp. 130–139, 2012.
- [261] D. Palanker, A. Vankov, and P. Jayaraman, “On mechanisms of interaction in electrosurgery,” *New Journal of Physics*, vol. 10, 2008.
- [262] K. Wang and A. P. Advincula, ““Current thoughts” in electrosurgery,” *International Journal of Gynecology and Obstetrics*, vol. 97, no. 3, pp. 245–250, 2007.
- [263] Bovie Corporation, “J-Plasma.” <https://apyxmedical.com/jplasma/>, 2020.
- [264] Bovie Corporation, “Transformational Helium Plasma Technology.” http://www.boviemedical.com/jplasma/?wpfb_dl=97, 2019.
- [265] N. Barekzi, M. Laroussi, G. Konesky, and S. Roman, “Effects of low temperature plasma on prostate cancer cells using the Bovie Medical J-Plasma® device,” *Plasma Processes and Polymers*, vol. 13, no. 12, pp. 1189–1194, 2016.
- [266] G. Daeschlein, M. Napp, S. Lutze, A. Arnold, S. von Podewils, D. Guembel, and M. Jünger, “Skin and wound decontamination of multidrug-resistant bacteria by cold atmospheric

- plasma coagulation,” *JDDG: Journal der Deutschen Dermatologischen Gesellschaft*, vol. 13, pp. 143–149, feb 2015.
- [267] US Food and Drug Administration, “Aaron 510(k) Letter K051956.” https://www.accessdata.fda.gov/cdrh_docs/pdf5/K051956.pdf, 2005.
- [268] Bovie Corporation, “Aaron 940 User Manual,” 2013.
- [269] S. Rohlf, “Laparoscopic Electrosurgery,” in *Prevention & Management of Laparoendoscopic Surgical Complications*, ch. Chapter 2, The Society of Laparoendoscopic Surgeons, 1999.
- [270] G. Glockler, “Complex formation,” *Transactions of the Faraday Society*, vol. 33, no. 224, p. 224, 1937.
- [271] X. Yuan and L. L. Raja, “Computational study of capacitively coupled high-pressure glow discharges in helium,” *IEEE Transactions on Plasma Science*, vol. 31, no. 4 II, pp. 495–503, 2003.
- [272] N. Ohno, M. A. Razzak, H. Ukai, S. Takamura, and Y. Uesugi, “Validity of Electron Temperature Measurement by Using Boltzmann Plot Method in Radio Frequency Inductive Discharge in the Atmospheric Pressure Range,” *Plasma and Fusion Research*, vol. 1, pp. 028–028, 2006.
- [273] I. Gibson, D. W. Rosen, and B. Stucker, “Additive manufacturing technologies: Rapid prototyping to direct digital manufacturing,” in *Additive Manufacturing Technologies: Rapid Prototyping to Direct Digital Manufacturing*, ch. Direct Wri, pp. 275–298, Boston, MA: Springer US, 2010.
- [274] J. A. Lewis and G. M. Gratson, “Direct writing in three dimensions,” *Materials Today*, vol. 7, no. 7, pp. 32–39, 2004.
- [275] K. K. Hon, L. Li, and I. M. Hutchings, “Direct writing technology-Advances and developments,” *CIRP Annals - Manufacturing Technology*, vol. 57, no. 2, pp. 601–620, 2008.

- [276] J. L. Wasserman, K. Lucas, S. H. Lee, A. Ashton, C. T. Crowl, and N. Marković, “Fabrication of one-dimensional programmable-height nanostructures via dynamic stencil deposition,” *Review of Scientific Instruments*, vol. 79, no. 7, 2008.
- [277] A. M. Abdul-Wahed, A. L. Roy, Z. Xiao, and K. Takahata, “Direct writing of metal film via sputtering of micromachined electrodes,” *Journal of Materials Processing Technology*, vol. 262, no. August 2017, pp. 403–410, 2018.
- [278] A. M. Abdul-Wahed, A. L. Roy, and K. Takahata, “Microplasma drawing of thermocouple sensors,” *Proceedings of IEEE Sensors*, pp. 1–3, 2017.
- [279] E. Dudley, *A Microplasma-Based Sputtering System for Direct-Write, Microscale Fabrication of Thin-Film Metal Structures*. Master’s thesis, Case Western Reserve University, 2016.
- [280] K. H. Church, C. Fore, and T. Feeley, “Commercial Applications and Review for Direct Write Technologies,” *MRS Proceedings*, vol. 624, p. 3, feb 2000.
- [281] S. E. Alexandrov and M. L. Hitchman, “Chemical vapor deposition enhanced by atmospheric pressure non-thermal non-equilibrium plasmas,” *Chemical Vapor Deposition*, vol. 11, no. 11-12, pp. 457–468, 2005.
- [282] T. Belmonte, G. Henrion, and T. Gries, “Nonequilibrium atmospheric plasma deposition,” *Journal of Thermal Spray Technology*, vol. 20, no. 4, pp. 744–759, 2011.
- [283] J. Benedikt, K. Focke, A. Yanguas-Gil, and A. Von Keudell, “Atmospheric pressure microplasma jet as a depositing tool,” *Applied Physics Letters*, vol. 89, no. 25, pp. 2004–2007, 2006.
- [284] J. Benedikt, V. Raballand, A. Yanguas-Gil, K. Focke, and A. Von Keudell, “Thin film deposition by means of atmospheric pressure microplasma jet,” *Plasma Physics and Controlled Fusion*, vol. 49, no. 12 B, 2007.
- [285] G. Kim, S. Park, H. Shin, S. Song, H. J. Oh, D. H. Ko, J. I. Choi, and S. J. Baik, “Two dimensional radial gas flows in atmospheric pressure plasma-enhanced chemical vapor deposition,” *AIP Advances*, vol. 7, no. 12, pp. 1–13, 2017.

- [286] S. Guruvenket, S. Andrie, M. Simon, K. W. Johnson, and R. A. Sailer, “Atmospheric-pressure plasma-enhanced chemical vapor deposition of a-SiCN:H films: Role of precursors on the film growth and properties,” *ACS Applied Materials and Interfaces*, vol. 4, no. 10, pp. 5293–5299, 2012.
- [287] J. L. Hodgkinson and D. W. Sheel, “Advances in atmospheric pressure PECVD: The influence of plasma parameters on film morphology,” *Surface and Coatings Technology*, vol. 230, pp. 73–76, 2013.
- [288] S. Kang, R. Mauchauffé, Y. S. You, and S. Y. Moon, “Insights into the Role of Plasma in Atmospheric Pressure Chemical Vapor Deposition of Titanium Dioxide Thin Films,” *Scientific Reports*, vol. 8, no. 1, pp. 1–13, 2018.
- [289] A. Perraudau, C. Dublanche-Tixier, P. Tristant, C. Chazelas, S. Vedraine, and B. Ratier, “Low-temperature deposition of TiO₂ by atmospheric pressure PECVD towards photoanode elaboration for perovskite and solid-state dye-sensitized solar cells,” *EPJ Photovoltaics*, vol. 10, pp. 0–4, 2019.
- [290] A. Dey, A. Lopez, G. Filipič, A. Jayan, D. Nordlund, J. Koehne, S. Krishnamurthy, R. P. Gandhiraman, and M. Meyyappan, “Plasma jet based in situ reduction of copper oxide in direct write printing,” *Journal of Vacuum Science & Technology B*, vol. 37, no. 3, p. 031203, 2019.
- [291] R. P. Gandhiraman, V. Jayan, J. W. Han, B. Chen, J. E. Koehne, and M. Meyyappan, “Plasma jet printing of electronic materials on flexible and nonconformal objects,” *ACS Applied Materials and Interfaces*, vol. 6, no. 23, pp. 20860–20867, 2014.
- [292] S. W. Lee, D. Liang, X. P. A. Gao, and R. M. Sankaran, “Direct Writing of Metal Nanoparticles by Localized Plasma Electrochemical Reduction of Metal Cations in Polymer Films,” *Advanced Functional Materials*, vol. 21, no. 11, pp. 2155–2161, 2011.
- [293] M. Meyyappan, L. Delzeit, A. Cassell, and D. Hash, “Carbon nanotube growth by PECVD: A review,” *Plasma Sources Science and Technology*, vol. 12, no. 2, pp. 205–216, 2003.

- [294] Thierry Corp, “Plasma Knowledge: PECVD Industrial Applications.” <https://www.thierry-corp.com/plasma/plasma-resources/plasma-knowledgebase/industrial-pecvd-applications/>, 2020.
- [295] US Food and Drug Administration, “Sec. 880.5090 Liquid bandage.” <https://www.accessdata.fda.gov/scripts/cdrh/cfdocs/cfcfr/CFRSearch.cfm?fr=880.5090>, 2019.
- [296] Neogen, “AluShield™ Aerosol Bandage.” <https://animalsafety.neogen.com/pdf/prodinfo/79100.pdf>, 2017.
- [297] K. L. Huebner, A. K. Kunkel, C. S. McConnel, R. J. Callan, R. P. Dinsmore, and L. S. Caixeta, “Evaluation of horn bud wound healing following cautery disbudding of preweaned dairy calves treated with aluminum-based aerosol bandage,” *Journal of Dairy Science*, vol. 100, no. 5, pp. 3922–3929, 2017.
- [298] A. Radhakrishnan, G. Kuppusamy, and V. V. S. R. Karri, “Spray bandage strategy in topical drug delivery,” *Journal of Drug Delivery Science and Technology*, vol. 43, pp. 113–121, 2018.
- [299] D. S. Yoon, Y. Lee, H. A. Ryu, Y. Jang, K. M. Lee, Y. Choi, W. J. Choi, M. Lee, K. M. Park, K. D. Park, and J. W. Lee, “Cell recruiting chemokine-loaded sprayable gelatin hydrogel dressings for diabetic wound healing,” *Acta Biomaterialia*, vol. 38, pp. 59–68, 2016.
- [300] N. Annabi, D. Rana, E. Shirzaei Sani, R. Portillo-Lara, J. L. Gifford, M. M. Fares, S. M. Mithieux, and A. S. Weiss, “Engineering a sprayable and elastic hydrogel adhesive with antimicrobial properties for wound healing,” *Biomaterials*, vol. 139, pp. 229–243, 2017.
- [301] P. M. Neumann, B. Zur, and Y. Ehrenreich, “Gelatin-based sprayable foam as a skin substitute,” *Journal of Biomedical Materials Research*, vol. 15, no. 1, pp. 9–18, 1981.
- [302] J. C. Salamone, A. B. Salamone, K. Swindle-Reilly, K. X. C. Leung, and R. E. McMahon, “Grand challenge in Biomaterials-wound healing,” *Regenerative Biomaterials*, vol. 3, no. 2, pp. 127–128, 2016.

- [303] D.-H. Kim, N. Lu, R. Ma, Y.-S. Kim, R.-H. Kim, S. Wang, J. Wu, S. M. Won, H. Tao, A. Islam, K. J. Yu, T.-i. Kim, R. Chowdhury, M. Ying, L. Xu, M. Li, H.-J. Chung, H. Keum, M. McCormick, P. Liu, Y.-W. Zhang, F. G. Omenetto, Y. Huang, T. Coleman, and J. A. Rogers, “Epidermal Electronics,” *Science*, vol. 333, pp. 838–843, aug 2011.
- [304] H. U. Chung, B. H. Kim, J. Y. Lee, J. Lee, Z. Xie, E. M. Ibler, K. H. Lee, A. Banks, J. Y. Jeong, J. Kim, C. Ogle, D. Grande, Y. Yu, H. Jang, P. Assem, D. Ryu, J. W. Kwak, M. Namkoong, J. B. Park, Y. Lee, D. H. Kim, A. Ryu, J. Jeong, K. You, B. Ji, Z. Liu, Q. Huo, X. Feng, Y. Deng, Y. Xu, K. I. Jang, J. Kim, Y. Zhang, R. Ghaffari, C. M. Rand, M. Schau, A. Hamvas, D. E. Weese-Mayer, Y. Huang, S. M. Lee, C. H. Lee, N. R. Shanbhag, A. S. Paller, S. Xu, and J. A. Rogers, “Binodal, wireless epidermal electronic systems with in-sensor analytics for neonatal intensive care,” *Science*, vol. 363, no. 6430, pp. 0–13, 2019.
- [305] S. Wang, J. Xu, W. Wang, G. J. N. Wang, R. Rastak, F. Molina-Lopez, J. W. Chung, S. Niu, V. R. Feig, J. Lopez, T. Lei, S. K. Kwon, Y. Kim, A. M. Foudeh, A. Ehrlich, A. Gasperini, Y. Yun, B. Murmann, J. B. Tok, and Z. Bao, “Skin electronics from scalable fabrication of an intrinsically stretchable transistor array,” *Nature*, vol. 555, no. 7694, pp. 83–88, 2018.
- [306] M. Kondo, M. Melzer, D. Karnaushenko, T. Uemura, S. Yoshimoto, M. Akiyama, Y. Noda, T. Araki, O. G. Schmidt, and T. Sekitani, “Imperceptible magnetic sensor matrix system integrated with organic driver and amplifier circuits,” *Science advances*, vol. 6, no. 4, p. eaay6094, 2020.
- [307] W. Gao, S. Emaminejad, H. Y. Y. Nyein, S. Challa, K. Chen, A. Peck, H. M. Fahad, H. Ota, H. Shiraki, D. Kiriya, D. H. Lien, G. A. Brooks, R. W. Davis, and A. Javey, “Fully integrated wearable sensor arrays for multiplexed in situ perspiration analysis,” *Nature*, vol. 529, no. 7587, pp. 509–514, 2016.
- [308] S. Z. Guo, K. Qiu, F. Meng, S. H. Park, and M. C. McAlpine, “3D Printed Stretchable Tactile Sensors,” *Advanced Materials*, vol. 29, no. 27, pp. 1–8, 2017.

- [309] P. A. Lopes, H. Paisana, A. T. De Almeida, C. Majidi, and M. Tavakoli, “Hydroprinted Electronics: Ultrathin Stretchable Ag-In-Ga E-Skin for Bioelectronics and Human-Machine Interaction,” *ACS Applied Materials and Interfaces*, vol. 10, no. 45, pp. 38760–38768, 2018.
- [310] A. J. Bandonkar, W. Jia, J. Ramírez, and J. Wang, “Biocompatible Enzymatic Roller Pens for Direct Writing of Biocatalytic Materials: “Do-it-Yourself” Electrochemical Biosensors,” *Advanced Healthcare Materials*, vol. 4, no. 8, pp. 1215–1224, 2015.
- [311] Z. Zhu, S. Z. Guo, T. Hirdler, C. Eide, X. Fan, J. Tolar, and M. C. McAlpine, “3D Printed Functional and Biological Materials on Moving Freeform Surfaces,” *Advanced Materials*, vol. 30, no. 23, pp. 1–8, 2018.
- [312] Y. Yu, J. Zhang, and J. Liu, “Biomedical Implementation of Liquid Metal Ink as Drawable ECG Electrode and Skin Circuit,” *PLoS ONE*, vol. 8, no. 3, pp. 8–13, 2013.
- [313] N. X. Williams, S. Noyce, J. A. Cardenas, M. Catenacci, B. J. Wiley, and A. D. Franklin, “Silver nanowire inks for direct-write electronic tattoo applications,” *Nanoscale*, vol. 11, no. 30, pp. 14294–14302, 2019.
- [314] M. Hitti, “New Liquid Bandage Approved.” <https://www.webmd.com/first-aid/news/20080208/new-liquid-bandage-approved>, 2008.
- [315] Avita Medical, “AVITA Medical Announces FDA Approval of the RECELL® System for the Treatment of Severe Burns in the U.S.” <https://www.avitamedical.com/uploads/pdf/AVITA-Medical-Press-Release-PMA-Approval-21-September-2018.pdf>, 2018.
- [316] US Food and Drug Administration, “Part 898 Performance Standard for Electrode Lead Wires and Patient Cables.” <https://www.accessdata.fda.gov/scripts/cdrh/cfdocs/cfcfr/CFRSearch.cfm?CFRPart=898&showFR=1>, 2019.
- [317] T. Maruyama and Y. Ikuta, “Copper thin films prepared by chemical vapour deposition from copper dipivalylmethanate,” *Journal of Materials Science*, vol. 28, no. 20, pp. 5540–5542, 1993.

- [318] Y. Sawada, H. Tamaru, M. Kogoma, M. Kawase, and K. Hashimoto, “The reduction of copper oxide thin films with hydrogen plasma generated by an atmospheric-pressure glow discharge,” *Journal of Physics D: Applied Physics*, vol. 29, no. 10, pp. 2539–2544, 1996.
- [319] I. Gibson, D. Rosen, and B. Stucker, *Additive Manufacturing Technologies*. New York, NY: Springer New York, 2015.
- [320] P. Zelinski, “Additive Manufacturing and 3D Printing Are Two Different Things.” <https://www.additivemanufacturing.media/blog/post/additive-manufacturing-and-3d-printing-are-two-different-things>, 2017.
- [321] Y. Huang, M. C. Leu, J. Mazumder, and A. Donmez, “Additive Manufacturing: Current State, Future Potential, Gaps and Needs, and Recommendations,” *Journal of Manufacturing Science and Engineering*, vol. 137, no. 1, p. 014001, 2015.
- [322] A. K. Ravi, A. Deshpande, and K. H. Hsu, “An in-process laser localized pre-deposition heating approach to inter-layer bond strengthening in extrusion based polymer additive manufacturing,” *Journal of Manufacturing Processes*, vol. 24, pp. 179–185, 2016.
- [323] V. Kishore, C. Ajinjeru, A. Nycz, B. Post, J. Lindahl, V. Kunc, and C. Duty, “Infrared preheating to improve interlayer strength of big area additive manufacturing (BAAM) components,” *Additive Manufacturing*, vol. 14, pp. 7–12, 2017.
- [324] Essentium LLC, “FlashFuse.” <https://essentium3d.com/flashfuse/>, 2020.
- [325] C. C. Shih, *Effects of Cold Plasma Treatment on Interlayer Bonding Strength in Fused Filament Fabrication (FFF) Process*. Master’s thesis, Texas A&M University, 2019.
- [326] C. B. Sweeney, *Electromagnetic Energy Coupled to Nanomaterial Composites for Polymer Manufacturing*. PhD thesis, Texas A&M University, 2017.
- [327] S. Jackson, “BASF and Essentium, Inc. create 3D printed prosthetic leg that maintains strength during life cycle modifications.” <https://www.basf.com/us/en/media/news-releases/2018/04/P-US-18-047.html>, 2018.

- [328] K. Cantekin and S. Avci, “Evaluation of shear bond strength of two resin-based composites and glass ionomer cement to pure tricalcium silicate-based cement (Biodentine ®),” *Journal of Applied Oral Science*, vol. 22, no. 4, pp. 302–306, 2014.

APPENDIX A

DOUBLE SPARK GAP DISCHARGE GENERATOR USER GUIDE

The user guide for the RC pulse generator circuit (see Section 4.4.1) that was delivered to the project sponsor (EP Technologies, LLC) is on the following pages. This includes more details on how the power supply behaved under various conditions (different values for C , R_2 , substrate, etc. as shown in Figure 4.4), as well as step-by-step operating instructions and a short troubleshooting guide.

Double Spark-Gap Discharge Device User Guide



Sections:

I. Safety Warnings

Describes warnings for the dangers during use of this device

II. Overview

Provides a discussion of the device's contents

III. Operating Instructions

Step-by-step operating instructions for using this device

IV. Normal Operation

Provides voltage-current graphs of the pulses and shows general ranges for achieving certain operating conditions

V. Troubleshooting

Provides instruction on how to correct certain issues that may come up in device operation

Contact: Matthew Burnette (burnetteml@tamu.edu) or David Staack (dstaack@tamu.edu)

I. Safety Warnings

Warning: For use only by properly trained personnel. Minimum training must include proper safety procedures around high voltage electrical equipment.

Warning: This double spark-gap discharge generator contains capacitors that can store electrical energy for long times. Always ensure the device is grounded and ALL capacitors are discharged before operating, INCLUDING capacitors not connected to the circuit.

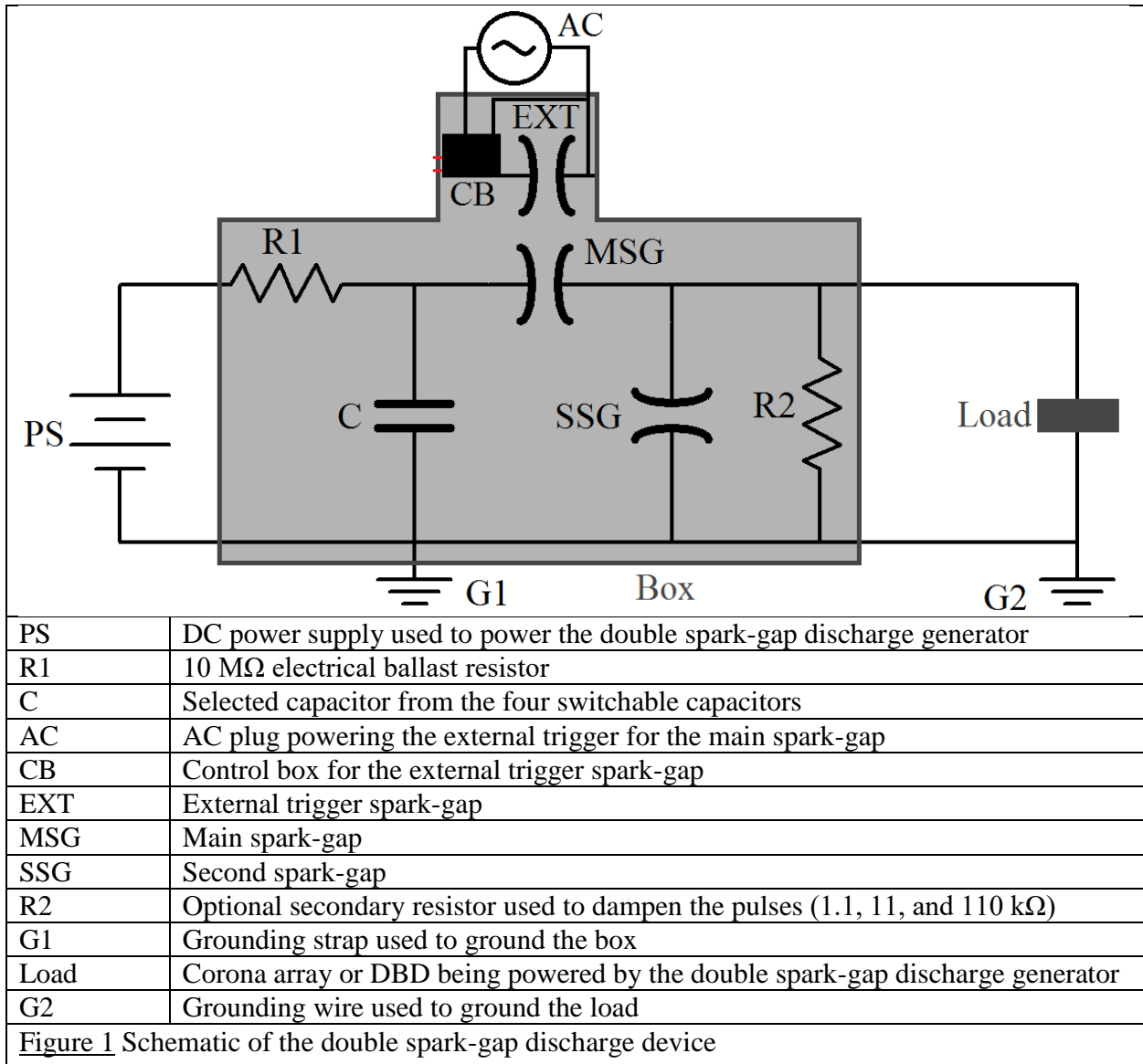
Warning: This double spark-gap discharge generator can output significant electromagnetic interference (EMI). During use, ensure the box is closed and locked with all acrylic shields in place.

Warning: High voltage is used to power this device. Ensure all wires are properly insulated, the box is properly grounded, and the load is grounded appropriately.

Warning: Do not exceed voltage, current, and power ratings of device. Failure can occur if ratings are exceeded which will destroy the device and create an electrical hazard for the operator.

II. Overview

The double spark-gap discharge generator contains a 10 MΩ electrical ballast resistor, four switchable capacitors (5 nF, 500 pF, 50 pF, and stray capacitance), an optional secondary resistor to dampen the pulses, two independently adjustable spark-gaps, and an external trigger box controlling a third external trigger spark-gap. The schematic is shown below in Figure 1 with a legend and the inside of the box is shown in Figure 2.



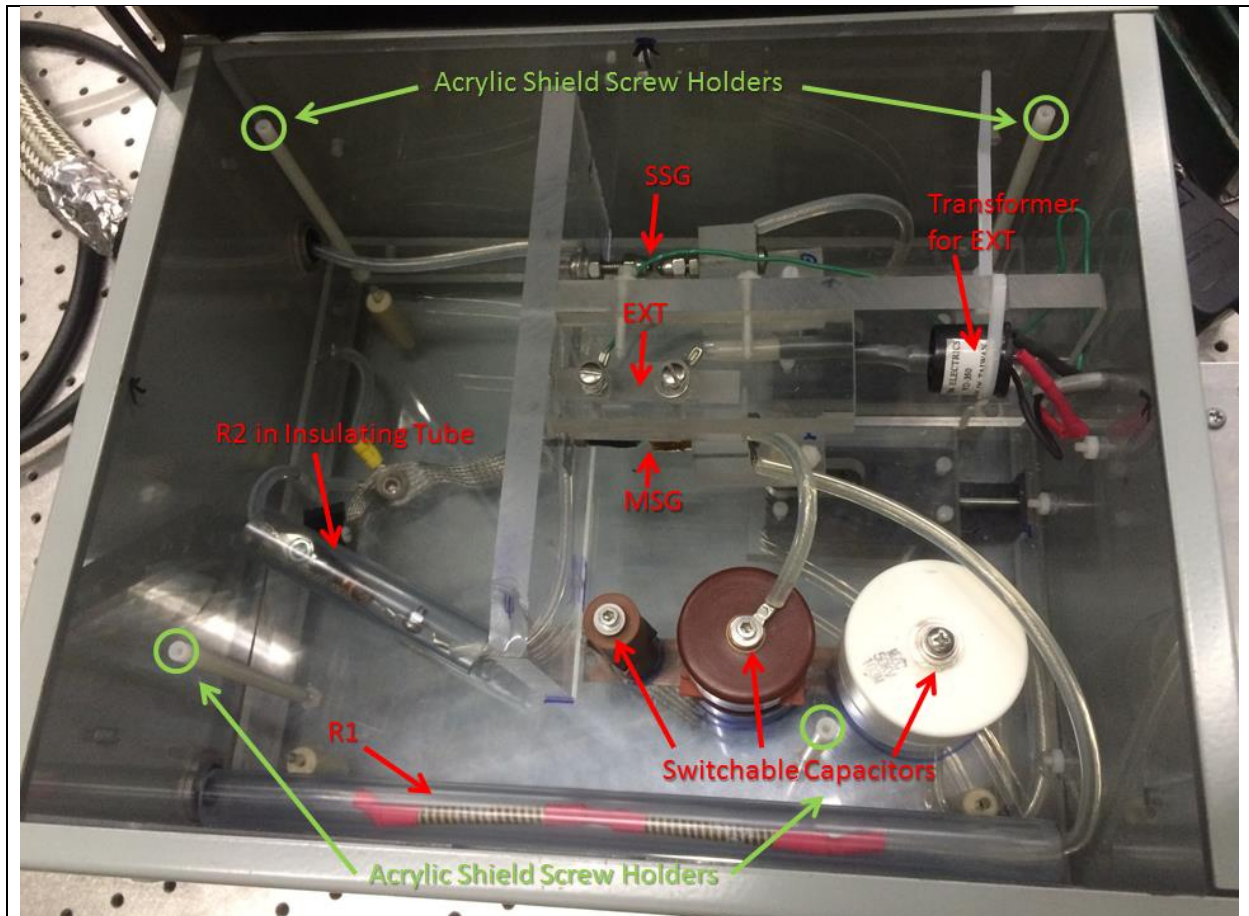


Figure 2 View inside of box showing various components of the double spark-gap discharge generator

The ballast resistor, R1, is used to control the rate the selected capacitor charges. Changing between the four switchable capacitors (5 nF, 500 pF, 50 pF, and stray capacitance) changes the energy per pulse coming from the double spark-gap discharge device. See section *IV. Normal Operation* for data on the pulse characteristics for each capacitor. Note that the capacitors do not have interchangeable screws; the 50 pF and 500 pF capacitors are screw size M4 (metric), and the 5 nF capacitor has screw size #10-24. Stray capacitance is achieved by securing the wire to the capacitors to the screw on the main spark-gap head (see Figure 3). This RC circuit is rated for a maximum of **40 kV, 2.5 mA, and 32 W**. There is a grounding rod attached to the box by the external trigger control box for discharging the capacitors.

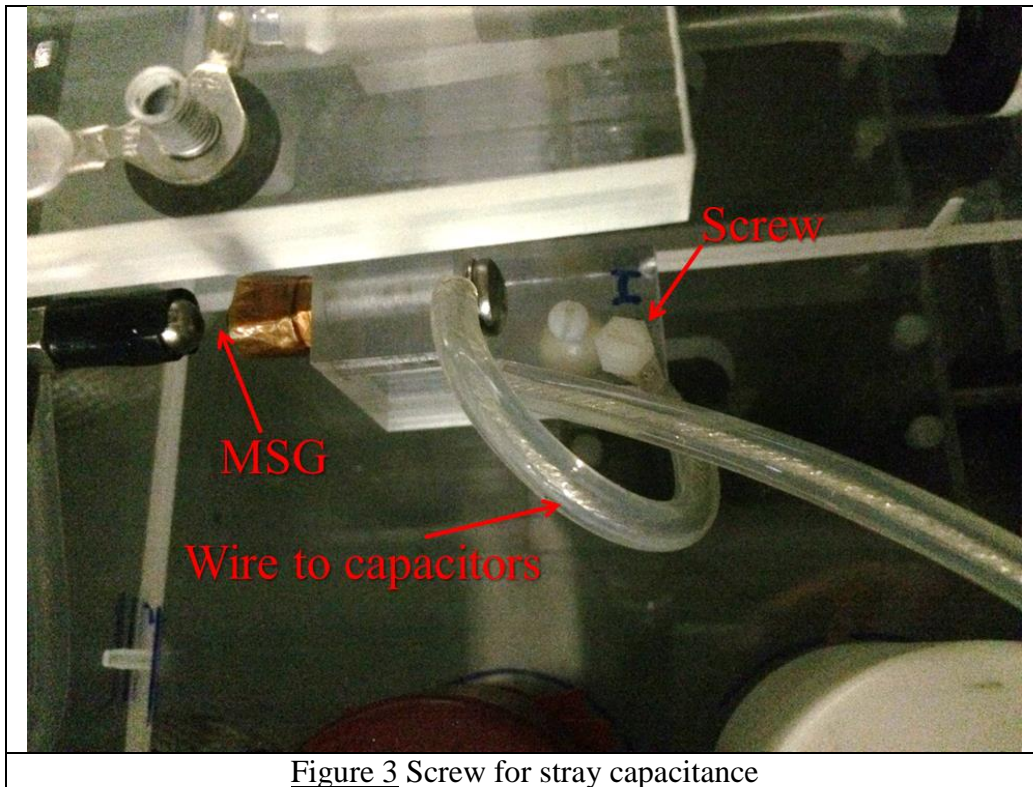
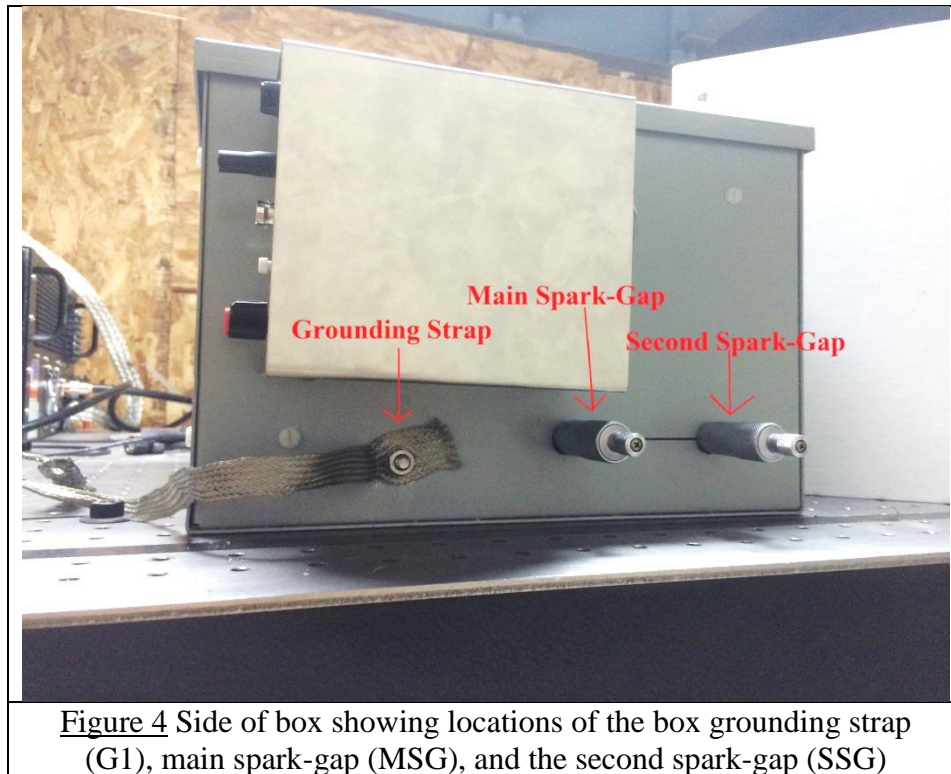


Figure 3 Screw for stray capacitance

The spark-gap micrometers are seen in Figure 4. The main spark-gap, MSG, is controlled by a micrometer which ranges from -0.087 in (note that the closed gap, when the two ends touch, is below the zero reading on the micrometer) to 0.95 in. Increasing this gap increases the amount of voltage per pulse. The second spark-gap, SSG, ranges from -0.092 in (note that the closed gap, when the two ends touch, is below the zero reading on the micrometer) to 0.95 in. Note that these zero-values changed upon rebuilding of the double spark gap generator after damage due to shipping to EP Technologies. Though any differences in distances are the same, there is a shift for accounting for a new zero location which is NOT accounted for in this document. For large distances, the second spark-gap controls the pulse width; decreasing it further has no significant effect on the pulse width, instead it reduces the pulse peak voltage. The secondary resistor, R2, is used to dampen any oscillatory behavior in the pulse by slowly discharging current delivered to the load as well as draining unwanted charge from the downstream side of the main spark-gap. The best damping behavior occurs for R2 values between 1 k Ω and 100 k Ω . Larger values do not leak charge fast enough and encourage corona breakdown initially, and much smaller resistance values reduce the pulse maximum voltage, since significant charge leaks off through the resistor rather than traveling to the load (for more information see section IV. *Normal Operation* subsection E. *Effect of R2* and section V. *Troubleshooting* number 4).



The two grounding locations are internally connected, thus they are not separate grounds, but used to ground two different locations. The grounding strap on the box (G1, seen in Figure 4) is used to ensure the box is at earth ground and will not build up charge. If this grounding location is replaced, ensure that it is only replaced with high gauge grounding strap wire. The load ground (G2) is the marked wire next to the load input wire and is used to connect the ground side of the load to the circuit ground, completing a current path for the voltage pulse.



The external trigger box is attached to the main box; it is powered by a 12 V AC wall adapter. The external trigger control panel is seen in Figure 5. It has the controls for various

ways to operate the external trigger spark-gap. The knob on the right controls the mode for the external trigger. The three modes are described in the Table 1.

Table 1: External Trigger Modes

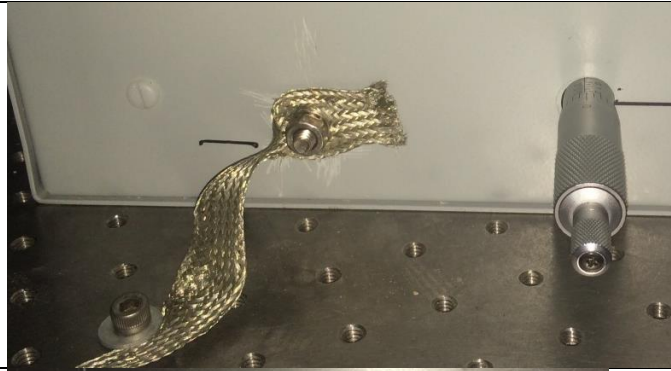
1-Single	Controls the trigger via the white Single button
2- Pulse	Controls the trigger via the ON/Pulse knob
3-Ext Trig	Controls the trigger via an external device connected into the Ext Trig BNC plug

The white Single button works in single mode. Pressing it causes the external trigger spark-gap to discharge. The Ext Trig plug connects to a 50 Ω BNC cable; a minimum voltage change of 650 mV is required to operate the trigger. The ON/Pulse knob controls both the power for the entire box **regardless of mode**, and it also controls the frequency of the pulse in pulse mode, varying between a frequency of 12 Hz (just past clicking into the ON position by turning clockwise) and 125 Hz (farthest turning of the knob clockwise). The voltage pulses outputted from the box are stepped up to approximately 12 kV by the transformer inside of the main box, thus breaking down the external trigger spark-gap, EXT.

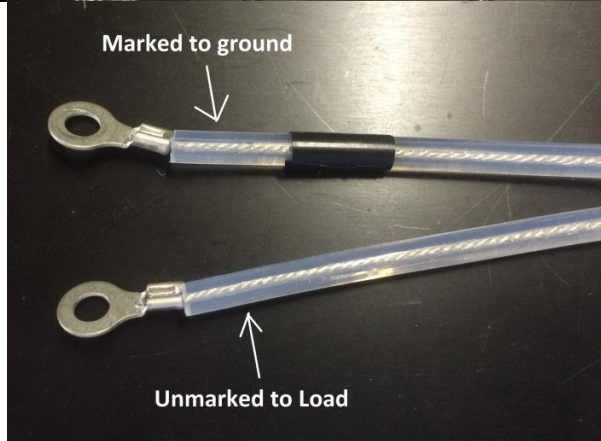
In addition to the three pulsing modes above, the box is also capable of being operated without an external trigger. In this self-pulsing mode, the frequency of pulses is controlled by the amount of current supplied from the power supply, with higher currents charging the capacitor more quickly thus increasing the pulsing frequency.

III. Operating Instructions

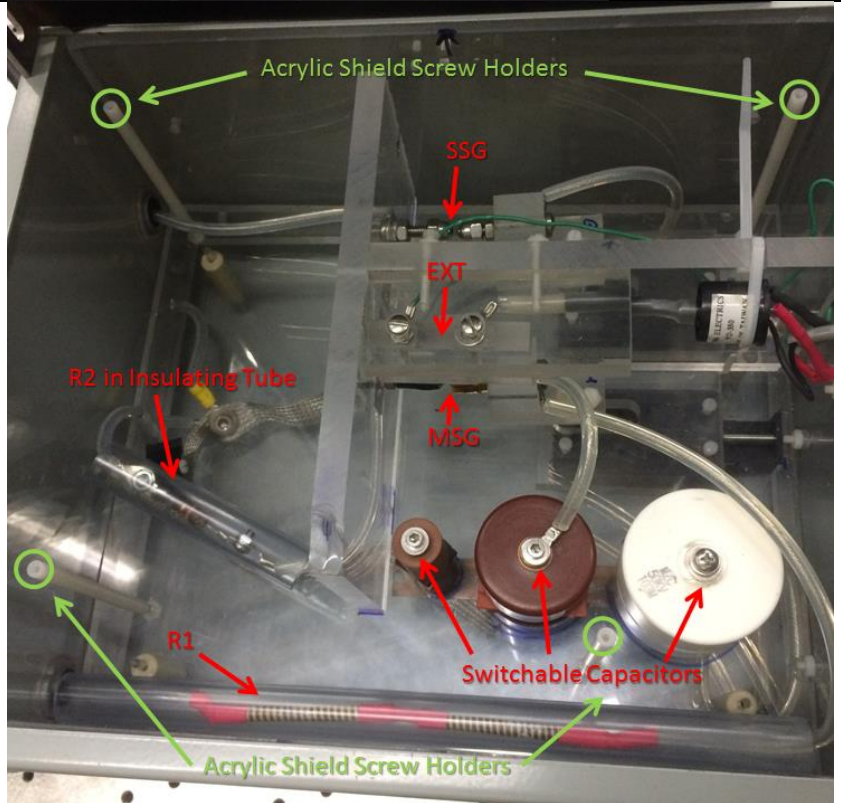
1. Connect the grounding strap (G1) on the outside of the box to earth ground. Ensure this is also the ground for the power supply used.



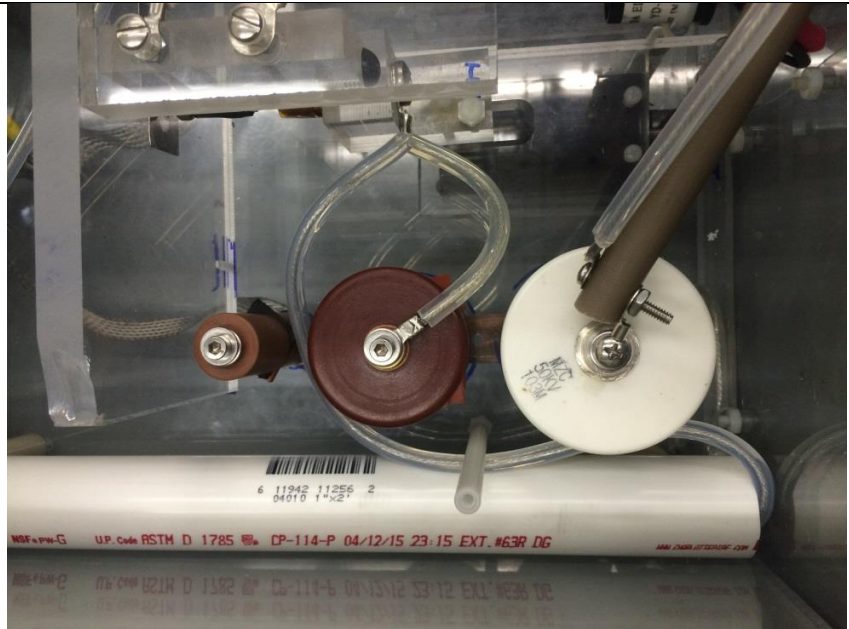
2. Connect the desired load (corona array or DBD) to the unmarked output wire and attach the marked output ground wire (G2) appropriately.



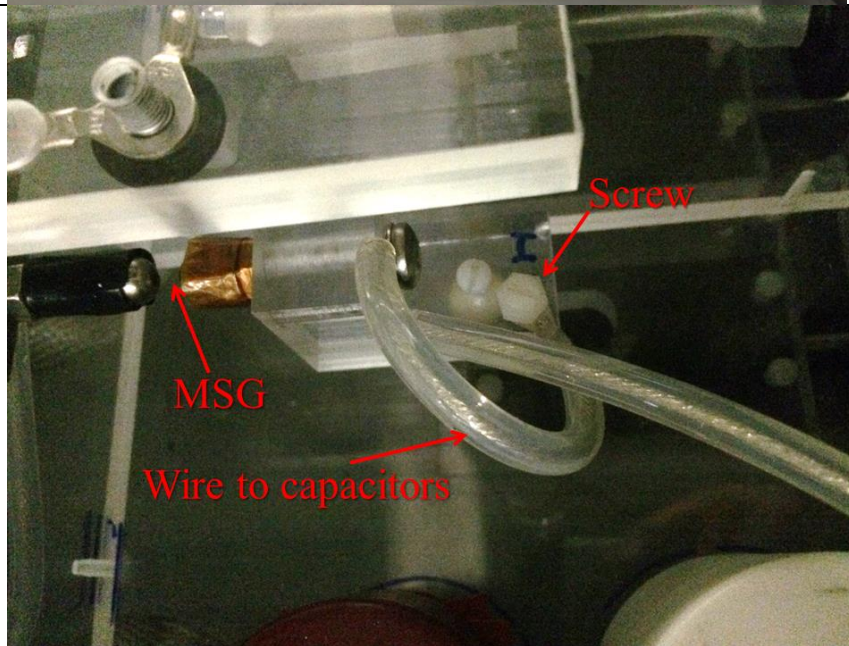
3. Open the box and remove the top acrylic shield held in place by 4 plastic screws.



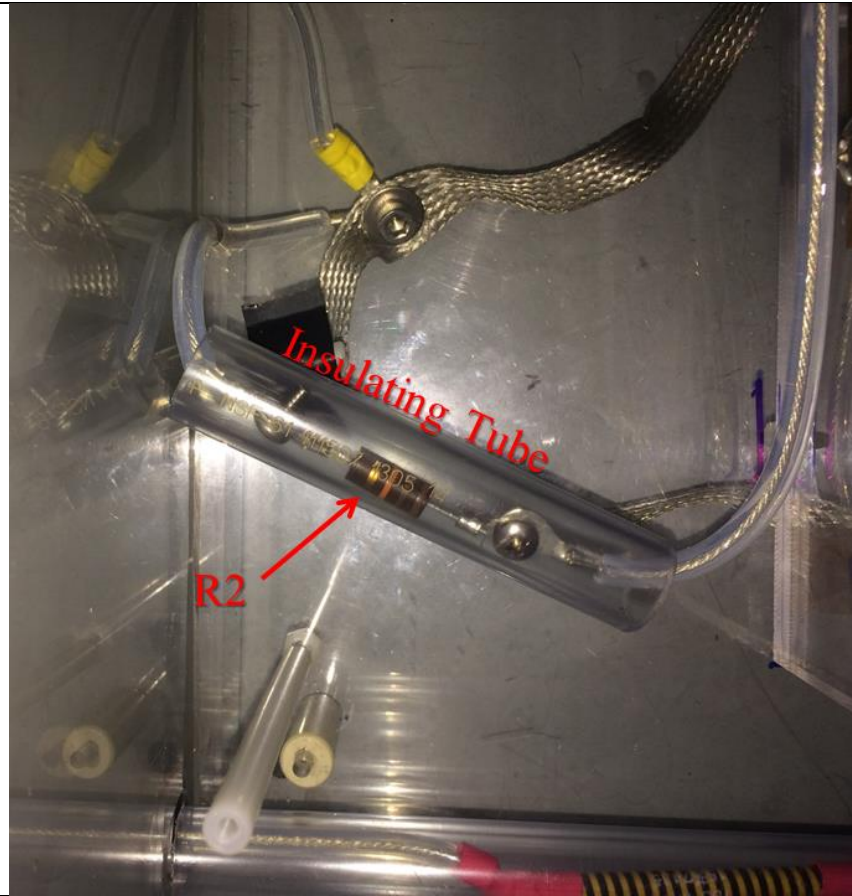
4. Using the attached grounding rod, ensure the capacitors are discharged. Check every capacitor, **including the ones not connected to the circuit.** Stray charge can build up on the capacitors even when they are not attached to the circuit. It is best to check each capacitor multiple times since they do not always fully discharge if good contact not made.



5. Attach the desired capacitor (C) to the main spark-gap. If stray capacitance is desired, remove the wire connecting the capacitors to the main spark-gap and secure it to the screw near the main spark-gap.



6. Replace the secondary (dampening) resistor (R2) as needed for the required dampening of the pulse, ensuring the resistor is inside of its insulating tube. For multiple resistors in series it may not be possible to insulate the resistors in the insulating tube. In which case, make sure they are as far away from other electrical connections as possible.



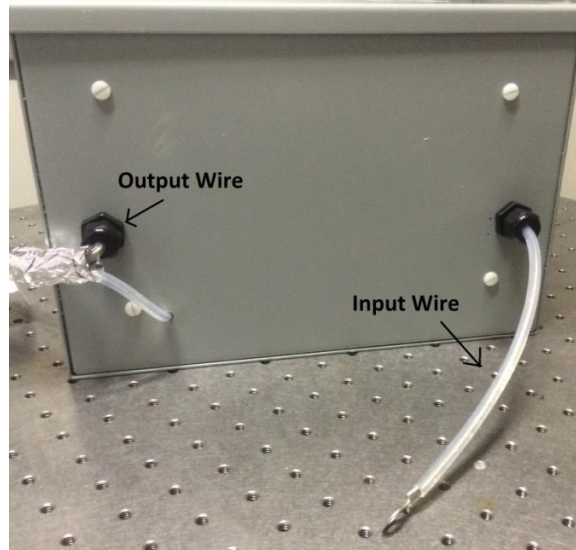
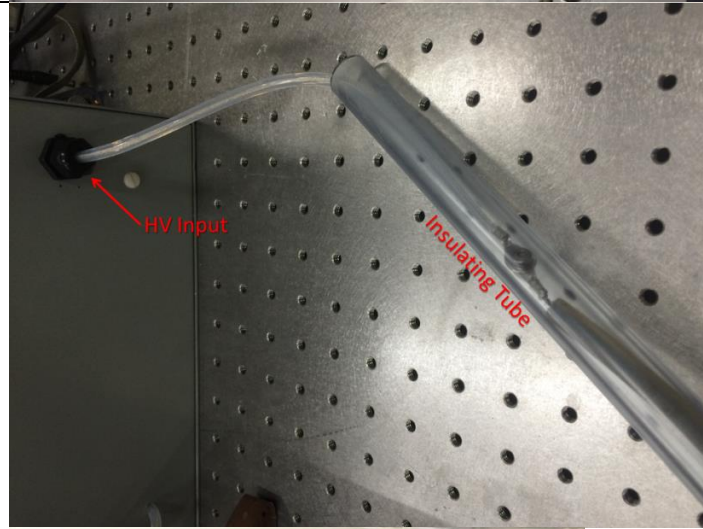
7. Visually ensure both spark-gaps are closed. (Note: the micrometer reading is not the actual spark-gap distance; the micrometers will be in a negative position to close the spark-gaps.)




8. Replace the top acrylic shield and screw it down. Then close and lock the box.

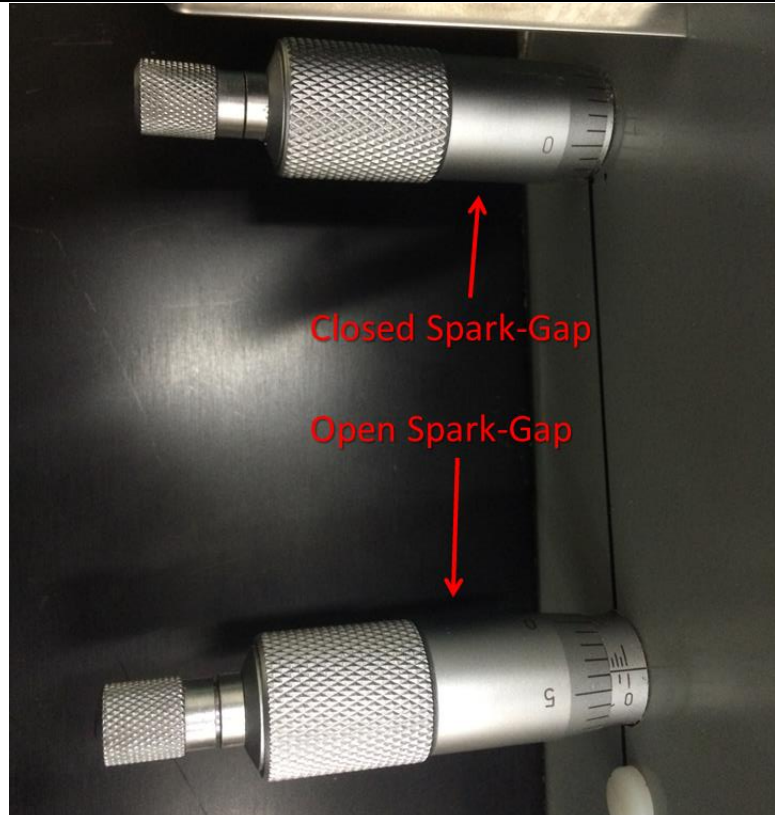


9. Connect the high voltage power supply to the input wire. Ensure it is properly insulated. PVC tubing or some other thick dielectric works well. Make sure the exposed electrical connections are at least 5 in inside of the dielectric. It is also advisable to wrap the exposed electrical connections with electrical tape as well for additional insulation.

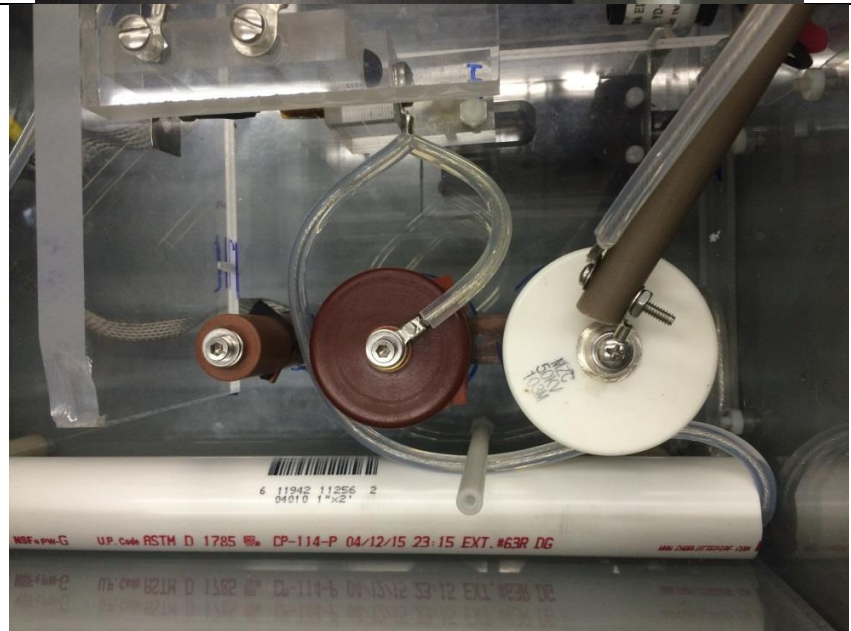


<p>10. If self-triggering of the box is desired:</p>	<p>10-a-1. Turn on the main high voltage power supply and slowly increase the voltage to the desired level while keeping current at minimum (zero if possible). DO NOT EXCEED 40 kV!</p> <p>10-a-2. Set the spark-gaps to the desired lengths. See section <i>IV. Normal Operation</i> for approximate values for spark-gaps.</p> <p>10-a-3. Slowly increase the current until the desired frequency of pulses is achieved. DO NOT EXCEED 2.5 mA or 32 W!</p>
<p>If external triggering of the box is desired:</p>	<p>10-b-1. Plug in the external trigger (smaller box attached to the box), and select the desired mode. Single is operated by the white 'Single' pushbutton. Pulse is operated by the ON/Pulse knob. Ext Trig is operated by the 50 Ω BNC input labeled Ext Trig.</p> <p>10-b-2. Set the spark-gaps to the desired lengths. See section <i>IV. Normal Operation</i> for approximate values for spark-gaps.</p> <p>10-b-3. Turn on the main high voltage power supply and slowly increase the voltage to the desired level while keeping current at minimum (zero if possible). DO NOT EXCEED 40 kV! The voltage should be set to approximately 100 V below the breakdown threshold for the main spark-gap.</p> <p>10-b-4. Increase the current on the main high voltage power supply, such that the desired frequency from the external trigger can be achieved. DO NOT EXCEED 2.4 mA or 32 W!</p> <p>10-b-5. Turn on the external trigger box using the ON/Pulse knob to operate the external trigger spark-gap, operating in the desired mode.</p>
<p>11. After testing, turn off the power supply. If applicable, turn off and unplug the external trigger.</p>	

12. Close the spark-gaps
(Note: the micrometer reading is not the actual spark-gap distance; the micrometers will be in a negative position to close the spark-gaps.)



13. If desired for long term storage, open the box and remove the top acrylic shield. Using the attached grounding rod ensure the capacitors are discharged. Check every capacitor, **including the ones not connected to the circuit.** Then, replace the top acrylic shield and screw it down. Close and lock the box.



IV. Normal Operation

A. Important Notes:

1. The voltage and current pulse shapes are **heavily load dependent**. The examples given below are simply a guide and may not reflect how the pulses behave for other loads. The two loads used in the data below are 1) a corona array directly under Pyrex petri dish with grounded salt water (i.e. a zero-gap distance) and 2) a corona array 5mm above a grounded metal plate. General trends are higher capacitive loads will have lower peak voltage pulses and less resistive loads will have shorter pulses.
2. There will always be some amount of ringing in the circuit after the initial pulse. This is minimized by decreasing the second resistor, but by decreasing the resistance too much (less than $\sim 200\Omega$) the pulse is affected.
3. The double spark-gap discharge device can be operated as a single spark-gap. This happens when the second spark-gap is too large to break down. The distance this occurs is affected by both the capacitor used and the main spark-gap.

B. Effect of Main Spark-Gap

The main spark-gap is used to control the breakdown voltage of the capacitor. Note that this is not the peak voltage of the pulse, which is discussed in *Subsection H* below. Figure 6 below shows the relation between the main spark-gap's setting (note that the closed gap, when the two ends touch, is below the zero reading on the micrometer) and breakdown voltage of the main spark-gap. The power supply voltage is also plotted, since this is also a controllable parameter through the power supply. The difference between the power supply voltage and the breakdown voltage is the voltage drop across the charging resistor, R1. (The self-pulsing frequency was around 1 to 10 Hz for every condition. The actual voltage drop across the resistor will vary depending on the amount of current supplied by the power supply.) The trend-line is a spline function used to fit the data. The data plotted consists of multiple substrates and all capacitors; hence it shows the breakdown voltage is not greatly affected by the capacitor or substrate used. Within an uncertainty of a few hundred volts, the breakdown voltage is only a function of the main spark-gap distance.

Effect of Main Spark-Gap

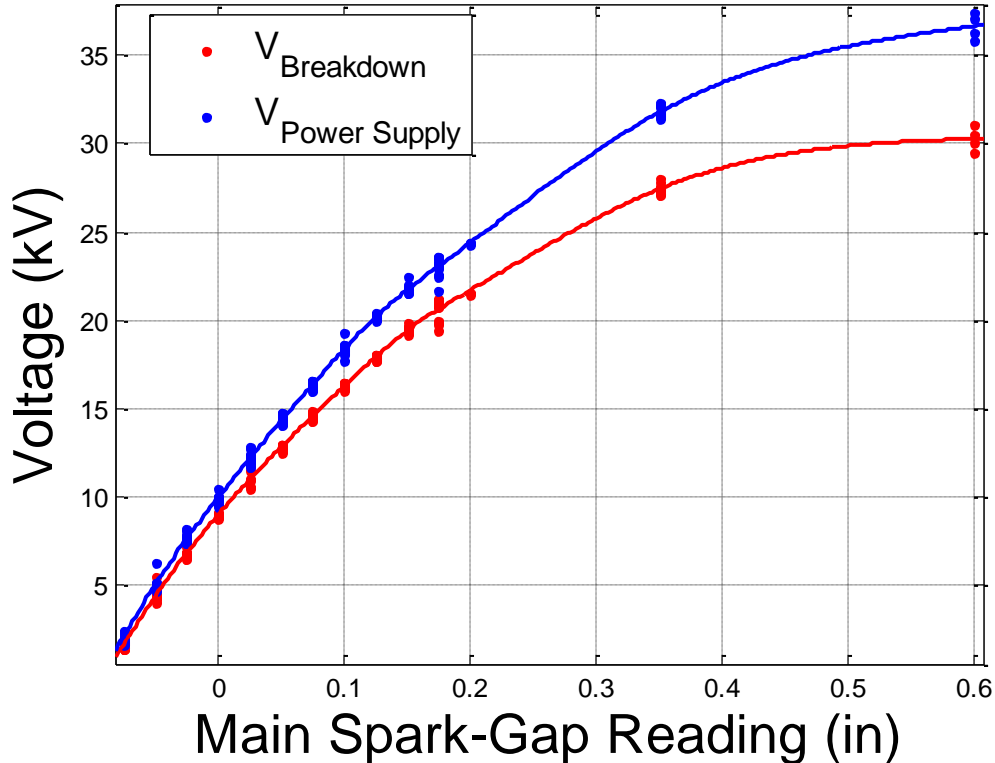


Figure 6: Various Capacitors, SSGs, Substrates, R2s, and loads; self-pulsing mode; **note that the actual results will be shifted due to a change in the zero-location of the micrometer after shipping**

For very large distances of the main spark-gap, corona discharges can become significant. This is noticeable as a larger current required to operate the device (i.e. the current is larger than that required by the resistors to operate at a particular voltage). There is not a sharp rise in voltage with a corona discharge, rather a slower increase due to some charge leaking across the main spark-gap before it fully breaks down, as can be seen in Figure 7, where the larger main spark-gap has a lower rise time due to corona breakdown initially.

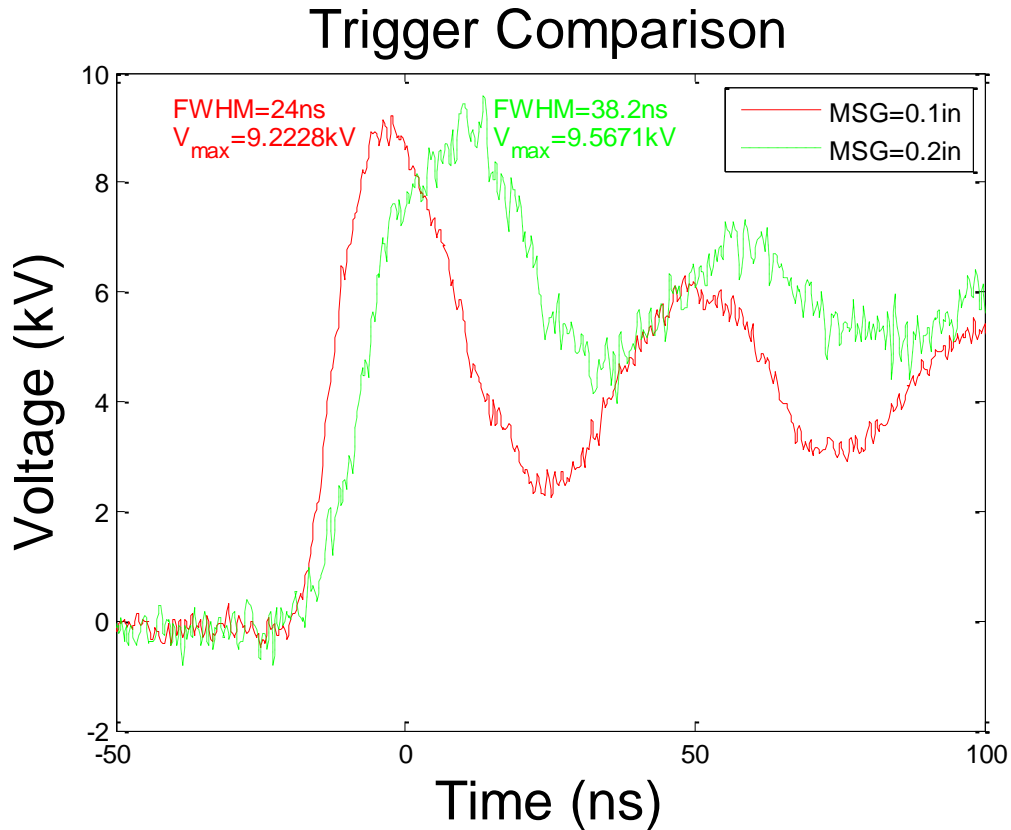


Figure 7: 50 pF Capacitor, single spark-gap configuration, R2=4.4 kΩ, corona array under Pyrex petri dish with grounded salt water, self-pulsing mode

C. Effect of Second Spark-Gap

The second spark-gap has an effect on both the voltage pulse magnitude and duration. At large gaps, the second spark-gap will not breakdown and the device operates in a single spark-gap configuration. This leads to very long voltage pulses for a capacitive load (like the solid red curve in Figure 8 below which last for microseconds), but does not greatly affect the pulse duration for conductive loads (e.g. spark-gaps, such as a discharge to a grounded metal plate in Figure 9 below). This is because the charge slowly dissipates through the resistor (R2) for a capacitive load, but for a conductive load the charge is able to quickly dissipate through the load. As the second spark-gap distance is shortened, the pulse duration and peak voltage both decrease.

Effect of Second Spark-Gap on Voltage Pulse

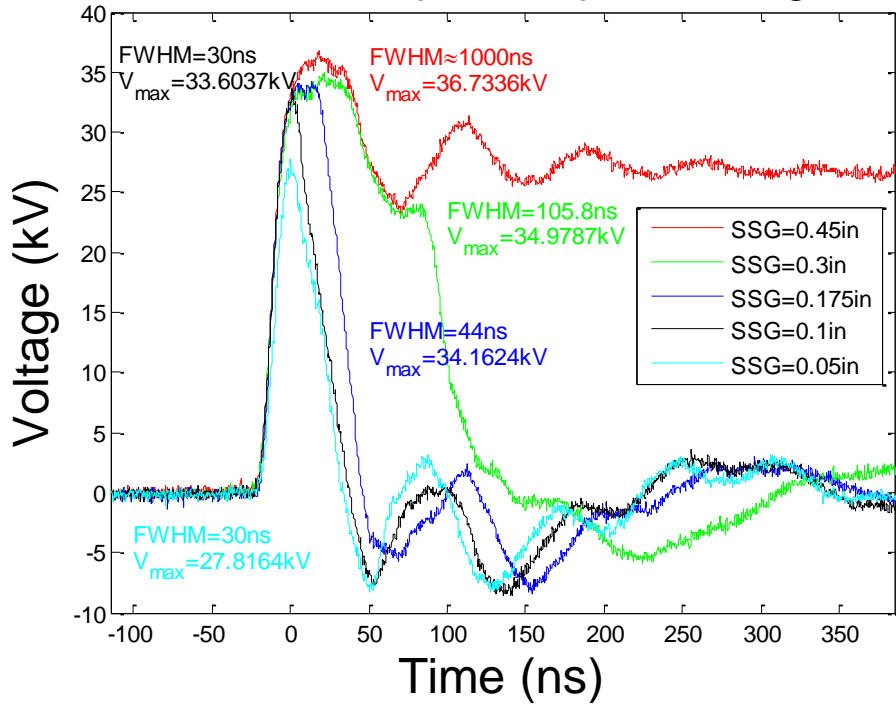


Figure 8: 5nF Capacitor, MSG=0.6 in, R2=4.4 k Ω , corona array under Pyrex petri dish with grounded salt water, self-pulsing mode

Effect of Second Spark-Gap on Voltage Pulse

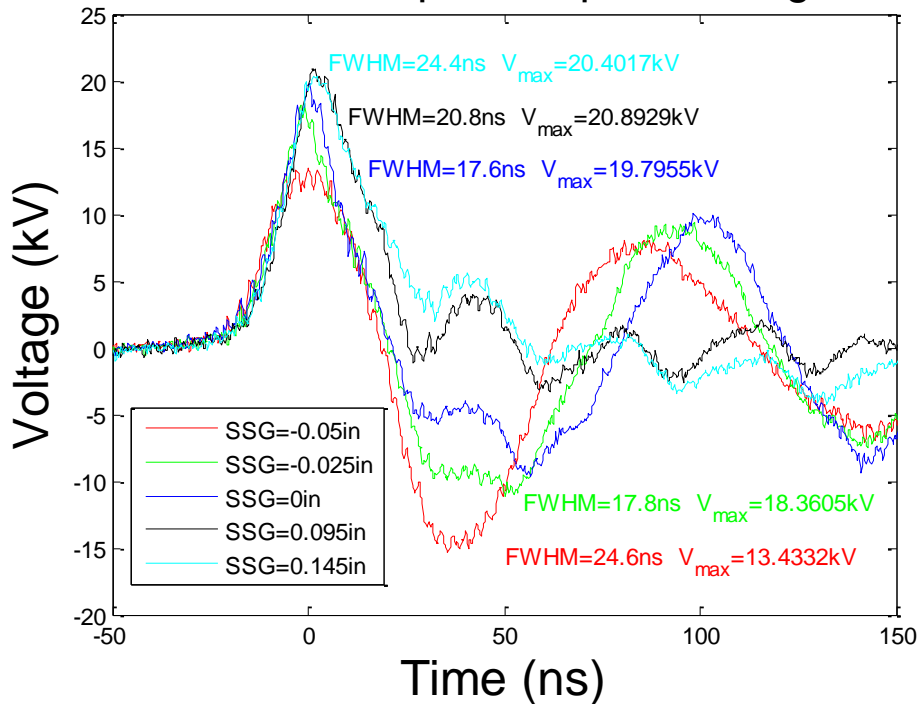


Figure 9: 500pF Capacitor, MSG=0.35 in, R2=4.4 k Ω , corona array 5 mm over grounded metal plate, self-pulsing mode

D. Effect of Capacitor

The capacitor has a large effect on the voltage pulse magnitude and as a result it affects the voltage pulse duration as well. As the capacitor is increased the voltage pulse magnitude increases as can be seen in Figure 10 below, where the only parameter changed between conditions is the capacitor. As the voltage pulse magnitude increases, the pulse duration also increases, since the pulses have approximately the same rise time per unit voltage. The larger capacitors are also capable of achieving larger voltage pulse magnitudes, as can be seen in Figure 11. This is due to the load being very capacitive. The capacitor discharges to the load, which has a voltage determined by its capacitance.

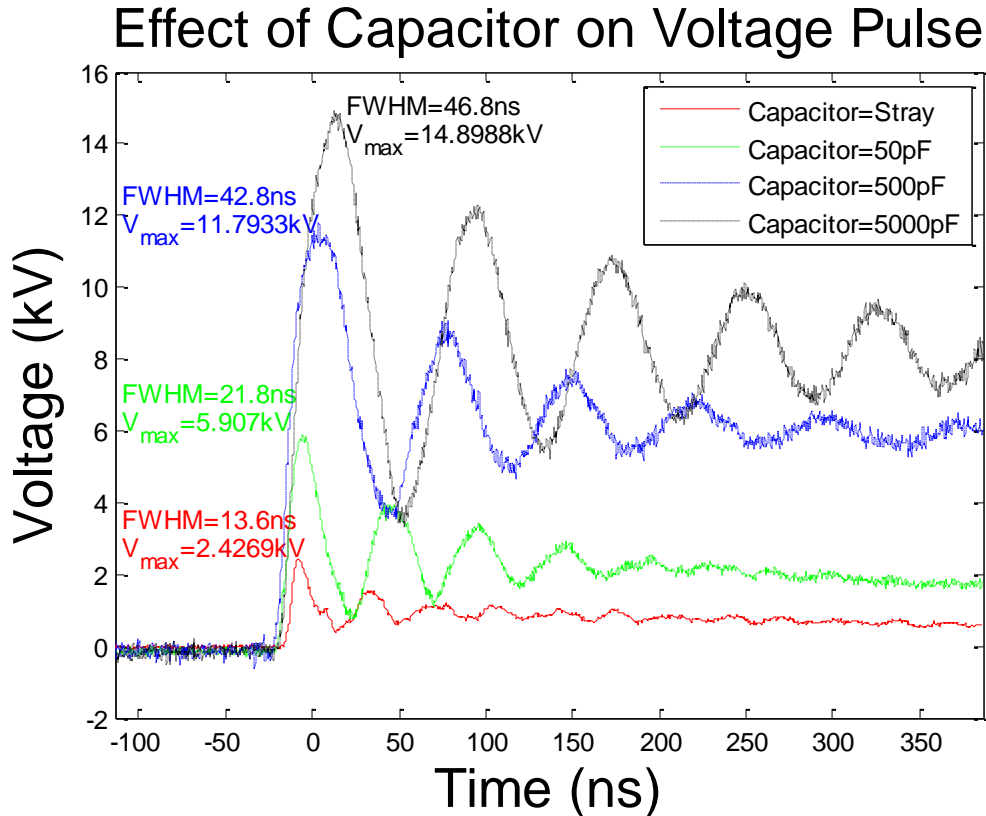


Figure 10: MSG=0 in, single spark-gap configuration (SSG=0 in), R₂=4.4 kΩ, corona array under Pyrex petri dish with grounded salt water, self-pulsing mode

Effect of Capacitor on Voltage Pulse

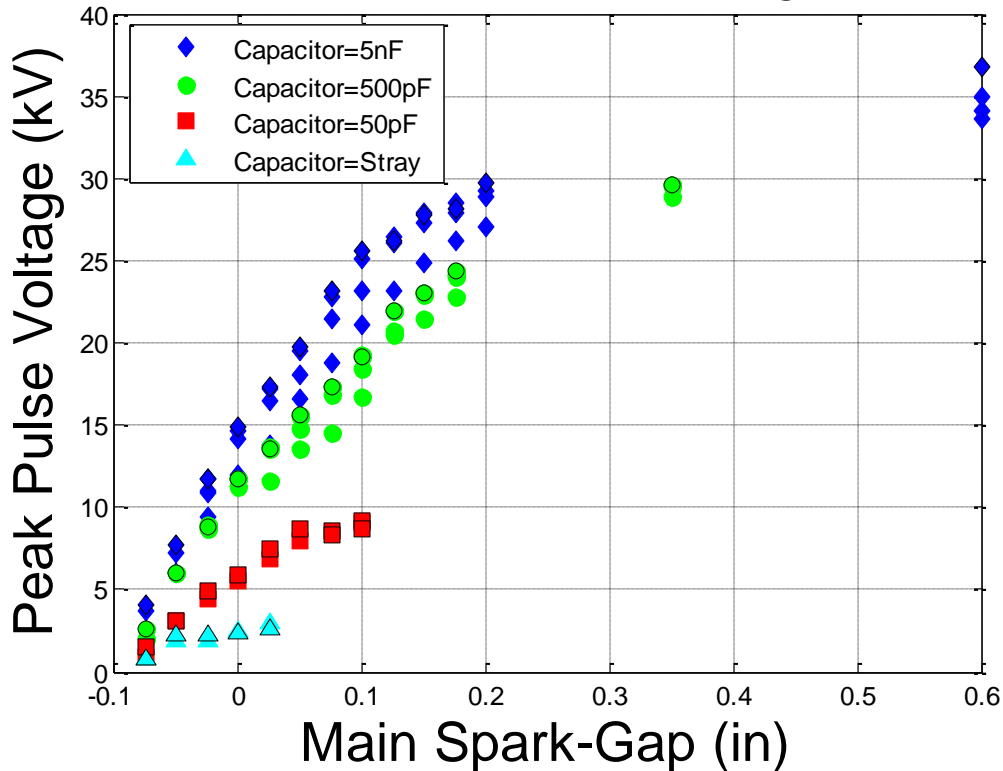


Figure 11: Various SSGs, $R_2=4.4\text{ k}\Omega$, corona array under Pyrex petri dish with grounded salt water, self-pulsing mode, black outline indicates single spark-gap configuration

E. Effect of R_2

The resistor acts as a second path to ground for any pulses; however it takes time for the charge to travel through the resistor. Smaller resistors drain off the charge faster, reducing the voltage quicker as seen in Figure 12. This helps reduce ringing in the voltage pulse. However, for a double spark-gap configuration (i.e. when the second spark-gap discharges) the resistor does not have much effect, as can be seen in Figure 13. For very large gaps, the resistor does not quickly reduce the charge build up on the downstream side of the main spark-gap, promoting corona discharges, as seen in section V. *Troubleshooting* number 4.

Effect of Resistor on Voltage Pulse

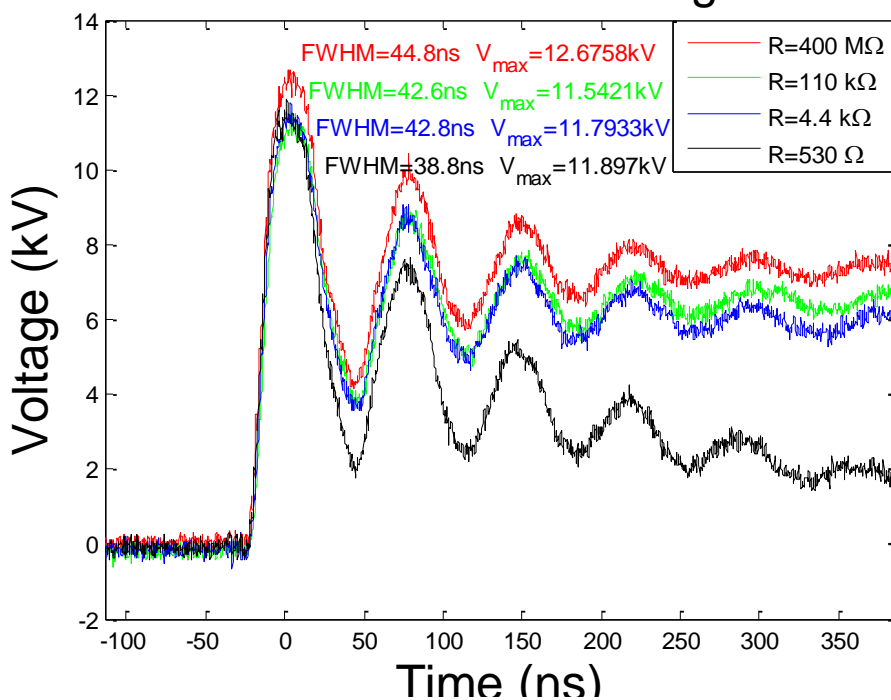


Figure 12: 500pF Capacitor, MSG=0 in, single spark-gap configuration (SSG=0 in), corona array under Pyrex petri dish with grounded salt water, self-pulsing mode

Effect of Resistor on Voltage Pulse

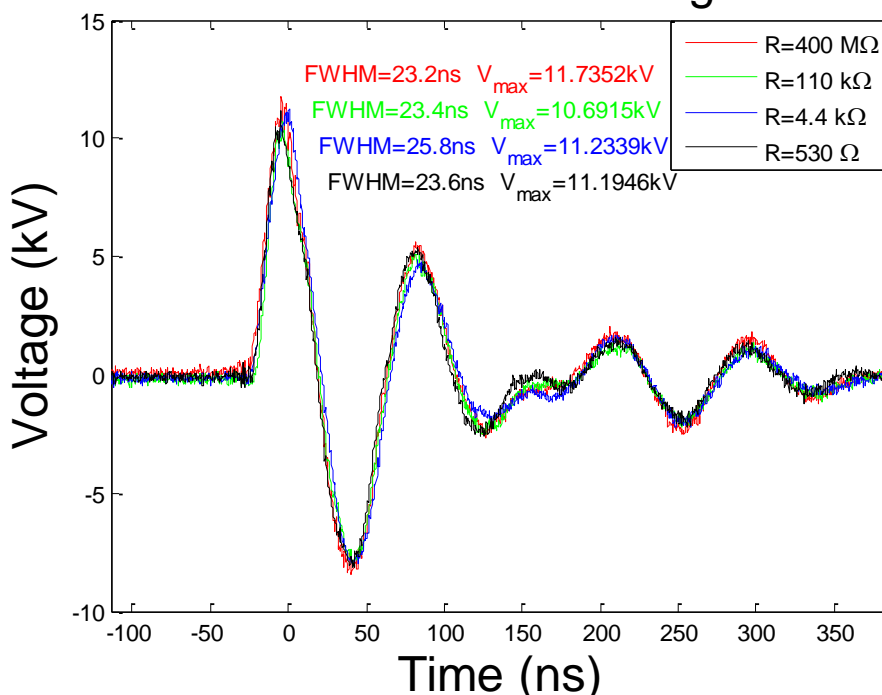


Figure 13: 500pF Capacitor, MSG=0 in, SSG=-0.045 in, corona array under Pyrex petri dish with grounded salt water, self-pulsing mode

F. Effect of Load

Two types of load were tested: 1) the corona array directly under a Pyrex petri dish filled with salt water connected to ground (gap distance is zero as seen in Figure 14) and 2) the corona array 5mm above a grounded metal plate (Figure 15). For small voltages, the two loads acted similarly, since the air between the corona array and metal acted as a dielectric, as can be seen in Figures 16 (double spark-gap configuration) and 17 (single spark-gap configuration) for the main spark-gap value of 0 in. However, for larger voltages the air began to breakdown and became conductive. The voltage pulse for the metal substrate was not reflected as well as the voltage pulse for the capacitive load (since the plasma acts as a conductive path), leading to lower peak voltages. The transition in the air acting as a dielectric to a conductor is noticeable in Figure 19 as a sharp decrease in the voltage at longer times after the pulse for larger main spark-gaps, which is not seen in Figure 18 for a purely dielectric load.

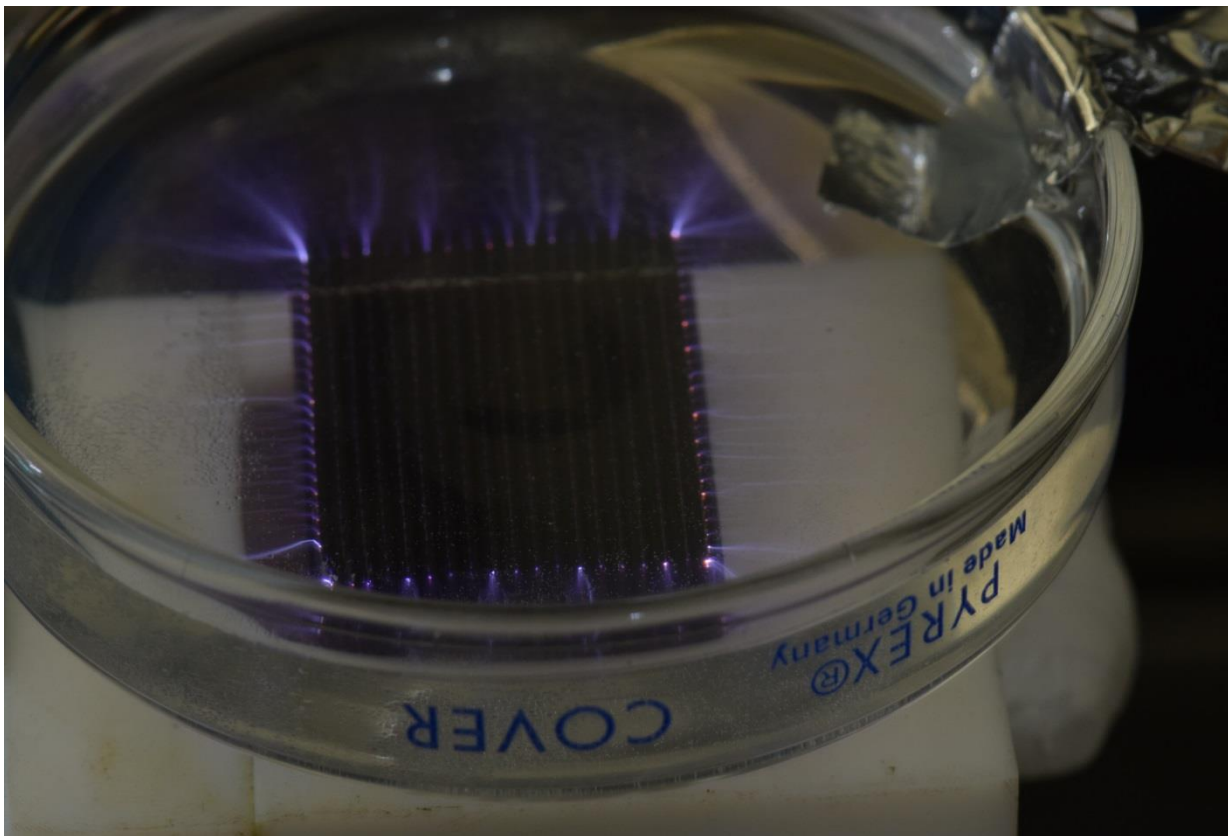


Figure 14: Image of corona array under Pyrex petri dish with grounded salt water

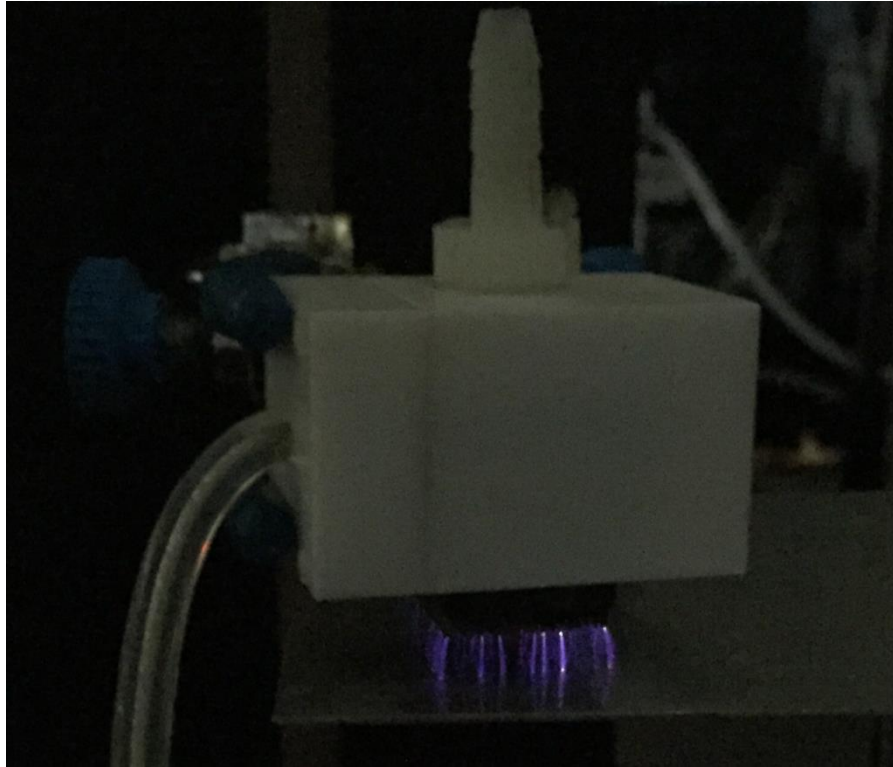


Figure 15: Image of corona array 5 mm over grounded metal plate

Effect of Load on Voltage Pulse

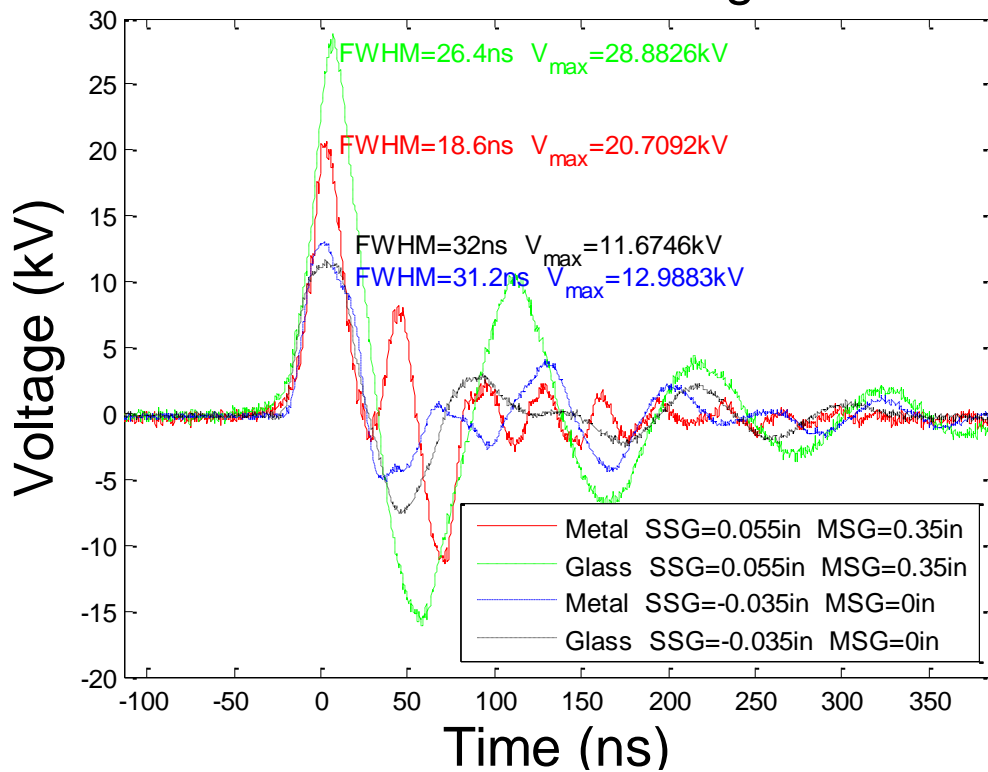


Figure 16: 500pF Capacitor, R2=4.4 kΩ, self-pulsing mode

Effect of Load on Voltage Pulse

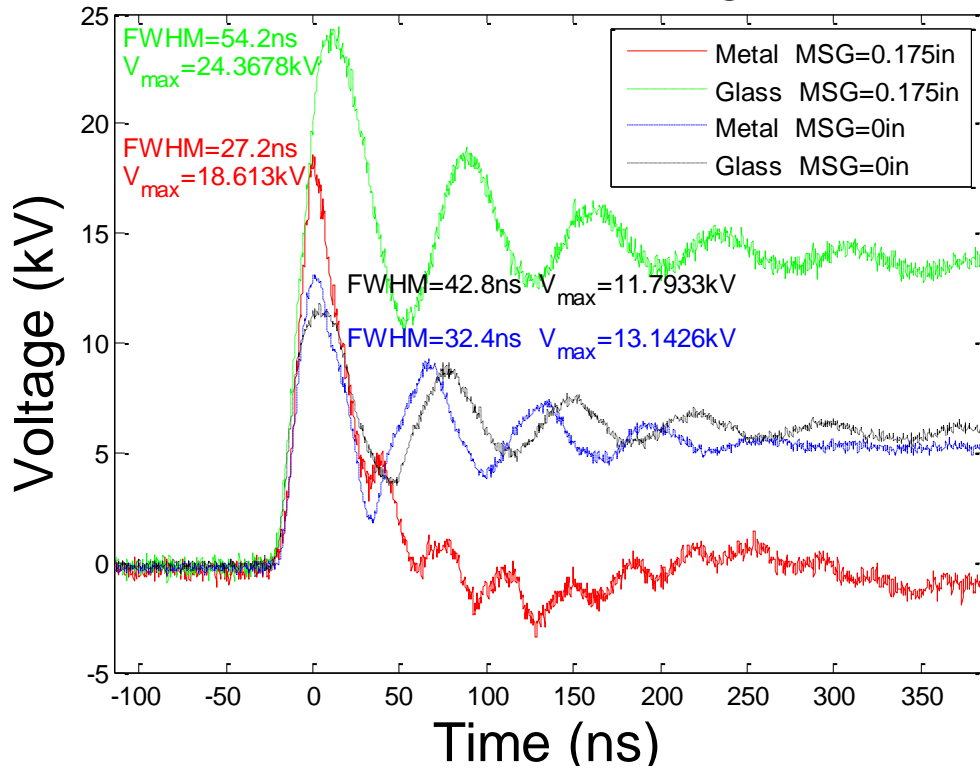


Figure 17: 500pF Capacitor, single spark-gap configuration, R2=4.4 kΩ, self-pulsing mode

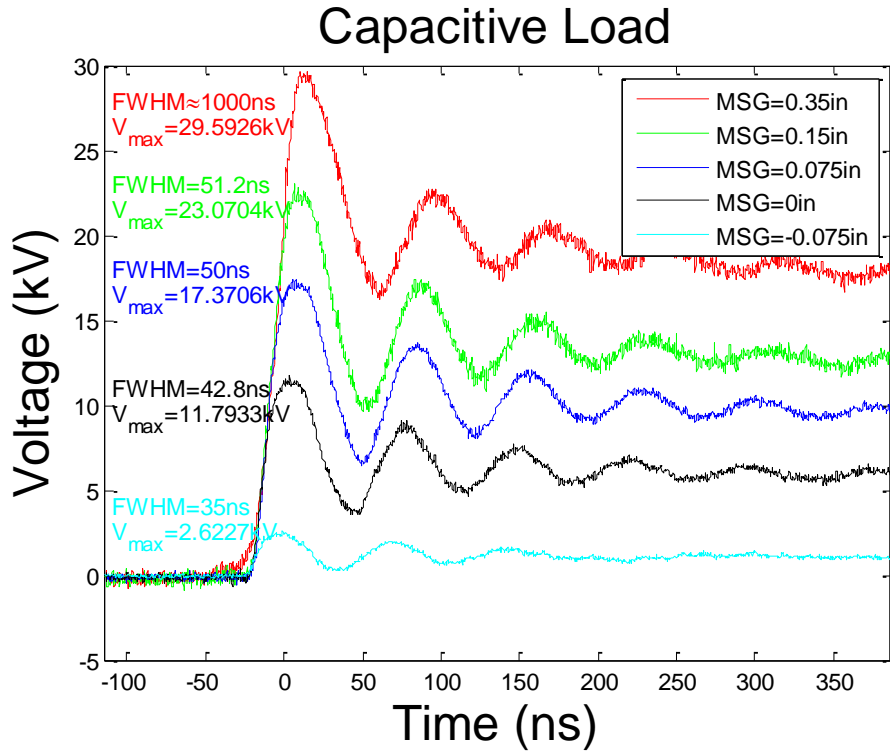


Figure 18: 500pF Capacitor, single spark-gap configuration, R2=4.4 kΩ, self-pulsing mode

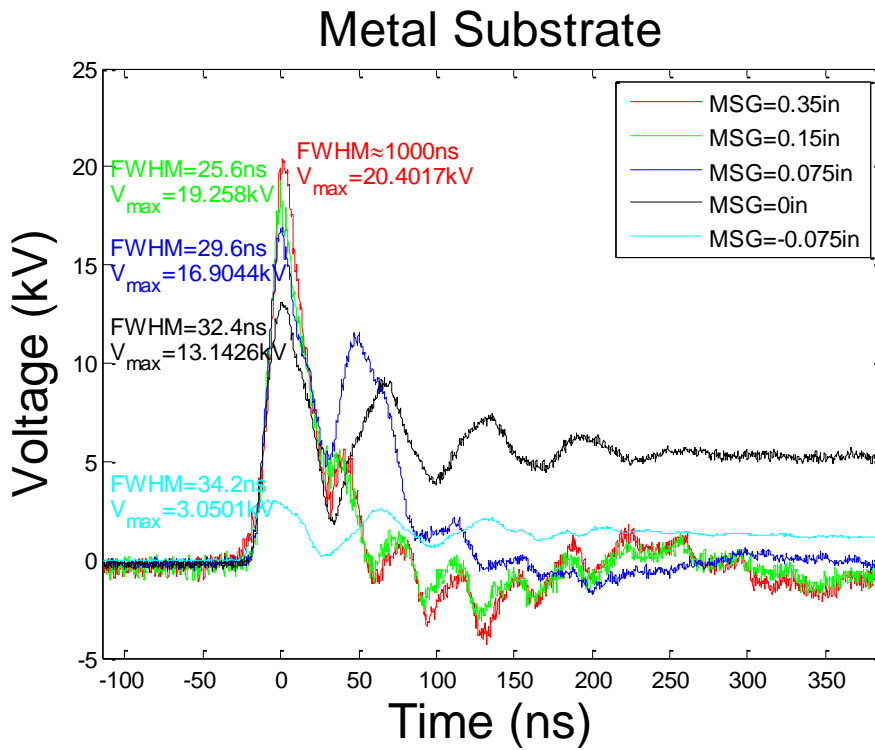


Figure 19: 500pF Capacitor, single spark-gap configuration, R2=4.4 kΩ, self-pulsing mode

G. Effect of Triggering Mechanism

The trigger does not have a large effect on the voltage pulse, as can be seen from Figure 20 below. Small differences may occur since the breakdown voltage is slightly different from the self-pulsing mode. The trigger is prone to error at high voltages. The two types of error that occur are incomplete discharge of the capacitor and discharge to the trigger ground. In incomplete discharge the main spark-gap breaks down, but it is a weak discharge with the capacitor only partially discharging. Often the second spark-gap will not discharge. This occurs more often for the smaller capacitors. In the second type of error, the main spark-gap breaks down to the trigger's ground electrode, creating no voltage pulse on the load. This is more common for the larger capacitors. Typically each discharge is independent of the others, so one faulty discharge will not affect other discharges, thus triggering the box again will result in a good discharge.

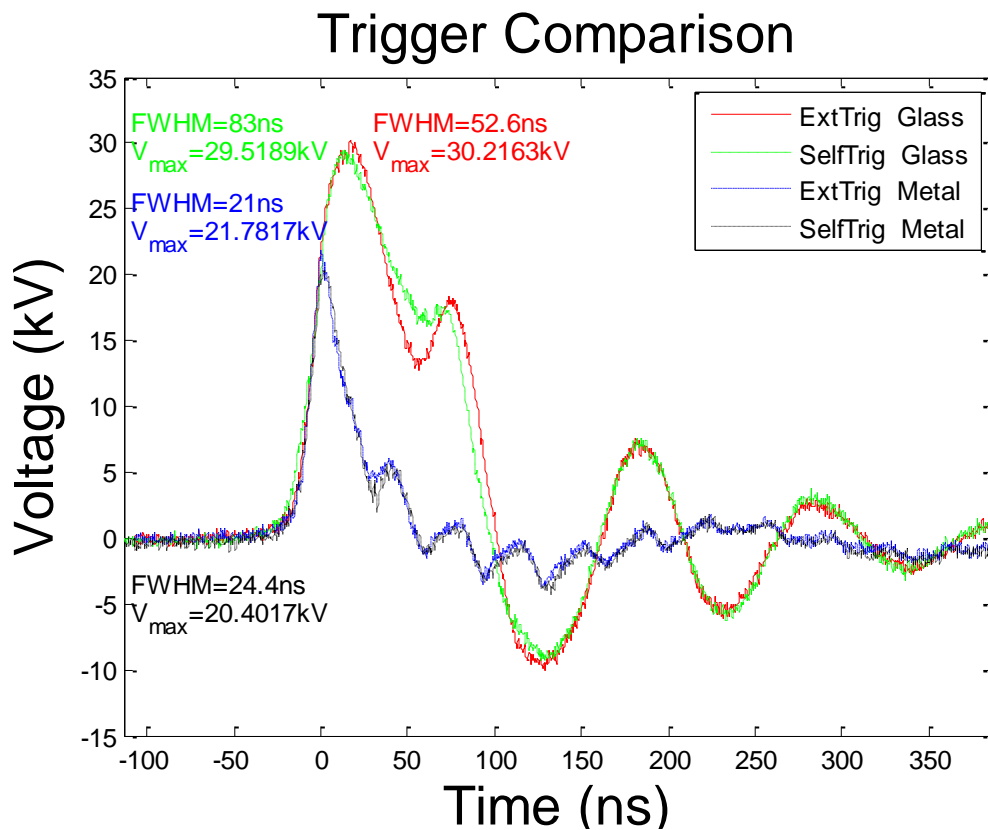


Figure 20: 500pF Capacitor, MSG=0.35 in, SSG=0.145 in, R2=4.4 kΩ

H. Voltage Pulse

Many factors influence the voltage pulse on the load, including the main spark-gap, the second spark-gap, the capacitor, and the load itself. The maximum peak voltage is partially controlled by the main spark-gap, which controls the breakdown voltage. The maximum peak pulse voltage is at most double the breakdown voltage on the capacitor, since the voltage pulse can be reflected in the transmission line (i.e. the high voltage wire connecting the load and box) if the load resistance is greater than the transmission line's impedance (This is often the case, since the transmission line has an impedance under 500 Ω). The resistivity of the load determines how much of the voltage pulse is reflected, with higher resistances reflecting more

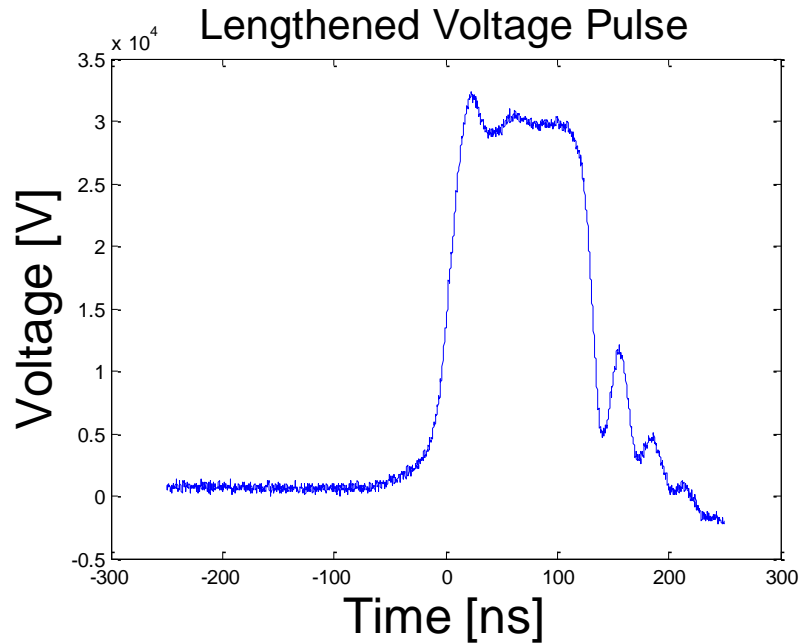
of the voltage and increasing the maximum peak voltage. The second spark-gap mostly affects the pulse duration, but too small of a second spark-gap begins to reduce the voltage pulse maximum, since the pulse has a fairly constant rise time per unit voltage, holding other parameters constant. Attempting to reduce the pulse duration below a certain threshold begins to significantly decrease the maximum voltage to keep the rise time per unit voltage the same. For large distances of the second spark-gap it will not discharge, operating in a single spark-gap configuration. The capacitor also controls the maximum peak voltage, with higher capacitances able to achieve higher voltages.

I. Taking Measurements

All probes have internal impedances which will affect measurements. Use high impedance probes to minimize the effect. The pulse generated from the main spark-gap discharging can generate very large currents (~1 kA). Due to natural inductance in all wires, measuring currents and voltages can become very difficult. In general, use the thickest and shortest wires possible. This is especially true for ground wires, including grounding wires attaching the various ground locations in the circuit and probes. If these are not very low inductance (i.e. not a solid block of metal, such as the metal optical table top used in all testing in Dr. Staack's lab) even the ground voltage can change, greatly affecting measurements. Some high voltage probes have multiple grounding locations which can be used. Electromagnetic interference (EMI) is also generated since the pulse has such a fast rise and fall time. Shielding all wires used can help reduce their susceptibility to EMI.

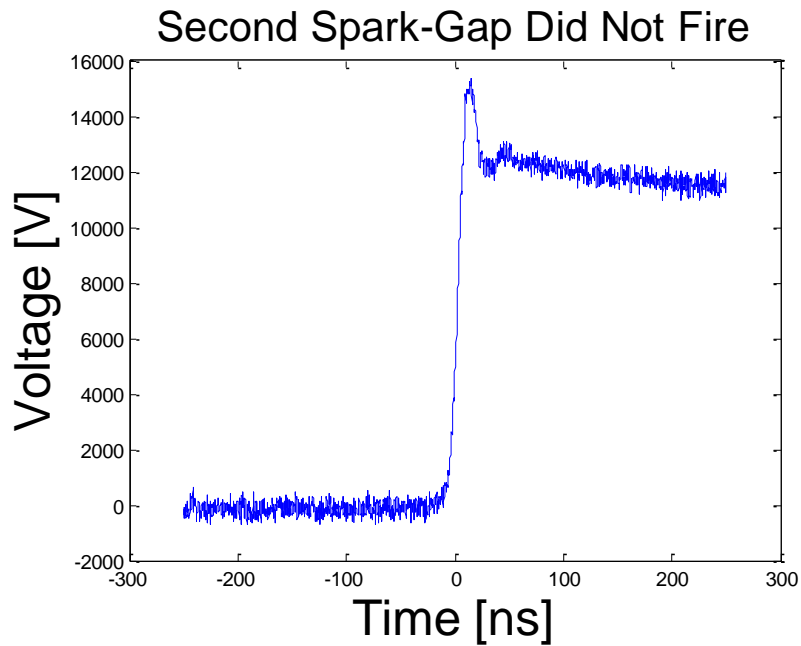
V. Troubleshooting

1. The voltage pulse appears lengthened.



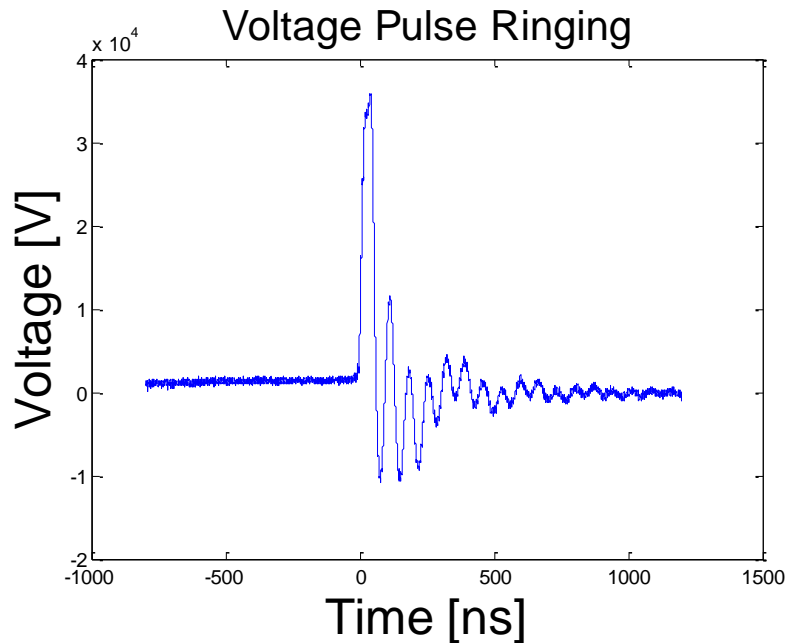
Solution: Shorten the second spark-gap. The second spark-gap is too large to reliably discharge.

2. The second spark-gap did not discharge. The voltage pulse does not have a sharp end, but gradually trails off.



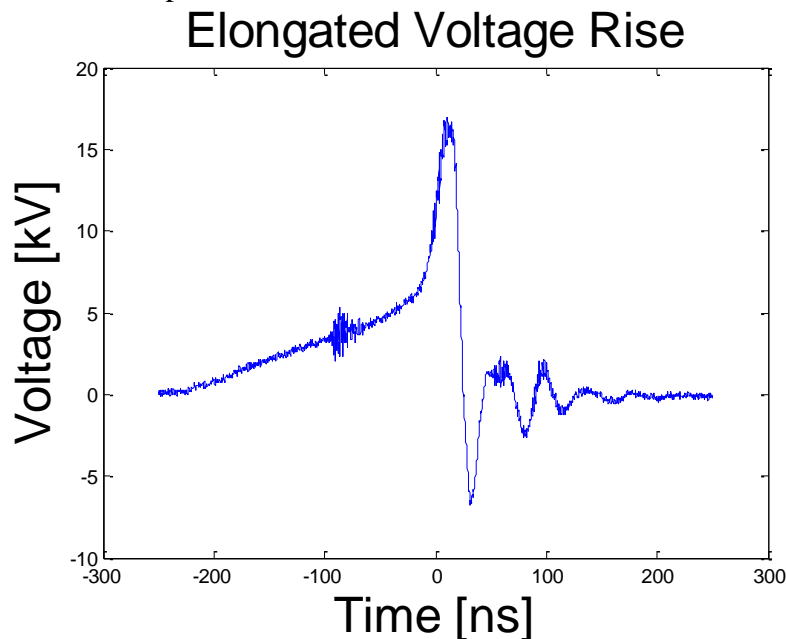
Solution: Shorten the second spark-gap. The second spark-gap is too large and did not discharge.

3. There is significant ringing in the pulse



Solution: Reduce the secondary resistor, R2. This will allow current to travel to ground over time, which will decrease some of the ringing and still maintain a high initial voltage pulse. However, most of the ringing is too fast for the time response of the resistor and cannot be controlled.

4. Pulse does not have a sharp rise.

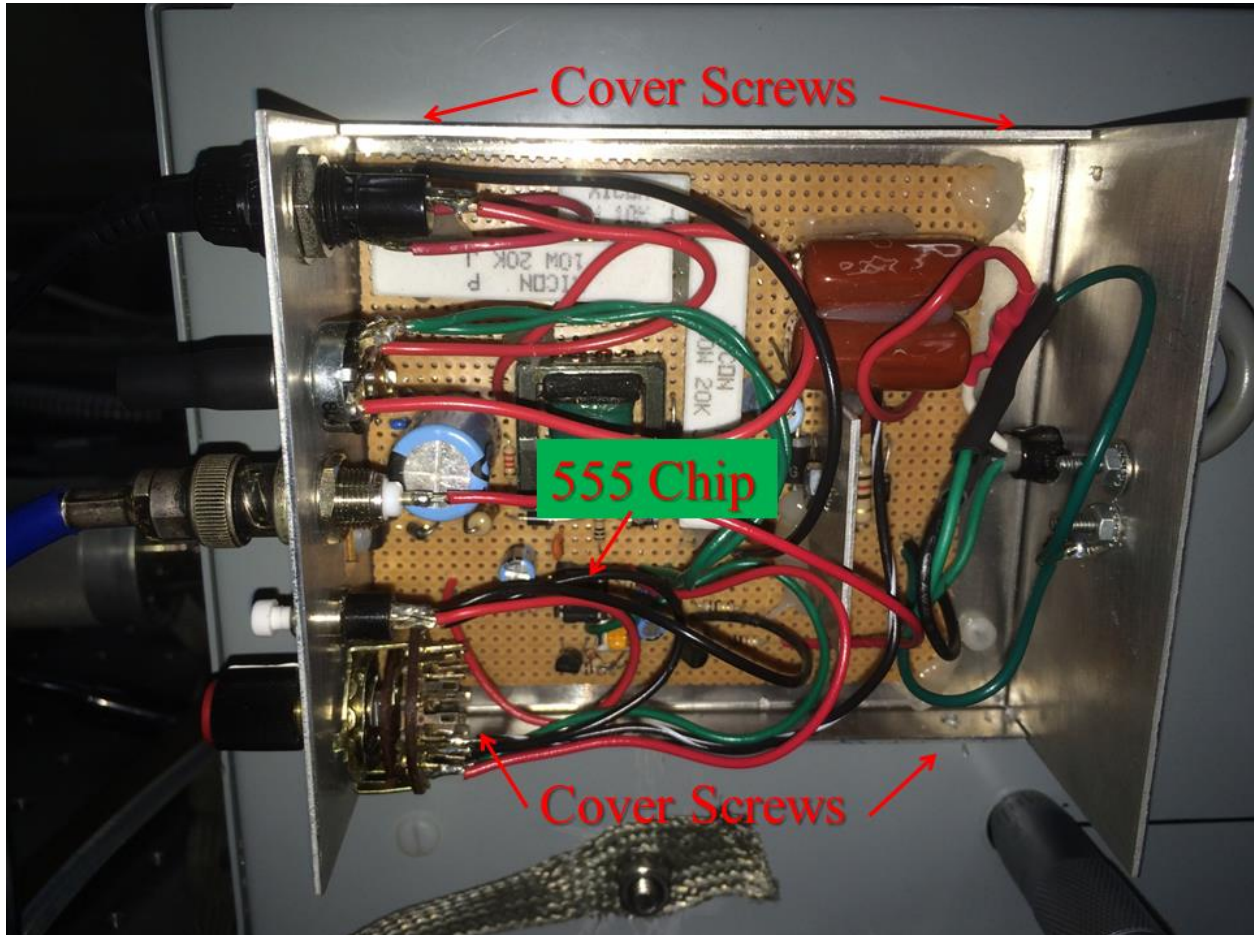


Solution: Reduce the value of R2. The second dampening resistor is too large, allowing charge to build up on the downstream side of the main spark-gap encouraging initial corona discharge followed by an arc.

5. The frequency of pulses is too high.

Solution: If in self-pulsing mode, reduce the current supplied to the box. If that is not possible, switch to the external trigger mode. If in external pulsing mode, lower the frequency knob. If that is not possible, switch to externally triggering the external trigger box using a function generator via the Ext Trig BNC connection on the external trigger box. The external trigger may also be operated in Single mode, being triggered manually by the operator.

6. The box does not work in Pulse mode for the external trigger, but does work in the other two modes.



Solution: Replace the 555 timer chip in the control box. There are 4 screws holding the stainless steel cover in place, which can be removed allowing access inside of the control box. A 7555 timer chip (uses less power) can be used instead if desired.

APPENDIX B

MATLAB CODE TO CONTROL THE 3D PRINTER

The MatLab code used for controlling the 3D printer in Chapter 6 is included below.¹ It consists of a main code, called `GCodeWriter.m`, that interfaces with the 3D printer and a function, called `GCodeParser.m`, that it calls if external GCode is used. This allows for greater versatility in deciding which GCode to run, as well as giving access to the specific commands to control the 3D printer even when supplied a GCode.

The function `GCodeWriter.m` connects to and sends commands to the 3D printer. It also contains a few custom geometries that can be written from MatLab code. In addition it offers the capability of plotting the GCode before in runs in three different ways: a step-by-step animation of the GCode, a colored plot of the steps, and a plot of the time per area in the code. The latter two are shown in Figure 6.4 for two different geometries, one case for “Staack’s Second Try” geometry and the other case from a GCode generated geometry by the Slic3r software.

The function `GCodeParser.m` takes in the filename for a GCode file and outputs the desired parameters. It contains a legacy code portion that was a first attempt at extracting changes in the x and y movements in the GCode, but this legacy code relied on certain lines that were in the GCode generated by the Slic3r software for certain cases only. As a result, a more generalized GCode was written, but the legacy code was retained in case replicating old results was necessary.

GCodeWriter.m

```
1  %% 3D Printer Code
2  % This code interacts with the 3D Printer to output a 2D
3  % drawing. It accounts for the fact that the x-axis control
4  % is broken, so the z-axis control is running the x-axis
5  % servo motor.
6
7  % Authors: Matthew Burnette, Chris Campbell, and David Staack
```

¹Thanks to Uwe Lelke’s code `m2tex.m` (MatLab File Exchange #24515) for generating the nicely formatted output used here.

```

 8 % Version: 1.2 (Better plotting & cleaner code)
 9 %   1.1.1 (Changed plotting to always have visual buffer)
10 %   1.1 (Added Matt's Annular Run)
11 % Last Updated: 5/16/2020 at 11:19PM
12 % Requires: GCodeParser
13
14 %% Initializing Code
15 clearvars
16 clc
17 close all
18 delete(instrfindall);
19
20 %% Options
21 Run3D_Printer=0;
22   %True runs printer
23 Show_Plots=1;
24   %Extra descriptive plots of pattern
25 Show_Plotting_Steps=0;
26   %Animation of the 3D printer pattern
27 SaveGIF=''; %'C:\Users\...\NewGif.gif';
28   %Absolute File Save Location
29   %Show_Plotting_Steps must also be on
30 StopTempError=1;
31   %Generally good to leave on
32   %Turn off if code is running too slow
33 GCodeFilename=''; %...\GCode\CircleD20mm3_new.gcode';
34   %if empty uses build in geometry below
35   %Otherwise looks for filename given
36
37 %% Open serial port to send commands to the 3D Printer
38 if Run3D_Printer
39     s=serial('COM3'); %#ok<SERIAL>
40     %This is upper USB port on the front of the computer
41     set(s,'BaudRate',2.5e5);
42     fopen(s);
43
44     %Wait for grbl to initialize
45     pause(1)
46     fread(s,s.BytesAvailable)
47 end
48
49 %% Set Speeds
50 zfactor_x= 40; %Constant
51 zfactor_v = 40; %Constant
52 speed = 1000; %mm/minute

```

```

53 x_speed=speed/zfactor_v;
54 % zaxis units/min since x-servo motor broke!
55 y_speed=speed; %% mm/min
56 num_passes=10;
57 Edim=0; %For servo controlling turning on/off plasma precursor
58
59 %% Geometry
60 if isempty(GCodeFilename)
61     %% Staack's First Try (Used for Initial 8 runs)
62     %{ Remove this text to comment out
63     nsegments = 10000;
64     %Note this starts at the top-center position
65     maxt = 100;
66     t = linspace(0,maxt,nsegments);
67     r = 10*cos(t/maxt*36*pi);
68     theta = t/maxt*500*pi;
69     x = r.*sin(theta);
70     y = r.*cos(theta);
71     NeedPause=true;
72     %}
73
74     %% Chris's Spiral Try
75     %Failed for some odd reason with printer
76     %The reason for this has not been fully explored
77     %{ Remove this text to comment out
78     nsegments = 25000; %Starts in center
79     maxt = 100;
80     t = linspace(0,maxt,nsegments);
81     radius_freq = 0.005;
82     % Try a few methods to get the best r
83     %r = 10.0.*(0.5.*sawtooth(2*pi*radius_freq*t,0.5)+0.5);
84     %r = 10.*abs(mod(floor(radius_freq*t),2).*...
85     %    sawtooth(2*pi*(t+0.5)*radius_freq)+...
86     %    mod(floor(radius_freq*t)+1,2).*...
87     %    sawtooth(-2*pi*radius_freq*(t+0.5)));
88     r = 10.*((t/maxt).^0.1).*cos(t/maxt*36*pi);
89     theta = t/maxt*pi*500;
90     x = r.*sin(theta);
91     y = r.*cos(theta);
92     NeedPause=false;
93     %}
94
95     %% Staack's Second Try (Path1) Starts in center
96     %{ Remove this text to comment out
97     Diameter = 20; % units mm circle diameter

```

```

98     speed = 250/60; %mm/min
99         % / 60 to get mm/s, this is the gcode speed.
100    % Note cartesian speed is constant not omega.
101    norbits = 140; %% large number of orbits increases
102    % uniformity but also increases total length of print
103    % these will take about 10 minutes
104
105    z = linspace(0,2*pi,norbits*90);% at least 2 deg
106    % resolution
107    ft = norbits; % theta rapidly changes helps
108    % Want to avoid spiral overlapping previous one...
109    %pri = max(primes(sqrt(ft+1)));
110        % trying to algorithm this but a guess works too
111    %fr = pri;
112        % should not have too many beating
113        %r should change rapidly also
114    fr=9; %better than 11...
115        %can't find way to do this programatically
116    r = Diameter/2*sawtooth(z*fr,0.5);
117        % saw tooth is the right function not sine
118    t = z*ft;
119
120    % try to correct middle by decimate small r
121    r_f = r(r>=0.5);
122    t_f = t(r>=0.5);
123    r = r_f;
124    t = t_f;
125
126    % no matter what start and end at zero
127    r = [0,r,0];
128    t = [0,t,0];
129
130    x = r.*sin(t);
131    y = r.*cos(t);
132    rnew = sqrt(x.^2+y.^2);
133    tnew = atan2(y,x);
134
135    dx = diff(x);
136    dy = diff(y);
137    dL = sqrt(dx.^2+dy.^2);
138
139    time = [0,cumsum(dL/speed)];
140    fcode = 24; % times per second new position is sent
141        %this must be large enough to resolve orbits
142    ncode = fcode*round(max(time));

```



```

143         % number of position points the lin time vector
144     linTime = linspace(0,max(time),ncode);
145     r_lin = interp1(time,rnew,linTime);
146         % these are evenly spaced in time
147     x_lin = interp1(time,x,linTime);
148         % these are evenly spaced in time
149     y_lin = interp1(time,y,linTime);
150         % these are evenly spaced in time
151     t_lin = interp1(time,tnew,linTime);
152         % these are evenly spaced in time
153     % if we send even in time points to program then
154     % matlab vector and gcode time will be the same
155
156     % send to printer code
157     x = x_lin;
158     y = y_lin;
159     NeedPause=false;
160     %}
161
162     %% Matt's Annular Pattern
163     %{ Remove this text to comment out
164     Diameter=20; %mm
165     dtheta=.01;
166     theta=dtheta:dtheta:360; %Do not double count 0/360;
167     x=Diameter/2*cos(theta*pi/180);
168     y=Diameter/2*sin(theta*pi/180);
169     NeedPause=false;
170     %}
171 else
172     [x,y]=GCodeParser(GCodeFilename,'NotLegacy');
173     x(1)=[]; %often bad first point to move build stage
174     y(1)=[]; %often bad first point to move build stage
175     NeedPause=true;
176 end
177
178 %% Outputing GCode
179 cp =[0,0];
180 x = x-x(1); %Centers Gcode starting location
181 y = y-y(1); %Centers Gcode starting location
182 x_c=x/zfactor_x; % zaxis units
183
184 num_steps=length(x);
185 e = Edim*ones(1,num_steps);
186 num_steps=length(x);
187 residuedur = 0;

```

```

188
189 if Show_Plotting_Steps || Show_Plots
190     maxX=max(x);
191     minX=min(x);
192     dX=maxX-minX;
193     maxY=max(y);
194     minY=min(y);
195     dY=maxY-minY;
196     dxy=.05;
197     XLims=[minX-dxy*dX  maxX+dxy*dX];
198     YLims=[minY-dxy*dY  maxY+dxy*dY];
199 end
200
201 if Show_Plotting_Steps
202
203     % Writing Animation of Steps
204     figSteps=figure('Color','w');
205     axSteps=axes('Parent',figSteps);
206     StepSize=round(num_steps/100);
207     % Only show it in 100 steps
208     % Otherwise this takes forever depending on the print!
209     for i = 1:StepSize:num_steps %Used for GIFs
210         plot(axSteps,x(1:i),y(1:i),'.-')
211         xlim(axSteps,XLims)
212         ylim(axSteps,YLims)
213         if ~isempty(SaveGIF)
214             drawnow
215             dfram=getframe(figSteps);
216             fram=frame2im(dfram);
217             [image,map]=rgb2ind(fram,256);
218             if i==1
219                 imwrite(image,map,SaveGIF,'gif',...
220                     'LoopCount',inf,'DelayTime',.001)
221             else
222                 imwrite(image,map,SaveGIF,'gif',...
223                     'WriteMode','append','DelayTime',.001)
224             end
225         else
226             title(i)
227             axis equal
228             pause(0.001)
229         end
230     end
231 end
232

```

```

233 if Show_Plots
234
235     %% Show The Full Print
236     fig=figure;
237     ax=axes('Parent',fig);
238     color=jet(length(y));
239     scatter(x,y,1,color)
240     xlabel(ax,'x [mm]')
241     ylabel(ax,'y [mm]')
242     xlim(ax,XLims)
243     ylim(ax,YLims)
244     axis equal
245     pause(2)
246     % Last second chance to abort if I realize this is not
247     % the print I want
248
249     %% Run Time-Per-Area Plot
250     %{ Remove this text to comment out
251     % Need to get points evenly spaced in time
252     dx = diff(x);
253     dy = diff(y);
254     dL = sqrt(dx.^2+dy.^2)';
255     if min(dL)==0
256         %Sometime there is a dwell at a location which will
257         %mess with code later. If this happens a lot in the
258         %code then this analysis is not accurate. Generally,
259         %though this happens when there is a z-height change,
260         %which is relatively infrequent (hopefully)
261         badI=(dL==0);
262         dL=dL(~badI);
263         badI(end+1)=false; %Add extra index for x and y
264         x2plot=x(~badI);
265         y2plot=y(~badI);
266     else
267         x2plot=x;
268         y2plot=y;
269     end
270
271     % Get a vector of cumulative time taken at each step
272     if isrow(dL)
273         time = [0,cumsum(dL/speed)];
274     else
275         time = [0;cumsum(dL/speed)];
276     end
277

```

```

278 % Now get a length vector for each time point
279 dt=diff(time);
280 fcode = 10/min(dt);
281 %times per second new position is sent-must be large
282 %enough to resolve orbits
283 ncode = ceil(fcode*max(time));
284 %number of position points in the linTime vector
285 linTime = linspace(0,max(time),ncode);
286
287 % Get x and y based on even-time spaced vector
288 x_lin = interp1(time,x2plot,linTime);
289 % these are evenly spaced in time
290 y_lin = interp1(time,y2plot,linTime);
291 % these are evenly spaced in time
292
293 % Guess a computational time per step
294 computetime = 5e-3;
295 % time to tell about next move estimated, because
296 % points are evenly spaced in time this should not
297 % affect uniformity
298 time_real = [0,cumsum(diff(linTime)+computetime)];
299 ResTime = mean(diff(time_real));
300
301 % Find Time in Each Cell of Grid
302 xResolution=20;
303 yResolution=20;
304 xCells = XLims(1):dX/xResolution:XLims(2);
305 yCells = YLims(1):dY/yResolution:YLims(2);
306 %Easier than using meshgrid to get x and y
307 for i=1:length(xCells)-1
308     for j = 1:length(yCells)-1
309         inds = x_lin>xCells(i) & x_lin<xCells(i+1) &...
310             y_lin>yCells(j) & y_lin<yCells(j+1);
311         xc(i,j) = (xCells(i)+xCells(i+1))/2; %#ok<*SAGROW>
312         yc(i,j) = (yCells(j)+yCells(j+1))/2;
313         tc(i,j) = length(find(inds))*ResTime;
314     end
315 end
316
317 % Output Time at Spot Figure
318 figMap=figure;
319 ax=axes;
320 surf(xc,yc,tc/max(max(tc))) %Normalized cell counts
321 view(0,90)
322 colormap jet

```

```

323     title('Time at Spot')
324     xlabel('x [mm]')
325     ylabel('y [mm]')
326     xlim(ax,XLims)
327     ylim(ax,YLims)
328     colorbar
329     axis equal
330     saveas(figMap,'TimeAtSpotPlot')
331     %Save figure
332     %}
333 end
334
335 %% Run the Printer
336 if Run3D_Printer
337     disp('Running the 3D printer now...')
338     pause(0.1)
339
340     %Final checks on code before running
341     if length(y)~=num_steps
342         error('Check length of y')
343     elseif length(e)~=num_steps
344         error('Check length of e')
345     end
346
347     % Looping over pattern iterations
348     for z = 1:num_passes
349
350         % Looping over pattern steps
351         for i = 1:num_steps
352             fprintf(['Executing Line %d/%d on Pass ',...
353                 '%d/%d\n'],i,num_steps,z,num_passes)
354             distance = sqrt((x(i)-cp(1))^2+(y(i)-cp(2))^2);
355             lengthx = abs(x(i)-cp(1));
356             lengthy = abs(y(i)-cp(2));
357             speed_m = ((lengthx/distance)*x_speed + ...
358                 (lengthy/distance)*y_speed);
359             %effective speed for this move
360             dur(i) = distance/speed*60;
361
362             %tosend1 = ['G01 E',num2str(e(i)), ' F1000',,];
363             % Turn on plasma if using E to control DBD
364             % jet flow. This never worked well, mostly
365             % manually controlled instead
366             tosend2 = ['G01 Z',num2str(x_c(i)),...%X = broken
367                 ' Y',num2str(y(i)),...

```

```

368         ' F', num2str(speed_m)]; % moves
369     if StopTempError
370
371         % Prevents printer from resetting due to
372         % temperature error, but we don't use the
373         % thermoplastic so temperature is irrelevant
374         fprintf(s, 'M999');
375         pause(0.001)
376         fprintf(s, 'M302');
377         pause(0.001)
378
379         % May need extra temperature reset to work
380         %fprintf(s,tosend1);
381         %pause(.001)
382         %fprintf(s, 'M999');
383         %pause(0.001)
384         fprintf(s,tosend2);
385
386         % May need pause to ensure sufficient time
387         % elapses for printer head movement time
388         if NeedPause
389             pause(dur(i)*0.95+0.001) %#ok<*UNRCH>
390             residuedur = residuedur+0.05*dur(i);
391         end
392     end
393 end %Loop over steps
394 end %Loop over print iterations
395 pause(residuedur+.02) %% finish up
396
397 %% Closing Link to Printer
398 fclose(s);
399 delete(s);
400 clear s;
401 end %if running printer
402
403 disp('Code Executed Without Errors')
```

GCodeParser.m

```

1 %% GCodeParser Reads X and Y locations from a GCode file
2 % [X,Y]=GCodeParser(filename) outputs X and Y locations
3 % from a GCode written by the slicer program from Staack's
4 % 3D printer. This may not work with other GCodes
```

```

5 %
6 % [X,Y,Z]=GCodeParser(filename) outputs X, Y, and Z
7 % locations from a GCode. This may yield different results
8 % from above, since it uses a different method for parsing
9 % the GCode file. X, Y, and Z will all be vectors of the
10 % same length. Any time a value is missing the previous
11 % value is assumed (starting with a value of 0 if not
12 % initially specified in the GCode).
13 %
14 % [X,Y]=GCodeParser(filename,'NotLegacy') outputs X and Y
15 % locations from a GCode using the newer GCode parsing
16 % method, which may yield different results from the old
17 % method.
18 %
19 % [X,Y,Z,PreVal1,PreVal2,...]=GCodeParser(___, 'Prefix', ...
20 %     {'pre1','pre2',...})
21 % outputs X, Y, and Z locations from a GCode along with the
22 % specified prefix's values (not strings!). Desired
23 % prefixes must be specified as a cell string array, which
24 % will yield as many outputs as prefixes. For example, the
25 % prefix 'F' can be used to see the feed (speed) rate and
26 % 'E' will yield the extrusion amount/rate. The value is
27 % assumed to come immediately after the prefix string (no
28 % spaces).
29 %
30 % [...] = GCodeParser(___, 'plot') also plots the GCode. The
31 % plot will either be a 2D or 3D line plot depending on
32 % whether Z was written.
33 %
34 % [...] = GCodeParser(___, 'Waitbar') adds a waitbar for files
35 % read in using the newer (non-legacy) method. This can
36 % substantially slow down the code with the waitbar's
37 % overhead, but closing the waitbar will let it get back to
38 % "full" speed (the waitbar will not open again)
39
40 % Author: Matthew Burnette
41 % Version: 2.1.1 (bug fix on waitbar)
42 % 2.1 (better error handling and bug fix)
43 % 2.0 (More general GCode parser)
44 % Last Updated: 2/13/2020 at 8:51PM
45
46 function [varargout]=GCodeParser(varargin)
47 %% Parse Inputs and Open File
48 if nargin<1 || ~ischar(varargin{1})
49     error('StaackLab:GCodeParser:ReadFile',...

```

```

50         'First input must be a file path')
51 end
52 filename=varargin{1};
53 fID=fopen(filename);
54 if fID<3
55     warning('StaackLab:GCodeParser:ReadFile',...
56         'Cannot find file')
57     return
58 end
59 PlotIt=false;
60 Legacy=true;
61 Prefix={};
62 Waitbar=false;
63 w=[];
64 i=2;
65 while i<=nargin
66     if ~ischar(varargin{i})
67         warning('StaackLab:GCodeParser:Input',...
68             'Invalid input!\nIgnoring input')
69     end
70     switch lower(varargin{i})
71     case 'notlegacy'
72         Legacy=false;
73     case 'prefix'
74         if i==nargin || ~iscellstr(varargin{i+1})
75             warning('StaackLab:GCodeParser:Prefix',...
76                 ['Invalid "Prefix" Input!\n',...
77                 'Ignoring input'])
78         else
79             Prefix=varargin{i+1};
80             i=i+1; %Extra one for Prefix input
81         end
82     case 'plot'
83         PlotIt=true;
84     case 'waitbar'
85         Waitbar=true;
86     otherwise
87         warning('StaackLab:GCodeParser:Input',...
88             'Invalid input!\nIgnoring input')
89     end
90     i=i+1; %Iterate on input index
91 end
92 if nargout~=2
93     Legacy=false;
94 end

```



```

95  if Waitbar
96      w=waitbar(0,'Preparing to parse the GCode');
97      %pause(0.5) %Assume the code will take long enough to run
98      %anyway, so no need to pause
99  end
100
101  %% Choose Parsing Method
102  try
103      if Legacy
104          [X,Y]=LegacyCode(fID,filename);
105          CellOutput={X,Y};
106      else
107          CellOutput=ParseGCode(fID,Prefix,Waitbar,w);
108      end
109      fclose(fID); %Close the file
110  catch ME
111      fclose(fID); %Program broke but close the file anyway
112      rethrow(ME)
113  end
114
115  %% Write Outputs
116  if Waitbar && ishandle(w)
117      waitbar(1,w,'Finished Parsing, now making outputs')
118      pause(.2)
119  end
120  X=[]; Y=[]; Z=[];
121  EnoughOutputs=true;
122  NumOut=nargout;
123  if nargout<2 && ~PlotIt %May just plot it, which is fine
124      warning('StaackLab:GCodeParser:Output',...
125          'Not Enough Outputs!\nOutputting X and Y anyway!')
126      EnoughOutputs=false;
127      NumOut=2;
128  end
129  for out=1:length(CellOutput)
130      switch out
131          case 1
132              X=CellOutput{1};
133              if NumOut>=1 %Warning already taken care of above
134                  varargout{1}=X;
135              end
136          case 2
137              Y=CellOutput{2};
138              if NumOut>=2 %Warning already taken care of above
139                  varargout{2}=Y;

```

```

140         end
141     case 3
142         Z=CellOutput{3};
143         if NumOut<3 || ~EnoughOutputs
144             if ~PlotIt %May just plot, which is fine
145                 warning(['StaackLab:GCodeParser:',...
146                     'Output'], ['Not Enough Outputs!'],...
147                     '\nNot outputting anything more ',...
148                     'outputs!'])
149                 EnoughOutputs=false;
150             end
151         else
152             varargout{3}=Z;
153         end
154     otherwise
155         if ~EnoughOutputs
156             warning('StaackLab:GCodeParser:Output',...
157                 ['Not Enough Outputs!\nNot ',...
158                 'outputting anything more outputs!'])
159             EnoughOutputs=false;
160         else
161             varargout{out}=CellOutput{out};
162         end
163     end
164 end
165
166 %% Plot if Desired
167 if PlotIt
168     if Waitbar && ishandle(w)
169         waitbar(1,w,'... and now plotting')
170         pause(.2)
171     end
172     figure %Ensure it's in a new figure
173     if isempty(Z)
174         plot(X,Y)
175     else
176         plot3(X,Y,Z)
177         zlabel('Z')
178     end
179     xlabel('X')
180     ylabel('Y')
181     axis equal %square
182 end
183 if Waitbar && ishandle(w)
184     waitbar(1,w,'Done!')

```

```

185     pause(.05)
186     delete(w)
187 end
188
189 %% Local Functions
190 function [X,Y]=LegacyCode(fID,filename)
191 %Keep for backwards compatibility with old codes...
192 LineToFind='G1 Z';
193 %Blocks of X Y locations are broken up by a Z motion line
194 text=fileread(filename);
195 newlines=strfind(text,sprintf('\n')); %#ok<SPRINTFN>
196 ZMoveLine=strfind(text,LineToFind);
197 T=cell(1);
198 T{1}=textscan(fID,'G1 X%7.3f Y%7.3f %*[\n]',...
199     'HeaderLines',24);
200 X=T{1}{1};Y=T{1}{1};
201 for n=2:length(ZMoveLine)
202     LineNumber=find(newlines>ZMoveLine(2),1,'first');
203     T{n}=textscan(fID,'G1 X%7.3f Y%7.3f %*[\n]',...
204         'HeaderLines',LineNumber);
205     X=[X;T{n}{1}]; %#ok<*AGROW>
206     Y=[Y;T{n}{2}];
207 end
208
209 function CellOutput=ParseGCode(fID,Prefix,Waitbar,w)
210 if Waitbar
211     % Loop first to get number of lines in file for waitbar
212     TotalLines=0;
213     fgetl(fID);
214     %This avoids off by 1 errors, since fgetl must first
215     %start reading to get line nums
216     while ~feof(fID)
217         fgetl(fID);
218         TotalLines=TotalLines+1;
219     end
220     frewind(fID) %Rewind file for reading the data
221     if ishandle(w) %In case it's closed...
222         str=sprintf('Parsing the GCode (%d lines)',...
223             TotalLines);
224         waitbar(0,w,str)
225     end
226 end
227 X=[]; Y=[]; Z=[];
228 pN=length(Prefix);
229 Pre=cell(1,pN);

```

```

230 Changed=false(1,pN+3);
231 LineNum=0;
232 FileLineNum=1;
233 while ~feof(fID)
234     line=fgetl(fID);
235     % Look for "G1 Xx" and get "x" as a floating point value
236     TagData=regexp(line,'G1.*X([-+]?[0-9]*\.[0-9]*)',...
237         'tokens');
238     if ~isempty(TagData)
239         val=str2double(TagData{1}{1});
240         if ~isnan(val)
241             X(LineNum+1)=val;
242             Changed(1)=true;
243         end
244     end
245     % Look for "G1 Yx" and get "x" as a floating point value
246     TagData=regexp(line,'G1.*Y([-+]?[0-9]*\.[0-9]*)',...
247         'tokens');
248     if ~isempty(TagData)
249         val=str2double(TagData{1}{1});
250         if ~isnan(val)
251             Y(LineNum+1)=val;
252             Changed(2)=true;
253         end
254     end
255     % Look for "G1 Zx" and get "x" as a floating point value
256     TagData=regexp(line,'G1.*Z([-+]?[0-9]*\.[0-9]*)',...
257         'tokens');
258     if ~isempty(TagData)
259         val=str2double(TagData{1}{1});
260         if ~isnan(val)
261             Z(LineNum+1)=val;
262             Changed(3)=true;
263         end
264     end
265     for p=1:pN
266         % Look for "PREx" and get "x" as floating point value
267         str=sprintf('%s%s',Prefix{p},...
268             '([-+]?[0-9]*\.[0-9]*)');
269         TagData=regexp(line,str,'tokens');
270         if ~isempty(TagData)
271             val=str2double(TagData{1}{1});
272             if ~isnan(val)
273                 Pre{p}(LineNum+1)=val;
274                 Changed(3+p)=true;

```

```

275         end
276     end
277 end
278 % Write previous value for any missing ones
279 if any(Changed)
280     if ~all(Changed)
281         for c=1:3+pN
282             if ~Changed(c)
283                 switch c
284                     case 1 %X
285                         if isempty(X)
286                             X=0;
287                         else
288                             X(LineNum+1)=X(LineNum);
289                         end
290                     case 2 %Y
291                         if isempty(Y)
292                             Y=0;
293                         else
294                             Y(LineNum+1)=Y(LineNum);
295                         end
296                     case 3 %Z
297                         if isempty(Z)
298                             Z=0;
299                         else
300                             Z(LineNum+1)=Z(LineNum);
301                         end
302                     otherwise
303                         if isempty(Pre{c-3})
304                             Pre{c-3}=0;
305                         else
306                             Pre{c-3}(LineNum+1)=...
307                                 Pre{c-3}(LineNum);
308                         end
309                 end
310             end
311         end
312     end
313     LineNum=LineNum+1; %A change so increment LineNum
314 end
315 FileLineNum=FileLineNum+1;
316 Changed=false(1,pN+3); %Reset to find next useful line
317 if Waitbar && ishandle(w) %In case it's closed...
318     waitbar(FileLineNum/TotalLines,w)
319 end

```

```
320 end
321 CellOutput=[{X,Y,Z},Pre];
```